

ISBN: 978-93-92403-94-1

BOOK OF ABSTRACTS
AND
TECHNICAL PROGRAM

*The 9th International Conference on
Theoretical Applied Computational
and Experimental Mechanics
(ICTACEM 2025)*

Organised by
*Aerospace Engineering Department
Indian Institute of Technology Kharagpur*



**TECHNICAL PROGRAM
AND
BOOK OF ABSTRACTS**

*The 9th International Conference on
Theoretical Applied Computational and Experimental Mechanics
(ICTACEM 2025)*

Conference Organizer and host institution
Aerospace Engineering Department, Indian Institute of Technology Kharagpur, India

EDITORS:

Prof. Naba Kumar Peyada

Prof. Prasun Jana

Prof. Ratan Joarder

Prof. Sunil Manohar Dash

ASSOCIATED EDITORS:

Prof. Akshay Prakash

Prof. Anup Ghosh,

Prof. Amardip Ghosh

Prof. Arnab Roy

Prof. Bhrgu Nath Singh

Prof. Chetankumar Sureshbhai Mistry

Prof. Dipak Kumar Maiti

Prof. Kalyan Prasad Sinhamahapatra

Prof. Manoranjan Sinha

Prof. Mira Mitra

Prof. Mohammed Rabius Sunny

Prof. Mrinal Kaushik

Prof. Sandeep Saha

Prof. Sikha Hota

Prof. Somnath Ghosh

Prof. Srinibas Karmakar

Prof. Suresh Chandra Pradhan

Prof. Susmita Bhattacharyya

First Impression: 2025

© Abstracts of Authors 2025

© IIT Kharagpur

© Typography Vidya Kutir Publications

No part of this publication may be reproduced or transmitted in any form by any means, electronic or mechanical, including photocopy, recording, or any information storage and retrieval system, without permission in writing from the copyright owners.

DISCLAIMER

Authors are solely responsible for the views, opinions, correctness, authenticity, and permissions required for the chapter. Editors or Publisher has no responsibility on behalf of the authors in whatsoever manners.

ISBN: 978-93-92403-94-1

FOREWORD

The Department of Aerospace Engineering, IIT Kharagpur, would be hosting the 9th International Conference on Theoretical, Applied, Computational and Experimental Mechanics, ICTACEM 2025, during 15-17 December 2025. The ICTACEM conference has been held every three years since 1998, and the Department of Aerospace Engineering, IIT Kharagpur, takes pride in hosting it once again this year. Ten plenary and invited talks by distinguished researchers and industry leaders, as well as more than one hundred and ten excellent contributory papers from India and abroad, will be presented at the conference. ICTACEM was conceived by its founder, Late Prof. P. K. Sinha, to bring together researchers from all disciplines of Mechanics to exchange, share and enrich their knowledge, with a special focus on recent advances in Aerospace science and technology. It is very encouraging to find a very active participation of a large number of young researchers at ICTACEM 2025, who hold the promise of taking this vision forward in the future.

The contributions of authors and speakers helped materialize the conference. Countless hours of hard work from conveners and sub-committee members, scholars, and staff members enabled conference preparation and execution. During the entire process, the support received from IIT Kharagpur authorities was invaluable. The financial support received from the conference sponsors imparted confidence. Mr. Deepak Kumar Singh, a third-year undergraduate student of the department, played a pivotal role in developing the website that was used for author registration, submission, and review of abstracts and full-length papers, and managing various other associated processes. Shri. Rana Nandi, Lab in Charge, AE Computer Lab, provided dedicated technical support throughout the conference preparation. Sincere gratitude goes out to one and all who contributed towards organizing this conference.

Finally, and most importantly, let the three days of intense technical deliberations during ICTACEM 2025 enrich the participants profusely and motivate them to explore the ever-receding horizons of mechanics.

TECHNICAL PROGRAM

Schedule of ICTACEM-2025, 15-17 Dec, 2025 at IIT Kharagpur

| 15 December | Venue | Vikramshila Foyer | | Duration |
|-------------|---|--|---|----------|
| | 8:00 | Registration | | |
| Venue | Kalidas Auditorium | | | |
| | <u>Inauguration Of The Conference --</u> <u>ICTACEM 2025</u> | | | |
| 9:00 | Welcome Address By Convenor | | | 0:05 |
| 09:05 | Address By Director, IIT Kharagpur | | | 0:15 |
| 9:20 | Address By Chief Guest : Prof. Joseph Mathew | | | 0:15 |
| 09:35 | Inaugural Talk : Turbulent Jets Prof. Joseph Mathew, Department of Aerospace Engineering, Indian Institute of Science | | | 0:45 |
| 10:20 | Session Chair: Prof. Kalyan Prasad Sinhamahapatra Inaugural Talk : Digital Technologies in Aerospace Dr. Kallappa Pattada, Executive Director — Boeing Technology & Innovation and Chief Engineer — Boeing Defense India Session Chair: Prof. Kalyan Prasad Sinhamahapatra | | | 0:45 |
| 11:05 | Tea Break | | | 0:25 |
| Venue | Gargi Auditorium (A1) | Maitrayee Auditorium (S1) | Kalidas Auditorium (C1) | |
| Session | Aerodynamics and Fluid Mechanics | Solid Mechanics and Dynamics | Flight Mechanics, Control and Navigation | |
| | Session Chair Prof. Somnath Ghosh | Session Chair Prof. D K Maiti | Session Chair Prof. Alok Kanti Deb | |
| 11:30 | A Scalar LPCE–ALE Framework for Sound Generation in Low-Mach Flows with Moving Boundaries : ICTACEM2025P813 | 2D Multiphysics Modeling Framework for Laser Ablation of Al2O3 Ceramic Coating : ICTACEM2025P987 | A Lyapunov Guidance Vector Field with Variable Guidance Gain for Elliptical Path Following : ICTACEM2025P880 | 0:15 |
| 11:45 | Kevin S. Swamy; Vaibhav Joshi | Nazim Khan; Abinesh K; Rajdip Mukherji; Somnath Bhownick; Pritam Chakraborty | Ishan Phanse ; Sayantan Pal ; Sikha Hota | |
| | Buckling load parameter analysis of Rectangular plate with Full and partial stiffeners under Uniaxial and Biaxial loading conditions : ICTACEM2025P709 | A Cohesive Zone Modelling approach for Fatigue Crack Growth and Life Prediction in Adhesively Bonded Joints: ICTACEM2025P601 | Altitude Control of Powered Parafoil Systems using Extended State Observer-Finite-time Sliding Mode Control (ESO-FTSMC) : ICTACEM2025P027 | 0:15 |
| | prabhash kumar yadav ; Dr. AKL Srivastava | Pradeep Kumar Sahoo; Mopidevi Naga Saradvani; Shrimukhi G Shastry | Nitin Pal ; Naba Kumar Peyada | |

| | | | | | | | | | |
|---------------------------|-------|---|---|---|------|--|--|--|--|
| 15 December | 12:00 | CFD Investigation of Transonic Bucket phenomena for Typical Grid Fin used on Re-Entry Stage Configuration : ICTACEM2025P856 | A comparative investigation of electromechanical vibration suppression in imperfect curved fiber laminates and straight fiber laminates with integrated piezoelectric layers: ICTACEM2025P031 | Comparative Analysis of Obstacle Avoidance Path Planning Algorithms for Robotic Manipulators: RRT, APF, and CHOMP : ICTACEM2025P898 | 0:15 | | | | |
| | | Anubhab Das ; Kunal Garg ; Amit Sachdeva ; Ankur Nagpal | Vanshika Anand; Ansh Kapoor; Narayan Sharma; Pawan Kumar; Prasant Kumar Swain | Adeetya Uppal ; Rakesh Kumar Sahoo ; Manoranjan Sinha | 0:15 | | | | |
| | | Computation of heat flux over Winged Reusable Launch Vehicle – Technology Demonstrator and comparison with flight data : ICTACEM2025P015 | A Meshfree Numerical Solver for a Fractional Calculus Approach to Continuum Damage Mechanics: ICTACEM2025P304 | Curvature-Constrained UAV Path Following Using Finite-Time Sliding Mode Control : ICTACEM2025P056 | 0:15 | | | | |
| | | Sundeep Kumar Epuri ; Jiju R Justus ; Vidya G ; Manokaran K | Malapeta Hemasundara rao; M Ramji; sai sidhardh | Panasa Pranav Kumar ; Sayantan Pal ; Sikha Hota | 0:15 | | | | |
| | | Design of Vent system for crew escape system-test vehicle compartments : ICTACEM2025P219 | A Reduced-order Homogenized Plate Model of Sandwich Structure Using Variational Asymptotic Method: ICTACEM2025P493 | Guidance Law for Surveillance by UAVs Using Curve Paths : ICTACEM2025P537 | 0:15 | | | | |
| | | VenkatshivaramJadav B ; Jathaveda.M ; G.Vidya | Anup Kumar Pathak; Pritam Chakraborty | Gururaj Khurd ; Parth Madure | 0:15 | | | | |
| | | Development and Validation of a Python-Based Preliminary Design Tool for Ramjet Engines : ICTACEM2025P683 | Analytical Investigation for Free Vibrations Analysis of Functionally Graded Sandwich Plates with Advanced Gradation Laws: ICTACEM2025P939 | Lame Curve Following by UAVs using Vector Field Guidance : ICTACEM2025P744 | 0:15 | | | | |
| | | Atharva Mangalkar ; Thivya Ranee ; Akshay Abhyankar | Ankitha Kamath; Supen Kumar Sah; Anup Ghosh | Hemant V Nair ; Sayantan Pal ; Sikha Hota | 0:15 | | | | |
| 13:00 | | LUNCH BREAK | | | 1:00 | | | | |
| Venue | | | | | | | | | |
| Kalidas Auditorium | | | | | | | | | |
| Venue | 14:00 | Plenary Session -1: Vertical takeoff of aircrafts: Some new possibilities Prof. P. A. Ramakrishna, Department of Aerospace Engineering, IIT Madras | | | 0:45 | | | | |
| | | Session Chair: Prof. Amardip Ghosh | | | | | | | |
| | | Plenary Session -2 : Wave Technologies in SHM of Built Facilities - Theory, Experiments and Practice Prof. Abhijit Mukherjee, School of Civil and Mechanical Engineering, Curtin University, Australia | | | | | | | |
| | | Session Chair: Prof. P K Datta | | | | | | | |
| Venue | | Maitrayee Auditorium (P1) | Kalidas Auditorium (S2) | Kalidas Auditorium (S3) | | | | | |

| Session | Propulsion | Solid Mechanics and Dynamics | Solid Mechanics and Dynamics | |
|----------------------------------|--|---|---|------|
| | Session Chair Prof. Srinibas Karmakar | Session Chair Prof. Vikranth Racherla | Session Chair: Prof. Kiran Vijayan | |
| 15:30 | Bluff Body Induced Regression Rate Enhancement in Hybrid Motor : ICTACEM2025P797 | The assessment to study the free vibration of edge cracked bi-directional SFGM plate with modified inverse hyperbolic shear deformation theory (m-IHSDT): ICTACEM2025P284 | Axially-Loaded Column under Earthquake Loading : ICTACEM2025P664 | 0:15 |
| | Ankush Vilas Khnadare ; Aditya Sanjay Patil ; Jogi Binit Patel ; Sachin Chandrakant Sonage ; Nagendra Kumar ; Narendra Deore | Rahul Sudam Kamble; Achchhe Lal; Bhrigu Nath Singh | Mahendra Gattu | |
| 15:45 | Correlation of Tulip Flame Formation and CH Chemiluminescence Bursts in Confined Propane-Air Combustion : ICTACEM2025P329 | ANN-based prediction of the deflection and free vibration characteristics of functionally graded plates for various boundary conditions: ICTACEM2025P996 | Comparative Ballistic Impact Simulation of NiTi SMA-Reinforced and Conventional GFRP Composites : ICTACEM2025P571 | 0:15 |
| | Abhishek kumar : Ratan Joarder | Dabeer Anwer Danish; Sukanta Chakraborty | Sibaram Patro ; Prof. Chandra Sekher Yerramalli ; Prof. Krishnendu Haldar | |
| 16:00 Tea Break | | | | 0:15 |
| Venue | Gargi Auditorium (A2) | Maitrayee Auditorium (S4) | Kalidas Auditorium (C2) | |
| Session | Aerodynamics and Fluid Mechanics | Solid Mechanics and Dynamics | Flight Mechanics, Control and Navigation | |
| Session Chair Prof. Chandan Bose | | Session Chair: Dr. Ganesh Soni | Session Chair Prof. Suman Maiti | |
| 16:15 | Direct Simulation Monte Carlo Study of Thruster Plume Impingement on Planetary Surface : ICTACEM2025P067 | Comparative bending response of imperfect variable-angle tow and straight fiber laminates with integrated PZT layers: ICTACEM2025P016 | Mobile Anti-Drone System: A SDR Approach for Defensive Disruption of UAVs : ICTACEM2025P630 | 0:15 |
| | Malakannan G ; Suman Chakraborty | Ansh Kapoor; Vanshika Anand; Narayan Sharma; Pawan Kumar; Rakesha Chandra Dash | Ajit Kumar ; Namra Patel ; Jagat Rath | |
| 16:30 | Effect of Flight velocity on Mean Flow of an Ideally Expanded Supersonic Jet – a CFD study : ICTACEM2025P990 | Deflection Characteristics of Piezoelectric Composite Plates under UDL and SSL Using Refined Second Shear Deformation Theory: ICTACEM2025P690 | Model-Less Feedback Control of Space-based Continuum Manipulators using Backbone Tension Optimization : ICTACEM2025P254 | 0:15 |

15 December

| | | | | |
|-------|--|--|--|------|
| | Sanjoy Kumar Saha ; Manoj T Nair | Raju Sidhu Pawar; Achchhe Lal | Shrreya Rajneesh ; Nikita Pavle ; Rakesh Sahoo ; Manoranjan Sinha | |
| 16:45 | On the Dynamic Mode Decomposition of Supersonic Cavity Flow : ICTACEM2025P439 | Deformation Behavior of Soft Electroelastic Membranes Subjected to Large Electric Fields: ICTACEM2025P886 | Wind-Aware Dubins-Inspired L1 Guidance for Faster Convergence with Bounded Continuous Curvature and Sliding Mode Tracking for UAVs : ICTACEM2025P678 | 0:15 |
| 17:00 | Satya Prakash ; Ram Kumar Yadav ; Avijit Chatterjee ; Aniruddha Sinha | Yadwinder Singh Joshan; Sushma Santapuri; Debashish Khan | Pradyumn Mahajan ; Sayantan Pal ; Sikha Hota | |
| 17:15 | Effect of Pivot Point Location on the Propulsive Performance of Rear Airfoil in Tandem Configuration : ICTACEM2025P440 | Design and Development of a Hybrid Model for Impact Analysis on Underwater Vehicles: ICTACEM2025P600 | Obstacle Avoidance of UAV in Dynamic Environments Using Direction and Velocity-Adaptive Artificial Potential Field : ICTACEM2025P943 | 0:15 |
| | Adeetya Uppal ; Rahul Ranjan ; Sunil Manohar Dash | Pankaj Meena; Rajiv Sharma | Nikita Vaibhav Pavle ; Shrreya Rajneesh ; Rakesh Kumar Sahoo ; Manoranjan Sinha | |
| | Effect of ply-orientation angle on flutter behaviour of laminated composite plates : ICTACEM2025P264 | Reliability analysis of uncertain vibration response in bidirectional sandwich structures using a direct probability integral approach : ICTACEM2025P735 | Parameter Estimation of BLDC Motor Using Nonlinear Least Square Method : ICTACEM2025P974 | 0:15 |
| | Shashank K S ; Subrata Barman ; Rajeev Nayan Gupta ; Saikat Ranjan Maity ; Dipak Kumar Maiti ; Sudip Dey | Narayan Sharma ; Pawan Kumar ; Prateek Chandrakar ; Dipak Kumar Maiti | Rajib Mandi ; N.K. Peyada | |
| 17:30 | Tea Break | | | 0:20 |
| 17:50 | Panel Discussion on : Opportunities and Challenges of AI implementation in Aerospace | | | |
| 18:50 | | | | 1:00 |

| | | | |
|---------|----------------------------------|--|--|
| # | Venue | Vikramshila Foyer | |
| | 8:00 | BREAKFAST | |
| | Venue | Kalidas Auditorium | |
| | 09:00 | Plenary Session -3: SPC-I and DPSM – two new developments in the field of NDE and SHM Prof. Tribikram Kundu, Department of Civil and Architectural Engineering and Mechanics, University of Arizona, USA Session Chair: Prof. Arghya Deb | 0:45 |
| | 9:45 | Hijli Detention camp to IIT-An Untold Saga | 0:45 |
| Venue | Gargi Auditorium (A3) | Maitrayee Auditorium (S5) | Kalidas Auditorium (C3) |
| Session | Aerodynamics and Fluid Mechanics | Solid Mechanics and Dynamics | Flight Mechanics, Control and Navigation |

| | Session Chair Prof. S M Dash | Session Chair Prof. Vikranth Racherla | Session Chair Prof. Sourav Patra | |
|------------------------|--|---|--|------|
| 16 December | Empirical expression to predict the first-mode resonant frequency of a pitching flexible panel : ICTACEM2025P467 | Effect of Localized Elastic Supports Representing Ribs and Mounts on the Flutter Behavior of Tailored Composite Panels: ICTACEM2025P427 | Real-Time Obstacle Avoidance for Waypoint Following of UAVs : ICTACEM2025P146 | 0:15 |
| | Abhinav Kumar KSN ; Parag Deshpande ; Ravi Dodamani | Abdul Sadiq; Aayush Gupta; Dipak Kumar Maiti | Heavenly Dadala ; Sayantan Pal ; Sikha Hota | |
| | Estimation of Flight Measured Pressure using CFD for a Typical Launch Vehicle : ICTACEM2025P287 | Effects of random orientation of bluff body on the onset speed of galloping-based piezoelectric energy harvester: ICTACEM2025P101 | Real-Time Tiny Object Detection and Tracking for High-Altitude UAVs Using Customized YOLO Architectures : ICTACEM2025P536 | 0:15 |
| | Sreenivasulu Juluri ; Sanjoy Kumar Saha ; Vidya G | Rakesha Chandra Dash | Vishnubhatla Aditya Shankar ; Devshree Kumar | |
| | Feature-Alignment Model Order Reduction (FAMOR) for Nonlinear Convective and Shock-Dominated Flows : ICTACEM2025P358 | Evaluation of anisotropy via non-destructive indentation in LPBF processed Co-Cr-Mo alloy: The role of scanning strategy: ICTACEM2025P892 | Moving Target Interception using Variable L1 guidance : ICTACEM2025P519 | 0:15 |
| | Aritro Ghosh ; Aniruddha Sinha ;Sanjay R. | Vinod Kumar Jat; R. U. Patil | Machavolu Venkata Sushanth ; Sayantan Pal ; Sikha Hota | |
| 11:15 Tea Break | | | | |
| Venue | Gargi Auditorium (A4) | Maitrayee Auditorium (S6) | Kalidas Auditorium (B1) | 0:15 |
| Session | Aerodynamics and Fluid Mechanics | Solid Mechanics and Dynamics | Bio-Inspired FSI | |
| | Session Chair Prof. K P Sinhamahapatra | Session Chair Prof. P K Datta | Session Chair: Prof. Sandeep Saha | |
| 16 December | Harnessing wind energy within the conduit-style tall building through the use of wind turbines : ICTACEM2025P104 | AI in Finite Element Analysis | Analysis of Temporal Oscillations of a Deflected Wake in a Plunging Foil Using Proper Orthogonal Decomposition : ICTACEM2025P007 | 0:15 |
| | Amlan Kumar Bairagi | Ganesh Soni | Mohamed Aniffa S : Sunetra Sarkar | |
| | Impact of Preheated Central Jet on Intermixing of Confined Multi-Annular Swirling Jets : ICTACEM2025P035 | | Flow-Induced Vibrations of a Circular Cylinder and an Upstream D-Cylinder of various Elliptical Ratios : ICTACEM2025P036 | 0:15 |
| | Ritesh Srivastava ; Vivek Kumar Patel | | Sachin S B ; Atul Sharma | |

| | | | | | | | | | |
|-------------|---|---|--|---|------|--|--|--|--|
| 16 December | 12:00 | Integrating CFD, Experiments, and Bayesian Inference for Aerodynamic Analysis of Serrated Delta Wings : ICTACEM2025P832 | Experimental Analysis of the Magneto-Viscous Responses of Magneto-Active Polymers: ICTACEM2025P419 | Response Dynamics of Bio-Inspired Morphing Aerofoils : ICTACEM2025P505 | 0:15 | | | | |
| | 12:15 | Sarat Kumar Maharana ; Anand M Raikar ; N. Chikkanna | Rahul Kumar Saini | Chandan Bose ; Hibah Saddal ; Lucky Jayswal | 0:15 | | | | |
| | 12:15 | Model Order Reduction for Cerebrovascular Hemodynamics: A POD-Galerkin and Hybrid Physics-Informed Approach : ICTACEM2025P717 | Experimental Fabrication and Characterization of E-Glass/Epoxy Composites Using Vacuum-Assisted Resin Infusion: ICTACEM2025P609 | Scaling laws for thrust generated from pitching foils : ICTACEM2025P492 | 0:15 | | | | |
| | 12:30 | Rahul Halder ; Arash Hajisarifi ; Kabir Bakhshaei ; Gianluigi Rozza | UMAKANTA MEHER; MOHAMMED RABIUS SUNNY; Praveen Shakya; Iqbal Ahmed | Mahesh K Sawardekar ; Ratnesh K Shukla | | | | | |
| | 12:30 | Numerical Analysis of Shockwave Boundary Layer Interaction : ICTACEM2025P616 | Experimental Static and Fatigue Damage Assessment of Adhesively Bonded CFRP Joints Under Mode II Loading Using AE Technique: ICTACEM2025P138 | Wake Modifications arising from a Bio-inspired Flexible Filament placed on NACA0012 Airfoil : ICTACEM2025P643 | 0:15 | | | | |
| | 12:45 | Prahlad V Deshpande ; Suraj J Warang ; Dhruv Bagora ; Pardeep Duneria | Bandaru Bangarraju; Sai Sidhardh; M Ramji | Thangavel Sudeep ; Sachin Yashavant Shinde | | | | | |
| | 12:45 | Numerical Investigation of a Novel Aerospike–Aero disk–Bleed Channel Configuration for Drag and Thermal Load Reduction in Hypersonic Vehicles : ICTACEM2025P518 | FE Modeling of Single Foam-filled Reentrant Unit Cell to Evaluate Deformation Mechanics and Energy Absorption: ICTACEM2025P165 | Wave Propagation Mechanisms for Enhanced Jet Impulse in Squid-Inspired Flexible Nozzles : ICTACEM2025P096 | 0:15 | | | | |
| | 13:00 | Sanjay Satish ; Vijay Suresh ; Aswathy K. S. ; A. Abhijith ; Antony J. K. ; Manoj Kumar M. | Viswasarathi N M; Bibhu Prasad Mahapatra; Prasun Jana | Paras Singh ; Daehyun Choi ; Halley Wallace ; Gourav Samal ; Saad Bhamla | | | | | |
| | LUNCH BREAK | | | | | | | | |
| | Venue | Kalidas Auditorium | | | | | | | |
| 14:00 | Plenary Session -4: Role of Real Fluid Behaviour & Multi-Physics Optimisation in Sustainable Energy System Prof. Jayanta Kapat, Department of Mechanical & Aerospace Engineering, University of Central Florida, USA Session Chair: Prof. C S Mistry | | | | | | | | |
| | Plenary Session -5: Designing Heavy Payload Unmanned Aerial Systems: The Helicopter Way Prof. Abhishek, Department of Aerospace Engineering, IIT Kanpur Session Chair: Prof. Sikha Hota | | | | | | | | |
| | Venue | Gargi Auditorium (A5) | | | | | | | |
| Session | Aerodynamics and Fluid Mechanics | Maitrayee Auditorium (S7) | | | | | | | |
| | Solid Mechanics and Dynamics | | | | | | | | |

| | | Session Chair: Prof. Akshay Prakash | Session Chair: Prof. M R Sunny | |
|-------------|----------------------------------|---|--|--|
| 16 December | 15:30 | Numerical Investigation of an Archimedean Spiral Wind Turbine Using Dynamic Mesh CFD in ANSYS Fluent : ICTACEM2025P217 | Finite Element Simulation of Magnetocaloric Effect in Gadolinium: ICTACEM2025P187 | 0:15 |
| | | Shivendraraj Godbole ; Krishnendu Haldar | Busi Swathi priya | |
| | 15:45 | NUMERICAL INVESTIGATION OF LOW-FREQUENCY OSCILLATIONS IN SEPARATED SHEAR FLOWS ; ICTACEM2025P194 | Flexural and ILSS Performance of GFRP Composites under Extreme Temperature Conditions: ICTACEM2025P970 | 0:15 |
| | | Digpriya; Rajesh Ranjan ; Pradeep Moise | Supal Tudu; Velmurugan Ramachandran | |
| 16:00 | | Tea Break Maitrayee Auditorium (S8) | | |
| Venue | Gargi Auditorium (A6) | | | Lecture Hall V1 (S9) |
| Session | Aerodynamics and Fluid Mechanics | Solid Mechanics and Dynamics | Solid Mechanics and Dynamics | |
| | | Session Chair: Dr. Parag Deshpande | Session Chair: Prof. P K Datta | Session Chair: Prof. Korak Sarkar |
| 16 December | 16:15 | Numerical Investigation on the Effect of Acoustic Cavity Geometry, Angle of Attack, and Injectant Molecular Weight for Drag and Heat Flux Reduction over a Blunt Body : ICTACEM2025P074 | Free Vibration Analysis of Cranked Sandwich Plates with CSCL Facesheets and Honeycomb Core Comparison: ICTACEM2025P654 | Machine Learning based approach to predict the life of damaged wind turbine blade : ICTACEM2025P622 |
| | | Sanjay Satish ; Arun B. S. ; Ashik Muhammad ; Manoj Kumar M. ; Antony J. K. | Gajavada Sanjeevkumar; Pritam Mondal; Jayant Prakash Varun; Prashanta kr Mahato | Praveen Shakya ; Umakant Meher : Sachin Kumar ; Danial Arias ; Abdennour C. Seibi ; Mohammad A. S. Masoum |
| | 16:30 | Numerical Prediction of Interaction Between Two Flying Robotic Butterflies : ICTACEM2025P288 | Investigation of Delamination Progression in Unidirectional Composite Laminates: ICTACEM2025P309 | Magneto-Stiffening Effects on Beam Vibrations Supported by Winkler Foundation : ICTACEM2025P296 |
| | | Aman Shukla ; Debajyoti Kumar ; Chandan Bose; Somnath Roy | Subhabrata Koley | Lakshita Patil |
| 16:45 | | Numerical Study on Drag Reduction of Various Bluff-body Geometries using the Passive Rotation of a NACA0012 Aerofoil : ICTACEM2025P055 | Investigation of Flexural Behavior of Functionally Graded Plates through Higher-Order Shear Formulation: ICTACEM2025P045 | Micromechanical Homogenization and Electromagnetic Characterization of Radar Absorbing Materials using Multiphysics Simulation : ICTACEM2025P595 |

| | | | | |
|-------|---|---|---|------|
| | Bibhas Chand ; Prabir Sikdar ; M S Harihara Sudhan ; Sunil Manohar Dash | Smruti Ranjan sahoo; Surendra Verma; Bhrigu Nath Singh | Omkar Bilawar ; Krishnendu Haldar | |
| 17:00 | Effect of Mach number on a Compressible Impinging Round Jet: An LES study : ICTACEM2025P072 | Investigation of transonic buffet loads on aeroelastic launch vehicle model using coupled CSD-CFD approach: ICTACEM2025P273 | Microstretch Continuum Theory Modeling for Nematic Liquid Crystalline Elastomers: Interplay Between Non-Affinity and Director Stretch : ICTACEM2025P192 | 0:15 |
| 17:15 | Priyakshi Goswami ; Somnath Ghosh | Amit Kumar Onkar; Mutturaj H Medar; Arun Kumar A; Rahul B Choudhary; Shivaprasad M V; Raja S | Aishwarya Kasarla ; Prof. Krishnendu Haldar | |
| | Predictive Multiphysics Simulation of Fluid–Structure Interaction in Deformable Microchannels for Biomedical Applications : ICTACEM2025P232 | Large deformation analysis of magneto-active polymer membranes under varying mechanical loads: ICTACEM2025P064 | Semi-analytical estimates for three phase elastomeric self-healing composite systems : ICTACEM2025P815 | 0:15 |
| | Satyabrata Podder ; Tapan Sarkar ; Amit Dhar ; Animesh Das ; Shantanu Dutta | Anuttar Jain; Krishnendu Haldar | Jayram Desai ; Vikranth Racherla | |
| 17:30 | Tea Break | | | 0:30 |
| 18:00 | Cultural Evening at Kalidas Auditorium followed by Conference Dinner at Vikramshila Foyer | | | |

| 17 December | Department of Aerospace Engineering | | | |
|-------------|-------------------------------------|---|--|--|
| | Venue | 8:00 | BREAKFAST | |
| | Venue | Seminar Room of Aerospace Engineering Annex Building | | |
| | | Plenary Session -6: Modelling and Simulation of Multiphase Flows: A Personal Perspective | | |
| | | Prof. J C Mandal, Department of Aerospace Engineering, IIT Bombay Session Chair: Prof. Somnath Ghosh | | |
| | Venue | Seminar Room of Aero Annex Building (A7) | Meeting Room Aero Annex Building (S10) | Seminar Room Aero Old Building (S11) |
| | Session | Aerodynamics and Fluid Mechanics | Solid Mechanics and Dynamics | Solid Mechanics and Dynamics |
| | | Session Chair: Prof. Ranadev Datta | Session Chair: Prof. Amit Shaw | Session Chair: Prof. Mainak Chakraborty |
| 17 December | | Prediction of Store Trajectory Using Domain-Decomposed Reduced-Order Modelling : ICTACEM2025P722 | Parametric study of friction characteristics of IRS rail steel using ball-on-disk experiments: ICTACEM2025P726 | Dynamic Response of Variable Fibre Spacing Composites Under Porous Hemispherical Nosed Impactor: ICTACEM2025P969 |
| | | Navdeep Pandey ; aysinh Jagdishchandra Patel ; Aniruddha Sinha | Shreedhar Sahoo; D S Kushan; Mayank Kumar; Vikranth Racherla | Aayush gupta; Abdul Sadiq; Dipak Kumar Maiti |
| | | | | 0:15 |

| | | | |
|---------|---|---|--|
| | | | |
| 10:00 | On the evolution of Lamb vector in pulsating transonic jet flows : ICTACEM2025P040 | Random Eigenvalue Characterization for Free Vibration of Centrifugally Loaded Euler-Bernoulli Beams: ICTACEM2025P599 | Role of Particle Shape in Fabric Evolution during Compressive Creep Failure of Concrete : ICTACEM2025P303 |
| 10:15 | Subhro Halder ; Debayan Das ; Ribhu Pal ; Satvik Jaiswal ; Arnab Roy | Jammu Sarath; Ravi Prakash Prajapati; Korak Sarkar | Subham Mukherjee ; Kumar Anjneya ; Arghya Deb |
| 10:15 | Shock-Tandem Bubble Interaction: The Effect of Inter-Bubble Gap on the Bubble Flow Dynamics : ICTACEM2025P549 | RBFN-based reliability analysis of thermally loaded variable fiber spacing composite plates with damage: ICTACEM2025P184 | Morphological Effects of Friction Modifiers for Railway Applications: Binder vs Solid Lubricant : ICTACEM2025P568 |
| 10:30 | Nithin Krishnan S ; Ribhu Pal ; Arnab Roy ; Parthasarathi Ghosh | Prateek Chandrakar; Narayan Sharma; Dipak Kumar Maiti | Kushan D S ; G S P J Ronith ; Shreedhar Sahoo ; Mayank Kumar ; Vikranth Racherla |
| 10:30 | Some Acoustic Measurements on a Thrust-Vectoring Biconical Jet : ICTACEM2025P504 | Simulation of Voltage Generation in Thermophotovoltaic (TPV) Cells Using FE Analysis: ICTACEM2025P992 | Thermo-elastic vibration characteristics of graphene-reinforced composite stiffened spherical panels : ICTACEM2025P751 |
| 10:45 | Saiphanendra Karuchola ; Deeksha Yadav ; Revathy R K ; Arun Kumar Perumal Ashoke De | Samanth Martis; Krishnendu Haldar | Pabitra Maji ; Poonam Kumari ; Bhrigu Nath Singh |
| 10:45 | Stability characteristics of ORV at Transonic and Supersonic Mach number : ICTACEM2025P161 | Strength and Environmental Durability of Epoxy/Graphene Oxide Composites:An AI-Driven Framework for UAV Applications: ICTACEM2025P166 | Thermo-Mechanical Analysis of thermally Autofrettaged Functionally Graded Disk : ICTACEM2025P949 |
| 11:00 | Nalin Singh Sirohi ; M Jathaveda ; Dileep K N ; G Vidya | Santosh Maharana; SK Maharana; R. Vijayakumar | Mohit Rajput ; .M. Kamal ; R.U. Patil |
| 11:00 | Thrust Vectoring of an Actively Controlled Supersonic Jet : ICTACEM2025P312 | Study of lamb wave propagation for sandwich plates of fiber-reinforced functionally graded transverse isotropic material with an adhesive modelled as linear elastic material with voids using frobenious method: ICTACEM2025P694 | Transonic flutter prediction of delta wings using coupled CSD-CFD approach : ICTACEM2025P760 |
| 11:15 | Mayank Kumar ; Saiphanendra Karuchola ; Arun Kumar Perumal ; Ashoke De | Rokkam Saketh; Tatipaka Anand | Arun Kumar A ; Amit K Onkar ; Rahul B Choudhary ; Arun K ; Raja S |
| | Tea Break | | |
| Venue | Seminar Room of Aero Annex Building (A8) | Meeting Room Aero Annex Building (S12) | Seminar Room Aero Old Building (S13) |
| Session | Aerodynamics and Fluid Mechanics | Solid Mechanics and Dynamics | Solid Mechanics and Dynamics |

| | Session Chair: Prof. Mrinal Kaushik | Session Chair: Prof. Prasun Jana | Session Chair: Prof. M R Sunny | |
|---|--|---|--|------|
| 11:30 | Venting analysis of a Typical Launch Vehicle Inter Stage Structure near to strapon nose cone : ICTACEM2025P605 | Temperature-Driven Deformation Mechanisms in CNT- and Graphene-Reinforced Al _{0.3} CoCrFeNi High-Entropy Alloys: A Molecular Dynamics Approach: ICTACEM2025P827 | Vibration-Based Energy Harvesting Using Mass-in-Mass Metamaterial with Piezoelectric Coupling : ICTACEM2025P307 | 0:15 |
| 11:45 | Darshit Gajera ; Sanjoy Kumar Saha | Subrata Barman; Sudip Dey | Subrata Barman ; Pushpa Pandey ; Hamed Haddad Khodaparast ; Tanmoy Mukhopadhyay ; Hadi Madinei ; Michael Friswell | 0:15 |
| 12:00 | Computational Investigation of Aerodisk Geometries in a Spiked Blunt Body for Hypersonic Heat Reduction : ICTACEM2025P875 | Analytical Modelling of Electro-Mechanical Impedance (EMI) in Adhesively Bonded Beams for Multi-Damage Detection: ICTACEM2025P019 | XFEM based Free vibration analysis of thin Circular plates using 2DOF on Multiple crack characteristics : ICTACEM2025P653 | 0:15 |
| 12:15 | Sanjay Satish ; Satheeshkumar S. ; Nivin Francis | Umakanta Meher; Mohammed Rabius Sunny | Babasaheb Kisan Varpe ; Achchhe Lal | |
| | Validating Combined Vector Field Approach With Full Quadrotor Dynamics ; ICTACEM2025P514 | Tailoring Flow-Induced Vibrations of Flexible Plates via Perforation: ICTACEM2025P108 | Aerodynamic Performance of a Multi-Element Flapping Foil Inspired from the Feathered Wings of Birds : ICTACEM2025P761 | 0:15 |
| | Dheeraj ; Sikha Hota | Shubham Giri; V. Kartik; Amit Agrawal; Rajneesh Bhardwaj | Avinash Kumar Pandey ; Rajneesh Bhardwaj ; Rajat Mittal | |
| Poster Presentation Sessions Will Take Place at the End of Oral Presentations. | | | | |
| Venue | Seminar Room of Aerospace Engineering Annex Building | | | |
| 12:30 | Valedictory Session of ICTACEM 2025 | | | |
| 13:00 | LUNCH BREAK | | | |

BOOK OF ABSTRACTS

Turbulent Jets

Joseph Mathew

Professor, Indian Institute of Science, Bangalore

Jets are canonical flows that have been the subject of many studies. Jets appear in many applications while also serving as a model for many kinds of fundamental studies. A round jet emerging from a nozzle can be viewed as a nearly uniform flow bounded by a thin cylindrical shear layer. This shear layer is susceptible to Kelvin-Helmholtz-like instability resulting in a wavy appearance that develops into a train of vortex rings. These rings undergo an azimuthal (Widnall) instability, and then a rapid breakdown, over a distance much smaller than jet diameter, into a turbulent round jet. Our complete viscous instability analysis of vortex rings, and tracking the linear growth of unstable modes ending in nonlinear processes, revealed the reasons for the very rapid breakdown. The turbulent jet is a canonical example of a self-preserving flow. It was the setting for our new understanding of turbulent entrainment. Essential principles for large eddy simulations were clarified by our studies of jets at very high Reynolds numbers, performed with a less widely known method that we had proposed at the beginning of this century. Examples from our studies will be presented, including some new phenomena in supersonic jets and scaling in twin jets.

SPC-I and DPSM – two new developments in the field of NDE and SHM

Tribikram Kundu

Professor, Department of Civil Engineering and Engineering Mechanics, University of Arizona, USA

Two techniques – 1) Sideband Peak Count–Index (SPC-I) and 2) Distributed Point Source Method (DPSM) have been recently developed by the speaker in collaboration with his students and colleagues. This talk will discuss the strengths and limitations of these two techniques. SPC-I is primarily a nonlinear ultrasonic technique that can be effectively used for monitoring damages at various stages - from microscopic dislocation and micro-crack generation to larger macro-crack propagation in metals, polymer composites and concrete structures. The SPC-I technique has been found to be more effective than traditional nonlinear ultrasonic techniques like higher harmonic generation, nonlinear wave modulation spectroscopy, nonlinear impact resonant acoustic spectroscopy etc. For modelling elastic and electromagnetic wave propagation the semi-analytical mesh-free technique DPSM developed by the speaker and his colleagues has been shown to be significantly more efficient than popular finite element-based techniques, especially for 3-dimensional problems. Experimental and model generated results will be presented to demonstrate the advantages of these two techniques.

Wave Technologies in SHM of Built Facilities – Theory, Experiments and Practice

Abhijit Mukherjee

John Curtin Distinguished Professor, School of Civil and Mechanical Engineering, Curtin University,
Australia

Wave technologies offer an exciting opportunity for continuous monitoring of the health of built facilities. Rapidly falling cost of hardware and data and great improvement of drone technologies have made scanning of the entire body of built facilities such as bridges or aircrafts possible. However, there are challenges of acquisition, transmission and interpretation of data. This talk will introduce the frontline technologies for such measurements. The theoretical background for data interpretation will be discussed. Recent developments in artificial intelligence technologies that facilitate automated data interpretation, their challenges and future research will be mentioned. Some case studies for field implementation will be discussed.

Designing Heavy Payload Unmanned Aerial Systems: The Helicopter Way

Abhishek

Professor, Department of Aerospace Engineering, Indian Institute of Technology, Kanpur

The talk would start with introduction to Unmanned Aerial Systems (UAS), following which the challenges associated with design and development of heavy payload (> 20 kg) unmanned aerial systems for operations in high altitude areas would be established. This would be followed by discussion on configuration selection. The description of multiple disciplinary design optimisation based iterative design process would be presented. Results from the design process would be summarised and explained. The final weight breakdown of the conceptual design and the final prototype would be compared and the efficacy of the design would be proved through flight testing in the relevant environment. The talk would end by highlighting important lessons learnt during the design process and how they were solved using knowledge of rotary wing aeromechanics.

Modelling and Simulation of Multiphase Flows: A Personal Perspective

J C Mandal

Professor, Department of Aerospace Engineering, Indian Institute of Technology Bombay, India

Accurate modelling of multiphase flows is central to the design and analysis of numerous engineering systems in aerospace, mechanical, chemical, civil, and marine applications. Phenomena such as fuel injection, atomization, boiling, cavitation, free-surface motion, and liquid sloshing all demand precise resolution of fluid–fluid interfaces and a deep understanding of the governing physics. These challenges, coupled with the need for robust and efficient numerical tools, make the development of reliable multiphase flow solvers a problem of enduring significance. This plenary lecture presents a personal perspective on our journey in modelling and simulation of multiphase flows, focusing not on a comprehensive survey of the field - which would be an immense undertaking - but on key ideas that shaped our approach.

A central theme of the talk is the interplay between the mathematical nature of the governing partial differential equations and the numerical strategies developed to solve them. Although the vast majority of work on multiphase flows adopts incompressible formulations - owing to their perceived simplicity and their relevance to many engineering applications - the incompressibility assumption brings with it subtle yet significant mathematical and numerical challenges. The incompressible Navier-Stokes equations exhibit a mixed parabolic-elliptic character, lack an explicit pressure evolution equation, and enforce a tight coupling between velocity and pressure. These features have led to a wide spectrum of numerical methodologies, including derived-variable formulations, pressure-projection schemes, artificial compressibility approaches, and weakly compressible models, each offering distinct advantages while carrying inherent limitations.

Our work has been guided by the view that many of the longstanding difficulties in incompressible flow simulation arise from the mixed parabolic-elliptic nature of the governing equations, which cannot be solved in a fully coupled manner either analytically or numerically with present-day techniques. Artificial Compressibility (AC) methods offer a powerful alternative by transforming the system into a parabolic-hyperbolic form, allowing all flow variables to evolve simultaneously and enabling the use of advanced algorithms originally developed for compressible flows. Weakly Compressible (WC) formulations - such as KRLNS, EDAC, and the General Pressure Equation (GPE) -further enhance computational scalability by providing explicit pressure evolution equations. We will also discuss our recent contributions to WC-based multiphase solvers, including approaches for discretizing non-conservative terms through Abgrall's steady-state constraint and path-conservative methods, which enable accurate interface representation and robust surface-tension modelling.

The talk will also address our efforts in compressible multiphase flow simulation, where density variations, shock interactions, and strong pressure coupling cannot be ignored. Diffuse Interface Methods (DIMs), including the 7-, 6-, and 5-equation models, have become indispensable for such problems. However, they face severe numerical stiffness in the low-Mach limit. We will outline the limitations of existing preconditioning-based remedies and present our pressure-scaling-based low-Mach correction, which restores accuracy and significantly improves convergence while highlighting the remaining challenges such as interface oscillations at high density ratios.

In conclusion, drawing from our years of research, we argue that compressible formulations - appropriately adapted - offer a unified and versatile framework for both compressible and incompressible multiphase flows. Since no real fluid is perfectly incompressible, compressible equations are, in principle, valid even in the incompressible limit, making them naturally suited for a wide range of flow regimes. Their ability to capture interface dynamics, strong transients, and diverse physical phenomena positions them as a promising foundation for future developments. Illustrative examples will be presented to demonstrate the potential of this perspective

Vertical takeoff of aircrafts: Some new possibilities

P. A. Ramakrishna

Professor, Department of Aerospace Engineering, Indian Institute of Technology Madras

Vertical take-off and landing are the capabilities of an aircraft to take off and land vertically without the need for a runway. Not relying on the runway for take-off and landing adds to the operational flexibility of the aircraft systems. Since the first powered flight in 1903, there have been many conceptual designs and prototypes for VTOL aircraft, of which only a few made it to the operational phase. Currently, rotorcraft systems like helicopters account for the major share of operational VTOL systems, and only very few fixed-wing aircraft with VTOL capabilities are operational. A fixed-wing VTOL-capable aircraft enhances the range, endurance and operational flexibility compared to a rotorcraft system. For VTOL, the propulsion unit should be capable of thrust modulation and control. In this regard, a hybrid rocket thruster is proposed to augment the thrust during vertical takeoff and landing. Classical hybrid rocket motors – having solid fuels and gaseous/liquid oxidisers – are controllable, although the precise thrust control of these hybrid motors is still being researched. In this study, compressed air was chosen as the oxidiser for the hybrid rocket motor. A wax-aluminium-based solid fuel was identified to work with air. Using this propellant combination, a lab-scale hybrid motor was developed. To achieve thrust control and modulation in this motor, an oxidiser flow control valve was designed and integrated into the motor. The thrust control capabilities of hybrid rocket thrusters were demonstrated using the lab-scale hybrid rocket motor, showcasing both closed-loop thrust control and open-loop throttling functionalities. During open-loop throttling, a thrust-turndown ratio of 5.5:1 was achieved for the lab-scale motor.

CAE Simulations for GenZ

Ganesh Soni

Quality Control Manager, Manufacturing Intelligence division, Hexagon, Pune

Today's Gen-Z engineers expect engineering tools that move as fast as they do. This talk explores how modern CAE simulation is evolving to meet that expectation through smarter workflows, AI-assisted engineering, and fully connected design-to-simulation ecosystems. We will walk through the journey of Hexagon's Design and Engineering portfolio, from classical solvers such as MSC Nastran, MSC Marc, Adams, Digimat and Cradle CFD, to their next-generation implementations within Hexagon's Multiphysics, Digital Materials, System Dynamics, Virtual Manufacturing and Virtual Mobility suites.

The session highlights how AI is transforming the way simulations are built, executed and interpreted. ODYSSEE will be introduced as Hexagon's AI platform that uses reduced-order modelling and machine learning to predict simulation results in seconds. It enables real-time response prediction, rapid design exploration and accessible digital twin creation for any user level. From automated model generation and surrogate models to intelligent meshing and real-time behaviour prediction, AI is reducing cycle times and making high-fidelity simulation accessible to early-career engineers. We will also explore how these advancements help customers solve problems faster, iterate more confidently and reduce dependence on physical prototypes.

Whether you work in CAE, design engineering or product development, this talk will show how simulation is being re-imagined for the next generation, and why Gen-Z is poised to drive one of the most significant shifts our industry has ever seen.

CONTENT

| S.No | Paper | Page No |
|------|--|---------|
| 1 | 2D Multiphysics Modeling Framework for Laser Ablation of Al₂O₃ Ceramic Coating Nazim Khan, Abinesh K, Rajdip Mukherji, Somnath Bhowmick and Pritam Chakraborty | 1-2 |
| 2 | A Cohesive Zone Modelling Approach for Fatigue Crack Growth and Life Prediction in Adhesively Bonded Joints Pradeep K Sahooa, M.N. Saradvanib, Shrimukhi G Shastry | 3-4 |
| | A comparative investigation of electromechanical vibration suppression in imperfect curved fiber laminates and straight fiber laminates with integrated piezoelectric layers Vanshika Anand, Ansh Kapoor, Narayan Sharma, Pawan Kumar, and Prasant Kumar Swain | 5-6 |
| 4 | A Lyapunov Guidance Vector Field with Variable Guidance Gain for Elliptical Path Following Ishan Phanse, Sayantan Pal and Sikha Hota | 7-8 |
| 5 | A Meshfree Numerical Solver for a Fractional Calculus Approach to Continuum Damage Mechanics Malapeta Hemasundara Rao, M. Ramji, and Sai Sidhardh | 9-10 |
| 6 | A Reduced-order Homogenized Plate Model of Sandwich Structure Using Variational Asymptotic Method Anup Kumar Pathaka, Pritam Chakraborty | 11-12 |
| 7 | A Scalar LPCE–ALE Framework for Sound Generation in Low-Mach Number Flows with Moving Boundaries Kevin S. Swamya and Vaibhav Joshia | 13-14 |
| 8 | Aerodynamic Performance of a Multi-Element Flapping Foil Inspired from the FeatheredWings of Birds Avinash Kumar Pandey, Rajneesh Bhardwaj, Rajat Mittal | 15-16 |
| 9 | Altitude Control of Powered Parafol Systems using Extended State Observer-Finite-time Sliding Mode Control (ESO-FTSMC) Nitin Pal and N.K. Peyada | 17-18 |
| 10 | Analysis of Temporal Oscillations of a Deflected Wake in a Plunging Foil Using Proper Orthogonal Decomposition Mohamed Aniffa S, Sunetra Sarkar | 19-20 |
| 11 | Analytical Investigation for Free Vibrations Analysis of Functionally Graded Sandwich Plates with Advanced Gradation Laws Ankitha Kamatha, Supen Kumar Sah, Anup Ghosh | 21-22 |
| 12 | Analytical Modelling of Electro-Mechanical Impedance (EMI) in Adhesively Bonded Beams for Multi-Damage Detection Umakanta Meher, Mohammed Rabius Sunny | 23-24 |

| | | |
|----|--|-------|
| 13 | ANN-based prediction of the free vibration characteristics of functionally graded plates for various boundary conditions Dabeer Anwer Danisha and Sukanta Chakraborty | 25-26 |
| 14 | Axially-Loaded Column under Earthquake Loading Mahendra Gattu | 27-28 |
| 15 | Bluff Body Induced Regression Rate Enhancement in Hybrid Motor Khandare A., Patil A., Patel J., Sonage S., Kumar N., Deore N. | 29-30 |
| 16 | Buckling load parameter analysis of Rectangular plate with Full and partial stiffeners under Uniaxial and Biaxial loading conditions | 31-32 |
| 17 | CFD Investigation of Transonic Bucket phenomena for Typical Grid Fin used on Re-Entry Stage Configuration Anubhab Das, Kunal Garg, Ankur Nagpal, Amit Sachdeva, G Vidya | 34-35 |
| 18 | Comparative Analysis of Obstacle Avoidance Path Planning Algorithms for Robotic Manipulators: RRT, APF, and CHOMP Adeetya Uppala, Rakesh Kumar Sahoo, Manoranjan Sinha | 36-37 |
| 19 | Comparative Ballistic Impact Simulation of NiTi SMA-Reinforced and Conventional GFRP Composites Sibaram Patro, Chandra Sekhar Yerramallib and Krishnendu Haldar | 38-39 |
| 20 | Comparative bending response of imperfect variable-angle tow and straight fiber laminates with integrated PZT layers Ansh Kapoora, Vanshika Anand, Narayan Sharma, Pawan Kumar, and Rakesha Chandra Dash | 40-41 |
| 21 | Computation of heat flux over Winged Reusable Launch Vehicle – Technology Demonstrator and comparison with flight data Jiju R. Justusa, Sundeep Kumar Epuri, Vidya G, Manokaran K | 42-43 |
| 22 | Computational Investigation of Aerodisk Geometries in a Spiked Blunt Body for Hypersonic Heat Reduction Sanjay Satish, Satheeshkumar S., Nivin Francis | 44-45 |
| 23 | Correlation of Tulip Flame Formation and CH Chemiluminescence Bursts in Confined Propane-Air Combustion Abhishek Kumar and Ratan Joarder | 46-48 |
| 24 | Curvature-Constrained UAV Path Following Using Finite-Time Sliding Mode Control Panasa Pranav Kumar, Sayantan Pal and Sikha Hota | 49-50 |
| 25 | Deflection Characteristics of Piezoelectric Composite Plates under UDL and SSL Using Refined Second Shear Deformation Theory Pawar Raju Sidhu,d, Achchhe Lal , Rahul Sudam Kamble | 51-52 |
| 26 | Deformation Behavior of Soft Electroelastic Membranes Subjected to Large Electric Fields Yadwinder Singh Joshana, Sushma Santapuri and Debashish Khan | 53-54 |

| | | |
|----|--|-------|
| 27 | Design and Development of a Hybrid Model for Impact Analysis on Underwater Vehicles Pankaj Meena and R. Sharmab | 55-56 |
| 28 | Design of Vent system for crew escape system-test vehicle compartments B.Venkat Shivaram Jadav, Jathaveda.M, G.Vidya | 57-58 |
| 29 | Development and Validation of a Python-Based Preliminary Design Tool for Ramjet Engines Thivya Ranee and Atharv Mangalkarb and Akshay Abhyankar | 59-60 |
| 30 | Direct Simulation Monte Carlo Study of Thruster Plume Impingement on Planetary Surface Malaikannan G and Suman Chakraborty | 61-62 |
| 31 | Dynamic Response of Variable Fibre Spacing Composites Under Porous Hemispherical Nosed Impactor Aayush Gupta, Abdul Sadiq and Dipak Kumar Maiti | 63-64 |
| 32 | Effect of Flight velocity on Mean Flow of an Ideally Expanded Supersonic Jet – a CFD study Sanjoy Kumar Saha and Manoj T Nair | 65-66 |
| 33 | Effect of Localized Elastic Supports Representing Ribs and Mounts on the Flutter Behavior of Tailored Composite Panels Abdul Sadiq, Aayush Gupta, Dipak Kumar Maiti | 67-68 |
| 34 | Effect of Mach number on a Compressible Impinging Round Jet: An LES study Priyakshi Goswami and Somnath Ghosh | 69-70 |
| 35 | Effect of Pivot Point Location on the Propulsive Performance of Rear Airfoil in Tandem Configuration Adeetya Uppala, Rahul Ranjana, Sunil Manohar Dasha | 71-72 |
| 36 | Effect of ply-orientation angle on flutter behaviour of laminated composite plates Shashank K Shankaregowda, Subrata Barman, Rajeev Nayan Gupta, Saikat Ranjan Maity, Dipak Kumar Maiti, Sudip Dey | 73-74 |
| 37 | Effects of random orientation of bluff body on the onset speed of galloping-based piezoelectric energy harvester Rakesha Chandra Dash | 75-76 |
| 38 | Empirical expression to predict the first-mode resonant frequency of a pitching flexible panel Abhinav Kumar KSN, Parag Deshpande and Ravi Dodamani | 77-78 |
| 39 | Estimation of Flight Measured Pressure using CFD for a Typical Launch Vehicle Sreenivasulu Juluri, Sanjoy Kumar Saha and Vidya G | 79-80 |

| | | |
|----|--|---------|
| 40 | Evaluation of anisotropy via non-destructive indentation in LPBF-processed Co-Cr-Mo alloy: The role of scanning strategy Vinod Kumar Jat, R. U. Patil | 81-82 |
| 41 | Experimental Analysis of the Magneto-Viscous Responses of Magneto-Active Polymers Rahul Kumar Saini and Krishnendu Haldar | 83-84 |
| 42 | Experimental Fabrication and Characterization of E-Glass/Epoxy Composites Using Vacuum-Assisted Resin Infusion Umakanta Meher, Praveen Shakya, Mohammad Rabius Sunny, Iqbal Ahmed | 85-86 |
| 43 | Experimental Static and Fatigue Damage Assessment of Adhesively Bonded CFRP Joints Under Mode II Loading Using AE Technique Bandaru Bangarraju, Sai Sidhardh, M Ramji | 87-88 |
| 44 | FE Modeling of Single Foam-filled Reentrant Unit Cell to Evaluate Deformation Mechanics and Energy Absorption Viswasarathi NM, Bibhu Prasad Mahapatra, Prasun Jana | 89-90 |
| 45 | Feature-Alignment Model Order Reduction (FAMOR) for Nonlinear Convective and Shock-Dominated Flows Aritro Ghosha, Sanjay R.b, Aniruddha Sinha | 91-92 |
| 46 | Finite Element Simulation of Magnetocaloric Effect in Gadolinium Busi Swathi Priya and Krishnendu Halder | 93-94 |
| 47 | Flexural and ILSS Performance of GFRP Composites under Extreme Temperature Conditions Supal Tudu and Velmurugan Ramachandran | 95-96 |
| 48 | Flow-Induced Vibrations of a Circular Cylinder and an Upstream D-Cylinder of various Elliptical Ratios Sachin S B and Atul Sharma | 97-98 |
| 49 | Free Vibration Analysis of Cranked Sandwich Plates with CSCL Face sheets and Honeycomb Core Comparison Gajavada Sanjeevkumar, Pritam Mondal Jayant Prakash Varun & Prashanta Kr Mahato | 99-100 |
| 50 | Free Vibration Analysis Of Multiple Central Cracked Rectangular Plate with Two Degrees of Freedom (2- Dof) Babasaheb Kisan Varpe and Dr. Achchhe Lal | 101-102 |
| 51 | Guidance Law for Surveillance by UAVs Using Curve Paths Parth Madure, Gururaj Khurda, Sayantan Pal, and Sikha Hota | 103-104 |
| 52 | Harnessing wind energy within the conduit-style tall building through the use of wind turbines Amlan Kumar Bairagi | 105-106 |

| | | |
|----|--|---------|
| 53 | Impact of Preheated Central Jet on Intermixing of Confined Multi-Annular Swirling Jets Ritesh Srivastava, Vivek Kumar Patel | 107-108 |
| 54 | Integrating CFD, Experiments, and Bayesian Inference for Aerodynamic Analysis of a Serrated Delta Wing Anand M.Raikar, S.K.Maharana, N.Chikkanna | 109-110 |
| 55 | Investigation of Delamination Progression in Unidirectional Composite Laminates Subhabrata Koley | 111-112 |
| 56 | Investigation of Flexural Behavior of Functionally Graded Plates through Higher-Order Shear Deformation Formulation Smruti Ranjan Sahoo, Surendra Verma, and B. N. Singh | 113-114 |
| 57 | Investigation of transonic buffet loads on aeroelastic launch vehicle model using couple CSD-CFD approach Amit K Onkar, Mutturaj H Medar, Arun Kumar A, Rahul B Choudhary, Shivaprasad M V, Raja S | 115-116 |
| 58 | Lam e Curve Following by UAVs using Vector Field Guidance Hemant V Nair, Sayantan Pal and Sikha Hota | 117-118 |
| 59 | Large Deformation Analysis of Magneto-Active Polymer Membranes under Varying Mechanical Loads Anuttar Jain and Krishnendu Haldarb | 119-120 |
| 60 | Machine Learning based approach to predict the life of damaged wind turbine blade Praveen Shakya, Umakant Meher, Sachin Kumar, Danial Arias, Abdennour C. Seibia, Mohammad A. S. Masoum | 121-122 |
| 61 | Magneto-Stiffening Effects on Beam Vibrations Supported by Winkler Foundation Lakshita Patila and Krishnendu Haldarb | 123-124 |
| 62 | Micromechanical Homogenization and Electromagnetic Characterization of Radar Absorbing Materials using Multiphysics Simulation Omkar Bilawar and Krishnendu Haldar | 125-126 |
| 63 | Microstretch Continuum Theory Modeling for Nematic Liquid Crystalline Elastomers: Interplay Between Non-Affinity and Director Stretch Ms. Aishwarya Kasarla and Prof. Krishnendu Haldar | 127-128 |
| 64 | Mobile Anti-Drone System: A SDR Approach for Defensive Disruption of UAVs Patel Namra, Ajit Kumar and Jagat Rath | 129-130 |
| 65 | Model Order Reduction for Cerebrovascular Hemodynamics: A POD-Galerkin and Hybrid Physics-Informed Approach | 131-132 |

| | | |
|----|---|---------|
| 66 | Model-Less Feedback Control of Space-based Continuum Manipulators using Backbone Tension Optimization Shrreya Rajneesh, Nikita Pavle, Rakesh Sahoo, Prof. Manoranjan Sinha | 133-134 |
| 67 | Morphological Effects of Friction Modifiers for Railway Applications: Binder vs Solid Lubricant Kushan D S, G S P J Ronith, Shreedhar Sahoo, Mayank Kumar, and Vikranth Racherla | 135-136 |
| 68 | Moving Target Interception using Variable L1 guidance Machavolu Venkata Sushanth, Sayantan Pal and Sikha Hota | 137-138 |
| 69 | Numerical Analysis of Shockwave Boundary Layer Interaction Suraj J Waranga, Prahlad V Deshpandea, Dhruv Bagoraa, Pardeep Duneriaa | 139-140 |
| 70 | Numerical Investigation of a Novel Aerospike–Aero disk–Bleed Channel Configuration for Drag and Thermal Load Reduction in Hypersonic Vehicles Sanjay Satish, Vijay Suresh, Aswathy K. S, A. Abhijith, Antony J. K, Manoj Kumar M | 141-142 |
| 71 | Numerical Investigation of an Archimedean SpiralWind Turbine Using Dynamic Mesh CFD in ANSYS Fluent Shivendraraj Godbole and Krishnendu Haldar | 143-144 |
| 72 | Numerical Investigation of Low-Frequency Oscillations in Separated Shear Flows Digpriya, Rajesh Ranjan and Pradeep Moise | 145-146 |
| 73 | Numerical Investigation on the Effect of Acoustic Cavity Geometry, Angle of Attack, and Injectant Molecular Weight for Drag and Heat Flux Reduction over a Blunt Body Sanjay Satish, Arun B. S, Ashik Muhammad, Manoj Kumar M, Antony J. K. | 147-148 |
| 74 | Numerical Prediction of Interaction Between Two Flying Robotic Butterflies Aman Shukla, Debajyoti Kumar, Chandan Bose, Somnath Roy | 149-150 |
| 75 | Numerical Study on Drag Reduction of Various Bluff-body Geometries using the Passive Rotation of a NACA0012 Aerofoil Bibhas Chand, Prabir Sikdar, M S Harihara Sudhan, and Sunil Manohar Dash | 151-152 |
| 76 | Obstacle Avoidance of UAV in Dynamic Environments Using Direction and Velocity-Adaptive Artificial Potential Field Nikita Pavle, Shrreya Rajneesh, Rakesh Kumar Sahoo, Manoranjan Sinha | 153-154 |
| 77 | On the Dynamic Mode Decomposition of Supersonic Cavity Flow Satya Prakash, Ram Kumar Yadav, Avijit Chatterjee, and Aniruddha Sinha | 155-156 |

| | | |
|----|---|---------|
| 78 | On the evolution of Lamb vector in pulsating transonic jet flows Subhro Halder, Debayan Das, Ribhu Pal, Satvik Jaiswal, and Arnab Roy | 157-158 |
| 79 | Parameter Estimation of BLDC Motor Using Nonlinear Least Square Method <i>Rajib Mandi, N. K. Peyada</i> | 159-160 |
| 80 | Parametric study of friction characteristics of IRS rail steel using ball-on-disk experiments Shreedhar Sahoo, D S Kushan, Mayank Kumar and Vikranth Racherla | 161-162 |
| 81 | Prediction of Store Trajectory Using Domain-Decomposed Reduced-Order Modelling Navdeep Pandey, Jaysinh Jagdishchandra Patel and Aniruddha Sinha | 163-164 |
| 82 | Predictive Multiphysics Simulation of Fluid–Structure Interaction in Deformable Microchannels for Biomedical Applications Satyabrata Podder, Tapan Sarkar, Amit Dhar, Animesh Das, Shantanu Dutta | 165-166 |
| 83 | Random Eigenvalue Characterization for Free Vibration of Centrifugally Loaded Euler-Bernoulli Beams Jammu Sarath, Ravi Prakash Prajapati and Korak Sarkar | 167-168 |
| 84 | RBFN-based reliability analysis of thermally loaded variable fiber spacing composite plates with damage Prateek Chandrakara, Narayan Sharma, Dipak Kumar Maiti | 169-170 |
| 85 | Real-Time Obstacle Avoidance for Waypoint Following of UAVs Heavenly Dadala, Sayantan Pal, and Sikha Hota | 171-172 |
| 86 | Real-Time Tiny Object Detection and Tracking for High-Altitude UAVs Using Customized YOLO Architectures V Aditya Shankar and Devshree Kumar | 173-174 |
| 87 | Reliability analysis of uncertain vibration response in bidirectional sandwich structures using a direct probability integral approach Narayan Sharma, Pawan Kumar, Prateek Chandrakar, and Dipak Kumar Maiti | 175-176 |
| 88 | Response Dynamics of Bio-Inspired Morphing Aerofoils Hibah Saddal, Lucky Jayswal, Chandan Bose | 177-178 |
| 89 | Role of Particle Shape in Fabric Evolution during Compressive Creep Failure of Concrete Subham Mukherjee, Kumar Anjneya, Arghya Deb | 179-180 |
| 90 | Scaling laws for thrust generated from pitching foils Mahesh K Sawardekar and Ratnesh K Shukla | 181-182 |
| 91 | Semi-analytical estimates for three phase elastomeric self-healing composite systems Jayram Desai and Vikranth Racherla | 183-184 |

| | | |
|-----|--|---------|
| 92 | Shock-Tandem Bubble Interaction: The Effect of Inter-Bubble Gap on the Bubble Flow Dynamics Nithin Krishnan S, Ribhu Pal, Arnab Roy and Parthasarathi Ghosh | 185-186 |
| 93 | Simulation of Voltage Generation in Thermophotovoltaic (TPV) Cells Using FE Analysis Samanth Martis and Krishnendu Haldar | 187-188 |
| 94 | Some Acoustic Measurements on a Thrust-Vectoring Biconical Jet SaiPhaneendra Karuchola, Deeksha Yadav, Revathy R K, Arun Kumar Perumal and Ashoke De | 189-190 |
| 95 | Stability characteristics of ORV at Transonic and Supersonic Mach number Nalin Singh Sirohi, M Jathaveda, Dileep K N, and G Vidya | 191-192 |
| 96 | Strength and Environmental Durability of Epoxy/Graphene Oxide Composites: An AI-Driven Framework for UAV Applications S. Maharana, S.K. Maharana and R. Vijayakumar, Anand M Raikar | 193-194 |
| 97 | Study of Lamb Wave Propagation for Sandwich Plates of Fiber-Reinforced Functionally Graded Transverse Isotropic Material with an adhesive modelled as linear elastic material with voids using Frobenious Method Rokkam Saketh and Tatipaka Ananda | 195-196 |
| 98 | Tailoring Flow-Induced Vibrations of Flexible Plates via Perforation Shubham Giri, V. Kartik, Amit Agrawal, Rajneesh Bhardwaj | 197-198 |
| 99 | Temperature-Driven Deformation Mechanisms in CNT- and Graphene-Reinforced Al_{0.3}CoCrFeNi High-Entropy Alloys: A Molecular Dynamics Approach Subrata Barman, Sudip Dey | 199-200 |
| 100 | The assessment to study the free vibration of edge cracked bi-directional SFGM plate with modified inverse hyperbolic shear deformation theory (m-IHHSDT). Rahul Sudam Kamble, Achchhe Lal, Bhrigu Nath Singh | 201-202 |
| 101 | Thermo-elastic vibration characteristics of graphene-reinforced composite stiffened spherical panels Pabitra Majia, Poonam Kumari and Bhrigu Nath Singha | 203-204 |
| 102 | Thermo-Mechanical Analysis of thermally Autofrettaged Functionally Graded Disk Mohit Rajputa, S.M Kamal, R. U. Patila | 205-206 |
| 103 | Thrust Vectoring of an Actively Controlled Supersonic Jet Mayank Kumar, SaiPhaneendra Karuchola, Arun Kumar Perumal, Ashoke De | 207-208 |
| 104 | Transonic flutter prediction of delta wings using coupled CSD-CFD approach Arun Kumar A, Amit K Onkar, Rahul B Choudhary, Arun K, Raja S | 209-210 |

| | | |
|-----|---|---------|
| 105 | Validating Combined Vector Field Approach With Full Quadrotor Dynamics Sikha Hota and Dheeraj | 211-212 |
| 106 | Venting analysis of a Typical Launch Vehicle Inter Stage Structure near to strapon nose cone Darshit Gajera and Sanjoy Kumar Saha | 213-214 |
| 107 | Vibration-Based Energy Harvesting Using Mass-in-Mass Metamaterial with Piezoelectric Coupling Subrata Barman, P. Pandey, H. Haddad Khodaparast, T. Mukhopadhyay, H. Madinei, M. I. Friswell, S. Dey | 215-216 |
| 108 | Wake Modifications arising from a Bio-inspired Flexible Filament placed on NACA0012 Airfoil Thangavel Sudeep and Sachin Yashavant Shinde | 217-218 |
| 109 | Wave Propagation Mechanisms for Enhanced Jet Impulse in Squid-Inspired Flexible Nozzles Paras Singh, Daehyun Choi, Halley Wallace, Gourav Samal, Saad Bhamla, Chandan Bose | 219-220 |
| 110 | Wind-Aware Dubins-Inspired L1 Guidance for Faster Convergence with Bounded Continuous Curvature and Sliding Mode Tracking for UAVs Pradyumn Mahajan, Sayantan Pal and Sikha Hota | 221-222 |
| 111 | Simulation-Based Performance Analysis of Fiber-Reinforced Particle Polymer Composites Using R-Abaqus Multiscale Framework Ajoy Kumar Bhowmick, Salil Haldar and Nipu Modak | 223-224 |
| 112 | Index | 225-228 |

CONTRIBUTED PAPERS

2D Multiphysics Modeling Framework for Laser Ablation of Al₂O₃ Ceramic Coating

Nazim Khan ^a, Abinesh K ^a, Rajdip Mukherji ^b, Somnath Bhowmick ^b, and Pritam Chakraborty^{c*}

^a Postdoctoral Fellow, Department of Aerospace Engineering, IIT Kanpur-208016, India.

^a Project Associate, Department of Aerospace Engineering, IIT Kanpur-208016, India.

^b Associate Professor, Department of Materials Science and Engineering, IIT Kanpur-208016, India.

^c* Associate Professor, Department of Aerospace Engineering, IIT Kanpur-208016, India.

ABSTRACT

This work presents the development of a two-dimensional multiphysics model for laser ablation of Al₂O₃ ceramic coatings to elucidate the ablation dynamics. The model integrates thermophysical effects through the governing equations of continuity, momentum, and energy, coupled with a level-set equation to dynamically track the interface during the ablation process. The model is implemented in COMSOL Multiphysics through the weak form of the heat and fluid flow models and level set equation, ensuring numerical stability with strong nonlinear couplings. The results highlight the transition from melting to vaporization and the subsequent interface recession with damage morphology, providing insights into the thermo-fluid mechanisms of the ablation process. The proposed framework provides a robust computational method for understanding laser–ceramic interactions and supports the optimization of material parameters to minimize the ablation-induced damage.

1. INTRODUCTION

Solid-state lasers are widely used to emulate high-energy laser threats, owing to their ability to produce highly focused beams that facilitate precise and controlled energy deposition on the target surface [1]. The rapid development of high-energy laser technologies poses increasing threats to aerospace applications. When the laser beam incident on the ceramic coating applied on the substrate, a fraction of energy is absorbed by the ablative material and the remaining energy is reflected to the ambient. This leads to a rapid increase in temperature of the material, ultimately causing ablation damage once the material's thermal tolerance is exceeded. The interaction of laser energy with the material can lead to melting, vaporizing, ionizing or spattering of ablative layer, depending on the intensity of the laser energy and exposure time. Direct observation of laser–material interaction in experiments can be challenging and expensive, particularly when involving high-power lasers and specialized materials. Thus, numerical simulation has become an essential tool for studying and predicting the complex physical processes associated with laser-induced ablation. The proposed multiphysics framework integrates the heat transfer and fluid flow model with a level-set method to predict the laser ablation behavior of ceramic coating.

2. MATHEMATICAL MODEL

The mathematical framework integrates thermo-physical phenomena such as conduction, convection, radiation, and material phase changes, utilizing a combination of heat and fluid flow models and level set function to capture interface dynamics. The mathematical framework of these processes includes as follows:

$$\nabla \cdot \mathbf{u} = \dot{m} \frac{\delta(\phi)}{d_m} \left(\frac{(\rho_l - \rho)}{\rho^2} \right) \quad (1)$$

$$\rho \left(\frac{\partial \mathbf{u}}{\partial t} + \mathbf{u} \cdot \nabla \mathbf{u} \right) = \nabla \cdot [-p\mathbf{I} + \mu(\nabla \mathbf{u} + \nabla(\mathbf{u}^T))] + \frac{F_\delta}{d_\delta} \quad (2)$$

$$\rho C_p(T) \left(\frac{\partial T}{\partial t} + \nabla \cdot (\mathbf{u} T) \right) = \nabla \cdot (k(T) \nabla T) + \left(\frac{A Q_L}{d_q} + \frac{Q_v}{d_v} - \frac{h(T - T^0)}{d_c} - \frac{\varepsilon K_B (T^4 - T_0^4)}{d_r} \right) \delta(\phi) \quad (3)$$

$$\frac{\partial \phi}{\partial t} + \mathbf{u} \cdot \nabla \phi + \frac{\dot{m} \delta(\phi)}{\rho d_\phi} = \gamma_{ls} \nabla \cdot \left(\varepsilon_{ls} \nabla \phi - \phi(1 - \phi) \frac{\nabla \phi}{|\nabla \phi|} \right) \quad (4)$$

where \mathbf{u} , ρ , p and T denotes velocity, density, pressure, and temperature. C_p is the material's specific heat capacity, ϵ is the emissivity, \dot{m} is the mass flux rate, A is the absorptivity, k is the thermal conductivity, κ_b is Boltzmann constant. F_δ is the surface tension due to Marangoni effect and d_i is the length scale representing the absorption depth used to convert surface force (energy) into volumetric. $\delta(\phi)$ represents the Dirac delta function of the level set (ϕ), defined as $\delta(\phi)=16\phi^3(1-\phi)^2$, γ_{ls} is the level set interface re-initialization velocity, ε_{ls} is the transition thickness, and Q_L is the Gaussian distribution of laser heat flux.

3. RESULTS

A 2D FEM model consisting of air and ceramic coating is shown in Figure 1. The size of the model is 4 mm (in the x-direction) and 1.3 mm (in the y-direction), with the laser irradiating the top surface of the ceramic coating. The domain consists of 0.3 mm ceramic coating and 1 mm thick layer of air. Multiphysics simulations integrating heat transfer, fluid flow, and the level-set method were performed to investigate the ablation behavior of Al_2O_3 ceramic coatings subjected to a laser power of 500 watts with r_{spot} of 0.8 mm. The contours of the level set function and temperature distribution are shown in Figure 2, highlighting the localized heating and progression of the ablation interface.

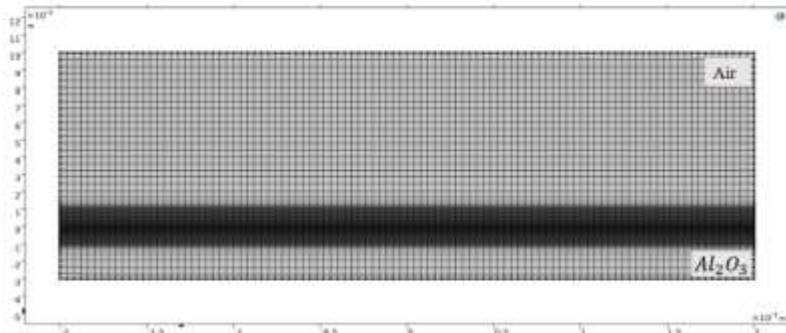


Figure 1. 2D FEM model for air and ceramic domains.

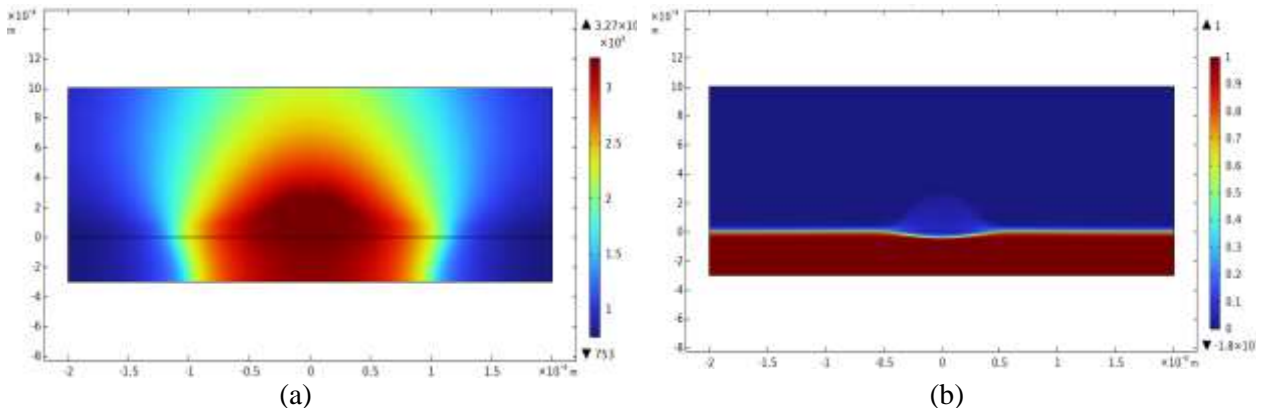


Figure 2. Contours of (a) temperature and (b) level set function after the onset of vaporization.

4. CONCLUSIONS

This study presents a multiphysics simulation of laser ablation in Al_2O_3 ceramic coatings, capturing the coupled interaction between heat transfer, fluid flow, and phase change using a level set function. The model highlights the strong coupling between temperature, velocity, and interface motion, providing a valuable framework for understanding laser–material interactions in the ablation process.

5. REFERENCES

- [1] S. Liu, Z. Tian, L. Shen, and M. Qiu, “Numerical simulation and experimental investigation of laser ablation of Al_2O_3 ceramic coating,” *Materials*, vol. 13, no. 23, p. 5502, 2020, doi: 10.3390/ma13235502

* Communicating Author: Pritam Chakraborty and email: cpritam@iitk.ac.in

A Cohesive Zone Modelling Approach for Fatigue Crack Growth and Life Prediction in Adhesively Bonded Joints

Pradeep K Sahoo^{a1}, M.N. Saradvani^{b, c}, Shrimukhi G Shastry^d

^aSr. Principal Scientist, Structural Technological Division, CSIR-National Aerospace Laboratories, Bangalore, India

^b Project Intern, Structural Technological Division, CSIR-National Aerospace Laboratories, Bangalore, India

^c Undergraduate Student, Aerospace Engineering Department, School of Mechanical Engineering, VIT Bhopal University, Sehore, Madhya Pradesh, India

^d PhD Scholar, Structural Technological Division, CSIR-National Aerospace Laboratories, Bangalore and Academy of Scientific and Innovative Research, Ghaziabad, India

1. INTRODUCTION AND OBJECTIVE

Adhesively bonded joints have become indispensable in aerospace and automotive engineering due to their superior strength-to-weight ratio and ability to distribute stresses uniformly across bonded surfaces. Despite these advantages, their structural integrity is highly influenced by fatigue crack growth under cyclic loading, which can significantly reduce service life. Traditional fatigue analysis approaches based on Linear Elastic Fracture Mechanics (LEFM) require the assumption of a pre-existing crack and become computationally expensive for cycle-by-cycle simulations of complex joint geometries. Cohesive Zone Modelling (CZM) offers a more generalised approach by capturing both damage initiation and crack propagation within a single framework [1]. While there are limited studies available in the literature explaining the CZM of adhesively bonded joints for predicting fatigue life, notable works have explored related aspects [2-4]. However, only a very small number of contributions have attempted to integrate CZM with fracture mechanics-based approaches, such as the Paris law, particularly in the context of adhesively bonded joints. This lack of combined frameworks highlights the need for further research in this direction. To address the identified gap, the current study aims to establish a computational framework for analysing the DCB configuration of Al-Al joints bonded with epoxy adhesive whose cohesive parameters were derived from a study on HTA/6376C carbon/epoxy composite joints [1]. This study develops a computationally efficient methodology for predicting fatigue life of adhesive joints by combining CZM with a cycle-jump approach in Abaqus. This eliminates the need for assumed cracks and extensive computational resources, thereby providing a practical tool for durability assessment.

2. METHODOLOGY

A Double Cantilever Beam (DCB) configuration is selected as the representative geometry under pure Mode I loading. The adherends are modelled as linear elastic beams, while the adhesive layer is represented using cohesive elements governed by a bilinear traction separation law. Quasi-static simulations are performed under representative peak loads, beginning with an intact adhesive layer. At each stage, cohesive element degradation ($SDEG = 1.0$) is used to determine the current crack length. The strain energy release rate (G_{max}) is extracted from simulation results and applied within a Paris-type fatigue law:

$$\frac{da}{dN} = C(G_{max})^m$$

where C and m are material constants obtained from fatigue experiments reported in the literature [1-4]. The number of cycles (ΔN) associated with each crack growth increment (Δa) is then estimated, where Δa corresponds to the cohesive element size to ensure accuracy. The process is repeated iteratively using a cycle-jump scheme until complete failure, thereby reducing computational effort compared to explicit cycle-by-cycle modelling [5-8]. The proposed methodology is validated by comparing the numerical predictions for crack growth rate and energy release rate with established experimental data from the literature, ensuring the accuracy of the model's predictions. [1]. While

¹ Communicating Author: Pradeep K Sahoo, pks@nal.res.in

demonstrated for Mode I, it can be extended to mixed-mode cases by employing suitable mixed-mode fatigue laws [7, 8].

3. RESULTS AND DISCUSSION

Initial simulations of the DCB specimen successfully captured adherend opening displacement and the onset of cohesive damage under applied loading. Crack initiation was observed without an assumed pre-crack, validating the CZM approach's capability. These preliminary findings confirm that the framework can be extended to fatigue analysis, where crack progression links directly to cohesive element failure [2-4, 10-12]. The combination of CZM and cycle-jump analysis enables the efficient prediction of fatigue life. The methodology strikes a balance between physical accuracy and computational practicality by replacing explicit cycles with quasi-static simulations. Future work will extend the approach to mixed-mode loading and explore applications with nano-reinforced adhesives for aerospace-grade joints [7, 8].

4. CONCLUSIONS

A cohesive zone model-based fatigue life prediction framework has been developed and implemented in the Abaqus software. By integrating a cycle jump methodology with Paris-type fatigue laws, the framework enables the modelling of fatigue crack initiation and growth in a unified scheme, eliminating the need for cycle-by-cycle simulation or pre-assumed cracks. This offers a practical and scalable approach for predicting the durability of adhesively bonded joints in advanced engineering applications.

Keywords: Fatigue Crack Growth, Adhesively Bonded Joints, Cohesive Zone Modelling, Abaqus, Paris Law, Cycle-Jump Method

REFERENCES

- [1] M. Alfano and F. Furgiuele, “A progressive damage model for the prediction of fatigue crack growth in bonded joints,” *J. Adhes.*, vol. 87, no. 4, pp. 385–407, 2011.
- [2] C. S. Lopes, A. Turon, and J. Costa, “Fatigue crack growth simulation in adhesively bonded composite joints,” *Fatigue Fract. Eng. Mater. Struct.*, vol. 41, no. 12, pp. 2595–2606, 2018.
- [3] A. Turon, J. Costa, P. P. Camanho, and C. G. Dávila, “CZM for high-cycle fatigue of adhesively bonded joints under mode I loading,” *Int. J. Solids Struct.*, vol. 51, no. 23–24, pp. 3915–3927, 2014.
- [4] L. Zhang, P. B. Aswath, and J. W. Gillespie Jr., “Fatigue damage modelling of adhesively bonded joints under variable amplitude loading using a CZM,” *Eng. Fract. Mech.*, vol. 78, no. 18, pp. 3248–3261, 2011.
- [5] R. D. Adams, S. S. da Silva, and A. Öchsner, “A cohesive zone element for mode I modelling of adhesives degraded by humidity and fatigue,” *Int. J. Fatigue*, vol. 116, pp. 160–170, 2018.
- [6] S. Kumar and P. P. Camanho, “Mode II modelling of adhesive materials degraded by fatigue loading using CZM elements,” *Theor. Appl. Fract. Mech.*, vol. 101, pp. 250–261, 2019.
- [7] F. Carbas, M. F. S. Figueiredo, and L. F. M. da Silva, “CZM for high-cycle fatigue of composite bonded joints under mixed-mode I+II loading,” *Eng. Fract. Mech.*, vol. 147, pp. 154–170, 2015.
- [8] P. K. Ray, H. R. Chai, and D. J. Kinloch, “A modified CZM for fatigue delamination in adhesive joints: Numerical and experimental,” *Compos. Struct.*, vol. 226, p. 111220, 2019.
- [9] J. P. Campilho, M. F. S. Figueiredo, and L. F. M. da Silva, “Development of a CZM for fatigue/fracture of composite joints under mode II loading,” *Int. J. Adhes. Adhes.*, vol. 54, pp. 11–20, 2014.
- [10] J. Blackman and A. Kinloch, “Cyclic CZM for simulation of fatigue failure in adhesive joints,” *Appl. Mech.*, vol. 85, no. 2, pp. 145–158, 2014.
- [11] Y. Zhao, H. Zhang, and Z. Li, “Fractional cyclic CZM for time-dependent fatigue of soft adhesives under mode II loading,” *Int. J. Fatigue*, vol. 175, p. 107574, 2024.
- [12] S. Wang, T. Nguyen, and A. M. Waas, “Experimental–CZM approach to predict fatigue life of adhesive joints under varying modes,” *J. Adhes.*, vol. 100, no. 6, pp. 515–532, 2024.

A comparative investigation of electromechanical vibration suppression in imperfect curved fiber laminates and straight fiber laminates with integrated piezoelectric layers

Vanshika Anand^a, Ansh Kapoor^a, Narayan Sharma^b, Pawan Kumar^c, and Prasant Kumar Swain^d

^a Student, Amity Institute of Defence Technology, Amity University, Noida, 201303, Uttar Pradesh, India

^b Assistant Professor, Amity Institute of Defence Technology, Amity University, Noida, 201303, Uttar Pradesh, India

^c Associate Professor, Department of Mechatronics, Manipal Institute of Technology, Manipal Academy of Higher Education, Manipal, 576104, Karnataka, India

^d Assistant Professor, Department of Mechanical Engineering, National Institute of Advanced Manufacturing Technology, Ranchi, India

1. INTRODUCTION & OBJECTIVE

Composite materials are gaining demand in aerospace industries due to their superior properties, such as, high strength to weight ratio, corrosion resistance, and the tailorabile properties. The combination of lamination sequences allows us to tailor the required properties according to the specific applications. For more than a decade, constant stiffness composites (CSC), in which fibers are kept at a fixed orientation within a plane, have been widely used. However, studies have shown that varying fiber orientation within a lamina can lead to improved mechanical properties [1]. These curved fiber composites (CFC) laminate can be optimized for various structural applications and have shown promising potential [2]. Recent advancement in manufacturing technology offered greater flexibility to fabricate high quality, multi-layered CFC laminated structures [3]. In CFC laminates, fiber orientations can be adjusted in a favorable manner to make the most effective use of stiffness variation, such as mode shape adjustment and the enhancement of the aeroelastic boundaries. The complex manufacturing of CFC laminate leads to some variation in material properties due to internal flaws (such as, fiber damage, incorrect matrix-fiber ratio, etc.). The presence of such imperfections may reduce the mechanical performance of the composite structures. Thus, to provide a better sustainable structure, it is essential to include the effect of imperfection for the structural analysis of CFC laminates. Imperfection in the composite is modelled using anisotropic damage model [4], which reduces the effective load-carrying area.

The present work investigates a comparative dynamic response of CFC and CSC including the effect of imperfection. The free vibration response is estimated for various lamination sequences and the boundary conditions and observe how imperfection is affecting vibration amplitude. Then, active feedback control with embedded piezoelectric layers of actuators and sensors are attached to the substrate to control the vibration amplitude. Considering the simultaneous impact of fiber path variation, structural imperfections, and active control using piezoelectric layers, this study helps in designing composite structures with better vibration attenuation and, more importantly, enhanced reliability and damage tolerance, elements that are vital in aerospace and other high-performance engineering applications.

2. METHODS OF ANALYSIS

The finite element model of the CFCs is developed using isoparametric 8-noded elements. Imperfection in the CFC laminates is modeled via a stiffness-degradation approach [4], which reduces the effective load-carrying area to simulate defects. The study conducts a comparative analysis of vibration suppression responses between CFC and SFC laminates. Furthermore, the use of piezoelectric layers is investigated for their ability to mitigate stiffness loss and enhance vibration suppression in imperfect composite structures.

2.1 Active control by sensors and actuators

When the piezoelectric sensor layer is used as a strain rate sensor, the output charge Q can be converted into the sensor voltage as [4]:

$$V^s = G_s \frac{dQ_s}{dt} = G_c [K_{us}] \dot{u} \quad (1)$$

Where G_c is the constant gain of the charge amplifier. The actuator voltage is then specified by:

$$V^a = G \{V^s\} \quad (2)$$

Here, G is the independent constant gain of the sensor-actuator pair. Substituting the expression for $\{V^s\}$ from Eqn (1) into Eqn (2), the actuator voltage becomes:

$$\{V^a\} = G_a [K_{us}] \dot{u}$$

Where $G_a = G \cdot G_c$

3. RESULTS AND DISCUSSION

This study focuses on a comparative analysis of vibration suppression in CFC and SFC laminates, particularly in the presence of damage within the composite layers. The study examines how embedded piezoelectric sensors and actuator layers, through active feedback control, can suppress vibrations. The analysis is conducted for both simply supported and cantilever boundary conditions, aiming to identify which lamination sequences, CFC and SFC laminates, provide superior vibration suppression under imperfect conditions. Furthermore, the dynamic response of the laminates is evaluated for varying levels of active feedback gain, reflecting the influence of actuator control on vibration mitigation. As illustrated in Figure 1, the imperfect laminates exhibit larger vibration amplitudes compared to healthy plates, demonstrating that the incorporation of piezoelectric sensors and actuator active feedback significantly enhances vibration suppression and helps restore the structural performance degraded by imperfections.

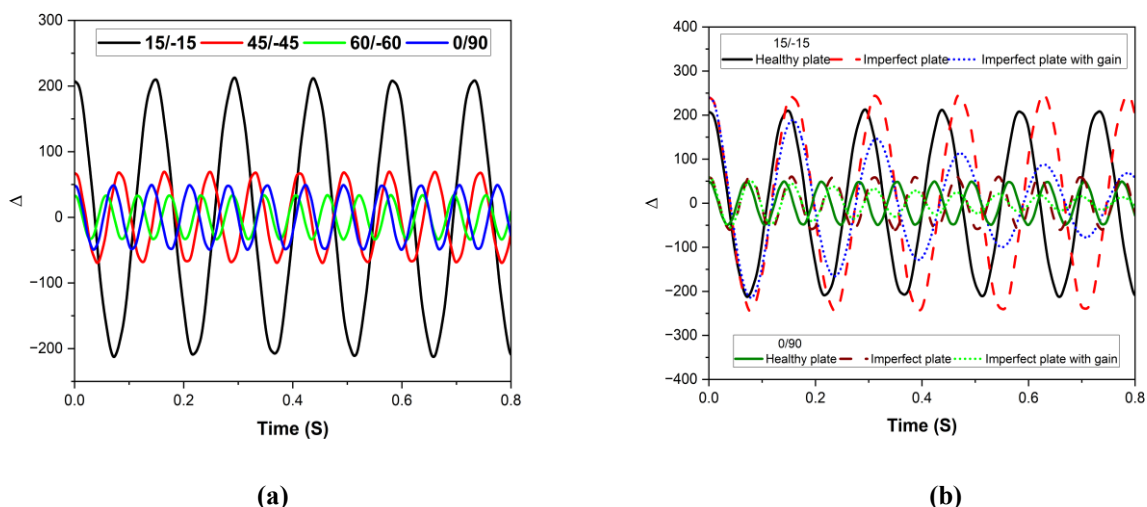


Figure 1: Vibration response of (a) healthy and (b) imperfect composite plates, including the effect of internal imperfection and piezoelectric sensors and actuator (gain $G=400$)

4. CONCLUSIONS

The use of piezoelectric sensors and actuators with active feedback control can effectively reduce vibrations. By integrating piezoelectric actuator layers and using sensor feedback to adjust the active control gain, vibration amplitudes amplified by imperfections can be significantly suppressed. Consequently, the combination of CFC laminates and actively controlled piezoelectric sensor–actuator systems provide an efficient strategy for vibration suppression, provided that an optimal sequence of fiber orientations and feedback gain settings is employed.

5. REFERENCES

- [1] Nozawa, Shuya, and Gokhan Serhat. "Topology and fiber path optimization of composite structures: A critical review." *Materials & Design* (2025): 113699.
- [2] Raju, Gangadharan, Zhangming Wu, and Paul M. Weaver. "Buckling and postbuckling of variable angle tow composite plates under in-plane shear loading." *International Journal of Solids and Structures* 58 (2015): 270-287.
- [3] Carosella, Stefan, Sebastian Hügle, Florian Helber, and Peter Middendorf. "A short review on recent advances in automated fiber placement and filament winding technologies." *Composites Part B: Engineering* 287 (2024): 111843.
- [4] Sharma, N., Swain, P. K., & Maiti, D. K. (2023). Static and dynamic control of smart damaged variable stiffness laminated composite plate with piezoelectric layers. *Mechanics Based Design of Structures and Machines*, 1-26.

* Communicating Author: Prasant Kumar Swain and pkswain@njamt.ac.in

A Lyapunov Guidance Vector Field with Variable Guidance Gain for Elliptical Path Following

Ishan Phanse^a, Sayantan Pal^b and Sikha Hota^c

^a Undergraduate Student, Department of Aerospace Engineering, Indian Institute of Technology Kharagpur, India

^b Research Scholar, Department of Aerospace Engineering, Indian Institute of Technology Kharagpur, India

^c Associate Professor, Department of Aerospace Engineering, Indian Institute of Technology Kharagpur, India

1. INTRODUCTION & OBJECTIVE

There is a strong need for efficient real-time trajectory tracking algorithms in Unmanned Aerial Vehicles (UAVs) that can execute critical maneuvers and follow preplanned trajectories while adhering to the operational constraints of the vehicle. Several proposed algorithms for generating continuous curvature paths based on the Virtual Target Point (VTP) method include the carrot-chasing algorithm, pure pursuit, Line-of-Sight (LOS), the Nonlinear Guidance Law, and the Trajectory Shaping guidance law. Vector field (VF) guidance has emerged as a widely used path-following technique for autonomous systems. Nelson et al. [1] proposed a VF guidance law accounting for constant wind disturbances, which Zhou et al. [2] extended, combining adaptive control to mitigate the impact of varying wind speeds. A classical framework of VF is the Lyapunov Guidance Vector Field (LGVF), which incorporates course-rate and curvature constraints by defining converging and circulation terms. In this direction, Liang et al. [3] constructed a combined VF for arbitrary two-dimensional (2D) and three-dimensional (3D) differentiable paths using Helmholtz's theorem. Harinarayana et al. [4] incorporated curvature constraints to generate a near time-optimal and smooth path. To track the trajectories generated by such guidance laws, a variety of controllers, such as PID Control, Sliding Mode Control (SMC), Linear Quadratic Regulators (LQR), Model Predictive Control (MPC), etc, are used.

This work addresses the elliptical path following problem for UAVs in a two-dimensional (2D) environment through a LGVF Guidance Law, in which the convergence and circulation terms are constructed using a cross-track error-dependent guidance gain. The Lyapunov stability of the guidance law is established. A second-order course-hold autopilot is used for trajectory tracking. Convergence to the desired ellipse is shown for various sets of gain values.

2. METHODS OF ANALYSIS

An LGVF is proposed with convergence and circulation terms using normalised odd and even functions derived from the decomposition of an exponential function. These terms can also be written in terms of hyperbolic tangent and secant functions, respectively, given as,

$$f_1 = V_a \tanh(cg(x, y))$$

$$f_2 = V_a \operatorname{sech}(cg(x, y))$$

where V_a is the airspeed, $g(x, y)$ is the cross-track error, and c is the guidance gain proposed as,

$$c = \frac{m(g(x, y))^2 + n}{(g(x, y))^2 + 1}$$

where m and n are positive constants.

Thus, the guidance gain c , used in the LGVF, is a function of the instantaneous cross-track error $g(x, y)$. It is observed that c converges to m at large distances ($g(x, y) \rightarrow \infty$), and to n as the UAV is near the desired ellipse ($g(x, y) \rightarrow 0$). Thus, it is possible to have better control over the convergence characteristics by suitably tuning the gains (m, n). The Lyapunov stability of the proposed guidance law is examined using a Lyapunov candidate function. A second-order course-hold autopilot tracks the desired course angle generated by the guidance law. The changes in UAV trajectories by changing m and n , once at a time, are analysed. The time of asymptotic convergence of the cross-track error is

compared across various gain settings. The variation of convergence and circulation terms is studied in the transition region (where the dominance of convergence and circulation terms switches), as well as in the area close to the desired ellipse.

3. RESULTS AND/OR HIGHLIGHTS OF IMPORTANT POINTS

The numerical simulations are conducted for a standard elliptical trajectory with $a = 80\text{ m}$ and $b = 40\text{ m}$, given the initial conditions as: position $(x_o, y_o) = (-120, -60)\text{ m}$, course angle $(\chi_{in}) = 0\text{ rad}$. A constant airspeed of 10 m/s is considered. Three different sets of gain values are chosen as $(m, n) = (1, 4)$, $(1, 6)$, and $(3, 6)$. The plots for UAV trajectory, cross-track error, and curvature profile are shown in Fig. (1). The response indicates that increasing the gain values increases the curvature, decreases the convergence time, as well as the path length.

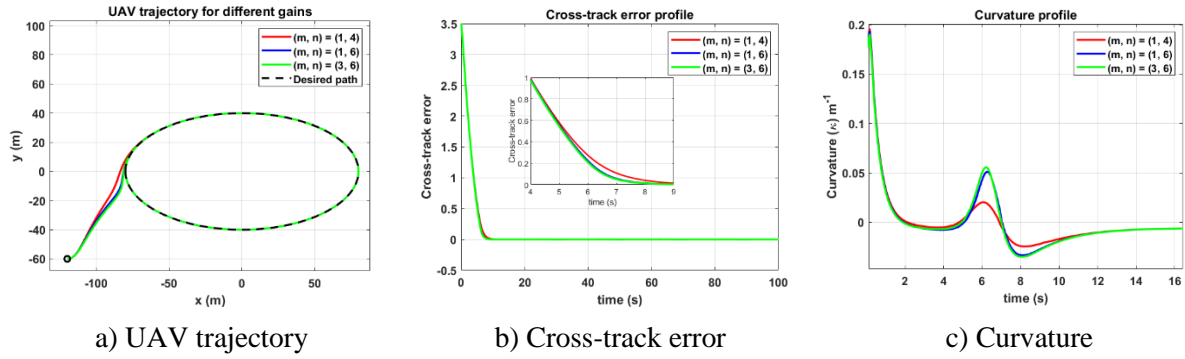


Fig. (1) Numerical simulation results

4. CONCLUSIONS

We propose a varying gain LGVF guidance law to follow an elliptical path in a 2D environment. The UAV successfully converges to the desired elliptical path with different gain values, with some tradeoffs in curvature and convergence speed. This varying gain LGVF guidance law helps to have more controlled convergence characteristics than an LGVF guidance law with a constant guidance gain. Additions to this research include parameter tuning using optimisation of the curvature, and extending the algorithm to three-dimensional (3D) space.

5. REFERENCES

- [1] Nelson, Derek & Barber, Duncan & McLain, Tim. (2006). Vector field path following for small unmanned air vehicles. 7 pp.. 10.1109/ACC.2006.1657648.
- [2] Zhou, Bingyu & Satyavada, Harish & Baldi, Simone. (2017). Adaptive path following for Unmanned Aerial Vehicles in time-varying unknown wind environments. 1127-1132. 10.23919/ACC.2017.7963104.
- [3] Liang, Yueqian & Jia, Yingmin. (2016). Combined Vector Field Approach for 2D and 3D Arbitrary Twice Differentiable Curved Path Following with Constrained UAVs. Journal of Intelligent & Robotic Systems. 83. 10.1007/s10846-015-0308-x.
- [4] Harinarayana T, Hota S, Kushwaha R. Vector field guidance for standoff target tracking. *Proceedings of the Institution of Mechanical Engineers, Part G: Journal of Aerospace Engineering*. 2022;236(14):2963-2973. doi:[10.1177/09544100211072320](https://doi.org/10.1177/09544100211072320)

* Communicating Author: Sikha Hota, Email ID: sikhahota@aero.iitkgp.ac.in

A Meshfree Numerical Solver for a Fractional Calculus Approach to Continuum Damage Mechanics

Malapeta Hemasundara Rao¹, M. Ramji², and Sai Sidhardh¹

¹*SMART Lab, Department of Mechanical and Aerospace Engineering, Indian Institute of Technology Hyderabad,
Kandi, Telangana 502285, India*

²*OPTICS Lab, Department of Mechanical and Aerospace Engineering, Indian Institute of Technology Hyderabad,
Kandi, Telangana 502285, India*

1. Introduction and Objective

Mesh-based numerical solvers, such as the Finite Element Method (FEM), often face challenges in meshing discontinuous geometries and in satisfying the enhanced continuity requirements. In contrast, the Element-Free Galerkin (EFG) method eliminates the need for a predefined mesh and utilizes the Moving Least Squares (MLS) formulation to construct higher-order continuous approximations. This study employs the EFG solver for a numerical solution of the integro-differential governing equations provided by a fractional-order constitutive model for nonlocal Continuum Damage Mechanics (CDM). The EFG solver is particularly well-suited for the present application, as it obviates the need for meshing and employs MLS-based approximants that can efficiently capture discontinuous geometries and complex boundary conditions. The EFG solver is particularly advantageous for fractional-order formulations, as it enables the effective capture of nonlocal effects. The present study leverages the strengths of fractional-order Continuum Damage Mechanics (f-CDM) while addressing the limitations of both local and conventional nonlocal formulations in modeling material degradation. The adoption of fractional-order strain-displacement relations eliminates pathological strain localization, thereby enhancing the robustness of the formulation. However, the MLS approximation alone is insufficient to guarantee mesh-independent softening responses in CDM problems. Furthermore, the proposed framework reduces the computational cost relative to conventional finite element approaches for damage modeling. Its effectiveness is demonstrated through numerical investigations of the material damage response.

2. Method of Analysis

Continuum Damage Mechanics (CDM) provides a powerful theoretical framework for describing the initiation and evolution of damage and fracture in solid materials [1]. The approach introduces an internal damage variable into the constitutive equations, enabling the representation of material degradation and softening effects. However, conventional local or integer-order CDM models face inherent challenges, particularly the tendency to produce pathological strain localization at the site where damage initiates [2]. This phenomenon often leads to artificial mesh sensitivity and unstable softening responses, highlighting the ill-posed character of local CDM formulations. In contrast, nonlocal continuum mechanics provides a more systematic means of mitigating strain localization. However, existing integer-order nonlocal formulations are not without drawbacks, as they may compromise objectivity and, therefore, require additional constraints to ensure consistency [2]. This highlights the need for a well-posed and robust framework for damage modeling. In this regard, the f-CDM framework has been developed in our previous works within the FEM solver [3]. Previous studies have demonstrated the efficacy of the f-CDM framework in delivering mesh-independent responses across both the linear elastic and softening regimes. While this establishes a well-posed and consistent approach for damage modeling, its mesh-based nature

¹ Corresponding author: Malapeta Hemasundara Rao (me23m25p100002@iith.ac.in)

entails certain limitations. In particular, achieving an accurate representation of damage requires mesh refinement in the vicinity of discontinuities and complex geometrical features within the structural domain. Moreover, implementing fractional calculus within mesh-based methods entails extensive bookkeeping to track the interactions among neighboring material points. This requirement significantly increases the computational cost, thereby limiting the efficiency of mesh-based approaches for large-scale damage simulations [4]. These limitations highlight a research gap in developing damage modeling strategies that reduce the computational cost associated with mesh-based methods. As an alternative, meshless methods have been increasingly employed in the literature to simulate structural behavior. In this study, a pseudo-meshfree approach, namely the EFG method, is adopted for damage modeling within the f-CDM framework. The EFG method facilitates the incorporation of fractional-order derivatives into the constitutive relations of the damage model. Furthermore, the EFG method eliminates the need for inter-element connectivity and efficiently constructs higher-order approximation functions through the MLS formulation [5, 6]. The MLS approximants are inherently slightly nonlocal, but they are not sufficient on their own to ensure mesh-independent softening responses in damage modeling. In this study, f-CDM is implemented within the EFG method to capture nonlocal effects in damage evolution accurately. The EFG method, utilizing MLS, enables the tracking of neighboring material points without the extensive bookkeeping typically required in mesh-based approaches when employing f-CDM. To demonstrate the effectiveness of the EFG method in conjunction with the f-CDM model, a numerical simulation of the damage model is conducted.

3. Highlights/Results

The f-CDM framework is successfully implemented within the EFG solver, demonstrating several significant advantages. The approach ensures mesh-independent softening responses, highlighting its robustness in capturing material degradation without sensitivity to discretization. The EFG method, which relies on MLS approximants, eliminates the need for predefined mesh connectivity and constructs smooth and continuous approximation functions across the domain. This flexibility enables the EFG solver to accurately handle complex geometrical features that commonly arise in structural domains during f-CDM modeling. Furthermore, the process of tracking neighboring material points becomes simpler, as the framework inherently manages point interactions without extensive bookkeeping, thereby reducing computational effort and improving overall efficiency.

4. Conclusions

The meshless EFG method coupled with the f-CDM framework provides an efficient and robust approach for damage modeling. It ensures mesh-independent softening responses while reducing computational cost. The framework is highly versatile and can be extended to study damage in heterogeneous materials, including composites.

5. References

1. Kachanov, L. Introduction to continuum damage mechanics, vol. 10 (Springer Science & Business Media, 1986).
2. Pijaudier-Cabot, G. & Bažant, Z. P. Nonlocal damage theory. *Journal of Engineering Mechanics* 113, 1512–1533 (1987).
3. Malapeta Hemasundara Rao; Shubham Kumar Singh; Ramji M, & Sai Sidhardh. Modeling Nonlocal Damage via Fractional-Order Constitutive Relations, “under review”
4. Rajan, A., Desai, S. & Sidhardh, S. Element-free Galerkin method for a fractional-order boundary value problem. *International Journal for Numerical Methods in Engineering* 125, e7429 (2024).
5. Belytschko, T., Lu, Y. Y. & Gu, L. Element-free galerkin methods. *International Journal for Numerical Methods in Engineering* 37, 229–256 (1994).
6. Lu, Y., Belytschko, T. & Gu, L. A new implementation of the element-free Galerkin method. *Computer methods in applied mechanics and engineering* 113, 397–414 (1994).

A Reduced-order Homogenized Plate Model of Sandwich Structure Using Variational Asymptotic Method

Anup Kumar Pathak^{a*} and Pritam Chakraborty^b

^aIPDF, Aerospace Engineering, Indian Institute of Technology Kanpur, India

^bAssociate Professor, Aerospace Engineering, Indian Institute of Technology Kanpur, India

*Communicating Author: Anup Kumar Pathak, Email: anupkp@iitk.ac.in

1. INTRODUCTION & OBJECTIVE

Sandwich structures offer high stiffness-to-weight ratio making them suitable for aerospace, automotive, and naval industries. These structures can be optimized for different scenarios and loading conditions by changing their core and facesheet geometry, and properties. However, modeling these structures in full 3D at the length-scale of components can be extremely costly, therefore, requiring the need to develop reduced-order homogenized plate models. The objective of the present work is to develop a mathematically rigorous and asymptotically correct homogenized reduced-order model for sandwich structures using the following two-step approach.

1. Variational Asymptotic Method (VAM) to reduce the 3D structure into an inhomogeneous 2D plate.
2. Homogenization of the fast periodic micro-response to obtain a homogeneous 2D plate model at the component scale.

2. METHODS OF ANALYSIS

Sandwich structures are 3D with one dimension (thickness) significantly smaller than the other two dimensions (length and width). VAM is applied to obtain an asymptotically correct 2D plate model by taking advantage of the small quantities inherent to the problem, like strains and thickness-to-length ratio [1,2]. The dimensional reduction is done by taking the through-the-thickness structure into account [3]. The resulting 2D plate model, comprising in-plane unit cells, is inhomogeneous. To homogenize it, this work uses two coordinate systems [4]:

- Global coordinates (x_1, x_2) for the whole plate.
- Local coordinates (y_1, y_2) for the unit cell.

Similar to the First-Order Shear Deformation Plate Theory (FSDT) [5, 6], the 2D plate model expresses the displacement field for the plate in terms of five in-plane primary variables – three displacements (u_i , $i = 1, 2, 3$) and two rotations (ϕ_α , $\alpha = 1, 2$). These variables are split into two parts:

$$\begin{aligned} u_i(x_1, x_2; y_1, y_2) &= v_i(x_1, x_2) + w_i(x_1, x_2; y_1, y_2), \\ \phi_\alpha(x_1, x_2; y_1, y_2) &= \psi_\alpha(x_1, x_2) + \theta_\alpha(x_1, x_2; y_1, y_2), \end{aligned} \quad (1)$$

where v_i and ψ_α are the average displacements and rotations, respectively. w_i and θ_α are the fluctuations over the averaged values.

By applying the principle of virtual work, the governing equations for the fluctuating fields and the averaged variables are obtained. The equations for the fluctuating components and the averaged variables are solved analytically and numerically, respectively, considering the continuity of the displacements across the boundaries of the unit cells.

3. RESULTS AND HIGHLIGHTS OF IMPORTANT POINTS

One typical example of such structures is shown in Fig. 1, where different colors represent different materials. For such structures, analytical solutions for the fluctuating components in terms of the averaged displacements are obtained.

These solutions are given as follows:

$$w_i = y_\alpha \frac{\partial v_i}{\partial x_\alpha}, \quad \theta_\alpha = y_\beta \frac{\partial \psi_\alpha}{\partial x_\beta} \quad (2)$$

The key highlights of the present work are as follows:

- The reduced-order model obtained using VAM captures the asymptotically correct deformation, avoiding *ad hoc* and *a priori* assumptions.
- The homogenized model includes the effect of in-plane periodic unit cells.
- The method reduces computational complexity while maintaining high accuracy.

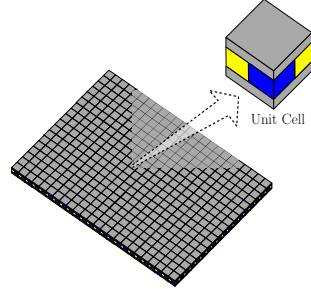


Figure 1: Inhomogeneous anisotropic plate with repetitive microstructure,

4. CONCLUSIONS

A simple and efficient method for analyzing inhomogeneous plates with repetitive microstructure is presented. The combination of VAM and two-scale homogenization gives a homogenized reduced-order plate model. This model can be used for advanced plate-like composite structures engineered for different scenarios. Future work will extend it to thermal and nonlinear problems.

5. REFERENCES

References

- [1] W. Yu, D. H. Hodges and V. V. Volovoi, “Asymptotic construction of Reissner-like composite plate theory with accurate strain recovery,” *Int. J. Solids Struct.*, vol. 39, no. 20, pp. 5185–5203, 2002.
- [2] A. K. Pathak, S. J. Singh and S. S. Padhee, “Asymptotically correct isoenergetic formulation of geometrically nonlinear anisotropic plates,” *Mech. Adv. Mater. Struct.*, 2024.
- [3] A. K. Pathak, S. J. Singh and S. S. Padhee, “Geometrically nonlinear analysis of composite plates through asymptotically accurate isoenergetic theory,” *Compos. Part A: Appl. Sci. Manuf.*, vol. 191, p. 108712, 2025.
- [4] W. Yu and T. Tang, “Variational asymptotic method for unit cell homogenization of periodically heterogeneous materials,” *Int. J. Solids Struct.*, vol. 44, pp. 3738–3755, 2007.
- [5] E. Reissner, “The effect of transverse shear deformation on the bending of elastic plates,” *J. Appl. Mech.*, vol. 12, pp. A69–A77, 1945.
- [6] R. D. Mindlin, “Influence of rotary inertia and shear on flexural motions of isotropic, elastic plates,” *J. Appl. Mech.*, vol. 18, no. 1, pp. 31–38, 1951.

A Scalar LPCE–ALE Framework for Sound Generation in Low-Mach Number Flows with Moving Boundaries

Kevin S. Swamy^a and Vaibhav Joshi^{a,*}

^aDepartment of Mechanical Engineering, Birla Institute of Technology & Science Pilani
K K Birla Goa Campus, NH 17B Bypass Road, Zuarinagar, Sancoale, Goa 403726, India

1. INTRODUCTION & OBJECTIVE

The study of sound generation in fluid flows has been a central theme in fluid mechanics and acoustics. Acoustic analogy by Lighthill [1, 2] reformulated the compressible Navier–Stokes equations into a wave equation with turbulence-driven source terms, providing a foundation for aeroacoustics. Extensions by Curle [3] and Ffowcs Williams–Hawkins (FW–H) [4] incorporated the effects of rigid and moving boundaries, enabling the treatment of more realistic fluid–structure configurations. Still, integral formulations face challenges when hydrodynamic and acoustic scales overlap, particularly in low Mach number flows.

To address these limitations, decomposition-based approaches were developed. Acoustic/viscous splitting by Hardin and Pope [5] separated acoustic fluctuations from vortical and entropic motions, paving the way for acoustic perturbation equations (APE) by Ewert and Schröder [6]. For improved efficiency in low Mach number regimes, the perturbed and linearized perturbed compressible equations (PCE/LPCE) were introduced by Seo and Moon [7, 8], which linearize the governing equations about an incompressible base flow, capturing acoustic propagation while suppressing spurious compressibility.

Moving boundary problems add another layer of difficulty, as deforming fluid domains cannot be represented adequately in a purely Eulerian framework. The arbitrary Lagrangian–Eulerian (ALE) method by Donea et al. [9] provides a robust approach by allowing mesh motion that follows boundary displacements while maintaining consistent fluid transport.

Building on these advances, the present work develops a computational hydroacoustic framework for low Mach number flows with moving boundaries. By deriving the scalar LPCE-wave equation in the ALE framework, the approach enables efficient and accurate simulation of hydrodynamic fluctuations and their associated acoustic radiation in deforming domains.

2. FORMULATION OF THE SCALAR LPCE IN THE ALE FRAME

Assuming linear acoustics, i.e. small perturbations and neglecting second-order terms, viscous stresses, and thermal effects, the LPCE in the ALE framework can be expressed as:

$$\begin{aligned} \frac{D\rho^a}{Dt}\Big|_{ALE} + \rho_0 \nabla \cdot \mathbf{v}^a = 0, \quad \frac{D\mathbf{v}^a}{Dt}\Big|_{ALE} + \frac{1}{\rho_0} \nabla p^a = 0, \text{ and} \\ \frac{Dp^a}{Dt}\Big|_{ALE} + \gamma P^{ic} \nabla \cdot \mathbf{v}^a + (\mathbf{v}^a \cdot \nabla) P^{ic} = -\frac{DP^{ic}}{Dt}\Big|_{ALE} \end{aligned} \quad (1)$$

Here $D/Dt|_{ALE} = \partial/\partial t|_{ALE} + (\mathbf{v}^{ic} - \mathbf{w}) \cdot \nabla$, where \mathbf{v}^{ic} and \mathbf{w} are the incompressible fluid velocity and the mesh velocity, respectively. P^{ic} is the incompressible fluid pressure, ρ_0 the reference density, and γ denotes the ratio of specific heats. Introducing the scalar acoustic potential ψ^a with $\mathbf{v}^a = -\nabla\psi^a$ yields the compact scalar LPCE:

$$\frac{D^2\psi^a}{Dt^2}\Big|_{ALE} - \frac{\gamma P^{ic}}{\rho_0} \nabla^2 \psi^a - \frac{1}{\rho_0} \nabla \psi^a \cdot \nabla P^{ic} = -\frac{1}{\rho_0} \frac{DP^{ic}}{Dt}\Big|_{ALE} \quad (2)$$

Equation 2 expresses the acoustic field in terms of a single scalar potential, providing a compact and efficient framework for sound propagation in deforming fluid domains.

3. MODEL VALIDATION USING FLOW OVER A CIRCULAR CYLINDER

The accuracy of the scalar LPCE–ALE formulation is evaluated using flow over a circular cylinder at low Mach numbers. Two benchmark configurations are considered to assess the model performance in both stationary and moving boundary conditions. In both cases, the acoustic pressure fluctuation Δp^a is defined following Seo and Moon [7] and Wang et al. [10] as $\Delta p^a = (\bar{P}^{ic} + p^a) - (\bar{P}^{ic} + p^a)$, where the overbar denotes the statistical mean of that quantity. For consistency across cases, Δp^a is further non-dimensionalised by the reference dynamic pressure scale $\rho_0 c_0^2$, where c_0 is the speed of sound in the medium.

First, the stationary cylinder benchmark of Seo and Moon [7] at $Re = \rho_0 U_\infty D / \mu = 200$ and $Ma = U_\infty / c_0 = 0.3$ is examined. Here, U_∞ is the freestream velocity, D is the diameter of the cylinder and μ is the dynamic viscosity

of the fluid. This case is widely used for validating low Mach number acoustic models, as it captures the coupling between vortex shedding and acoustic radiation. Figure 1a shows the predicted acoustic pressure distribution along the line at $\theta = 90^\circ$. The present results are in close agreement with the direct numerical simulation (DNS) data of Seo and Moon [7], demonstrating the ability of the formulation to resolve hydrodynamic–acoustic coupling.

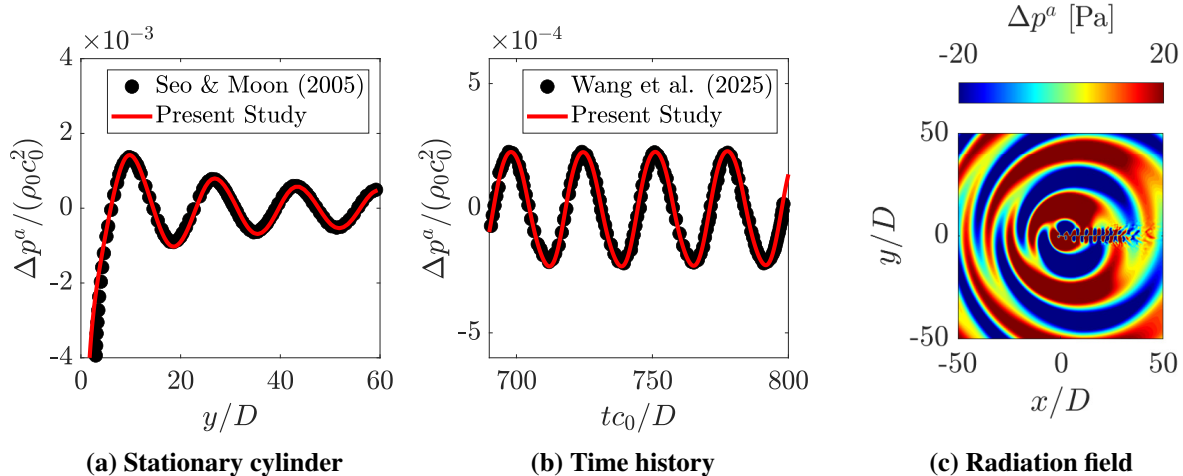


Figure 1: Validation of the scalar LPCE–ALE formulation: (a) acoustic pressure distribution along $\theta = 90^\circ$ for the stationary cylinder compared with DNS data by Seo and Moon [7], (b) time history of acoustic pressure at $r = 75D$, $\theta = 90^\circ$ for the oscillating cylinder compared with reference data by Wang et al. [10], and (c) acoustic radiation contours for the oscillating cylinder.

Second, a forced oscillating cylinder at $Re = 150$ and $Ma = 0.2$ with sinusoidal motion, as described by Wang et al. [10], is considered. This case introduces moving boundary effects and thereby tests the robustness of the ALE framework under coupled flow–structure motion. Figure 1b presents the time history of acoustic pressure at a monitoring point located at $r = 75D$ and $\theta = 90^\circ$, showing good agreement with reference data. The corresponding acoustic radiation field is shown in Figure 1c. A qualitative comparison with the reference contour of Wang et al. [10] confirms that the present model accurately reproduces the radiation patterns associated with boundary oscillation.

4. CONCLUSIONS

The scalar LPCE in the ALE framework was validated using stationary and oscillating cylinder benchmarks. The model successfully captured hydrodynamic–acoustic coupling and sound radiation from moving boundaries, confirming its consistency and efficiency for incompressible flows with structural motion.

5. REFERENCES

- [1] M. J. Lighthill, “On sound generated aerodynamically I. General theory,” *Proceedings of the Royal Society of London. Series A. Mathematical and Physical Sciences*, vol. 211, no. 1107, pp. 564–587, 1952.
- [2] ——, “On sound generated aerodynamically II. Turbulence as a source of sound,” *Proceedings of the Royal Society of London. Series A. Mathematical and Physical Sciences*, vol. 222, no. 1148, pp. 1–32, 1954.
- [3] N. Curle, “The influence of solid boundaries upon aerodynamic sound,” *Proceedings of the Royal Society of London. Series A. Mathematical and Physical Sciences*, vol. 231, no. 1187, pp. 505–514, 1955.
- [4] J. F. Williams and D. L. Hawkings, “Sound generation by turbulence and surfaces in arbitrary motion,” *Philosophical Transactions for the Royal Society of London. Series A, Mathematical and Physical Sciences*, pp. 321–342, 1969.
- [5] J. C. Hardin and D. S. Pope, “An acoustic/viscous splitting technique for computational aeroacoustics,” *Theoretical and computational fluid dynamics*, vol. 6, no. 5, pp. 323–340, 1994.
- [6] R. Ewert and W. Schröder, “Acoustic perturbation equations based on flow decomposition via source filtering,” *Journal of Computational Physics*, vol. 188, no. 2, pp. 365–398, 2003.
- [7] J.-H. Seo and Y. J. Moon, “Perturbed compressible equations for aeroacoustic noise prediction at low Mach numbers,” *AIAA journal*, vol. 43, no. 8, pp. 1716–1724, 2005.
- [8] J. H. Seo and Y. J. Moon, “Linearized perturbed compressible equations for low Mach number aeroacoustics,” *Journal of Computational Physics*, vol. 218, no. 2, pp. 702–719, 2006.
- [9] J. Donea, A. Huerta, J.-P. Ponthot, and A. Rodríguez-Ferran, “Arbitrary Lagrangian–Eulerian methods,” *Encyclopedia of computational mechanics*, 2004.
- [10] K. Wang, G. Jin, T. Ye, Y. Chen *et al.*, “Aerodynamic and acoustic analysis of a self-excited oscillation cylinder in a low Mach flow using a hybrid method,” *Journal of Fluids and Structures*, vol. 136, p. 104339, 2025.

*Communicating Author: Vaibhav Joshi, vaibhavj@goa.bits-pilani.ac.in.

Aerodynamic Performance of a Multi-Element Flapping Foil Inspired from the Feathered Wings of Birds

Avinash Kumar Pandey^{1,2}, Rajneesh Bhardwaj², Rajat Mittal¹

¹Department of Mechanical Engineering, Johns Hopkins University, Baltimore, MD, USA.

²Department of Mechanical Engineering, Indian Institute of Technology Bombay, Mumbai, India

1 Introduction and Objective

The evolution of biological flight has produced diverse structural and kinematic strategies for generating aerodynamic forces. Insects rely on lightweight wings reinforced with veins to balance stiffness and flexibility, while bats use compliant membranes to achieve high maneuverability. Birds are distinct, as their wings are composed of multiple feathers attached to a skeletal framework, where each feather can deform and rotate independently, creating complex aerodynamic interactions [1, 2]. This modularity is hypothesized to act as a biomechanical check-valve, reducing resistance during the wing's recovery phase [3]. However, the aerodynamic role of multiple interacting feathers and their contribution to the aerodynamic force generation is not fully understood.

Inspired by the arrangement of feathers in bird wings, we propose a simplified model of a multi-element flapping foil composed of feather-like membranes undergoing combined heaving and pitching motions (figure 1). This study investigates the aerodynamic role of biased feather pitching, examining how passive upstroke rotations affect lift and power, how multi-feather arrangements compare to a single feather, the influence of feather-length combinations on performance, and the impact of Strouhal number and heave amplitude on optimal configurations through inter-feather interactions.

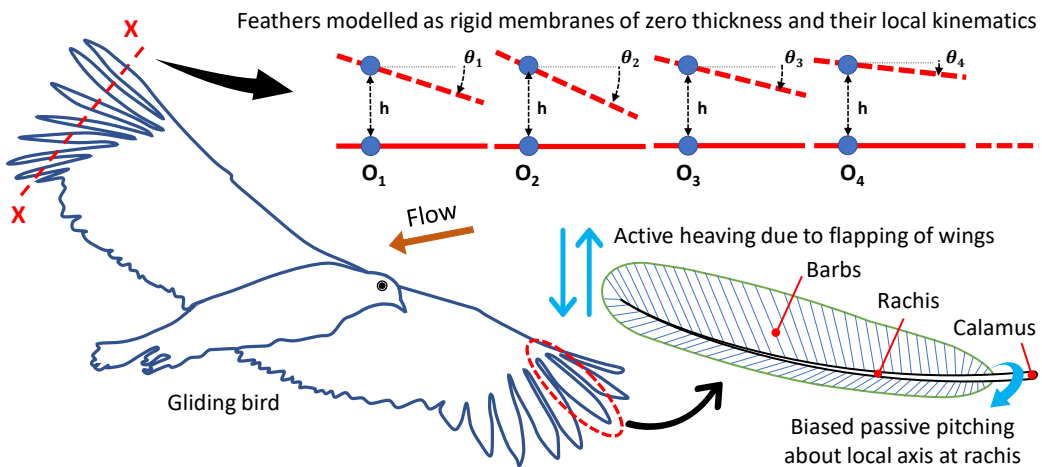


Figure 1: Schematic of a bird wing in a forward avian flight, and the anatomy and local kinematics of a typical feather. Considering a cross-section across the bird wing, the collective fluid-structure interaction of multiple feathers is modeled as a series of rigid membranes undergoing combined pitching and heaving motion about their leading edge.

2 Computational Methodology and Parametric Space

In the present numerical study, we consider a simplified configuration of three thin rigid membranes—referred to as feathers—arranged in tandem along the chord of a flapping foil (figure 1). These mimic the local kinematics of avian primary and secondary feathers. Each feather undergoes collective wing motion, modeled as a sinusoidal heave, as well as localized passive rotation via flow-induced biased pitching about its leading edge. The feathers are one-way coupled to an incompressible flow field, capturing the combined effects of heaving and pitching motions on the aerodynamic performance.

Two-dimensional fluid-structure interaction (FSI) simulations are performed using the in-house solver ViCar3D. The system is governed by seven non-dimensional parameters: L_1 , L_2 , C , I , Re , h_0 , and St . Feather lengths are defined as $L_k = L_k^*/C$ ($k = 1, 2, 3$), with $L_1 + L_2 + L_3 = C = 1$. Assuming thin, rigid membranes, the moment of inertia scales as $I_k \approx L_k^3$. Simulation parameters reflect typical avian flight conditions [4, 5]. The Reynolds number is fixed at $Re = 5000$ [4]. The Strouhal number is based on the peak-to-peak heave amplitude ($2h_0 = 2h_0^*/C$), given by $St = 2h_0 f_h$, where f_h is the heave frequency. Three Strouhal numbers ($St = 0.08, 0.12, 0.2$) and heave amplitudes ($h_0 = 0.1, 0.2, 0.3$) are examined, representing values typical of cruising flight in small and medium-sized birds [5]. Aerodynamic performance is evaluated using the mean lift (F_L), mean power (P), and their ratio ($\eta = F_L/P$), while flow structures are analyzed via vorticity, pressure, and leading-edge vortex (LEV) dynamics.

3 Results and Key Findings

The baseline single-feather configuration demonstrates the fundamental role of biased pitching. With unbiased rotation, the feather produces symmetric wakes and negligible net lift. In contrast, imposing bias during the upstroke suppresses positive vorticity beneath the foil and yields a positive mean lift ($F_L \approx 0.28$).

With multiple feathers, the aerodynamic benefits increase substantially. In general, feathers exhibit non-linear yet periodic pitching after the initial transient, producing a periodic lift response. Optimal length combinations produce up to twice the lift of a single-feather configuration without additional power input. The best-performing designs achieve $\eta \approx 1.9$ at $St = 0.08$, $\eta \approx 1.73$ at $St = 0.12$, and $\eta \approx 1.2$ at $St = 0.20$. Because higher St corresponds to increased heaving frequency, the associated rise in power input reduces the lift-to-power ratio. These configurations minimize negative lift during the upstroke, and in some cases even generate small positive lift, while sustaining strong positive lift in the downstroke, thereby enhancing overall mean lift. Wake visualizations reveal that constructive and destructive LEV interactions are the dominant mechanism behind these improvements. At higher St , destructive interference mitigates positive vorticity during the upstroke, while constructive interference enhances pressure differences during the downstroke. Power consumption is redistributed, with downstream feathers requiring less input energy due to favorable wake interactions.

The Strouhal number strongly influences the optimal feather configuration, shifting the peak location in (L_1, L_2) space as St varies. In contrast, changes in heave amplitude have minor effects. Inter-feather interactions redistribute lift and power, highlighting the role of multiple feathers in enhancing the lift-to-power ratio. These interaction effects are pronounced at the higher Strouhal numbers ($St = 0.2$).

4 Conclusions

This study proposes a feather-inspired, segmented flapping foil design and demonstrates that it can substantially enhance aerodynamic performance compared to a foil with single-feather. The key mechanisms include suppression of negative lift during the upstroke and constructive inter-feather vortex interactions that redistribute lift and power, thereby increasing the lift-to-power ratio. These results suggest that segmented feathers significantly influence bird wing aerodynamics and provide valuable insights for bio-inspired applications in micro- and unmanned aerial vehicles.

References

- [1] H. R. Vejdani, D. B. Boerma, S. M. Swartz, and K. S. Breuer, “The dynamics of hovering flight in hummingbirds, insects and bats with implications for aerial robotics,” *Bioinspiration & Biomimetics*, vol. 14, no. 1, p. 016003, 2018.
- [2] U. M. Norberg, *Vertebrate flight: mechanics, physiology, morphology, ecology and evolution*, vol. 27. Springer Science & Business Media, 2012.
- [3] T. L. Hedrick, J. R. Usherwood, and A. A. Biewener, “Wing inertia and whole-body acceleration: an analysis of instantaneous aerodynamic force production in cockatiels (*nymphicus hollandicus*) flying across a range of speeds,” *Journal of Experimental Biology*, vol. 207, no. 10, pp. 1689–1702, 2004.
- [4] J. H. Park and K.-J. Yoon, “Designing a biomimetic ornithopter capable of sustained and controlled flight,” *Journal of Bionic Engineering*, vol. 5, no. 1, pp. 39–47, 2008.
- [5] G. K. Taylor, R. L. Nudds, and A. L. Thomas, “Flying and swimming animals cruise at a strouhal number tuned for high power efficiency,” *Nature*, vol. 425, no. 6959, pp. 707–711, 2003.

Altitude Control of Powered Parafoil Systems using Extended State Observer-Finite-time Sliding Mode Control (ESO-FTSMC)

Nitin Pal and N.K. Peyada

Research Scholar, Dept. of Aerospace Engineering, Indian Institute of Technology Kharagpur, Kharagpur, India.

Associate Professor, Dept. of Aerospace Engineering, Indian Institute of Technology Kharagpur, Kharagpur, India.

1. INTRODUCTION & OBJECTIVE

The powered parafoil is a highly safe and controllable aircraft that evolved from air sports and is now broadly used in military and civilian applications like airdrops and reconnaissance. Due to the addition of a power system, it offers enhanced stagnation capability and controllability, making its control algorithm a key research area. While methods like Feedback Linearization Control and Adaptive Fuzzy Back-stepping have been explored, this complex, flexible aircraft remains sensitive to disturbances and modeling uncertainties.

To achieve robust control despite system perturbations, this study proposes a novel Extended State Observer-Finite-time Sliding Mode Control (ESO-FTSMC) strategy. Based on an established 8-DOF parafoil dynamics model, the goal is to leverage the ESO to estimate system uncertainties and disturbances and then use an exponential approach sliding mode controller. The effectiveness and superior anti-disturbance performance of the ESO-FTSMC method will be verified through simulation under gust disturbances and compared against traditional SMC.

2. METHODS OF ANALYSIS

The development of the powered parafoil system's dynamics model relies on establishing a set of coupled differential equations that accurately capture the system's motion. This study employs an 8-Degrees-of-Freedom (DOF) dynamic model based on the Kirchhoff equation of motion, which is necessary to account for the crucial relative pitch (θ_r) and relative yaw (ψ_r) motion between the payload (carrier) and the flexible parafoil canopy. This involves establishing coupled differential equations for the momentum (P) and momentum moment (H) for both parts, accounting for forces (F) like aerodynamics, gravity, thrust, and rope tension. The final model's is demonstrated in its state vector X , which is a combined set of 8 independent variables:

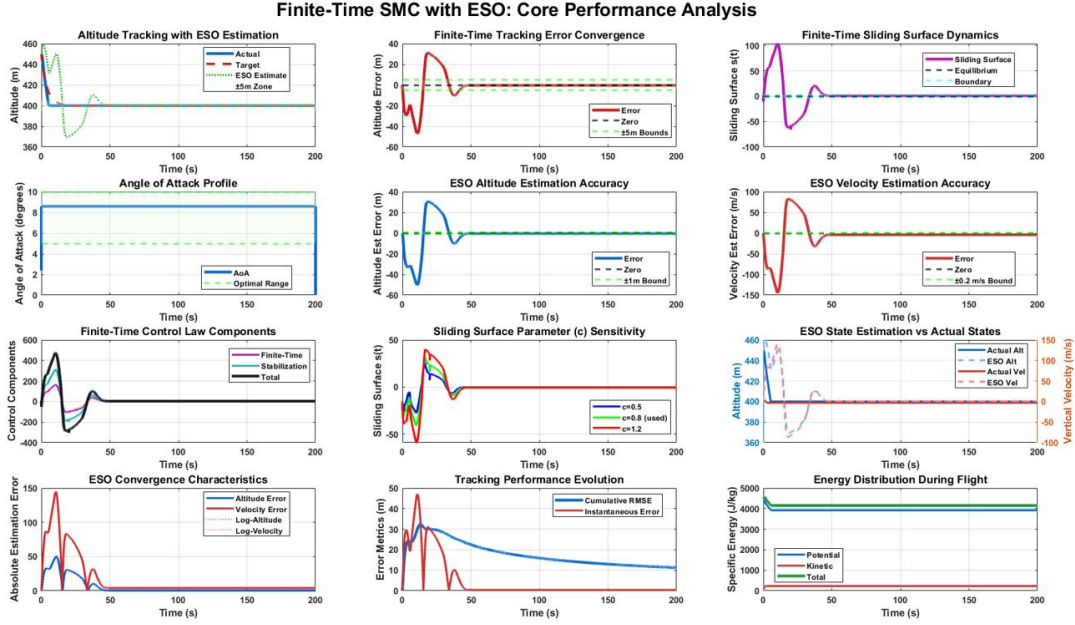
$$X = [V_w^T, W_w^T, V_s^T, W_s^T, \psi_r, \theta_r]^T$$

This vector includes the linear and angular velocities of both the payload and the parafoil, as well as the two relative angular motions (ψ_r and θ_r), resulting in the 8-DOF system.

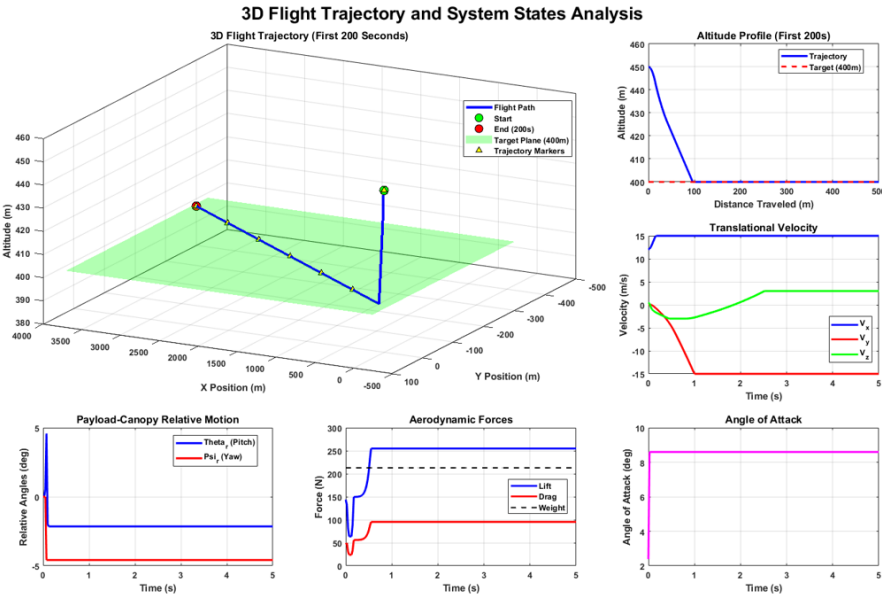
The control method developed for the highly nonlinear parafoil system is the Extended State Observer-Finite-time Sliding Mode Control (ESO-FTSMC), designed to ensure precise altitude tracking despite system complexities and external disturbances. The Extended State Observer is the system's real-time disturbance compensator. It estimates not only measurable states (like altitude and vertical speed) but also a special extended state that lumps together all un-modeled dynamics, internal uncertainties, and external disturbances (such as wind gusts). By accurately predicting, the ESO effectively simplifies the control problem. Unlike standard SMC, the FTSMC uses a modified sliding surface reaching law designed to guarantee that the system reaches the sliding surface in a finite, amount of time. This ensures faster convergence and better transient performance than asymptotic convergence. Thus the proposed strategy combines the ESO's robust disturbance rejection with the FTSMC's finite-time convergence which provides strong anti-disturbance capabilities and superior response speed, ensuring the parafoil quickly and accurately converges to maintains the target altitude, even under adverse conditions, surpassing the performance of traditional control methods.

3. RESULTS

The complex nonlinear 8 DOF model of the powered parafoil is modeled in MATLAB 2021a using the appropriate parameters to effectively demonstrate the parafoil motion's characteristics.



Figures present a comprehensive analysis of the finite-time sliding mode controller (SMC) with extended state observer (ESO) performance for powered parafoil altitude control. The plots demonstrate excellent altitude tracking convergence, with the system rapidly stabilizing at the 400-meter target altitude within tight ± 5 -meter bounds. The ESO effectively estimates both altitude and velocity states, showing minimal estimation errors while accurately compensating for system disturbances.



4. CONCLUSIONS

The finite-time sliding mode controller with extended state observer successfully achieves precise altitude tracking with robust disturbance rejection. The system demonstrates excellent convergence properties and maintains stable flight performance throughout the mission.

5. REFERENCES

- [1]. S. Nie, Y. Cao, Z. Wu, Numerical simulation of parafoil inflation via a Robin–Neumann transmission-based approach, Proc. Inst. Mech. Eng., G J. Aerosp. Eng. 232(4) (2018) 797–810, <https://doi.org/10.1177/0954410016688925>.
- [2]. S. Luo, Q. Sun, W. Wu, et al., Accurate flight path tracking control for powered parafoil aerial vehicle using ADRC-based wind feedforward compensation, Aerospace Sci. Technol. 84 (2019) 904–915, <https://doi.org/10.1016/j.ast.2018.11.022>.
- [3]. J. Stein, C. Madsen, A. Strahan, An overview of the guided parafoil system derived from X-38 experience, in: 18th AIAA Aerodynamic Decelerator Systems Technology Conference and Seminar, 2005, p.1652.
- [4]. C. Dek, J. Overkamp, A. Toeter, et al., A recovery system for the key components of the first stage of a heavy launch vehicle, Aerospace Sci. Technol. 100 (2020) 105778, <https://doi.org/10.1016/j.ast.2020.105778>.
- [5]. Q. Sun, L. Yu, Y. Zhengetal. Aerospace Science and Technology 122(2022)107406
- [6]. J. Tao, Q. Sun, Z. Chen, et al., NSGAII based multi-objective homing trajectory planning of parafoil system, J. Cent. South Univ. 23 (2016) 3248–3255, <https://doi.org/10.1007/s11771-016-3390-8>.

Analysis of Temporal Oscillations of a Deflected Wake in a Plunging Foil Using Proper Orthogonal Decomposition

Mohamed Aniffa S^a, Sunetra Sarkar^{b*}

^a Post-Doctoral Fellow, Department of Aerospace Engineering, Indian Institute of Technology Madras, Chennai, India

^b Professor, Department of Aerospace Engineering, Indian Institute of Technology Madras, Chennai, India

1. INTRODUCTION & OBJECTIVE

Flapping wings and fins generate unsteady vortices that influence thrust, drag, and efficiency in bio-inspired systems such as MAVs and energy harvesters. These motions are typically represented by pitching or plunging kinematics and are quantified using the non-dimensional plunge velocity, $kh = \frac{2\pi f_0 h_0}{U_\infty}$, where f_0 is the pitch/plunge frequency, h_0 is the plunge amplitude, and U_∞ is the freestream velocity [1, 2].

At low kh , the wake forms a classical von Kármán vortex street, which is typically associated with drag [1]. Beyond a critical kh , the wake transitions to a reverse von Kármán pattern, generally producing thrust through a jet-like velocity profile [1]. For $kh \leq 1$, vortices remain symmetric about the mean plunging line [3]. However, when $kh > 1$, the wake often deflects, and this deflection may evolve in an irregular (dynamically quasi-periodic or intermittent) manner. The temporal oscillation of the wake deflection is usually estimated using the wake deflection angle [4]. Estimating this angle at different time instants is challenging, since the centerline of the deflected wake may follow a curved [2] or even an undefined path. To the best of our knowledge, no alternative method has been reported in the literature for determining the temporal oscillation/dynamics of the deflected wake.

Therefore, we ask: *Is there an alternative way to determine the temporal oscillations/dynamics of the deflected wake in the flow field?* To address this question, we employ Proper Orthogonal Decomposition (POD), as it isolates the dominant global features of the wake in terms of modes and their associated energies. Moreover, POD provides both spatial and temporal information of the modes. It should be noted that other modal decomposition methods, such as Dynamic Mode Decomposition (DMD) and Spectral POD, are not considered here because wake deflection is not limited to a single temporal scale or frequency.

2. METHODS OF ANALYSIS

An elliptical foil with unit chord length c and thickness-to-chord ratio of 0.12 is considered in the present study. Its sinusoidal plunging motion is defined as $y_c(t) = h \sin(kt)$, where y_c is the non-dimensional displacement, $h = h_0/c$ is the non-dimensional plunge amplitude, and $k = \frac{2\pi f_0 c}{U_\infty}$ is the reduced frequency.

The flow is simulated using a discrete-forcing immersed boundary method (IBM) solver for the incompressible two-dimensional Navier–Stokes equations [3], at a Reynolds number of $Re = U_\infty c / \nu = 300$. Following the earlier study [3], four cases are considered under the same flow conditions: (i) an undeflected wake ($kh = 0.5$), (ii) a slightly deflected wake where the deflection angle does not change with time ($kh = 1$), and (iii–iv) deflected wakes where the deflection angle changes with time ($kh = 1.5$ and 1.7). These regimes are confirmed using instantaneous vorticity contours, which are not shown here for brevity. To identify the dominant flow structures and their spatio-temporal variations, uv -POD analysis is carried out. The fluctuating streamwise (u) and vertical (v) velocity components in the wake (downstream of the trailing edge) are used to construct a snapshot matrix, \mathbf{Q} . A singular value decomposition (SVD) is then performed on \mathbf{Q} , yielding

$$\mathbf{Q}' = \text{SVD}(\mathbf{Q}) = \mathbf{U} \mathbf{S} \mathbf{V}^T, \quad (1)$$

where \mathbf{U} contains spatial modes, \mathbf{S} the modal energies, and \mathbf{V} the temporal coefficients.

It is noted that the velocity data corresponding to 54 oscillation cycles of the elliptical body, excluding the initial transient dynamics, were considered for the POD analysis. The data were sampled at a frequency approximately 64 times the plunge frequency, which is sufficient to resolve the temporal dynamics of the wake. Furthermore, the convergence of the sampling duration was verified by examining the variation of modal energies with sampling time; however, these results could not be presented here for brevity but will be discussed during the conference presentation.

3. RESULTS

The temporal coefficients of the first and second POD modes for all kh values considered in this study exhibit periodic oscillations, as shown in figure 1(a–d, i–j). This behavior is expected due to the presence of traveling structures in the

*Communicating Author: sunetra.sarkar@gmail.com

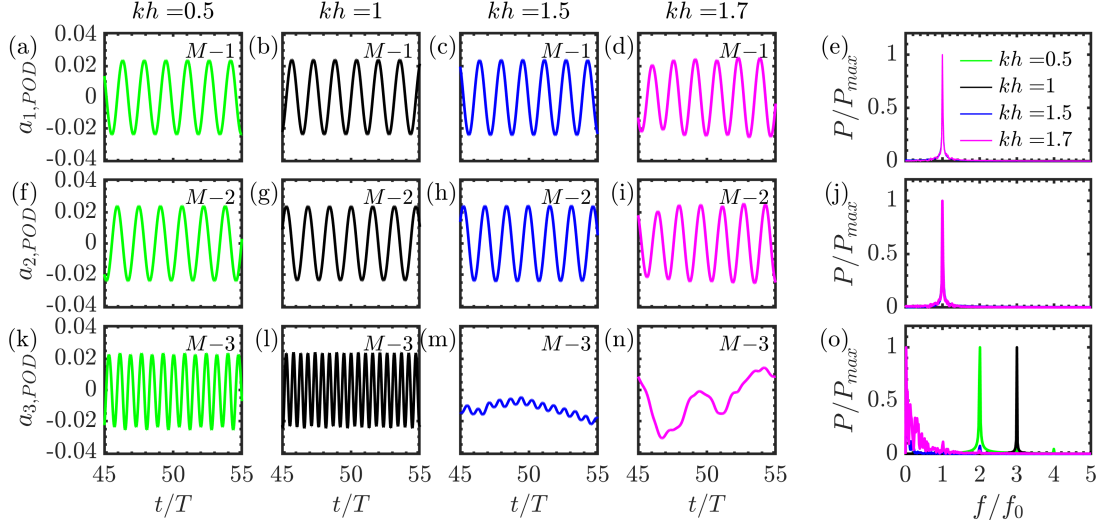


Figure 1: Temporal coefficients of the POD modes and their corresponding frequency spectra for different values of kh .

wake, and their peak frequencies coincide with the plunging frequency, as seen in figure 1(e, j).

In contrast, the temporal coefficients of the third POD mode display distinct characteristics across all kh values, as shown in figure 1(k–n). For $kh = 0.5$ and 1, the dominant peaks occur at superharmonic frequencies ($f/f_0 = 2$ and 3, respectively), as illustrated in figure 1(o). At higher kh values (1.5 and 1.7), no clear peak is observed; instead, the energy is distributed over a range of low frequencies, which is also evident in figure 1(o). Our analysis indicates that this behavior originates from the temporal change of maximum wake deflection, supported by the correlation between the temporal variation of $a_{3,POD}$ and the maximum wake deflection (not shown here for brevity). To the best of our knowledge, this link between the temporal dynamics of the deflected wake and the third POD mode has not been reported previously in the literature. It is noted that the oscillation frequency of the deflected wake does not have any clear relation to the plunge frequency. This may be because of the irregular interaction between the vortices that leads to sustain the wake deflection and possible switching [3].

4. CONCLUSIONS

The wake of the plunging elliptical body was analyzed using *uv*-POD for $kh = 0.5, 1, 1.5$, and 1.7 at $Re = 300$. For $kh = 0.5$ and 1, where the wake deflection does not change with time, the temporal coefficients of the first three dominant POD modes show periodic oscillations. The peak frequencies of the first two modes coincide with the plunging frequency of the body, while the third mode shows a superharmonic response. For $kh = 1.5$ and 1.7, where the wake deflection changes over time, the periodicity of the third mode weakens, and its dynamics correlate with the temporal variation of the maximum wake deflection. These results demonstrate that *uv*-POD can reliably capture both the qualitative behavior (temporal oscillations) and the quantitative features (characteristic time scales) of deflected wakes in flapping-body flows.

5. REFERENCES

- [1] J. C. S. Lai and M. F. Platzer, “Jet characteristics of a plunging airfoil,” *AIAA J.*, vol. 37, no. 12, pp. 1529–1537, 1999.
- [2] C. Bose, S. Gupta, and S. Sarkar, “Dynamic interlinking between near-and far-field wakes behind a pitching-heaving airfoil,” *J. Fluid Mech.*, vol. 911, p. A31, 2021.
- [3] D. Majumdar, C. Bose, and S. Sarkar, “Capturing the dynamical transitions in the flow-field of a flapping foil using immersed boundary method,” *J. Fluids Struct.*, vol. 95, p. 102999, 2020.
- [4] D. Majumdar, C. Bose, and S. Sarkar, “Effect of gusty inflow on the jet-switching characteristics of a plunging foil,” *Phys. Fluids*, vol. 32, no. 11, 2020.

Analytical Investigation for Free Vibrations Analysis of Functionally Graded Sandwich Plates with Advanced Gradation Laws

Ankitha Kamath^a, Supen Kumar Sah^{b*}, Anup Ghosh^c

^aSchool of Mechanical Engineering, VIT Bhopal University, Madhya Pradesh, India

^bDepartment of Mechanical Engineering, SRM University, Andhra Pradesh, India

^cDepartment of Aerospace Engineering, IIT Kharagpur, West Bengal, India

1. Introduction and Objective

Functionally graded materials (FGMs) with engineered gradations of composition offer enhanced mechanical performance, but their vibrational behavior under realistic structural parameters remains under-explored. In this work, a comprehensive free vibration analysis of rectangular FGM sandwich plates is presented, incorporating advanced gradation laws such as Exponential law, Four Parameter Law, Trigonometric Law, and the classical Power Law over five thickness ratios of configurations (1-1-1, 1-2-1, 1-1-2, 2-1-2, and 2-2-1) and varying aspect ratios (a/h , a/b) over a representative range. The analytical model is based on a Hyperbolic Shear Deformation Theory (HPSDT), with governing equations derived via Hamilton's principle and Navier-type closed-form solutions for simply supported boundary conditions. The analyses yield natural frequency parameters, illustrating how the combined effects of porosity type, material gradation law, thickness ratio, and geometric slenderness interact to substantially modify frequency spectra. This study fills a gap in vibration modelling with gradation laws in FGMs with insights such higher sensitivity of the trigonometric law to geometric variations, increasing frequency for asymmetric layering and deviation with respect to power law. These data and insights prove critical for the design and analysis of high-performance plates in aerospace, mechanical, and civil engineering applications.

2. Methods of Analysis

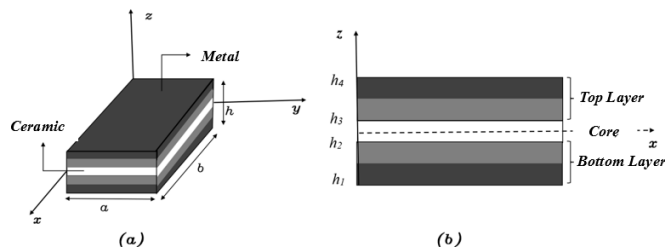


Fig. 1. (a) Geometry of FG sandwich plate (b) Layup of FG materials

| Sr. no. | Thickness Ratio | Height of each Layer |
|---------|-----------------|--|
| 1. | 1-1-1 | $h_4 = +h/2, h_3 = +h/6, h_2 = -h/6, h_1 = -h/2$ |
| 2. | 1-2-1 | $h_4 = +h/2, h_3 = +h/4, h_2 = -h/4, h_1 = -h/2$ |
| 3. | 1-1-2 | $h_4 = +6h/10, h_3 = +h/8, h_2 = -h/8, h_1 = -3h/10$ |
| 4. | 2-1-2 | $h_4 = +h/2, h_3 = +h/10, h_2 = -h/10, h_1 = -h/2$ |
| 5. | 2-2-1 | $h_4 = +6h/10, h_3 = +h/5, h_2 = -h/5, h_1 = -4h/10$ |

Fig. 2. Thickness ratios with heights of each layer

The FGM plate geometry consists of three layers: top and bottom-most metal-based layers that vary according to the gradation laws. The mathematical formulation for vibration analysis has been carried out for simply supported FGM plates using HPSDT to get the non-dimensional frequency. The analytical model developed in MATLAB is first validated for frequency parameters with A.M. Zenkour [1] for power law. Later, the frequency parameters are calculated and compared for varying a/h ratios, volume fraction index and gradation laws.

3. Results

This section presents the non-dimensional frequency parameters obtained in the analytical method for FG sandwich plate with Al_2O_3 (ceramic) core and Al (metal) top and bottom layers to compare the effects of the advanced gradation laws with the power law as per the objective of the study confirming that both gradation law and geometry play a significant role in governing the dynamic response of FGM sandwich plates.

Table 1. Percentage deviation of non-dimensional frequency parameter with respect to a/h ratios (at $n=2$, $a=b$), relative to Power law; (Expo = Exponential Law, Four = Four Parameter Law, Trigo = Trigonometric Law)

| a/h | FGM Model | | | Decrement (%) | | | Increment (%) | | | Decrement (%) |
|-------|-----------|-------|--------|---------------|-------|--------|---------------|-------|--------|---------------|
| 5 | 1-1-1 | Power | 3.4252 | 1.79 | Power | 3.4252 | 8.82 | Power | 3.4252 | 3.90 |
| | | Expo | 3.3636 | | Four | 3.7275 | | Trigo | 3.2914 | |
| | 1-2-1 | Power | 3.7055 | 1.13 | Power | 3.7055 | 5.27 | Power | 3.7055 | 2.35 |
| | | Expo | 3.6636 | | Four | 3.9011 | | Trigo | 3.6182 | |
| | 1-1-2 | Power | 3.2732 | 2.38 | Power | 3.2732 | 10.96 | Power | 3.2732 | 5.31 |

| | | | | | | | | | | |
|-------|-------|---------|---------|-------|---------|---------|---------|---------|---------|------|
| | | Expo | 3.1951 | | Four | 3.6320 | | Trigo | 3.0993 | |
| 2-2-1 | Power | 3.5125 | 1.50 | Power | 3.5125 | 7.98 | Power | 3.5125 | 3.26 | |
| | Expo | 3.4596 | | Four | 3.7930 | | Trigo | 3.3977 | | |
| 2-1-2 | Power | 3.1641 | 2.54 | Power | 3.1641 | 13.10 | Power | 3.1641 | 5.73 | |
| | Expo | 3.0837 | | Four | 3.5789 | | Trigo | 2.9826 | | |
| | | | | | | | | | | |
| 10 | 1-1-1 | Power | 6.8562 | 1.83 | Power | 6.8562 | 8.73 | Power | 6.8562 | 3.96 |
| | | Expo | 6.7305 | | Four | 7.4550 | | Trigo | 6.5846 | |
| 1-2-1 | Power | 7.4125 | 1.13 | Power | 7.4125 | 5.25 | Power | 7.4125 | 2.37 | |
| | | Expo | 7.3281 | Four | 7.8021 | Trigo | 7.2368 | | | |
| 1-1-2 | Power | 6.5474 | 2.33 | Power | 6.5474 | 11.02 | Power | 6.5474 | 5.15 | |
| | | Expo | 6.3944 | Four | 7.2694 | Trigo | 6.2096 | | | |
| 2-2-1 | Power | 7.0736 | 1.52 | Power | 7.0736 | 7.35 | Power | 7.0736 | 3.25 | |
| | | Expo | 6.9658 | Four | 7.5941 | Trigo | 6.8434 | | | |
| 2-1-2 | Power | 6.3436 | 2.63 | Power | 6.3436 | 12.8 | Power | 6.3436 | 5.88 | |
| | | Expo | 6.1766 | Four | 7.1578 | Trigo | 5.9703 | | | |
| | | | | | | | | | | |
| 25 | 1-1-1 | Power | 17.1445 | 1.84 | Power | 17.1445 | 8.70 | Power | 17.1445 | 3.97 |
| | | Expo | 16.8287 | | Four | 18.6376 | | Trigo | 16.4628 | |
| 1-2-1 | Power | 18.5323 | 1.14 | Power | 18.5323 | 5.25 | Power | 18.5323 | 2.37 | |
| | | Expo | 18.3208 | Four | 19.5053 | Trigo | 18.0923 | | | |
| 1-1-2 | Power | 16.3694 | 2.32 | Power | 16.3694 | 11.04 | Power | 16.3694 | 5.11 | |
| | | Expo | 15.9891 | Four | 18.1778 | Trigo | 15.5320 | | | |
| 2-2-1 | Power | 17.7178 | 1.52 | Power | 17.7178 | 7.18 | Power | 17.7178 | 3.25 | |
| | | Expo | 17.4469 | Four | 18.9912 | Trigo | 17.1414 | | | |
| 2-1-2 | Power | 15.8703 | 2.65 | Power | 15.8703 | 12.75 | Power | 15.8703 | 5.92 | |
| | | Expo | 15.4483 | Four | 17.8944 | Trigo | 14.9293 | | | |

4. Conclusions

The following conclusions can be drawn from the table above and overall findings of the research study:

- a. Across all thickness and aspect ratios, the exponential and four parameters yield slightly higher or comparable values unlike trigonometric law which generally gives lowest frequency values showing greater sensitivity to geometric variations.
- b. The increase in aspect ratio a/h (from 5 to 25), significantly increases the frequency parameters. The relative differences between gradation laws remain consistent across the a/h ratios.
- c. Symmetric thickness ratios (eg, 1-1-1) tend to show higher stability and smaller deviations between gradation laws where non-symmetric thickness ratio (1-1-2, 2-2-1) display greater decrements highlighting that asymmetric layering increasing frequency,
- d. Compared to the power-law distribution, the exponential and trigonometric laws generally yield lower frequency parameters, whereas the four-parameter law predicts consistently higher values, indicating its stiffening effect on the plate response.

5. References

- [1] Zenkour, A., “A comprehensive analysis of functionally graded sandwich plates: Part 1 Deflection and stresses,” International Journal of Solids and Structures, Vol. 42, 2005. <https://doi.org/https://doi.org/10.1016/j.ijsolstr.2005.02.015>
- [2] Thai, H.-T., Nguyen, T.-K., Vo, T. P., and Lee, J., “Analysis of functionally graded sandwich plates using a new first-order shear deformation theory,” European Journal of Mechanics - A/Solids, URL <https://www.sciencedirect.com/science/article/abs/pii/S099775381300168X>
- [3] Sah, S. K., and Ghosh, A., “Free vibration and buckling analysis of FGM plates using inverse trigonometric shear deformation theory,” Aircraft Engineering and Aerospace Technology, Vol. 93, 2021. <https://doi.org/10.1108/AEAT-01-2020-0001>.
- [4] Reissner, E., “The Effect of Transverse Shear Deformation on the Bending of Elastic Plates,” Journal of Applied Mechanics, Vol. 12, No. 2, 2021, pp. A69–A77. <https://doi.org/10.1115/1.4009435>
- [5] A.M.A. Neves, A.J.M. Ferreira, E. Carrera, M. Cinefra, C.M.C. Roque, R.M.N. Jorge, C.M.M. Soares, A quasi-3D hyperbolic shear deformation theory for the static and free vibration analysis of functionally graded plates, Composite Structures, Volume 94, Issue 5, 2012, Pages 1814-1825, ISSN 0263-8223, <https://doi.org/10.1016/j.compstruct.2011.12.005>.

Analytical Modelling of Electro-Mechanical Impedance (EMI) in Adhesively Bonded Beams for Multi-Damage Detection

Umakanta Meher^{1,2}, Mohammed Rabius Sunny²

¹ School of Aerospace Engineering, KIIT Deemed to be University, Bhubaneswar, India

²Department of Aerospace Engineering, IIT Kharagpur, India

1. INTRODUCTION & OBJECTIVE

Weight efficient adhesively bonded joints are commonly found in various engineering applications due to their associated advantages such as smooth stress distribution, preservation of material integrity, improved fatigue and vibration resistance etc. However, these structures are susceptible to disbonds/delaminations which poses a potential threat to long term structural integrity and reliability. The EMI method which incorporates surface-bonded PZT transducers has emerged as a promising NDT/NDE tool for damage localization and quantification due to its sensitivity to small minor defects that leads to modification of local stiffness and boundary conditions [1].

The present method proposes a low-computational cost 1D analytical EMI model for damage detection that preserves the principal structural dynamic properties such as mass, stiffness and damping etc. of a real-life 3D structure. The analytical framework includes the modelling of single, double and triple disbonds inside an adhesively bonded metallic beams.

2. METHODOLOGY

The test structure represents a cantilever beam with a surface bonded PZT 5H transducer and is formed by joining two individual aluminum beam by means of epoxy adhesive. The electro-mechanical coupling of the PZT-structure interaction has been captured in terms of electro-mechanical impedance (EMI) signatures. The EMI response which is a function of dynamic stiffness of the structure can be represented mathematically as follows:

$$Z(\omega) = \frac{1}{i\omega C} \left(1 - k_{31}^2 \frac{K_{str}(\omega)}{K_{PZT} + K_{str}(\omega)} \right)^{-1} \quad (1)$$

where $K_{str}(\omega)$ is the dynamic stiffness of the structure; K_{PZT} is the stiffness of the PZT transducer and the other terms represent the piezo-electric properties of the attached PZT.

As axial vibration modes are more prone to higher natural frequencies, the axial vibration is neglected in the present model. The structural stiffness (K_{str}) experienced by the PZT due to PZT-host structure interaction which is a function of the natural frequencies and mode-shapes of the structure is given as follows:

$$K_{str} = \frac{F_{PZT}}{u_{PZT}} = \left\{ \frac{\left(\frac{d}{2}\right)^2}{\rho A} \sum_n \frac{[W_n'(Loc1) - W_n'(Loc2)]^2}{\omega_n^2 + 2i\zeta\omega\omega_n - \omega^2} \right\}^{-1} \quad (2)$$

Where ' Loc_1 ' and ' Loc_2 ' are the location of two extreme ends of the PZT patch.

W_n' is the mode shape of the structure

Application of appropriate boundary condition gives rise to determination of natural frequencies and corresponding mode shapes which can be utilized to determine the EMI response of the structure. Each damage scenarios involve solving roots of system of transcendental equations to find the natural frequencies and hence the mode shapes, with the continuity and compatibility conditions at region interfaces.

3. RESULTS AND DISCUSSIONS

Consider two aluminum beams of dimension $150\text{mm} * 25\text{mm} * 1\text{mm}$ are attached by means of epoxy adhesive. A PZT patch of dimension $15\text{mm} * 15\text{mm} * 0.4\text{mm}$ is fitted on the surface of beam. The frequency range $20\text{kHz}-80\text{kHz}$ has been investigated for the pristine state structure which consists of 11 numbers of natural modes. The analytical model has been validated with ANSYS simulation. A comparison of impedance spectrum between analytical and ANSYS model demonstrates an excellent agreement in terms of number of resonant peaks, peak locations and overall pattern of the spectrum (refer Fig. 1). The impedance responses of the structure are now obtained for (i) Single damage state, (ii) Two damage state and (iii) Three damage state from the analytical model respectively. Figure 2 describes a comparison of impedance response between pristine state and multiple damage states of the structure obtained from respective analytical models.

From Figure 2 it can be seen that presence of any damage significantly modifies the EMI response of the structure as compared to the healthy state. Resonance frequency shifting can be spotted due to the multiple damages present in the structure. Presence of damage reduces the stiffness of the structure which in turn decreases the natural frequencies of the system. The conclusive sign of damage present inside the structure can be seen through the left shift of resonant frequencies which in turn indicates the reduction in structural stiffness and hence decrement of natural frequencies.

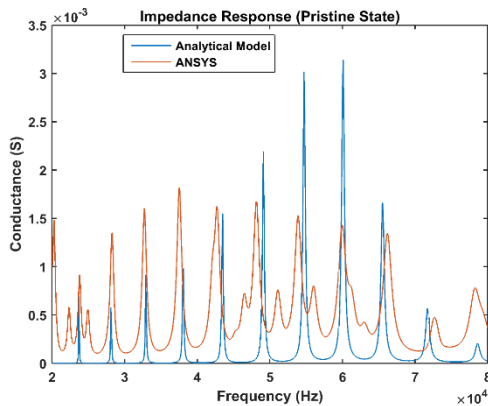


Figure 1 . Comparison of Impedance Response between the Analytical Model and ANSYS

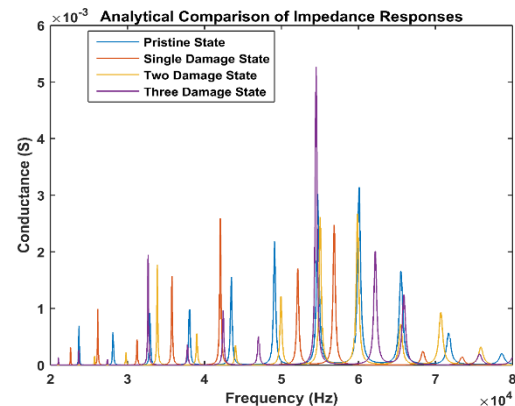


Figure 2 Comparison of Impedance Responses for Different Damage State Obtained from Respective Analytical Model

4. CONCLUSION

The present method proposes a computationally inexpensive 1D alternative model to a full-scale 3D-simulation, especially for preliminary diagnostics. The proposed analytical model is robust enough to preserve the basic structural dynamics properties when compared with a 3D simulation model, which significantly reduces the computational complexity of EMI data generation. The model offers an accurate prediction of resonant frequencies and hence subsequent impedance-spectrum, making it a valuable tool for early damage prediction.

5. REFERENCES

- [1] Bhalla S, and Soh CK. Electro-mechanical impedance technique. In: Smart Materials in Structural Health Monitoring, Control and Biomechanics. Zhejiang University Press. doi:10.1007/978-3-642-24463-6

ANN-based prediction of the free vibration characteristics of functionally graded plates for various boundary conditions

Dabeer Anwer Danish^{a*} and Sukanta Chakraborty^b

^aResearch Scholar, Department of Civil Engineering, IIT (ISM) Dhanbad, Dhanbad, India

^bAssociate Professor, Department of Civil Engineering, IIT (ISM) Dhanbad, Dhanbad, India

1. INTRODUCTION & OBJECTIVE

A new class of advanced composites known as functionally graded materials (FGMs) is characterised by a gradual variation in structure and composition, which results in seamless transition in mechanical and thermal properties across the thickness. This gradation helps FGMs to overcome the interfacial and delamination issues that are commonly found in conventional laminated composites. In recent decades, the static and dynamic performance of FGM plates has gained significant attention, and a number of analytical and computational techniques have been put forth to precisely capture their responses. A detailed study on the free vibration behaviour of thin FGM rectangular plates has been reported by Baferani et al. [1], illustrating how the material gradient index and boundary conditions affect natural frequencies. To connect static and dynamic reactions under a range of loading and boundary conditions for thin FGM plates, Li et al. [2] calculated the scaling factors for bending, buckling, and free vibration of isotropic functionally graded material (FGM) thin plates and compared them to isotropic homogeneous plates. Despite the high accuracy of finite elements used in these studies, their computational cost remains significantly higher. Thus, an efficient machine learning based predictive model is desperately needed to replicate the high-fidelity results with considerably reduced computational efforts.

The present study aims to develop an ANN-based predictive framework to estimate the:

- Impact of various grading indices on the vibration response of the functionally graded (FG) plate under various boundary conditions using ANN.
- Behaviour of ANN when a single database is prepared using various methods (FEM, experimental, etc.) and compared with the database prepared using only analytical methods to check the robustness of the proposed ANN model.

2. METHODS OF ANALYSIS

Finite element software is used to perform a static analysis for the calculation of central deflection and a free vibration analysis for calculating the natural frequency of the thin FGM plate. The outcomes are matched with existing literature as well as analytical solutions. A metal/ceramic ($\text{Al}/\text{Al}_2\text{O}_3$) FGM plate is considered. The plate's top face is considered ceramic, while the bottom face is of metal. Although the material's properties are isotropic in-plane, they progressively and continuously vary with thickness. A database was compiled related to the free vibration of FGM plates under three different boundary conditions. To forecast the FGM plate's natural frequency and central displacement, an artificial neural network (ANN) model is created.

3. RESULTS AND HIGHLIGHTS OF IMPORTANT POINTS

The natural frequency of thin FGM plates with various gradient indices is investigated, and the outcomes are compared with Yin et.al [3]. This paper's natural frequency has been normalised in relation to the material attributes and plate geometries. The normalised natural frequencies of the first five modes are compared with those derived from literature and simplified analytical solutions in Figure 1. The results clearly show that prediction by ANN offers either slightly less, greater, or extremely close to the actual test data. On a similar note, Figure shows the comparison of the dimensionless deflection of a thin square Sigmoid Functionally Graded Material (S-FGM) plate with those obtained from analytical solution and Chi & Chung [4]. The figure clearly validates the result obtained from analytical solution and Finite element modelling with the existing literature. An Artificial Neural Network (ANN) model developed by Sarkar et al. [5] is used as a reference to develop the ANN model.

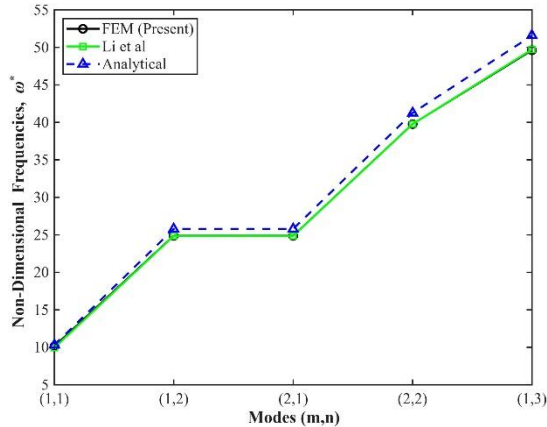


Figure 1: Comparison of Non-dimensional natural frequencies, $\omega^* = \omega\pi^2(a^2/t)\sqrt{\rho_m/E_m}$ of first five modes of Metal/Ceramic (Al/Al₂O₃) plate with grading index, $n = 0.5$

4. CONCLUSIONS

Utilising ANN methods to forecast the central deflection and natural frequency of the FG plate is presented in this study. Different network types, activation functions, hidden layer counts, epochs, and neuron counts were used to optimise the ANN model. Two separate ANN models were created using data from analytical methods only in one model, and data obtained using various other methods, FEM results, in another model. The predicted results by both the ANN models were compared. The network's performance was assessed by estimating the principal error using the Mean Squared Error (MSE). The R^2 value obtained in both studies undoubtedly suggests the accuracy of the suggested ANN model in predicting the natural frequency of the thin FGM plate, but the high MSE value in the 2nd model (prepared using various methods) suggests the lack of robustness to generalise the model to predict natural frequency accurately.

5. REFERENCES

- [1] A. H. Baferani, A. R. Saidi, and E. Jomehzadeh, “An exact solution for free vibration of thin functionally graded rectangular plates,” *Proceedings of the Institution of Mechanical Engineers, Part C: Journal of Mechanical Engineering Science*, vol. 225, no. 3, pp. 526–536, 2010, doi: 10.1243/09544062JMES2171.
- [2] S. R. Li, X. Wang, and R. C. Batra, “Correspondence Relations between Deflection, Buckling Load, and Frequencies of Thin Functionally Graded Material Plates and Those of Corresponding Homogeneous Plates,” *J. Appl. Mech. Trans. ASME*, vol. 82, no. 11, pp. 1–8, 2015, doi: 10.1115/1.4031186.
- [3] S. Yin, T. Yu, and P. Liu, “Free vibration analyses of FGM thin plates by isogeometric analysis based on classical plate theory and physical neutral surface,” *Advances in Mechanical Engineering*, vol. 2013, Art. no. 634584, pp. 1–10, 2013, doi: 10.1155/2013/634584.
- [4] S.-H. Chi and Y.-L. Chung, “Mechanical behavior of functionally graded material plates under transverse load—Part II: Numerical results,” *International Journal of Solids and Structures*, vol. 43, no. 12–13, pp. 3675–3691, 2006. doi: 10.1016/j.ijsolstr.2005.04.010.
- [5] S. Sarkar, S. Chakraborty, and S. Nayak, “ANN-Based Axial Strength Prediction of Short Columns with Double and Bar-Reinforced Concrete-Filled Steel Tubes Subjected to Concentric and Eccentric Loading,” *Arabian Journal for Science and Engineering*, vol. 49, pp. 4947–4968, 2024. doi: 10.1007/s13369-023-08285-8.

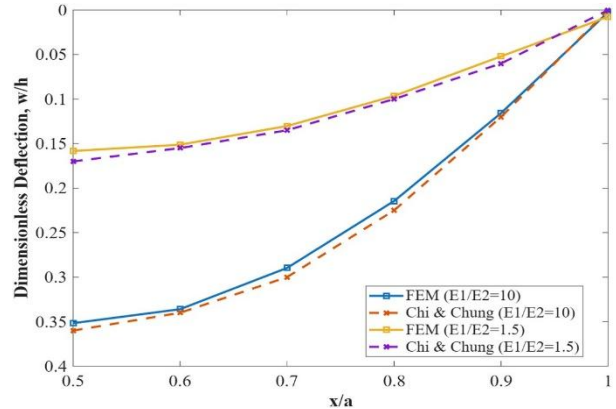


Figure 2: Comparing the S-FGM plate's dimensionless deflection, w/h , along the x-direction for various E_1/E_2

* Communicating Author: Dabeer Anwer Danish, Email: 24dr0060@iitism.ac.in.

Axially-Loaded Column under Earthquake Loading

Mahendra Gattu^{a*}

^aAssistant Professor, Department of Civil Engineering, National Institute of Technology-Rourkela, India.

1. INTRODUCTION & OBJECTIVE

The fundamental vibration frequency of columns decreases with increasing axial compressive load.

1. This paper carries out the free vibration analysis of a beam using the finite element method. The frequencies and mode shapes are determined. The vibration behavior of the beam under axial load is investigated analytically and using the finite element method. The results show that the square of the frequency reduces linearly with an increase in axial load. At the critical buckling load, this frequency goes to zero. Experimental work to determine the buckling load of a column can be carried out indirectly from an axial load versus frequency plot.
2. The effect of axial load on the dynamic response of columns under earthquake ground motion is analyzed. Using Euler-Bernoulli beam theory, we derive the governing differential equation. We model the column using the 4-degree-of-freedom beam element. We calculate the displacement-time response numerically using Newmark's method.
3. We introduce Rayleigh damping in the analysis and examine the deformation response spectrum for different earthquake ground motions with and without axial load.

2. METHODS OF ANALYSIS

The finite element method is used with the Newmark's method [1] to obtain the response spectrum of the columns subjected to ground motion with and without axial load (Figure 1).

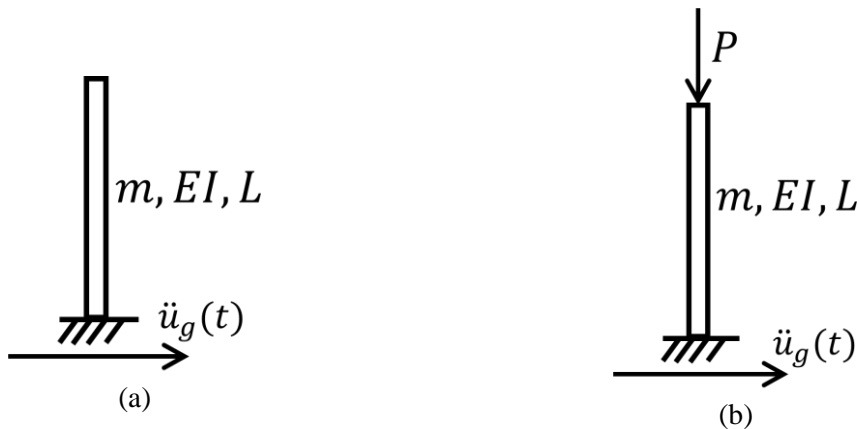


Figure 1: Response to seismic ground motion $\ddot{u}_g(t)$: a) Column with no axial b) Column with axial load

3. RESULTS

We determine the frequency ω for varying axial load, P_{axial} . We observe that an increase in axial load reduces the frequency of vibration (Figure 2).

*Communicating Author: Mahendra Gattu, gattum@nitrkl.ac.in

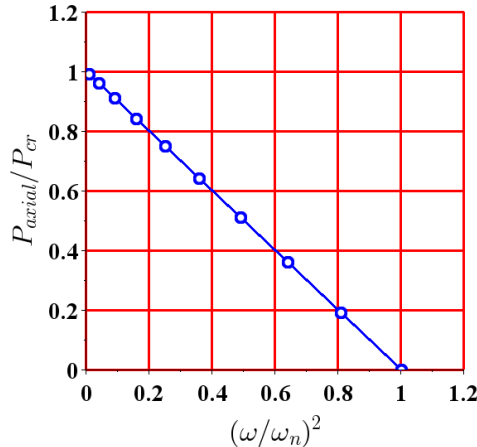


Figure 2: Axial load P_{axial} versus ω^2 frequency plot

4. CONCLUSIONS

Axial load reduces the fundamental frequency of vibration of the axially loaded column. This paper aims to evaluate the effect of axial loading on the response spectrum of the axially loaded column subjected to seismic loading, which is important in design of engineering structures [2], [3].

5. REFERENCES

- [1] A. K. Chopra, *Dynamics of Structures: Theory and Applications to Earthquake Engineering*, 2007th ed. in Prentice-Hall international series in civil engineering and engineering mechanics. Pearson Education India.
- [2] D. T. W. Looi, R. K. L. Su, B. Cheng, and H. H. Tsang, “Effects of axial load on seismic performance of reinforced concrete walls with short shear span,” *Engineering Structures*, vol. 151, pp. 312–326, Nov. 2017, doi: 10.1016/j.engstruct.2017.08.030.
- [3] J. Cai, J.-B. Ye, Q.-J. Chen, X. Liu, and Y.-Q. Wang, “Dynamic behaviour of axially-loaded RC columns under horizontal impact loading,” *Engineering Structures*, vol. 168, pp. 684–697, Aug. 2018, doi: 10.1016/j.engstruct.2018.04.095.

*Communicating Author: Mahendra Gattu, gattum@nitrkl.ac.in

Bluff Body Induced Regression Rate Enhancement in Hybrid Motor

Khandare A.¹, Patil A.¹, Patel J.¹, Sonage S.², Kumar N.², Deore N.¹

¹Mechanical Engineering Department, Pimpri Chinchwad College of Engineering, Pune, India

²Aerospace Engineering Department, Indian Institute of Technology, Bombay, India

1 Introduction

Hybrid rocket propulsion combines the simplicity of solid fuels and the flexibility of liquid oxidizers, offering safer operation and reduced system complexity compared to traditional propulsion systems [1]. However, their major drawback is the low regression rate of fuel, which limits performance. Researchers have addressed this issue through three approaches: optimizing fuel properties (e.g., paraffin blends, metallic additives), employing advanced injection and grain design techniques (e.g., swirl injection, radial flow) [2,3]. This study focus on bluff bodies by placing geometric obstructions in the combustion chamber to improve turbulence, improve fuel-oxidizer mixing, and stabilize the flame, thus increasing the regression rate [2,4]. Three shapes of bluff body; conical, cuboid and hemispherical has been tested in the study. A fuel mixture of 30% microcrystalline wax and 70% paraffin wax was used due to its low cost and manufacturability despite weak mechanical properties [4,5]. Oxygen gas served as the oxidizer, and experiments were conducted with a single-port grain configuration on a custom-built thrust bed test setup at IIT Bombay.

2 Methodology

Wax-based propellants theoretically offer regression rates 3–5 times higher than conventional solid fuels [6]; however, experimental results indicate a lower rate of around 2.28 mm/s [7]. The fuel used is fabricated in a single port grain configuration for simplicity and reduced preparation time. The grains were produced using the melt-and-cast method described by Dinesh and Kumar (2024) [8], in which the melted wax was poured into the mould with a mandrel coated with silica grease. To minimize shrinkage and defects, cooling was controlled in a hot air oven starting at 60°C and reduced by 5°C per hour; additional wax was added during cooling to maintain grain length. After being cooled to 45 °C, the grains were air dried to room temperature and extracted. Further, computational studies were performed to determine the dimensions of the most efficient bluff bodies. The hemispherical design (9.5 mm radius with 2.5 mm step) creates uniform recirculation, the conical design (6 mm length, 19 mm diameter) generates sharp turbulent flows, and the cuboid design (9.5 mm side) induces strong shear layers and larger recirculation zones. The hybrid rocket motor comprised an SS 304 combustion chamber, showerhead injector, and a graphite convergent–divergent nozzle, with oxidizer flow (63 g/s) regulated by a solenoid valve and sequential timer. Regression rates were determined using the weight-loss method by measuring grain mass before and after firing. Oxidizer mass flux was calculated using the port area and oxidizer flow rate, and (1) was established from the test data.

$$r' = a(G_{ox})^n \quad (1)$$

where, r' is the regression rate in mm/s, a is the mass flux constant, G_{ox} is the mass flux in gm/s and n is the mass flux exponent.

3 Results and Discussion

Table 1 presents the comparison of experimental and numerical regression rates for different bluff body configurations with the error percentage.

¹ Corresponding author: ankushkhandare0003@gmail.com

Table 1: Experimental and numerical regression rates for different bluff body configurations

| Configuration | Exp. (mm/s) | Num. (mm/s) | Error (%) |
|---------------|-------------|-------------|-----------|
| Hemispherical | 4.68 | 4.72 | 0.85 |
| Conical | 5.30 | 5.15 | 2.83 |
| Cuboid | 3.05 | 2.80 | 8.20 |
| Baseline | 2.28 | — | — |

The conical bluff body showed the highest regression rate of 5.30 mm/s, followed by the hemispherical shape (4.68 mm/s). Numerical predictions using ANSYS Fluent agreed closely, with maximum deviation below 3% for these shapes. Both conical and hemispherical bluff bodies generated strong recirculation zones, enhancing mixing and heat transfer near the head end, which increased regression rates significantly compared to the baseline (2.28 mm/s). In contrast, the cuboid shape exhibited lower performance and higher numerical error due to weaker flow disturbances. A slight increase near the nozzle end was observed, attributed to erosive burning effects.

4 Conclusion

From the experimental evaluation of bluff body geometries in hybrid rocket motors, it is evident that geometry plays a crucial role in enhancing the fuel regression rate. Among the tested configurations, the conical bluff body delivered the highest performance (5.3 mm/s), which is 2.3 times greater than the baseline without a bluff body, followed by the hemispherical shape (4.68 mm/s) (about 2 times the baseline) and the cuboid (3.05 mm/s) with 1.3 times the baseline. The influence of bluff bodies was most pronounced near their location, with regression rates decreasing along the axial length of the fuel port due to the limited span of turbulence and flow disturbance. Overall, the results highlight the effectiveness of conical and hemispherical bluff bodies in improving fuel regression rates in hybrid rocket motors.

References

- [1] G. Sutton and O. Biblarz, *Rocket Propulsion Elements*. New York: Wiley, 2000.
- [2] M. Chiaverini, “Review of solid-fuel regression rate behaviour in classical and nonclassical hybrid rocket motors,” in *Fundamentals of Hybrid Rocket Combustion and Propulsion, Progress in Astronautics and Aeronautics*, pp. 37–125, AIAA, 2006.
- [3] D. Pastrone, “Approaches to low fuel regression rate in hybrid rocket engines,” *International Journal of Aerospace Engineering*, vol. 2012, pp. 1–12, 2012.
- [4] K. R. Brahma, H. and P. Ramakrishna, “Improving the mechanical properties of paraffin-based hybrid fuels,” in *Ninth International Conference on Flow Dynamics*, pp. 254–255, GCOE Institute of Fluid Science, Tohoku University, Japan, 2012.
- [5] I. T. S. K. Maruyama, S. and I. Nakagawa, “Study on the mechanical characteristics of paraffin-based fuel,” in *Eighth International Conference on Flow Dynamics*, pp. 306–307, GCOE Institute of Fluid Science, Tohoku University, Japan, 2011.
- [6] A. D. Karabeyoglu, M.A. and B. Cantwell, “Combustion of liquefying hybrid propellants: Part 1,” *Journal of Propulsion and Power*, vol. 18, no. 3, pp. 610–620, 2002.
- [7] D. Mengu and R. Kumar, “Development of eva-sebs based wax fuel for hybrid rocket applications,” *Acta Astronautica*, vol. 152, pp. 325–334, 2018.
- [8] S. S. Dinesh, M. and K. Nagendra, “Demonstration of dual-thrust capability in hybrid rockets using multi-layered tubular fuel grains,” *FirePhysChem*, 2024.

Buckling load parameter analysis of Rectangular plate with Full and partial stiffeners under Uniaxial and Biaxial loading conditions

Prabhash Kumar Yadav ^a and A.K.L. Srivastava ^b

^aResearch scholar, civil engineering department, national institute of technology Jamshedpur,india

^bProfessor, civil engineering department, National Institute of Technology Jamshedpur, India

1. Introduction and objective

One popular and economical method for enhancing the performance of plates and shells is to add stiffeners. Stiffened plates are lightweight, highly durable structural components that are frequently found in roofing units, offshore drilling rigs, aircraft, ships, submarines, bridges, and pressure vessels. Operating in dynamic situations is necessary for the majority of these structures. By improving the basic structure's cross-sectional second moment of inertia, the stiffeners make them more rigid. Stiffened plates are structural elements made up of plates that have been strengthened by a rib system to increase their capacity to support weight.

In the present study, the plate is modeled using an quadratic isoperimetric element is used, with every node carrying five degrees of freedom, allowing both membrane and bending behaviour to be accurately captured. The stiffener is designed to be positioned anywhere within the plate element, and interpolation functions are used for the stiffener as well to ensure compatibility between the plate and stiffener. Structural engineering application requires an accurate prediction of the system behaviour of a stiffened plate. In the case of optimum design of structural components, it is necessary to have a fundamental understanding of their deformation, vibration, buckling behaviour, etc. In this work, the finite element method has been used to formulate the equation of motion of the stiffened plate and compared with the result obtained from FORTRAN 90 software. The variables of analysis are the aspect ratio of the plate, the arrangement of the stiffeners and their location, different boundary conditions to the plate, and the direction of loading. Using these results, the relation between aspect ratio and buckling parameters for various boundary conditions is analysed.

2. Method of analysis

Finite element formulation

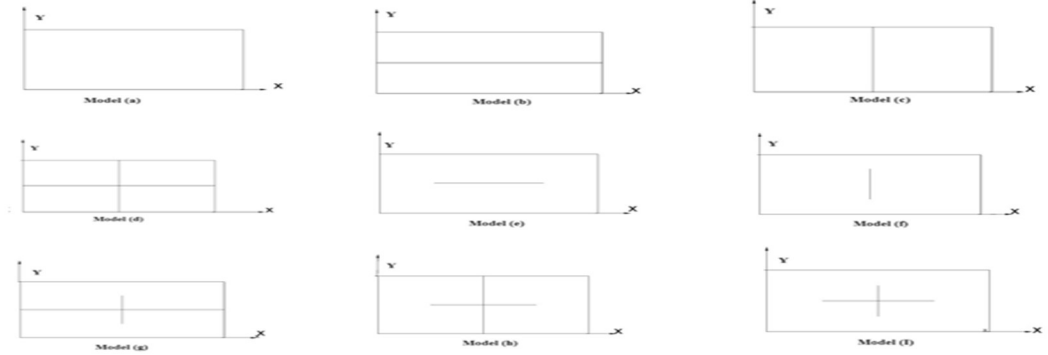
The analysis here focuses on a rectangular plate ($a \times b$) subjected to in-plane forces , stiffener configuration. The structure is subjected to compressive loading, with the plate edges held either by simple supports or by clamping. According to Mindlin's plate theory, the expressions for the plate's total potential energy and kinetic energy, including the effects of shear deformation and rotary inertia. To make use of the structural and loading symmetries of the plate, the buckling modes are classified into symmetric and anti-symmetric types with respect to the axis or axes of symmetry. This classification helps simplify the analysis by reducing computational effort and exploiting the natural behavior of the structure.

Computer Program

A custom-built computer program has been used to handle all the calculations required for the analysis. The plate is modeled using a grid of rectangular elements arranged in two dimensions. To prevent issues like shear locking, the elastic stiffness of each element is calculated using 2×2 Gauss integration points. The same integration scheme is applied for

mass matrix computation, as higher-order integration offers little benefit—this is supported by the convergence results

3. Results



The basic configuration considered here is the simple rectangular plate with various types of partial stiffener arrangements for isotropic stiffened plate Figures 1- 4. Numerical results are obtained with different boundary conditions. In the discussion that followed, S and C denote simply supported, clamped edges respectively. Various models of rectangular plates with different arrangement of full and partial stiffeners as shown in figures a to i which are analyzed by finite element method and using FORTRAN 90 software for coding.

4. Conclusion

Buckling load parameter increases as the restraint at the edges increases for all cases of studies. So the buckling parameters of the edge condition SCSC is more than simply supported (SSSS) and less than that for the clamped condition (CCCC).

Shear deformation has a stronger influence on clamped plates compared to simply supported plates.

5. References

1. K. Bathe, E. L. Wilson and F. E. Peterson, SAPIV A Structural Analysis Program for Static and Dynamic Response of Linear Structures, Report EERC 73-11, University of California, Berkeley, CA (1973).
2. Arun Roy, Y., Shastry, B. P., & Venkateswara Rao, G. Stability of partially stiffened square plates using high precision finite elements. *Computers & structures*, 37(4); 613-615:1990.
3. Mali, Kiran D., and Pravin M. Singru. 'Determination of modal constant for fundamental frequency of perforated plate by Rayleigh's method using experimental values of natural frequency.' *International Journal of Acoustics and Vibrations* 20.3 (2015): 177-184.

Communicating Author: Prabhash Kumar Yadav
2023rsce015@nitjsr.ac.in

Dr. A.K.L. Srivastava
aklsriv.civil@nitjsr.ac.in

CFD Investigation of Transonic Bucket phenomena for Typical Grid Fin used on Re-Entry Stage Configuration

Anubhab Das^{a*}, Kunal Garg^b, Ankur Nagpal^b, Amit Sachdeva^a, G Vidya^c

^aACDD/ADSG/AERO, VSSC, ISRO, Thiruvananthapuram, Kerela, India

^bACMD/ADSG/AERO, VSSC, ISRO, Thiruvananthapuram, Kerela, India

^cADSG/AERO, VSSC, ISRO, Thiruvananthapuram, Kerela, India

1. INTRODUCTION & OBJECTIVE

Reusable Launch Vehicle stages use several types of control surfaces during descent phase of the flight like interstage segments, planar fins, grid fins etc. Grid fins are lattice-like control surfaces used on reusable rocket stages (e.g., Starship, Falcon-9, Hyperbola-1, RETALT [2]) to provide aerodynamic stability and steering during atmospheric descent. Positioned near the fore-end of the stage, they are deployed based on mission requirements generally during descent/landing phase and function by deflecting airflow, each cell act as a nozzle, to generate necessary torque. The lattice architecture gives its unique characteristics, which are depicted in Figure 1 [1]. This phenomenon is called transonic bucket (the dip in normal force coefficient in transonic regime) which is central idea of this study. This study brings out the same phenomena for the vehicle in study and further the physical aspects and flow features are discussed in detail.

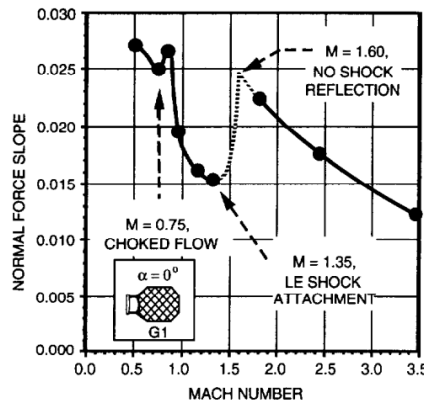


Figure 1. Transonic bucket phenomena for Grid Fin

2. METHODS OF ANALYSIS

The reusable stage of a typical Launch Vehicle has been considered for the study is shown in Figure 2 along with the cut plane mesh. Half symmetry is considered for simulation to decrease computation overhead. Pointwise v23R3 is employed for mesh generation, volume mesh using voxel method is around 155 million; Quad dominated surface mesh with volume refinement near grid fins and nozzle-landing gear allows for better flow capture with less cell count. First cell height is fixed to 1.0 microns to obtain $y^+ \sim 1$. RANS simulations has been carried out in CFD++ v20.1 employing SST-k ω turbulence model. Simulations has been carried out for Mach numbers (M): 0.8, 0.95, 1.05, 1.2, 1.6, 1.8 at an angle of attack of 176° (typical 4° angle of attack for launch vehicle configuration).

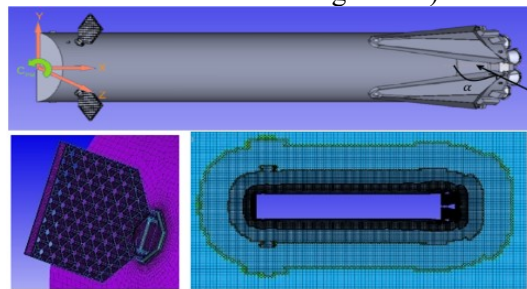


Figure 2. Sign Convention, Grid fin Surface Mesh, Mesh Cut Section

3. RESULTS & DISCUSSION

Figure 3 shows the trend of C_N (normal force coefficient) with M of both windward and leeward fins. We can observe that the C_N for Windward Fin dips from $M = 0.95$, however the dip in Leeward Fin is delayed (starts from $M = 1.05$).

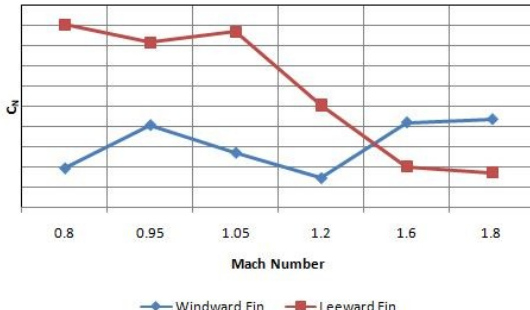


Figure 3. C_N vs Mach number

Leeward fin force contribution is 3-5 times higher than that of windward fin, which is very counter-intuitive. The detailed flow structure for the vehicle and fin cross-section for both side fins at angle of attack 176° is depicted in Figure 4. Further investigation reveals that the approach M to windward fin is different than that of leeward fin, due to angle of attack. Therefore, attributed to grid fin characteristics, based on local approach Mach number the windward fin is choked whereas the leeward fin isn't. This also causes the delay in reduction of C_N for leeward fin. Further details will be discussed in the full paper.

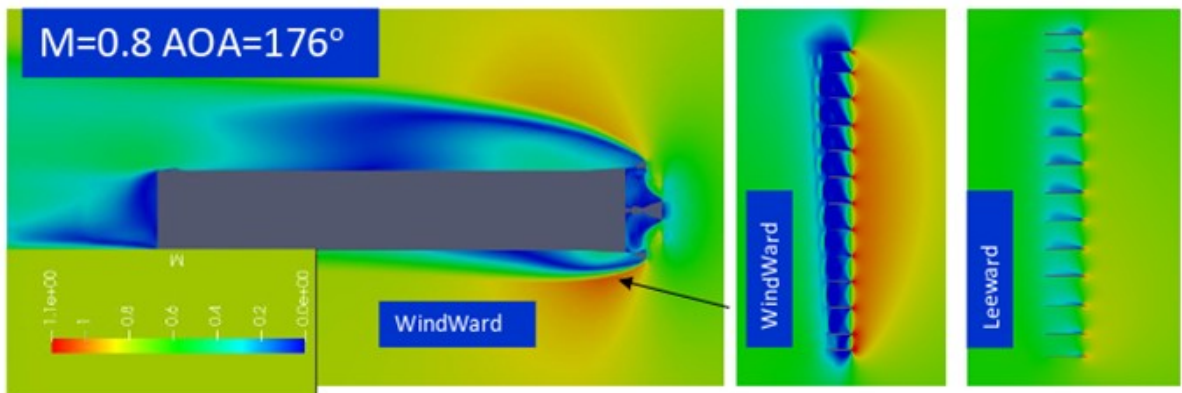


Figure 4. Detailed flow structure for the vehicle and fin cross-section

4. CONCLUSIONS

CFD simulations are carried out for grid fin based reusable rocket stage. Transonic bucket phenomenon is investigated for grid fin, $M = 0.80-2.0$. Details for other Mach numbers will be discussed in full paper. Large variation in force generation between windward fin and leeward fin studied is found to be related to transonic bucket phenomena which depends on the local approach M .

5. REFERENCES

- [1] W. D. Washington and M. S. Miller, "Experimental investigations of grid fin aerodynamics: A synopsis of nine wind tunnel and three flight tests," in *Proceedings of the NATO RTO Applied Vehicle Technology Panel Symposium on Missile Aerodynamics (RTO-MP-5)*, Sorrento, Italy, 1998, pp. 10-1–10-14.
- [2] A. Marwege, A. Güllhan, J. Klevanski, C. Hantz, S. Karl, M. Laureti, G. De Zaiacomo, J. Vos, M. Jevons, C. Thies, A. Krammer, M. Lichtenberger, J. Carvalho, and S. Paixão, "REALT: review of technologies and overview of design changes," *CEAS Space Journal*, vol. 14, pp. 433-445, 2022.

*Communicating Author: ANUBHAB DAS <anubhab_das@vssc.gov.in>

Comparative Analysis of Obstacle Avoidance Path Planning Algorithms for Robotic Manipulators: RRT, APF, and CHOMP

Adeetya Uppal^a, Rakesh Kumar Sahoo^{b*}, Manoranjan Sinha^c

^{a,b*,c}Department of Aerospace Engineering, Indian Institute of Technology Kharagpur,
West Bengal, 721302, India

1. INTRODUCTION

Robotic manipulators operating in 3D environments containing obstacles should be able to generate and follow collision-free and dynamically feasible trajectories. This allows the manipulators to safely navigate the unstructured environment with obstacles, enabling them to complete their allocated task [1]. As the robotic manipulators are often required to work in constrained, unstructured or cluttered spaces, collision-free and smooth trajectories are emphasized. Several algorithms have been proposed over the years to address the central challenges of path planning and obstacle avoidance in modern robotics, each having their distinct advantages and limitations in terms of computational efficiency, convergence time and robustness [2][3]. The objective of this paper is to analyze and compare the performance of RRT [2], APF [3] and CHOMP [4][5] algorithms for trajectory generation for robotic manipulators in 3D space. The study focuses on the capability of these algorithms to generate trajectories from a start to a goal, avoiding collisions in a 3D environment containing various obstacles under identical simulation conditions. By analyzing the advantages and limitations of the algorithms, their feasibility for practical applications and real world integration can be highlighted.

2. METHODOLOGY

Precise modeling of the kinematics and dynamics of a robotic manipulator are essential for control and planning. For a given set of joint angles, the pose of the end-effector of the manipulator can be found using forward kinematics. The Denavit–Hartenberg (D-H) convention is used to describe each joint of the manipulator using four parameters: a_i (link length), α_i (link twist), d_i (link offset) and θ_i (joint angle). The Kinova Gen3 robotic manipulator has 7 revolute joints. The homogenous transformation matrix from the base to the end-effector is given by:

$${}^0T_7 = \prod_{i=1}^7 {}^{i-1}T_i \quad (1)$$

where ${}^{i-1}T_i$ is obtained by four basic transformations - rotation about z-axis by θ_i , translation about z-axis by $d - I$, rotation about x-axis by α_i and translation about x-axis by a_i [1]. The influence of forces and torques on the motion can be seen by dynamic modeling which considers inertial, centrifugal, Coriolis and gravitational effects. For dynamic modeling, the Euler-Lagrange formulation is typically used for robotic manipulators, and is mathematically expressed as:

$$\frac{d}{dt} \left(\frac{\partial \mathcal{L}}{\partial \dot{q}_i} \right) = \frac{\partial \mathcal{L}}{\partial q_i}, \quad \text{for } i = 1, 2, \dots, n \quad (2)$$

where \mathcal{L} is the Lagrangian operator. The Lagrangian of the system is expressed as a difference between the total kinetic and potential energy of the system [1].

3. RESULTS AND DISCUSSION

The performance of three planning algorithms - RRT, APF and CHOMP - was evaluated for path planning and obstacle avoidance using a Kinova Gen3 7-DoF robotic manipulator. The algorithms were tested in an identical environment containing three fixed obstacles and were given identical start and goal configurations. The plot in Fig.1 compares the optimized 3D trajectory planned by the RRT algorithm to the 3D trajectory executed by the robotic manipulator. The RRT algorithm generates a path which keeps a safe distance from the obstacles, however, this path appears to be rough and jagged at certain sections of the path profile. This behavior is expected from RRT and is present due to the random sampling utilized by the algorithm to build its tree. This random tree-expansion approach, and the unconstrained sampling method of connecting the closest points rather than moving in a direct smooth path, of RRT results in abrupt changes in the curvature of the path and the end effector of the robotic manipulator has to follow a trajectory with sharp and varying turns. The plot in Fig.2 compares the optimized 3D trajectory planned by the Artificial Potential Field algorithm to the 3D trajectory executed by the robotic manipulator. The APF algorithm generates a smoother and more continuous trajectory curve as compared to the path generated by RRT. The generated path keeps an optimum distance from the obstacles, bending smoothly around them. This creates a curvilinear motion profile without any sharp turns or abrupt changes. The gradient-descent based approach of the APF algorithm can be seen as

it generates a shorter and more direct path as compared to RRT. However, a key limitation of APF is the issue of local minima, where entrapment can occur due to the cancellation of attractive and repulsive forces by each other. The plot in Fig.3 compares the optimized 3D trajectory planned by CHOMP to the 3D trajectory executed by the robotic manipulator. CHOMP generates a very smooth trajectory from the start to the goal while also avoiding any obstacles in the vicinity of the path. CHOMP prioritizes the smoothness of the motion profile, thereby generating a path that is not only feasible but also optimized for smooth execution as abrupt changes in motion will result in undesirable joint torques and control efforts. Unlike the APF's gradient-descent approach and RRT's random tree-expansion method, CHOMP generates an elegant and globally smooth and consistent trajectory as it adjusts the trajectory by ensuring gradual transitions in direction, slope and curvature. The relative translation position of the end effector with respect to the goal is compared in Fig.4 for all three algorithms. RRT rapidly converges towards the goal in about 1.7 seconds, and is the first to reach the goal. However, the curve shows non-monotonic fluctuations, with some disturbances that reflect the jagged nature of path generated using RRT. APF converges to towards the goal in about 2.2 seconds, showing a smooth and monotonic decrease in the distance towards the goal. APF shows a smooth and efficient trajectory, balancing the convergence time and the quality of generated path. CHOMP converges towards the goal more gradually, without much oscillations or disturbances as compared to RRT and APF. This is due to the priority given by CHOMP to the smoothness and execution of path which results in a moderate convergence time.

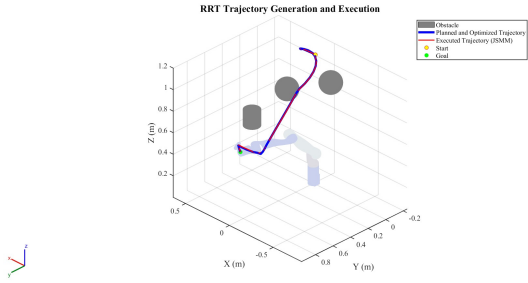


Figure 1: 3D trajectory generated by RRT.

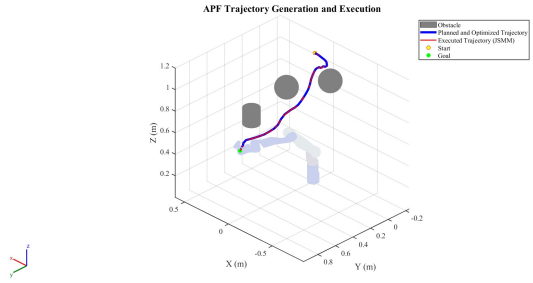


Figure 2: 3D trajectory generated by APF.

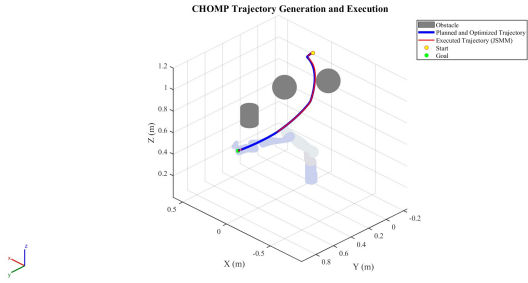


Figure 3: 3D trajectory generated by CHOMP.

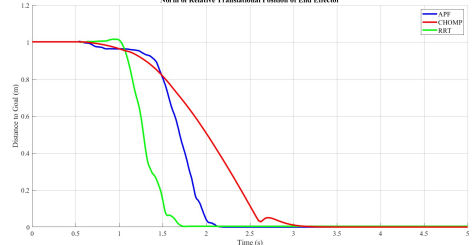


Figure 4: Norm of relative translational position of the end-effector w.r.t. the goal.

4. CONCLUSIONS

In this paper, we have implemented, analyzed and compared three algorithms - RRT, APF and CHOMP, which are widely used for path planning and obstacle avoidance for robotic manipulators in 3D space, using a Kinova Gen3 7-Degree-of-Freedom Robotic Manipulator. RRT-based path converges the fastest towards the goal, but with a jagged profile, which could result in abrupt joint movements. APF-based path shows a balance between the quality of path and convergence time, however, one should be cautious of the issue of local minima. CHOMP yields the globally smoothest part. The compromise in convergence time is justified by the dynamic feasibility and execution of the trajectory.

References

- [1] A. Uppal, R. K. Sahoo, and M. Sinha, "Collision-free trajectory planning and control of robotic manipulator using energy-based artificial potential field (E-APF)," *arXiv preprint arXiv:2508.07323*, 2025.
- [2] S. M. LaValle and J. J. Kuffner, "Randomized kinodynamic planning," *The International Journal of Robotics Research*, vol. 20, no. 5, pp. 378–400, May 2001.
- [3] O. Khatib, "Real-time obstacle avoidance for manipulators and mobile robots," *The International Journal of Robotics Research*, vol. 5, no. 1, pp. 90–98, March 1986.
- [4] N. Ratliff, M. Zucker, J. A. Bagnell, and S. S. Srinivasa, "CHOMP: Gradient optimization techniques for efficient motion planning," in *Proc. IEEE Int. Conf. Robotics and Automation (ICRA)*, Kobe, Japan, May 2009, pp. 489–494.
- [5] M. Zucker, N. Ratliff, A. D. Dragan, M. Pivtoraiko, M. Klingensmith, C. M. Dellin, J. A. Bagnell, and S. S. Srinivasa, "CHOMP: Covariant Hamiltonian optimization for motion planning," *The International Journal of Robotics Research*, vol. 32, no. 9–10, pp. 1164–1193, Aug. 2013.

Comparative Ballistic Impact Simulation of NiTi SMA-Reinforced and Conventional GFRP Composites

Sibaram Patro ^a, Chandra Sekhar Yerramalli^b and Krishnendu Haldar ^b

^a M.Tech Student, Aerospace Dept., IIT Bombay, Mumbai, India

^b Professor, Aerospace Dept., IIT Bombay, Mumbai, India

1. INTRODUCTION & OBJECTIVE

Shape Memory Alloys (SMAs) can recover their original shape upon heating after deformation and dissipate mechanical energy through reversible hysteresis during cyclic loading. Nickel-Titanium (NiTi) is the most commonly used SMA due to its high strength, corrosion resistance, and stable phase transformation. The Shape Memory Effect (SME) is the recovery of the original shape when a deformed martensitic SMA is heated above the austenite finish temperature, while pseudoelasticity occurs above this temperature when stress induces a reversible transformation from austenite to martensite, allowing large recoverable strains upon unloading. These properties make SMAs ideal for energy-absorbing and self-recovering composite reinforcements. This study numerically compares the ballistic response of NiTi SMA-reinforced GFRP hybrids with conventional GFRP laminates, focusing on energy absorption, contact force, and damage mitigation using ABAQUS/Explicit.

2. METHOD OF ANALYSIS

Finite-Element simulations were conducted in ABAQUS/Explicit and validated against low-velocity impact data from Naik et al. [1], confirming the reliability of the model setup and contact definitions. A square steel plate with dimensions ($0.2m \times 0.2m \times 0.008m$) is analyzed under impact loading conditions. The impactor is modeled as a spherical mass with a mass of $32g$. Figure 1 indicates the contact force developed at the point of impact.

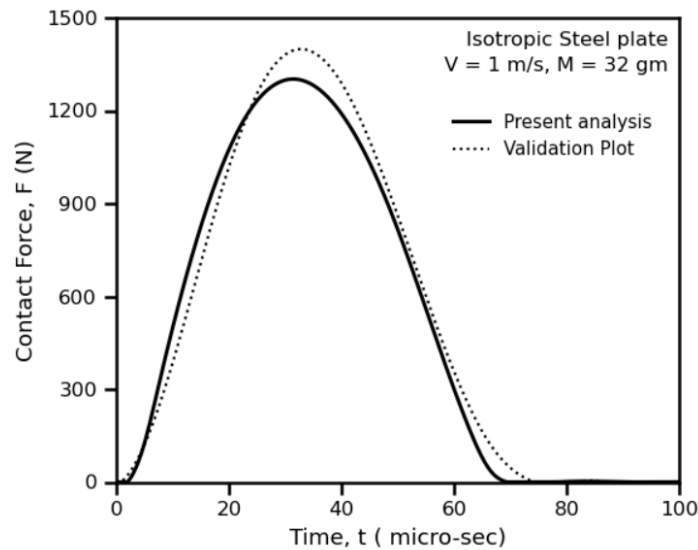


Figure 1: Contact force v/s time plot validated against [1]

3. RESULTS

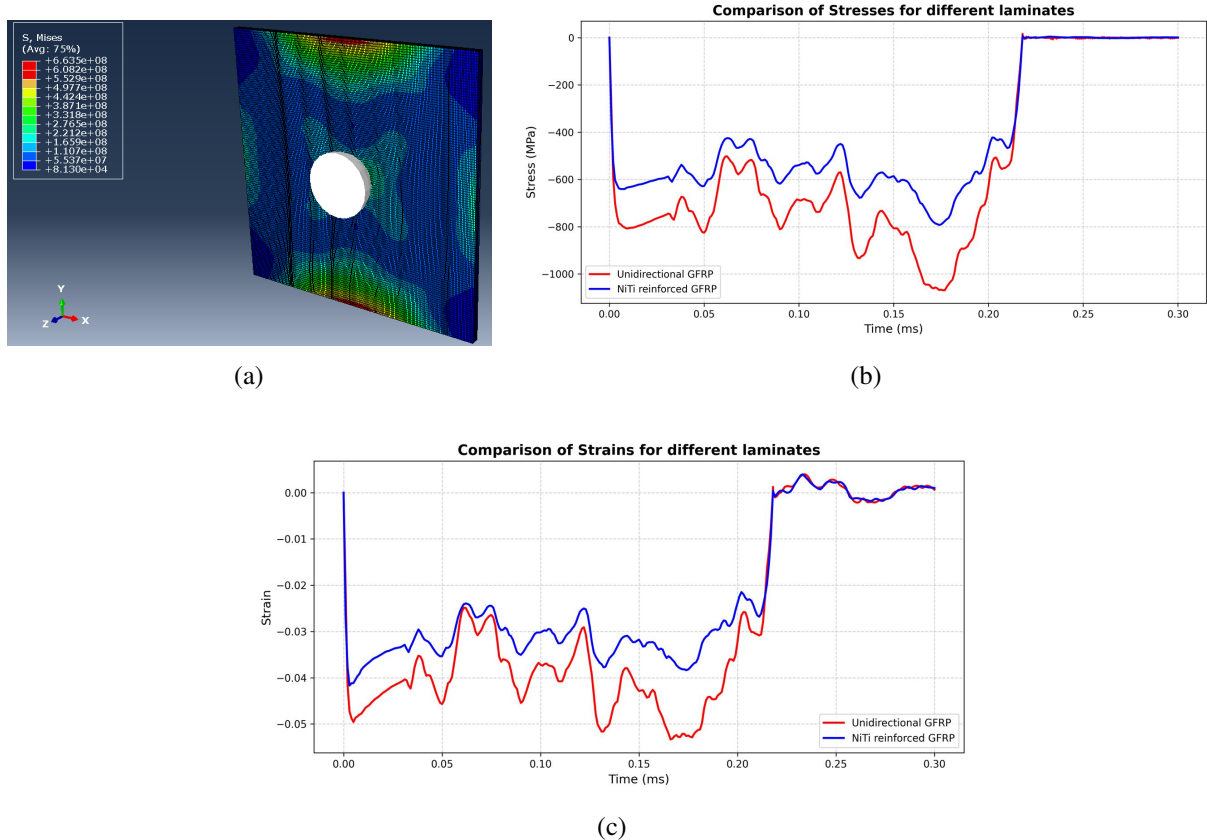


Figure 2: (a) FE stress distribution of laminate plate (b) Comparison of stress for different laminates and (c) Comparison of strain for different laminates

Ballistic impact analyses were carried out for two configurations: a conventional unidirectional glass-epoxy laminate, and an SMA wire-reinforced hybrid laminate. The NiTi SMA-reinforced laminate demonstrated a noticeable improvement in impact resistance compared to the conventional laminate. Figure 2b and Figure 2c indicate the stress distribution and strain developed for different laminates. The incorporation of SMA wires approximately reduced the peak stress by 27% while increasing the energy absorption.

4. CONCLUSIONS

NiTi SMA reinforcement significantly enhanced the ballistic performance of GFRP composites by improving energy absorption, load distribution, and post-impact recovery. The combination of pseudoelasticity and the shape memory effect allowed the hybrid laminate to dissipate impact energy while maintaining structural integrity. These results highlight the potential of SMA-GFRP hybrid composites as promising candidates for lightweight, damage-tolerant aerospace and defense applications.

REFERENCES

- [1] N. K. Naik and Y. C. Sekher. Damage in laminated composites due to low velocity impact. *Journal of Reinforced Plastics and Composites*, 17(15):1355–1369, 1998.
- [2] Dimitris C. Lagoudas and P. K. Kumar. *Shape Memory Alloys: Modeling and Engineering Applications*. Springer, New York, 2008.

* **Communicating Author:** Krishnendu Haldar, krishnendu@aero.iitb.ac.in

Comparative bending response of imperfect variable-angle tow and straight fiber laminates with integrated PZT layers

Ansh Kapoor^{a*}, Vanshika Anand^a, Narayan Sharma^b, Pawan Kumar^c, and Rakesha Chandra Dash^d

^a Student, Amity Institute of Defence Technology, Amity University, Noida, 201303, Uttar Pradesh, India

^b Assistant Professor, Amity Institute of Defence Technology, Amity University, Noida, 201303, Uttar Pradesh, India

^c Associate Professor, Department of Mechatronics, Manipal Institute of Technology, Manipal Academy of Higher Education, Manipal, 576104, Karnataka, India

^d Assistant Professor, Department of Mechanical Engineering, Birla Institute of Technology, Pilani, India

1. INTRODUCTION & OBJECTIVE

Composite materials have become an indispensable part of modern engineering, especially in the aerospace industry, owing to their superior properties such as high strength-to-weight ratio, corrosion resistance, and the flexibility to tailor material properties for targeted performance. Conventionally, fiber-reinforced composites are fabricated using straight fiber paths, producing Constant Stiffness Composite (CSC) laminates. CSC laminas provide flexibility to tailor the properties using various lamination sequences, however within lamina, fiber orientation is fixed, thus stiffness is constant within a plane. However, the advancement in manufacturing approach allows the lamina with curved fiber in a plane, called variable angle tow (VAT) laminates. The fiber paths can be optimized to obtain the maximum buckling resistance [1], thermomechanical performances [2], thus, it offers a design versatility that cannot be achieved with the conventional CSC composites.

As the manufacturing of curved fiber laminates is an intricate process, there might be possibilities of variation in properties due to the internal flaws (such as, fiber damage, incorrect matrix-fiber ratio, etc.). The presence of defects is quite difficult to detect. Thus, it is important to consider the effect of internal flaws for the analysis of VAT laminas. The imperfection within the composite is modelled using stiffness degradation approach. An anisotropy damage model is integrated with the finite element modeling to investigate the bending response of the imperfect composites [3,4]. Further, PZT actuators are attached to the top and bottom of the composites to enhance the bending performance which were reduced by the internal flaws.

This work investigates a comparative bending response of VAT and CSC laminates under different stacking sequences and boundary conditions. The study first examines how damage influences the bending behavior of both VAT and CSC laminates. Then, it explores the effect of applying different voltage inputs to PZT actuators and records the corresponding structural responses. By highlighting how piezoelectric actuation can alter the bending response of damaged VAT structures, the research provides valuable insights for designing smart, damage-tolerant composite systems.

2. METHODS OF ANALYSIS

The first order-based displacement values are considered for the finite element modelling of composites. The imperfections in the VAT composite have been taken into account by means of a stiffness-degradation approach [3], which reduces the effective load-carrying area. The research focus on the comparing the bending response of CSC and VAT composites and investigates the possible contribution of PZT actuators toward compensation for the stiffness loss caused by imperfections in composite materials.

2.1 STATIC ANALYSIS

Implementing Hamilton's principle and minimizing the equation, the governing equation is obtained as follows [4]:

$$\begin{aligned}[M]\{\ddot{u}\} + [K_{uu}]\{u\} - [K_{ua}]\{\beta^a\} - [K_{us}]\{\beta^s\} &= \{F\} \\ [K_{au}]\{u\} + [K_{aa}]\{\beta^a\} &= \{Q\} \\ [K_{su}]\{u\} + [K_{ss}]\{\beta^s\} &= 0\end{aligned}$$

In the equations, $[M]$, $[K_{uu}]$, and $\{u\}$ represent the global mass matrix, stiffness matrix, and displacement vector, respectively. The terms $[K_{ua}]$ and $[K_{us}]$ are the electromechanical matrices for the actuator and

sensor, while $[K_{aa}]$ and $[K_{ss}]$ are their corresponding permittivity matrices. Finally, $\{F\}$ and $\{Q\}$ are the mechanical and electrical force vectors generated by an applied surface charge.

3. RESULTS AND DISCUSSION

The present study focuses on a comparative analysis of the effect of damage within the composite layers of curved-fiber and straight-fiber laminates. Furthermore, it examines how the application of a piezoelectric actuator can help recover the stiffness lost due to such damage. The analysis is conducted for both simply supported and cantilever boundary conditions to determine which lamination sequences, among those with curved and straight fibers, yield better performance under damage. Additionally, the bending response of the laminates is examined for varying levels of input voltage. Figure 1 illustrates the bending response of the laminates, showing that the imperfect plate undergoes greater deflection. The inclusion of actuator response is therefore beneficial in recovering the stiffness lost due to imperfections.

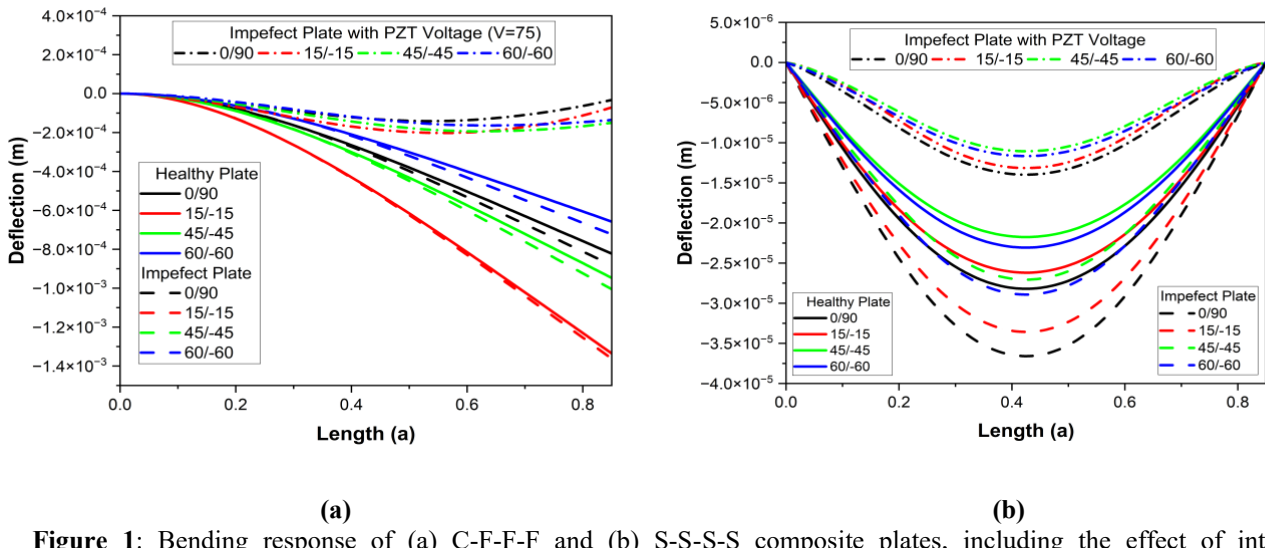


Figure 1: Bending response of (a) C-F-F-F and (b) S-S-S-S composite plates, including the effect of internal imperfection and PZT actuator at various voltages

4. CONCLUSIONS

The incorporation of PZT actuators can effectively compensate for stiffness loss arising from imperfections within composite structures. By integrating PZT actuator layers, the bending response degraded by imperfections can be significantly improved. Therefore, the synergy between VAT laminas with curved fibers and PZT layers can be highly beneficial, provided that an optimal sequence of fiber orientations is selected.

5. REFERENCES

- [1] Hyer, M. W., & Lee, H. H. (1991). The use of curvilinear fiber format to improve buckling resistance of composite plates with central circular holes. *Composite Structures*, 18(3), 239-261.
- [2] Abdalla, M. M., Gürdal, Z., & Abdelal, G. (2008). Thermomechanical response of variable stiffness composite panels. *Journal of Thermal Stresses*, 32(1-2), 187-208.
- [3] Valliappan, S., Murti, V., & Wohua, Z. (1990). Finite element analysis of anisotropic damage mechanics problems. *Engineering Fracture Mechanics*, 35(6), 1061-1071.
- [4] Sharma, N., Swain, P. K., & Maiti, D. K. (2023). Static and dynamic control of smart damaged variable stiffness laminated composite plate with piezoelectric layers. *Mechanics Based Design of Structures and Machines*, 1-26.

* Communicating Author: Ansh Kapoor and ansh.kapoor1@s.amity.edu

Computation of heat flux over Winged Reusable Launch Vehicle – Technology Demonstrator and comparison with flight data

Jiju R. Justus^{a*}, Sundeep Kumar Epuri^b, Vidya G^c, Manokaran K^d

^aACMD/ADSG/AERO, VSSC/ISRO, Trivandrum, Kerala, India

^bAATD/ADSG/AERO, VSSC/ISRO, Trivandrum, Kerala, India

^cADSG/AERO, VSSC/ISRO, Trivandrum, Kerala, India

^dASTD/AHTG/AERO, VSSC/ISRO, Trivandrum, Kerala, India

1. INTRODUCTION & OBJECTIVE

Reentry vehicles are of various types such as ballistic, semi-ballistic and winged reentry vehicles. RLV HEX mission using a winged reentry vehicle was accomplished successfully few years ago. The aerodynamic parameters such as force coefficients, hinge moment coefficients as well as pressure distribution as estimated using in-house Cartesian mesh based CFD solver during descent phase have been validated with flight data earlier [1,2]. In this paper, the heat flux is estimated on the windward side of the vehicle using CFD solver in typical ascent and descent environments and compared with the flight measured data.

2. METHODOLOGY

Body-fitted unstructured mesh with prism layers has been generated using 'Pointwise' software. The ascent flight conditions correspond to Mach number 4.6 and at altitude of 33 km, whereas descent phase conditions correspond to Mach number 3.5 and altitude of 26 km. The angle of attack in ascent phase is low (1.3^0) whereas the angle of attack in descent phase is moderately high (17.6^0). The study configuration (Figure 1), details of mesh and boundary conditions (Figure 2) and the heat flux distribution on the complete vehicle (Figure 3) is presented in the paper.

2. RESULTS AND DISCUSSION

The nose cap and the leading edges of wing and vertical tail face higher heat flux in ascent phase due to higher dynamic pressure as compared to descent phase. However, the fuselage windward side faces higher heat flux in descent phase because of higher angle of attack. The results for the fuselage windward side heat flux have been validated with flight data available in [3].

Keywords: CFD, winged reentry vehicle, CFD++, heat flux, RLV, ascent and descent phases

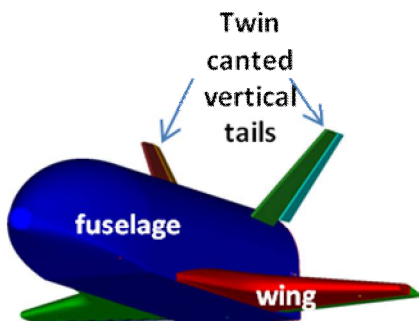


Figure 1: *Study configuration*

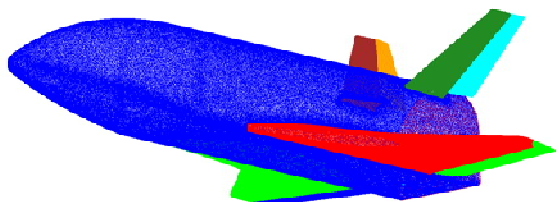


Figure 2: *Unstructured surface mesh*

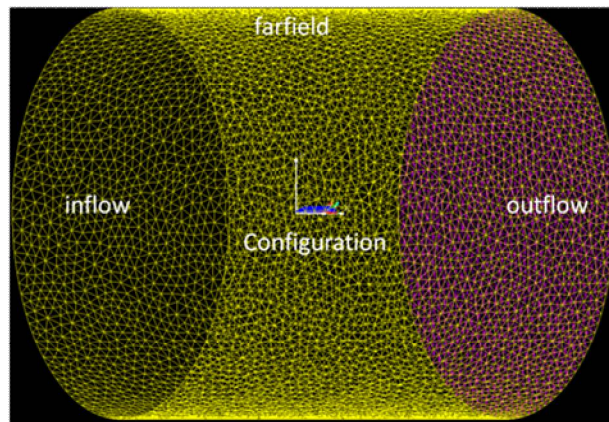


Figure 3: *Computational domain and boundary conditions*

References

1. G Vidya et al., Aerodynamic design, characterization and parameter estimation from flight data, (2017), Journal of Aerospace Sciences and Technologies, 69(3A), pp 423-439.
2. G Vidya, K Manokaran, C Babu, Haroon Rasheed, Dipankar Das, M M Patil, V Ashok, Validation of PARAS3D RANS pressure data with flight results over a wing-body RLV configuration at supersonic high angle of attack conditions, (2019), Journal of Aerospace Sciences and Technologies, Vol.71, No14, pp.30-35
3. Rony Varghese, et.al, Aero-thermal Design, Analysis, Thermo-Structural Testing & Qualification of RLV-TD, (2017), Journal of Aerospace Sciences and Technologies, 69(3A), pp 423-439.

COMPUTATIONAL INVESTIGATION OF AERODISK GEOMETRIES IN A SPIKED BLUNT BODY FOR HYPERSONIC HEAT REDUCTION

Sanjay Satish^a, Satheeshkumar S.^{b*}, Nivin Francis^c

^aAssistant Professor, Department of Mechanical Engineering, Rajiv Gandhi Institute of Technology, Kottayam, Kerala

^b*Student, College of Engineering Trivandrum, Trivandrum, Kerala

^cAssistant Professor, Department of Aeronautical Engineering, ACE College of Engineering, Trivandrum, Kerala

1. INTRODUCTION & OBJECTIVE

Hypersonic vehicles face severe aerodynamic drag and thermal loads, challenging efficiency and structural integrity. This study investigates passive and active flow-control strategies—headed aerospikes, multiple flat aero-disks, and rear opposing jets—using CFD. A conical spiked blunt body with multiple aero-disks and a rear opposing jet reduced both drag and surface heat flux compared to a conventional blunt body. Drag reduction was primarily due to shock detachment by the aero-disks, while the rear jet lowered wake-region heating. Various spike head geometries—flat-faced, hemispherical, conical, hybrid, and single-disk—were compared to identify the optimal combination of spike shape, disk placement, and jet parameters for minimizing drag and heat flux.

2. METHODS OF ANALYSIS

Numerical simulations were performed using ANSYS Fluent, with the computational mesh generated in ICEM-CFD. A 2D axisymmetric domain modelled the spiked blunt-body configuration. The flow was solved using RANS equations with the SST $k-\omega$ turbulence model to capture shock-boundary layer interactions. Air was treated as an ideal gas with viscosity computed from Sutherland's law. A density-based solver with a CFL number of 0.5 ensured stability. Convergence was achieved when residuals decreased by three orders of magnitude and net mass imbalance was below 0.001 kg/s. The spike length and body diameter were 100 mm ($L/D=1$). Three aero-disks were placed along the spike at an axial spacing ratio of 2:1:3, with radii of 14.41 mm, 21.82 mm, and 29.24 mm, optimized for shock detachment and drag reduction.

A comparative study examined various spike head geometries: flat-faced, hemispherical, flat aero-disk, hybrid (flat + hemispherical), and conical. Percentage reduction in drag and surface heat flux served as the key performance metric. Geometric configurations are shown in the figures.

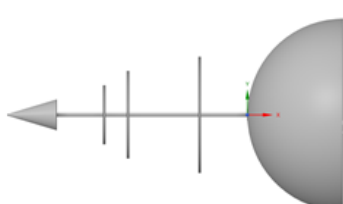


Fig.2.1. Conical Aerospike

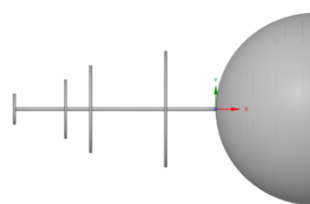


Fig.2.2. Flat Aerospike

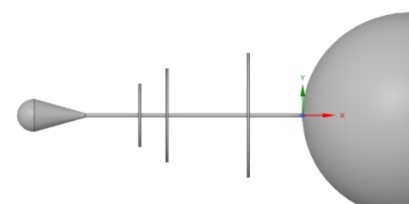


Fig.2.3. Flat face combined with hemispherical Aerospike

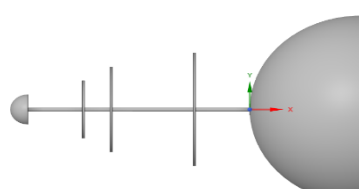


Fig.2.4. Hemispherical Aerospike

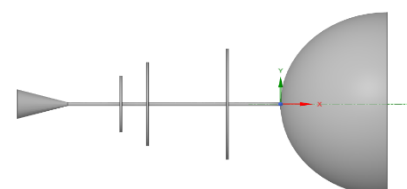


Fig.2.5. Flat faced Aerospike

*Communicating Author: satheeshkumars2019@gmail.com

Table 1: Boundary Conditions

| | Mach No. | Static Temperature (K) | Static Pressure (Pa) | Velocity (m/s) |
|---------------------|----------|------------------------|----------------------|----------------|
| Freestream | 6 | 247.02 | 21.96 | 1890.45 |
| Opposing jet | 1.5 | 300 | 4.4 | |

3. RESULTS

The optimum configuration and its corresponding Mach number contour are presented in Figure 3.1, while the comparative surface heat flux for different geometries is shown in Figure 3.2. Results indicate that the hemispherical aerospike attached to the blunt body provides superior reduction in both aerodynamic drag and surface heat flux compared to the other configurations.

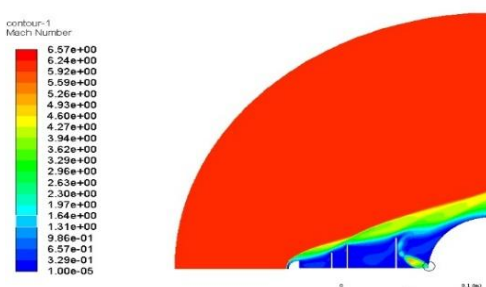


Fig.3.1. Mach Contour

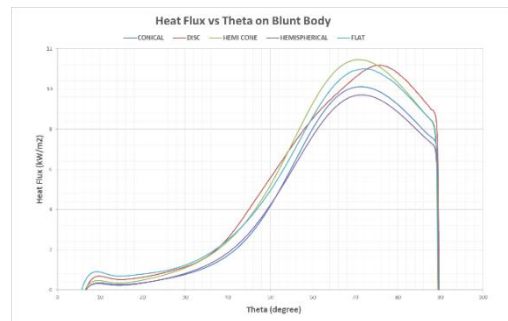


Fig.3.2. Heat flux v/s Theta on blunt body

4. CONCLUSIONS

1. Multiple flat aero-disks enhance freestream compression and reduce the intensity of the reattachment shock wave.
2. The rear opposing jet, with a jet pressure ratio of 0.2, effectively pushes the reattachment shock away from the blunt surface, lowering both shock strength and surface temperature.
3. Injection of low-temperature gas through the opposing jet provides additional cooling of the blunt body region.
4. The hemispherical aerospike configuration achieved the best overall performance, with a 0.344% reduction in drag and a 3.306% reduction in heat flux compared to the baseline conical configuration.
5. The combined use of optimized aero-disks and a properly tuned rear jet offers an effective passive-active approach for drag and heat mitigation in hypersonic vehicles.

5. REFERENCES

- [1] Zhenkang Zhang, Wanwu Xu, Wei Ye, Zhiyan Li, "Study on hypersonic drag and heat reduction of a spiked blunt body with multiple flat aerodisks and rear opposing jets", Case Studies in Thermal Engineering, 2023.
- [2] Senthilkumar S, Aarohi Anmol Mudholkar and Sanjay K J., "A Comparative study on Aerodynamic Drag Reduction of a blunt Nose Body using Aerospike and Aerodisk", ELSEVIER 2021.
- [3] Jie Huang a, Wei-Xing Yao, "Parameter study on drag and heat reduction of a novel combinational spiked blunt body and rear opposing jet concept in hypersonic flows", ELSEVIER, 2020.
- [4] S.Manigandan, K N Sruthisree, KaushaliAich, P.Gunasekar, S.Nithya, J.Devipriya, S.Venkatesh, "Numerical analysis of slotted aerospike for drag reduction", Journal of physics, IOP Publishing, 2019.
- [5] Jie Huang a, Wei-Xing Yao, "Multi-objective design optimization of blunt body with spike and aerodisk in hypersonic flow", ELSEVIER, 2019.

*Communicating Author: satheeshkumars2019@gmail.com

Correlation of Tulip Flame Formation and CH Chemiluminescence Bursts in Confined Propane-Air Combustion

Abhishek Kumar^a and Ratan Joarder^b

^a Research Scholar, Department of Aerospace Engineering, IIT Kharagpur, India

^b Associate Professor, Department of Aerospace Engineering, IIT Kharagpur, India

Abstract: In this work, we studied how the fuel–air equivalence ratio changes the way propane–air flames propagate and become unstable in a rectangular chamber. For this, we used a high-speed camera (5000 fps) along with CH* chemiluminescence detection, so that flame images and heat release signals were recorded at the same time. The experiments were carried out for equivalence ratios between 1.1 and 1.47. From the flame images, we looked at how the flame front developed, its speed, and how the shape changed from finger type to tulip flame and further. The chemiluminescence signal (CH*) was tracked in time, and this was compared with flame development. It was noticed that with richer mixtures, the tulip flame formed earlier, and also the CH* signal was stronger, showing sudden bursts exactly when instabilities appeared. A clear relation was observed between the maximum CH* intensity and the key points of flame deformation. This indicates that CH* emission can be used as an early marker of instability for rich propane–air flames. The study adds a useful understanding of how heat release and flame dynamics are connected at higher equivalence ratios, which is important for designing and checking the stability of confined combustion systems.

1. Introduction:

The study of flame propagation in premixed combustible mixtures is important for understanding combustion stability, safety, and efficiency in confined chambers. Among different gaseous fuels, propane is widely used in industrial and domestic applications, yet detailed investigations on its flame dynamics at rich equivalence ratios are still limited compared to methane or hydrogen. The equivalence ratio plays a key role in deciding flame structure, burning velocity, and the onset of instabilities such as the well-known tulip flame formation.

Most of the previous studies have focused on global flame parameters or on lean-to-stoichiometric mixtures, whereas the flame behaviour at higher equivalence ratios ($\phi \approx 1.4\text{--}1.5$) has not been explored in detail. In particular, the combined use of high-speed flame imaging and chemiluminescence diagnostics provides an opportunity to link visual flame morphology with heat release processes. The CH* radical emission near 430 nm is a commonly accepted marker for local heat release and can therefore be correlated with flame instabilities.

The present work addresses this gap by studying premixed propane–air flames in a rectangular chamber using simultaneous high-speed imaging and CH* chemiluminescence. The focus is on how increasing fuel richness affects flame propagation speed, morphology transitions (from finger-shaped front to tulip flame), and the timing of instabilities. By linking these features with the temporal evolution of CH* intensity, the work aims to provide new insights into the coupling of heat release and flame dynamics at elevated equivalence ratios.

2. Experimental Facility and Methodology

The experiments were carried out in a rectangular acrylic combustion chamber ($400 \times 40 \times 40$ mm) built in-house, with 12 mm thick optical windows on the front and back and 20 mm thick plates on the top and bottom for strength. A thin diaphragm on the right side acted as a safety vent. Propane and air were supplied through mass flow controllers to set ϕ between 1.1 and 1.47, and the mixture was allowed to mix for 10 minutes before ignition at $x = 50$ mm, $w = 20$ mm, $h = 20$ mm.

Flame propagation was captured using a Photron AX Mini 50 at 5000 fps (exposure = 1/frame rate). Under the same conditions, CH* chemiluminescence at 430 nm was recorded by mounting a bandpass filter on the same camera. The recorded videos were cropped to the propagation part and processed in ImageJ to track flame fronts along the centreline and walls. Pixel data were converted to position (mm) using calibration, and position-time and velocity-time plots were generated in Excel. Flame shape evolution (finger, tulip, oscillatory stages) was identified and marked. CH* intensity was integrated over time and compared with flame images at the same timestamps to relate heat release with flame dynamics. Preliminary efforts are also underway to approximate heat release rate from CH* signals.

3. Preliminary Results and Discussion:

Flame Front Evolution from Imaging: Figure 1 shows the direct flame images at two instants (12.8 ms and 28.0 ms), along with the corresponding CH* chemiluminescence images recorded at the same times. At 12.8 ms, the flame front in the direct image is smooth and finger-shaped, representing the early propagation stage. The CH* image at this instant shows a compact, bright emission zone confined to the leading edge of the flame, indicating that active heat release is localised in a much narrower region than the luminous flame thickness seen in normal imaging.

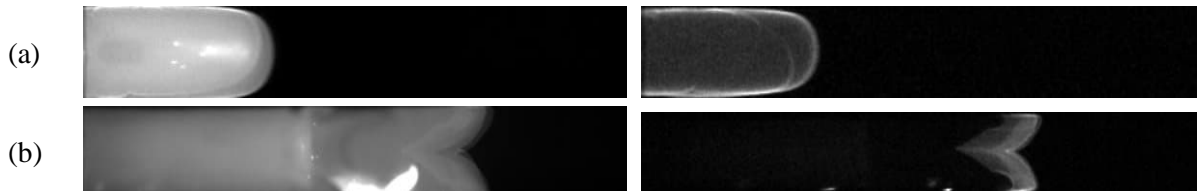


Figure 1. Comparison of flame images and CH* chemiluminescence at $\phi = 1.47$. (a) $t = 12.8$ ms, finger flame; (b) $t = 28$ ms, tulip flame.

At around 28 ms, the normal flame picture shows the tulip flame very clearly, where the front has flipped in shape because of the chamber walls and pressure effects. In the CH* image at the same time, the light is brighter and not uniform. It looks patchy along the flame front. This means that when the tulip flame forms, the burning not only becomes stronger but also uneven in different parts of the flame.

Position–Velocity Characteristics at $\phi = 1.47$: The position and velocity data of the flame front for equivalence ratio $\phi = 1.47$ are presented in Figure 2. The flame advances steadily, reaching a maximum position of about 302 mm, close to the chamber end wall. The flame speed goes up quickly after ignition and reaches about 20 m/s at nearly 13 ms. After that the flame slows down as it travels toward the end of the chamber and starts to get unstable. This matches what is seen in the images, because the finger flame begins to turn into a tulip shape just after the velocity peak.

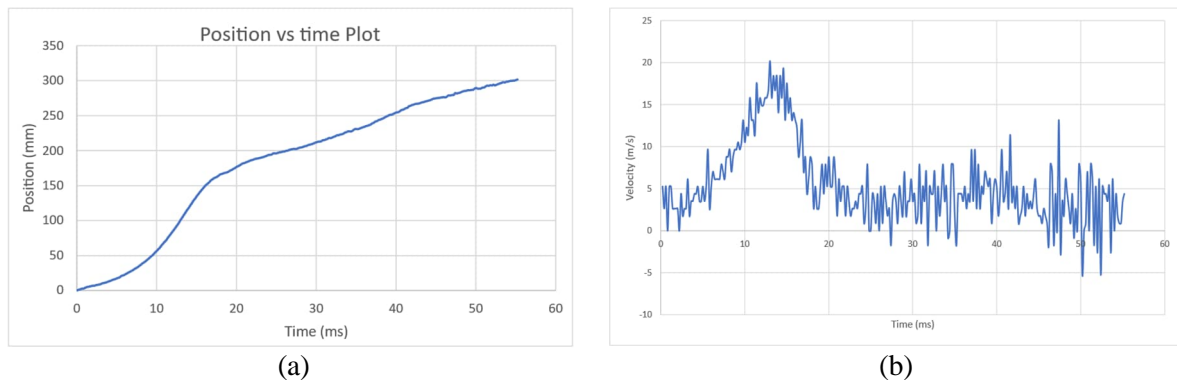


Figure 2. Position–time (a) and velocity–time (b) plots of flame front for propane–air combustion at $\phi = 1.47$.

Combined Interpretation: When we look at the pictures together with the velocity data, we can see the link more clearly. The highest speed at 13 ms also lines up with the time when the CH* signal begins to grow, so flame acceleration and heat release are happening together. Later, when the tulip shape

appears around 28 ms, the CH* signal is not smooth anymore but scattered in patches, showing bursts of burning at different spots.

In summary, while the direct flame images give information about the overall shape and front movement, the CH* chemiluminescence highlights the chemically active zones and provides a more accurate picture of heat release. The velocity data bridges these two diagnostics by showing that mechanical flame acceleration and chemical activity peaks occur at closely linked times, particularly around instability onset.

Curvature-Constrained UAV Path Following Using Finite-Time Sliding Mode Control

Panasa Pranav Kumar*, Sayantan Pal** and Sikha Hota***

*Undergraduate Student, Aerospace Engineering, Indian Institute of Technology Kharagpur, Kharagpur, India

**Research Scholar, Aerospace Engineering, Indian Institute of Technology Kharagpur, Kharagpur, India

***Associate Professor, Aerospace Engineering, Indian Institute of Technology Kharagpur, Kharagpur, India

1. INTRODUCTION & OBJECTIVE

In modern-day applications of Unmanned Aerial Vehicles (UAVs), there are many instances where the physically allowable maximum turning rate is limited to a certain bound, especially in the case of a fixed-wing UAV. As a result, the time to converge cannot be set arbitrarily low. In addition, external disturbance can cause the UAV to deviate from the path during the turn. So, there is a need for an approach that is fast-converging and robust to external disturbance. The Sliding Mode Controller serves the purpose, as it is robust to external disturbances, as proven in [1], and a Fast-Terminal Sliding Mode Control approach, as in [2], would compensate for the increased convergence time. In this study, we propose an enhanced Sliding Mode strategy that converges in finite time and achieves a higher convergence rate, under various constraints on turning rate.

2. METHODS OF ANALYSIS

Consider the UAV with $(x_{init}, y_{init}) \in \mathbb{R}^2$ as initial position and $\psi_{init} \in \mathbb{R}$ as initial heading angle flying at a constant altitude with planar engagement at a speed, $v \in \mathbb{R}_+$ relative to steady wind with a velocity, $\mathbf{V}_{wind} = w_x \hat{\mathbf{e}}_x + w_y \hat{\mathbf{e}}_y$ such that $|\mathbf{V}_{wind}| \ll v$. Let the instantaneous position be denoted by $(x, y) \in \mathbb{R}^2$ and the instantaneous heading angle be denoted by $\psi \in \mathbb{R}$ at a specific moment. Then the kinematic equations that govern the motion of the UAV can be expressed as:

$$\dot{x} = v \cos(\psi) + w_x; \quad \dot{y} = v \sin(\psi) + w_y; \quad \dot{\psi} = \frac{a_c}{v}$$

Let r represent the perpendicular distance between the desired path and the instantaneous position of the UAV at the specific moment, which is updated in real time. It should be noted that the actual turn rate of the path, $\dot{\psi}_r$, is not available to the guidance algorithm and is considered an unknown bounded uncertainty. Also, the turn rate of the UAV is constrained so that the maximum turn-rate can be $\dot{\psi}_{max}$. The rate of approach can be expressed as $\dot{r} = v \sin(\psi - \psi_r)$ and its dynamics as $\ddot{r} = a_c \cos(\psi - \psi_r) + \epsilon$, where ϵ is a bounded uncertainty. Now, consider a non-linear sliding surface, $S = \dot{r} + \beta r^\gamma + \lambda \tanh(kr) r^\eta$. By choosing our control law as in Eq.(1), we can prove that the system is stable with respect to Lyapunov stability criterion.

$$a_c = -\frac{1}{|\cos(\psi - \psi_r)|} \left(k_1 |S|^{\frac{1}{2}} \operatorname{sgn}(S) + \phi(r) \dot{r} \right); \quad (1)$$

where $\phi(r) = (\beta \gamma r^{\gamma-1} + \lambda (k \operatorname{sech}^2(kr) r^\eta + \eta \tanh(kr) r^{\eta-1}))$. Without loss of generality, $\beta, \gamma, \lambda, \eta, k, k_1$ are all chosen to be positive. Considering the reachability condition, we obtain that γ is odd and η is even. The time to converge to the desired path is finite and is expressed as

$$t = t_0 + \int_0^{r_0} \frac{dr}{\beta r^\gamma + \lambda \tanh(kr) r^\eta} \leq t_0 + \int_0^{r_0} \frac{dr}{r^\eta} \leq t_0 + \frac{r_0^{1-\eta}}{1-\eta} \quad (2)$$

where t_0, r_0 are the time taken to reach the sliding surface and the initial perpendicular distance, respectively. Hence, for finite-time convergence, γ and η are chosen such that $\gamma < 1$ and $\eta < 1$.

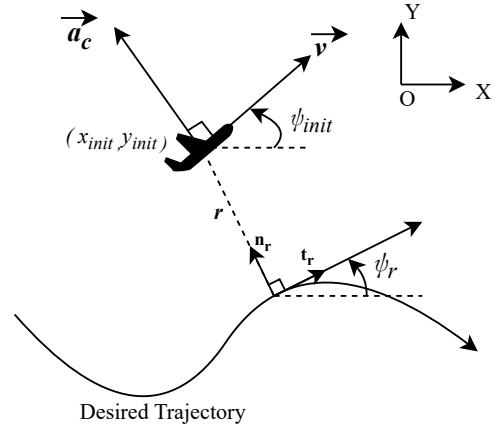


Figure 1: Schematic of a UAV path-following problem

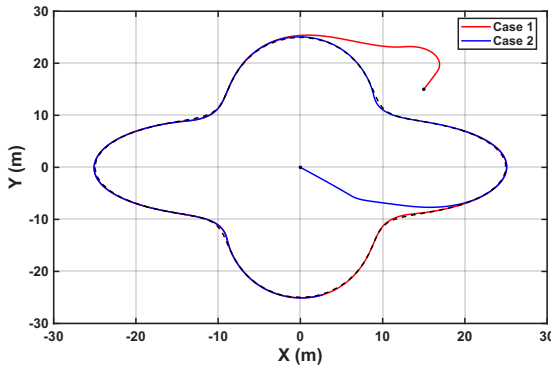
The control law ensures that the UAV is directed towards the sliding surface for all configurations except in the cases where the initial heading angle ψ_{init} is perpendicular to the slope at the closest point in the path, $\psi_{init} - \psi_r \neq \pm \frac{\pi}{2}$. It must not normally be towards the surface in the case of a straight line only, as there will be no change in the effect of ψ_r . In simpler terms, the UAV should not initially be directed away from the desired path.

3. RESULTS AND/OR HIGHLIGHTS OF IMPORTANT POINTS

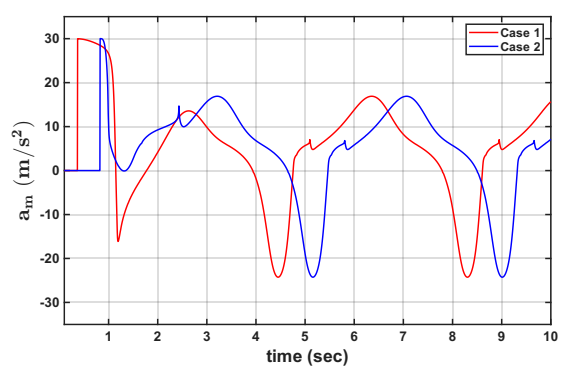
The UAV is made to follow an arbitrary path defined by equations $x(t) = r(t) \cos(t)$ and $y(t) = r(t) \sin(t)$ where $r(t) = 20 (1 + \frac{1}{4} \cos(4t))$, with the following initial conditions.

Case 1: $(x_{init}, y_{init}) = (15, 15)$ $\psi_{init} = 60^\circ$
 $t_0 = 1.209224$ s, $r_0 = 5.987850$ m
 $t = 3.335056$ s < 8.361169 s $= t_0 + \frac{r_0^{(1-\eta)}}{1-\eta}$

Case 2: $(x_{init}, y_{init}) = (0, 0)$ $\psi_{init} = 330^\circ$
 $t_0 = 0.786857$ s, $r_0 = 15.000000$ m
 $t = 2.379224$ s < 9.380717 s $= t_0 + \frac{r_0^{(1-\eta)}}{1-\eta}$



(a)



(b)

Figure 2: Simulation results

The simulations are performed in MATLAB R2025a. The speed of the UAV is set to be 10 m/s, and the wind speed is considered to be 1 m/s at an angle of 45° to both axes. The parameters $\beta, \gamma, \lambda, \eta, k$ and k_1 are chosen to be 3, 0.6, 0.6667, 0.8, 0.01 and 20, respectively. The trajectories followed by the UAV to converge to the desired path are illustrated in Fig 2(a), and the corresponding control input, that is, the lateral acceleration plots, are depicted in Fig 2(b). It can be seen that acceleration is restricted between -30 m/s^2 and 30 m/s^2 and the convergence time satisfies the inequality derived in Eq.(2).

4. CONCLUSIONS

This work introduces a finite-time sliding mode control strategy that navigates the UAV towards the planned path subject to constraints on turn radius or turn rate. The approach is extended to follow arbitrary paths whose curvature is within the given turning rate of the UAV, and also, the algorithm does not require any prior knowledge of the exact curvature of the planned path. By performing simulations under various paths and initial conditions, it is observed that the proposed algorithm ensures finite-time convergence to the desired path, as well as robustness against external disturbances and uncertainties.

5. REFERENCES

- [1] S. Kumar, S. R. Kumar, and A. Sinha, “Separate guidance and control design for autonomous path-following,” *IFAC-PapersOnLine*, vol. 55, no. 22, pp. 212–217, 2022, 22nd IFAC Symposium on Automatic Control in Aerospace ACA 2022. [Online]. Available: <https://www.sciencedirect.com/science/article/pii/S240589632300294X>
- [2] C. Hisar, G. Balta, N. Altin, and I. Sefa, “An improved fast terminal sliding mode control for step-down converter,” in *2023 15th International Conference on Electronics, Computers and Artificial Intelligence (ECAI)*, 2023, pp. 1–5.

*Communicating Author: Panasa Pranav Kumar, panasapranavkumar@gmail.com

Deflection Characteristics of Piezoelectric Composite Plates under UDL and SSL Using Refined Second Shear Deformation Theory

Pawar Raju Sidhu^{a,d}, Achchhe Lal^{b*}, Rahul Sudam Kamble^c

^{a,c} Ph. D Student, Department of Mechanical Engineering, SVNIT Surat, Gujarat, India;

^b Associate Professor, Department of Mechanical Engineering, SVNIT Surat, Gujarat, India.

^d Assistant Professor, Department of Mechanical Engineering, Gokhale Education Society's R. H. Saput College of Engineering, Management Studies and Research, Nashik, Maharashtra, India.

1. INTRODUCTION & OBJECTIVE

Piezoelectric laminated plates are widely used in aerospace, automotive, and electronic systems due to their multifunctional capabilities in sensing, actuation, and vibration control. Accurate prediction of deflection and stress distribution in these plates is critical for ensuring structural reliability and performance. Deflection behavior is influenced by various factors including loading type, boundary conditions, stacking sequence, material properties, and electromechanical coupling. Classical plate theories, such as Classical Laminate Plate Theory (CLPT) and First-Order Shear Deformation Theory (FSDT), often fail to capture the behavior of moderately thick and thin laminated plates under complex loadings. To address this limitation, refined higher-order theories have been developed. The Refined Second Shear Deformation Theory (RSSDT), incorporating Grover-type kinematic assumptions, provides improved accuracy in predicting deflection and stress while eliminating the need for shear correction factors. Various refined shear deformation theories have been proposed by various authors for accurately predict the transverse central deflection and stresses. In this direction, [1] developed Refined Second Shear Deformation Theory (RSSDT) for accurately predict the transverse central deflection and stresses of laminated sandwich plate. In the same direction, [2] and [3] developed various nonpolynomial shear deformation theories (NDSTs) and successfully applied to thick and moderately thick laminated and sandwich composite plate with suitable penalty parameters. They predict that penalty parameters are significant for thick plate and green Lagrange nonlinearity played a significant role for better convergence specially for thick plate. [4] proposed various polynomial and nonpolynomial shear deformation theories for accurately predict the structural response using higher order shear deformation theories. They accurately predicted the structural response and compared with closed solution using various polynomial and nonpolynomial theories. The effect of nonlinear free vibration response of piezo-laminated composite plate using VK nonlinearity for various input parameters are analysed by [4]. In the present study, recently proposed NDSTs such as TSDT and RSSDT are proposed to accurately predict the transverse central deflection and applied successfully for nonlinear analysis of piezo laminated composite plate.

2. GENERAL FORMULATION

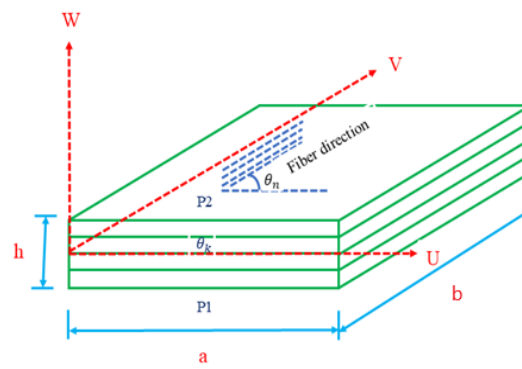


Figure. 1. Piezoelectric Composite Plates

Figure 1 shows the rectangular multilayered Piezoelectric Composite Plate of 'n' elastic orthotropic layers stacked in particular sequence ($\theta_1 / \theta_2 / \theta_3 / \theta_4 / \dots / \theta_n$) is considered. The plate dimensions are named as length a , width b , and uniform thickness ' h '. A Cartesian coordinate system, with x y plane consisting with middle plane of the plate, is chosen as shown in Figure 1. In this study, recently developed refined second shear deformation theory (RSSDT) [1], [5] is applied as. $f(z) = \sinh^{-1} \left(\frac{rz}{h} \right) - \frac{2rz}{h\sqrt{4+r^2}}$, Where $r = 3$

Corresponding author: achchhel@med.svnit.ac.in

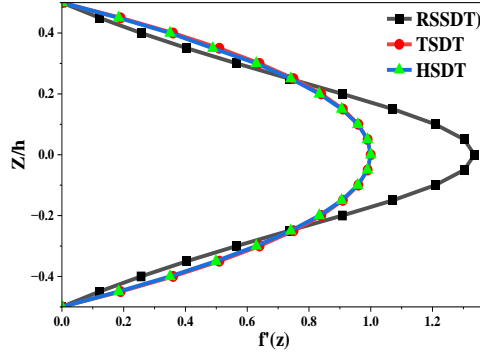


Figure. 2. The variation of $f'(x)$ for proposing transverse shear strain functions

Figure 2 shows the variation of derivative of $f(z)$ using TSDT, HSDT and RSSDT through the thickness. It shows that the transverse shear function shows the parabolic (quadratic) variation of transverse shear strain and stress across the thickness.

3. SOLUTION TECHNIQUES

3.1 Governing equation for forced vibration

The governing equation for forced vibration of laminated composite plate reinforced with SMA fiber can be derived using Variational principle, which is generalization of the principle of virtual displacement.

$$[\bar{K}]\{\mathbf{q}\} = \{\mathbf{F}\} \quad (1)$$

Where $[\bar{K}] = [K_q] - [K_{q\phi}][K_\phi]^{-1}[K_{q\phi}]^T$ is the nonlinear governing equation of transverse central deflection problem and can be solved by iterative procedure using Newton's Raphson method.

4. RESULTS AND DISCUSSION

4.1 Validation and parametric study

Table 1 Normalized central deflection (W) of simply supported (SSSS1) square laminated $0^0/90^0/90^0/0^0$ plate subjected to sinusoidal distributed load (SSL) with parameters ($a/h = 10$, SSSS1)

| a/h | Q | IHSIDT [2] | Present (RSSDT) |
|-------|-----|------------|-----------------|
| 10 | 50 | 0.3474 | 0.33116 |
| | 100 | 0.6501 | 0.58082 |
| | 200 | 1.1147 | 0.91482 |
| | 300 | 1.4605 | 1.4563 |

5. CONCLUSIONS

This study presented an analytical investigation into the deflection behavior of piezoelectric laminated composite plates subjected to uniformly distributed (UDL) and sinusoidal surface loadings (SSL) under simply supported (SSSS) and fully clamped (CCCC) boundary conditions. The good matching of results with FEM-TSDT confirmed the accuracy and validity of the developed formulation.

5. REFERENCES

- [1] N. Grover, B. N. Singh, and D. K. Maiti, "New nonpolynomial shear-deformation theories for structural behavior of laminated-composite and sandwich plates," *AIAA Journal*, vol. 51, no. 8, pp. 1861–1871, Aug. 2013, doi: 10.2514/1.J052399.
- [2] B. R. Thakur, S. Verma, B. N. Singh, and D. K. Maiti, "Dynamic analysis of folded laminated composite plate using nonpolynomial shear deformation theory," *Aerospace Sci Technol*, vol. 106, Nov. 2020, doi: 10.1016/j.ast.2020.106083.
- [3] S. Verma, B. R. Thakur, B. N. Singh, and D. K. Maiti, "Geometrically nonlinear flexural analysis of multilayered composite plate using polynomial and non-polynomial shear deformation theories," *Aerospace Sci Technol*, vol. 112, May 2021, doi: 10.1016/j.ast.2021.106635.
- [4] P. Dash and B. N. Singh, "Nonlinear free vibration of piezoelectric laminated composite plate," *Finite Elements in Analysis and Design*, vol. 45, no. 10, pp. 686–694, Aug. 2009, doi: 10.1016/j.finel.2009.05.004.
- [5] R. Kumar, A. Lal, B. N. Singh, and J. Singh, "New transverse shear deformation theory for bending analysis of FGM plate under patch load," *Compos Struct*, vol. 208, pp. 91–100, Jan. 2019, doi: 10.1016/j.compstruct.2018.10.014.

Deformation Behavior of Soft Electroelastic Membranes Subjected to Large Electric Fields

Yadwinder Singh Joshan^{a*}, Sushma Santapuri^b and Debasish Khan^c

^aAssistant Professor, Department of Mechanical Engineering, Indian Institute of Technology (BHU) Varanasi, UP, 221005, India

^bAssociate Professor, Department of Applied Mechanics, Indian Institute of Technology Delhi, New Delhi, 110016, India

^cProfessor, Department of Mechanical Engineering, Indian Institute of Technology (BHU) Varanasi, UP, 221005, India

1. INTRODUCTION & OBJECTIVE

Dielectric elastomers are electroelastic materials that are capable of undergoing large strains under applied electric field. Modeling these materials requires integration of nonlinear electrodynamics with continuum mechanics for hyperelastic materials. When dielectric elastomers are placed between two deformable electrodes and electric field is applied, these materials undergo spontaneous polarization. The positive and negative charges produced due to potential difference compresses the elastomer due to force of attraction between them, which causes in-plane stretching due to incompressible nature of the elastomer. Due to the high strain ability of dielectric elastomers, these materials have wide applications as actuators and sensors in the field of soft robotics and biomedical engineering. In the present work, dielectric elastomers are analyzed for the design of soft membrane actuators. The membrane actuators are modelled using an $O(h)$ non-linear membrane theory incorporating finite deformations. Specifically, deformations and limit point instability in circular and cylindrical membrane actuators and their dependence on material properties is analyzed for varying pressure and voltage inputs. The utility of this computational framework in design of actuators is demonstrated through these examples.

2. MATHEMATICAL FORMULATION

The electroelastic membranes are modelled using $O(h)$ membrane theory under applied internal pressure and electric field. The pointwise 2D electrostatic governing equations are given by [1]

$$\text{Div}(\mathbf{1}\mathbf{D}_0) = 0, \quad \mathbf{D}_0 \cdot \mathbf{N}_3 = -\sigma_F \quad (1)$$

where **Div** represent Lagrangian divergence operator, $\mathbf{1} = \mathbf{I} - \mathbf{N}_3 \otimes \mathbf{N}_3$, \mathbf{I} is the identity tensor, \mathbf{N}_3 is the normal to the mid-surface of the membrane, \mathbf{D}_0 denotes the electric displacement tensor in reference configuration and σ_F is the applied surface charge density. It is important to note that the electric field outside the dielectric membrane is zero, which eliminates Maxwell-stress-induced traction on the exterior boundary. Similarly, the governing equations for the pressurized membrane are expressed as [1]:

$$\text{Div}(\mathbf{1}\mathbf{P}_0) = -\{(p^+ - p^-)/h\}(J\mathbf{F}^T)_0 \mathbf{N}_3, \quad \mathbf{P}_0 \mathbf{N}_3 = \mathbf{0}, \quad (2)$$

where \mathbf{P}_0 represents the Piola stress tensor on membrane mid-plane, p^+ and p^- are the applied pressure on the top and bottom surface of the membrane, respectively. J represents the determinant of the deformation tensor \mathbf{F} . These equations are subsequently specialized for cylindrical and circular membranes subjected to axisymmetric loading and a through-thickness electric potential.

3. RESULTS AND DISCUSSION

The deformation, stretches and limit point instability in electroelastic membranes due to applied electromechanical load are analyzed. Our results are verified with literature for passive membranes (in the absence of applied electric field) for circular and cylindrical membranes and different cases are analyzed to study deformation behavior of electroelastic membranes.

For verification of our results, the limit point insatiability in passive hyperelastic circular membrane under nondimensionalized uniform pressure Δp^* is analyzed. The pressure gradient is evaluated for a specified nondimensional deformation z^* ($R^*=0$) and load-deformation curves are presented in Fig. 1 for different values of nondimensional material parameter δ .

Our results are verified with Saxena et al. [2] for the case of Neo-Hookean material i.e. $\delta=1$. It may be noted that the results of Neo-Hookean ($\delta=1$) and Mooney-Rivlin ($\delta<1$) hyperelastic models are almost identical for smaller deformations $z^*<0.8$. However, the post limit point deformation is dependent on the choice of nondimensional material parameter δ . The pressure limit point is not observed for Mooney-Rivlin material $\delta>0.96$.

*Communicating Author: Yadwinder Singh Joshan, Email: yadwinder.mec@itbhu.ac.in

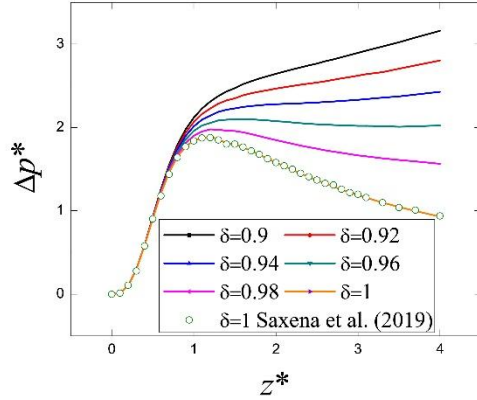


Fig. 1: Limit point instability plot for passive circular membrane for different nondimensional material parameter δ .

Further, the dielectric cylindrical membrane is analyzed under a constant pressure gradient $\Delta p^*=0.844$ and variable electric load $V^*=0.005-0.017$. The results are presented in Figure 2. It may be noted the bulge formation is observed at the center $z^*=0$ and the bulge evolves with the increase in the electric load.

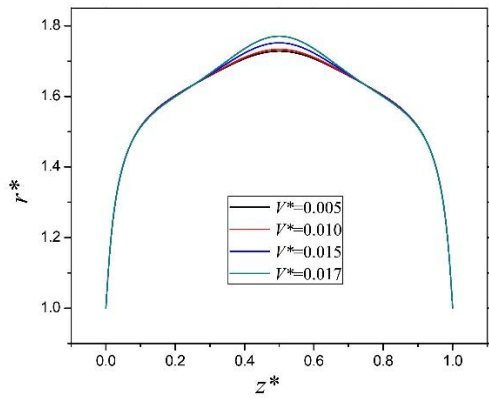


Fig. 2: Deformation plots for electroelastic cylindrical membrane under applied pressure and electric load.

4. CONCLUSIONS

An $O(h)$ finite deformation membrane theory is presented for electroelastic membranes. The membrane theory is used to model circular and cylindrical membranes. The constitutive behavior of the dielectric elastomer membrane is modelled using Mooney-Rivlin type electroelastic model. The deformation, stretches, and limit point instability in electroelastic membranes under transverse pressure and an electric field is analyzed. Our limit point results are validated with existing literature for a passive hyperelastic membrane. The model is further used to study deformation and limit point behaviour due to applied electric field in electroelastic membranes. It is observed that applied electric field increases the radial deformation and axial stretches in the membrane actuators. The applied electric field tends to decrease the value of limit point pressure and also decrease the pressure required in post limit point deformation. Thus, the applicability of electroelastic membrane theory toward the analysis and computational design of dielectric elastomer membrane actuators is demonstrated.

5. REFERENCES

- [1] A. Mishra, Y. S. Joshan, S. K. Wahi, and S. Santapuri, “Structural instabilities in soft electro-magneto-elastic cylindrical membranes,” *Int. J. Non-Linear Mech.*, vol. 151, pp. 104368, 2023.
- [2] P. Saxena, N. H. Reddy, and S. P. Pradhan, “Magnetoelastic deformation of a circular membrane: wrinkling and limit point instabilities,” *Int. J. Non-Linear Mech.*, vol. 116, pp. 250–261, 2019.

Design and Development of a Hybrid Model for Impact Analysis on Underwater Vehicles

Pankaj Meena^a and R. Sharma^{b*}

^a Research scholar, Design and Simulation Laboratory, Department of Ocean Engineering, Indian Institute of Technology Madras, Chennai (TN) - 600 036, India

^b Professor, Design and Simulation Laboratory, Department of Ocean Engineering, Indian Institute of Technology Madras, Chennai (TN) - 600 036, India

ABSTRACT

This article aims to design and develop a hybrid model for impact analysis and presents the preliminary results showing the effect of material properties on crack development and distribution of stresses and strains after explosion/impact, etc. Proposed hybrid approach has two components, i.e. Analytical model and numerical model. Analytical model is based upon the classical theories (i.e. Griffith and classical mechanics theories) and the numerical model is built upon the large deformation finite element analysis. Presented results examine the role of different materials (i.e. mild steel, Aluminum 7178-T651, Titanium Ti-6Al-4V, Glass, AISiC metal matrix composite and Epoxy etc.) under the uniform pressure load. Based upon the results and their analyses suitable design guidelines are derived.

Keywords: Submarine, stresses and crack-width, deep water, crack propagation, different beams etc.

1. INTRODUCTION

In the modern times, the incidence of terrorist attacks has risen, and regrettably, current trends indicate a potential further increase in the future, also. Normally, conventional structures are more prone to damage because potential explosive loads have magnitudes significantly exceeding typical design loads [1-2] and this scene demands the design and development of new age structures that can resist the impact loads.

2. OBJECTIVE

Our objective is to design and develop a FEA based model to study the impact through explosion for analyzing both the metal and composite plates.

3. METHODOLOGY

Following [2-3], we model an explosive using a high explosive burn material model represented as an equivalent TNT explosive for the PEK I explosive and the pressure in a high explosive element at any time is given:

$$p = F \times p_{eos}(V, E) \quad (1)$$

where p_{eos} is the pressure from the equation of state, F is the burn fraction, V is the relative volume, and E is the internal energy density per unit initial volume. Explosive is represented by the JWL equation of state in which the detonation pressure is expressed [4]:

$$p_{eos} = A \left(1 - \frac{\omega}{R_1 V}\right) e^{-R_1 V} + B \left(1 - \frac{\omega}{R_2 V}\right) e^{-R_2 V} + \frac{\omega E}{V} \quad (2)$$

where p_{eos} is the detonation pressure, E is the specific internal energy per unit mass, V is the specific volume and A, B, R1, R2, and ω are the explosive constants, respectively. The JWL equation parameters considered for the model and analysis are listed in Table 1.

*Communicating Author: Further author information: (Send correspondence to P. Meena)

P. Meena: E-mail: pankajmn92@gmail.com, Telephone: +91 8764384833

R. Sharma: E-mail: rajivatri@iitm.ac.in, Telephone: +91 8122636837, Address: Department of Ocean Engineering, Indian Institute of Technology Madras, Chennai (TN) - 600 036, India.

Table 1. List of the JWL equation of state parameters adapted from [4], and the computed maximum stresses, strains and displacements for the mild steel aluminum and carbon fiber

| Material | MA-AL-2014-T6 | MC-Steel-A36 | MD-Carbon-Fiber | JWL Parameters | |
|------------------------|---------------|--------------|-----------------|----------------|-------------|
| Max. Mises stress (Pa) | +8.124e+06 | +5.417e+06 | +3.606e+06 | A (GPa) 371.2 | R_2 0.95 |
| Max. strain | +4.743e-05 | +2.188e-05 | +7.924e-05 | B (GPa) 3.23 | w 0.3 |
| Max. displacement (m) | +2.488e-04 | +7.850e-05 | +3.492e-04 | R_1 4.145 | E (kJ/kg) 7 |

Basic flow chart followed in the designed and developed model is shown in Figure 1 (A). Generated mesh of the plate is shown Figure 1 (B). Our studies consider square plate in which three different types of plate materials and the plate is fixed from all the sides and we use explosive TNT. This is shown in Figure 1 (C). Plate dimensions are: 0.3 m \times 0.3 m and thickness of plate is 0.01 m. Mass of TNT is taken 1 kg and the MC-Steel-A36 with density of 7850 kg/m³, Young's modulus 203 GPa, and Poisson's ratio 0.3 is considered.

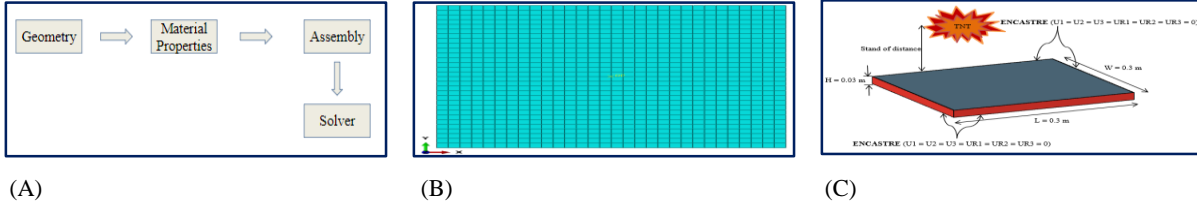


Fig. 1. (A) Basic flow chart followed in the designed and developed model, (B) Generated mesh of the plate, and (C) Square plate subjected to blast

4. RESULTS AND HIGHLIGHTS OF IMPORTANT POINTS

We compute the stresses and strains and examine extensively the role of different strains, the role of different material properties and plate thicknesses. Computed Mises stresses in the plate, for mild steel, at different heights of TNT detonations are shown in Figure 2. A comparative study is conducted on the three materials: MA-AL-2014-T6, MC-Steel-A36, and MD-Carbon-Fiber. Results in Table 2. Maximum stress obtained in ML-AL-2014-T6 is high as compared to MC-Steel-A36 and MD-Carbon-Fiber. Maximum strain and displacement obtained in MD-Carbon-Fiber is high as compared to ML-AL-2014-T6 and MC-Steel-A36.

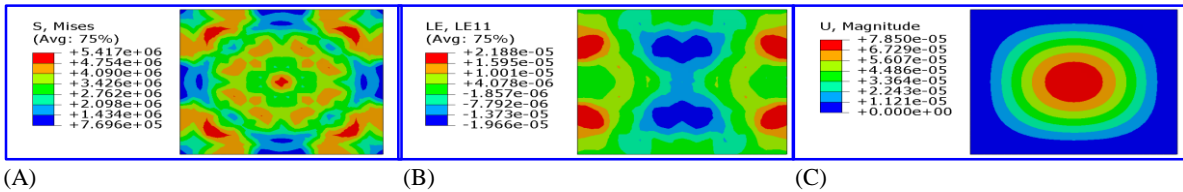


Figure 2. 2A - computed Mises stresses, 2B – computed strains and 2C – computed displacements in the plate, for the mild steel material.

5. CONCLUSIONS

Under the impact loads composite materials show higher energy absorption but they show weak performance in tension, buckling and bending/torsion. Because of these reasons in the application where, all the structural deformations are critical, e.g. in underwater vehicles, composite are useful only in certain specific areas where only impact loads dominate, like the front and tail ends, and not in other areas like middle parts, fins, etc.

REFERENCES

- [1] Iqbal, K. M. A. Senthil, Bhargava P., and Gupta N. K., The characterization and ballistic evaluation of mild steel, *International Journal of Impact Engineering*, 2015, vol. 78, p. 98–113.
- [2] Zhijian H., Chao L., Blast Loads on Concrete Bridges, *Advanced Materials Research*. 217–218 (2011) 445–450.
- [3] R. Sharma, Monograph on Structural Analysis and Design of Pressure Vessels Submarine Design and Engineering, CCE IIT Madras, ISBN: 978-93-80689-32-6, India, 2019.
- [4] B. M. Dobratz, LLNL explosive handbook. UCRL-52997, (1981).

Design of Vent system for crew escape system-test vehicle compartments

B.Venkat Shivaram Jadav^{a*}, Jathaveda.M^b, G.Vidya^c

^aSenior Manager, Launch vehicle building, NewSpace India Ltd, Bengaluru, India.

^b Scientist/Engineer, FMTD, ADSG, Aeronautics Entity, Vikram Sarabhai Space Centre, Thiruvananthapuram, India.

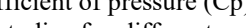
^c Group director, ADSG, Aeronautics Entity, Vikram Sarabhai Space Centre, Thiruvananthapuram, India.

1. INTRODUCTION

ISRO has come a long way from launching a sounding rocket in 1963 to completing complex missions like Mangalyaan, chandrayaan-3 and Aditya mission in recent years. ISRO's Gaganyaan program is going to be the next big milestone in terms of expanding its technical expertise in the field of space technology. The main aim of the program is to place an Indian in the space and Gaganyaan program is envisaged to do the job. Prior to the successful launch of the Gaganyaan mission with human on-board, all the systems and subsystems of the Gaganyaan vehicle have to be tested and validated. In this process, to validate the atmospheric Crew Escape System (CES) for various flight events, a test vehicle project (TV) with a single stage liquid propelled vehicle was conceived (as seen in figure 1) and launched on 21st October 2023.

Many systems and sub-systems in the Crew Escape System (CES) were qualified in the flight. Out of the many systems qualified, one of the major systems validated in the test vehicle flight was depressurisation/vent system for different structures like CES interface adaptor, Equipment Bay and base shroud compartments.

Venting or the depressurization system [1] is one of the important aspects of structural design. It plays an important role in relieving the entrapped air inside the compartments to outside. Vent schemes are provided to estimate the differential pressure across the compartments. In the test vehicle vent system was designed to meet the structural constraint of difference of compartment pressure to ambient pressure within $\pm 10\text{kPa}$. Design of vent system was carried out using in-house software MPVENT [2]. Inputs such as Coefficient of pressure (C_p) were taken from CFD studies, Discharge coefficient of vents were taken from wind tunnel studies for different configurations [3]. Design was implemented in the vehicle in the form of vent ports on the adaptor region. Results were validated with the pressure data acquired from the sensors mounted in the flight compartments



2. THEORETICAL ANALYSIS

Theoretical studies were carried out by using an in-house code MPVENT (multipath vent code) to assess the differential pressure across the compartment through venting process. MPVENT takes care of venting process through multiple ports and multiple compartments at any given time. A typical compartment of volume V is filled with air at pressure P_c , density ρ_c , and temperature T_c . The flow conditions at the exit of the vent holes are P_e (P_L), ρ_e , and T_e . Differential pressure values across the compartment are calculated by the following expression (1).

$$\frac{dP_c}{dt} = \sum_k C_{d_k} \frac{A_k}{V} \sqrt{P_c \rho_c} \sqrt{\frac{2\gamma}{\gamma-1} \left(1 - \left(\frac{P_e}{P_c}\right)_k^{\frac{\gamma-1}{\gamma}}\right) \left(\frac{P_e}{P_c}\right)_k^{\frac{2}{\gamma}} \left(\frac{P_c}{P_o}\right)_k^{\frac{\gamma-1}{2\gamma}} P_c} \dots \quad (1)$$

The differential equation for the compartment pressure is integrated using RK4 method.

Inputs for design of vent system, such as Coefficient of pressure



Figure1: Test vehicle at SDSC, SHAR

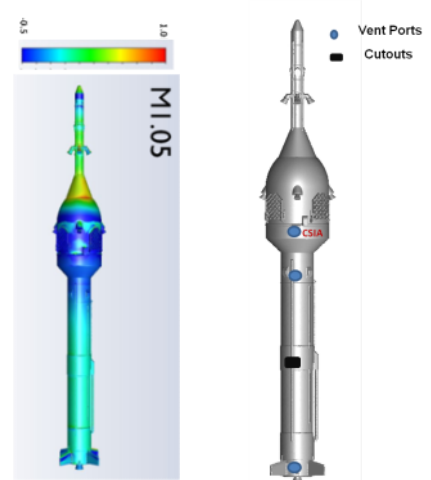


Figure 2: Cp
palette over CES-
TV at M=1.05



Figure 3: Vent port types and location

(C_p) were taken from CFD for different Mach numbers. C_p palette over the entire vehicle at $M=1.05$ is seen in figure 2. The different types of vent schemes in the vehicle are shown in figure 3.

All the compartments in the test vehicle were connected. Hence multi compartment vent analysis approach was considered during the design of the vent system. Also, un-intentional opening was observed during the integration of the flight. Various other inputs of compartment free volume, vent area of the ports, trajectory of the vehicle and other inputs like C_p (Coefficient of pressure) & C_d (Discharge coefficient), are taken for the analysis. The dispersions on the C_p and the discharge coefficients are also taken to obtain the off-nominal bounds. Compartment pressure values and the differential pressure values across the compartment are generated for regular time intervals.

3. RESULTS

Design of the venting system in the CES test vehicle compartments met the specification of keeping the compartment differential pressure values within the design limits successfully i.e. $P_c - P_{inf}$ within $\pm 10\text{kPa}$. Differential pressure across CES adaptor compartment can be seen in figure 4. Due to the varying volumes in the different compartments, venting process through the provided vents was different, but the differential pressures across all the compartments of CES-TV were found to be similar. Details of various other inputs used and results across other compartments and comparison with flight will be given in full paper.

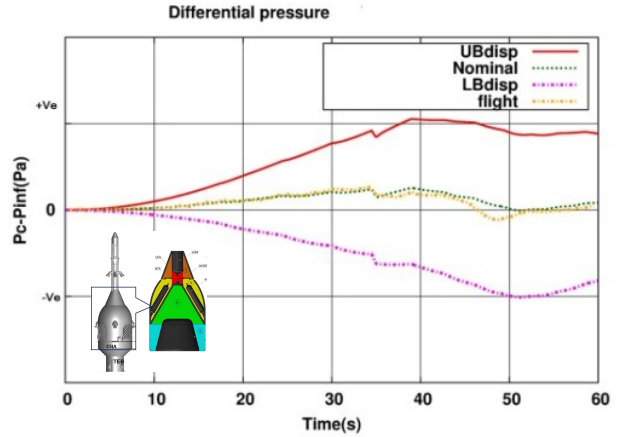


Figure4: Differential pressure across CES adaptor compartments

4. CONCLUSIONS

The main objective of the studies carried out in the present paper is to design the vent system for the ISRO's human mission Gaganyaan test vehicle (TV). Design was carried out using an in-house software Multi Path Vent program (MPVENT). Compartment pressure, mass flow rate and differential pressure across the compartments for the entire flight duration was computed and the design studies were validated with the flight acquired data. The design specification of the studies was mainly to contain the differential pressure ($P_c - P_\infty$) values of all the compartments within $\pm 10\text{kPa}$ $\pm 0.1\text{bar}$. The differential pressures across all the compartments of CES-TV were found to be within the limits of design specification and were following the Theoretical predictions during the flight conditions . Hence the design methodology was validated for all the compartments of the test vehicle. Details of the data acquired from flight across all other compartments will be provided in the full-length paper.

5. REFERENCES

- [1] J.T. Fransisco and A.L.Braslow, "NASA Space vehicle design criteria (Structures)-Compartment venting", NASA SP-8060 (1970).
- [2] B.Venkat Shivaram Jadav and Dipankar Das, "Venting system design and analysis for a typical launch vehicle compartment", Proceedings-27th National Convention of Aerospace Engineers, India (2013).
- [3] Saravanan.R et.al, "Experimental determination of Discharge Coefficient (C_d) of vent port", National conference on wind tunnel testing (NCWT-03), August 23-24, 2013, Thiruvananthapuram.

Development and Validation of a Python-Based Preliminary Design Tool for Ramjet Engines

Thivya Ranee^a and Atharv Mangalkar^{b*}, and Akshay Abhyankar^c

^{a,b} Defence Institute of Advanced Technology (DIAT-DRDO), Pune, India

^c Modern Education Society's Wadia College of Engineering, Pune, India

1. INTRODUCTION & OBJECTIVE

Ramjet engines represent a critical propulsion technology for high-speed flight applications, particularly in the supersonic regime. The preliminary design phase of ramjet engines requires extensive parametric analysis to optimize performance across various operating conditions. Traditional design approaches often involve time-consuming iterative calculations and computational fluid dynamics simulations. This work presents the development and validation of a comprehensive Python-based tool for preliminary ramjet engine design that can rapidly generate performance predictions across multiple operating conditions. The primary objective is to create an efficient, accurate design tool that can streamline the initial design process while maintaining reliability comparable to advanced simulation methods.

2. METHODS OF ANALYSIS

A Python-based computational tool was developed to perform comprehensive preliminary design analysis of ramjet engines. The tool incorporates thermodynamic models, gas dynamics equations, and empirical correlations to predict engine performance across a wide range of operating conditions. The code capabilities include: (1) parametric analysis across multiple altitudes (0-50,000 ft) and Mach numbers (1.4-4.0); (2) calculation of flow properties at various engine stations; (3) optimization of inlet and nozzle geometry; (4) prediction of performance metrics including thrust, efficiency, specific impulse, and fuel consumption; (5) range estimation based on fuel requirements; and (6) detailed nozzle design with expansion ratio optimization. To validate the code, comprehensive ANSYS simulations were performed for three representative operating conditions (0 ft, 25,000 ft, and 50,000 ft) at Mach 0.95. The numerical values from the Python code were compared with ANSYS results to assess accuracy and reliability.

3. RESULTS AND/OR HIGHLIGHTS OF IMPORTANT POINTS

The Python-based design tool successfully generated comprehensive performance predictions across the entire operating envelope. Parametric analysis revealed distinct performance characteristics at different flight conditions, with optimal thrust efficiency observed at specific combinations of altitude and Mach number. The validation against ANSYS simulations demonstrated excellent agreement, with average discrepancies of less than 5% for critical parameters such as static pressure, total pressure, and temperature. For instance, at 25,000 ft altitude, the code predicted a static pressure of 589,551 Pa compared to the ANSYS result of 589,551 Pa, while at sea level, the predicted total pressure of 2,846,480 Pa closely matched the ANSYS value of 2,846,480 Pa. The tool also effectively captured the complex

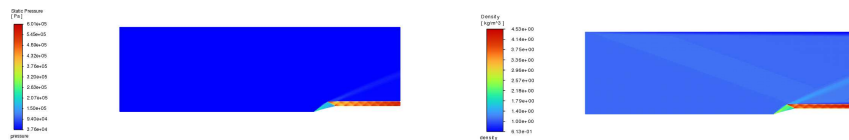
flow phenomena in the inlet and nozzle sections, accurately predicting shock wave patterns and expansion characteristics. The computational efficiency of the Python tool was remarkable, reducing analysis time from hours (required for CFD simulations) to seconds while maintaining acceptable accuracy for preliminary design purposes.

4. CONCLUSIONS

The developed Python-based tool demonstrates significant potential as a reliable and efficient preliminary design methodology for ramjet engines. The strong agreement with ANSYS simulations validates the accuracy of the computational approach across various operating conditions. This tool enables rapid parametric analysis and optimization, significantly reducing the time and resources required during the initial design phase. The capability to quickly generate performance predictions across multiple operating conditions makes it particularly valuable for conceptual design studies and mission planning. Future work will focus on expanding the tool to include additional design variables, incorporating more advanced combustion models, and developing an integrated graphical user interface to enhance accessibility for design engineers.

5. APPENDIX

Some Images from Ansys simulations



Code Excel Sheet Output

* Communicating Author: Atharv Mangalkar and atharvamangalkar@gmail.com.

Direct Simulation Monte Carlo Study of Thruster Plume Impingement on Planetary Surface

Malaikannan G*^a and Suman Chakraborty^{b*}

^a Post-doctoral fellow, Department of Mechanical Engineering, IIT Kharagpur, India.

^b Professor and Director, Department of Mechanical Engineering, IIT Kharagpur, India

1. INTRODUCTION & OBJECTIVE

In order to successfully return samples, it is necessary to be able to land on the surfaces of planetary bodies without creating any damage. When the jet plume from the lander strikes the surface of the planet, it effectively penetrates the surface, which in turn leads to the development of craters. Accurate modeling allows for the complete investigation of dust impingement on the lander module and Extra-Vehicular Activity (EVA) systems, as well as system failures owing to scouring regolith; this, in turn, leads to the success of the space mission. The lander in the sample collection mission is critical to the mission's success. The lander will be placed on the target planets/moons using thrusters. The high-velocity plume of hot gases created by the thrusters impacts the planets' surfaces with great force. In addition to severely damaging the planet's surface, this plume also severely damages the lander [1]. Surface contamination from impingement has a major impact on the sample collection mission. Flow physics are made more complicated by the plume surface interaction (PSI). The PSI results in a number of physical changes, including cratering of regolith, erosion of planetary surfaces or viscous erosion, diffused gas eruption, and ejecta [2, 3].

Modeling intricate physics of the PSI and recreating the desired environment are both tasks that necessitate the use of numerical techniques. PSI is inherently multiphysics due to the expansion of the continuum plume into near vacuum conditions. Continuum flow is changing to rarefied flow, which ultimately becomes free-molecular flow. Numerous phenomena, such as local scouring, entrainment, and particle collisions, are to be expected and observed when the plume impinges on the surface regolith [4]. A shock wave forms in advance of the obstacle as the wall jet propagates radially outward and a viscous boundary layer develops along the abrasive lunar surface due to the supersonic nature of the flow.

As long as the flow regime is continuum, the physics of the flow can be accurately resolved using conventional CFD solvers based on the Navier-Stokes equations. Rarefaction causes the continuum assumption to fail at very high altitudes. Because of this, Direct Simulation Monte Carlo (DSMC) [5] and other kinetic particle based approaches are commonly utilised in this regime. The DSMC technique, proposed by Prof. Bird [5], accurately represents flows spanning from the continuum to the free-molecular regime. Therefore, in the present study, the DSMC method was employed to accurately simulate the plume–surface interaction (PSI).

2. METHODOLOGY

DSMC is the probabilistic simulation technique in which the real molecules are represented by the simulation particles of physical size and coupled to physical time. This method sets the initial state of the particle, and the particles are distributed into cells with initial position and velocity. Then the particles move and interact with the boundaries. Collision pairs are selected, and intermolecular collisions are performed. Finally, flow properties are sampled, and solutions are obtained. The simulations are performed using the DSMC code called Stochastic Parallel Rarefied-gas Time-accurate Analyzer. Variable Hard Sphere (VHS) is the collision model used for particle-particle collision. A fully diffuse reflection wall is considered for gas-surface interaction. The exhaust mixture from the thruster consists of multiple species; however, for simplicity, only water vapor is considered in the present simulation, with throat conditions of 144,630 Pa pressure, 1,214 m/s velocity, and 2,458 K temperature.

3. RESULTS AND DISCUSSIONS

The DSMC simulation is carried out to investigate the impact of a nozzle thruster on a planetary regolith using both a convergent-divergent (C-D) nozzle and a Bezier nozzle. The simulation primarily focuses on the divergent section of the nozzle, where the flow expands into a vacuum. Two scenarios are considered: in the first, the exhaust flow expands freely into the vacuum without obstruction; in the second, the expanding plume impinges on a flat planetary surface. In the latter case, the plume–surface interaction generates a shock wave that propagates outward from the surface, subsequently deflecting the flow and causing a portion of it to reflect back toward the lander. This backflow can potentially influence the local flow field near the lander and may lead to surface erosion or contamination effects. Figures 1 and 2 show the vertical velocity distribution of the thruster plume impingement in vacuum and on the planetary surface, respectively.

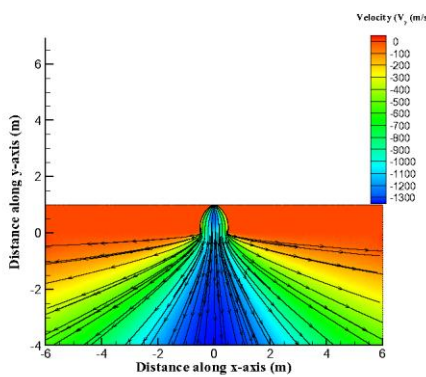


Figure.1: Thruster plume impingement in vacuum

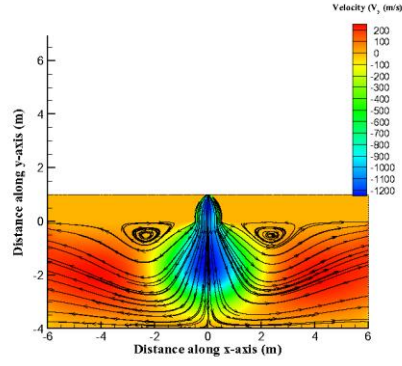


Figure.2: Thruster plume impingement on flat planetary surface

4. CONCLUSIONS

DSMC simulations are carried out to examine thruster plume impingement behaviour under vacuum and planetary surface conditions, employing both convergent-divergent and Bezier nozzles. The results reveal that, in vacuum, the exhaust plume expands symmetrically without any flow disturbance, whereas in the presence of a planetary surface, the impinging jet generates a significant shock wave that propagates outward and reflects toward the nozzle exit. This backflow affects the local flow field adjacent to the lander, and resulting in surface erosion or contamination impacts. The comparison of the two nozzle designs reveals that the Bezier nozzle offers a more uniform expansion and enhanced control over plume divergence, thus diminishing the intensity of flow deflection upon surface hit. The results show that plume-surface interaction modelling and nozzle geometry are important for predicting lander performance and safe planetary descent operations.

5. REFERENCES

- [1] Metzger, Philip T., Christopher D. Immer, Carly M. Donahue, Bruce T. Vu, Robert C. Latta III, and Matthew Deyo-Svendsen. "Jet-induced cratering of a granular surface with application to lunar spaceports." *Journal of Aerospace Engineering* 22, no. 1 (2009): 24-32.
 - [2] Calle, C. I., C. R. Buhler, J. L. McFall, and S. J. Snyder. "Particle removal by electrostatic and dielectrophoretic forces for dust control during lunar exploration missions." *Journal of Electrostatics* 67, no. 2-3 (2009): 89-92.
 - [3] Gaier, James R., Khrissaundra Journey, Steven Christopher, and Shanon Davis. "Evaluation of brushing as a lunar dust mitigation strategy for thermal control surfaces." In *41st International Conference on Environmental Systems*, no. NASA/TM-2011-217231. 2011.
 - [4] Metzger, Philip T., Jacob Smith, and John E. Lane. "Phenomenology of soil erosion due to rocket exhaust on the Moon and the Mauna Kea lunar test site." *Journal of Geophysical Research: Planets* 116, no. E6 (2011).
 - [5] Bird, Graeme A. *Molecular gas dynamics and the direct simulation of gas flows*. Oxford university press, 1994.
- * Malaikannan G:malaikannan.g25t@kgpian.iitkgp.ac.in, Suman Chakraborty:suman@mech.iitkgp.ac.in.

Dynamic Response of Variable Fibre Spacing Composites Under Porous Hemispherical Nosed Impactor

Aayush Gupta^{1,*}, Abdul Sadiq¹ and Dipak Kumar Maiti²

¹Research Scholar, Department of Aerospace Engineering, IIT Kharagpur, Kharagpur, India

²Professor, Department of Aerospace Engineering, IIT Kharagpur, Kharagpur, India

1. INTRODUCTION

The assessment of bird impact on aircraft structures has gained significant attention due to the growing risk of foreign object damage to critical components such as wings, nacelles, and windshields. Composite materials are widely employed in modern aerospace structures for their superior strength-to-weight ratio. However, conventional composites with uniform fibre distribution and homogeneous properties often exhibit stress concentrations, premature delamination, and limited energy absorption under impact loading. In contrast, composites with variable fibre spacing (VFSC) can enable improved stress redistribution [1, 2], delayed damage initiation, and enhanced impact tolerance. Typical bird models with 5–10% porosity effectively represent the compressibility and fluid-like behaviour of bird tissue, yielding better agreement with experimental observations [3, 4]. Such models also capture the attenuated pressure pulse and reduced structural damage, consistent with experimentally observed impact phenomena. Furthermore, Cwiklak et al. [3] demonstrated that hemispherical-nose configurations better replicate experimental deformation and energy dissipation patterns observed in actual bird strike tests.

In this work, we investigate the soft impact response of a composite plate using an impactor that is both hemispherical-nosed and porous, and with the plate having variable fibre spacing distributions, to explore how the combination of impactor geometry, porosity, and spatial material variation affects damage initiation, propagation, and energy dissipation.

2. METHODOLOGY

The dynamic response of a square composite plate subjected to high-velocity impact was investigated using finite element simulations in Abaqus/Explicit. The composite plate was modelled with a symmetric angle-ply layup and fixed boundary conditions, and the impactor was positioned at the centre of the plate with velocity of 200m/s . A user-defined field (VUSDFLD) subroutine was implemented to assign spatially varying material properties across the plate, allowing for controlled variations in fibre volume fraction and stiffness.

3. RESULTS AND DISCUSSION

From Fig.1a and 1b, it is observed that stresses are lower for the hemispherical impactor even when total energy is same, indicating that the cylindrical case overestimates the parameters. Fig.1c and 1d show that peak stress are higher with porosity compared to the non-porous model despite having lower total energy.

For the VFSC in Fig.1e and 1f, displacements and damage dissipation energies are lower than in constant-spacing composites, indicating improved damage absorption. The damage dissipation energy is smaller for VFSCs, indicating smaller permanent damage.

Email: gupta/ay1594@gmail.com^{*}, abdulsadiqshahid@gmail.com, dkmaiti@aero.iitkgp.ac.in

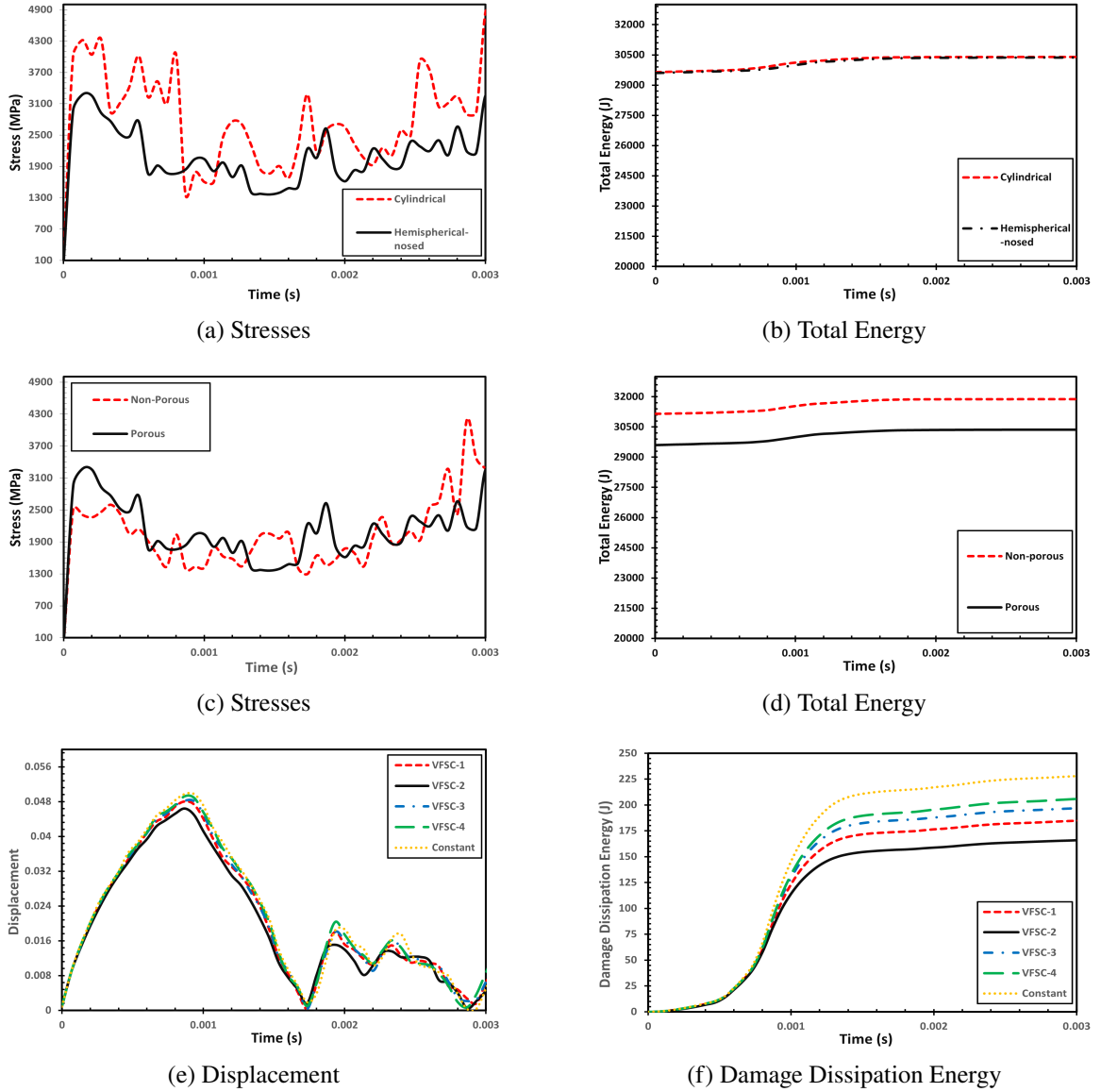


Figure 1: Stresses and Total Energy for different Impactors (a,b) and Porosity (c,d); Displacements and Damage Dissipation Energy for VFSCs (e,f)

4. CONCLUSIONS

The non-uniform VFSC architecture contributes to improved stiffness, reduced susceptibility to extensive damage, and more efficient absorption of elastic energy.

REFERENCES

1. P. Chandrakar, N. Sharma, and D. K. Maiti, “Stochastic buckling response of variable fibre spacing composite plates under thermal environment,” **J. Compos. Mater.**, 2023.
2. N. Sharma, P. K. Swain, D. K. Maiti, and B. N. Singh, “Stochastic aeroelastic analysis of laminated composite plates with variable fibre spacing,” **J. Compos. Mater.**, 2021.
3. J. Cwiklak, E. Kobialka, and A. Gos, “Experimental and numerical investigations of bird models for bird strike analysis,” **Energies**, 2022.
4. A. Kalam, R. Kumar, R. Ranga, and G. Janardhana, “SPH high-velocity impact analysis—Influence of bird shape on rigid flat plate,” **Mater. Today Proc.**, 2017.

Effect of Flight velocity on Mean Flow of an Ideally Expanded Supersonic Jet – a CFD study

Sanjoy Kumar Saha^{a1} and Manoj T Nair^b

^aScientist / Engineer, VSSC, Trivandrum, Kerala, India.

^bProfessor, IIST / ISRO, Trivandrum, Kerala, India

1. INTRODUCTION & OBJECTIVE

In the area of aeroacoustics, one of the primary research is focused on the reduction of the jet noise specially when the thrust obtained from the nozzle is higher. Use of bypass flow in the jet engine is very helpful in reducing the aircraft noise. It is later proven through experimental and numerical analysis that the presence of the flight velocity i.e co-flow reduces the acoustic levels significantly. Hence, studying the effects of co-flow stream outside the jets is very useful. Studies show that forward flight motion modifies the jet development by axially stretching the potential core and lengthening of shock cells due to reduction in mixing layer growth. All these reduces radiated noise. To understand these phenomena of jet development in presence of free-stream, numerical studies are carried out for fully expanded jet using commercial code and the mean flow characteristics of jet are monitored.

2. METHODS OF ANALYSIS

Fluent code with Reynolds Averaged Naiver Stokes (RANS) solver is used to simulate the flow. The turbulent kinetic energy fields, potential core length etc obtained through RANS simulations are further investigated to understand the effect of velocity on acoustic generation. The nozzle considered here for the simulations is a CD nozzle which is designed to deliver a Mach number (M_j) 2.0 with area ratio of 1.757 [1]. Computational domain along with the grid distribution pattern used is shown in Figure 2. Seven different flight velocities ($U_f = 0, 30, 50, 75, 100, 150, 200 \text{ m/s}$) are studied here. The temperature of the jet at chamber is 300K and chamber pressure of 7.82 bar.

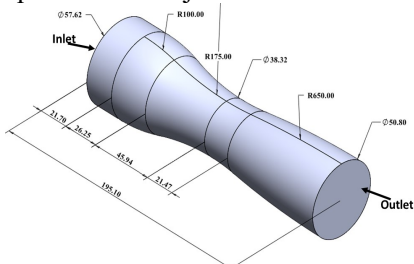


Figure 1: 3D view of simulated nozzle

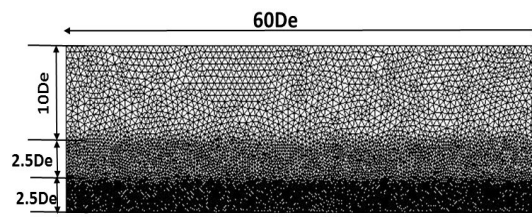


Figure 2: Domain and grid distribution

3. RESULTS

Normalised velocity (U/U_j) palette for different simulations case shows that as the co-flow velocity (U_f) increases, the spreading of the jet reduces (Figure 3) due to stretching of jets [1]. Jet becomes narrower, mixing with ambient reduces and higher Mach number prevails over a larger region. Similar observation is reported in literature also [2]. The variation of the center line velocity variation shows that as the co-flow velocity increases, the initial portion of the jet velocity remains similar and later they start deviating. Beyond the potential core the velocity falls very sharply with the decrease of co-flow velocity (Figure 4). This is due to the enhanced mixing of the ambient flow with jet with the decrease of co-flow velocity (U_f). With the increase of the free-stream velocity, the jet gets elongated and hence, the length of potential core increases. The length of the potential core is 12.9D when there is no co-flow but it enhanced to 16.27D for co-flow velocity of 200m/s. Beyond potential core ($x/D=20$), the max Mach number has reduced significantly and jet spread over a much longer distance ($>3D$ radially without co-flow).

The acoustic radiation from a jet is dependent on the turbulence within the jet plume. Turbulent kinetic energy (TKE) indicates the growth of fluctuation in the flow. The increase of co-flow velocity, reduces the growth of mixing layer and hence, TKE level also decreases. The max turbulent level which is

¹ Sanjoy254@gmail.com

an indication of the source of maximum acoustic level occurs close to the end of the supersonic core [3]. The location of peak TKE moves further down with the increase in the co-flow velocity. The peak axial turbulent intensity also decreases with the increase in the co-flow velocity (Figure 5). When the co-flow velocity is about 200m/s, the TKE levels along the nozzle center line is about 50% of the TKE values when there is no co-flow (Figure 6).

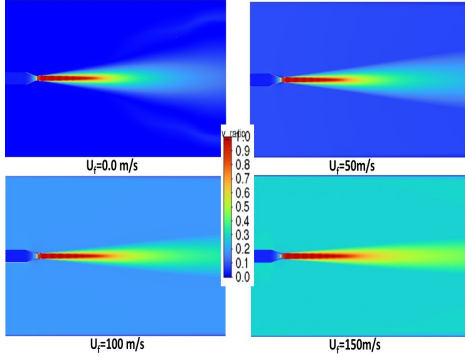


Figure 3: Jet velocity palette with co-flow

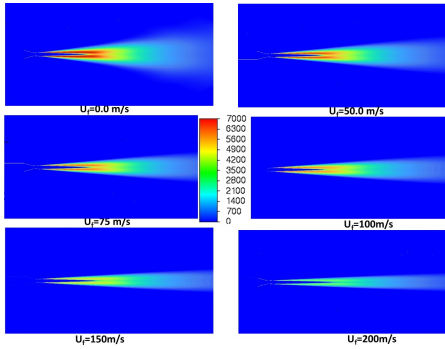


Figure 5: TKE palette along the jet symmetry plane Figure 6: Variation of TKE along the jet center line

The shock-cell strength can be expressed by $P_{\max}/P_{\min} - 1$ as suggested by Tam [4], with P_{\max} (P_{\min}) the maximum (minimum) pressure in each cell. The amount of pressure jump decreases as one moves downstream due to the dissipation of the energy of the flow because of the shear action between the jet and free-stream. An increase in the strength of the shock cells as the co-flow velocity increases after first few shock cell [5]. This is also due to the reduction on the shear strength with the increase in the co-flow velocity.

4. CONCLUSIONS

A series of numerical simulations are carried out for a fully expanded supersonic jet using Reynolds average Navier-Stokes calculation with 2 equation turbulence model to understand the mean flow characteristics of jet. The velocity of the ambient fluid i.e. surrounding fluid has been varied from 0 to 200m/s to understand the effect of co-flow on the mean flow field of the jet. Analysis shows that the trend of jet velocity decay, TKE variations, shock cell length etc match well with the literature data.

5. REFERENCES

- [1] Nicholas J. Georgiadis and Mark P. Wernet, "Mach Number and Heating Effects on Turbulent Supersonic Jets", AIAA Aviation 2021 forum, DOI: 10.2514/6.2021-2834
- [2] Tanna, H. K., & Morris, P. J. (1977). In-flight simulation experiments on turbulent jet mixing noise. Journal of Sound and Vibration, 53(3), 389–405. doi:10.1016/0022-460x(77)90422-9
- [3] Nagamatsu, H. T. and Horvay, G. "Supersonic Jet Noise," AIAA Paper No. 70-237, (1970).
- [4] Tam, C. K. W. (1992). Broadband shock associated noise from supersonic jets measured by a ground observer. AIAA Journal, 30(10), 2395–2401. doi:10.2514/3.11239
- [5] Norum, T., & Shearin, J. (1986). Shock noise from supersonic jets in simulated flight to Mach 0.4. 10th Aeroacoustics Conference. doi:10.2514/6.1986-1945

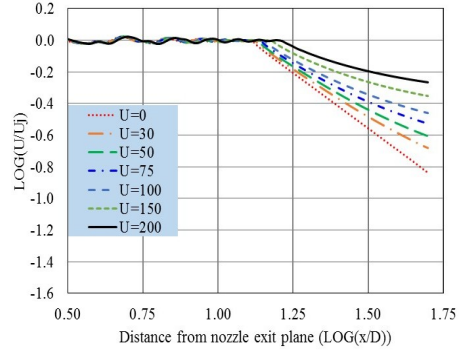


Figure 4: Variation of centre line velocity (U/U_j).

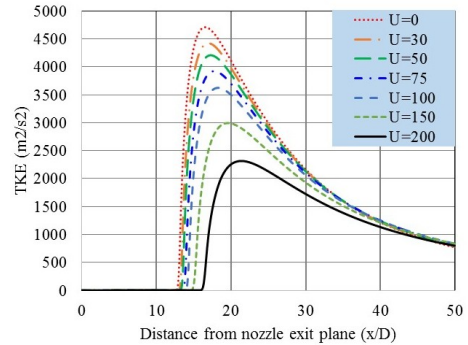


Figure 5: TKE palette along the jet symmetry plane Figure 6: Variation of TKE along the jet center line

Effect of Localized Elastic Supports Representing Ribs and Mounts on the Flutter Behavior of Tailored Composite Panels

Abdul Sadiq ^{1,a*}, Aayush Gupta ^{2,b}, Dipak Kumar Maiti ^{3,c}

^{1,2} Research Scholar, Department of Aerospace Engineering, Indian Institute of Technology Kharagpur, Kharagpur, 721302, West Medinipur, West Bengal, India

³ Professor, Department of Aerospace Engineering, Indian Institute of Technology Kharagpur, Kharagpur, 721302, West Medinipur, West Bengal, India

INTRODUCTION

Thin plates are commonly utilized in aerospace structures [1], such as the skins of aircraft fuselages and wings. These plates are subdivided into smaller panels by longitudinal stiffening elements (e.g., stringers, wing spars) and transverse reinforcements (e.g., frames, ribs). These panels are commonly supported by internal substructures such as ribs, stringers, and mounting points, which introduce localized elastic restraints rather than idealized boundary conditions. This study investigates the aeroelastic flutter behavior of a tailored stiffness (variable fiber-spacing) laminated composite panel incorporating spring supports at selected locations to simulate the stiffness contribution of internal substructures. The influence of spring stiffness and support location on the natural frequencies and flutter boundaries is systematically analyzed.

Leissa and Martin [2] conducted a comprehensive study on the free vibration and buckling behavior of rectangular laminated composite plates with spatially varying fiber distributions. Their analysis revealed that optimizing the fiber arrangement can lead to a significant enhancement in structural performance. Sharma et. al [3] investigated the stochasticity of flutter velocity in VFSC laminates for different boundary conditions. Watkins and Barton [4] analyzed the vibrations of an isotropic rectangular plate with point elastic supports by applying eigen-sensitivity analysis. Meanwhile, Setoodeh and Karami [5] used a three-dimensional, elasticity-based, layer-wise finite element approach to investigate general laminated thick composite plates resting on both distributed and point elastic supports.

METHODOLOGY

This study aims to perform free vibration and flutter analysis of tailored stiffness composite plates with elastic supports, using a coupled framework that integrates finite element (FE) coding with MSC.NASTRAN. The modal properties are determined through an in-house FE code based on First-Order Shear Deformation Theory (FSDT), which accurately accounts for transverse shear effects and ensures compatibility with MSC.NASTRAN data structures. These modal parameters are then used to compute unsteady aerodynamic forces in MSC.NASTRAN via the Direct Matrix Abstraction Program (DMAP) interface. Finally, flutter characteristics are assessed using the p-k eigenvalue method implemented in MATLAB.

RESULTS AND DISCUSSION

For both free vibration and flutter analyses, a symmetric ply laminate made up of graphite epoxy with ply layup sequence $[0/0/0/90]_s$ is considered. For this study a panel of length 1m, width 1m and thickness of 6 mm is used. The elastic properties of fiber and matrix are: $E_f = 275.790$ GPA, $E_m = 3.447$ GPA, $v_f = 0.20$, $v_m = 0.35$, $G_f = 114.9$ GPA, $G_m = 1.277$ GPA, $\rho_f = 1411.6671$ Kg/m³, $\rho_m = 1217.9158$ Kg/m³. The distribution of fibers within the lamina is controlled by fiber volume fraction V_f , which is a function of μ and Ω . With an effective fiber volume fraction of 0.5, following distribution function for V_f are considered for the present analysis. For lamina having 0° or 90° fibers: VFSC-1: $V_f = 0.5$, VFSC-2: $V_f = A_1(1-\mu)$, VFSC-3: $V_f = A_2(1-\mu^2)$, VFSC-4: $V_f = A_3(1-\mu^4)$ VFSC-5: $V_f = A_4(1-\mu^6)$, VFSC-6: $A_5(1-\mu^2)^2$
Where, $A_1 = 0.5$, $A_2 = 0.75$, $A_3 = 0.625$, $A_4 = 0.584$, $A_5 = 0.9375$

^aabdulsadiqshahid@gmail.com, ^bgupta.ay1594@gmail.com, ^cdkmaiti@aero.iitkgp.ac.in

The plate is supported by spring constraints at points (L/4, W/4), (L/4, W/2), (L/2, W/2) and (L/2, W/4). Where L and W are the length and width of the plate.

Free Vibration

For free vibration analysis, a simply supported laminated plate is considered and non-dimensional frequency parameters are calculated for different VFSCs. The spring stiffness (k_0) is taken as 10^3 , 10^4 , 10^5 , 10^6 , 2×10^6 , 4×10^6 , 6×10^6 , 10^7 and 10^8 N/m. The variation of non-dimensional frequency parameter with spring stiffness (k_0) is represented in Fig. 1(a).

Flutter Analysis

The study in this section comprises the comparison of fiber distribution patterns with elastic spring stiffness with respect to flutter velocity. The spring stiffness (k_0) is taken as 10^2 , 5×10^2 , 10^3 , 10^4 , 10^5 , 10^6 , 2×10^6 , 4×10^6 and 6×10^6 N/m. Different type of fiber distribution patterns with an effective fiber volume fraction of 0.5 are considered. Flutter velocities are obtained for cross ply laminated composite plate with C-F-F-F boundary condition. The variation of flutter speed with spring stiffness is shown in Fig. 1(b).

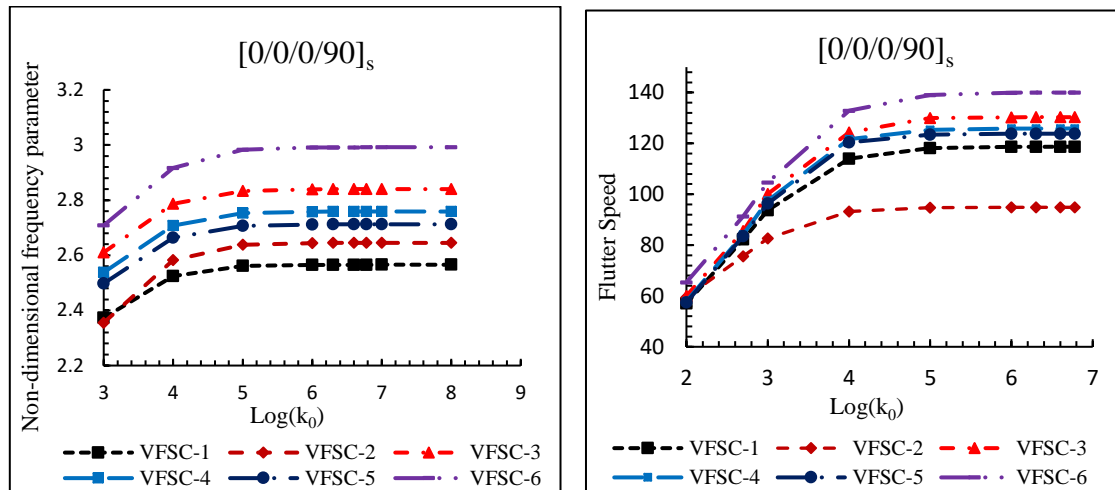


Fig. 1. Variation of (a) non-dimensional frequency parameter (b) flutter speed, with spring stiffness

CONCLUSIONS

Results reveal that localized spring supports and fiber distribution substantially alter the dynamic characteristics and aeroelastic stability of the panel, emphasizing the necessity of accurately modeling internal elastic restraints in the aeroelastic design of composite aircraft structures.

REFERENCES

- [1]. Ren, R., Ma, X.Y., Yue, H.H., Yang, F. and Lu Y.F., "Stiffness enhancement methods for thin-walled aircraft structures: A review," *Thin Wall Struct.*, 201, 111995, 2024.
- [2]. Leissa, A. and Martin, A., "Vibration and buckling of rectangular composite plates with variable fiber spacing," *Compos Struct.*, 14: 339–357, 1990.
- [3]. Sharma, N., Swain, P.K., Maiti, D.K. and Singh, B.N. "Stochastic Aeroelastic Analysis of Laminated Composite Plate with Variable Fiber Spacing," *Journal of Composite Materials*, vol. 55, pp. 4527-4547, 2021.
- [4]. Watkins, R.J. and Barton, O., "Characterizing the vibration of an elastically point supported rectangular plate using eigen sensitivity analysis", *Thin-Walled Struct.* 48(4–5), 327–333, 2010.
- [5]. Setoodeh, A.R., Karami, G., "Static, free vibration and buckling analysis of anisotropic thick laminated composite plates on distributed and point elastic supports using a 3-D layer-wise FEM", *Eng. Struct.* 26(2), 211–220, 2004.

Effect of Mach number on a Compressible Impinging Round Jet: An LES study

Priyakshi Goswami^a and Somnath Ghosh^{b*}

^a Research Scholar, Department of Aerospace Engineering, Indian Institute of Technology, Kharagpur, India

^b Associate Professor, Department of Aerospace Engineering, Indian Institute of Technology, Kharagpur, India

1. INTRODUCTION

We often encounter impinging jets in engineering applications like turbine blade cooling, rocket propulsion and Short Take Off-Vertical Landing aircrafts. Such impingement of high-speed compressible jet on a flat surface at a close distance from the inlet can result in a complex interplay of shock waves, turbulent shear layers and acoustic feedback loop that results in discrete acoustic tones. In the early stages of research, Powell [1] proposed that large-scale vortical structures are initiated from the Kelvin-Helmholtz instability which are generated in shear layer of the flow. Krothapalli et al. [2] investigated flow and acoustic characteristics of axisymmetric supersonic impinging jets at Mach numbers 1 and 1.5. To better understand the flow field and acoustic characteristics of compressible impinging jets with inlet to plate distance variations, Large Eddy Simulation of impinging round jet is performed at Mach number 0.9 and Reynolds number 25000 in this study. Two flow cases are studied, with Mach numbers 0.9 and 1.5 and fixed impingement distance. The objectives of this study are to perform LES based on high-order compact finite difference scheme and an explicit filtering to study compressible impinging jets and to investigate the influence of impingement distance on the instantaneous fields, mean flow characteristics and flow statistics in both the cases.

2. METHODOLOGY

2.1 Governing Equations and Numerical Methods

The governing equations are written in a characteristic form [3] for compressible flow, in generalized curvilinear coordinates in terms of the primitive variables and solved using a 6th order compact central finite difference scheme for discretizing spatial derivatives. A low storage 3rd Runge–Kutta scheme is used for time-marching, LES is performed using an explicit filtering approach based on the approximate deconvolution method. Additionally, an adaptive filtering approach is used filtering closer to the shocks [4].

2.2 Computational Parameters

The domain is taken as $h \times 2\pi r_0 \times 24r_0$, with impingement distance of $h=8r_0$ and Mach numbers 0.9 and 1.5 for the two cases. Here, r_0 is jet radius at the inflow. The Reynolds number is 25,000, based on inflow jet diameter and inflow velocity. The grid points taken are $640 \times 192 \times 400$ in axial, azimuthal and radial directions respectively. In the radial direction, we have applied a *sinh* stretching is applied. The simulations are then run on 64 cores on Paramshakti, IIT Kharagpur.

2.3 Boundary Conditions

The axial velocity profile at the inflow is specified. A vortex inflow forcing method [4], which causes the transition of initially laminar shear layer to turbulence is used to add disturbance. Near the radial outflow, we specify a sponge layer [4] from $z_s = z/r_0 = 15$ to $z_f = z/r_0 = 24$, which is to absorb outgoing waves and thus prevent spurious reflections. Transverse terms of the governing equation are zero at the inflow. At the axial end of our domain, the isothermal ($T_w = 300$ K) no slip wall boundary condition is applied.

3. RESULTS

3.1 Instantaneous fields:

Instantaneous axial velocity, normalised with the inlet centreline velocity in an axial radial plane is shown shown in figure 1 which show the appearance of weak shocks and upstream propagation of acoustic waves responsible for the feedback loop is noticed.

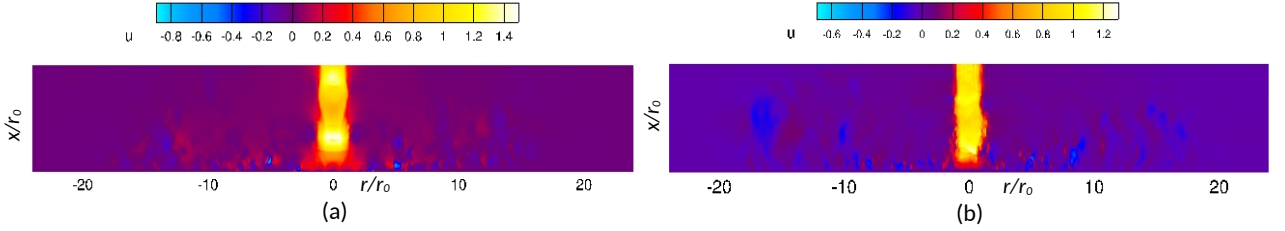


Figure 1: Instantaneous velocity variations for (a) $M=0.9$ case and (b) $M=1.5$ case

3.2 Mean flow characteristics:

The variation of centreline mean axial velocity and centreline pressure in the axial direction for the two flow cases are shown in figure 2. Here, axial velocity is normalized using centreline velocity (u_j) at the inflow, centreline pressure is normalized using ambient pressure and axial coordinate is normalised by impinging distance. Alternate expansion zones and compression are observed in the free jet region. As shown in the figure, mean pressure value is maximum near the stagnation point and the pressure jump is more for the supersonic case, as expected. The intensity of the shocks is also higher in case of the supersonic jet.

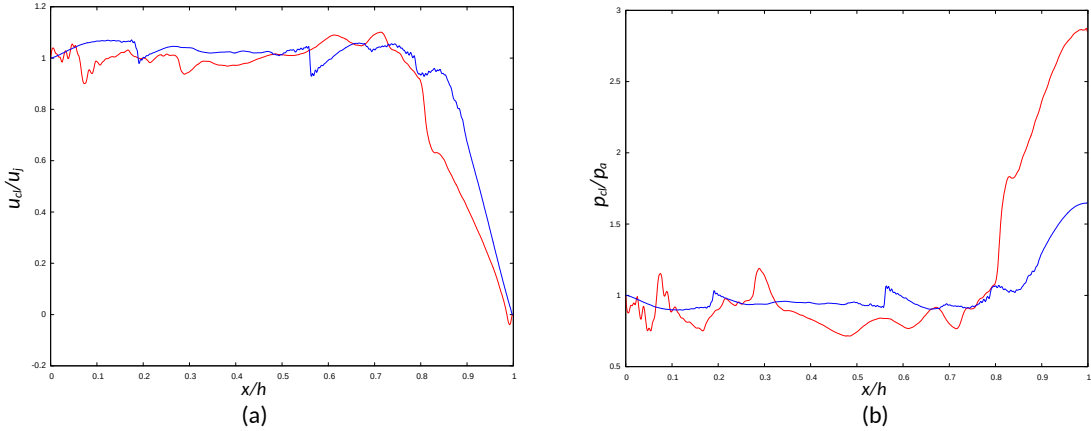


Figure 2: Variation of (a) Centreline axial velocity and (b) Centreline pressure

4. CONCLUSIONS

Large Eddy Simulation is performed for a compressible round jet impinging on a flat plate at inlet-to-plate distance of $h=8r_0$, where r_0 is the jet radius at the inlet. Two cases are studied with Mach numbers 0.9 and 1.5. Reynolds number is 25,000. The governing equations [3] are solved using 6th order compact finite difference scheme and an explicit filtering based LES approach [4]. Instantaneous and mean flow fields show the appearance of weak shocks in the flows. The centreline velocity and pressure variations are also plotted that show the weak shocks in the flow and how the intensity of these shocks are higher in the supersonic case. Further, we plan to present detailed turbulence statistics and methodology in the full paper. The effect of Mach number on the flow parameters and shocks can then be observed in more details.

5. REFERENCES

- [1] A. Powell, “On Edge Tones and Associated Phenomena,” *Acta Acustica United with Acustica*, Vol. 3, No. 4, 1953, pp. 233–243.
- [2] A. Krothapalli, E. Rajkuperan, F. Alvi and L. Lourenco, “Flow Field and Noise Characteristics of a Supersonic Impinging Jet,” *Journal of Fluid Mechanics*, Vol. 392, Aug. 1999, pp. 155–181. doi: 10.1017/S0022112099005406.
- [3] J. Sesterhenn, “A Characteristic-Type Formulation of the Navier–Stokes Equations for High Order Upwind Scemes,” *Computers & Fluids*, Vol. 30, No. 1, 2000, pp. 37–67. doi: 10.1016/S00457930(00)00002-5
- [4] S. Pradhan, P. Thaker and S. Ghosh, “Analysis of the Dominant Structures of an Impinging Round Jet at $M=0.9$,” *AIAA Journal*, Vol. 62, No. 2, 2024, pp. 602–619. doi: 10.2514/1.J063282.

* Communicating Author: Dr. Somnath Ghosh, sghosh@aero.iitkgp.ac.in.

Effect of Pivot Point Location on the Propulsive Performance of Rear Airfoil in Tandem Configuration

Adeetya Uppal^a, Rahul Ranjan^{a,*}, Sunil Manohar Dash^a

^aDepartment of Aerospace Engineering, Indian Institute of Technology, Kharagpur, India

* Communicating Author: Rahul Ranjan rr24@kgpian.iitkgp.ac.in

1. INTRODUCTION

The flight of insects, birds, and aquatic animals has long inspired engineers to design highly maneuverable and energy-efficient vehicles. Among the various configurations found in nature, the tandem airfoil system - seen in dragonflies - stands out for its ability to combine lift generation with precise control [1]. By flapping two airfoils in a coordinated manner, these creatures exploit complex wake interactions that can either enhance or diminish performance, depending on the timing and spatial arrangement [2].

This paper investigates the thrust and aerodynamic performance, as well as the flow physics, of two-dimensional tandem flapping elliptic airfoils by varying the pivot point locations on the rear airfoil in an incoming flow with a Reynolds number of 5000, while maintaining an aspect ratio of 8 for both the front and rear airfoils. Three pivot point locations are chosen for the rear airfoil: Pivot Points A = 0.25c, B = 0.5c and C = 0.75c from the leading edge, c being the chord length. The front airfoil has a fixed location of pivot point, B = 0.5c from the leading edge, and the airfoil spacing between the two elliptic airfoils is set at 1c. The size ratio of the two airfoils is fixed as 1. The Strouhal number, St , is varied from 0.1 to 0.7 for three angle of attack amplitudes ($\alpha_0 = 10^\circ$, 15° and 20°). The transient thrust and lift are denoted by C_T and C_L , respectively, and the time-averaged thrust and lift are denoted by $\overline{C_T}$ and $\overline{C_L}$, respectively.

2. METHODOLOGY

The front and rear 2D elliptical airfoils in tandem configuration follow an in-phase sinusoidal heaving and pitching profile of motion, and the phase difference between the heaving motion and the pitching motion is set to 90° . The kinematics of the simple harmonic motions of heaving and pitching, which are used to emulate the flapping motion of an airfoil, can be mathematically represented as: $h_{F/R}(t) = h_0 \cos(\omega t)$ and $\theta_{F/R}(t) = \theta_0 \cos(\omega t - \phi)$, where h_0 (= 0.75c) and θ_0 (= 30°) are the heaving and pitching amplitudes, and $h_{F/R}$ and $\theta_{F/R}$ are the functions of instantaneous heaving and pitching, respectively, for the front and rear airfoils, $\omega = 2\pi f$ is the angular frequency, f is the corresponding flapping frequency and ϕ (= 90°) is the phase angle between heaving and pitching motion [5]. A commercial Computational Fluid Dynamics (CFD) software package, ANSYS FLUENT v19.1, utilizing the Finite Volume Method (FVM) [2], was employed to conduct the numerical simulations on elliptical flapping airfoils in tandem configurations within a $60c \times 40c$ domain. The governing equation, a conservative integral form of the 2D unsteady, incompressible Navier-Stokes equation, is solved using the Arbitrary Lagrangian-Eulerian (ALE) formulation [3]. The Pressure-Implicit with Splitting Operators (PISO) algorithm was applied for the coupling of pressure and velocity [5]. User-defined functions (UDFs) were written in C programming language and compiled in FLUENT to simulate the flapping motion profile in the numerical solver [4][5].

3. RESULTS & DISCUSSION

The present study analyzes the thrust and lift characteristics of 2D elliptical flapping airfoils in tandem configuration. The characteristics of the front airfoil remain largely unchanged with respect to variations in rear airfoil pivot location, hence the study primarily focuses on the rear airfoil. The flapping cycle is divided into a downstroke ($t^* < 0.5$) and an upstroke ($t^* > 0.5$) for better visualization of the trends in the figures. It is observed that the time-averaged thrust ($\overline{C_T}$) and time-averaged lift ($\overline{C_L}$) coefficients decrease for every α_0 (Fig.

1) as the pivot point location moves from near the leading edge towards the trailing edge on the rear airfoil. It is also observed that for every pivot location, $\overline{C_T}$ increases with an increase in α_0 (Fig. 1). These trends can be further analyzed with the transient plots as seen in Fig. 2. Pivot A produces higher peaks of both C_T and C_L , while Pivot B produces lower peaks and small negative valleys. Pivot C produces diminished peaks and deeper negative valleys. These variations can be attributed to the influence of pivot point location on the formation and development of the Leading Edge Vortex (LEV) on the rear airfoil. Due to a change in the location of the pivot point, the linear velocity distribution on the surface of the rear airfoil changes. This causes a change in the interaction of the LEV and the vortex shed from the front airfoil, leading to the different trends in the thrust and lift characteristics. The detailed flow physics is discussed in the full paper.

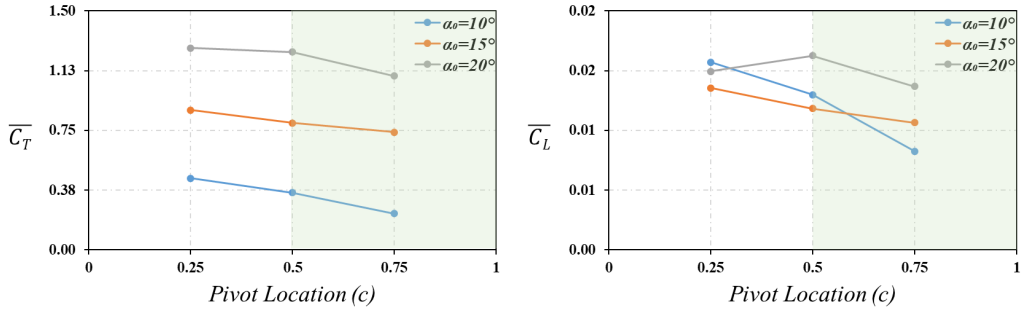


Figure 1: $\overline{C_T}$ and $\overline{C_L}$ vs. Pivot Locations at $St = 0.4$ for various α_0 .

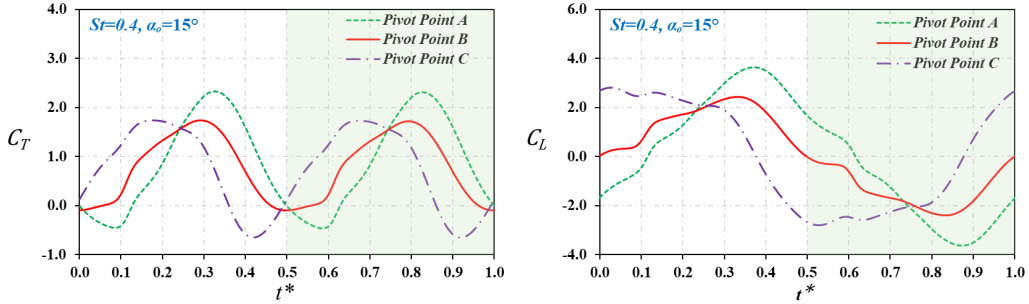


Figure 2: C_T and C_L vs. Pivot Locations at $St = 0.4$, $\alpha_0 = 15^\circ$.

4. CONCLUSIONS

In this study, we have simulated 2D elliptical flapping airfoils in tandem configuration and analyzed the variations in thrust and lift characteristics with a change in the location of the pivot point of the rear airfoil. The change in pivot point location results in a change in the linear velocity distribution on the surface of the airfoil, which significantly affects the interaction between the LEV and the vortex shed from the front airfoil, leading to variations in the thrust and lift characteristics of the rear airfoil. Pivot A produces higher thrust and lift peaks, as compared to Pivot B and Pivot C, which have lower peaks and negative valleys. The net thrust and lift decrease as the location of the pivot point is shifted from near the leading edge towards the trailing edge.

References

- [1] K. B. Lua, S. M. Dash, T. T. Lim, and K. S. Yeo, "On the thrust performance of a flapping two-dimensional elliptic airfoil in a forward flight," *Journal of Fluids and Structures*, vol. 66, pp. 91–109, Oct. 2016, doi: 10.1016/j.jfluidstructs.2016.07.012.
- [2] K. B. Lua, H. Lu, X. H. Zhang, T. T. Lim, and K. S. Yeo, "Aerodynamics of two-dimensional flapping airfoils in tandem configuration," *Physics of Fluids*, vol. 28, no. 12, p. 121901, Dec. 2016, doi: 10.1063/1.4971859.
- [3] J. H. Ferziger, M. Perić, and R. L. Street, *Computational Methods for Fluid Dynamics*, 3rd ed., Berlin: Springer-Verlag, 2002.
- [4] J. Sinha, N. Sreedharan, and S. M. Dash, "Effect of the Pivot Point Locations on the Wake Dynamics and Thrust Performance of a Flapping Elliptic Airfoil: A Numerical Study," in *Fluid Mechanics and Fluid Power (FMFP)*, pp. 193–201, 2021.
- [5] R. Ranjan, A. Singh, J. Sinha, and S. M. Dash, "Effects of Flapping Frequency on the Aerodynamic Performance of the Elliptical Tandem Flapping Wings," in *Fluid Mechanics and Fluid Power*, Lecture Notes in Mechanical Engineering, Singapore: Springer, 2024, pp. 395–408, doi: 10.1007/978-981-99-5752-1-33.

Effect of ply-orientation angle on flutter behaviour of laminated composite plates

Shashank K Shankaregowda^a, Subrata Barman^b, Rajeev Nayan Gupta^c, Saikat Ranjan Maity^d, Dipak Kumar Maiti^e, Sudip Dey^f

^{a,b,c,f} Mechanical Engineering Department, National Institute of Technology Silchar, India

^d Mechanical Engineering Department, NIT Jamshedpur, India

^e Aerospace Engineering Department, IIT Kharagpur, India

1. INTRODUCTION & OBJECTIVE

Laminated composite panels are widely used in aerospace and high-speed vehicle structures owing to their high stiffness-to-weight ratio, corrosion resistance, and tenable mechanical behaviour through ply stacking. However, their anisotropic nature gives rise to complex aeroelastic interactions, making them vulnerable to flutter - a dynamic instability that can lead to structural failure under supersonic flow. Accurate prediction and control of this phenomenon remain essential for safe and efficient design. Conventional analyses based on classical plate theory (CPT) or low-order finite elements often neglect transverse shear deformation and higher-order coupling effects, limiting their accuracy for multi-layered laminates. Moreover, the influence of ply-orientation angle on flutter onset and modal coalescence has not been systematically investigated [1,2]. This study presents a computational case analysis on the effect of ply-orientation angle (θ) using a nine-node isoparametric quadrilateral finite element model formulated within the first order shear deformation theory (FSDT) [3]. Aerodynamic forces are represented through first-order piston theory, and the governing equations are derived via Lagrange's energy principle [4]. The objective is to quantify the role of ply angle in altering mode coupling and critical flutter boundaries for laminated composite panels.

2. METHOD OF ANALYSIS

The present numerical formulation is developed using the first-order shear deformation theory (FSDT), which accounts for transverse shear deformation effects without relying on empirical correction factors. The laminated composite plate is discretized with nine-node isoparametric quadrilateral elements, each node having five degrees of freedom - three translational and two rotational. This high-order element ensures displacement continuity and accurate curvature representation, offering superior accuracy over conventional four-node elements. The laminate stiffness matrices are formulated using classical lamination theory (CLT), wherein the orthotropic stiffness coefficients of each ply are transformed according to its ply-orientation angle (θ). This enables direct inclusion of anisotropy and stacking sequence effects in the global stiffness matrix. Aerodynamic pressure under supersonic flow (Mach>1) is modeled using first-order piston theory, expressed as [4],

$$[M]\{(\delta_{,t})_t\} + g[K_d]\{\delta_{,t}\} + ([K] + \lambda[K_s])\{\delta\} = 0 \quad (1)$$

where, $[M]$: global mass matrix, $[K]$: panel stiffness matrix, $[K_d]$: aerodynamic damping matrix, $[K_a]$: aerodynamic stiffness matrix, $\{\delta\}$: global displacement vector, λ : non-dimensional dynamic pressure, g : aerodynamic damping parameter.

3. RESULTS AND DISCUSSION

The numerical results demonstrate a significant influence of the ply-orientation angle on the flutter boundaries of laminated composite plates. As shown in the Fig.1 the ply angle increases from 0° to

45° , the critical flutter dynamic pressure decreases, indicating a stronger coupling between in-plane and out-of-plane modes. Beyond 45° , a gradual increase in flutter pressure is observed, signifying improved stiffness alignment along the fiber direction. This behaviour underscores the anisotropic response of the laminate under aerodynamic loading. The analysis also captures smooth and continuous eigenvalue progression, accurately distinguishing between mode veering and coalescence phenomena. The first two coupled modes primarily govern flutter onset, while higher modes exhibit stable trends throughout. Overall, the proposed finite element formulation effectively characterizes the interaction between structural anisotropy, flow direction, and modal coupling-offering a physically consistent representation of the flutter mechanism in laminated composite plates.

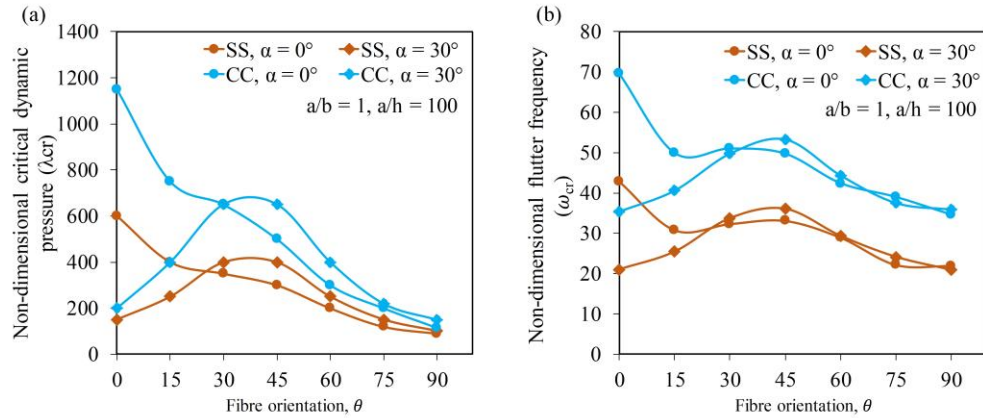


Figure 1. Variation of flutter characteristics of a square composite plate with the fibre orientation: (a) Non-dimensional critical pressure parameter (λ_{cr}), (b) Non-dimensional flutter frequency (ω_{cr}).

4. CONCLUSIONS

This present study numerically examined the effect of ply-orientation angle on the flutter behavior of laminated composite plates under supersonic flow. The non-dimensional flutter frequency and critical pressure vary notably with ply orientation, with off-axis plies showing reduced stability margins. The developed computational framework efficiently captured eigenvalue coalescence and mode veering, accurately identifying the critical flutter boundary. Results confirm that ply orientation strongly governs aeroelastic stability-off-axis plies exhibit increased flutter tendency due to higher bending-torsion coupling, whereas symmetric orientations provide improved stability margins. The proposed FSDT-based formulation offers a reliable and computationally efficient approach for supersonic flutter prediction, establishing a solid foundation for future developments in stochastic uncertainty modelling, multiscale integration, and experimental validation of advanced aerospace composite structures.

REFERENCES

- [1] Xia, W. and Ni, Q., 2011. Parametric study on supersonic flutter of angle-ply laminated plates using shear deformable finite element method. *Acta Mechanica Sinica*, 27(5), pp.749-756.
- [2] Attaran, A., Majid, D.L., Basri, S., Rafie, A.M. and Abdullah, E.J., 2011. Structural optimization of an aeroelastically tailored composite flat plate made of woven fiberglass/epoxy. *Aerospace Science and Technology*, 15(5), pp.393-401.
- [3] Lee, I., Oh, I.K. and Lee, D.M., 1997, November. Vibration and flutter analysis of stiffened composite plate considering thermal effect. In *ASME International Mechanical Engineering Congress and Exposition* (Vol. 18350, pp. 133-141). American Society of Mechanical Engineers.
- [4] Mohapatra, S., Sharma, N., Dewangan, H.C. and Panda, S.K., 2025. Flutter characteristics of multi-layered composite shell panels under supersonic flow with curvature effect. *Waves in Random and Complex Media*, 35(4), pp.6952-6970.

Effects of random orientation of bluff body on the onset speed of galloping-based piezoelectric energy harvester

Rakesha Chandra Dash^a

^a Assistant Professor, Department of Mechanical Engineering, Birla Institute of Technology Pilani, Pilani, India

1. INTRODUCTION & OBJECTIVE

Vibration-based energy harvesters offer promising solutions to meet the growing power needs of small-scale devices. Considerable attention has been directed toward galloping-based piezoelectric energy harvesters (GPEH), particularly because wind energy represents a sustainable and renewable resource. The positioning of a vertical cylinder in the wind flow path is known to critically influence energy harvesting performance. Even slight forward or backward tilts of this cylinder can have a marked impact on the amount of power generated [3]. Since manual installation of the vertical cylinder on a cantilever beam can introduce small orientation errors, understanding these effects is crucial. The speed at which galloping begins, the onset speed (U_g), is key to harvesting efficiency, as oscillations and thus energy generation only occur beyond this threshold. This study explores how minor random misalignments of the vertical cylinder affect the onset speed of galloping. Monte Carlo simulations are employed to assess the influence of these variations, with conclusions drawn from the resulting probability distribution analysis.

2. METHODS OF ANALYSIS

In this study, Forward and backward tilts were defined as positive and negative, respectively Figure 1. Inclination angles within -10° to $+10^\circ$ were generated from a Gaussian distribution using Latin Hypercube Sampling (LHS). The governing equations of the piezoelectric harvester were expressed in state-space form [1], and the onset speed was determined from the linear coefficient of the aerodynamic galloping force [4]. This force was modeled using quasi-steady theory, where the lift coefficient was represented by a 7th-order polynomial fit for higher accuracy [2]. The linear coefficient was further curve-fitted with an Artificial Neural Network (ANN) to capture inclination effects. Finally, Monte Carlo simulations with 10,000 samples were carried out to estimate the probability distribution of onset speeds.

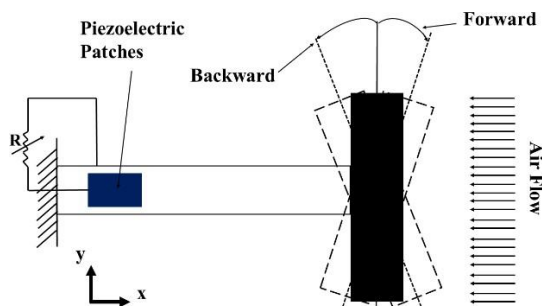


Figure 1: GPEH system with forward and backward inclination

3. RESULTS AND/OR HIGHLIGHTS OF IMPORTANT POINTS

Figure 2(b) presents the probability density function (PDF) of the onset speed of galloping, obtained from Monte Carlo simulations where inclination angles were sampled from a normal distribution

centered at 0° . The results show that the onset speed is not fixed but exhibits statistical variability due to random orientation of the bluff body. The peak probability density occurs in the range of 1.75–1.8, representing the most probable onset speed. The distribution is skewed toward higher speeds, with values extending up to ~ 2.1 , which correspond to backward inclinations delaying the initiation of galloping. This asymmetry highlights that forward inclinations facilitate galloping at lower speeds, enhancing energy harvesting initiation, while backward inclinations increase the onset threshold, thereby reducing efficiency.

To further illustrate this behavior, Figure 2 (a) shows the deterministic variation of onset speed with inclination angle. A clear trend emerges: onset speed decreases progressively from negative inclinations (backward tilt) toward a minimum near $+5^\circ$, after which it increases again with larger forward inclinations. This U-shaped dependence explains the probabilistic spread observed in the Monte Carlo simulations. Specifically, the lower onset speeds associated with forward inclinations dominate the probability distribution, while the higher speeds from backward inclinations contribute to the tail.

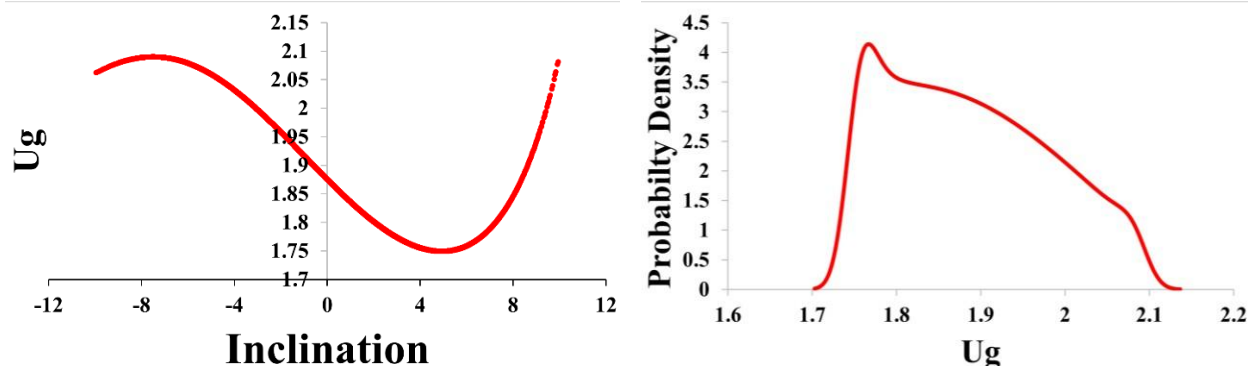


Figure 2 : (a) Onset speed of galloping vs. Inclination plot (b) PDF plot for onset speed of galloping

4. CONCLUSIONS

This study investigated the onset speed of galloping in a galloping-based piezoelectric energy harvester (GPEH) under varying bluff body inclinations. Using a quasi-steady aerodynamic model with a 7th-order polynomial fit, the linear stability parameter was identified and evaluated through Artificial Neural Network (ANN) curve-fitting across inclination angles generated via Latin Hypercube Sampling (LHS). Monte Carlo simulations with 10,000 samples revealed that forward inclinations consistently lower the onset speed, while backward inclinations delay galloping and contribute to a skewed probability distribution. These results demonstrate that even small orientation changes can significantly affect stability and harvesting performance. Hence, maintaining a slight forward inclination is recommended for experimental setups and practical deployments to ensure earlier and more consistent galloping initiation.

5. REFERENCES

- [1] Dash, R. C., Maiti, D. K., & Singh, B. N. (2020). Dynamic stability and performance analysis of a galloping-based piezoelectric energy harvester for different order representations of the aerodynamic force. International Journal of Non-Linear Mechanics, 121, 103463.
- [2] Dash, R. C., Maiti, D. K., & Singh, B. N. (2022). Nonlinear dynamic analysis of galloping based piezoelectric energy harvester employing finite element method. Mechanics of Advanced Materials and Structures, 29(26), 4964-4971.
- [3] Hu, G., K. T. Tse, and K. C. S. Kwok. 2015. Galloping of forward and backward inclined slender square cylinders. Journal of Wind Engineering and Industrial Aerodynamics 142:232–45. doi:10.1016/j.jweia.2015.04.010.
- [4] U. Javed, A. Abdelkefi, Role of the galloping force and moment of inertia of inclined square cylinders on the performance of hybrid galloping energy harvesters, Applied Energy, Volume 231, 2018, Pages 259-276, ISSN 0306-2619, <https://doi.org/10.1016/j.apenergy.2018.09.141>.

* Communicating Author: Rakesha Chandra Dash and email ID: rakesha.dash@pilani.bits-pilani.ac.in.

Empirical expression to predict the first-mode resonant frequency of a pitching flexible panel

Abhinav Kumar KSN[#], Parag Deshpande^{\$#} and Ravi Dodamani^{\$}

UAV Design and Integration Division

^{\$} CSIR-National Aerospace Laboratories, Bangalore-560017, India

[#] Academy of Scientific and Innovative Research, Ghaziabad-201002, India

abhinav.ksn@gmail.com

INTRODUCTION & OBJECTIVES

Knowing the resonant frequency for a flexible propulsor undergoing oscillatory motion is indispensable while evaluating its propulsive performance. Euler-Bernoulli (E-B) beam theory is used by many investigators to determine the resonant frequency of a fluid-structure system analytically by modelling the effect of high-density fluid using the added mass term. Yadykin, Tenetov, and Levin (2003) proposed a theoretical approach in which they showed that the added mass scales with ρL , where L is the length of the plate and ρ is the fluid density. Smits (2019) mentioned that the scaling of added mass can be done based on the aspect ratio of the flexible panel undulating in water. For example, for $AR \ll 1$, added mass can be scaled as ρsc , whereas for $AR \gg 1$, it can be taken as ρs^2 , where s and c are the span and chord of the rectangular panel.

In general, the E-B theory is applicable only for low forcing amplitudes, where the pitching motion of the foil/panel is analogous to the vibrating cantilever beam in a dense fluid medium. Thus, the effect of amplitude on the resonance of the fluid-panel system is not included in the formulation. However, Deshpande and Abhinav Kumar (2025) showed experimentally that the resonant frequency is a strong function of the pitch angle. Thus, the added mass scaling should be done by incorporating the amplitude term.

In the present study, we are proposing an empirical expression to determine the first-mode resonant frequency of the fluid-panel system by modelling the added mass term as the area swept by the panel into the density of the fluid. To benchmark the proposed expression, various panels having different flexural stiffness are selected, and their first-mode natural frequency is determined using trailing-edge amplitude measurements as well. Thereafter, the propulsive performance characteristics of various flexible panels obtained through propulsive force and power measurements for the range of forcing amplitudes and frequencies will be elucidated with a perspective of designing bio-inspired propulsion for underwater vehicle applications.

METHODS OF ANALYSIS

The present study is being carried out in a newly designed recirculation-type water tunnel at CSIR-NAL, Bangalore. The details about the setup can be found in Deshpande and Abhinav Kumar (2025). The present study considers four panels of varying thickness (h) and the same aspect ratio (AR) of 2.0, with a fixed chord length (c) of 100 mm and a width (b) of 200 mm. The Panel parameters will be given in the full-length paper. Sinusoidal pitching motion $\theta_m = \cos(2\pi ft + \pi)$ was given to the pitching shaft. The trailing edge instantaneous position and the trajectory are determined using a high-speed camera, which is used to determine the first mode resonant frequency. Propulsive force and torque experienced by the panels are measured using a six-component ATI mini 40 F/T sensor, which was mounted above the servo.

RESULTS

In the case of a rigid panel, the trailing edge excursion a_0 can be determined as $a_0 = 2cs\sin\theta$. In the case of a flexible panel, due to elastic deformation, the trailing edge excursion a_1 would be higher than a_0 , and the frequency at which a_1 reaches peak becomes the first mode resonant frequency of that panel.

$$m_s = \rho 2A_s = \rho 2 \frac{2\theta}{360} \pi c^2 \quad \dots \dots \dots (1)$$

$$f_{np} = \beta \sqrt{\frac{Eh^3}{12m_s c^3}} \quad \dots \dots \dots (2)$$

Figure 1 shows the area swept by the rigid and flexible panels during pitching. The rigid panel is found to sweep the area as the sector area, with the pitch angle being the apex angle of the sector. We

calculated the mass of the fluid swept by the rigid panel per unit span in expression 1, where A_s is the Sector area traced by the trailing edge during a half pitching cycle, ρ is the fluid density.

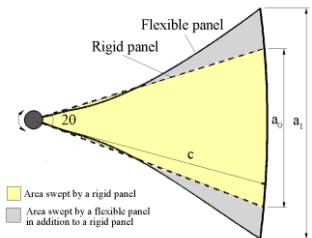


Figure 1: Schematic of the area swept by the panel during pitching

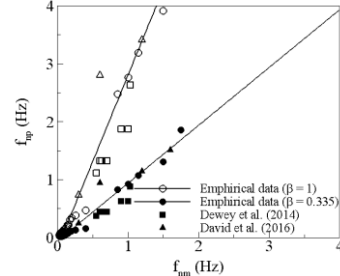


Figure 2: Comparison of predicted first mode resonant frequency (f_{np}) using expression 1 with the experimentally obtained first mode resonant frequency (f_{nm}) for various flexible panels

Based on flexural stiffness per unit span of the panel and fluid mass swept by the rigid panel, the expression to determine the first mode resonant frequency is given below. In expression 2, the factor β is the proportionality constant which accounts for the actual fluid mass swept by the flexible panel. The grey shaded region in the schematic depicted in Figure 1 is the area swept by the flexible, in addition to the rigid panel, pitching at the same amplitude.

Initially, taking $\beta = 1$, we estimated the f_{np} and the comparison of f_{np} and measured f_{nm} is shown in Figure 2. The linear curve fitting shows a very good value of $R^2 > 0.98$. The literature data also shows less scatter around the linear data fitting curve. It means that in the proposed relation, the inclusion of swept fluid mass instead of added mass happens to be a reasonable assumption. Since the slope of the curve is 2.98 indicates that the predicted resonant frequency is higher than the actual, and this is because the actual fluid mass swept by the flexible panels must be higher than that for the rigid panel. To account for extra mass, we simply considered β as the inverse of the slope of the curve so that after multiplication by $\beta = 0.335$, the new curve will have a slope of 1; thus, the predicted resonant frequency will have a good match with the actual resonant frequency.

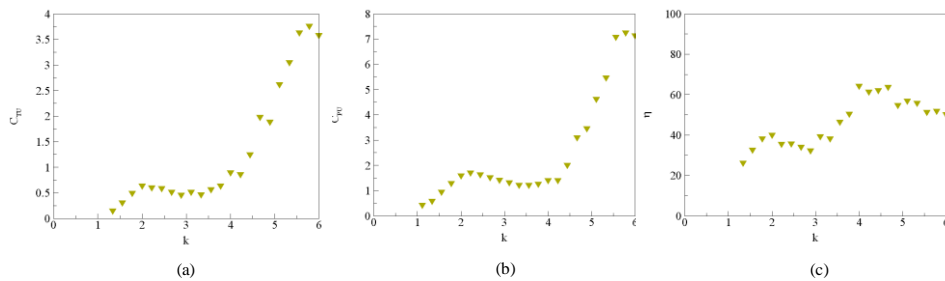


Figure 3: Experimentally obtained propulsive performance characteristics of a flexible panel
(a) C_{TU} vs k , (b) C_{PU} vs k , and (c) η vs k

Figure 3 shows the propulsive performance data for a 0.125 mm thick panel pitching with an incoming flow ($U = 90$ mm/s) will be elucidated in the full-length paper.

SUMMARY:

- Proposed an empirical expression to determine the first mode resonant frequency of the fluid-panel system by modelling the added mass term as the area swept by the rigid panel into the density of the fluid.
- For the flexible panel having a 0.125 mm thickness, the propulsive efficiency up to 60 % is recorded.

REFERENCES:

- Yadykin Y, Tenetov V., Levin D., The added mass of a flexible plate oscillating in a fluid, Journal of Fluids and Structures, 17, (2003), 115–123.
- Alexander J Smits, Undulatory and oscillatory swimming, Journal of Fluid Mechanics 874 (2019).
- Parag J. Deshpande and K.S.N. Abhinav Kumar, Effect of amplitude on resonance and propulsive characteristics of a pitching flexible panel, Ocean Engineering 316 (2025), 119809.

Estimation of Flight Measured Pressure using CFD for a Typical Launch Vehicle

Sreenivasulu Juluri^a, Sanjoy Kumar Saha^b and Vidya G^c

^a Scientist/Engineer, Aero Entity, Vikram Sarabhai Space Centre, Trivandrum

^b Division Head, ACD/ADSG/AERO, Vikram Sarabhai Space Centre, Trivandrum

^c Group Director, ADSG/AERO, Aero Entity, Vikram Sarabhai Space Centre, Trivandrum

1. INTRODUCTION & OBJECTIVE

Aerodynamic characterization over a typical launch vehicle in presence of jet was carried out using CFD (PARAS-3D software [1]). Non-dimensional forces and moments along with C_p distribution over the vehicle has been generated and this data is essential for structural, mission and thermal design of the vehicle. This data is essential to be validated with flight data measured during the mission. C_p derived from the pressure measurements during the actual flight are compared with the pre-flight estimated C_p data generated using CFD. In the paper, details about these comparisons are discussed.

2. METHODS OF ANALYSIS

Pressure port location:

To measure the pressure on the external surface, a total 10 pressure ports were instrumented over the complete vehicle. Schematic locations of external pressure ports in typical launch vehicle are given in Figure 1. One port on Pay Load Fairing (PLF), 2 ports on cylindrical region and 7 ports on 1st stage (2 on flare region, 1 port on fixed fin side panel, 2 ports on shroud base and 2 ports at base of the fins) are located in the actual flight.

Trajectory parameters (angle of attack, dynamic pressure, Mach number etc as a function of time) were given in Figure 2. The maximum flight dynamic pressure occurs at about 48 sec of flight. The total angle of attack is $< 1^\circ$ for majority of the flight regime.

Offset correction of measured pressure data is carried out based on the pressure measured (101350 Pa) on the day of launch. These corrections are estimated at time=0sec and assumed constant throughout the flight duration. The flight measured pressure thus obtained are converted to C_p (coefficient of pressure) using the following expression

$$C_p = (P - P_\infty) / q_\infty$$

Where, P =Flight measured pressure, Pa

P_∞ =Free stream pressure, Pa; q_∞ =Free stream dynamic pressure, Pa

2. RESULTS AND DISCUSSION

Variation of C_p with Mach numbers on PLF for flight is shown in Figure 3. C_p palette over PLF at various Mach numbers as obtained from CFD is shown in Figure 4. At the beginning of the nose cone, C_p reaches the maximum value due to flow stagnation. In the expansion region like ogive and the cylinder-boat tail junction, the static pressure goes below the free stream pressure. It is noticed from the C_p palette that at lower Mach numbers ($M < 0.95$), the expansion of flow on the ogive region does not reach to the port location. This leads to a pressure very close to ambient value ($C_p \sim 0$) at the port location. At $M=0.95$, flow over the ogive-cylinder region accelerates beyond $M>1.0$ and gets terminated by a λ shock on the cylinder. The port location, being ahead of the λ shock, experiences very low pressure. With increase of Mach number, the shock passes over cylinder end and the pressure over port gradually increases to free-stream value. CFD data matches well with the flight measured C_p except at

Mach 0.95 where less expansion is observed in flight as compared to CFD as shown Figure 3. Axi-symmetric simulations are carried out over PLF using CFD++ code. The obtained data show similar behaviour like PARAS data.



Figure 1: Location of pressure ports

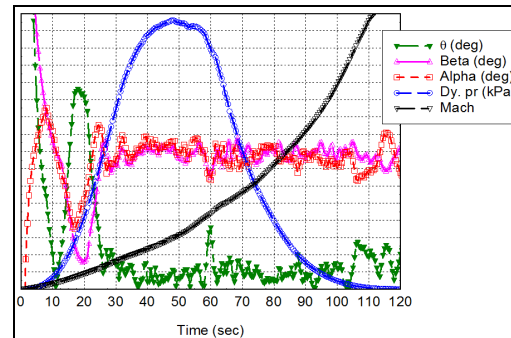


Figure 2: Typical flight trajectory parameters (during actual flight) over the configuration

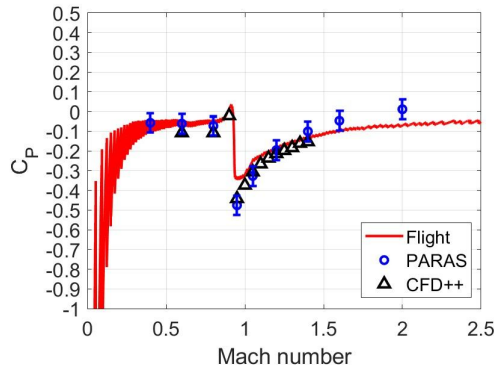


Figure 3: Comparison of C_p distribution over PLF at various Mach numbers

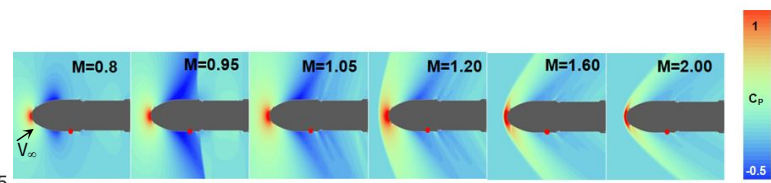


Figure 4: C_p palette over PLF at various Mach numbers

4. CONCLUSIONS

CFD analysis carried out over typical launch vehicle at various Mach numbers under jet-on condition. Steady pressure data has been estimated for the flight measured ports. Pre-flight estimated C_p data (using CFD) is used to compare with the flight measured data CFD data estimated from PARAS-3D and CFD++ matches very well with the flight data.

5. REFERENCES

- [1]. Harichand M V., "Acceleration of an Adaptive Cartesian Mesh CFD Solver in the Current Generation Processor Architectures", 25th International conference on High Performance Computing (HIPC-2018), Bangalore.

6. ACKNOWLEDGEMENT

Authors would like to thank present and former DD, AERO for their encouragement. The computations presented here were carried out using NARL HPC system and authors also thank NARL team for their support during the simulations. Authors also thank Shri. Gnanasekar, APD, VSSC for providing the necessary inputs.

* Communicating Author: Juluri Sreenivasulu, jksnivas@gmail.com or sreenivas_j@vssc.gov.in

Evaluation of anisotropy via non-destructive indentation in LPBF-processed Co-Cr-Mo alloy: The role of scanning strategy

Vinod Kumar Jat *, R. U. Patil

Department of Mechanical Engineering, Indian Institute of Technology Jammu, Jammu & Kashmir 181221, India

Abstract: This work investigates the anisotropy of Co-Cr-Mo alloy produced via laser powder bed fusion (LPBF) using a non-destructive indentation (NDI) technique based on Knoop hardness (KHN) testing. Stripe, meander, and chessboard scanning strategies were used to fabricate the samples. The resulting hardness values were used to generate yield locus plots. These plots revealed significant anisotropy along the X-direction for all scanning strategies, whereas stress was found to be isotropic along the Y-direction.

Keywords: Co-Cr-Mo alloy, Anisotropy, Yield strength, Knoop hardness, Scanning strategy.

1 INTRODUCTION AND OBJECTIVE

The Co-Cr-Mo alloy has been extensively used in biomedical implants [1] as well as aerospace components. Nowadays, these parts are often complex and can be efficiently manufactured using LPBF. The LPBF process involves intricate thermal cycling, which promotes directional solidification and leads to a pronounced texture in the material. This increases the likelihood of anisotropy in mechanical properties. Therefore, investigating the anisotropic behavior of Co-Cr-Mo alloys processed by LPBF is essential. Yielding behavior is commonly recognized as a key basis for describing mechanical anisotropy. Wheeler and Ireland [2] proposed a relatively simple approach to estimate anisotropy in materials using a KHN. In this study, the influence of scanning strategy on the yield locus of LPBF-processed Co-Cr-Mo alloy was examined using the KHN test.

2 MATERIAL AND METHOD

Co-Cr-Mo samples were LPBF-printed using stripe, meander, and chessboard scan strategies. The LPBF process parameters, scanning strategy parameters and powder characteristics used in this study are consistent with those reported by Vinod et al. [3]. The Innova Test Falcon 400 hardness tester was used for micro-hardness. The load employed with 200 grams and was subjected to a dwell period of 10 seconds. The microhardness measurement via knoop was conducted on the plane aligned with the build direction, the plane perpendicular to it, and the plane perpendicular to both. The Wheeler and Ireland method was employed to evaluate the material's yield surfaces [2].

3 RESULTS AND DISCUSSION

The yield locus qualitatively reflects the material's anisotropy. The points where the yield locus intersects the horizontal and vertical axes represent the σ_x and σ_y values under compressive and tensile loading conditions [4]. Isotropic behavior, or the consistency of a material's properties in all directions, is suggested by a yield locus that is perfectly elliptical. Any deviation from the elliptical form suggests anisotropy, indicating that the material exhibits direction-dependent behavior. The NDI yield locus for

* Corresponding author E-mail address: vinod.jat@iitjammu.ac.in

LPBF-printed Co-Cr-Mo alloy samples with stripe (S), meander (M), and chessboard (CH) scanning strategies is presented in [Figure 1](#). The anisotropy observed in the samples may result from the intricate thermal behavior integral to the LPBF process and the direction-dependent mechanical response of the material [\[5\]](#).

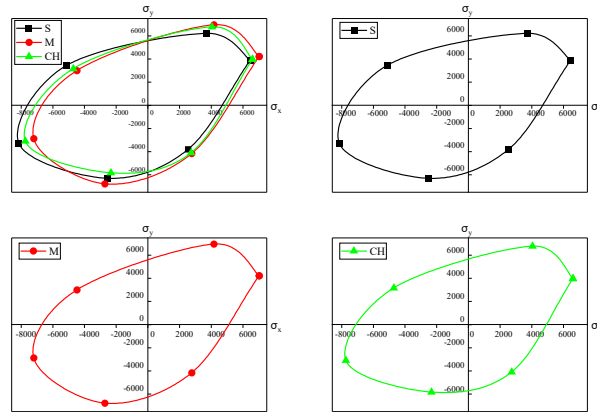


[Fig. 1.](#) The yield locus of LPBF-processed Co-Cr-Mo alloy samples for S, M and CH scanning strategies. (Both axes are in MPa)

4 CONCLUSIONS

The results of the present study indicate that the LPBF-processed Co-Cr-Mo alloy exhibits noticeable anisotropy along the X-direction for all three scanning strategies as confirmed by the plotted yield loci. In contrast, along the Y-direction, the stress ratio was found to be nearly unity for all scanning strategies, suggesting that the material behaves almost isotropically in this direction. Furthermore, the area enclosed by the yield loci showed minimal variation among the different scanning strategies.

REFERENCES

- [1] L. E. Murr, S. M. Gaytan, E. Martinez, F. Medina, and R. B. Wicker, “Next Generation Orthopaedic Implants by Additive Manufacturing Using Electron Beam Melting,” *Int. J. Biomater.*, vol. 2012, pp. 1–14, 2012.
- [2] R. G. Hheeler, R. Washington, C. Contrac, and E. Unit, “Multiaxial plastic flow of Zircaloy-2 determined from hardness data,” *Electrochem. Technol.*, vol. 4, 1965.
- [3] V. K. Jat, R. U. Patil, and S. S. Samant, “Influence of Scanning Strategies on the Tensile and Fatigue Properties of Direct Metal Laser Sintering-Printed Co-Cr-Mo Alloy,” *J. Mater. Eng. Perform.*, vol. 34, no. 9, pp. 7479–7495, May 2025.
- [4] S. Suwas, I. Lahiri, R. Ray, and S. Bhargava, “The Knoop hardness yield locus of Ti–24Al–11Nb alloy,” *Mater. Lett.*, vol. 57, no. 21, pp. 3251–3256, Jul. 2003.
- [5] K. S. Kim, J. W. Hwang, and K. A. Lee, “Effect of building direction on the mechanical anisotropy of biocompatible Co–Cr–Mo alloy manufactured by selective laser melting process,” *J. Alloys Compd.*, vol. 834, p. 155055, Sep. 2020.

Experimental Analysis of the Magneto-Viscous Responses of Magneto-Active Polymers

Rahul Kumar Saini ^a and Krishnendu Haldar ^{b*}

^a M.Tech Student,Aerospace,IIT Bombay, Mumbai,India

^b Professor,Aerospace, IIT Bombay, Mumbai, India

1. INTRODUCTION & OBJECTIVE

Magneto active polymers are special polymers whose properties change when a magnetic field is applied [1]. To fabricate them, magnetic particles like iron are mixed into a normal polymer matrix, so the material becomes responsive to magnets and stiffens as we increase the magnetic field [1]. Depending on how strong a magnetic effect we need, different types and amount of magnetic fillers can be added. These polymers are very useful in different areas. For example, they are used in robot arms for pick and place objects, in medical devices like MRI machines, and even in space antennas to get better coverage. They are also applied in actuators, dampers, and other smart devices [2].

2. METHODS OF ANALYSIS

MAP Specimen Preparation

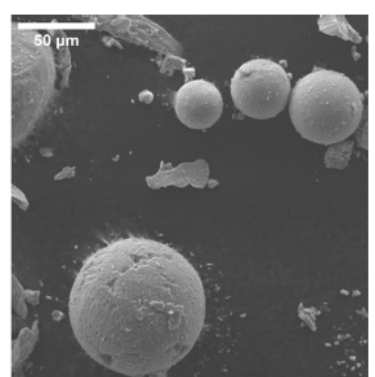
Magnetically active polymer (MAP) samples Figure 1a were fabricated by blending iron powder with Ecoflex-0030. Subsequently, epoxy and hardener were mixed in a 1:1 weight ratio, followed by the incorporation of 20% magnetic fillers. The mixture was vigorously stirred for 2 minutes to ensure a homogeneous dispersion of Fe_3O_4 particles within the matrix, and then placed under vacuum desiccation for 2 minutes to eliminate air bubbles in cylindrical molds. All samples were cast with a diameter of 12 mm. The curing process was carried out for 2 hours at 70°C, followed by 24 hours at room temperature, to achieve the desired mechanical properties.



(a) Specimen



(b) Slice cut for SEM test



(c) SEM test

Microstructural characterization

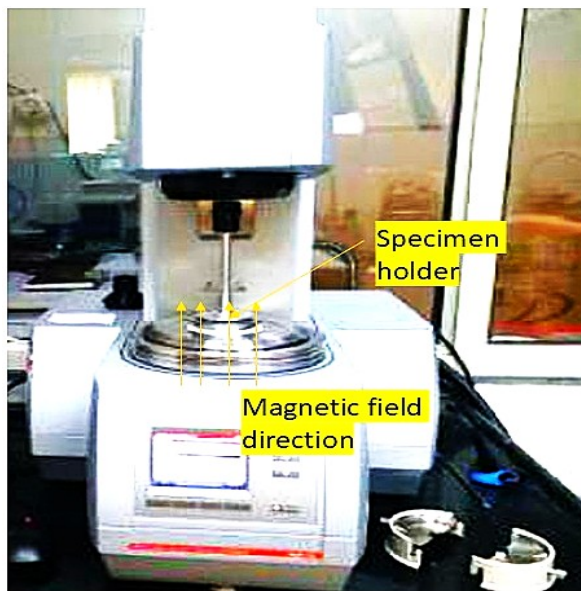
Figure 1

In Scanning Electron Microscopy (SEM) was employed to investigate the morphology, size, and elemental composition of the synthesized Fe_3O_4 particles. Figure 1c Both surface and cross-sectional views of the MAP samples were analyzed to evaluate the microstructural characteristics. SEM examination confirmed a uniform dispersion of Fe_3O_4 particles within the polymer matrix and allowed detection of any possible cluster formation. Furthermore, detailed micrographs of the matrix revealed particle sizes in the range of 40–60 μm .

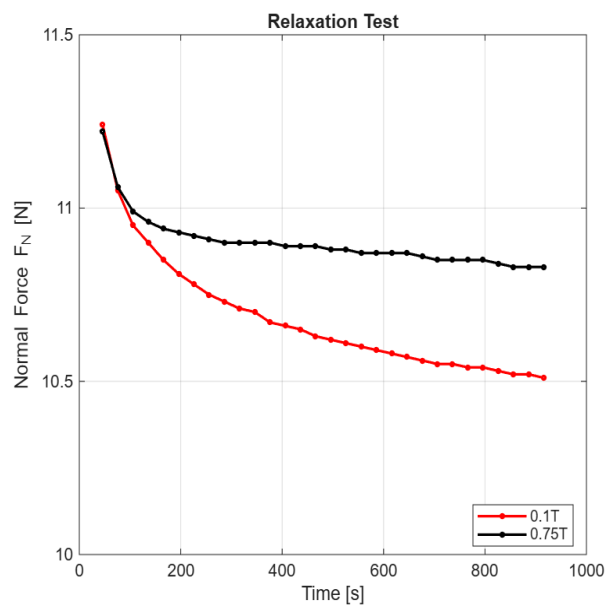
Mechanical Testing

Relaxation Test

Relaxation tests [3] were conducted to investigate the viscoelastic characteristics of the MAP specimens. The experiments were performed under magnetic field strengths of 0.1 T and 0.75 T, with the samples subjected to 30% strain and held for 15 minutes. Figure 2a The application of the magnetic field increased the stiffness of the specimens with rising field intensity. Moreover, the weak relaxation behavior observed indicates the low viscosity of the MAP material, consistent with its magneto-elastic response.



(a) Experimental Setup at IITB facility



(b) Relaxation tests at 0.1 T and 0.75 T

Figure 2

3. RESULTS AND/OR HIGHLIGHTS OF IMPORTANT POINTS

In Figure 2b The graph shows stress relaxation under constant strain at two magnetic fields: 0.1 T and 0.75 T. At 0.1 T, stress relaxes faster, while at 0.75 T, stress relaxation is slower, meaning the material holds stress longer. This indicates higher magnetic fields slow down relaxation by stabilizing material structure, important for understanding magnetic field effects on material behavior.

4. CONCLUSIONS

This study presents the fabrication process, microstructural characterization, and deformation behavior of magneto-active polymers (MAPs). The MAP fillers were analyzed using Scanning Electron Microscopy (SEM) to verify their size and purity. Mechanical behavior was examined through compression tests under applied magnetic fields. It was observed that at 0.1 T, stress relaxation occurs faster, while at 0.75 T, relaxation is slower, indicating the material retains stress longer. This suggests that higher magnetic fields slow stress relaxation by stabilizing the material's structure.

REFERENCES

- [1] Arijit Garai and Krishnendu Haldar. Experiments and modeling of magneto-stiffening effects for magnetoactive polymer. *International Journal of Mechanical Sciences*, 286:109860, 2025.
- [2] Jingze Xue, Zhuangzhuang Tian, Xinze Xiao, Chuankai Du, Shichao Niu, Zhiwu Han, and Yan Liu. Magnetoactive soft materials with programmable magnetic domains for multifunctional actuators. *ACS Applied Materials & Interfaces*, 15(48):56223–56232, 2023. PMID: 37988636.
- [3] Krishnendu Haldar. Constitutive modeling of magneto-viscoelastic polymers, demagnetization correction, and field-induced poynting effect. *International Journal of Engineering Science*, 165:103488, 2021.

* Communicating Author: krishnendu@aero.iitb.ac.in

Experimental Fabrication and Characterization of E-Glass/Epoxy Composites Using Vacuum-Assisted Resin Infusion

Umakanta Meher^a, Praveen Shakya^c, Mohammad Rabius Sunny^b, Iqbal Ahmed^{d,*}

^a Assistant Professor, School of Aerospace Engineering, KIIT University, Bhubaneswar, India

^b Associate Professor, Department of Aerospace Engineering, IIT Kharagpur, India

^c Post Doctoral Research Fellow, Mechanical & Civil Engineering, Utah Valley University, UT, USA

^d Research Scholar, Department of Aerospace Engineering, IIT Kharagpur, India

1. INTRODUCTION & OBJECTIVE

Fibre-reinforced polymer (FRP) composites have gained significant attention in recent years due to their superior mechanical properties, lightweight characteristics, and corrosion resistance. These materials are increasingly employed in various engineering sectors, including aerospace, automotive, marine, and civil infrastructure. Among the different fabrication methods available, Vacuum-Assisted Resin Infusion (VARI) has emerged as a cost-effective and reliable technique for producing high-quality composite laminates with consistent resin distribution and reduced void content.

This study focuses on the fabrication of E-glass/epoxy composite laminates using the VARI process, followed by experimental evaluation through burn-off testing to determine the fibre and resin content. The calculated fibre volume fraction and composite density serve as key indicators of fabrication quality. The findings contribute to optimizing process parameters for structural composite manufacturing and lay the groundwork for future mechanical and functional integration, such as embedded sensing for health monitoring applications.

2. METHODS OF ANALYSIS

The composite laminates were fabricated using biaxial woven E-glass fibre as the reinforcement and a thermosetting epoxy resin system consisting of L-12 epoxy resin and K-6 hardener. Additional consumables required for the Vacuum-Assisted Resin Infusion (VARI) process included vacuum bagging film, sealant tape, peel ply, infusion mesh, infusion spiral, and silicon connectors. A square glass sheet was used as the mould surface. Eight layers of E-glass fibre, each of 0.28 mm thickness and 25 g weight, were used in each laminate to achieve the desired thickness and structural integrity. The fabrication was carried out in three main stages: (i) fibre lay-up, (ii) vacuum bagging, and (iii) resin infusion.



Figure 1 Prepared composite sample of dimension 30cm×30cm

* Communicating Author: Iqbal Ahmed, iqahmed42@gmail.com

3. RESULTS

Volume and weight ratios play an important role in design and fabrication of composites. So, after completion of fabrication these quantities are calculated. The resin burn-off method involves the heating of the composite up to a certain temperature at which resin melts and the fibre remains stable. Four composite samples of dimension 25mm×25mm×2.1mm were kept inside a muffle furnace at 600°C for 20minutes and then the furnace was switched off. It took around 15minutes to reach 600°C from room temperature. After 24hrs the samples were recollected. Some calculated findings after the burn-off test are listed in Table1.

| Specimen Number | Composite Weight (gms) | Fibre Weight (After Burn-off test) in (gms) | Resin Weight (gms) | Fibre ratio (%) | Resin ratio (%) |
|-----------------|------------------------|---|--------------------|-----------------|-----------------|
| Burn-off | | | | | |
| 1 | 2.0320 | 1.3664 | 0.6656 | 67.24% | 32.76% |
| 2 | 2.0518 | 1.4144 | 0.6374 | 68.93% | 31.07% |
| 3 | 2.0744 | 1.4246 | 0.6498 | 68.67% | 31.33% |
| 4 | 2.0748 | 1.4622 | 0.6126 | 70.47% | 29.53% |

The fibre volume ratio has been calculated after the Burn-off test and the values are given below.

$$\text{Fibre weight} = 1.3664 \text{ gm}$$

$$\text{fibre density} = 2.3 \text{ gm/cc}$$

$$\text{Composite weight} = 2.0320 \text{ gm}$$

$$\text{resin density} = 1.2 \text{ gm/cc}$$

$$\text{Resin weight} = \underline{\underline{0.6656}} \text{ gm}$$

$$\text{fibre volume} = \underline{\underline{0.594}} \text{ cubic cm}$$

$$\text{Fibre weight ratio} = \underline{\underline{67.24\%}}$$

$$\text{fibre/resin weight ratio} = \underline{\underline{2.053}}$$

$$\text{Resin weight ratio} = \underline{\underline{32.76\%}}$$

$$\text{Matrix volume ratio}(V_m) = \underline{\underline{48.28\%}}$$

$$\text{Fibre volume ratio } (V_f) = \underline{\underline{51.72\%}}$$

4. CONCLUSIONS

The average fibre volume ratio obtained was approximately 51.72%, indicating effective resin impregnation and compaction. This parameter is critical in estimating the mechanical properties of the composite, particularly its elastic modulus. The results confirm the VARI process as a reliable and low-cost method for producing high-quality fibre-reinforced composites suitable for structural and lightweight engineering applications. Future work will focus on mechanical characterization and potential integration with sensing techniques for advanced structural health monitoring.

5. REFERENCES

- [1] Meher, U., Shakya, P., & Sunny, M. R. (2022). Electro-mechanical Impedance response of a delaminated glass-fibre composite beam. In Aerospace and Associated Technology (pp. 437-441). Routledge.

* Communicating Author: Iqbal Ahmed, iqahmed42@gmail.com

Experimental Static and Fatigue Damage Assessment of Adhesively Bonded CFRP Joints Under Mode II Loading Using AE Technique

Bandaru Bangaraju^a, Sai Sidhardh^a, M Ramji^b

^a*SMART Lab, Department of Mechanical and Aerospace Engineering, Indian Institute of Technology Hyderabad, Telangana, India-502284*

^b*Engineering Optics Lab, Department of Mechanical and Aerospace Engineering, Indian Institute of Technology Hyderabad, Telangana, India-502284*

1. INTRODUCTION & OBJECTIVE

Adhesively bonded joints are increasingly used in aerospace, automotive, and renewable energy sectors due to their ability to reduce structural weight and enhance design flexibility compared to traditional mechanical fasteners. Unlike bolts and rivets, adhesive bonding allows for more uniform load transfer while preserving fiber continuity in carbon fiber reinforced polymer (CFRP) laminates. Nevertheless, such joints are susceptible to fatigue damage under cyclic loading, where micro-cracks may initiate within the adhesive or at the interface, eventually growing into critical failures that compromise structural integrity.

The fracture and fatigue behaviour of bonded joints under shear loading, particularly Mode II, is limited. De Moura et al. [1] and Fernández et al. [2] characterised fracture toughness and fatigue response of composite bonded joints under pure Mode II loading, emphasising the role of shear stresses in crack initiation and propagation. Paliwal and Ramji [3] investigated damage mechanics in CFRP joints under tensile loading, while Mahesh et al. [4] applied Acoustic Emission (AE) techniques to classify damage modes in composite laminates subjected to combined tension and shear. Mohapatra et al. [5] proposed an energy-based model to predict the mechanical behaviour of adhesively bonded CFRP laminates by employing the cohesive zone model (CZM).

Building upon these findings, this study explores the fatigue performance of CFRP adhesive joints under Mode II loading using the End-Notch Flexure (ENF) test configuration. Crack growth is estimated using the Compliance-Based Beam Method (CBBM), and AE monitoring is employed to capture the damage progression during fatigue loading. The study offers a comprehensive understanding of fatigue mechanisms and supports the development of more durable adhesive joint designs.

2. METHODS OF ANALYSIS

2.1 Specimen preparation:

The End-Notched Flexure (ENF) specimens are fabricated using unidirectional CFRP laminates, each ply having a nominal thickness of 0.2 mm. The adherends consist of $[0^\circ]_{10}$ unidirectional prepreg layers stacked to achieve a total thickness of 2 mm and are cured in an autoclave following the manufacturer's recommended temperature and pressure cycle. The bonding surfaces are joined using a two-part structural epoxy adhesive (Araldite® 2015), with the bond-line thickness maintained at approximately 0.2 mm using steel spacers. A specially designed fixture is employed during bonding to maintain uniform bond line thickness and introduce a pre-crack of 30 mm length across all test specimens.

2.2 Testing configuration:

The ENF setup imposed pure Mode II loading under three-point bending conditions as shown in Fig.1. Tests are performed on an MTS servo-hydraulic machine with displacement control for static and load control for fatigue at stress ratios $R=0.1$ and sinusoidal waveform, frequency 4 Hz. A maximum load level of 50% is chosen based on prior static Mode II fracture toughness (G_{IIC}) tests.

During loading, acoustic emission (AE) signals are recorded using a single wide-band sensor (100–1000 kHz, Physical Acoustic Corporation) mounted on the specimen with silicone grease as the coupling medium. Before each test, the threshold is incrementally adjusted to suppress noise, with 40 dB determined as optimal. An AE response is calibrated according to ASTM E976 using a pencil lead break on each specimen before testing.

2.3 Compliance-Based Beam Method (CBBM):

The CBBM is employed to determine the equivalent crack length and Mode II strain energy release rate from global load-displacement data, eliminating the need for direct crack-length measurement. This approach accounts for the influence of the fracture process zone (FPZ) ahead of the crack tip, ensuring more accurate estimation of fracture parameters. By incorporating beam theory corrections, CBBM effectively captures nonlinear deformation and shear effects in bonded joints [1]. Its application enhances the reliability of Mode II fracture characterisation, particularly for adhesive layers where visual crack tracking is challenging.

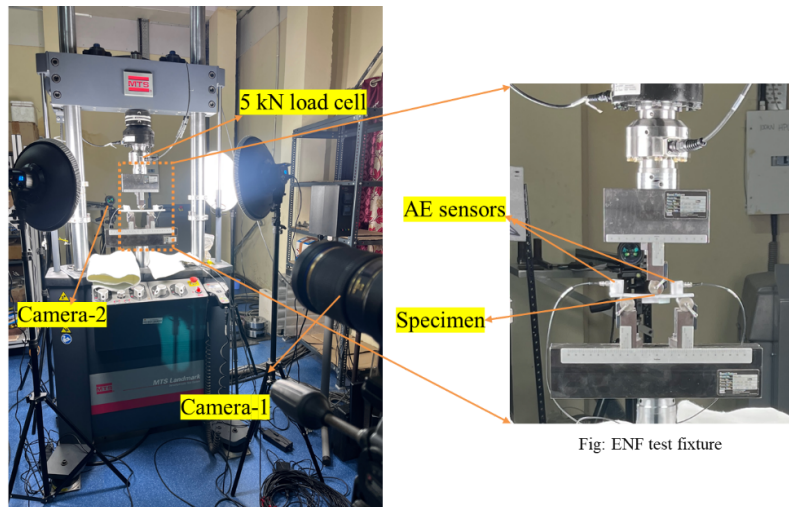


Fig. 1. Image of the experimental setup along with the AE sensors mounted over the ENF specimen

3. RESULTS

Fatigue testing under pure Mode II loading reveals a progressive increase in compliance and equivalent crack length with the number of cycles, as determined using the CBBM. The steady compliance evolution confirms continuous interfacial degradation and stable crack growth during most of the fatigue life, followed by rapid propagation near failure. Acoustic Emission (AE) monitoring identifies distinct peak frequency bands associated with matrix cracking and adhesive debonding, while cumulative energy evolution strongly correlates with crack growth estimated from CBBM. The Paris law relationship between the normalised strain energy release rate and crack growth rate exhibits a consistent power-law trend, validating the applicability of fracture mechanics-based fatigue models for bonded CFRP joints.

4. CONCLUSIONS

ENF testing under Mode II loading effectively characterises the fatigue response of adhesively bonded CFRP joints through the CBBM framework. The CBBM enables the estimation of the equivalent crack length and Mode II strain energy release rate without direct visual tracking. The acoustic emission response during fatigue loading of adhesively bonded CFRP joints reveals a clear damage progression. As cyclic loading continues, a pronounced increase in cumulative energy and higher-frequency activity signifies the transition to interfacial debonding and rapid crack propagation. This methodology provides a robust basis for fatigue life assessment. It enhances understanding of damage evolution in bonded composite joints, aiding us in the development of durable structural designs for aerospace and renewable energy applications.

5. REFERENCES

- 1) M.F.S.F. de Moura, R.D.S.G. Campilho, J.P.M. Gonçalves, "Pure mode II fracture characterization of composite bonded joints," *International Journal of Solids and Structures*, Volume 46, Issue 6, 2009, Pages 1589-1595, ISSN 0020-7683, doi:10.1016/j.ijsolstr.2008.12.001.
- 2) Maria V. Fernández, Marcelo F.S.F. de Moura, Lucas F.M. da Silva, António T. Marques, Characterization of composite bonded joints under pure mode II fatigue loading, *Composite Structures*, Volume 95, 2013, Pages 222-226, ISSN 0263-8223.
- 3) Isha Paliwal, M. Ramji, "A detailed study on the damage evolution and failure assessment of single-lap hybrid joints in CFRP laminates under tensile loading," *Composite Structures*, Volume 299, 2022, 116021, ISSN 0263-8223, doi:10.1016/j.compstruct.2022.116021.
- 4) P. Mahesh, Viswanath Chinthapenta, Gangadharan Raju, M. Ramji, "Classification of damage modes in scaled open-hole composite laminates under combined tension-shear loading using acoustic emission technique," *Engineering Fracture Mechanics*, Volume 308, 2024, 110390, ISSN 0013-7944, doi:10.1016/j.engfracmech.2024.110390.
- 5) Rashmiranjan Mohapatra, Hetram Sonwani, Sai Sidhardh, V. Narayananamurthy, M. Ramji, "An energy-based 2D model for predicting mechanical behavior of adhesively bonded CFRP laminates," *Engineering Failure Analysis*, Volume 163, Part A, 2024, 108589, ISSN 1350-6307.

* Communicating Author: Bandaru Bangaraju and me24resch01009@iith.ac.in.

FE Modeling of Single Foam-filled Reentrant Unit Cell to Evaluate Deformation Mechanics and Energy Absorption

Viswasarathi NM*, Bibhu Prasad Mahapatra, Prasun Jana

*Department of Aerospace Engineering, Indian Institute of Technology, Kharagpur, West Bengal
721302, India*

1. Introduction

Auxetic structures are a type of mechanical metamaterial that expand in the lateral direction when stretched and contract when compressed [1]. They are noted for their negative Poisson's ratio, which is in contrast to the expected behaviour of most materials. The concept of auxetic materials dates back to the demonstration by Lakes [2] in 1987. Re-entrant honeycomb structures have become the benchmark for recently engineered auxetic materials, due to enhanced energy absorption, collision resistance, and the ability to undergo large deformations. These structures are being applied more frequently across a wide range of fields including automotive, aerospace, sports, and marine industries. Despite these advantages, conventional re-entrant honeycomb auxetic structures are prone to excessive local buckling or collapse of cell walls under heavy and repetitive loads, restricting their use for certain practical applications. Foam infill enhances the overall energy absorption and improves the stiffness of the structure, without compromising much its lightweight nature [3]. The work presented in this paper aims to investigate the effects of foam infill on the mechanical properties of conventional re-entrant honeycomb structures using finite element methods.

2. Methods and Analysis

The reentrant unit cell is modeled using an elastic–perfectly plastic material formulation, while the PU foam is represented through a crushable foam material model. A tie constraint is imposed between the foam and lattice surfaces to prevent sliding or separation (refer Figure 1).

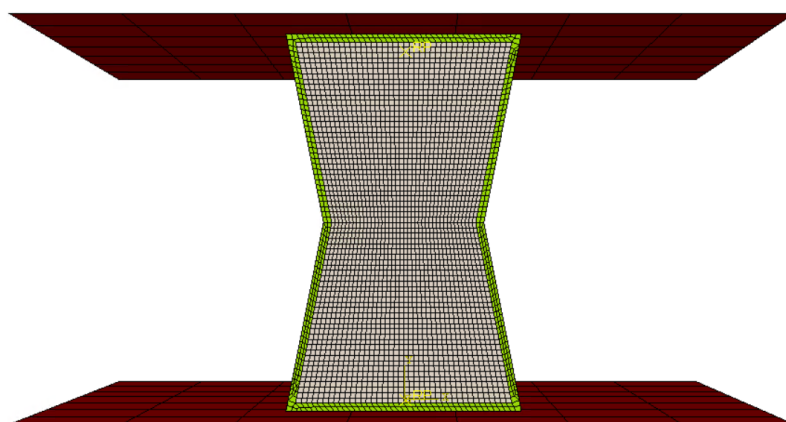


Figure 1 Schematic of the numerical model of foam-filled reentrant unit cell

3. Results and discussions

The numerical model is validated against experimental data available in the literature (Yu et al., 2020 [3]) ensuring accurate capture of deformation patterns and specific energy absorption (SEA) (refer Figure 2). A mesh convergence study is performed to determine an optimal element size for reliable predictions. Additionally, a parametric study examines the influence of key geometric design parameters, namely the internal angle (θ) and cell wall thickness (t), on the SEA of the single unit cell.

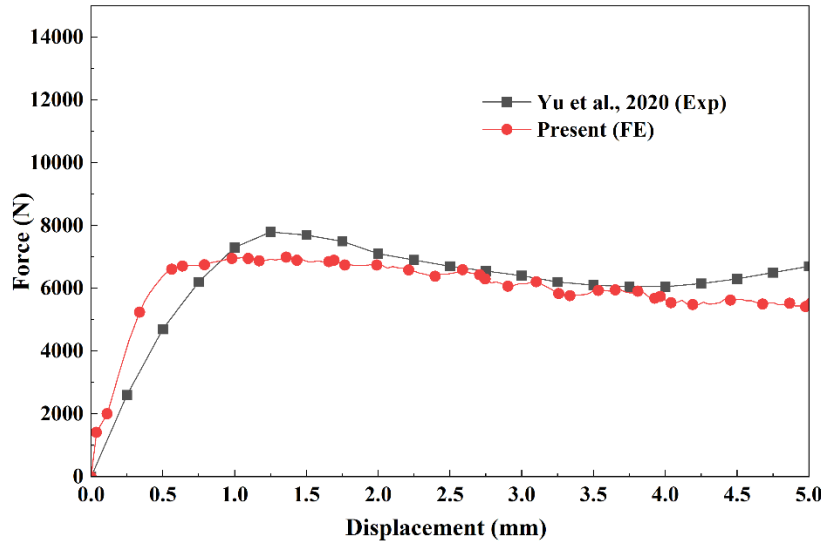


Figure 2 Comparison of force vs. displacement for foam-filled reentrant unit cell.

4. Conclusions

The study demonstrates that the quasi-static compression response and specific energy absorption of a foam-filled aluminum reentrant unit cell are strongly influenced by its geometric parameters, particularly the internal angle and cell wall thickness. The validated FE model provides an accurate framework for capturing local deformation mechanics and optimizing the energy absorption performance of individual meta-cells for impact mitigation applications.

References

1. L. J. Gibson and M. F. Ashby, *Cellular Solids: Structure and Properties*, 2nd edn, 1997, (Cambridge: Cambridge University Press)
2. Lakes, R. (1987). Foam structures with a negative Poisson's ratio. *Science*, 235(4792), 1038-1040.
3. Yu, R., Luo, W., Yuan, H., Liu, J., He, W., & Yu, Z. (2020). Experimental and numerical research on foam filled re-entrant cellular structure with negative Poisson's ratio. *Thin-Walled Structures*, 153, 106679.

Feature-Alignment Model Order Reduction (FAMOR) for Nonlinear Convective and Shock-Dominated Flows

Aritro Ghosh^a, Sanjay R.^b, Aniruddha Sinha^c

^aSenior Research Fellow, ^bFormer Master's student, ^cAssociate Professor,
Department of Aerospace Engineering, IIT Bombay, India

1. Introduction And Objective

Reduced-order modelling (ROM) is a cornerstone in medium-fidelity computational fluid dynamics (CFD) simulations, especially for parametric studies and design optimization. Classical linear ROMs, such as Proper Orthogonal Decomposition (POD) combined with Galerkin-based approaches, often struggle with flow discontinuities that are poorly represented in linear modal decompositions. Recent approaches – like Transported Snapshot Model Order Reduction (TSMOR) by Nair & Balajewicz (NB2019) and ROM with Implicit Feature Tracking (ROM-IFT) by Mirhoseini & Zahr [MZ2022] – addressed this challenge by embedding mesh deformation for feature alignment into the ROM framework making it nonlinear. Whereas TSMOR leveraged a global coarse parametrization of the mesh deformation (e.g. using Fourier basis), MZ2022 introduced a fine-grained parametrization affording much more fidelity of representation. The deformation maps were parameterized by arbitrary nodal degrees of freedom (DOFs) on the mesh, not restricted to truncated Fourier coefficients.

Both TSMOR and ROM-IFT attempt to minimize governing-equation residuals in the online (or inference or predictive) stage. ROM-IFT continues to do the same in the learning (or offline) stage also (hence the ‘implicit’), whereas TSMOR attempts to minimize the feature-tracking error directly. Since the latter is possibly a simpler task, we borrow this aspect from TSMOR. In this work, we introduce Feature-Alignment Model Order Reduction (FAMOR), which combines the philosophy of TSMOR (especially its offline stage) with the fine-grained parametrization of mesh deformation proposed in MZ2022.

This abstract demonstrates the preliminary implementation of the FAMOR methodology. Some results are presented for a 2D supersonic forward-facing step problem, a canonical shock-dominated flow exhibiting separation, reattachment, and multiple interacting features, introduced in NB2019.

2. FAMOR Algorithm

Offline phase: A central aspect of FAMOR (following MZ2022) is the set of maps $x = G(X)$ that take the corresponding training snapshots (on the x -coordinate system) to the reference domain (with the X -coordinate system). That is, each training snapshot is mapped to a reference configuration by optimizing the alignment of features (e.g., shocks), and thereby determining the corresponding map G . At its simplest, the map parameters are the nodal displacements that respect the domain boundaries. E.g., a node on a boundary in a 2D problem has a single DOF whereas an interior node has two. Following NB2019, FAMOR minimizes the misfit or misalignment, measured as the L_p -norm of the error between the mapped snapshot and the reference data. The constraint to be satisfied in this endeavour is that the deformed mesh should not have any ‘folded wrinkles’; i.e., all cell ‘volumes’ should remain positive.

Each training snapshot is used in turn, building up a library of reference snapshots, all having their salient features approximately aligned. Successive training snapshots attempt to match a linear combination of the reference snapshots already found till – the latter using POD. At the end of the offline phase, a separate POD is performed on all the maps obtained, which encapsulate the salient mesh deformation required for the flow problem. A schematic of the offline algorithm is given in fig. 1.

Online phase: For a new parameter query, the optimization problem is formulated over both mapping and solution POD coefficients. These are optimized to minimize the L_p -norm of the governing equations’ residual, as well as the non-trivial boundary conditions. The constraint on positivity of mesh cell volumes still applies.

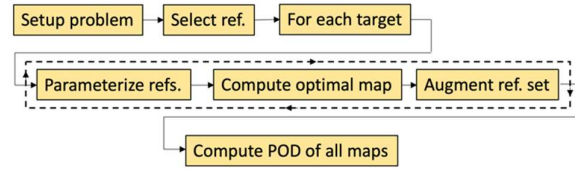


Figure 1: Schematic of offline phase of FAMOR

3. Preliminary Results

The methodology is applied to the steady, inviscid 2D forward-facing step-in-a-channel problem at supersonic inflow Mach numbers 3.3, 3.45, 3.6, 3.75 and 3.9. These five training solutions (for the flow variables $[\rho, \rho U, \rho V, \rho E]$) have been kindly provided by NB2019. Preliminarily, we have implemented the parameterization of the map G . To evaluate the working of this method, we have resorted to the Fourier-mode based map derived from TSMOR for this problem, specifically the mapping of the $M = 3.45$ snapshot to the $M = 3.6$, treated as reference. The density contours for these two undeformed cases are shown in fig. 2. The global coarse parameterization of the map in the TSMOR approach cannot respect the step due to the construction of the domain geometry as the boundary nodes do not have respective direction DOFs. So a mask is used for the step region while the entire rectangular domain is used for the solution. The flexible node-by-node parameterization of the map in FAMOR does allow this. However, since we are directly using the TSMOR-generated map (only as the initial guess), there is some inevitable ‘clipping’ of the mesh displacement that shows up as artefacts in the contour plots due to the fact that we map each boundary nodal DOF constituting the shelf and the step-region, restricting the movement of internal nodes only till the step corner to avoid highly skewed cells; this may easily be ameliorated in the subsequent offline optimization step. The figure shows how the former snapshot is deforming such that the flow features are getting more or less aligned with the reference.

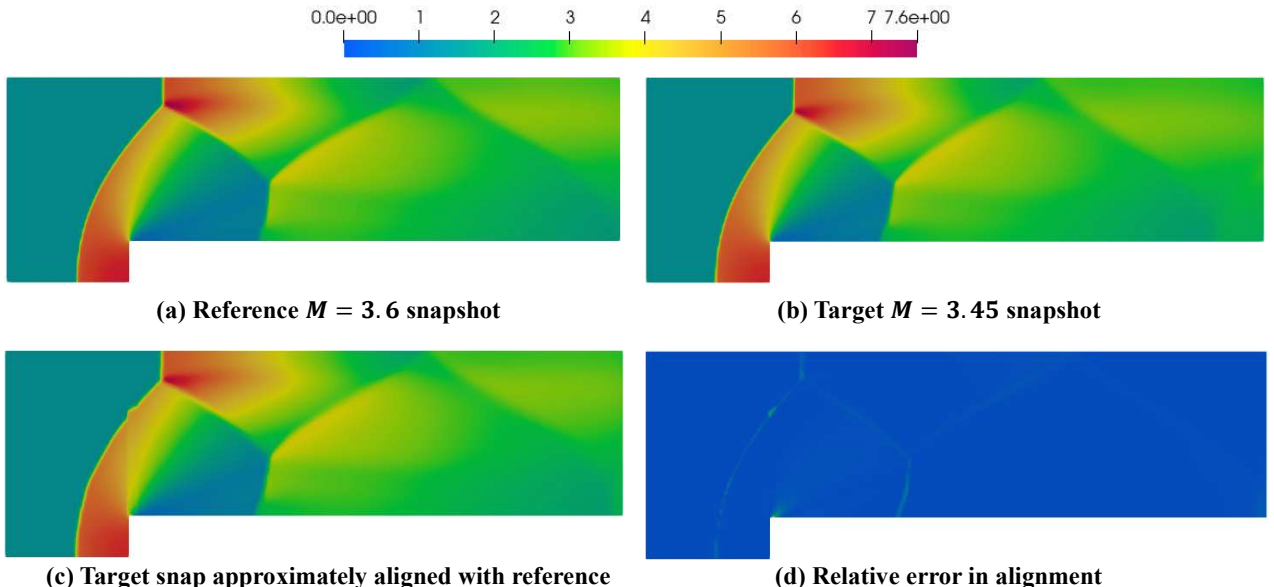


Figure 2: (a-b) Original density data of two snapshots. (c) Target snapshot approximately aligned with reference, using TSMOR deformation but implemented in FAROM framework. (d) Relative error in density.

4. Summary

We presented **FAMOR**, a new feature-aligned reduced order modelling framework that extends the concepts of TSMOR and ROM-IFT. The method differs from existing approaches by:

- Allowing arbitrary nodal DOFs for displacement fields, enabling local and fine-grained feature tracking.
 - Reducing offline costs by minimizing alignment errors, deferring physics enforcement to the online stage.

Preliminary results for the 2D forward-facing step demonstrate the plausibility of the proposed approach. The final paper will present results from the complete implementation of the offline and online stages of FAMOR. Further, we will present a cost-benefit comparison against TSMOR of NB2019 and ROM-IFT of MZ2022. It is expected that the proposed FAMOR will be costlier but more accurate than TSMOR. At the same time, it is hypothesized that FAMOR will be less expensive than ROM-IFT, but no less accurate or versatile.

5. References

- [MZ2022] M. A. Mirhoseini and M. J. Zahr, “Model reduction of convection-dominated partial differential equations via optimization-based implicit feature tracking”, *J. Comp. Phys.*, 2022 **473**:111739. DOI: [10.1016/j.jcp.2022.111739](https://doi.org/10.1016/j.jcp.2022.111739).

[NB2019] N. J. Nair and M. Balajewicz, “Transported snapshot model order reduction approach for parametric, steady-state fluid flows containing parameter-dependent shocks”, *Int. J. Num. Methods Engg.*, 2019; **117**:1234-1262. DOI: [10.1002/nme.5998](https://doi.org/10.1002/nme.5998).

Finite Element Simulation of Magnetocaloric Effect in Gadolinium

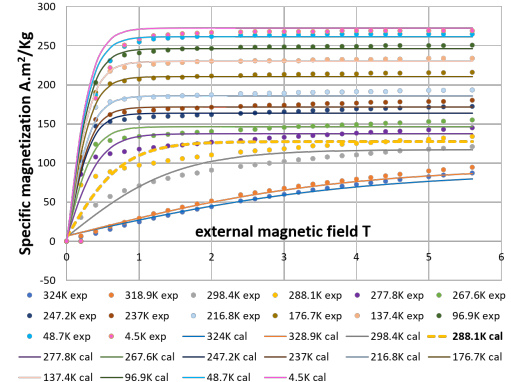
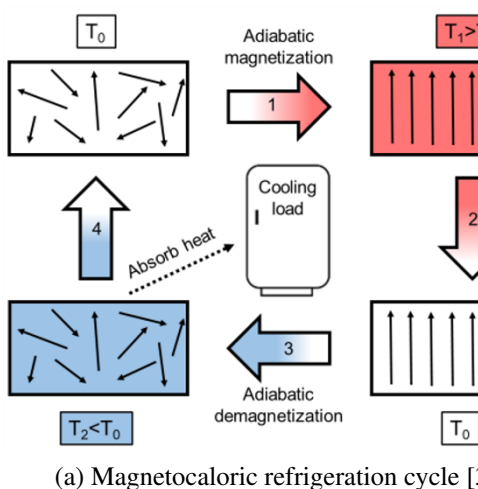
Busi Swathi Priya^a and Krishnendu Halder^{b,*}

^a Student, Aerospace, Indian Institute of Technology, Bombay, India

^b Professor, Aerospace, Indian Institute of Technology, Bombay, India

1. INTRODUCTION & OBJECTIVE

Magnetocaloric effect is a material's ability to change its temperature due to a change in the magnetic field. These materials are potential green energy sources that could serve as an alternative to conventional refrigeration. In the magnetocaloric refrigeration cycle shown in Figure 1a, a material at its Curie temperature (T_0) is magnetized, causing its temperature to rise, and a working fluid transfers heat to the surroundings. Upon demagnetization, the material cools below T_0 , allowing the working fluid to absorb heat, thereby completing the cycle.



(b) Analytical(Cal) and experimental(exp) graph of specific magnetization(m) vs $\mu_0 H$ of gadolinium; 288.1K analytical curve is plot of interest [1]

Figure 1

Gadolinium (Gd) is widely regarded as the benchmark material for magnetocaloric refrigeration with an operating temperature range of $293 \pm 10K$. Using the laws of thermodynamics and Maxwell relations, the change in entropy and temperature caused by the external magnetic field [2] is

$$\Delta S(T, H) = \int_0^H \left[-\mu_0 \frac{\partial M}{\partial T} \right]_H dH \left[\frac{J}{kg K} \right], \quad \Delta T_{ad} = \int_0^H \frac{\mu_0 T}{C_p} \left[\frac{\partial M}{\partial T} \right]_H dH [K] \quad (1)$$

The objective is to simulate the temperature (T) change in the gadolinium for applied magnetic fields and material temperatures.

2. METHODS OF ANALYSIS

Magnetization (M) of gadolinium under varying magnetic fields was modeled using a nonlinear constitutive response calibrated from experimental data in Figure 1b and implemented in COMSOL Multiphysics to capture magnetic saturation behavior, assuming a non-dissipative system.

$$M(H, T) = \frac{C_1(T) - C_2(T)}{1 + e^{\frac{\mu_0 H}{C_3(T)}}} + C_2(T) \quad (2)$$

The material domain inside a vacuum, as shown in Figure 2a, which is subjected to boundary conditions that impose a uniform magnetic flux density (B) along the x-axis, is formulated through the magnetic vector potential (\mathbf{A}). Within the Gd region, a magnetization model based on Ampère's law is incorporated.

$$\nabla \times \mathbf{A} = \mathbf{B}, \quad \nabla \times \mathbf{H} = 0, \quad \mathbf{B} = \mu_0(\mathbf{H} + \mathbf{M}) \quad (3)$$

The finite element framework couples the magnetic and thermal fields by solving the governing equations 3, thereby enabling a detailed analysis of the temperature-dependent magnetic field distribution and the associated magnetization behavior as shown in Figure 2b.

3. RESULTS AND/OR HIGHLIGHTS OF IMPORTANT POINTS

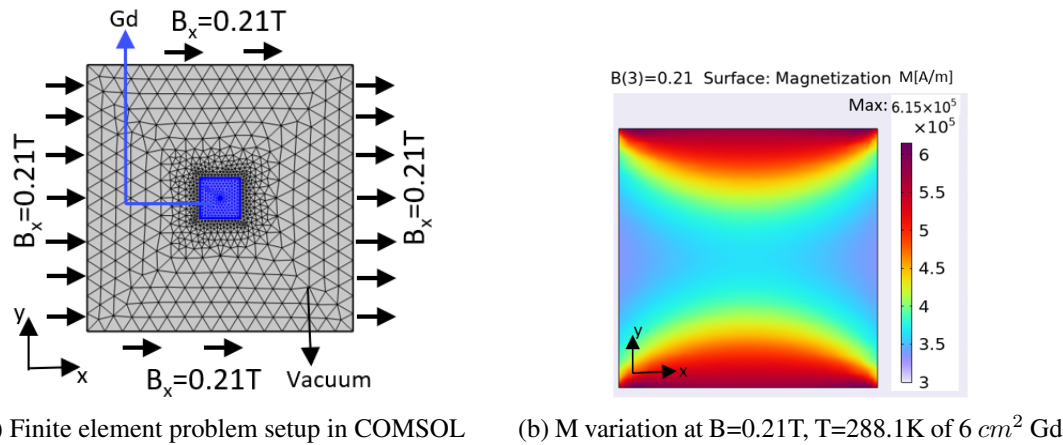


Figure 2

Magnetization in Gd in Figure 2b has maximum along the x-axis and minimum along the y axis due to aligning and opposing magnetic fields from Gd respectively. The magnetization variation causes varying temperature over the surface due to MCE. This effect is predicted to be maximum at curie temperature

4. CONCLUSIONS

This study explains gadolinium's magnetic behavior incorporated in the finite element analysis at constant temperature. The developed framework will be extended to compute ΔT_{ad} through coupled heat transfer physics. Future work will focus on assessing the coefficient of performance (COP) and optimizing the system for an efficient magnetocaloric refrigeration cycle.

REFERENCES

- [1] S. Yu. Dan'kov and A. M. Tishin, "Magnetic phase transitions and the magnetothermal properties of gadolinium," *Ames Laboratory and Department of Materials Science and Engineering*, Iowa State University, Ames, IA, USA, 1998.
- [2] R. Bjørk, "Designing a magnet for magnetic refrigeration," Ph.D. dissertation, Technical University of Denmark, 2020.
- [3] "Research topics in functional materials," *Technische Universität Darmstadt*, [Online]. Available: https://www.mawi.tu-darmstadt.de/fm/research_fm/research_topics_fm/neu_overview.en.jsp. [Accessed: Sep. 25, 2025].

* Communicating Author: Krishnendu Halder, krishnendu@aero.iitb.ac.in

Flexural and ILSS Performance of GFRP Composites under Extreme Temperature Conditions

Supral Tudu^{a*} and Velmurugan Ramachandran^b

^aResearch scholar, Department of Aerospace Engineering, IIT Madras, Chennai, India

^bInstitute Chair Professor, Department of Aerospace Engineering, IIT Madras, Chennai, India

1. INTRODUCTION AND OBJECTIVE

Glass Fiber Reinforced Polymer (GFRP) composites are widely used in aerospace, automotive, and marine applications due to their high strength-to-weight ratio, high stiffness, corrosion resistance, and design-tailorable properties [1]. These properties make GFRP an attractive alternative to traditional metals, particularly in weight-sensitive structures such as satellites, spacecraft, and supersonic aircraft. They can withstand harsh conditions without losing strength, which makes them very useful in aerospace engineering. GFRP composites are expected to operate efficiently within a temperature range of +50 °C to -75 °C, where both thermal stability and mechanical performance are crucial [2].

The primary objective of this study is to investigate the flexural and interlaminar shear behavior of Glass Fiber Reinforced Polymer (GFRP) composites under varying thermal environments ranging from -75 °C to 100 °C. The study aims to evaluate the effect of temperature on the flexural and interlaminar shear strength, as well as the failure mechanisms, of GFRP. Additionally, the study focuses on analysing the viscoelastic behaviour of the composites to understand their time- and temperature-dependent deformation. Fractography analysis of failed specimens was done to identify failure modes, crack propagation patterns, and microstructural damage, providing insights for improving material design and reliability in extreme environments.

2. METHODS OF ANALYSIS

The experimental investigation involved analyzing the flexural and interlaminar shear behavior of GFRP composites under varying thermal conditions. Three-point bending and Short Beam Shear (SBS) tests were conducted using a Universal Testing Machine (UTM) equipped with an environmental chamber to maintain controlled temperatures of -75 °C, -50 °C, 30 °C, 80 °C, and 100 °C. Flexural testing was conducted in accordance with ASTM D7264, while interlaminar shear strength (ILSS) was evaluated according to ASTM D2344 standards. Dynamic Mechanical Analysis (DMA), as specified in ASTM D7028, was conducted to investigate the storage modulus, loss modulus, and damping characteristics, providing insight into the viscoelastic behaviour. The specimens were in situ-conditioned at each temperature before testing to ensure thermal equilibrium. A fractography test was conducted using Scanning Electron Microscopy to identify the failure mechanisms, including matrix cracking, delamination, and fiber pull-out.

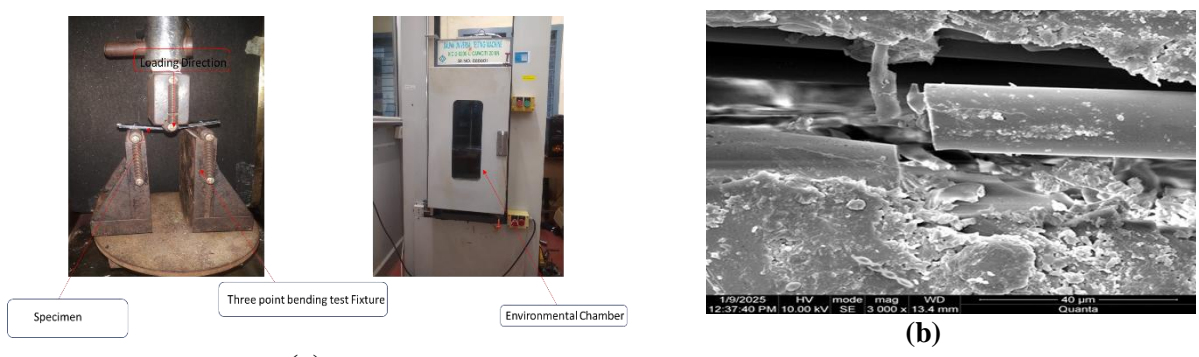


Fig.1. (a) Experimental setup, (b) SEM

3. RESULTS AND DISCUSSIONS

The flexural behaviour of GFRP is shown in Fig. 2, with significant temperature dependence. At -50°C , the composite exhibited the highest strength and strain-to-failure due to enhanced fibre–matrix bonding and reduced molecular chain mobility. At elevated temperatures (75°C – 100°C), a reduction in flexural strength was observed due to matrix softening and weakening of interfacial adhesion. Interlaminar shear strength (ILSS) increased by 44% at -50°C , indicating strong fibre–matrix adhesion, while it decreased by 86% at 80°C due to resin degradation and bond failure. The graph in Fig. 2 shows the thermal sensitivity of flexural and ILSS properties of GFRP. Fig. 3 illustrates the viscoelastic properties of GFRP at various temperatures and frequencies. Fractography studies of failure specimens were conducted using SEM to examine fibre breakage and matrix cracking, as shown in Fig.1 (b).

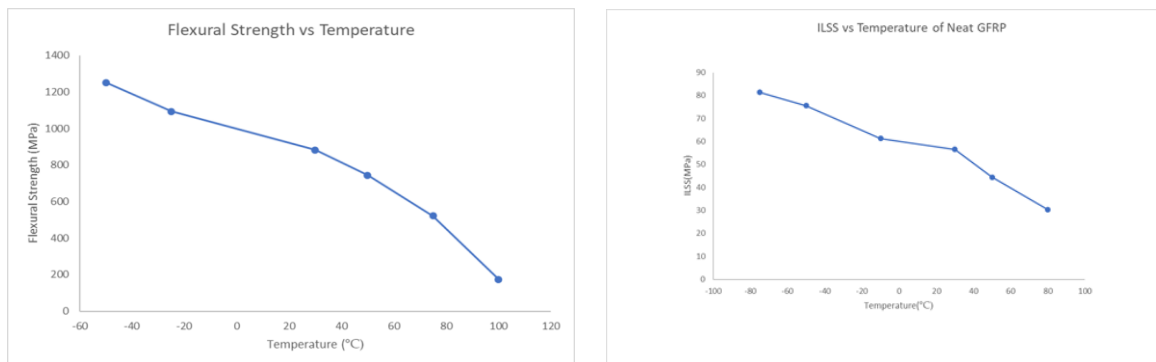


Fig.2 Flexural strength and ILSS vs Temperature

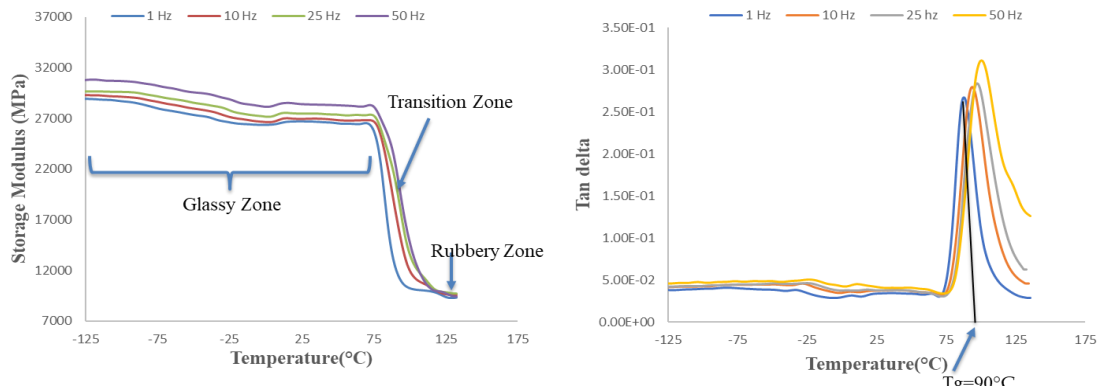


Fig.3 Dynamic mechanical analysis plot

4. CONCLUSIONS

GFRP composites exhibit higher mechanical performance at low temperatures due to enhanced fibre–matrix bonding. However, elevated temperatures decrease strength because of matrix softening and interfacial degradation. Comprehensive testing, including mechanical, DMA, and fractographic analysis, confirms the importance of evaluating GFRP across a wide temperature range for reliable aerospace and structural applications.

5. REFERENCES

- [1] Dasari, Srinivasu, Sushant Saurabh, Savita Gupta, Bankim Chandra Ray, and Rajesh Kumar Prusty. "Experimental amelioration of flexural behavior under cryogenic conditioning through inter-ply fiber hybridization in FRP composites." Materials Today: Proceedings 27 (2020): 1618-1624.
- [2] Huang, W. J., Y. T. Li, Y. M. Zhang, Z. M. Xiao, and W. G. Li. "Experimental and numerical investigations of interlaminar shear behaviors of CFRP composites at cryogenic and high temperatures." Composite Structures 352 (2025): 118681

Flow-Induced Vibrations of a Circular Cylinder and an Upstream D-Cylinder of various Elliptical Ratios

Sachin S B^{1*} and Atul Sharma²

¹sachinsb932@gmail.com,²atulsharma.iitb@gmail.com

^{1,2}Department of Mechanical Engineering, Indian Institute of Technology Bombay, Powai 400076, India

I. INTRODUCTION & OBJECTIVE

Due to their practical relevance in offshore, civil, and energy systems, the dynamics of flow-induced vibrations (FIV) of bluff bodies remain a central topic in fluid–structure interaction research. While canonical studies have extensively examined the behaviour of isolated circular and D-section cylinders, the coupled response of these bodies in tandem configurations is less understood. The present work highlights that coupling effects in tandem arrangements introduce additional complexity to both the wake dynamics and structural response for both cylinders. In particular, when a D-section cylinder is placed upstream of a circular cylinder, the wake interference gives rise to complex vibration characteristics susceptible to the body geometry. The elliptical ratio of the upstream D-section governs the wake topology, modifies vortex shedding patterns, and consequently alters the amplitude and frequency response of the downstream circular cylinder. Elucidating its influence on fluid–structure coupling provides new insight into the mechanisms governing multi-body VIV involving closely spaced structures exposed to cross-flow.

The paper investigates numerically the Flow-Induced coupled Vibration of both elastically mounted D-cylinders with different elliptical ratios (ER) and circular cylinders in tandem arrangement. The upstream cylinder has a varying ER values of 0.25, 0.5, 1.0 & 2.0, the two cylinders are placed in tandem arrangement with varying gap ratios of $G^* = 0.1, 0.5 & 2.0$. The circular cylinder is moved from the wake interference region to the proximity-wake interference region by decreasing the gap ratio.

II. METHODS OF ANALYSIS

Our computational domain consists of both an elastically mounted upstream D-section cylinder with a downstream circular cylinder in tandem arrangement with equal mass ratio ($m^* = 2.0$) with damping ratio $\zeta = 0.005$ and diameter (D) in a free stream flow, as shown in Fig. 1(a). The domain's dimensions, the outer limits' location relative to the center of the upstream cylinder, and the boundary conditions are presented in Fig 1(a). The reduced velocity is varied within the range ($U^* \in [3 - 12]$), while the Reynolds number ($Re = 100$) remains constant. The computational method employs an in-house LS-IIM code [3], LS-IIM involves a block-iterative hybrid Lagrangian–Eulerian method coupled with the finite volume method [2],[1] on a non-uniform Cartesian grid. The Navier models the fluid flow–Stokes equations, cylinder motion by a linear oscillator, and the fluid-structure interface dynamics are governed by specific non-dimensional boundary conditions.

III. RESULTS AND DISCUSSION

The simulations yield the following results, Fig. 1(b) – (e): (i) For upstream cylinders with $ER = 0.25$ and 0.5 , similar behavior is observed at $G^* = 0.1$ and 0.5 , where the vibration response increases peak amplitude and an expanded lock-in region. In contrast, for $G^* = 2.0$, the response resembles that of the isolated case. (ii) For $ER = 1.0$ and 2.0 , the upstream cylinders behave similarly at $G^* = 0.5$ and 2.0 , showing a galloping response similar to the isolated case. However, at $G^* = 0.1$, the cylinders with $ER = 1.0$ and 2.0 experience galloping suppression, though after a critical U^* , the cylinder with $ER = 2.0$ exhibits an increase in amplitude. (iii) For the downstream circular cylinder, the vibration response varies with the ER of the upstream cylinder for each G^* value. At $G^* = 2.0$, the circular cylinder undergoes wake-induced vibration for $ER = 0.25, 0.5$, and 1.0 , whereas $ER = 2.0$ shows a gradually increasing trend. (iv) At $G^* = 0.5$, the circular cylinder exhibits a monotonically increasing trend similar to galloping for $ER = 1.0$ and 2.0 , while $ER = 0.25$ and 0.5 show wake-induced vibration. At $G^* = 0.1$, for $ER = 0.25$ and 0.5 , the vibration response of the circular cylinder is similar to that of the upstream cylinder, while $ER = 1.0$ and 2.0 exhibits a modified-VIV response.

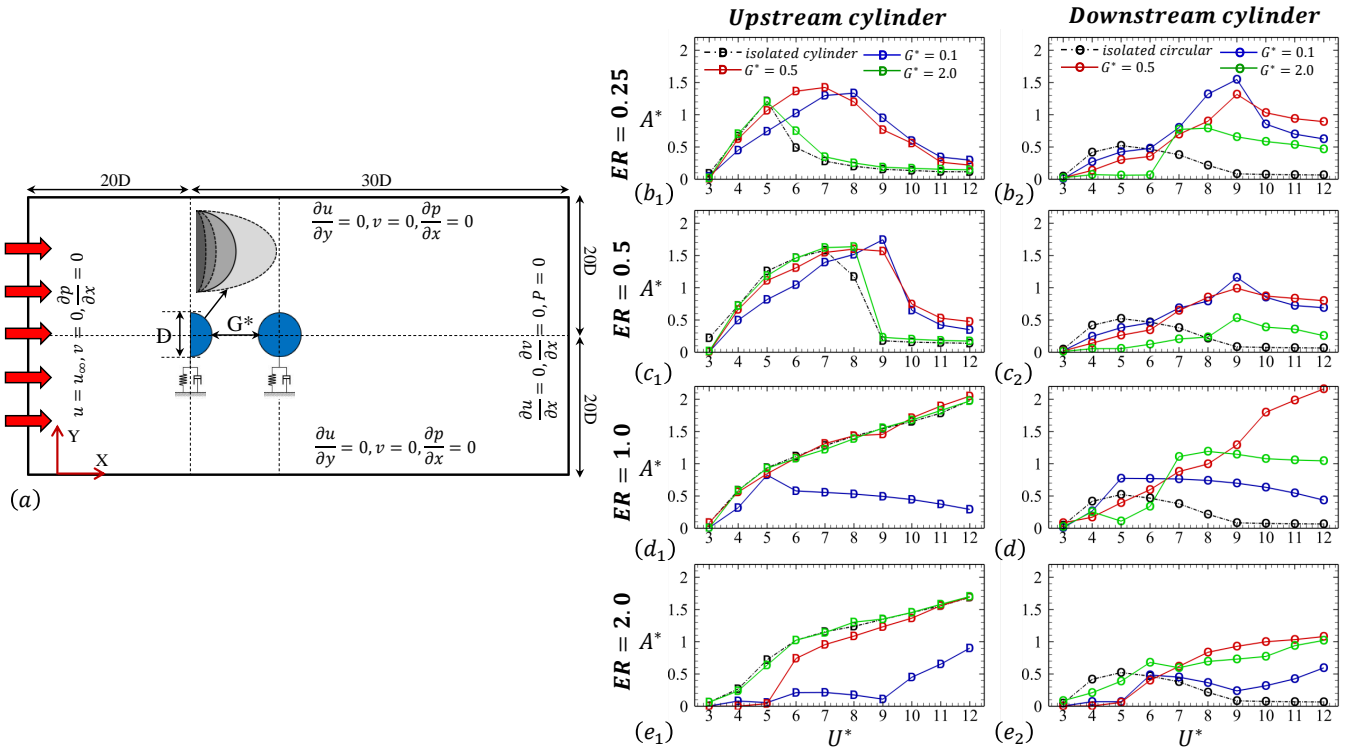


Figure 1: (a) Computational setup for free-stream flow across an elastically mounted D-(with different ER) and circular cylinder in tandem arrangement. Effect of non-dimensional gap G^* and reduced velocity U^* . Amplitude response A^* of (1) Upstream and (2) Downstream cylinders compared with their respective isolated counterpart for $ER = 0.25, 0.5, 1.0$ & 2.0 respectively for various gap ratios $G^* = 0.1, 0.5$ & 2.0

IV. CONCLUSIONS

The present study explores the impact of elliptical ratios (ER) of upstream cylinder and different gap ratios (G^*) on the vibration responses of elastically mounted tandem cylinders. The elliptical ratio (ER) is critical in modifying the vibrational response. Smaller ER values resulted in higher vibration amplitudes and more pronounced peaks at specific reduced velocities, while larger ER values led to more stable and consistent vibrational behavior. At the smallest gap ($G^* = 0.1$), the proximity effect led to substantial wake interference, amplifying the vibration response of the downstream cylinder. The interaction was most pronounced when the gap was minimal, with enhanced vibrations and erratic behavior observed in the amplitude response. As the gap ratio increased to $G^* = 0.5$, the wake interference diminished, but the downstream cylinder still experienced notable wake effects, resulting in elevated vibrational amplitudes compared to isolated cylinders. For a larger gap ($G^* = 2.0$), the interaction between the upstream and downstream cylinders was significantly reduced, allowing both cylinders to behave more independently. The vibrational characteristics of the downstream cylinder approached those of the isolated case, with minimal wake interference from the upstream body. This highlights the importance of geometric and flow parameters in determining the vibrational dynamics of tandem-mounted bodies.

REFERENCES

- [1] Atul Sharma, *Introduction to computational fluid dynamics: development, application and analysis*, John Wiley & Sons, 2016.
- [2] Namshad Thekkethil and Atul Sharma, *Hybrid lagrangian-eulerian method-based cfsd development, application, and analysis, Immersed Boundary Method: Development and Applications* (2020), 361–394.
- [3] Namshad Thekkethil, Atul Sharma, and Amit Agrawal, *Self-propulsion of fishes-like undulating hydrofoil: A unified kinematics based unsteady hydrodynamics study*, Journal of Fluids and Structures **93** (2020), 102875.

Free Vibration Analysis of Cranked Sandwich Plates with CSCL Face sheets and Honeycomb Core Comparison

Gajavada Sanjeevkumar^{a*}, Pritam Mondal^b, Jayant Prakash Varun^c & Prashanta Kr Mahato^d

^aResearch Scholar, Department of Mechanical Engineering, IIT (ISM) Dhanbad, Jharkhand, India

^bResearch Scholar, Department of Mechanical Engineering, IIT (ISM) Dhanbad, Jharkhand, India

^cResearch Associate, Department of Mechanical Engineering, IIT (ISM) Dhanbad, Jharkhand, India

^dProfessor, Department of Mechanical Engineering, IIT (ISM) Dhanbad, Jharkhand, India

1. INTRODUCTION

Sandwich composite plates with stiff face sheets and lightweight cores offer high stiffness-to-weight efficiency, making them ideal for aerospace and high-performance structures. Cranked geometries as shown in Fig. 1, introduce stiffness redistribution and modal coupling, significantly affecting vibration behaviour. Although honeycomb cores and cranked plates have been studied individually, their combination with Constant Stiffness Composite Laminate (CSCL) face sheets remains largely unexplored.

Building on previous work on cantilever sandwich plates with variable stiffness face sheets and re-entrant honeycomb cores[1], [2], this study extends the analysis to cranked sandwich configurations with CSCL face sheets and hexagonal or re-entrant (auxetic) cores. The focus is to assess the influence of core topology on stiffness and dynamic characteristics, with numerical results presented in the full paper.

A MATLAB-based finite element framework using First-Order Shear Deformation Theory (FSDT) is employed. Initial findings show cranked geometry alters modal frequencies by 10–15%, sandwich construction increases frequencies by 5–32% while reducing weight by ~40%, and core topology has minimal effect (<2%) on vibration performance[1], [2].

2. OBJECTIVES:

The primary objective of this study is to determine the natural frequencies and mode shapes of cranked sandwich plates featuring constant stiffness composite laminate (CSCL) face sheets. A comparative analysis is conducted to evaluate the dynamic behaviour of hexagonal and re-entrant (auxetic) honeycomb cores under identical geometric and mass conditions. Additionally, the influence of cranked geometry on modal characteristics is assessed to understand its impact on structural dynamics.

3. METHODS OF ANALYSIS

To achieve these goals, the cranked plate planform is modelled using a transformation-based meshing technique that ensures accurate nodal generation. The finite element model is developed in MATLAB using First-Order Shear Deformation Theory (FSDT) and incorporates cantilever boundary conditions. Both hexagonal and re-entrant core configurations are designed with identical thickness and density ratios to isolate the effect of core topology. The generalized eigenvalue problem ($K - \omega^2 M$) $u = 0$ is solved to extract the first few natural frequencies and corresponding mode shapes.[3], [4]

4. RESULTS & HIGHLIGHTS OF IMPORTANT POINTS

The natural frequencies and corresponding mode shapes of cranked sandwich plates featuring Constant Stiffness Composite Laminate (CSCL) face sheets are calculated by finite element analysis. The inclusion of crank geometry altered the stiffness distribution along the plate span, leading to variations in modal frequency patterns and introducing coupling effects relative to flat plate

configurations. The sandwich construction exhibited distinct dynamic characteristics compared with single-layer laminates. Comparisons between hexagonal and re-entrant honeycomb cores, designed with identical geometric and mass parameters, indicated minimal variation in modal responses and similar overall vibration trends. The mode shapes revealed localized deformation near the crank junction, with geometric features influencing the orientation and placement of nodal lines. Additionally, variations in laminate layer count and fibre orientation are expected to modify the stiffness matrix, thereby affecting both the natural frequency spectrum and mode shape characteristics.

5. CONCLUSIONS

This study presented the modelling and vibration analysis of cranked sandwich plates with CSCL face sheets and honeycomb cores using a MATLAB-based finite element framework developed under First-Order Shear Deformation Theory (FSDT). Core configurations were designed to maintain uniform geometric and mass properties, enabling an isolated comparison of topology effects. The analysis facilitated the extraction of modal parameters and the assessment of geometric influences on vibration behaviour. Although the present work focused on constant stiffness laminates, future studies incorporating variations in layer count and fibre orientation may further influence the modal response and support tailored dynamic performance in cranked sandwich structures.

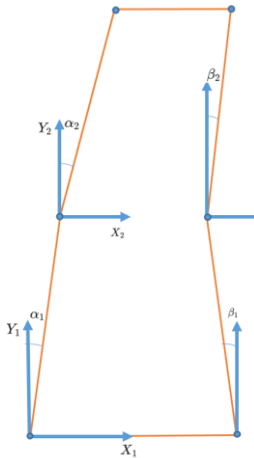


Fig 1: Cranked laminated wing like plate configuration

6. REFERENCES:

- [1] P. Mondal, J. P. Varun, and P. Kr Mahato, “Subsonic flutter behavior of cantilever sandwich plates with variable stiffness composite face sheets and re-entrant honeycomb cores,” *Mechanics Based Design of Structures and Machines*, pp. 1–24, 2025. doi:10.1080/15397734.2025.2560564
- [2] P. Mondal and P. K. Mahato, “Closed-loop subsonic flutter control of smart symmetric variable stiffness composite laminates in tapered-swept configurations,” *European Journal of Mechanics-A/Solids*, p. 105875, 2025. doi:10.1016/j.euromechsol.2025.105875
- [3] X. Peng, Y. Zhong, J. Shi, and Z. Shi, “Free flexural vibration analysis of composite sandwich plate with reentrant honeycomb cores using homogenized plate model,” *Journal of Sound and Vibration*, Apr. 2022, doi: 10.1016/j.jsv.2022.116955.
- [4] M. Belarbi, A. Tati, H. Ounis, and A. Khechai, “ON THE FREE VIBRATION ANALYSIS OF LAMINATED COMPOSITE AND SANDWICH PLATES: A LAYERWISE FINITE ELEMENT FORMULATION,” *Latin American Journal of Solids and Structures*, vol. 14, pp. 2265–2290, Sept. 2017, doi: 10.1590/1679-78253222.

*Communicating Author: Gajavada Sanjeevkumar, sanjeevkumargajavada@gmail.com

Free Vibration Analysis Of Multiple Central Cracked Rectangular Plate with Two Degrees of Freedom (2- Dof)

^aBabasaheb Kisan Varpe and ^bDr. Achchhe Lal

^aResearch Scholar, Department of Mechanical Engineering, S.V. National Institute of Technology, Surat. India.

^bAssociate Professor, Department of Mechanical Engineering, S.V. National Institute of Technology, Surat. India.

1. Introduction & Objective

The dynamic integrity of rectangular plates, common in aerospace, marine and mechanical systems is critically impacted by presence of cracks. Analysing their free vibration response is essential in structural health monitoring and damage- tolerant design. Traditional methods are struggles with modelling multiple interacting cracks due meshing complexities. This study aims to develop a robust numerical framework using XFEM to investigate the free vibration of rectangular plates with multiple cracks using two degrees of Freedom.

2. Methods of Analysis

The analysis is done using XFEM. The XFEM is employed to model the cracks by enriching standard finite element approximation with Heavyside crack tip function This allows the cracks to be represented independently of mesh. The key features of this model are use of 2 DOF per node, which is sufficient to capture the essential bending behaviour of the plates. The governing eigen value equation is derived and solved to obtain natural frequencies. The comprehensive parametric study is conducted for plates under clamped and simply supported boundary conditions, varying the crack configurations.

3. Results

The results evaluated a significant reduction in natural frequencies of plates with introduction of multiple cracks. The interaction between closely spaced cracks shows pronounced loss of the stiffness than the isolated crack of same length. The mode shape exhibits clear localization phenomena around the crack tips and 2DOF-XFEM model successfully capture these complex deformation patterns without numerical instability.

4. Conclusion

The developed XFEM framework with 2 DOF model proves to be an efficient and powerful tool for the free vibration analysis of cracked plates. It effectively overcomes meshing constraint of conventional FEM. This study concludes that characteristics of multiple cracks are dominating factors in dictating the dynamic response, leading to substantial change in natural frequencies. These findings provide critical insights in predicting dynamic behaviour of cracked structures.

Table. 1. Natural frequencies

| Crack Length | Boundary Condition | Thickness Ratio, A/H | | |
|-------------------|-----------------------|----------------------|--------|--------|
| | | 1 | 1.5 | 2 |
| Natural Frequency | | | | |
| 0.1 | CCCC | 2.4757 | 2.0845 | 1.8644 |
| 0.2 | CCCC | 2.6573 | 2.1576 | 1.8909 |
| 0.3 | CCCC | 2.7698 | 2.1593 | 1.8721 |
| 0.4 | CCCC | 2.8037 | 2.1125 | 1.77 |
| 0.5 | CCCC | 0.0796 | 1.9807 | 1.3745 |
| 0.6 | CCCC | 2.5991 | 1.6744 | 1.221 |

Figure 1. Rectangular plate with multiple central crack propagation in longitudinal direction

Figure 1. shows the length (l) and breadth (b) of the plate are shown on x and y axes respectively, with central crack, $a = 0.4$, and thickness ratio of 1.5. The crack face, crack tip, and crack angle are clearly shown in the figure.

We investigate the free vibration behaviour of a cracked isotropic homogenous plate. A mesh of 10X10 elements with a nine-node iso-parametric element is used for the analysis of a Rectangular isotropic plate with dimensions $15x15x0.1cm^3$.

The first five natural frequencies of the rectangular plate with a central crack and full Clamped boundary conditions (CCCC) are compared to previous works.

The results demonstrate excellent agreement with previous works. Additionally, it is noticed that the presence of crack has a direct effect on the dynamic properties of the plate. As shown in Table. 1, the natural frequencies decrease with an increase in the crack length.

Clamped edge (C): On all edges: $u=0, v=0, w=0, \theta_x = \theta_y = 0$

References

Samah Maoudja, Rachid Tiberkaka, Mohamed Essedik Lazara, Madjid Ezzraimia, Mourad Bacheneb, and Saïd Rechakc, “Free vibration analysis of cracked composite plates reinforced with CNTs using extended finite element method (XFEM)”, *Mechanics of Advanced Materials and Structures* 2024, VOL. 31, NO. 27, 9710–9721 <https://doi.org/10.1080/15376494.2023.2279703>

*Communicating Author: Dr. Achchhe Lal, achchhelal@med.svnit.ac.in

Guidance Law for Surveillance by UAVs Using Curve Paths

Parth Madure^a, Gururaj Khurd^a,
Sayantan Pal^b, and Sikha Hota^c

^aStudent, Dept. of Aerospace Engg., IIT Kharagpur, India

^bResearch Scholar, Dept. of Aerospace Engg., IIT Kharagpur, India

^cFaculty, Dept. of Aerospace Engg., IIT Kharagpur, India

Department of Aerospace Engineering,
Indian Institute of Technology Kharagpur, West Bengal, India – 721302

1 INTRODUCTION & OBJECTIVE

Unmanned Aerial Vehicles (UAVs) are increasingly deployed in surveillance and monitoring due to their ability to cover large areas, access hazardous regions, and reduce risks to human operators [1, 2]. Fixed-wing UAVs, however, face turning constraints that limit the effectiveness of conventional circular or elliptical surveillance paths.

Generalized curve paths, such as Lame' curves (super ellipses), provide smooth closed trajectories that approximate rectangular or arbitrary boundaries while respecting UAV kinematics [3]. The objective of this work is to design a stable, fast-converging guidance law for generic curve path tracking and to integrate a fluid-inspired obstacle avoidance strategy, enabling safe and efficient UAV surveillance in cluttered environments.

2 METHODS OF ANALYSIS

A vector field guidance law based on a shaping function is developed, where the desired heading, ψ_d , is defined as the sum of the tangent heading, ψ_t , and a shaping term, ψ_o . Unlike earlier formulations, the exponential shaping function ensures smooth convergence with vanishing derivatives near the path, preventing oscillations.

Stability analysis is performed using a Lyapunov function, proving that the tracking error ($\beta - 1$) converges asymptotically to zero for arbitrary initial conditions.

For obstacle avoidance, a potential fluid-inspired vector field is superimposed on the nominal curve path guidance. A continuous weighting function blends the curve-heading with a tangential avoidance direction, ensuring smooth transitions. Then a dual-path selection rule chooses the minimum-deviation trajectory (left or right bypass).

Simulations were performed in MATLAB/Simulink for a fixed-wing UAV model at a constant speed of 15 m/s, with a heading controlled by a PD feedback law.

3 RESULTS AND/OR HIGHLIGHTS OF IMPORTANT POINTS

Key highlights of the proposed method are:

- **Improved convergence:** Faster path convergence compared to the reference method [3], with up to 15% shorter convergence distance.
- **Stable tracking:** The exponential shaping function eliminates oscillatory corrections near the boundary.
- **Obstacle avoidance:** The UAV successfully bypasses obstacles located directly on the curve path and rejoins smoothly downstream.
- **Generality:** The method is effective for circular, elliptical, Lame', and other curve trajectories.

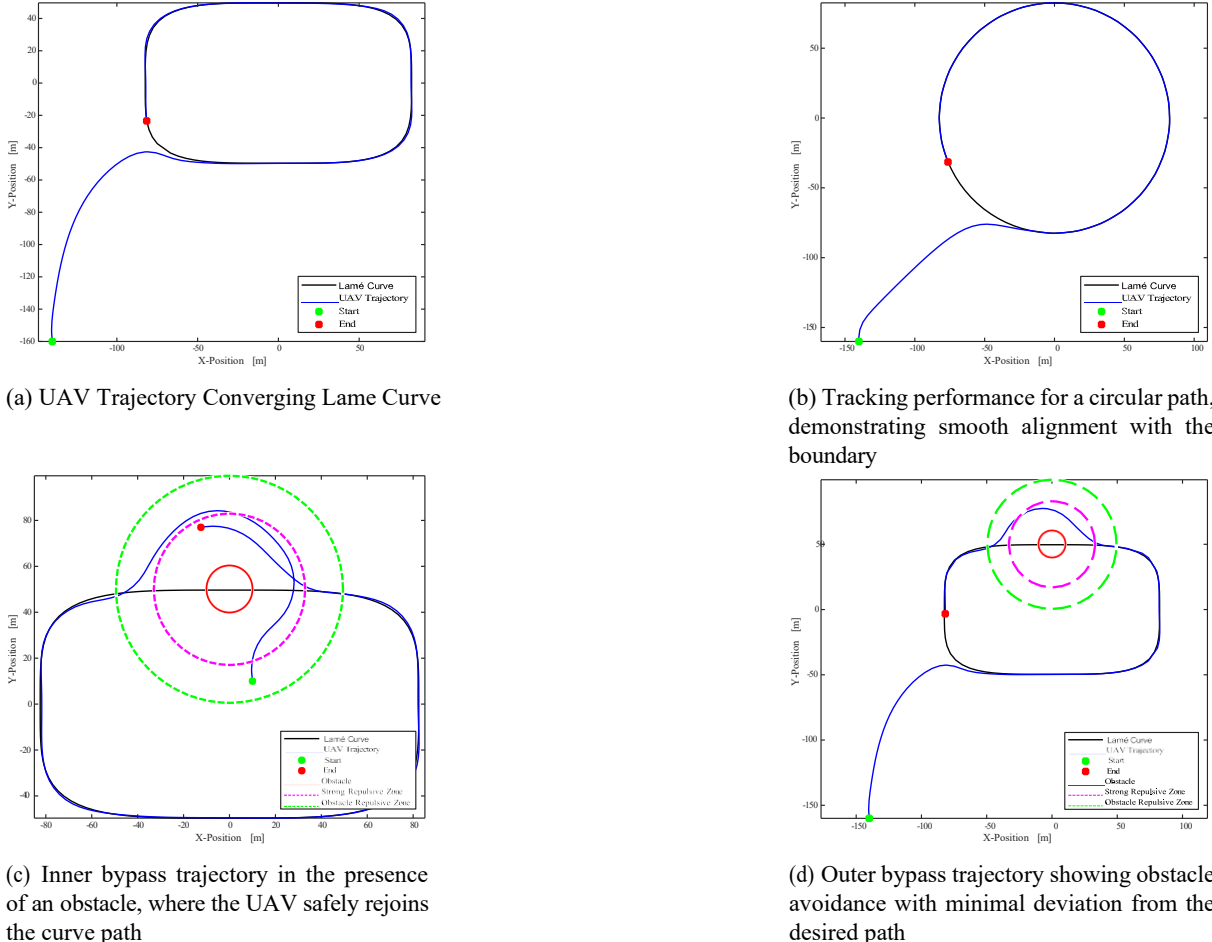


Figure 1: Representative UAV surveillance trajectories for different scenarios

4 CONCLUSIONS

This work introduces an improved curve-path-based guidance law that ensures faster convergence, and robust obstacle avoidance. The proposed strategy provides computational efficiency suitable for real-time implementation in UAV surveillance missions.

Future work will address cooperative multi-UAV coordination and experimental validation in real flight scenarios.

REFERENCES

- [1] D. McLean, *Automatic Flight Control Systems*. Prentice Hall, 1990.
- [2] B. L. Stevens and F. L. Lewis, *Aircraft Control and Simulation*, 2nd ed. Wiley, 2003.
- [3] A. Shivam and A. Ratnoo, “Surveillance guidance using Lamé’ curve paths,” *Journal of Guidance, Control, and Dynamics*, vol. 48, no. 5, pp. 1124–1137, 2025.
- [4] A. H. J. De Ruiter and O. Owlia, “Autonomous obstacle avoidance for fixed-wing UAVs using potential fluid flow theory,” *The Aeronautical Journal*, vol. 119, no. 1219, pp. 1431–1449, 2015.
- [5] H. Das and A. Ratnoo, “Potential fluid flow inspired guidance for obstacle avoidance in UAVs,” in *AIAA Scitech 2025 Forum*, Orlando, FL, USA, 2025.

^{1*}* Communicating Author: Gururaj Khurd; gururajsk858@kgpian.iitkgp.ac.in

Harnessing wind energy within the conduit-style tall building through the use of wind turbines

Amlan Kumar Bairagi^{1*} [0000-0003-4042-8805]

¹Former research scholar, Department of Civil Engineering, Indian Institute of Engineering Science and Technology, Shibpur, Howrah, India.

*Corresponding author, E-mail: bairagiak@gmail.com

Keywords: Conduit-type building, Fluid dynamics, Power output, Tall buildings, Wind energy

1. INTRODUCTION & OBJECTIVE

A sudden change in the flow area of the fluid increases the velocity. This is designated as the Venturi effect. Wind velocity in the environment continuously changes, and it has a large impact on building structures. While wind flows inside the conduit-type opening in the tall buildings, it increases its velocity. This study concentrated on harvesting wind energy by installing a wind turbine inside the conduit. Past research work was studied by rectangular, circular geometry conduit and placed horizontally [1], [2]. But this study considered both horizontal and vertical type conduits. Environmental wind passes through the conduit and increases its velocity.

2. DESCRIPTION OF MODELS

This study considered 1:1:4 square plan shape tall building models. Where length (l) = 100mm, breadth (b) = 100mm and height (h) = 400mm. Horizontal square duct of size 50×50 mm placed near the top of the model. The vertical duct size is 50×50mm. This duct is connected to the horizontal duct. Similarly, other models are considered a tapered duct of 45° angle in both side openings as shown in Fig 1.

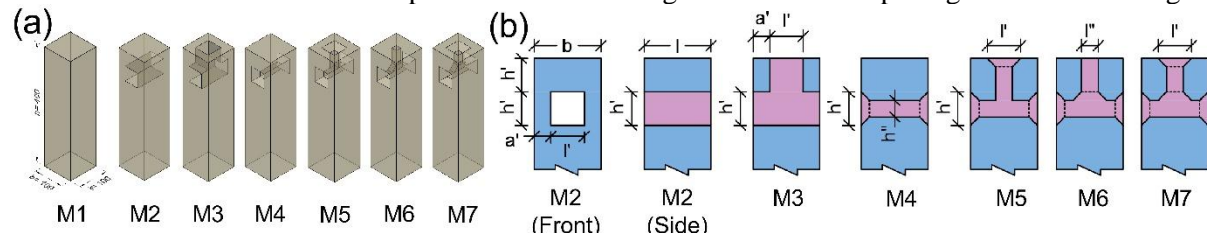


Fig 1 (a) Different square plan shape tall building models with horizontal and vertical conduits having sharp and chamfered edges (b) Dimension details of horizontal and vertical conduit openings.

3. METHODS OF ANALYSIS

A Computational Fluid Dynamics (CFD) study was implemented for the study. Considered models are simulated inside the domain, and the calculated wind velocity inside the conduit. Attacking wind angle is considered for the 0° case. This study can be done for the 90° or other wind angles. But this study considered for 0° wind angle due to the paucity of pages.

4. Computational Fluid Dynamics (CFD) simulation

4.1. Computational domain and boundary conditions

The domain design considered the tetrahedral meshing for the proper flow generation around the models. The inlet of the domain is considered 5 h from the extreme face of the model. Side walls are considered as 5 h . The outlet of the domain was designed at 15 h from the back side face of the model. Here, h is represented as the height of the model. The side walls are considered as a no-slip condition and the building walls are arranged as free slip condition. The top of the domain is considered 6 h from the base of the model. The growth rate is considered as 1.2, and the $y+$ value is 3, which is <5.

4.2. Meshing and Grid Sensitivity Study

The present study considered three different types of grids, namely Gr-1(course), Gr-2(medium), and Gr-3 (fine) as shown in Fig 2 (a). Velocity on the leeward side of the model was calculated for both Gr-1, Gr-2 and Gr-3 grids as shown in Fig 2 (b).

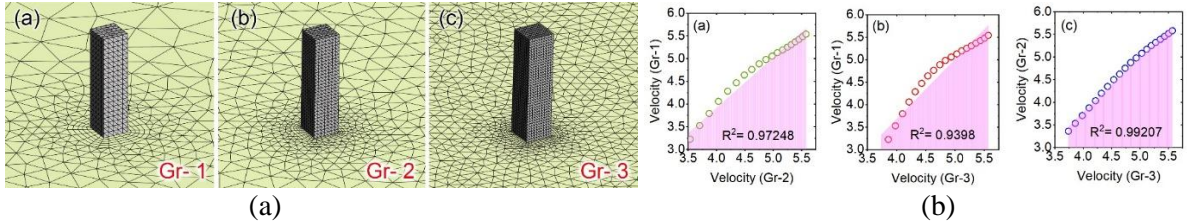


Fig 2 (a) Considered grid size of M1 model for grid sensitivity study, (b) Comparative study of mean wind velocity inside the domain between Gr1-Gr2, Gr1-Gr3, and Gr2-Gr3 grids

5. Authentication of the study

Mean velocity (U) was calculated using the power law on the M1 model using the RNG $k-\varepsilon$ turbulence method. The comparative study employed the past experimental study and the Large Eddy Simulation (LES) study as shown in Fig 3.

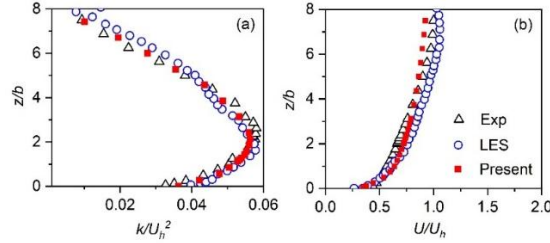


Fig 3(a) Comparison of wind velocity ratio (U/U_h) and (b) Turbulence Kinetic Energy (TKE) inside the domain

6. RESULTS AND HIGHLIGHTS OF IMPORTANT POINTS

For implementing the wind turbine inside the conduit, it is important to know the power generation capacity due to the wind flow. To achieve this, the study calculated power generation inside the conduit by calculating wind velocity inside the different conduits. Velocity ratio at the center of the conduit is compared between M2, M3, M4, M5, M6 and M7 models as shown in Fig 4.

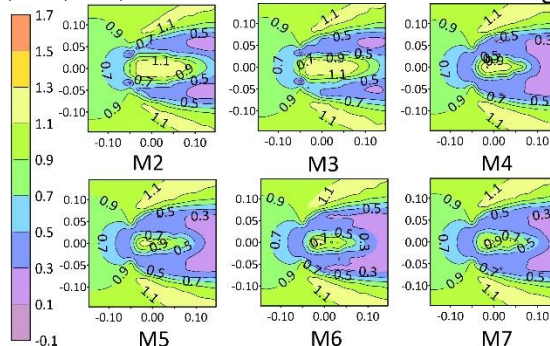


Fig 4 Comparison of velocity ratio (at x-y plane) between M2, M3, M4, M5, M6 and M7 at the center of the horizontal conduit for 0° attacking wind

7. CONCLUSIONS

After carefully studying the simulation, it was found that both horizontal and vertical top-opening conduits are efficient for the wind harvesting purpose.

8. REFERENCES

- [1] C. Alanis, I. Kalkman, and B. Blocken, “Aerodynamic design optimization of ducted openings through high-rise buildings for wind energy harvesting,” *Build. Environ.*, vol. 202, no. June, p. 108028, 2021, doi: 10.1016/j.buildenv.2021.108028.
- [2] M. Alanani, T. Brown, and A. Elshaer, “Multiobjective Structural Layout Optimization of Tall Buildings Subjected to Dynamic Wind Loads,” *J. Struct. Eng.*, vol. 150, no. 7, 2024, doi: 10.1061/j.sendh.steng-12366.

Impact of Preheated Central Jet on Intermixing of Confined Multi-Annular Swirling Jets

Ritesh Srivastava ^{a*}, Vivek Kumar Patel ^b

^a Research Scholar, Department of Applied Mechanics, MNNIT Allahabad, Prayagraj, India

^b Associate Professor, Department of Applied Mechanics, MNNIT Allahabad, Prayagraj, India

*Corresponding Author: ritesh.2022ram03@mnnit.ac.in

1. INTRODUCTION & OBJECTIVE

Efficient mixing of air and fuel within the gas turbine combustor is essential requirement for stable combustion and flame stability. However, in multi-annular configurations, the addition of an extra annular jet increases shear layer interactions between the jets, which enhance mixing within the confinement [1-2]. Swirling flows are widely employed in combustor design because they enhance turbulence, promote large-scale recirculation zones, and stabilize the flame. Mixing of coaxial swirling jets in confinement has been investigated experimentally and numerically over past decades. There is comparatively limited understanding of confined multi-annular jet configurations, especially under the combined influence of swirl, confinement, and thermal effects. The present study examines the flow and mixing behavior of a configuration featuring three swirling air jets: one central jet and two annular jets. This investigation is conducted in two scenarios: expanded confinement with an expansion ratio of 1.8 and non-expanded confinement with an expansion ratio of 1. The central jet, which represents the fuel jet, is analyzed under two conditions: one that is non-heated at 300 K and another that is preheated at 473 K. The main objective is to evaluate how heating the central jet affects the formation of recirculation zones and the decay of axial velocity, both of which are essential indicators of mixing performance.

2. METHODS OF ANALYSIS

The investigation is conducted through computational fluid dynamics (CFD) simulations using ANSYS Fluent. A two-dimensional axisymmetric computational domain is employed to model the confined flow field, as shown in Figure 1. The confinement is designed with a 15° angular outlet and incorporates a 30° counter-swirl intensity in each jet [3]. The central jet and the two surrounding annular jets are treated as air jets. Swirl is imposed on each jet; the swirl number for the central jet is 0.385, and the inner and outer annular jets are -0.470 and 0.478, respectively.

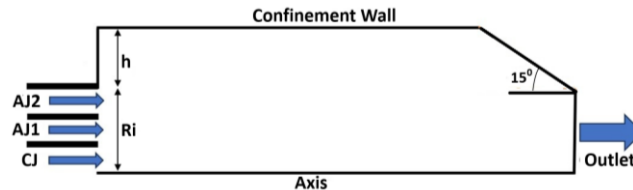


Figure 1. Geometry details 2D axisymmetric multi-annular confinement

The realizable k- ϵ turbulence model is adopted for turbulence closure. This choice was based on a validation exercise in which numerical results were compared with existing experimental data reported in the literature for confined swirling jets.

3. RESULTS

Comparison of centerline axial velocity (CLAV) depicted in Figure 2 for the non-expanded confinement ($e=1.0$) reveals that the velocity decay profiles are nearly identical, and the size of the recirculation zone remains almost unchanged, as shown in Figure 4 and Figure 6. This indicates that heating the central jet to 473 K does not significantly influence jet-jet interaction as the confinement limits the radial expansion and thermal diffusion of the heated jet. Consequently, the overall mixing behavior remains nearly the same in both cases. In the case of expanded confinement ($e = 1.8$), a greater decay in centerline axial velocity (CLAV) is observed when the central jet is heated, as shown in Figure 3. Furthermore, the axial extent of the recirculation zone increases for the heated jet compared to the non-heated case, as shown in Figures 5 and 7.

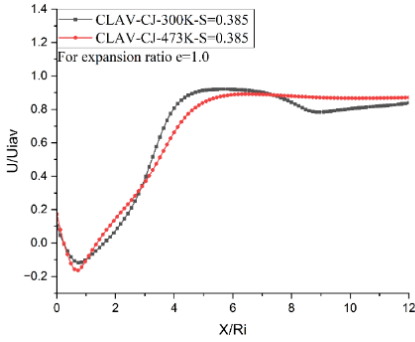


Figure 2. Central line axial velocity for expansion ratio $e=1.0$

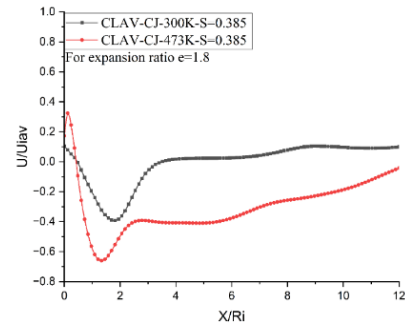


Figure 3. Central line axial velocity for expansion ratio $e=1.8$

This behavior indicates stronger jet–jet interaction and enhanced mixing within the expanded confinement due to the increased thermal energy effects associated with the heated central jet.

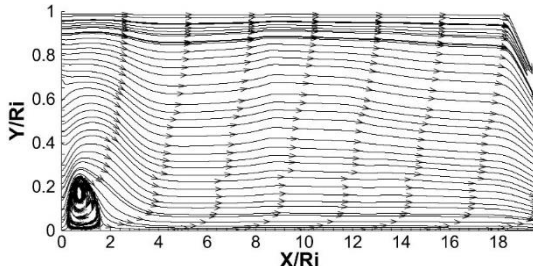


Figure 4. Central recirculation zone for expansion ratio $e=1.0$ with non-heated central jet

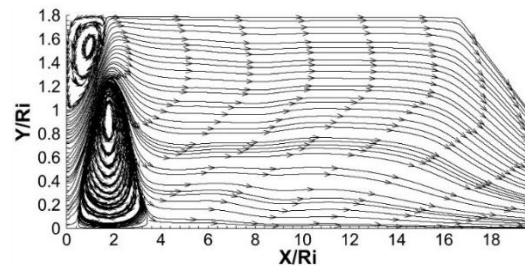


Figure 5. Central recirculation zone for expansion ratio $e=1.8$ with non-heated central jet

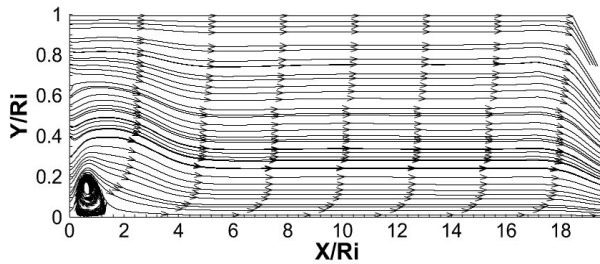


Figure 6. Central recirculation zone for expansion ratio $e=1.0$ with heated central jet

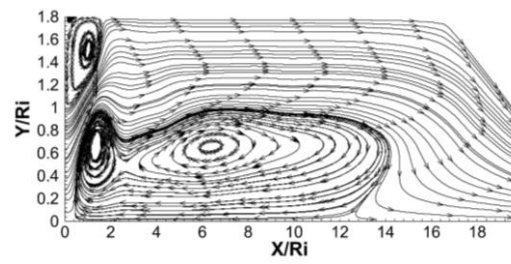


Figure 7. Central recirculation zone for expansion ratio $e=1.8$ with heated central jet

4. CONCLUSIONS

- In the non-expanded ($e=1.0$) confinement, heating the central jet to 473 K had minimal influence on the centerline axial velocity (CLAV) decay and the recirculation zone size, indicating that the confined geometry restricted jet-jet interaction and thermal spreading.
- For the expanded confinement ($e=1.8$), preheating the central jet led to a faster decay of CLAV and an axially enlarged recirculation zone.
- The results highlight that geometric expansion and jet pre-heating play a critical role in controlling flow structure and mixing performance in multi-annular swirling jet configurations.

5. REFERENCES

- [1] Singh, S. N., and D. P. Agrawal. “Effect of Swirl and Dump Expansion on Reverse Flow Structure in Multiannular.” *International Journal of Turbo and Jet Engines*, Vol.11, No. 4, pp.293-300, Dec1994, <https://doi.org/10.1515/tjj.1994.11.4.293>.
- [2] Tarnacha, R.S., Singh, S.N. and Rai, L., “Flow development of multi-annular jets in a confinement: effect of expansion ratio”. *Journal of Aerospace Sciences and Technologies*, pp.390-401, 2009.<https://doi.org/10.61653/joast.v6i3.2009.556>
- [3] Srivastava, R., Balyan, R. and Patel, V.K., “Effect of various angular outlets on mixing of swirling multi-annular jets in different expanded confinement.” *Aerospace Systems*, pp.1-24, 2024.<https://doi.org/10.1007/s42401-024-00333-x>

Integrating CFD, Experiments, and Bayesian Inference for Aerodynamic Analysis of a Serrated Delta Wing

Anand M.Raikar^a, S.K.Maharana^{b*}, N.Chikkanna^c

^aDept. of Aerospace Engineering, Ramaiah Institute of Technology, Bengaluru, Karnataka, India

^bDept. of Aerospace and Automotive Engineering, Ramaiah University of Applied Sciences, Bengaluru, Karnataka, India

^cDept. of Aerospace Engg., Visvesvaraya Technological University, Chickaballapura, Karnataka, India

1. INTRODUCTION

Bayesian inference has emerged as a transformative statistical framework in aerodynamic performance estimation, offering a principled way to quantify and propagate uncertainty[1]. In this study, Bayesian modeling is integrated with CFD and experimental data to analyze the aerodynamic characteristics of a serrated double delta wing, compared to a non-serrated baseline[2]. Serrations along the leading edge are hypothesized to control vortex evolution, delay flow separation, and enhance aerodynamic efficiency under high angles of attack.

2. OBJECTIVES

1. To develop an integrated Bayesian–CFD–Experimental framework for assessing the aerodynamic performance of serrated and non-serrated double delta wings under varying angles of attack.
2. To quantify uncertainty and validate aerodynamic coefficients (lift, drag, and lift-to-drag ratio) by merging CFD predictions with experimental data using Bayesian inference

3. METHODS

A hierarchical Bayesian model was constructed, where Gaussian priors were assigned to lift (C_L) and drag (C_D) coefficients based on preliminary CFD estimates ($C_L \sim N(0.8, 0.05^2)$, $C_D \sim N(0.12, 0.01^2)$). The likelihood function was defined as $p(D|\theta) \propto \exp[-(y - f(\theta))^2 / (2\sigma^2)]$, where y represents experimental observations and $f(\theta)$ the CFD predictions. Markov Chain Monte Carlo (MCMC) sampling was employed for posterior estimation, with convergence verified through Gelman–Rubin diagnostics ($\hat{R} < 1.02$) and effective sample size (ESS > 1000) criteria[3].

4. HIGHLIGHTS OF IMPORTANT POINTS

The posterior distributions revealed a 12–15% increase in mean lift coefficient and an 8–10% reduction in drag for the serrated configuration across the range of angles of attack. The lift-to-drag ratio improved by approximately 18%, with a corresponding increase in vortex circulation strength of 22% compared to the non-serrated wing. 95% credible intervals for C_L and C_D were found to be [0.76, 0.92] and [0.10, 0.13], respectively, demonstrating robust predictive consistency between CFD and experimental datasets[4]. Uncertainty bounds narrowed by 25% post-Bayesian updating, confirming effective data fusion.

This integrated approach illustrates how Bayesian inference can rigorously reconcile CFD and experimental discrepancies while quantifying aerodynamic uncertainty. The probabilistic

insights obtained not only confirm the aerodynamic benefits of serrated delta wings but also establish a systematic pathway for uncertainty-informed aerodynamic optimization.

5. CONCLUSIONS

The study validates Bayesian inference as a reliable framework for aerodynamic design under uncertainty. The serrated double delta wing exhibits significant aerodynamic enhancement with quantified confidence levels, thereby contributing to the advancement of probabilistic design and decision-making in next-generation aerospace configurations.

6. REFERENCES

- [1] T. A. Oliver and P. Castonguay, “Bayesian inference applied to aerodynamic analysis and design,” *AIAA Journal*, vol. 50, no. 5, pp. 1176–1189, 2012.
- [2] M. Gad-el-Hak, “Flow control: passive, active, and reactive flow management,” *Cambridge University Press*, Cambridge, 2007.
- [3] A. Gelman, J. B. Carlin, H. S. Stern, D. B. Dunson, A. Vehtari, and D. B. Rubin, *Bayesian Data Analysis*, 3rd ed., CRC Press, Boca Raton, FL, 2013.
- [4] A. K. Gopalarathnam and J. E. Chambers, “Characterization of leading-edge vortices on delta and double-delta wings,” *Journal of Aircraft*, vol. 42, no. 2, pp. 356–365, 2005.

Corresponding Author, Email: skmaha123@gmail.com

Investigation of Delamination Progression in Unidirectional Composite Laminates

Subhabrata Koley^{a*}

^a Department of Aerospace Engineering and Applied Mechanics, IEST Shibpur, West Bengal, India

1. INTRODUCTION and OBJECTIVE

Delamination refers to the separation of layers within a laminate, arising from the failure of the interlaminar interface between adjacent plies. This phenomenon can be triggered by interlaminar stresses generated at free edges, geometric discontinuities, impact loading, or load path eccentricities. Additionally, delamination may originate during manufacturing due to incomplete curing or the presence of foreign inclusions. In certain instances, it can lead to sudden and catastrophic failure without prior indication, thereby limiting the widespread use of advanced composite materials in structural applications. To capture the delamination behaviour, the interlaminar interface is modelled as a damageable three-dimensional layer between two adjacent plies. The degradation of material properties due to damage evolution is described using a homogenization-based formulation combined with standard mechanics principles. The primary objectives of this study are (a) to model and predict progressive delamination in unidirectional composites without introducing any initial crack; (b) to define an isotropic damage variable that quantitatively represents the damage state in terms of the void volume fraction, thus providing a clear physical interpretation; and (c) to develop a generalized model capable of predicting various forms of interfacial failure, including delamination in principal modes as well as failure caused by through-thickness cracks.

2. METHODS OF ANALYSIS

In the case of delamination, the initiation of damage and the formation of an initial crack are explained using damage mechanics, which integrates both strength theories and concepts of crack growth. Several criteria have been proposed to predict the onset of delamination, most of which are based on the macroscopic damage concepts introduced by Kachanov [1]. These criteria range from simple single-stress threshold models to more complex formulations involving combinations of multiple stress components. The evolution of micro-level damage into macroscopic cracks has led to the development of Continuum Damage Mechanics (CDM) [2]. For the preliminary analysis, a Double Cantilever Beam (DCB) specimen was selected, as it effectively represents the primary and most common mode of delamination. Two modelling approaches were examined—one with a 2-D interfacial representation and another with a 3-D interfacial layer of thickness $e_1 = 0.0275$ mm. However, interfacial failure and the ensuing delamination may manifest in multiple ways that cannot be adequately captured by 2-D models, primarily due to their inability to replicate the true three-dimensional nature of the phenomenon. To overcome this limitation, a new interfacial model is proposed that provides a physically meaningful representation of damage. In this framework, a Representative Volume Element (RVE) is employed to encapsulate the damage zone, where the quantified damage parameter is directly related to the size of the defect within the RVE. The micromechanical analysis is conducted based on the mathematical framework of homogenization theory [3].

In the current study, voids in the matrix are assumed to be spherical and locally periodic in the damage zone. Unit-cell RVE of size $e \times e \times e$ is assumed and $e \ll \min(L, l)$ where L is the length scale of the lamina and l is the characteristic size of the problem. Far field, or nonlocal influences, are not considered here. The local displacement field in the cell can be given as

$$u(x; y) \approx u_0(x) + \varepsilon u_1(y)$$

Where, $u_0(x)$ is the macro response and $u_1(y)$ is the periodic micro corrections. $u_1(y)$ can be obtained for each of the six fundamental macro strains e_{ij}^x by solving the periodic cell problems

$$-\frac{\partial}{\partial y_j} [C_{ijkl}^{\varepsilon} e_{kl}^y (\chi^{rs})] = \frac{\partial}{\partial y_j} (C_{ijrs}(y)), \chi^{rs} \text{ is } y\text{-periodic}$$

The above equation results from assuming the general solution of the micro problem $u^{(1)}$ to be of the following form

$$u^{(1)}(x, y) = \chi^{rs} e_{rs}^x(v_0(x))$$

The above equation means that the micro solution is written as a combination of solutions corresponding to individual macrostrains e_{rs}^x . Here, we use a DCB unidirectional specimen, a [0/0] laminate constituted of carbon-epoxy T300-M10 laminae, shown in Fig. 1.

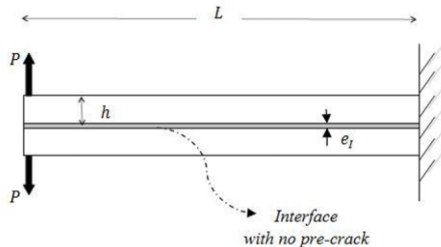


Fig. 1 Schematic diagram of the DCB specimen for delamination onset

3. RESULTS

The analysis reveals that delamination initiates at a time step of 0.7, corresponding to the point where the damage variable d of the interfacial mid-plane element at the loading end reaches its critical value $d_c = 0.38$. Hence, the onset of delamination is defined as the stage at which the interfacial elements reach this critical damage threshold. The corresponding traction force at this iteration is 68 N/mm^2 , which shows good agreement with the experimental value of 60 MPa reported in [4]. This consistency indicates that the proposed damage model accurately captures the initiation of delamination.

4. CONCLUSIONS

The following key observations are drawn from the present study:

1. The degradation of elastic properties due to damage exhibits a nonlinear behaviour, though its effect remains isotropic in nature.
2. The elastic properties do not reduce to zero even when the damage variable at a given point reaches its critical value.
3. The proposed damage model effectively captures the onset of delamination, yielding results that show good agreement with experimental findings.

5. REFERENCES

- [1] L.M. Kachanov, "Rupture time under creep conditions," *Izvestia Akademii Nauk SSSR, Otdelenie tekhnicheskikh nauk*, vol. 8, pp. 26-31, 1958.
- [2] J. Janson and J. Hult, "Fracture mechanics and damage mechanics: a combined approach," *J. mechanique appliquee*, vol. 1, no. 1, pp. 69-84, 1977.
- [3] Engquist, Björn, and Panagiotis E. Souganidis. "Asymptotic and numerical homogenization." *Acta Numerica* 17 (2008): 147-190.
- [4] O. Allix, P. Ladevèze and A. Corigliano, "Damage analysis of interlaminar fracture specimens," *Composite Structures*, vol. 31, pp. 61-74, 1995.

* Communicating Author: Dr Subhabrata Koley, subhabrata.aero@faculty.iests.ac.in

Investigation of Flexural Behavior of Functionally Graded Plates through Higher-Order Shear Deformation Formulation

Smruti Ranjan Sahoo^a*, Surendra Verma^b, and B. N. Singh^c

^aResearch Scholar, Aerospace, IIT Kharagpur, India.

^bAssistant Professor, Mechanical, IIT BHU (Varanasi), India.

^cProfessor, Aerospace, IIT Kharagpur, India.

1. INTRODUCTION & OBJECTIVE

Functionally graded (FG) materials represent a type of advanced composites in which the features of the material change steadily throughout the thickness in accordance with a predefined law, typically a power-law distribution of constituents. Unlike traditional laminated composites, FGMs eliminate sharp interfaces and stress discontinuities, leading to improved thermal and mechanical performance.

The flexural analysis of such FGM plates is of prime importance for aerospace, nuclear, and mechanical systems operating under large deflection or high temperature gradients. This study aims to examine the **linear flexural response of 'FGM plates'** using a '**Higher-Order Shear Deformation Theory**' (HSDT) formulation. The main objectives are: (i) to develop an HSDT-based finite element model for flexural analysis, (ii) to study the impact of material gradation (power-law index), boundary conditions, and 'aspect ratio' on deflection, and (iii) to validate the obtained results with available benchmark solutions.

2. METHODS OF ANALYSIS

A linear finite element model has been developed using a seven degrees-of-freedom (7-DOF) C^0 continuous HSDT displacement field, which includes independent rotations and higher-order shear terms. The 'material properties' are graded across the thickness following a power-law distribution based on the volume fraction of ceramic and metal constituents. The displacement field assumed for the HSDT is expressed by eq(1-3):

$$u(x', y', z') = u_0(x', y') + z \phi_x(x', y') + f(z) \psi_x(x', y') \quad (1)$$

$$v(x', y', z') = v_0(x', y') + z \phi_y(x', y') + f(z) \psi_y(x', y') \quad (2)$$

$$w(x', y', z') = w_0(x', y') \quad (3)$$

In this equation, the displacements of the plate at the mid-surface are denoted by the symbols u_0 , v_0 , and w_0 . The terms ϕ_x and ϕ_y represent the rotations of the 'normal to the mid-surface' about the y- and x-axes, respectively. The functions ψ_x and ψ_y account for higher-order shear deformation effects, providing a realistic representation of the transverse shear strain variation across the plate thickness. By selecting $f(z)$ in such a way that the transverse shear stresses disappear at the plate's upper and lower surfaces, ensuring shear stress-free boundary conditions.

Communicating Author: 'Smruti Ranjan Sahoo' (Email: smrutisahoo500@gmail.com)

3. RESULTS

Table 1: Deflection of simply supported FGM plates under ‘sinusoidal load’

| k | a/h | HSNDT | FEM-HSDT* |
|-----|-------|--------|-----------|
| 1 | 4 | 0.7284 | 0.7267 |
| | 10 | 0.5889 | 0.5887 |
| | 100 | 0.5625 | 0.5625 |
| 4 | 4 | 1.1611 | 1.1601 |
| | 10 | 0.8817 | 0.8820 |
| | 100 | 0.8287 | 0.8287 |
| 10 | 4 | 1.3916 | 1.3862 |
| | 10 | 1.0088 | 1.0082 |
| | 100 | 0.9361 | 0.9362 |

*represents present results

Table 1 presents the normalized central deflection of simply-supported square FGM plates under a ‘sinusoidal mechanical load’. A comparison between the available literature and the present Finite Element Method based on Higher-Order Shear Deformation Theory (FEM-HSDT) demonstrates excellent agreement, validating the accuracy and reliability of the developed numerical model. Deformation behavior and stiffness of FGM plates are affected by geometric factors and material gradation, as seen by the normalized deflection values.

4. CONCLUSIONS

In accordance with the HSDT theory, a linear finite element formulation has been developed for analyzing the static bending of functionally graded plates. The study demonstrates that the deflection behavior of FGM plates is significantly influenced by both the gradation index and the geometric aspect ratio. The study clearly indicates that as the power-law index increases, the normalized deflection also increases, which can be attributed to the higher metallic content and the corresponding reduction in overall stiffness of the plate. This trend demonstrates that the stiffness of FGM plates is highly sensitive to the gradation profile, and a higher proportion of metal leads to greater flexibility and deformation under mechanical loading. The developed model can serve as a computationally efficient tool for the flexural analysis of FGM structures in high-performance engineering applications.

5. REFERENCES

- [1] B. Adhikari and B. N. Singh, “Dynamic response of functionally graded plates resting on two-parameter-based elastic foundation model using a quasi-3D theory,” *Mech. Based Des. Struct. Mach.*, vol. 47, no. 4, pp. 399–429, 2019.

Investigation of transonic buffet loads on aeroelastic launch vehicle model using couple CSD-CFD approach

Amit K Onkar^{a1}, Mutturaj H Medar^a, Arun Kumar A^a, Rahul B Choudhary^a, Shivaprasad M V^a, Raja S^a

^a Structural Technological Division, CSIR-National Aerospace Laboratories, Bangalore 560017, India

1. INTRODUCTION & OBJECTIVE

Transonic buffet response in a flexible launch vehicle is an aeroelastic phenomenon that arises due to the interaction between aerodynamic forces and the vehicle's structural dynamics. This phenomenon, classified as a fluid-structure interaction (FSI), is characterized by several complex flow features, including shock wave oscillations, boundary layer separation, turbulence, and vortex shedding [1]. These unsteady aerodynamic effects make transonic buffeting a critical concern in the design and analysis of launch vehicles, as it can significantly influence the structural integrity and performance of the vehicle during ascent. The present study aims to develop a hi-fidelity FSI simulation framework to study the buffet load and buffet response on flexible launch vehicle. The numerical buffet load measured on the scaled aeroelastic launch vehicle is also compared with the in-house WT test data in the transonic regime.

2. METHODS OF ANALYSIS

The FSI framework adopted for the transonic buffet studies is based on coupled computational fluid dynamics (CFD) – computational structural dynamics (CSD) approach. CFD solver is based on unsteady N-S equations with turbulence modelled using Detached Eddy Simulation (DES) technique and CSD solver is based on time integration of the structural dynamic equations using HHT algorithm. A partitioned FSI approach is adopted, where aerodynamic forces and structural displacements are updated at the end of every physical time step. Mesh morphing of the CFD grid is modelled using the B-spline interpolation technique.

3. NUMERICAL RESULTS

Figure 1(a) shows the schematic representation of a scaled aeroelastic launch vehicle model with sting considered in this study. All the major dimensions indicated in the figure are in mm. A modular construction is used in the form of spar-rings-skin for the design of scaled launch vehicle model. Metallic materials such as aluminium and steel are chosen to build the skeleton and GFRP (glass fiber reinforced plastic) composite is used for skin. The material properties chosen for different components of the model are: Spar and Ring (Aluminium): $E_1 = E_3 = 70$ GPa, $\nu_{12} = \nu_{13} = \nu_{23} = 0.3$, $\rho = 2850$ kg/m³; Ring and Sting (Steel): $E_1 = E_3 = 210$ GPa, $\nu_{12} = \nu_{13} = \nu_{23} = 0.3$, $\rho = 7800$ kg/m³; Skin (GRPF): $E_1 = E_2 = 130$ GPa, $G_{12} = G_{13} = G_{23} = 4.2$ GPa, $\nu_{12} = \nu_{13} = \nu_{23} = 0.22$, $\rho = 1900$ kg/m³.

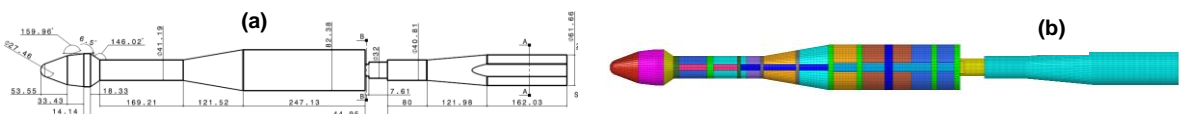


Figure 1: Schematic representation of scaled aeroelastic launch vehicle model with sting, and its finite element model

The finite element model of the scaled aeroelastic launch vehicle is shown in Fig. 1(b). It consists of hexahedral solid elements and quadrilateral shell elements. The total number of elements and nodes are 134610 and 157209 respectively. The model is constrained at the sting root in all the degrees of freedom.

¹ Communicating Author: Amit K Onkar and aeroamit@nal.res.in.

The dynamics of the scaled launch vehicle is studied through free vibration analysis in terms of natural frequencies and mode shapes. The 1st mode is observed to be 1st bending with natural frequency of 116.93 Hz and the 2nd mode is observed to be second bending with natural frequency of 551.32 Hz. These natural frequencies are also compared with the in-house ground vibration test results.

Figures 2 shows the CFD model with the following parameters. Farfield = 50 m, 1st cell height = 1e-6 m, prism layer total thickness = 2.7 mm, No. of prism layers = 35. The shock regions and shear layer regions are appropriately refined. The number of cells obtained in CFD grid is approx 17 million.

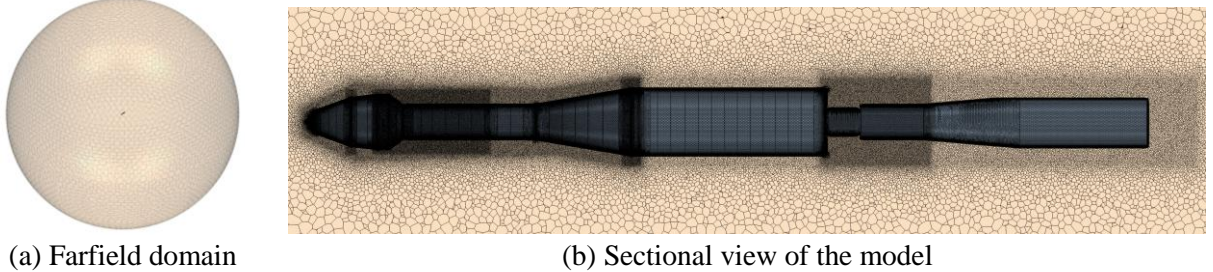


Figure 2: CFD model of scaled launch vehicle with sting

FSI analyses are carried out for various combinations of Mach number (M) and angles of attack (α), and results in terms of the mean and RMS of pressure coefficients on the launch vehicle are studied. These numerical results are also compared with the wind tunnel test data conducted at CSIR-NAL. Figure 3 shows the comparison of mean and RMS of pressure coefficient with test data at $M = 0.9$ and $\alpha = 0^\circ$. The figure also includes the rigid unsteady simulation results to show the effect of flexibility. The simulation results successfully capture the front and rear peaks of the Mean C_p distribution, demonstrating a good agreement with the WT measurements. However, a forward shift in the flow reattachment region is observed in the numerical simulations. Further, the amplitude of RMS C_p (unsteady pressure fluctuations) in the simulations is overestimated relative to the experimental data. It indicates that further refinements in the computational model may be necessary to achieve better buffet response predictions.

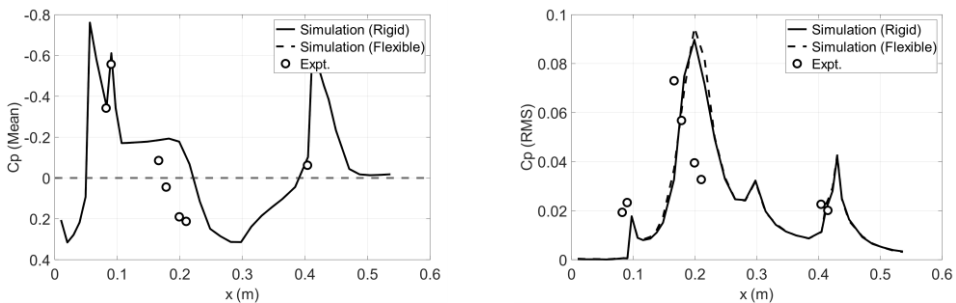


Figure 3: Comparison of mean and RMS C_p coefficients at $Mach = 0.9$ and $\alpha = 0^\circ$

4. CONCLUSIONS

The present study focuses on establishing a hi-fidelity FSI framework for transonic buffet investigations on a scaled aeroelastic launch vehicle. The simulated buffet results are also systematically compared with the in-house wind tunnel test data conducted at CSIR-NAL. The comparative analysis reveals that a good correlation in the buffet load trends is observed. However, some discrepancies between numerical results and experiment data in terms of flow reattachment region and peak RMS C_p are observed.

5. REFERENCES

- [1] J. M. Ramey, M. K. Sekula, D. J. Piatak, P. S. Heaney, and F. Soranna, "Development of Buffet Forcing Functions using Frequency-Dependent Coherence Factors," in *AIAA Scitech 2021 Forum*. doi: 10.2514/6.2021-1653.

Lamé Curve Following by UAVs using Vector Field Guidance

Hemant V Nair⁺, Sayantan Pal* and Sikha Hota

⁺Undergraduate Student, Aerospace Engineering, Indian Institute of Technology Kharagpur, Kharagpur, India

*Research Scholar, Aerospace Engineering, Indian Institute of Technology Kharagpur, Kharagpur, India

1. INTRODUCTION & OBJECTIVE

Prior work on path following has primarily focused on optimizing curvature, minimizing time-to-approach, or enriching control laws with additional tuning parameters to enhance alignment with a desired path. We take a complementary route by reducing controller complexity through path reconfiguration. Specifically, we recast Lamé curves as a family of concentric circles whose radii vary with angular position, and apply an existing sliding-mode control law on this surrogate geometry. This geometric abstraction preserves the target shape while yielding a simple control interface with fewer tuning parameters.

2. METHOD OF ANALYSIS

On employing the vector-field guidance (VFG) law for circular orbits [1] to navigate through a system of concentric circles switching the target radius inward once the vehicle enters a small threshold band δ around the current circle, an inward-coiling trajectory is thereby produced, similar to a spiral as shown in Fig. [1]. Increasing the number of intermediate circles improved smoothness by reducing the jump in commanded curvature at each switch.

$$r(t) = \begin{cases} r_1, & \text{for } t \in [t_0, t_1), \\ r_2, & \text{for } t \in [t_1, t_2), \\ \vdots \\ r_N, & \text{for } t \in [t_{N-1}, t_N) \end{cases} \quad \text{where } |d(t_i) - r_i| < \delta. \quad (1)$$

$d(t_i)$: Radial Distance of UAV from center of circles

r_i : Radius of i^{th} circle

δ : Threshold to cross over from r_i to r_{i+1}

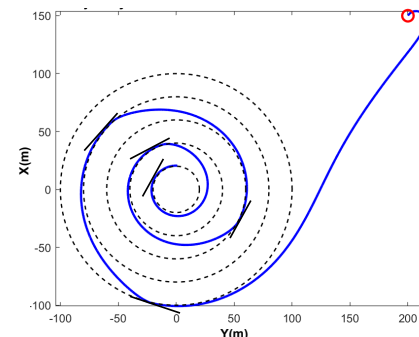


Figure 1: Spiral Representation

We can represent Lamé curves via an equivalent “radius as a function of bearing” with semi-axes a, b and degree of curve n , as shown in [2].

$$r(\theta) = \frac{ab}{\sqrt[n]{(a \sin \theta)^n + (b \cos \theta)^n}} \quad (2)$$

In piece-wise form [2] can be written as,

$$r(\theta) = \begin{cases} a, & \theta \in \{0, \pi\}, \\ r_1, & \theta \in \{\pm\theta_1, \pm(\pi - \theta_1)\} \\ \vdots \\ b, & \theta \in \{\pm\frac{\pi}{2}\} \end{cases} \quad (3)$$

θ : angular position of UAV

r_i : angular radius corresponding to $\pm\theta_i, \pm(\pi - \theta_i)$

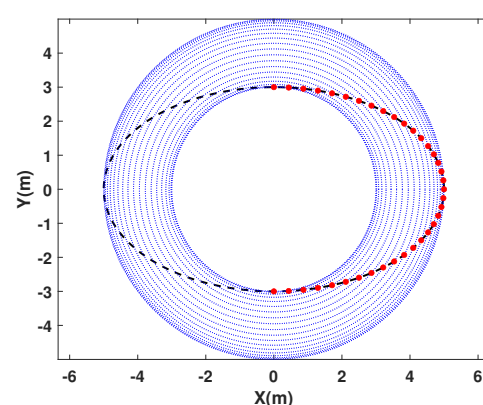


Figure 2: Ellipse Representation

It can be noted that the time-indexed radii representation [1] has been extended to angle-indexed radii representation as shown in [3]. The VFG then operates on these surrogate circular targets at each bearing, while preserving the intended geometry like in the case of an ellipse in Fig. [2].

3. RESULTS AND/OR HIGHLIGHTS OF IMPORTANT POINTS

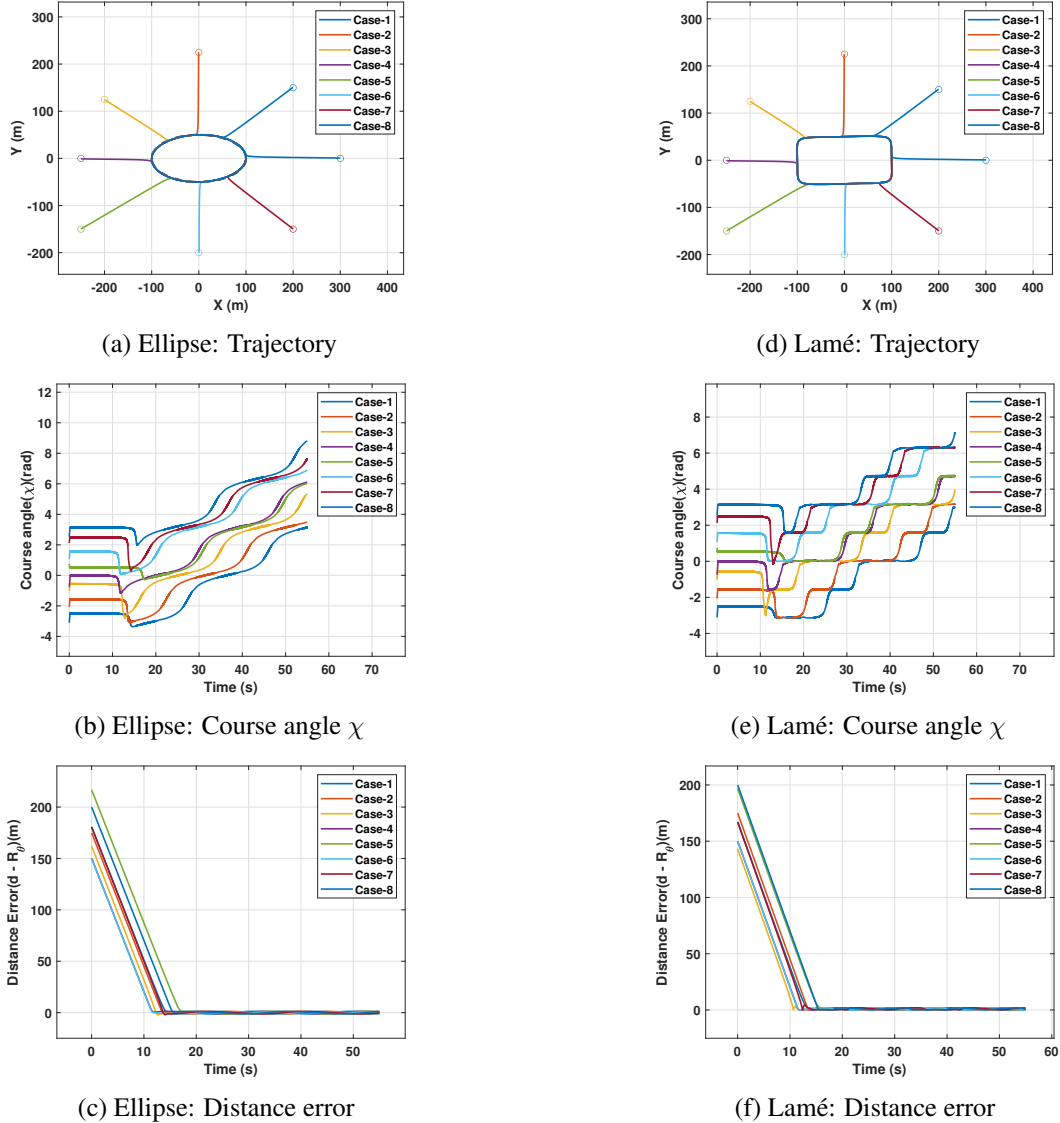


Figure 3: Results for Simulation of Ellipse ($\frac{x^2}{100^2} + \frac{y^2}{50^2} = 1$) and Lamé Curve ($\frac{x^5}{100^5} + \frac{y^5}{50^5} = 1$)

4. CONCLUSIONS

We reduce controller complexity by reconfiguring geometry: Lamé curves become concentric circles whose radii vary with angle, enabling a sliding-mode vector-field law. Demonstrated on ellipse and Lamé curve of $n = 5$, this preserves shape, simplifies planning, and ensures asymptotic convergence for fixed-wing UAV surveillance, offering a scalable, real-time solution for surveillance missions.

5. REFERENCES

- [1] D. R. Nelson, D. B. Barber, T. W. McLain, and R. W. Beard, “Vector field path following for miniature air vehicles,” *IEEE Transactions on Robotics*, vol. 23, no. 3, pp. 519–529, 2007.
- [2] A. Shivam and A. Ratnoo, “Surveillance guidance using lamé curve paths,” *Journal of Guidance, Control, and Dynamics*, pp. 1–14, 2025.
- [3] S. Pal and S. Hota, “Vector field guidance with curvature constraint for uavs,” in *AIAA SCITECH 2025 Forum*, 2025, p. 0523.

Large Deformation Analysis of Magneto-Active Polymer Membranes under Varying Mechanical Loads

Anuttar Jain^a and Krishnendu Haldar^{b,*}

^a B.Tech. Student, Dept. of Aerospace Engineering, Indian Institute of Technology Bombay, Mumbai, India

^b Associate Professor, Dept. of Aerospace Engineering, Indian Institute of Technology Bombay, Mumbai, India

1. INTRODUCTION

Magneto-active polymers (MAPs) have emerged as promising smart materials for aerospace structures, particularly in vibration suppression and adaptive damping applications [1]. Recent experimental studies by Garai et al. [2] demonstrated that the axial stiffness of cylindrical MAPs increases significantly with magnetic field strength, enabling tunable and controllable mechanical behavior.

Classical frameworks, such as the Föppl–von Kármán theory, provide a basis for analyzing thin elastic membranes by decoupling bending and stretching energies through order-of-magnitude arguments. Building on these foundations, Healey et al. [3, 4] extended the formulation to hyperelastic materials, allowing for a more accurate description of large deformations. Motivated by these developments, the present study explores the mechanical response of hyperelastic magneto-active polymer membranes.

2. MATHEMATICAL FORMULATION

A two-dimensional rectangular domain is adopted to represent the thin membrane, constrained along all edges, and subjected to a uniformly distributed load acting downwards over its face. Under the small-thickness assumption, variations of stress and strain across the thickness are neglected, and mid-plane quantities characterise the response. Following the order-of-magnitude arguments of the Föppl–von Kármán model [5], the total free energy is expressed as the sum of decoupled membrane and bending components, with the latter modelled using a linearised bending strain, introducing negligible error [6]. The membrane consists of a PDMS matrix embedded with magnetite particles [2], modelled using an incompressible Mooney–Rivlin constitutive law reduced for a 2D membrane using the 3D incompressible formulation.

The total Helmholtz free energy per unit reference area is

$$\Psi_{Total} = \Psi_E(\mathbf{C}) + \Psi_B(\mathbf{K}) + \Psi_M(\mathbf{H})$$

where Ψ_E , Ψ_B , and Ψ_M denote membrane, bending, and magneto-elastic coupling energies, respectively. Ψ_E is derived from the incompressible Mooney–Rivlin model reduced for a 2D membrane, with \mathbf{C} being the right Cauchy-Green tensor. Ψ_B is expressed in the linearized form, with \mathbf{K} being the curvature tensor. The volumetric contribution to the free energy is neglected owing to the 3D incompressibility assumption. In the absence of the magnetic field, $\mathbf{H} = 0$, which yields $\Psi_M = 0$ for our case.

$$\begin{aligned}\Psi_E(\mathbf{C}) &= h[1.08(tr \mathbf{C} + (det \mathbf{C})^{-1} - 3) + 1.37(det \mathbf{C} + tr \mathbf{C}(det \mathbf{C})^{-1} - 3)] \times 10^5 \\ \Psi_B(\mathbf{K}) &= \frac{Eh^3}{24(1-\nu^2)}[\nu(tr \mathbf{K})^2 + (1-\nu)\mathbf{K} : \mathbf{K}]\end{aligned}$$

The equilibrium solution is obtained by minimising the total free energy functional, leading to the corresponding Euler–Lagrange equations

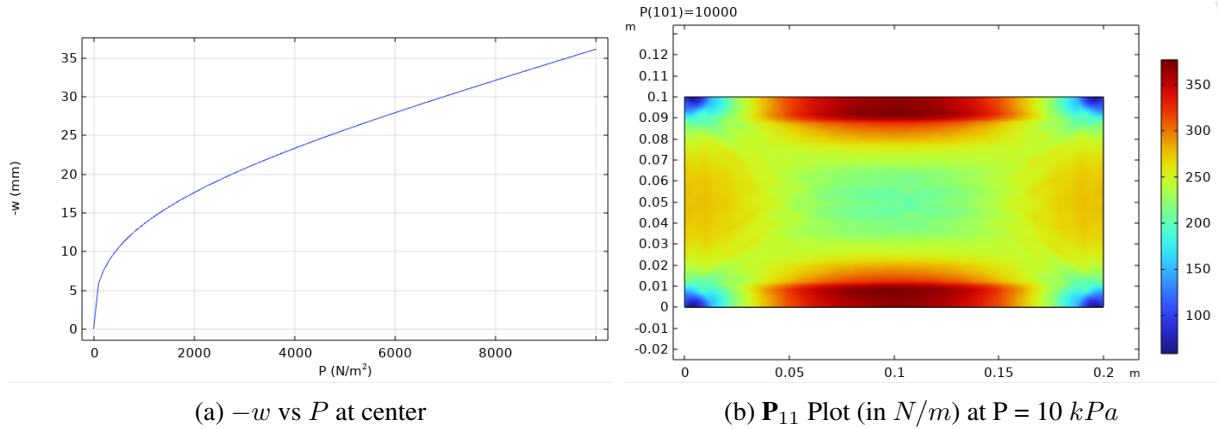
$$\nabla \cdot [(\mathbf{I} + \nabla \mathbf{u})\mathbf{N}] = \mathbf{0}, \quad D\Delta^2 w - \nabla \cdot (\mathbf{N}\nabla w) = -P$$

* Communicating Author: Krishnendu Haldar, krishnendu@aero.iitb.ac.in

where $\mathbf{u} = (u_1, u_2)$ represents the in-plane displacements, w is the transverse displacement, $\mathbf{N} = 2\partial_C\Psi_E$ is the membrane second Piola–Kirchhoff stress tensor, \mathbf{I} is the Identity tensor, P is the distributed load and h is the membrane thickness. $D = \frac{Eh^3}{12(1-\nu^2)}$ is a dimensional constant. Here, ∇ is the 2D gradient operator and Δ^2 denotes the biharmonic operator.

3. NUMERICAL IMPLEMENTATION

Owing to the nonlinear nature of the governing equations, solutions were obtained via finite-element simulations in COMSOL Multiphysics for $0 \leq P \leq 10kNm^{-2}$. A Newton–Raphson solver was used at each load step to solve the geometrically nonlinear plate equations. Figure (a) shows the transverse displacement (w) at the membrane center versus applied load P , and Figure (b) presents the spatial distribution of the first Piola–Kirchhoff stress component $\mathbf{P}_{11} = (\mathbf{FN})_{11}$ at $P = 10kNm^{-2}$ load, confirming the expected coupling between transverse deflection and in-plane membrane stresses.



4. CONCLUSION

This study proposes a hyperelastic constitutive model for a magneto-active polymer membrane (in the absence of applied magnetic fields) and uses COMSOL Multiphysics to compute stresses and strains under varying mechanical loads. Continuing this study, we will extend the model to a fully coupled magneto-mechanical formulation, derive the explicit expression for $\Psi_M(\mathbf{H})$, and carry out parametric numerical simulations to compare the mechanical responses with and without magnetic fields.

REFERENCES

- [1] A. M. Bazinenkov, D. A. Ivanova, I. A. Efimov, et al., "Study of Mechanical Properties of a Magnetorheological Elastomer for an Active Vibration Isolation System," *Russ. Engin. Res.* vol. 41, no. 11, pp. 1040—1044, 2021, doi: 10.3103/S1068798X21110034
- [2] A. Garai and K. Haldar, "Experiments and modeling of magneto-stiffening effects for magnetoactive polymer," *Int. J. Mech. Sci.*, vol. 286, no. 109860, Jan. 2025, doi: 10.1016/j.ijmecsci.2024.109860
- [3] T. J. Healey, Q. Li and R.-B. Cheng, "Wrinkling behavior of highly stretched rectangular elastic films via parametric global bifurcation," *J. Nonlinear Sci.*, vol. 23, no. 5, pp. 777–805, Apr. 2013, doi: 10.1007/s00332-013-9168-3.
- [4] Q. Li and T. J. Healey, "Stability boundaries for wrinkling in highly stretched elastic sheets," *J. Mech. Phys. Solids*, vol. 97, pp. 260–274, Dec. 2016, doi: 10.1016/j.jmps.2015.12.001.
- [5] B. Audoly and Y. Pomeau, *Elasticity and Geometry: From hair curls to the non-linear response of shells*, Oxford, U.K.: Oxford Univ. Press, 2010.
- [6] E. Yang, M. Zhang, J. Zeng and F. Tian, "Wrinkling and restabilization of a hyperelastic PDMS membrane at finite strain," *Soft Matter*, vol. 18, no. 29, pp. 5465–5473, Jul. 2022, doi: 10.1039/d2sm00406b

Machine Learning based approach to predict the life of damaged wind turbine blade

Praveen Shakya^a, Umakant Meher^b, Sachin Kumar^c, Danial Arias^d, Abdennour C. Seibi^a, Mohammad A. S. Masoum^d

^a Mechanical & Civil Engineering, Utah Valley University, UT, USA

^b Department of Aerospace Engineering, KIIT Bhubaneswar, India

^c Department of Aerospace Engineering, IIT Kharagpur, India

^d Electrical & Computer Engineering, Utah Valley University, UT, USA

1. INTRODUCTION & OBJECTIVE

With the growing significance of wind energy in sustainable power generation, the ability to accurately predict damage in wind turbine systems has become a critical research focus. Recent advancements have highlighted the potential of machine learning techniques in addressing these challenges, particularly within the wind power sector. Several studies have demonstrated that artificial neural networks (ANNs) and other machine learning (ML) algorithms can effectively model the complex, nonlinear relationships governing turbine behavior and have shown promising results in predicting fatigue loads, remaining life in critical components, such as rotor blades [1-2]. This predictive capability is essential for improving structural reliability, reducing maintenance costs, and extending the operational lifespan of wind turbines. In this study, ML algorithms such as Support Vector Machine (SVM), Random Forest, and XGBoost were implemented to determine the remaining life of the blade in term of number of cycles.

2. METHODS OF ANALYSIS

A small-scale wind turbine blade (Air Silent X) is used to estimate the remaining fatigue life in terms of the number of cycles using ANSYS Workbench. To replicate typical damage observed in operational wind turbine blades, intentional defects such as cracks, surface erosion, and holes are introduced, representing common degradation mechanisms caused by lightning strikes, material failure, and environmental factors such as rain and severe weather conditions. The blade geometry is initially modeled in SolidWorks, and the effects of these anomalies are analyzed using a combination of Computational Fluid Dynamics (CFD) and Finite Element Analysis (FEA). Aerodynamic loads are obtained through CFD simulations conducted in ANSYS FLUENT 22R1, which solves the Reynolds-Averaged Navier–Stokes (RANS) equations closed by the k–ω SST turbulence model to achieve accurate results within practical computational limits. A one-way fluid–structure coupling strategy is adopted, where aerodynamic loads obtained from CFD are mapped as boundary conditions for the structural analysis in FEA. Crack defects are represented as semi-elliptical geometries using the fracture tool in ANSYS Mechanical, and the fatigue life in terms of the number of cycles is evaluated through SMART crack growth analysis. An automation script was developed in ANSYS to generate remaining life data, expressed in terms of the number of cycles, for various crack configurations on the wind turbine blade. This dataset was subsequently utilized for machine learning analysis.

3. RESULTS

A total of 6,500 data points representing the number of cycles were generated at different locations on the Air Silent X blade. For the purpose of this study, the problem is formulated as a classification task by

discretizing the remaining life into predefined cycle ranges; for instance, a cycle range of 0–1000 is assigned the label “1.” Figure 1 illustrates the distribution of the generated remaining life data across these ranges. Machine learning (ML) algorithms, including SVM Random Forest, and XGBoost, were employed to predict the remaining life in terms of the number of cycles. Among these, XGBoost and Random Forest demonstrated the highest predictive performance, achieving an accuracy of 77%. Figure 2 shows the comparison of these three ML algorithms.

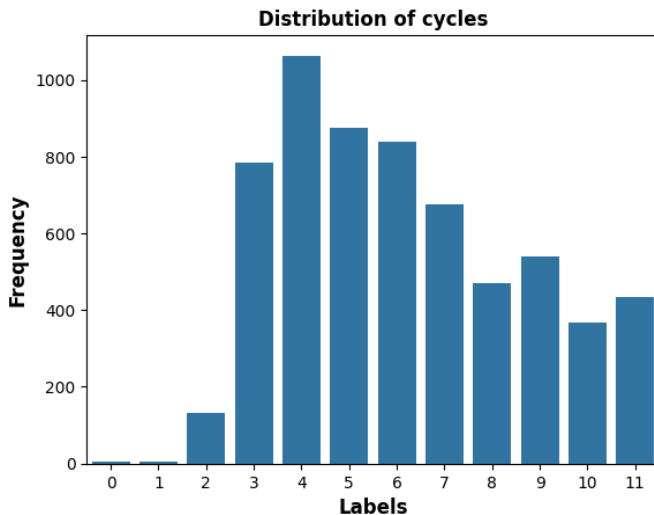


Figure 1 The distribution of remaining life of blade

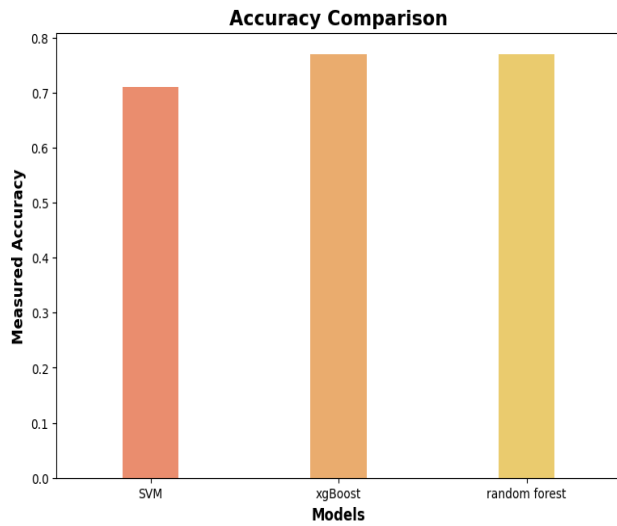


Figure 2 Comparison of ML algorithms

4. CONCLUSION

This study demonstrated an integrated computational framework for predicting the remaining fatigue life of small-scale wind turbine blades with induced damage, combining CFD, FEA, and machine learning techniques. By introducing realistic defect scenarios, including cracks, erosion, and holes, and simulating aerodynamic loads through ANSYS FLUENT coupled with structural responses in ANSYS Mechanical, a comprehensive dataset of 6,500 life cycles was generated. The discretization of fatigue life into classification ranges enabled the application of machine learning algorithms for predictive modeling. Among the tested approaches, Random Forest and XGBoost achieved the highest accuracy of 77%, highlighting their effectiveness in capturing the nonlinear relationships between blade damage and fatigue life.

5. REFERENCES

- [1] Yuan, X., Huang, Q., Song, D., Xia, E., Xiao, Z., Yang, J., Dong, M., Wei, R., Evgeny, S. and Joo, Y.H., 2024. Fatigue Load Modeling of Floating Wind Turbines Based on Vine Copula Theory and Machine Learning. *Journal of Marine Science and Engineering*, 12(8), p.1275.
- [2] Gajendran, M.K., Kabir, I.F.S.A., Vadivelu, S. and Ng, E.Y.K., 2023. Machine learning-based approach to wind turbine wake prediction under yawed Conditions. *Journal of Marine Science and Engineering*, 11(11), p.2111.

Magneto-Stiffening Effects on Beam Vibrations Supported by Winkler Foundation

Lakshita Patil^a and Krishnendu Haldar^{b,*}

^a M.Tech Student, Department of Aerospace Engineering, IIT Bombay, India

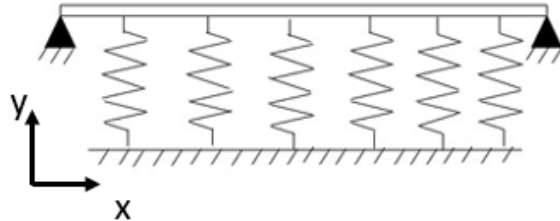
^b Associate Professor, Department of Aerospace Engineering, IIT Bombay, India

1 INTRODUCTION & OBJECTIVE

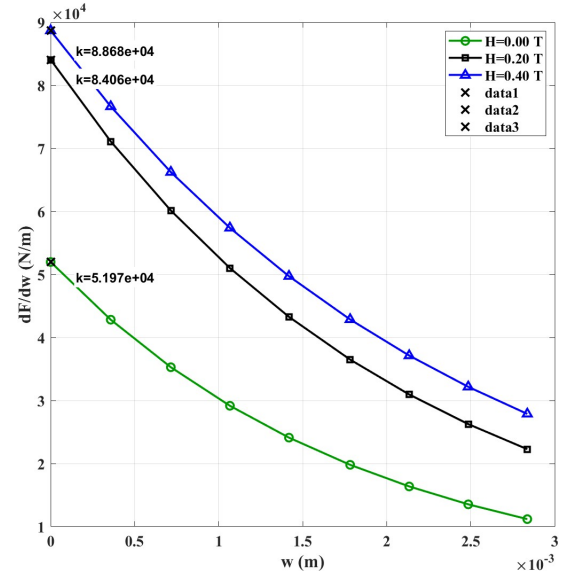
Magnetoactive polymers (MAPs) are smart composites with ferromagnetic particles embedded in a viscoelastic matrix, allowing magnetic-field-induced tuning of stiffness and damping [1]. Experimental studies and modeling of a beam on an elastic foundation showed that magnetic fields alter foundation stiffness, shifting natural frequencies and reducing resonance amplification. Despite challenges such as nonlinear viscoelasticity and integration complexity, MAPs present a lightweight, tunable, and energy-efficient solution for adaptive vibration control in aerospace and precision engineering.

2 METHODS OF ANALYSIS

To model the system dynamics, the beam–foundation interaction was governed by the classical Euler–Bernoulli beam equation with an elastic foundation term, as expressed in Eq. (1) [2]. Here, EI is the flexural rigidity, k_f represents foundation stiffness, which varies with magnetic field.



(a) Beam on winker foundation



(b) Change in stiffness due to magnetic field

Figure 1

$$EI \frac{\partial^4 w}{\partial x^4} + \rho A \frac{\partial^2 w}{\partial t^2} + k_f w = 0 \quad (1), \quad F = A_1 + A_2 e^{H/A_3} + \left(A_4 + A_5 e^{-H/A_6} \right) e^{\frac{w}{A_7 + A_8 e^{-H/A_9}}} \quad (2)$$

Stress-strain curves obtained from controlled loading tests were converted to force-displacement data using specimen geometry [3]. The stiffness variation with displacement and magnetic field is represented by fig 1(b).

The $k-w$ relationship was derived by fitting experimental force–displacement data to a nonlinear analytical model, effectively capturing the material’s magneto-viscoelastic stiffness behaviour and it is given by eq (2).

3 RESULTS AND/OR HIGHLIGHTS OF IMPORTANT POINTS

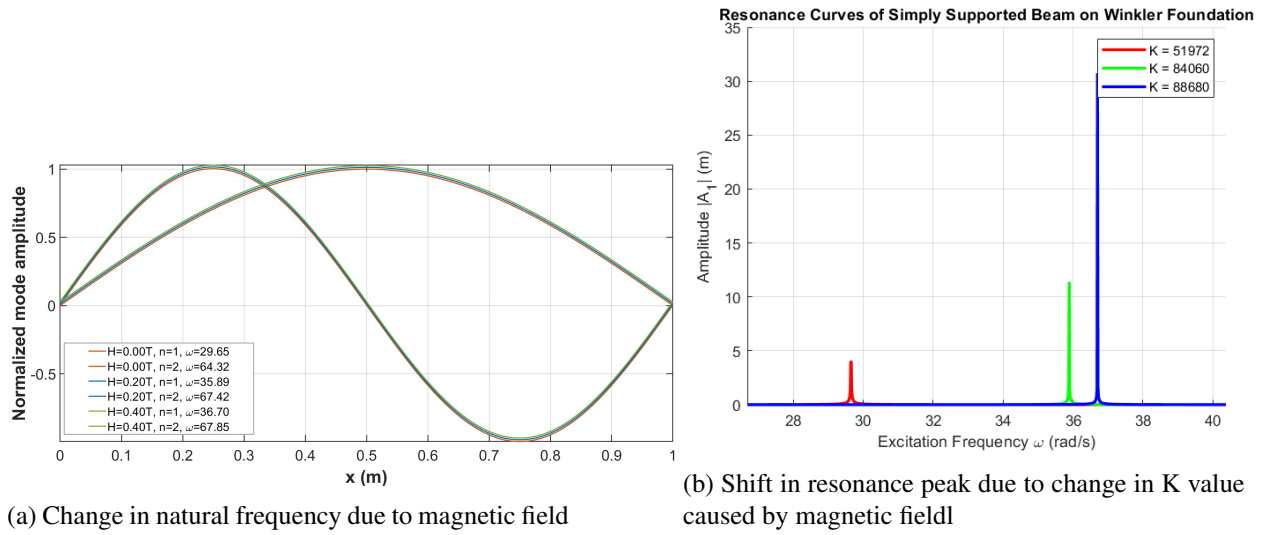


Figure 2

The above figure clearly shows that the natural frequency of the system increases with the enhancement of the magnetic field, indicating a magnetic field–induced stiffening effect due to magneto-mechanical coupling. As the magnetic field intensity increases, the resonance curves shift toward higher frequencies, confirming the tunable stiffness and improved vibration performance of the magnetoactive system.

4 CONCLUSIONS

This study demonstrated the tunable mechanical behavior of magnetoactive polymers (MAPs) under the influence of an external magnetic field. The analysis showed a clear shift in resonance frequency and variation in stiffness with increasing magnetic field strength, confirming the magneto-mechanical coupling effect. These results indicate that MAPs can effectively alter their stiffness and natural frequency through magnetic control, showing strong potential for future vibration isolation applications.

References

- [1] T. A. Nadzharyan et al., "Theoretical Modeling of Magnetoactive Elastomers on Mesoscopic Level and Its Numerical Realization," *Polymers*, vol. 14, no. 19, p. 4096, Sep. 2022, doi: 10.3390/polym14194096.
- [2] S. S. Rao, *Mechanical Vibrations*, 5th ed. Upper Saddle River, NJ: Pearson Prentice Hall, 2011.
- [3] A. Garai and K. Haldar, "Experiments and modeling of magneto-stiffening effects for magnetoactive polymer," *International Journal of Mechanical Sciences*, vol. 286, p. 109860, 2025, doi:10.1016/j.ijmecsci.2024.109860.

* Communicating Author: Krishnendu Halder, krishnendu@aero.iitb.ac.in

Micromechanical Homogenization and Electromagnetic Characterization of Radar Absorbing Materials using Multiphysics Simulation

Omkar Bilawar^a and Krishnendu Haldar^b

^a M.Tech Student, Department of Aerospace Engineering, IIT Bombay, India

^b Associate Professor, Department of Aerospace Engineering, IIT Bombay, India

1. INTRODUCTION & OBJECTIVE

Radar absorbing materials (RAM) play a crucial role in stealth technology by reducing the radar cross-section of platforms. Accurate prediction of their effective electromagnetic and mechanical properties from microstructural characteristics is essential for material design. This work presents a comprehensive multiphysics framework implemented in COMSOL Multiphysics for micromechanical homogenization of composite RAMs, facilitating the calculation of homogenized permittivity, permeability, and conductivity. The framework extends conventional homogenization theory to coupled electromagnetic-mechanical fields, enabling simultaneous characterization of stiffness and absorption properties. The simulated results are validated with classical mixing rules and extended to radar cross-section analysis, aiming to evaluate stealth performance and material stability under operational conditions.

2. METHODS OF ANALYSIS

Representative volume elements (RVEs) with spherical inclusions in a cubic matrix are modeled to capture heterogeneous RAM microstructures. Multiphysics simulations couple Solid Mechanics with Electrostatics and Magnetic Fields, using periodic boundary conditions to extract effective tensors. The deformation gradient is $\mathbf{F} = \mathbf{I} + \nabla \mathbf{u}$, and the homogenized elasticity tensor \mathbf{C}^{eff} is obtained from volume-averaged stress-strain relations.[2]

$$\langle \boldsymbol{\sigma} \rangle = \mathbf{C}^{\text{eff}} : \langle \boldsymbol{\varepsilon} \rangle \quad (1)$$

Similarly, effective permittivity ϵ_r^{eff} , permeability μ_r^{eff} , and conductivity σ^{eff} are determined from:

$$\langle \mathbf{D} \rangle = \epsilon_0 \epsilon_r^{\text{eff}} \langle \mathbf{E} \rangle, \quad \langle \mathbf{B} \rangle = \mu_0 \mu_r^{\text{eff}} \langle \mathbf{H} \rangle, \quad \langle \mathbf{J} \rangle = \sigma^{\text{eff}} \langle \mathbf{E} \rangle \quad (2)$$

where angle brackets denote volume averaging over the RVE. The computed effective properties are then used in full-wave electromagnetic simulations to evaluate radar cross-section (RCS) and reflection loss performance.[1] The reflection coefficient Γ for normal incidence is calculated as:

$$\Gamma = \frac{Z_s - Z_0}{Z_s + Z_0}, \quad \text{RL(dB)} = 20 \log_{10} |\Gamma| \quad (3)$$

where $Z_s = \sqrt{\mu_r^{\text{eff}} / \epsilon_r^{\text{eff}}} Z_0$ is the surface impedance and Z_0 is the free space impedance.

3. RESULTS AND DISCUSSION

The numerical homogenization framework predicts elastic moduli and electromagnetic properties as functions of inclusion volume fraction v_f and material contrasts. For spherical inclusions[3], the bulk modulus follows Hashin-Shtrikman bounds, while electromagnetic properties align with classical mixing formulations.[4]

$$\sigma^{\text{eff}} = \sigma_m \frac{\sigma_i + 2\sigma_m + 2v_f(\sigma_i - \sigma_m)}{\sigma_i + 2\sigma_m - v_f(\sigma_i - \sigma_m)} \quad (4)$$

where σ_m and σ_i are matrix and inclusion conductivities, respectively based on MG method. A multi-physics simulation framework has been developed to calculate the radar cross-section (RCS) and reflection loss of composite radar absorbing materials. The simulation requires three fundamental effective material properties—permittivity, permeability, and conductivity—computed using Numerical solutions and validated against classical analytical models.

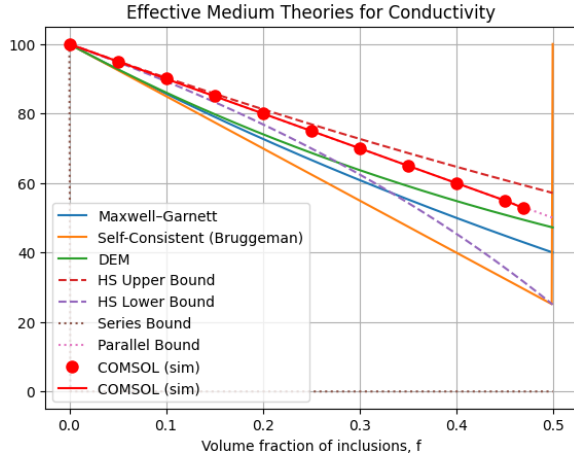


Figure 1: Effective Conductivity vs. inclusion volume fraction

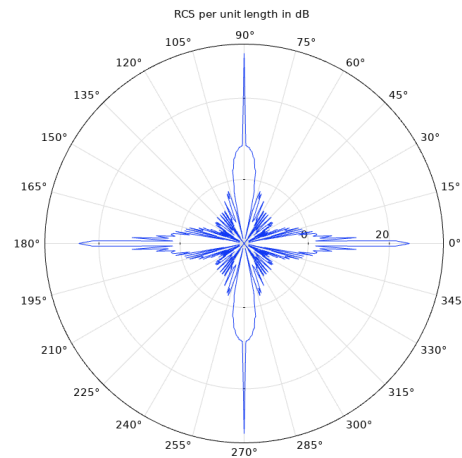


Figure 2: Bistatic RCS variation

Bistatic RCS calculations demonstrate angular stability across various incidence angles.[5] The impedance matching condition enables effective electromagnetic wave absorption, resulting in minimal reflection. The integrated approach enables rational RAM design tailored for stealth applications while ensuring structural reliability.

4. CONCLUSIONS

A periodic homogenization framework in COMSOL accurately captures coupled electromagnetic–mechanical behavior and predicts RAM performance. The approach bridges microscale heterogeneity to macroscale properties and demonstrates significant RCS reduction and reflection loss capabilities. Future work will extend this framework to include thermal and mechanical stability analyses, optimize material configurations for enhanced stealth performance, and validate the predictions through experimental measurements.

REFERENCES

- [1] R. K. Gupta and T. A. Venkatesh, “Electromechanical response of 1-3 piezoelectric composites: Effect of poling characteristics,” *J. Appl. Phys.*, vol. 98, no. 5, p. 054102, 2005.
- [2] COMSOL Multiphysics, “Micromechanical Model of a Particulate Composite,” Application Library, Structural Mechanics Module, 2023.
- [3] J. C. Maxwell, “A Treatise on Electricity and Magnetism,” Clarendon Press, Oxford, 1873.
- [4] Z. Hashin and S. Shtrikman, “A variational approach to the theory of the elastic behaviour of multi-phase materials,” *J. Mech. Phys. Solids*, vol. 11, no. 2, pp. 127–140, 1963.
- [5] E. F. Knott, J. F. Shaeffer, and M. T. Tuley, “Radar Cross Section,” 2nd ed., Artech House, Norwood, MA, 1993.

* Corresponding Author: Prof. Krishnendu Haldar, krishtnendu@aero.iitb.ac.in

Microstretch Continuum Theory Modeling for Nematic Liquid Crystalline Elastomers: Interplay Between Non-Affinity and Director Stretch

Ms. Aishwarya Kasarla^a and Prof. Krishnendu Haldar^{b,*}

^a Ph.D. Scholar, Department of Aerospace Engineering, Indian Institute of Technology, Bombay, India

^b Associate Professor, Department of Aerospace Engineering, Indian Institute of Technology, Bombay, India

1. INTRODUCTION & OBJECTIVE

Nematic Liquid Crystalline Elastomers (LCEs) are soft, anisotropic solids that exhibit the remarkable ability to undergo large, reversible deformations due to the coupling between polymer network elasticity and the orientational order of mesogenic units. This coupling results in unique phenomena such as spontaneous strain, soft elasticity, and reversible shape transformations, enabling a wide range of applications in soft robotics, artificial muscles, and adaptive optical devices.

Classical models—such as the Warner–Terentjev neo-classical theory and its subsequent continuum extensions—capture the fundamental order–mechanical coupling but typically assume affine chain distribution and inextensible directors. However, experimental studies have revealed that real networks exhibit non-affine molecular rearrangements (1; 2) and finite director stretch, both of which strongly influence macroscopic elasticity and soft modes of the elastomer.

The present work aims to develop a microstretch continuum framework for LCEs that integrates these two critical mechanisms—non-affinity and director stretch—into a unified thermodynamically consistent formulation. The objective is to explore and interpret how microscopic chain-level non-affinity and director extensibility together dictate the macroscopic mechanical response and anisotropy of nematic elastomers.

2. METHODS OF ANALYSIS

Building upon the non-affine network theory of Mao et al. (1998) (3), the polymer network is modeled as a collection of chains comprising N freely jointed rod-like segments of length a oriented along local director $\Xi = |\Xi|\bar{\Xi}$. The end-to-end vector of a chain transforms under deformation as

$$\mathbf{r} = \mathbf{F}\mathbf{R} + \gamma(\mathbf{F}\Xi - \xi).$$

where \mathbf{F} is the deformation gradient, ξ is the current director, and γ quantifies the non-affine coupling between the macroscopic deformation and local chain orientation. The entropic free energy of the network, derived from the mean-field probability distribution of chain configurations, is expressed as:

$$\begin{aligned} \psi_{\text{entropic}} = -k_B T < \ln P(\mathbf{r}) >_{P_0(\mathbf{R})} &= \frac{\mu}{2} \{ \text{Tr}(\tilde{\mathbf{l}}_0 \mathbf{F}^t \tilde{\mathbf{l}}^{-1} \mathbf{F}) - \ln \det(\tilde{\mathbf{l}}^{-1} \tilde{\mathbf{l}}_0) \\ &+ \chi \text{Tr}(\tilde{\mathbf{l}}^{-1} (\mathbf{F}\Xi \otimes \mathbf{F}\Xi)) + \chi \text{Tr}(\tilde{\mathbf{l}}^{-1} (\xi \otimes \xi)) \\ &- 2\chi \text{Tr}(\tilde{\mathbf{l}}^{-1} (\mathbf{F}\Xi \otimes \xi)) - 3 \}, \end{aligned}$$

where $\chi = \frac{3\gamma^2}{2}$.

In addition to this modified elastic energy, we define the semi-soft energy ($\psi_{\text{semi-soft}}$) to compensate for the director rotation and also the penalty for microstretching ($\psi_{\text{microstretching}}$), these are given as

$$\psi_{\text{semi-soft}} = \frac{\alpha\mu}{2} \text{Tr}[(\mathbf{I} - \Xi \otimes \Xi) \mathbf{F}^t \bar{\xi} \otimes \bar{\xi} \mathbf{F}], \quad \text{and} \quad \psi_{\text{stretching penalty}} = \frac{\kappa_j}{2} \left(\ln \frac{|\xi|}{|\Xi|} \right)^2.$$

3. RESULTS AND/OR HIGHLIGHTS OF IMPORTANT POINTS

The model is applied for the simple case of uniaxial stretching with $F = \text{diag}[\lambda, \lambda_1, 1/(\lambda\lambda_1)]$. The results below show stress-stretch response and final director orientation vs stretch plots for the initial director being oriented at an angle $\theta = 75^\circ$ with respect to the stretching axis.

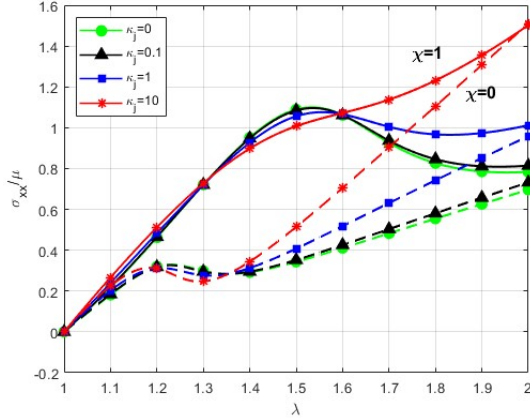


Figure 1: Stress vs stretch for $\theta = 75^\circ$,
 $\alpha = 0.1$.

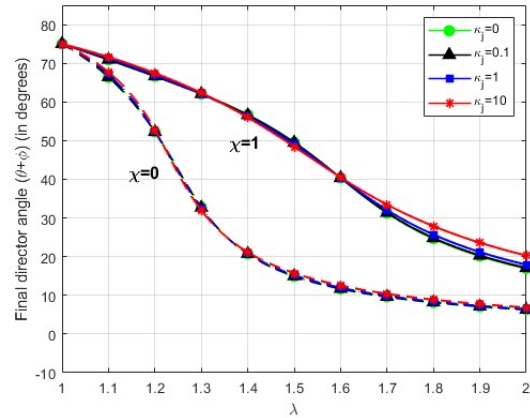


Figure 2: $\theta + \phi$ for $\theta = 75^\circ$,
 $\alpha = 0.1$.

We observe that increasing χ strengthens the coupling between macroscopic deformation and director alignment. Moderate χ facilitates director reorientation, producing soft elastic plateaus, while larger χ suppresses reorientation, yielding stiffer responses. The predicted stress–stretch curves show strong dependence on the initial director angle, consistent with experimental observations of anisotropic elasticity.

4. CONCLUSIONS

A thermodynamically consistent microstretch continuum model has been developed to describe nematic elastomers with stretchable directors and non-affine network deformation. The study reveals that:

- The non-affinity parameter χ governs the energetic interaction between deformation and director reorientation, dictating the transition from soft to stiff response regimes.
- The director-stretch stiffness κ_j regulates the ease of director magnitude variation, controlling the emergence of soft deformation modes.

The proposed framework provides a physical and computational bridge between microstructural mechanisms and macroscopic response.

5. REFERENCES

- [1] A. Basu, Q. Wen, X. Mao, T. Lubensky, P. A. Janmey, and A. Yodh, “Nonaffine displacements in flexible polymer networks,” *Macromolecules*, vol. 44, no. 6, pp. 1671–1679, 2011.
- [2] S. C. Lamont and F. J. Vernerey, “Generalized continuum theory for nematic elastomers: Non-affine motion and characteristic behavior,” *Journal of the Mechanics and Physics of Solids*, vol. 190, p. 105718, 2024.
- [3] Y. Mao, M. Warner, E. M. Terentjev, and R. Ball, “Finite extensibility effects in nematic elastomers,” *The Journal of chemical physics*, vol. 108, no. 20, pp. 8743–8748, 1998.

* Communicating Author: Prof. Krishnendu Haldar, Contact: krishnendu@aero.iitb.ac.in

Mobile Anti-Drone System: A SDR Approach for Defensive Disruption of UAVs

Patel Namra¹, Ajit Kumar^{1*} and Jagat Rath²

¹Institute of Infrastructure, Technology, Research and Management (IITRAM) Ahmedabad, India-380026

²Motilal Nehru National Institute of Technology Allahabad, Prayagraj, India-211004

1. INTRODUCTION & OBJECTIVE

The rapid proliferation of unmanned aerial systems (UAS) has increased the risk they pose to critical infrastructure, mass gatherings, and sensitive operations, motivating modern defensive countermeasures that combine sensing and targeted interruption. Prior work has examined electronic warfare and cyberattack vectors against UAV avionics, GPS jamming/spoofing methods, and experimental neutralization techniques.[1] This compact study presents a mobile, defensive anti-drone system that integrates real-time spectrum monitoring with selective disruption using software-defined radios (SDRs). The platform is explicitly designed for defensive use: to detect and classify suspicious ArduPilot/Pixhawk-based UAV activity originating from a ground control station (GCS), and to interrupt hostile links while minimizing collateral impact and indiscriminate RF interference. This work builds on SDR-based anti-UAV approaches reported in the literature. [2-4]

Objectives:

- (i) Evaluate observable system-level disruption effects on a Pixhawk/ArduPilot quadcopter using a mobile SDR-based defensive platform.
- (ii) Characterize UAV and autopilot behaviors and failure modes under targeted disruption (communications and/or GNSS degradation).

2. METHODS OF ANALYSIS

The test system used two HackRF SDRs and a single-board computer controlling the mobile platform. One HackRF was dedicated to continuous spectrum monitoring and waterfall visualization; the second HackRF served as the transmitter for producing the disruptive RF energy. The UAV under test was a quadcopter equipped with a Pixhawk flight controller running ArduPilot; the telemetry link operated at 433 MHz and the autopilot was connected to a laptop running the ArduPilot ground station software.

2.1 Experiment procedure: Each trial followed a simple structure: verify baseline operation and stable telemetry/command link, enable the monitoring/tracking chain, perform a disruption attempt by transmitting the noise signals through SDR, and record the autopilot and ground-station logs during and after the event. The ground station (laptop) and on-board logs captured messages and status changes; additionally, spectrum waterfall captures, and a demonstration video were recorded for post-analysis.

2.2 Outcome metrics - We captured and annotated occurrences of (a) loss of telemetry, (b) loss of manual command/arming capability, and (c) autopilot fail-safe behaviors. Observations were made from on-board flight logs and the ArduPilot ground-station console.

3. RESULTS / HIGHLIGHTS OF IMPORTANT POINTS

Primary observations - When the disruptive transmitter was active under the tested conditions, the ArduPilot (ground station) console's reported “**No response from MAV**”. At the same time, attempts to issue the arm command from the ground station did not succeed (the vehicle did not arm). These effects were reproducibly observed in the conducted trials under the controlled conditions noted above.

The demonstrable outcomes were (i) transient or sustained loss of telemetry as observed on the ground-station console, and (ii) inability to arm the motors via the ground station during the disruption interval. In multiple demonstration runs these behaviors were consistent with an interruption of the vehicle’s command/telemetry link; the quadcopter responded according to its configured fail-safe policy once nominal conditions were restored. Exact figures for trial counts and time-to-effect may be included in a full-length manuscript. The experimental process is visually documented in Figures 1 and 2.

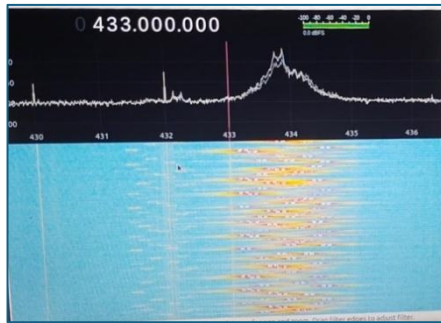


Figure 1: Baseline spectrum at 433 MHz with no active SDR transmission.

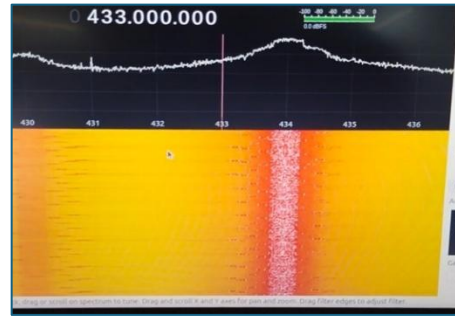


Figure 2: The disruptive signal from the SDR overpowering the 433 MHz band.

A recorded demonstration video was recorded during the experiments and illustrated the spectrum activity and ground-station messages contemporaneous with the observed vehicle responses. These files are available as supplementary material for reviewers (or upon request to the corresponding author under appropriate controls).

4. CONCLUSIONS

This experimental evaluation shows that, under controlled test conditions and using SDR hardware, it is possible to produce effective disruption of telemetry and command pathways for a Pixhawk/ArduPilot quadcopter using a 433 MHz telemetry link. The ground station reported loss of connection (“**No response from MAV**”), and the vehicle did not accept arm commands during the disruption intervals. Future work should emphasize detection mechanisms, GPS spoofing & command replay attacks.

5. REFERENCES

- [1]. Yu, Aaron, et al. "Electronic Warfare Cyberattacks, Countermeasures and Modern Defensive Strategies of UAV Avionics: A Survey." *IEEE Access* (2025).
- [2]. Ferreira, Renato, et al. "Effective GPS jamming techniques for UAVs using low-cost SDR platforms." *Wireless Personal Communications* 115.4 (2020): 2705-2727.
- [3]. Zidane, Younes, José Silvestre Silva, and Gonçalo Tavares. "Jamming and spoofing techniques for drone neutralization: An experimental study." *Drones* 8.12 (2024): 743.
- [4]. Ferreira, Renato, et al. "A software defined radio based anti-UAV mobile system with jamming and spoofing capabilities." *Sensors* 22.4 (2022): 1487.

Corresponding Author: Ajit Kumar (ajit.aiitk@gmail.com)

Model Order Reduction for Cerebrovascular Hemodynamics: A POD–Galerkin and Hybrid Physics-Informed Approach

Rahul Halder, Arash Hajisarifi, Kabir Bakhshaei, Gianluigi Rozza

Mathematics Area, mathLab, SISSA, via Bonomea 265, I-34136 Trieste, Italy

INTRODUCTION & OBJECTIVE: High-fidelity patient-specific simulation of cerebrovascular flow is important for the risk assessment of cerebral diseases such as aneurysm growth or rupture. However, it remains computationally expensive for parametric studies and real-time analysis. We propose two reduced-order frameworks: (i) a Proper Orthogonal Decomposition (POD) with a Galerkin projection-based approach, and (ii) a hybrid scheme that combines POD-Galerkin projection of the incompressible Navier-Stokes equations with a reservoir-computing (RC) framework [1] those leverages reduced-order physics as a residual. The RC network requires minimal training compared to traditional deep neural networks, since only the output layer is trained whereas the internal reservoir dynamics are kept fixed. We demonstrate accurate velocity reconstructions and error fields on a cerebrovascular system, demonstrating near real-time (first approach) and real-time (second approach) flow-field prediction suitable for hemodynamic analysis.

(a) Governing Equations: On a vascular domain $\Omega \subset \mathbb{R}^3$ with boundary conditions for velocity (\mathbf{u}) and pressure (p), kinematic viscosity, ν the dynamics satisfy:

$$\frac{\partial \mathbf{u}}{\partial t} + (\mathbf{u} \cdot \nabla) \mathbf{u} = -\nabla p + \nu \nabla^2 \mathbf{u}, \quad \nabla \cdot \mathbf{u} = 0.$$

We have assumed time-varying inlet boundary conditions and stress-free outlet conditions. For this proof of concept, we have adopted a simplified laminar Newtonian model with generic outlets. However, turbulence, non-Newtonian rheology, and time-varying pressure outlets (Bakhshaei et al. [2]) should be considered as future extensions of the present work.

(b) Reduced Order Modelling: The key concept behind reduced-order modelling is to find a spatial basis that spans a subspace \mathcal{S} to express the state vectors (velocity, pressure, etc.) in full-order. N_u and N_p denote the retained velocity and pressure modes considered for the POD-Galerkin projection of the Navier-Stokes equations. The velocity (\mathbf{u}) and pressure (p) fields can be approximated as:

$$\mathbf{u}(\mathbf{x}, t) \approx \sum_{i=1}^{N_u} \boldsymbol{\varphi}_i(\mathbf{x}) a_i(t), \quad p(\mathbf{x}, t) \approx \sum_{j=1}^{N_p} \chi_j(\mathbf{x}) b_j(t).$$

The optimal POD basis space for velocity, $E_u^{\text{POD}} = [\boldsymbol{\varphi}_1, \boldsymbol{\varphi}_2, \dots, \boldsymbol{\varphi}_{N_u}]$, is constructed by minimizing the difference between the snapshots and their orthogonal projection onto the basis in the L^2 norm:

$$E_u^{\text{POD}} = \arg \min_{\boldsymbol{\varphi}_1, \dots, \boldsymbol{\varphi}_{N_u}} \frac{1}{N_s^u} \sum_{n=1}^{N_s^u} \left\| \mathbf{u}(\mathbf{x}, t_n) - \sum_{i=1}^{N_u} (\mathbf{u}(\mathbf{x}, t_n), \boldsymbol{\varphi}_i(\mathbf{x}))_{L^2(\Omega)} \boldsymbol{\varphi}_i(\mathbf{x}) \right\|_{L^2(\Omega)}^2,$$

with L^2 orthonormal modes $(\boldsymbol{\varphi}_i, \boldsymbol{\varphi}_j) = \delta_{ij}$. N_s^u are total number of snapshots collected. Galerkin projection of [1] yields the following Ordinary Differential Equation (ODE).

$$\begin{aligned} M_r \dot{a} + C_r(a)a - \nu A_r a + B_r b &= f_r(t) \\ D_r b + G_r(a)a - \nu N_r a - T_r \dot{a} &= 0 \end{aligned}.$$

Where, $M_r, A_r, C_r, B_r, D_r, G_r, N_r$ and T_r are reduced operators computed from the governing equations and POD modes. f_r encodes boundary/forcing effects. The details of the approach can be found in [3] and [4].

(b.1) Hybrid reservoir-augmented ROM

Although the POD-Galerkin ROM provides an accurate representation of the governing physics, prediction of the flow physics at a new parameter or input is not real-time; As the number of pressure and velocity modes increases, the degrees of freedom associated with the reduced order system increases and thereby increasing the computational time. Therefore, we propose a physics-informed computing framework for real-time analysis of velocity and pressure fields at any prescribed inlet boundary conditions. The reservoir state is updated using this relationship: $\mathbf{r}_{k+1} = (1 - \alpha)\mathbf{r}_k + \alpha \operatorname{tanh}(W_{\text{in}} f_k + W\mathbf{r}_k)$, and we train only a linear readout $a_k = W_{\text{out}} \mathbf{r}_k + \mathbf{b}$ considering ridge regression. W , W_{in} and W_{out} are the weight matrices.

(c) Results: We evaluate cerebrovascular system with pulsatile inflows. Training is carried out using a multi-harmonic signal at the input boundary. A sinusoidal input is used with a mean flow of 0.2 m/s, amplitude of 0.04 m/s, and frequency of 0.4 Hz over 0 to 10s for testing. The fluid viscosity is 0.0035 Pa·s. 3 pressure modes, and 3 velocity modes are considered here for the development of reduced order system. Fig: 1 shows the velocity fields at the maximum amplitude location of the test signal using the POD-Galerkin projection-based approach.

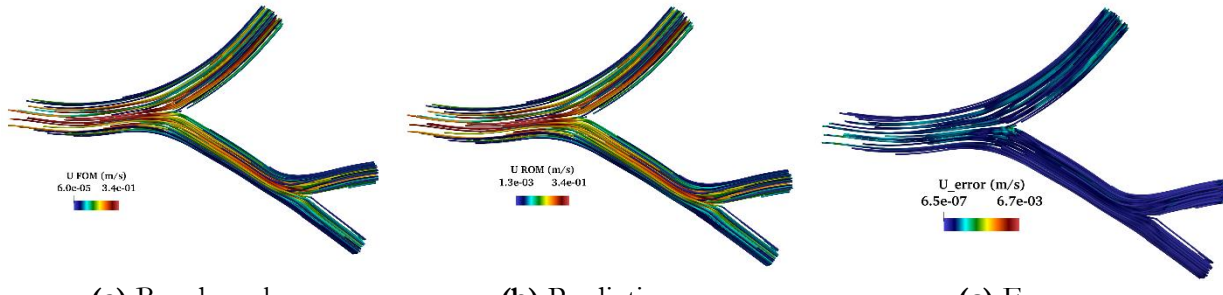


Fig: 1 Velocity fields (benchmark vs. prediction) and absolute errors on a representative time instant of 3.12 s.

(d) Conclusion:

We have shown that the POD-Galerkin projection-based model order reduction enables accurate prediction of unsteady velocity and pressure fields of cerebrovascular hemodynamics. The results of the hybrid extension: coupling the reduced-order physics with a reservoir computing framework will be presented in the full paper.

*Communicating Author: Rahul Halder (rhalder@sissa.it)

References:

- [1] Arash Hajisharifi, Michele Girfoglio, Annalisa Quaini, and Gianluigi Rozza. Combining extended convolutional autoencoders and reservoir computing for accurate reduced-order predictions of atmospheric flows. arXiv preprint arXiv:2504.01097, 2025.
- [2] Kabir Bakhshaei, Sajad Salavatidezfouli, Giovanni Stabile, and Gianluigi Rozza. Stochastic parameter prediction in cardiovascular problems. Computer Methods in Biomechanics and Biomedical Engineering, pages 1–25, 2025.
- [3] Rahul Halder, Giovanni Stabile, and Gianluigi Rozza. Coupling physics informed neural networks with external solvers. arXiv preprint arXiv:2509.24615, 2025.
- [4] S Kelbij Star, Giovanni Stabile, Francesco Belloni, Gianluigi Rozza, and Joris Degroote. A novel iterative penalty method to enforce boundary conditions in finite volume POD-Galerkin reduced order models for fluid dynamics problems. arXiv preprint arXiv:1912.00825, 2019.

Model-Less Feedback Control of Space-based Continuum Manipulators using Backbone Tension Optimization

Shrreya Rajneesh*, Nikita Pavle*, Rakesh Sahoo†, Prof. Manoranjan Sinha‡

* Undergraduate Student, Department of Aerospace Engineering, Indian Institute of Technology Kharagpur, West Bengal, 721302, India

† PhD Research Scholar, Department of Aerospace Engineering, Indian Institute of Technology Kharagpur, West Bengal, 721302, India

‡ Professor, Department of Aerospace Engineering, Indian Institute of Technology Kharagpur, West Bengal, 721302, India

Abstract— Continuum manipulators represent a class of robots with infinite degrees of freedom, deriving flexibility from continuous deformation across their entire structure. Inspired by biological systems such as octopus tentacles or elephant trunks, these manipulators hold promise in navigating confined environments. This work presents a novel framework for space applications, integrating model-less feedback control with a backbone tension optimization strategy. By unifying opposing tendon forces through a backbone tension function, we address limitations of traditional rigid manipulators in microgravity, enhancing stability, efficiency, and robustness in constrained orbital environments. Experimental validation demonstrates improved trajectory tracking, reduced tendon co-activation, and stable Jacobian estimation under dynamic constraints.

I. INTRODUCTION

Continuum manipulators provide unique advantages in traversing constrained environments by continuously bending and conforming to complex geometries. Unlike traditional rigid manipulators, they enable safe navigation in cluttered workspaces [1]. In space exploration, robotic arms such as the Canadarm2 excel in large-scale operations but struggle in precision tasks within confined geometries due to limited flexibility and large reaction forces from center-of-mass shifts in microgravity, which destabilize spacecraft attitude and demand continuous thrust correction. These drawbacks hinder critical operations such as satellite solar panel repair and deep-space probe maintenance. By contrast, the continuous structure of continuum manipulators, with their infinite degrees of freedom, allows complex maneuvers that rigid-link robots cannot achieve, reducing mechanical stress on both the manipulator and surrounding structures. This makes them ideal for delicate repairs and assembly tasks in unpredictable and constrained environments of space missions. Previous studies have shown that tendon-driven continuum robots can maintain effective path-following motions under extensibility and environmental constraints [3], while model-less feedback strategies offer robustness in uncertain or constrained conditions [2], highlighting their potential to enhance mission safety and success in long-duration space operations.

II. OBJECTIVE AND METHODOLOGY

We propose the use of continuum manipulators with a *model-less feedback control* strategy [1], [2], coupled with a unified backbone tension function

$$T_{\text{backbone}} = f(T_{\text{left}}, T_{\text{right}}),$$

to coordinate antagonistic tendon forces. Instead of relying on pre-programmed kinematic models, our approach empirically estimates the Jacobian from real-time sensor feedback, ensuring robustness against environmental uncertainties in space such as thermal cycling, radiation, material degradation, and vacuum effects. This strategy minimizes tendon co-activation, reduces axial compression, and enables smooth trajectory execution. The backbone tension optimization is formulated as

$$\min_{\Delta y} \|\tau + \Delta\tau\|_2, \quad (1)$$

$$\text{subject to } \Delta\tau = K\Delta y, \quad \tau + \Delta\tau \geq \epsilon, \quad (2)$$

while the Jacobian update follows

$$\hat{J}_{k+1} = \hat{J}_k + \Delta\hat{J}, \quad (3)$$

$$\min \|\Delta\hat{J}\|_F \text{ subject to displacement constraints.} \quad (4)$$

Together, these mechanisms ensure stable and efficient operation under uncertain, space-induced conditions.

III. RESULTS AND DISCUSSION

Experimental validation confirms improvements in trajectory tracking accuracy and operational stability. Tip trajectories under tension management followed predefined paths with high precision, while tendon tensions remained within safety bounds. The unified backbone tension function reduced co-activation, prevented buckling under thermal cycling, and enhanced stability.

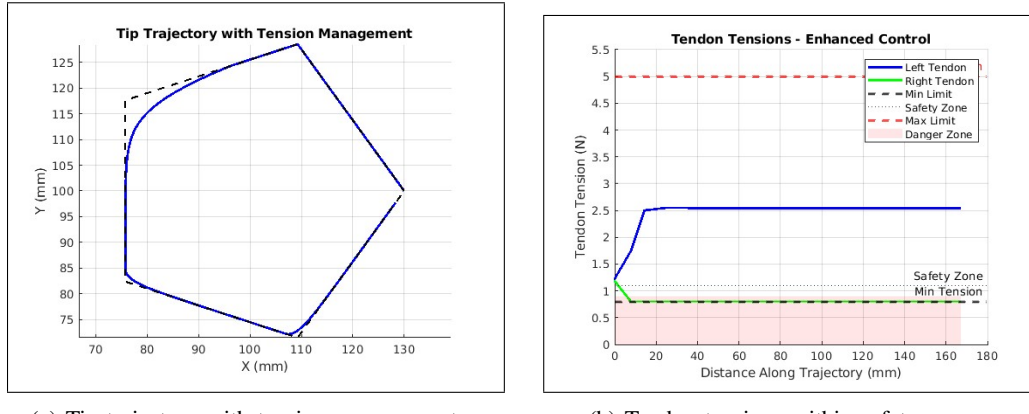


Fig. 1: Trajectory tracking and tendon tension profiles under backbone tension optimization.

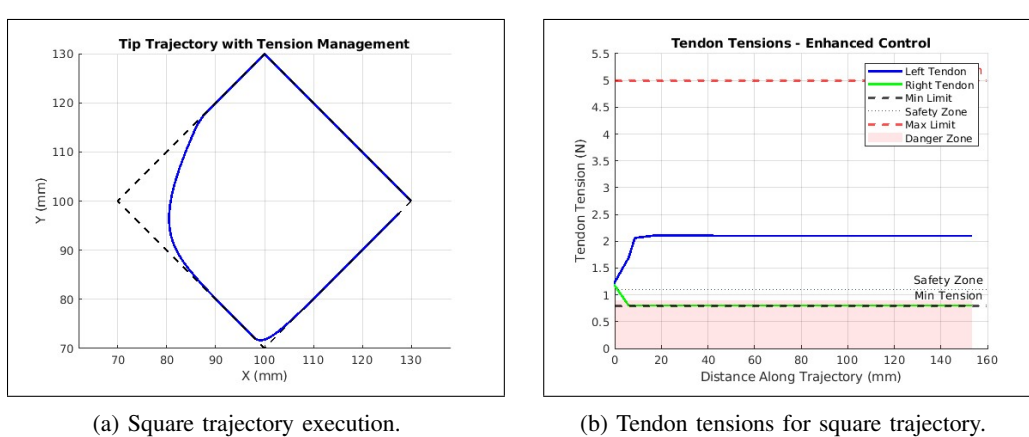


Fig. 2: Square trajectory tracking and tendon tension regulation.

Figure 1 and Figure 2 confirm that consistent tendon tension profiles validate backbone tension optimization. Testing across geometric paths (square, circular, and pentagon) demonstrated robustness in executing both sharp transitions and smooth curvature motions, highlighting versatility for space maintenance tasks such as docking or satellite repair.

IV. CONCLUSION

This study demonstrates the feasibility of model-less feedback control with backbone tension optimization for continuum manipulators in space operations. The proposed framework ensures stable, efficient, and resilient performance in microgravity without reliance on detailed kinematic models. Experimental validation confirmed superior trajectory tracking, optimal tension management, and reliable Jacobian estimation under uncertain conditions, making the approach particularly suitable for long-duration missions. By reducing power consumption, enhancing structural integrity, and improving operational smoothness, this work represents a step forward in continuum manipulator control. Future efforts will extend the framework to full 3D operations and integrate advanced sensing for greater autonomy in complex space environments.

REFERENCES

- [1] M. C. Yip and D. B. Camarillo, "Model-Less Feedback Control of Continuum Manipulators in Constrained Environments," *IEEE Transactions on Robotics*, vol. 30, no. 4, pp. 880–889, Aug. 2014. doi:10.1109/TRO.2014.2309194.
- [2] M. C. Yip and D. B. Camarillo, "Model-Less Hybrid Position/Force Control: A Minimalist Approach for Continuum Manipulators in Unknown, Constrained Environments," *IEEE Robotics and Automation Letters*, vol. 1, no. 2, pp. 844–851, July 2016. doi:10.1109/LRA.2016.2526062.
- [3] E. Amanov, T.-D. Nguyen, and J. Burgner-Kahrs, "Tendon-driven continuum robots with extensible sections—A model-based evaluation of path-following motions," *International Journal of Robotics Research*, vol. 40, no. 2-3, pp. 7–23, 2021.

Morphological Effects of Friction Modifiers for Railway Applications: Binder vs Solid Lubricant

Kushan D S^a, G S P J Ronith^{b*}, Shreedhar Sahoo^c, Mayank Kumar^a, and Vikranth Racherla^d

^aProject Officer, Centre for Railway Research, Indian Institute of Technology Kharagpur, Kharagpur, India

^bBTech Student, Department of Ocean Engineering and Naval Architecture, Indian Institute of Technology Kharagpur, Kharagpur, India

^cPhD Research Scholar, Department of Mechanical Engineering, Indian Institute of Technology Kharagpur, Kharagpur, India

^dProfessor, Department of Mechanical Engineering, Indian Institute of Technology Kharagpur, Kharagpur, India

1. INTRODUCTION

Wheel–rail interaction in railways plays a vital role in maintaining ride safety. Surface problems like corrugation, wear, and other degradations can create serious risks. The controlled application of friction modifiers (FMs) provides an effective solution by reducing wear, lowering curve-induced squeal noise, and optimizing the coefficient of friction (CoF).

Different rail sections require specific CoF levels. For straight tracks, a CoF of about 0.3–0.4 at the top-of-rail (TOR) ensures effective braking and traction, while curved segments demand a lower CoF of nearly 0.2 at the gauge face (GF) or wheel flange contact to reduce wear [1]. Moreover, FMs help establish favorable frictional conditions, essential for controlling the squealing noise caused by lateral creepage.

Extensive studies on friction modifiers (FMs) have primarily examined the role of top-of-rail (TOR) applications in reducing wheel–rail wear, limiting rolling contact fatigue (RCF) crack growth, suppressing plastic flow, and mitigating curve-induced squealing noise. TOR FMs have also proven effective in lowering and stabilizing the coefficient of friction. Nonetheless, research on water-based FMs—especially those investigated through ball-on-disk experimental methods remains relatively scarce.

The novelty of this study lies in introducing a new approach to evaluating binder and solid lubricant FMs and their influence on the wear mechanism using ball-on-disk experiments combined with scanning electron microscopy. The effects of binder and solid lubricant FM constituents were assessed using a tungsten carbide ball and a disk fabricated from rail-grade material. Post-experiment, worn samples were examined under a scanning electron microscope (SEM) to observe FM deposition and wear mechanism, with the impact of wear on elemental distribution using Energy Dispersive X-Ray Spectroscopy (EDX).

2. MATERIALS AND METHOD

This study investigates water-based FMs, focusing on the binder FM (Bentonite) and solid lubricant FMs (Molybdenum Disulphide (MoS_2) and Graphite). The disk samples used in the ball-on-disk experiments were fabricated from rail-grade material. Each disk sample was then ground and polished upto 1000# grade using silicon carbide polishing paper. After grinding, each sample was coated with the FM using a twin-fluid atomizer system (schematically shown in Figure 1) and ball-on-disk experiments were performed on the coated samples.

3. RESULTS

a. WEAR MECHANISM

- The binder as well as both the lubricants show abrasive wear marks formed due to ball rubbing.
- The tribo-oxide layer is found to be intact for the no FM case, as well as for the case of MoS_2 . Contrastingly, in case of bentonite and graphite, the substrate is observed to be exposed.

*G S P J Ronith (gspjronith7785@kgpian.iitkgp.ac.in)

- Delamination is observed to occur more frequently in the binder than in the lubricants.

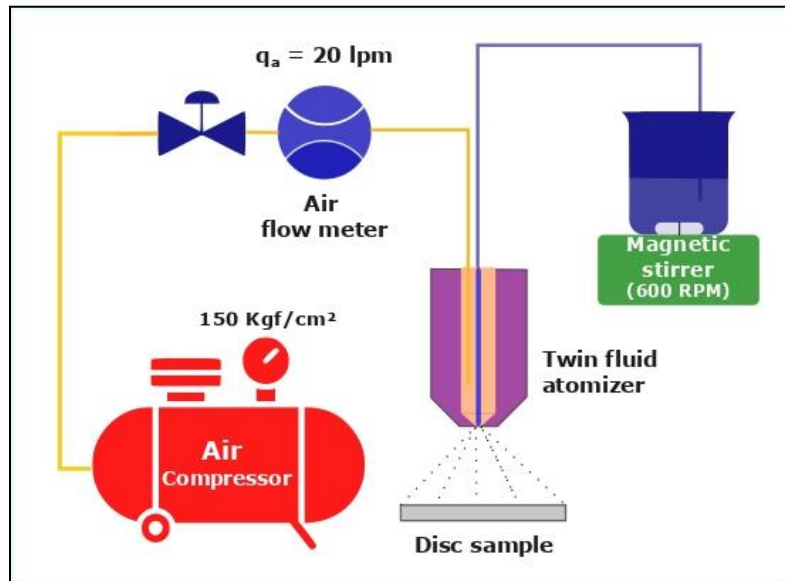


Figure 1 Schematic diagram depicting spraying setup

b. ELEMENTAL ANALYSIS

- The removal of the tribo-oxide layer (delamination) leads to loss of oxygen at that zone. This resulted in an increase in iron and/or carbon content in the delamination region.
- The opposite has been observed in the cases of no FM and MoS_2 .
- The high intensity of oxygen confirms the presence of the tribo-oxide layer.
- Traces of tungsten were also observed in all the cases, showing the slight inclusion of tungsten from the WC ball in the wear track during the test.

4. CONCLUSION

Binder and lubricant constituents of a friction modifier (FM) were individually applied on the surface of the disk, followed by ball-on-disk testing. After the experiments, the worn disk surfaces were examined using scanning electron microscopy. Based on these observations, the following conclusions were drawn.

- Among the FMs, MoS_2 was found to be the most adhesive, followed by bentonite. Graphite was found to be the least adhesive FM.
- Due to its adhesive nature, MoS_2 exhibited the least abrasive wear. However, the other two FMs showed abrasive wear.
- Delamination was observed more in the binder FM and the flaky lubricant FM than in the adhesive lubricant FM.

REFERENCES

- [1] Stock, Richard, Stanlake, Louisa, Hardwick, Chris, Yu, Marcia, Eadie, Donald, Lewis, Roger, "Material concepts for top of rail friction management – Classification, characterisation and application", *Wear*, vol. 366-367, pp. 225-232 (2016).

Moving Target Interception using Variable L_1 guidance

Machavolu Venkata Sushanth*, Sayantan Pal** and Sikha Hota***

*Undergraduate Student, Aerospace Engineering, Indian Institute of Technology Kharagpur, Kharagpur, India

**Research Scholar, Aerospace Engineering, Indian Institute of Technology Kharagpur, Kharagpur, India

***Associate Professor, Aerospace Engineering, Indian Institute of Technology Kharagpur, Kharagpur, India

1. INTRODUCTION & OBJECTIVE

The use of guided missiles in modern military combat and defense applications is increasing substantially by the day. They play a vital role in diverse fields such as target interception, air defence, and precision air strikes. Interception of a moving target optimally is becoming a key topic of interest in recent literature. Many guidance laws have been proposed based on Proportional Navigation (PN), Virtual Target Point (VTP)-based guidance, etc., to address this problem. This paper employs a technique that uses L_1 guidance to track a Dubins path that converges to the straight line along which the non-maneuvering target is traversing, with a turn-radius constraint in 2D. Consider a 2D interception geometry where a target, initially at (x_{T_0}, y_{T_0}) , is moving with a constant speed v_T along a straight line $y = mx + c$. The interceptor is initially at (x_o, y_o) , with a constant speed v and an initial heading angle ψ_o . Also, the interceptor is assumed to have a maximum lateral acceleration limit, expressed in terms of turn radius as having minimum turn radius r_m . The problem is to generate a C_2 -continuous path that the interceptor will track to engage with the target.

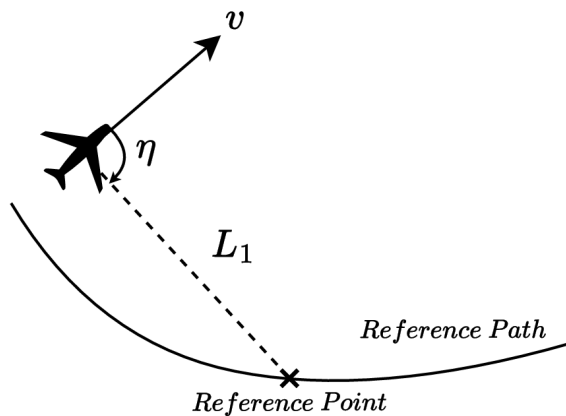


Figure 1: L_1 guidance law

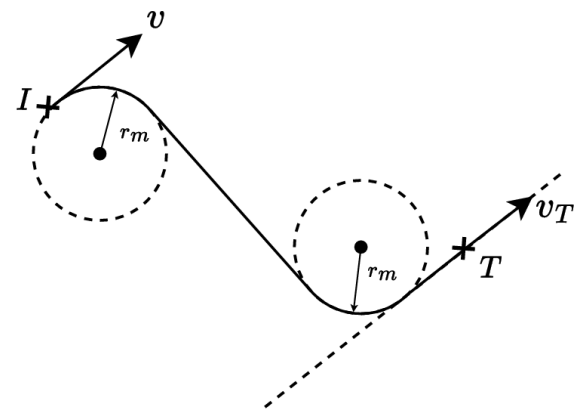


Figure 2: Interceptor-Target Engagement

2. METHOD OF ANALYSIS

In [1], it has been mathematically proved that the time-optimal path between two points where the initial and final orientations are fixed, and with a minimum turn-radius, is constructed with straight lines and circular arcs. This path converges to the straight line along which the target is moving, and the target will be intercepted along this line. But, this path, known as Dubins path, is not C_2 -continuous. This implies that its lateral acceleration is not continuous, which cannot be followed realistically. Hence, L_1 guidance is used to tackle this issue. This guidance law, known for its simplicity in implementation, presumes by considering a reference point at a distance L_1 ahead of the interceptor on a reference path. This setup is used to generate a lateral command acceleration (a_s) according to [1], resulting in a trajectory that converges smoothly with the reference path. The angle η represents the angle between the instantaneous velocity vector and the line joining the interceptor and the reference point as given in Fig. [1]. In [2], constant L_1 -guidance was proposed and applied to the problem of straight-line and circular convergence. But, it was found that it has slow

* Communicating Author: Machavolu Venkata Sushanth, sushanthmachavolu@gmail.com

convergence and overshoots the reference trajectory. To address this problem, a variable L_1 guidance law is being proposed, where L_1 is set to be equal to the absolute value of the cross-track error (d), added with a small positive constant ϵ to avoid singularities, as given in [2]. This paper proceeds by using L_1 guidance to generate a trajectory that closely matches the time-optimal Dubins path and also addresses the problem of C_2 -continuity. For this, L_1 guidance law uses the Dubins path that converges to the final straight line as its reference path, as given in Fig. [2].

$$a_s = \begin{cases} \frac{2v^2}{L_1} \sin \eta, & r \geq r_m \\ \frac{v^2}{r_m}, & r < r_m \end{cases} \quad (1)$$

$$L_1 = |d| + \epsilon \quad (2)$$

3. RESULTS AND/OR HIGHLIGHTS OF IMPORTANT POINTS

In this section, preliminary simulation results are presented. The simulations given are simulated using MATLAB 2024b and Simulink. A 2D engagement scenario was considered with the interceptor initially at $(0, 2000)m$, with a speed $250m/s$ and initial heading angle of 0° . The target is initially at $(2000, 0)m$, with a speed $50m/s$ moving along the x-axis. ϵ is taken to be $300m$. Results are given in Fig. [3], where Fig. [3](a) shows the trajectory plot and Fig. [3](b) shows the lateral acceleration profile. It is noted that the impact time is $17.7s$.

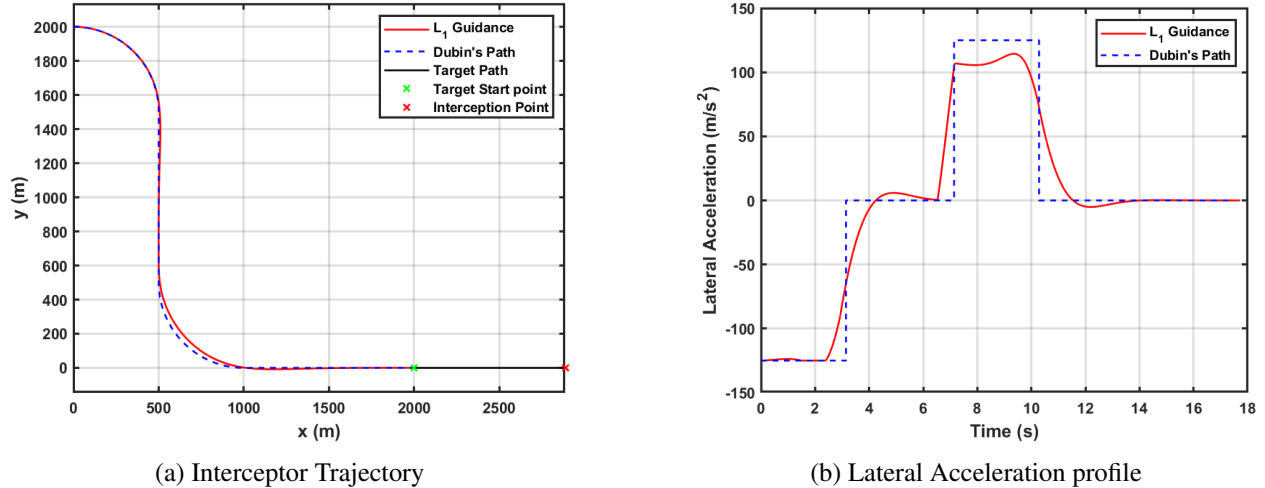


Figure 3: Results obtained from the simulation

4. CONCLUSIONS

In conclusion, this paper proposes a new guidance technique for moving target interception using Variable L_1 guidance and time-optimal Dubins path. This method has successfully generated a path that an interceptor can track to intercept the target in 2D. This work can be extended in the future to intercept targets with the Impact angle and the Field-of-View (FOV) angle constraints in 3D.

5. REFERENCES

- [1] L. E. Dubins, “On curves of minimal length with a constraint on average curvature, and with prescribed initial and terminal positions and tangents,” *American Journal of mathematics*, vol. 79, no. 3, pp. 497–516, 1957.
- [2] S. Park, J. Deyst, and J. How, “A new nonlinear guidance logic for trajectory tracking,” in *AIAA guidance, navigation, and control conference and exhibit*, 2004, p. 4900.

Numerical Analysis of Shockwave Boundary Layer Interaction

Suraj J Warang^a, Prahlad V Deshpande^a, Dhruv Bagora^a, Pardeep Duneria^a

^aNaval Institute of Aeronautical Technology, Naval Base, Kochi, Kerala – 682004.

1. INTRODUCTION AND OBJECTIVE

Shock wave Boundary Layer interactions occur when a shock wave and a boundary layer converge and, since both can be found in almost every supersonic flow, these interactions are commonplace. The most obvious way for them to arise is for an externally generated shockwave to impinge onto a surface on which there is a boundary layer that has been tripped. Another way of producing these interactions is if the gradient of the body surface changes in a manner to produce a sharp compression of the flow near the surface. If the flow is supersonic, a compression of this sort usually produces a shock wave that has its origin within the boundary layer. The effect on the viscous flow is analogous to that of an impinging shockwave coming from an external source.

The external consequences of SBLI include control loss, excessive aerodynamic heating, and unsteadiness. The internal consequences of SBLI include pressure losses, distortion intensification, and engine unstart in extreme conditions. Looking at the rapid progression of high-speed aircraft, this topic has become one of high importance and interest to mitigate the major consequences leading to failure of several aircraft.

These consequences of SBLI can be mitigated using flow control techniques. There are mainly 2 types of flow control techniques viz. Active Control techniques like Steady/ Pulsed Micro jets, Suction, and Plasma Jets. Another classification of flow control technique is the Passive Control technique which includes the use of Vortex Generators, Bumps, and Cavities on the surface on which the boundary layer is tripped, and the shockwave impinges.

This study includes the computational analyses of two models, one standard model and another model with vortex generators mounted on the flat plate as a control technique.

2. METHODS OF ANALYSIS

The computational geometry was created using the SolidWorks 2024 student edition software. The standard geometry comprises a wedge of half angle 12.5 degrees, which was used to create the shockwave. A flat plate was placed parallel to the wedge at a distance of 25mm. The second geometry included the vortex generators mounted on the top surface of the flat plate. Meshing has been done using the ANSYS workbench software. Figure 4 shows the computational mesh of the standard model. The mesh for all the models has been done using similar conditions. The physics preference has been set to the CFD. A grid independent study was also conducted to validate the meshing. The figure below depicts the meshing done on the computational domain.

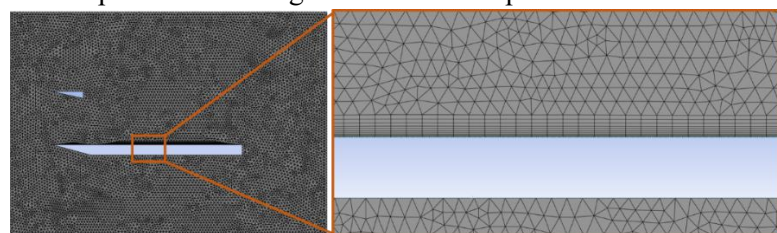


Figure 1: Grid generation of standard geometry

The boundary conditions applied to the computational domain is as described: The inlet of the domain is of pressure Farfield type. The gauge pressure at inlet is at 6000 Pa. The turbulence modelling of this domain has been done using k- ω SST model as it serves as the best model for boundary interaction solutions.

3. RESULTS

a. Velocity Contours

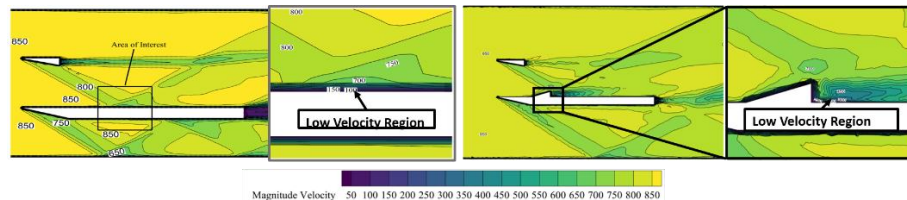


Figure 2: Velocity Contours

The velocity contours for both the computational domain is as depicted in above Figure. In the standard model we observe a prominent reflection of the shockwave, but in the case of the model with the vortex generators, we observe that the magnitude of the reflected shockwave is reduced to such an extent that the reflection is not at all prominent. Now looking at the region of impingement of shock, it is observed that in the case of the standard model, the size of the separation bubble is significant. The velocity in the local region reduces to about 100 m/s at the impingement point. In the case of the VG model, we observe that streamwise vortices are formed which facilitate in high – momentum transfer rates between boundary layer to near – wall regions. This increases the boundary layer thickness thus reducing the effect of the SBLI, by increasing the resistance to the shock induced separation.

b. Temperature Contours

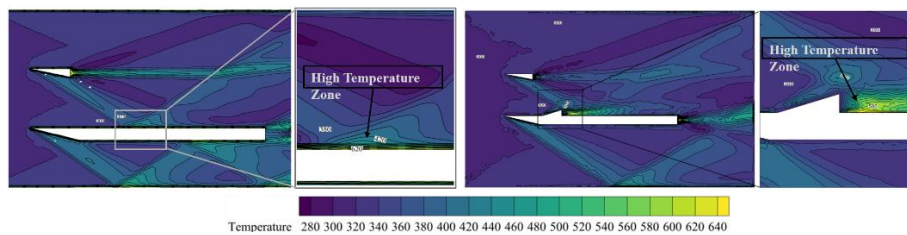


Figure 3: Temperature Contours

The temperature distribution contours facilitate us in understanding the variation of the temperature in the computational domain. In the case of the standard model, we observe a maximum temperature of about 640K wholly due to the shock impingement onto the flat plate. Now in the case of the VG model, the maximum temperature computed is at about 580K, there is a significant reduction due to higher rate of mixing. The reduction of maximum temperature is good evidence of reduction of local aerodynamic heating.

4. CONCLUSION

The study involved the computational analysis of shockwave boundary layer interaction, the results for which are obtained in the form of contours of Velocity, Pressure, Temperature, and Density. The results obtained for both the models are compared and it is found that in the case of Velocity contours, there is formation of streamwise vortices formed in the case of the VG model. Due to this, there is significantly higher momentum transfer from the boundary layer to the near wall regions. In the case of the temperature contours, there is reduction of the maximum temperature obtained in the computational domain.

5. REFERENCES

- [1] R. H. M. Giepmans, F. F. J. Schrijer, and B. W. van Oudheusden, “High-resolution PIV measurements of a transitional shock wave–boundary layer interaction,” *Experiments in Fluids*, vol. 56, no. 6, May 2015, doi: <https://doi.org/10.1007/s00348-015-1977-8>.
- [2] M. Grilli, P. J. Schmid, S. Hickel, and N. A. Adams, “Analysis of unsteady behaviour in shockwave turbulent boundary layer interaction,” *Journal of Fluid Mechanics*, vol. 700, pp. 16–28, Feb. 2012, doi: <https://doi.org/10.1017/jfm.2012.37>.
- [3] F. Gnani, H. Zare-Behtash, and K. Kontis, “Pseudo-shock waves and their interactions in high-speed intakes,” *Progress in Aerospace Sciences*, vol. 82, pp. 36–56, Apr. 2016, doi: <https://doi.org/10.1016/j.paerosci.2016.02.001>.

Numerical Investigation of a Novel Aerospike–Aero disk–Bleed Channel Configuration for Drag and Thermal Load Reduction in Hypersonic Vehicles

Sanjay Satish^a, Vijay Suresh^{b*}, Aswathy K. S.^c, A. Abhijith^d, Antony J. K.^e, Manoj Kumar M.^f

^{a,e}Assistant Professor, Department of Mechanical Engineering, Rajiv Gandhi Institute of Technology, Kottayam, Kerala, India

^{b*,c,d}Student, Department of Mechanical Engineering, Rajiv Gandhi Institute of Technology, Kottayam, Kerala, India

^fAssociate Professor, Department of Mechanical Engineering, Rajiv Gandhi Institute of Technology, Kottayam, Kerala, India

INTRODUCTION & OBJECTIVE

Hypersonic vehicles experience significant aerodynamic drag and thermal loads due to intense shock interactions at high Mach numbers. Blunt forebodies offer structural protection, but generate detached bow shocks that elevate surface pressure and heat flux. Various flow-control strategies, including aerospikes, opposing jets, and hybrid systems, have been explored to mitigate these effects. Opposing jets, for instance, create a counterflow that modifies the bow-shock structure and can reduce stagnation heating. However, they require onboard propellant and may increase local heat flux through jet impingement and mixing, which limits their practical applicability. This study proposes a novel aerodisk-bleed channel system designed to extract high-enthalpy air from the stagnation region and expel it through an annular ring, reshaping the forebody flow. A Mach 6, 30-km flight scenario is analysed to assess the effects of annular ring positions ($Lr = 0.1, 0.5, 0.9$), bleed channel spacing ratios (2:2:2, 1:3:2, 2:1:3), and angles of attack (0°, 4°, 8°).

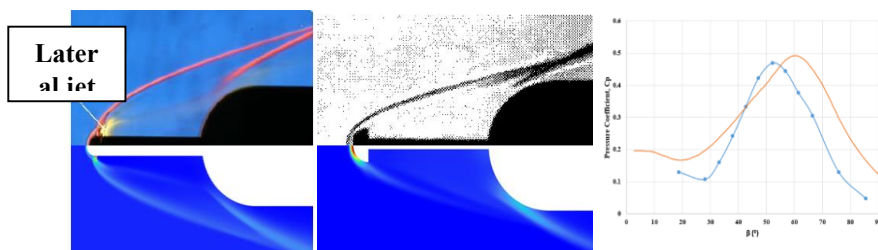
METHODS OF ANALYSIS

Geometry, Grid & Boundary Conditions

The computational model of a hemispherical blunt body ($R=20\text{mm}$) equipped with a spike–aerodisk assembly was adopted from the literature [2]. To ensure that $y^+ < 1$ for accurate near-wall resolution using the SST $k-\omega$ model, a structured grid was generated in ICEM-CFD. The computational domain was defined as ten times the characteristic length (i.e., the blunt-body diameter) to minimize boundary effects, and the first-layer cell height was set to 0.01 mm. Boundary conditions included a far-field inlet, no-slip isothermal walls maintained at 300 K, and a pressure outlet. The free stream conditions corresponding to Mach 6 at 30 km altitude, with a static pressure of 1197 Pa and Static temperature of 226.5 K.

Numerical Model

The flow field was resolved using a density-based, double-precision solver in ANSYS FLUENT. Spatial discretization used a second-order upwind scheme with AUSM flux formulation. Air was treated as an ideal gas with viscosity modelled via Sutherland's law. A CFL number of 0.5 and suitable under-relaxation factors. Convergence was achieved when residuals decreased by at least three orders of magnitude and the net mass imbalance across domain boundaries was below 0.001 kg/s.



a) Pressure contour [3] b) Pressure contour [4] c) Pressure coefficient [4]

Figure 1: Comparison of Pressure coefficients and experimental schlieren images with numerical contour

*Communicating Author: vijaysureshvijay123@gmail.com

RESULTS AND HIGHLIGHTS OF IMPORTANT POINTS

The effect of aero disk position is illustrated in the figure 2(a). The three different locations are analysed. The locations are defined by the distance between disks. $l_1: l_2: l_3$ corresponding to 2:2:2, 1:3:2, 2:1:3 was analysed. The position of annular ring is defined by a non-dimensional parameter L_r , three positions corresponding to $L_r=0.1$, $L_r=0.5$, $L_r=0.9$ are analysed in this study as shown in the Figure 2(b). Three different angles of attack (0, 4, 8 degrees) are evaluated to assess the effect of angle of attack in the flow field structure around the blunt body and heat flux reduction Figure 2(c)

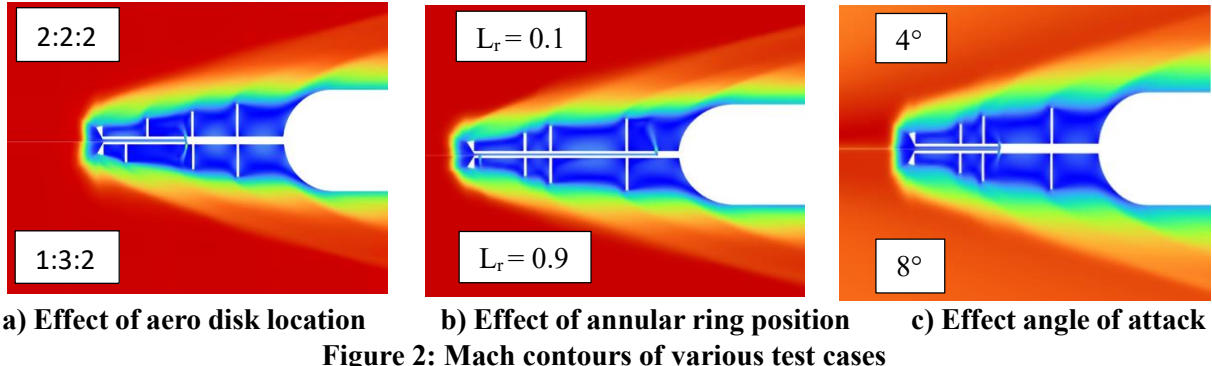


Figure 2: Mach contours of various test cases

CONCLUSION

- 1) It is found that, aerodisk position affects the recirculation zone size and flow through annular ring results in downstream movement of the reattachment shockwave. This further affects the heat flux and drag on blunt body.
- 2) The heat flux and pressure distribution is found to be reduced by keeping the annular ring position at the middle of aerospike.
- 3) By increasing angle of attack, the capture area of bleed channel is got affected and subsequently the flow through channel got varied. This further resulted in changes in the shape and size of recirculation zone.

The study is in progress and the quantitative results of above-mentioned conclusions will be incorporated in the full-length paper.

REFERENCES

- [1] Zijian Ni, Shuzhou Fang, et. al., “Three-dimensional numerical study on reducing hypersonic blunt body drag and aeroheating with spike-aerodisk-bleed air channel”, *J. Acta Astronica*, vol.215,pp.674-688,2024,doi: <https://doi.org/10.1016/j.actaastro.2023.12.058>
- [2] Zhenkang Zhang, Wanwu Xu ,et. al., “ Study on hypersonic drag and heat reduction of a spiked blunt body with multiple flat aerodisks and rear opposing jets”, *J. Case Studies in Thermal Engineering*,vol.42,pp.102714, January2023,doi: <https://doi.org/10.1016/j.csite.2023.102714>
- [3] Yunfeng Liu, Zonglin Jiang , “Concept of Non-Ablative Thermal Protection System for Hypersonic Vehicles”, *J. AIAA*, Vol. 51, pp.3,March 2013, doi: <https://doi.org/10.2514/1.J051875>
- [4] Noboru Motoyama, Ken Mihara, et. al., “*Thermal Protection And Drag Reduction With Use Of Spike In Hypersonic Flow*”, *J. American Institute of Aeronautics and Astronautics*, 24-27 April 2001
- [5] WeiHuang, LiYan, et. al., “Drag and heat reduction mechanism in the combinational opposing jet and acoustic cavity concept for hypersonic vehicles”, *J. Aerospace Science and Technology*, vol.42, pp. 407-414, February 2015, doi: <http://dx.doi.org/10.1016/j.ast.2015.01.029>

*Communicating Author: vijaysureshvijay123@gmail.com

Numerical Investigation of an Archimedean Spiral Wind Turbine Using Dynamic Mesh CFD in ANSYS Fluent

Shivendraraj Godbole ^a and Krishnendu Haldar ^{b*}

^a M.Tech Student,Aerospace,IIT Bombay, Mumbai,India

^b Professor,Aerospace, IIT Bombay, Mumbai, India

1. INTRODUCTION & OBJECTIVE

Small-scale wind systems are vital for urban areas where horizontal-axis turbines face turbulence, directional, and spatial constraints. The Archimedean Spiral Wind Turbine (ASWT), inspired by seashell geometry, combines lift and drag forces across wide inflow angles, achieving peak power coefficients $C_p \approx 0.25\text{--}0.27$ at low tip-speed ratios $\theta = 60^\circ$ [1]. This study numerically investigates ASWT [2] performance using ANSYS Fluent with a dynamic mesh and the standard $k-\varepsilon$ model to analyze transient flow interaction, pressure and velocity fields, and aerodynamic torque. Results at $Re \approx 54,000$ and $Ma = 0.024$ are validated against benchmarks, demonstrating ASWT's potential for efficient urban wind energy harvesting.

2. METHODS OF ANALYSIS

2.1 ASWT Geometry and Computational Domain

A three-bladed spiral rotor with radius $R = 0.05$ m, opening angle $\theta = 60^\circ$, and pitch $P = 1.5R$ was embedded in a cylindrical domain of $14.2R \times 5R \times 5R$ to minimize blockage. A rotating inner zone (diameter $1.2R$) containing the rotor was linked to a stationary outer domain via non-conformal sliding interfaces.

2.2 Mesh Generation and Dynamic Mesh Strategy

ANSYS Meshing generated a hybrid mesh: tetrahedral elements in the outer domain, prism layers near rotor surfaces for $y^+ \approx 30\text{--}100$. Dynamic mesh smoothing and local remeshing maintained mesh quality during rotor motion.

2.3 Turbulence Model and Solver Configuration

The standard $k-\varepsilon$ model solves:

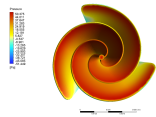
$$\frac{\partial(\rho k)}{\partial t} + \frac{\partial(\rho k u_i)}{\partial x_i} = \frac{\partial}{\partial x_j} \left[\left(\mu + \frac{\mu_t}{\sigma_k} \right) \frac{\partial k}{\partial x_j} \right] + P_k - \rho \varepsilon \quad (1)$$

$$\frac{\partial(\rho \varepsilon)}{\partial t} + \frac{\partial(\rho \varepsilon u_i)}{\partial x_i} = \frac{\partial}{\partial x_j} \left[\left(\mu + \frac{\mu_t}{\sigma_\varepsilon} \right) \frac{\partial \varepsilon}{\partial x_j} \right] + C_{1\varepsilon} \frac{\varepsilon}{k} P_k - C_{2\varepsilon} \rho \frac{\varepsilon^2}{k} \quad (2)$$

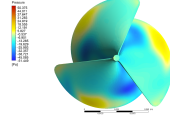
with

$$\mu_t = \rho C_\mu \frac{k^2}{\varepsilon} \quad (3)$$

A pressure-based transient solver with second-order discretization and coupled pressure–velocity scheme was used. Boundary conditions: uniform inlet velocity 8 m/s, zero-gauge outlet pressure, no-slip rotor walls, slip at far-field.



(a) Pressure side.



(b) Suction side.

Figure 1: Pressure contours of Archimedean Spiral

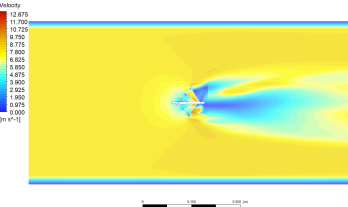


Figure 2: Velocity contour of spiral due to moving fluid

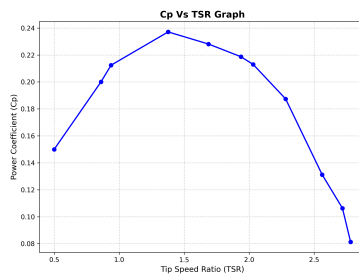


Figure 3: Cp vs TSR

3. RESULTS AND/OR HIGHLIGHTS OF IMPORTANT POINTS

CFD results show a pressure differential of ≈ 100 Pa across the rotor, consistent with previous ASWT studies. Concentric high-pressure contours Figure 1a and corresponding low-pressure regions Figure 1b confirm the lift–drag torque mechanism. Velocity contours Figure 2 reveal near-wake deficits below 3 m/s (60–70% extraction) and peripheral acceleration up to 12.6 m/s, with gradual downstream recovery favorable for array deployment.

4. CONCLUSIONS

ANSYS Fluent with dynamic mesh and $k-\varepsilon$ modeling accurately captured ASWT aerodynamics pressure differentials (≈ 100 Pa) generated distributed torque loading, while wake velocity deficits of 60–70% indicated effective momentum extraction. The standard $k-\varepsilon$ model accurately resolved boundary-layer and turbulent mixing effects. At $Re = 54,144$ and $Ma=0.024$, the flow remained fully turbulent. The maximum $C_p = 0.235$ at $TSR = 1.3$ as shown in Figure 3 aligned with reported ASWT benchmarks for a 60° spiral angle.

REFERENCES

- [1] Hyeyonmu Jang, Dongmyeong Kim, Yechan Hwang, Insu Paek, Seungjoo Kim, and Joonho Baek. Analysis of archimedes spiral wind turbine performance by simulation and field test. *Energies*, 12(24):4624, 2019.
- [2] Kyung Chun Kim, Ho Seong Ji, Yoon Kee Kim, Qian Lu, Joon Ho Baek, and Rinus Mieremet. Experimental and numerical study of the aerodynamic characteristics of an archimedes spiral wind turbine blade. *Energies*, 7(12):7893–7914, 2014.

* Communicating Author: Krishnendu Haldar, krishnendu@aero.iitb.ac.in

NUMERICAL INVESTIGATION OF LOW-FREQUENCY OSCILLATIONS IN SEPARATED SHEAR FLOWS

Digpriya¹, Rajesh Ranjan² and Pradeep Moise²

¹Graduate Student, Department of Aerospace Engineering, Indian Institute of Technology Kanpur, Kanpur, India

²Assistant Professor, Department of Aerospace Engineering, Indian Institute of Technology Kanpur, Kanpur, India

1. INTRODUCTION & OBJECTIVE

Mitigating flow separation is critical in many aerodynamic and hydrodynamic applications—such as aircraft wings, turbine blades, and vehicle surfaces—since the drag penalty and load fluctuations caused by separation-induced oscillations can severely degrade performance. Recent experiments have shown that self-sustained, low-frequency oscillations can arise when the separated shear layer reattaches to form a laminar separation bubble (LSB) [1,2]. However, the underlying dynamics of these oscillations remain relatively unexplored. Motivated by this, the present study investigates flow oscillations associated with separated shear layers. Following the experimental configuration of Aniffa et al. [3], two- and three-dimensional numerical simulations are conducted on a flat plate subjected to an imposed adverse pressure gradient generated by a contoured upper wall, leading to LSB formation. To extract the inherent frequencies and dominant coherent structures, Spectral Proper Orthogonal Decomposition (SPOD) is employed on the spatio-temporal datasets.

2. NUMERICAL SETUP

The flow is assumed to be unsteady, incompressible, viscous, and laminar. Incompressible Navier-Stokes equations are solved using the open-source finite-volume-based CFD solver, OpenFOAM. To solve the coupled pressure-velocity equations, the PIMPLE (Pressure Implicit Method for Pressure Linked Equations) algorithm is used.

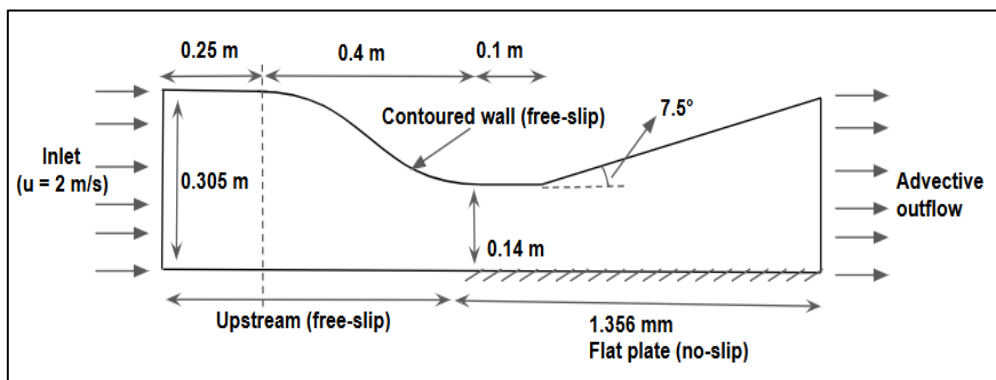


Figure 1. Computational Domain and Boundary Conditions

The computation domain is shown in Fig. 1. The domain spans from -0.25 m to 1.756 m in the streamwise direction and 0 to 0.305 m in the transverse direction. The shape of the upper wall is contoured based on the experimental configuration of Aniffa et al. [3] to impose an adverse pressure gradient on the boundary layer. The flow has been simulated at a relatively low Reynolds number (based on the inlet velocity, U_∞ , and throat height) of $Re = 18667$. A free slip boundary condition is applied on the upper boundary and on the lower boundary for $x < 0.4$ m. A no-slip boundary condition is applied for $x \geq 0.4$ m. At the inflow boundary, a uniform velocity of 2 m/s is applied, while an advective boundary condition is used at the outlet boundary.

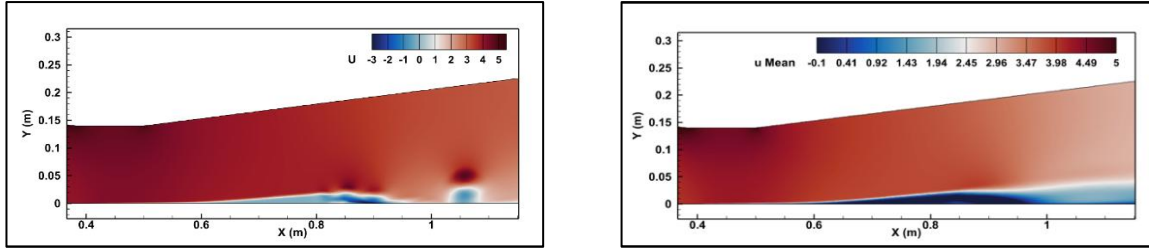


Figure 2. Flowfield using velocity contours. (a) Instantaneous flow, (b) Mean flow

3. RESULTS & DISCUSSIONS

Figure 2 shows the instantaneous and mean flow obtained from the two-dimensional simulations. The instantaneous contour shows the formation of a laminar separation bubble (LSB) and the presence of vortices downstream, which is likely due to the phenomenon of bubble bursting. The mean flow is similar to that obtained in experiments [3], with an LSB present between $x = 0.6\text{m}$ and $x = 0.95\text{m}$. To analyse the unsteady behaviour of the flow, multiple probes are used at the separated flow as well as the reattachment region of the bubble. A power spectral density (PSD) of the axial velocity fluctuation in the shear layer region is plotted in figure 3(a), which shows that there are two dominant peaks, associated with low- and high-frequency oscillations. The SPOD mode shapes shown in figure 3(b) show that the high-frequency oscillations correspond to vortex shedding. By contrast, the low-frequency oscillation is seen to have significant energy content near the separation bubble region, indicating that it is related to bubble bursting. Further, it closely resembles the mode shapes seen for low-frequency oscillations in incompressible flow over aerofoils, which occur as a precursor to stall.

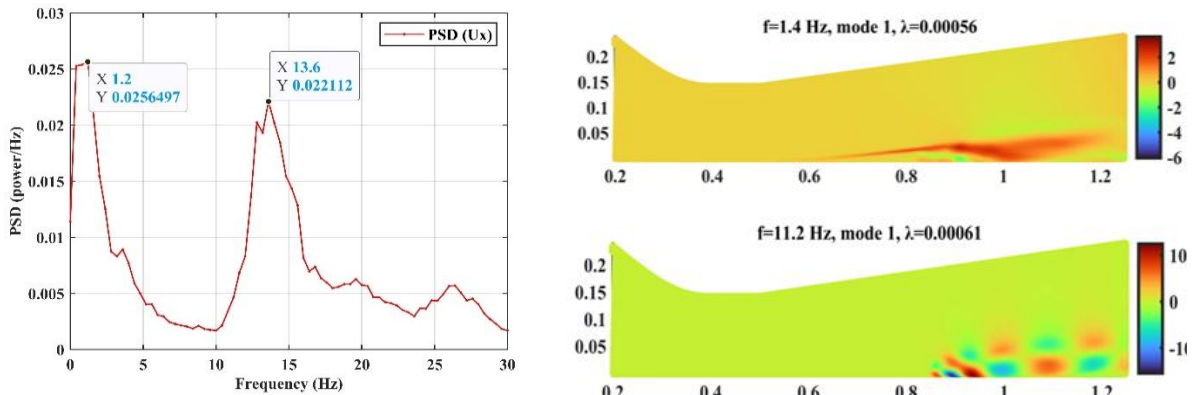


Figure 3. Flow dynamics. (a) Frequencies using probes, (b) Dominant SPOD modes

4. CONCLUSIONS

The dynamics of the laminar separation bubble are analysed using computational simulations followed by unsteady flow analysis. The SPOD spectrum reveals two dominant peaks: low-frequency “bubble bursting” and high-frequency vortex shedding. The final paper will further include insights from three-dimensional analyses and comparisons with other commonly observed separated flow phenomena.

5. REFERENCES

- [1] F. Malmir, G. Di Labbio, A. Le Floc'h, L. Dufresne, J. Weiss, and J. Vétel, “Low-frequency unsteadiness in laminar separation bubbles,” *J. Fluid Mech.*, vol. 999, p. A99, 2024, doi: 10.1017/jfm.2024.962.
- [2] P. Moise, M. Zauner, and N. D. Sandham, “Connecting transonic buffet with incompressible low-frequency oscillations on aerofoils,” *J. Fluid Mech.*, vol. 981, p. A23, 2024, doi:10.1017/jfm.2023.1065.
- [3] S. M. Aniffa and A. C. Mandal, “Experiments on the low-frequency oscillation of a separated shear layer,” *Phys. Rev. Fluids*, vol. 8, no. 2, p. 023902, Feb. 2023, doi:10.1103/PhysRevFluids.8.023902

Numerical Investigation on the Effect of Acoustic Cavity Geometry, Angle of Attack, and Injectant Molecular Weight for Drag and Heat Flux Reduction over a Blunt Body

Sanjay Satish^a, Arun B. S.^{b*}, Ashik Muhammad^c, Manoj Kumar M.^d, Antony J. K.^e

^{a,e}Assistant Professor, Department of Mechanical Engineering, Rajiv Gandhi Institute of Technology, Kottayam, Kerala, India

^{b,c}Student, Department of Mechanical Engineering, Rajiv Gandhi Institute of Technology, Kottayam, Kerala, India

^dAssociate Professor, Department of Mechanical Engineering, Rajiv Gandhi Institute of Technology, Kottayam, Kerala, India

INTRODUCTION & OBJECTIVE

Hypersonic vehicles experience high aerodynamic drag and severe thermal loads, which can reduce performance and cause structural degradation. Blunt body configurations are preferred for their robustness and thermal protection; however, the detached bow shock generates high surface pressure and heat flux at stagnation region. Various techniques have been proposed to mitigate these effects. This study investigates a novel combination of an acoustic cavity and an opposing jet to reduce drag and heat flux simultaneously. Different acoustic cavity geometries (trapezoidal, circular, and rectangular) are analysed. The effects of angle of attack ($0^\circ, 4^\circ, 8^\circ, 12^\circ$) and injectant gases ($\text{CH}_4, \text{H}_2, \text{N}_2$) on aerodynamic and thermal performance are quantified using surface pressure distributions and Stanton numbers along the blunt body.

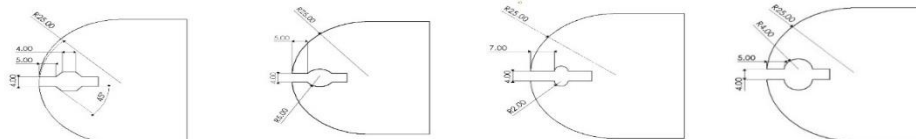
METHODS OF ANALYSIS

1) Geometry, Grid & Boundary Conditions

The blunt body with a cavity at the stagnation point is shown in Figure 1. Four acoustic cavity geometries were analysed to investigate drag and heat flux reduction. The computational grid, generated using ANSYS ICEM-CFD, was refined near the wall with $y^+ < 1$ to accurately resolve the boundary layer using the SST k- ω model. Boundary conditions, following Hayashi et al. [2].

Table 1: Boundary conditions

| | Mach No. | Total Pressure, P_0 (K) | Total Temperature, T_0 (Pa) |
|-------------------|----------|---------------------------|-------------------------------|
| Freestream | 3.98 | 1370000 | 397 |
| Injectant | 1 | 822000 | 300 |



a) Test case 01

b) Test Case 02

c) Test Case 03

d) Test Case

Figure 1: Geometries of acoustic cavity.

2) Numerical Setup

The flow field was resolved using a density-based, double-precision solver in ANSYS FLUENT. Spatial discretization used a second-order upwind scheme with AUSM flux formulation. Air was treated as an ideal gas with viscosity modelled via Sutherland's law. A CFL number of 0.5 and suitable under-relaxation factors. Convergence was achieved when residuals decreased by at least three orders of magnitude and the net mass imbalance across domain boundaries was below 0.001 kg/s.

RESULTS AND HIGHLIGHTS OF IMPORTANT POINTS

The numerical setup was validated using experimental data and schlieren images from the literature [2] (Figure 2).

*Communicating Author: arunarun7191@gmail.com

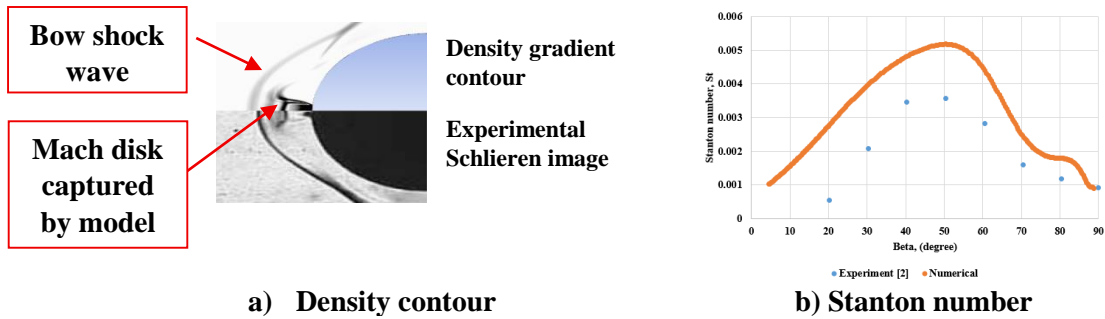


Figure 2: Comparison of experimental schlieren image and density gradient contour and static pressure distribution along blunt body

1) Comparison of turbulence models

The SST k- ω turbulence model is used in this study and the effect of turbulence model in the results is quantified by comparing density contours as shown in Figure 3.

2) Effect of cavity geometry

Four acoustic cavity geometries causes different recirculation zones.

3) Effect of angle of attack

Four angles of attack were analysed and found that increase in angle enlarges the recirculation zone in front of blunt body

4) Effect of molecular weight of injectant

Low molecular weight injectant shows better reduction in heat fluxes.

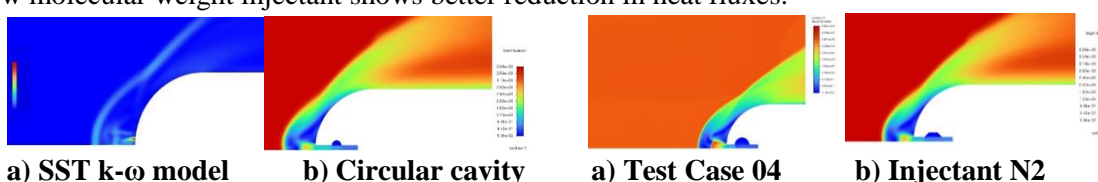


Figure 3: Numerical schlieren image of blunt body with opposing jet for validation [2] and Mach contours of different test cases

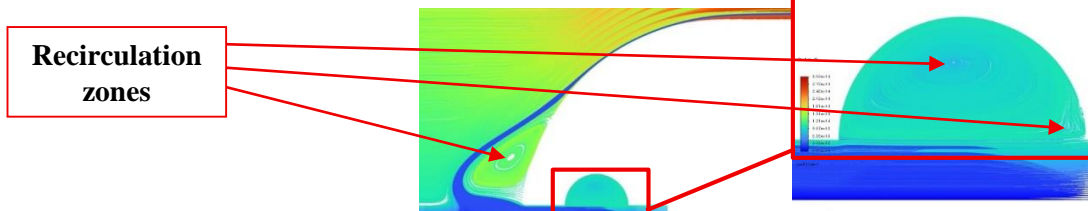


Figure 4: Recirculation zones captured by the model

CONCLUSION

The SST k- ω model captures Mach disk and shock interactions more accurately than the standard k- ϵ model. Circular cavities generate larger recirculation zones, causing reduction in surface pressure and Stanton number. Increasing angle of attack enlarges the recirculation zone and lowers surface pressure and heat transfer. Lower molecular weight injectants (e.g., H₂) are preferable for better heat reduction. The study is in progress and the quantitative results of above-mentioned conclusions will be incorporated in the full-length paper.

REFERENCES

- [1] WeiHuang, LiYan, et. al., "Drag and heat reduction mechanism in the combinational opposing jet and acoustic cavity concept for hypersonic vehicles", *J. Aerospace Science and Technology*, vol.42, pp. 407-414, February 2015, doi: <http://dx.doi.org/10.1016/j.ast.2015.01.029>
- [2] K. Hayashi, S. Aso, Y. Tani, Experimental study on thermal protection system by opposing jet in supersonic flow, *J. Spacecr. Rockets* 43(1) (2006) 233–235. doi: <https://doi.org/10.2514/1.15332>
- [3] M.Y.M. Ahmed, N. Qin, Forebody shock control devices for drag and aero-heating reduction: a comprehensive survey with a practical perspective, *Prog. Aero. Sci.* 112 (2020), 100585. doi: <https://doi.org/10.1016/j.paerosci.2019.100585>

*Communicating Author: arunarun7191@gmail.com

Numerical Prediction of Interaction Between Two Flying Robotic Butterflies

Aman Shukla ^a, Debajyoti Kumar ^b, Chandan Bose ^c, Somnath Roy ^{a,b,1}

^a Department of Mechanical Engineering, IIT Kharagpur, India

^b Centre for Computational and Data Sciences, IIT Kharagpur, India

^c Aerospace Engineering, School of Metallurgy and Materials, University of Birmingham, United Kingdom

1. INTRODUCTION & OBJECTIVE

Butterflies often fly close to each other, generating complex wake interactions. Based on this, butterfly-inspired micro air vehicles (MAVs) are designed to operate in swarms, where individuals may fly in close proximity. A butterfly generates thrust by flapping its wings backward and lift by flapping them downward [1]. In this context, the present study focuses on understanding how a follower flyer is affected by the unsteady wake vortices of a leading flyer by visualizing flow structures and analysing variations in aerodynamic forces and their coefficients at different separations.

2. METHODS OF ANALYSIS

Three-dimensional, time-dependent computational fluid dynamics (CFD) simulations were performed using an in-house developed solver. The fluid domain was discretized using a coarse background mesh, while overset mesh blocks, consisting of fine grids overlapping with the background mesh, were used around each flyer to resolve unsteady wing motions. At each time step, interpolation between overlapping grids enables free movement of the butterflies without grid deformation. An immersed boundary method (IBM) was used to capture the complex, time-varying wing geometries within the structured mesh framework. The flow is modelled using the Navier-Stokes equations (incompressible form):

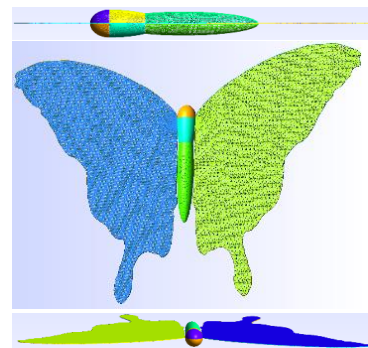


Figure 1 Geometry of the butterfly model.

$$\nabla \cdot \mathbf{u} = 0, \quad (2.1)$$

$$\frac{D\mathbf{u}}{Dt} = -\nabla p + \frac{1}{Re} \nabla^2 \mathbf{u} \quad (2.2)$$

where \mathbf{u} is the dimensionless fluid velocity, p is the dimensionless pressure and Re is the Reynolds number based on the wing span. The wing motion was prescribed using time-dependent kinematic profiles adopted from [1]. The angles $\theta(t)$ and $\alpha(t)$ represent the flapping angle and angle of attack at time t , respectively, given by

$$\theta(t) = \theta_m \cos(2\pi(St)t), \quad (2.3)$$

$$\alpha(t) = \frac{\alpha_m}{2} [1 + \cos(2\pi(St)t + \gamma)] \quad (2.4)$$

where θ_m is the flapping amplitude, α_m denotes the maximum angle of attack, γ is the phase shift, St is the Strouhal number based on wing flapping frequency and t is the dimensionless time. Numerical simulations will be carried out over a range of Reynolds and Strouhal numbers to explore how variations in these parameters influence the flow dynamics and the resulting aerodynamic forces.

¹ Communicating Author: Somnath Roy (somnath.roy@mech.iitkgp.ac.in)

3. RESULTS

The visualizations (Figure 2) capture the complex three-dimensional vortex structures resulting from the flapping motion of two robotic butterflies flying in parallel in the negative X direction and separated vertically. The dashed boxes indicate the positions of the butterflies. The simulations reveal unsteady wake interactions as the flapping wings shed vortices that move downstream.

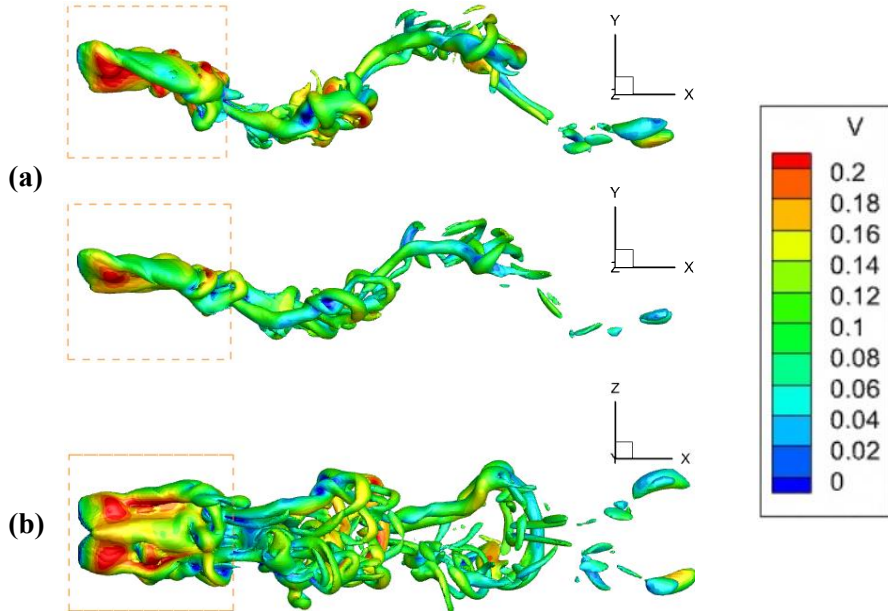


Figure 2 Iso-surfaces of vorticity magnitude coloured by velocity magnitude (V) showing the wake interaction of two robotic butterflies flying one above the other: (a) Side view of the pair in forward flight and (b) top view of the same configuration.

Further analysis will quantify aerodynamic forces and coefficients, including lift and drag, to assess how wake interactions affect the aerodynamic performance of each flyer across varying Reynolds and Strouhal numbers.

4. CONCLUSIONS

This study demonstrates that the airflow generated by one flyer can significantly affect a neighbouring butterfly when flying in proximity. Vortices and pressure zones alter the aerodynamic forces, while increased spacing reduces these interactions, eventually approaching single-flyer behaviour. Previous work [2] shows that the presence of free vortices in the wake region provides a stabilizing effect. These findings highlight the importance of spacing between flyers and provide useful insight into the design of flapping-wing robots flying in formation.

5. REFERENCES

- [1] Kosuke Suzuki et al., “Lift and thrust generation by a butterfly-like flapping wing body model: immersed boundary lattice Boltzmann simulations,” *Journal of Fluid Mechanics*, vol. 767, pp. 659–695, Mar. 2015, doi: 10.1017/jfm.2015.57
- [2] Kei Senda, Takuya Obara et al., “Modeling and emergence of flapping flight of butterfly based on experimental measurements,” *Robotics and Autonomous Systems*, vol. 60(5), pp. 670–678, 2012, doi: 10.1016/j.robot.2011.12.007

Numerical Study on Drag Reduction of Various Bluff-body Geometries using the Passive Rotation of a NACA0012 Aerofoil

Bibhas Chand^a, Prabir Sikdar^{*b}, M S Harihara Sudhan^a, and Sunil Manohar Dash^a

^aDepartment of Aerospace Engineering, Indian Institute of Technology Kharagpur, Kharagpur, India

^bDepartment of Mechanical Engineering, Indian Institute of Technology Bombay, Mumbai, India

1. INTRODUCTION

Flows over bluff bodies are generally found in both nature and engineering applications where alternate vortex shedding induces time-periodic drag and lift forces on the structure. In this regard, the drag reduction can be achieved by controlling the vortex shedding process and restructuring the near wake of a structure. Generally, the wake regime control is categorized into two groups: passive and active control. Among active controls, pitching and oscillating devices such as splitter plates and aerofoils delay the shear layer roll up, increase the base pressure, leading to a reduction in drag force on the cylinder. Bao et al. [1] investigated a detached, streamwise oscillating elliptic aerofoil on the cylinder's rear side and noticed that for an optimum gap spacing, the wake unsteadiness can be completely suppressed. Han et al. [2] explored the effect of pitching the NACA0012 aerofoil behind the circular cylinder and achieved a drag reduction up to 50% under optimal parametric conditions. However, the active control methods need external energy for practical deployment, which reduces the effectiveness of drag reduction. In contrast, the passive control method extracts energy from flow-induced forces. In the literature, studies on the effect of passive oscillation of the NACA0012 aerofoil on drag reduction of different bluff body geometries remain limited. Therefore, the present study numerically investigates the drag reduction of various bluff body geometries, including circular, square, semi-circular, and triangular, by using a downstream NACA0012 aerofoil that undergoes vortex-induced passive rotation. Here, numerical simulations are conducted using an in-house developed flexible forcing immersed boundary scheme-based one-step simplified lattice Boltzmann method (FFIB-OSLBM) solver [3]. The objective is to investigate the effect of aerofoil's passive rotation on wake patterns and the resultant flow-induced forces acting on the bluff bodies at a Reynolds number of $Re = 100$.

2. METHODS OF ANALYSIS

The computational domain and its size are illustrated in Fig. 1. This configuration consists of a stationary front cylinder and a downstream NACA0012 aerofoil, which undergoes a passive rotation induced by the aerodynamic moments. The height of the front stationary cylinder is D , while the chord length of the NACA0012 aerofoil is $2D$. The non-dimensional streamwise distance between the rear base point of the cylinder and the leading edge of the aerofoil is $L/D = 3$. Four different front body geometries, including circular, square, semi-circular, and triangular, are considered, each having the same characteristic length D . The Reynolds number is defined as, $Re = UD/v$, where v is the kinematic viscosity of the fluid. A uniform velocity ($u = U$, $v = 0$) is set at the inlet, upper, and lower walls of the computational domain. A pressure outlet condition is employed at the outlet boundary. The simulations are carried out using the FFIB-OSLBM solver, and its detailed algorithm can be found in reference [3].

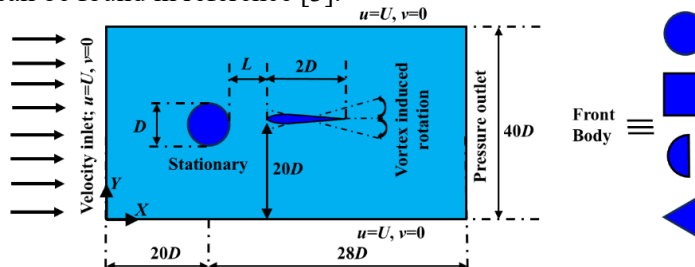


Fig. 1. The computational setup of the present study.

The vortex-induced rotation of the aerofoil is governed by Eq. 1. Here, θ , $C_m = \frac{2M_\theta}{\rho D^2 U^2}$, $I^* = \frac{I_s}{\rho D^4}$, and $U_\theta^* = \frac{U}{Df_\theta}$ are the rotational angle, pitching moment coefficient, the non-dimensional moment of inertia of the aerofoil, and the reduced velocity. ρ , M_θ , I_s , and f_θ are the density of the fluid, the torque acting on the aerofoil, the mass moment of the aerofoil, and the natural frequency, respectively. The simulations are performed at $Re = 100$, $I^* = 5$. The U_θ^* is varied from 4 to 14 at an interval of 2.

$$\ddot{\theta} + \left(\frac{2\pi}{U_\theta^*}\right)^2 \theta = \frac{C_m}{2I^*} \quad (1)$$

3. RESULTS AND DISCUSSIONS

Fig. 2 (A-D) shows the variation of aerofoil rotational amplitude θ_{max} and total time-averaged drag coefficient \bar{C}_d as a function of reduced velocity U_θ^* for different bluff body geometries. For all configurations, θ_{max} initially increases and then gradually decreases with increasing U_θ^* . A similar trend is observed for the total \bar{C}_d , defined as the combined drag coefficient of the front cylinder and the downstream aerofoil. As compared to the isolated front cylinder, the tandem configuration (front cylinder and aerofoil) exhibits a substantial reduction in total drag. This demonstrates the effectiveness of passive rotation in reducing the drag. The lowest \bar{C}_d for all front body shapes is observed at $U_\theta^* = 4$. Furthermore, the instantaneous vorticity contours around the cylinder and aerofoil at $U_\theta^* = 6$ are shown in Fig. 2 (E-H). It indicates that the vortex formation behind the cylinder is delayed due to the passive rotation of the aerofoil. Moreover, for all the front body shapes, a parallel vortex street is formed within the gap region of two bodies, followed by the development of a classic von Karman vortex street in the wake of the aerofoil. It is further noticed that for semi-circular and triangular cylinders, the vortex formation occurs closer to the aerofoil as compared to the circular and square cylinder cases. This contributes to the higher drag observed for these geometries.

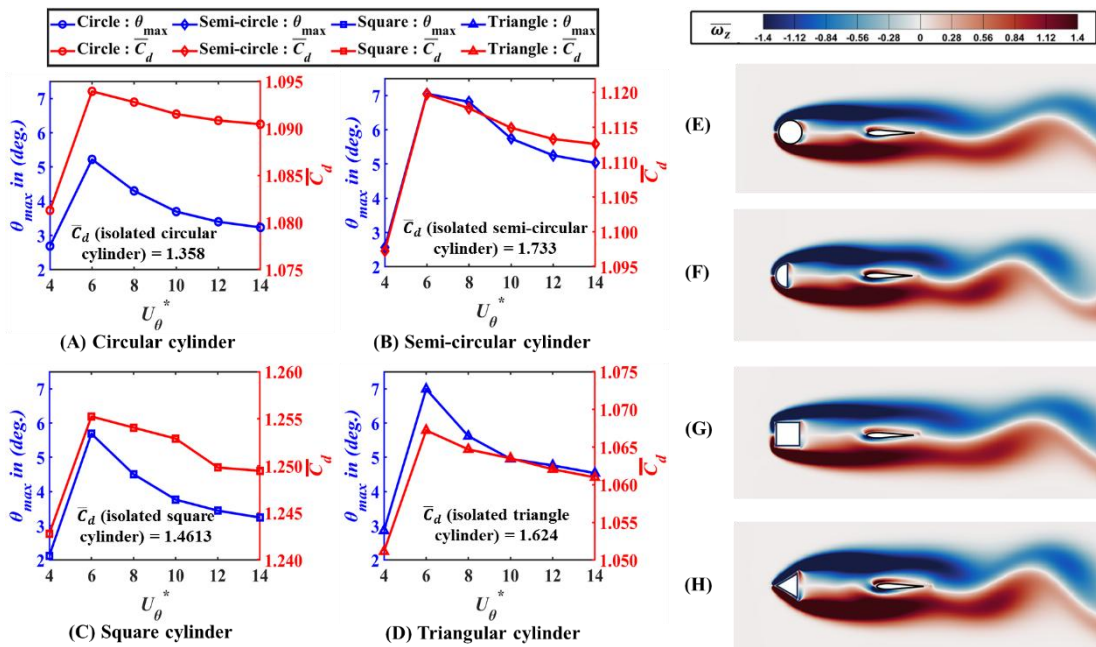


Fig. 2. The variation of θ_{max} of the aerofoil and total \bar{C}_d with U_θ^* when the front body is (A) circle, (B) semi-circular, (C) square, (D) triangle-shaped cylinder. Subplots (E-F) Instantaneous vorticity contours for different bluff body geometries with a passively rotating NACA0012 aerofoil at $Re = 100$ and $U_\theta^* = 6$.

4. CONCLUSION

This study numerically investigates the drag reduction of various bluff-body geometries, such as circular, semi-circular, square, and triangular, by using a downstream NACA0012 aerofoil which undergoes a passive rotation at $Re = 100$ and a reduced velocity range of $U_\theta^* = 4 - 14$. It is observed that the triangular and semi-circular geometries exhibit higher rotational amplitudes θ_{max} compared to the circular and square cylinders. Furthermore, for a fixed cylinder, the total time-averaged drag coefficient \bar{C}_d has a direct correlation with θ_{max} ; the \bar{C}_d value reduces when θ_{max} is decreased and vice versa. The passive rotation of the aerofoil delayed the vortex shedding to a further downstream region. Consequently, the tandem configuration exhibits a lower value of total \bar{C}_d than that of the isolated front body across all geometries.

5. REFERENCES

- [1] Bao, Yan & Tao, Jianjun, "Active control of a cylinder wake flow by using a streamwise oscillating foil," *Physics of Fluids*, vol. 25, May 2013, doi: 10.1063/1.4802042.
- [2] Han, Rong, Wei Liu, Xiao-Liang Yang, and Xing-Hua Chang, "Effect of NACA0012 Aerofoil Pitching Oscillation on Flow Past a Cylinder," *Energies*, vol. 14, no. 17, Sep. 2021, doi:10.3390/en14175582
- [3] Sikdar Prabir, Sunil Manohar Dash, and K Sinhamahapatra, "A Flexible Forcing Immersed Boundary Scheme-based One-step Simplified Lattice Boltzmann Method for Two-dimensional Fluid-solid Interaction Problems," *Computers & Fluids*, vol. 265, Jun. 2023, doi: 10.1016/j.compfluid.2023.105996.

Obstacle Avoidance of UAV in Dynamic Environments Using Direction and Velocity-Adaptive Artificial Potential Field

Nikita Pavle*, Shrreya Rajneesh*, Rakesh Kumar Sahoo†, Manoranjan Sinha‡

* Undergraduate Student, Department of Aerospace Engineering, Indian Institute of Technology Kharagpur, West Bengal, 721302, India

† PhD Research Scholar, Department of Aerospace Engineering, Indian Institute of Technology Kharagpur, West Bengal, 721302, India

‡ Professor, Department of Aerospace Engineering, Indian Institute of Technology Kharagpur, West Bengal, 721302, India

I. INTRODUCTION

The increasing prevalence of Unmanned Aerial Vehicles (UAVs) in civilian and commercial applications, from package delivery to infrastructure inspection, necessitates highly reliable and efficient autonomous navigation systems. A critical challenge for UAVs to navigate in cluttered and dynamic airspace, is collision avoidance. A widely-used approach for collision avoidance, owing to its computational cost and reactive nature, is the Artificial Potential Field (APF) method. APF works by assigning an attractive potential to the target and repulsive potentials to obstacles. The UAV traverse along the gradient of the combined potential field while avoiding obstacles. However, APF suffers from local minima issue that restricts its general applicability. In local minima condition, the attractive and repulsive forces balance out each other, causing the UAV to become prematurely trapped. To address this, various sophisticated methods have been explored in the literature, including modifications to the potential field like black-hole potential field [1], vortex potential field [2], and integration with optimization techniques such as RRT [3]. However, these approaches often require complex modifications of conventional potential functions, and the optimization techniques involved are computationally expensive. Crucially, even with local minima solutions, the standard APF doesn't account for the relative velocity V_e of moving obstacles with respect to the UAV. This deficiency is particularly problematic in high-speed scenarios, where relying solely on obstacle position and distance provides insufficient time and context for an appropriate evasive maneuver, often leading to a collision. To address the limitations of conventional APF in highly dynamic environments, we introduce a Direction and Relative Velocity Weighted APF approach. This novel method modifies the repulsive force using a bounded weighting function, which dynamically scales repulsion based on both the obstacle's direction and its relative speed. By integrating the instantaneous velocity threat into the potential function, our approach significantly enhances the safety, predictability, and real-time performance of collision avoidance for UAVs in dynamic airspace.

II. OBJECTIVES

The primary objective is to enhance the robustness of the Artificial Potential Field (APF) method for autonomous collision avoidance in dynamic environments. Specifically, we aim to:

- 1) Formulate a novel, bounded repulsive weighting function, $\omega(\theta, \vec{V}_e)$, that systematically incorporates both obstacle direction (θ) and relative velocity (\vec{V}_e) to accurately quantify the collision threat and scale the postential function.
- 2) Develop a stable APF extension by defining and enforcing bounds ($1 \leq \omega(\theta, \vec{V}_e) \leq \omega_{max}$) on the final weighting function to ensure predictable system behavior under high-threat conditions.
- 3) Validate the proposed APF extension in critical dynamic scenarios, particularly those involving fast-moving obstacles, to quantitatively demonstrate superior safety and performance compared to traditional and simple direction-weighted APF approaches.

III. METHODOLOGY

The methodology for this research begins by establishing the standard Artificial Potential Field (APF) repulsive potential as the baseline, which is solely dependent on obstacle distance ρ . This is defined as:

$$U_{rep} = \frac{1}{2}k_{rep} \left(\frac{1}{\rho} - \frac{1}{\rho_0} \right)^2 \quad \text{for } \rho \leq \rho_0$$

Recognizing the need for threat awareness, we first transition to the Direction-Weighted APF, where the repulsive potential is modulated by a directional weight, $U_{rep} = \omega(\theta)U'_{rep}$. However, this approach fails to adequately address high-speed, dynamic obstacles, as it treats a static obstacle and a rapidly moving one identically.

To close this critical safety gap, our main methodological contribution is the introduction of a Relative Velocity component into the weighting function. This is achieved by computing a threat factor, σ , which captures the instantaneous velocity of the obstacle (\vec{V}_e) along the line of sight (\hat{n}_e):

$$\sigma = \vec{V}_e \cdot \hat{n}_e$$

The final stage involves creating a new combined weighting function that integrates both the directional and relative velocity components. Crucially, this composite function is rigorously bounded ($1 \leq \omega_{final} \leq \dots$) to ensure the repulsive force scales appropriately under all conditions. The performance of this new approach is validated on a quadrotor simulation platform and compared against the Standard APF and the Direction-Weighted APF using key metrics like collision rate and minimum separation distance in various dynamic scenarios.

RESULTS AND DISCUSSION

The simulated performance of the proposed **Direction and Relative Velocity Weighted Artificial Potential Field (APF)** algorithm for quadrotor obstacle avoidance is outlined. The method is evaluated against critical dynamic scenarios, focusing on high-speed frontal and rear obstacle approaches, and compared against the **Standard APF** and a simpler **Direction-Weighted APF**. Key findings demonstrate that incorporating the relative velocity component provides timely and robust evasive maneuvers, leading to a quantifiable **reduction in collision rate** and a measurable **increase in minimum separation distance** across all dynamic test cases. The bounded nature of the new weighting function ensures predictable and stable avoidance behavior. Figure 1 illustrates the different obstacle cases considered, and Figure 2 shows a typical avoidance trajectory generated by the proposed algorithm in a cluttered environment.

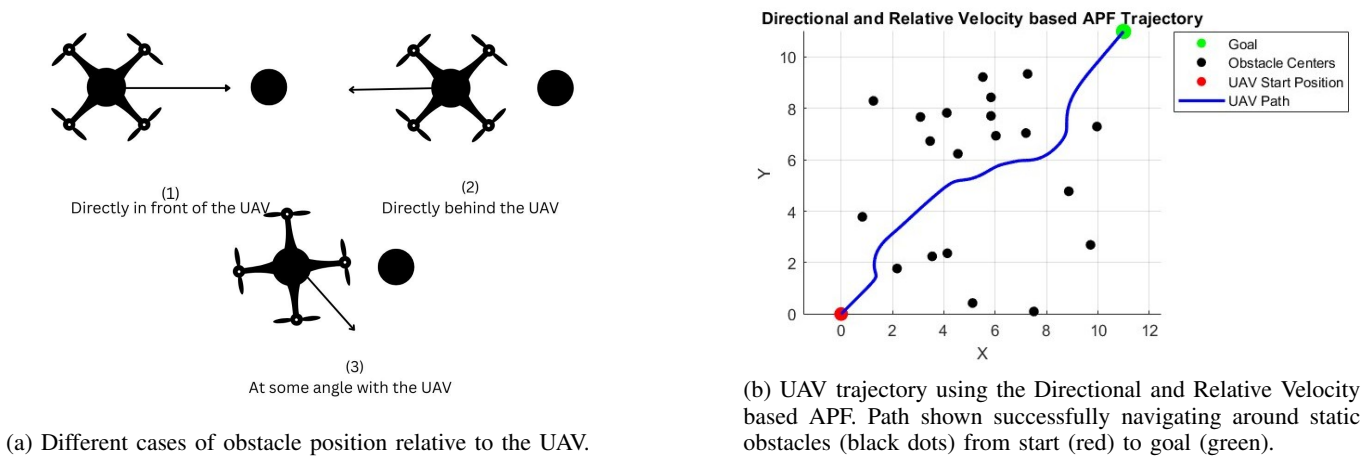


Fig. 1: Conceptual and simulation results of the proposed APF method.

CONCLUSION

This abstract presented a novel Direction and Relative Velocity Weighted Artificial Potential Field (APF) approach to enhance UAV collision avoidance in dynamic environments. By defining a new, bounded weighting function, $\omega(\theta, \vec{V}_e)$, which explicitly integrates directional bearing (θ) and the relative velocity threat factor ($\sigma = \vec{V}_e \cdot \hat{n}_e$), our method successfully addresses the critical limitations of traditional APF in high-speed scenarios. The proposed approach ensures the repulsive force is accurately scaled and system stability is guaranteed. Simulation results demonstrate that this enhanced APF significantly improves minimum separation distance and lowers the collision rate compared to previous APF models, leading to more reliable and safer autonomous navigation.

REFERENCES

- [1] Yao, Q., Zheng, Z., Qi, L., Yuan, H., Guo, X., Zhao, M., Liu, Z. and Yang, T., 2020. Path planning method with improved artificial potential field—a reinforcement learning perspective. *IEEE access*, 8, pp.135513-135523.
- [2] Nasuha, A., Priambodo, A.S. and Pratama, G.N.P., 2022, December. Vortex artificial potential field for mobile robot path planning. In *Journal of Physics: Conference Series* (Vol. 2406, No. 1, p. 012001). IOP Publishing.
- [3] Zhang, B. and Li, C., 2024. The Optimization and Application Research of the RRT-APF-Based Path Planning Algorithm. *Electronics*, 13(24), p.4963.

On the Dynamic Mode Decomposition of Supersonic Cavity Flow

Satya Prakash^{*1, 2}, Ram Kumar Yadav^{*1}, Avijit Chatterjee^{†2}, and Aniruddha Sinha^{‡2}

¹ Aeronautical Development Agency, Bengaluru 560017, INDIA

² Department of Aerospace Engineering, IIT Bombay, Mumbai, 400076, INDIA

1. INTRODUCTION

Open-cavity flows in high-speed regimes often exhibit strong tonal oscillations known as Rossiter modes, arising from feedback coupling between the shear-layer instability and acoustic resonance inside the cavity [1,2]. These oscillations generate intense pressure fluctuations and acoustic tones across subsonic, transonic, and supersonic regimes - though their amplitude and modal stability are strongly influenced by Mach number, compressibility, and cavity geometry [3]. The suppression of these oscillations has long been a subject of research owing to their significance in aircraft weapon bays, landing gear wells, and other aerodynamic cavities.

In this work, we apply POD [4,5] and DMD [6,7] to a three-dimensional supersonic cavity flow at a freestream Mach number of 1.4 and Reynolds number, $Re_L=1.7 \times 10^6$, comparing a baseline cavity with a passively controlled cavity outfitted with a cylindrical spoiler at the leading edge. Our goals are: (i) to perform a POD convergence study to determine how many snapshots suffice to resolve dominant energetic structures, and (ii) to analyze the dynamic characteristics of both the baseline and passively controlled cavity flows by conducting a DMD-based comparison, focusing on coherence, modal suppression, and feedback disruption mechanism.

2. GEOMETRICAL CONFIGURATION AND FLOW DATABASE

The cavity geometry is representative of a generic weapon bay. The flow is computed using Improved Delayed Detached Eddy Simulation [8], to resolve unsteady shear-layer dynamics, acoustic coupling and resulting tonal noise (Fig.1), while maintaining computational tractability. Two configurations are analyzed: a baseline cavity and a controlled cavity with a spanwise cylindrical spoiler placed just upstream of the cavity leading edge.

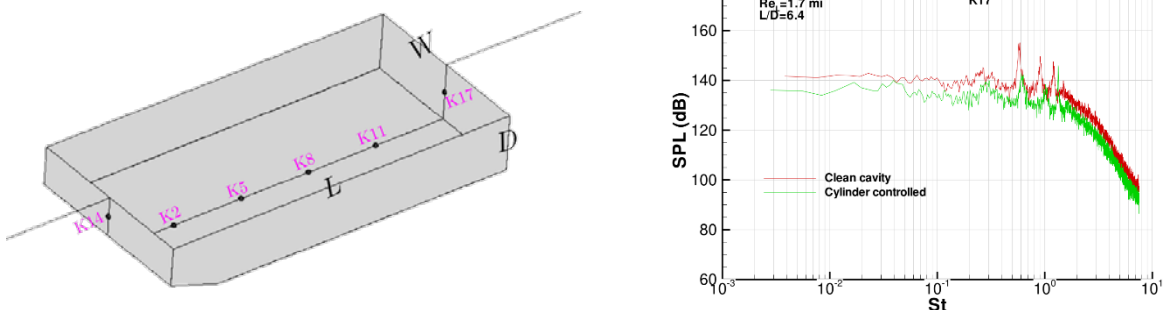


Fig 1: Baseline cavity configuration (left), sound pressure levels at the rear mid wall w/ & w/o control (right)

2.1 MODAL ANALYSIS

To guide snapshot selection, a preliminary POD convergence study is conducted using a 2D analogue of the cavity geometry under similar flow conditions. Up to 8000 snapshots were generated with a spacing of 0.067 flow time units, and various permutations and combinations of snapshot sets were pursued. This exercise helps guide the 3D dataset size to ensure statistically reliable modal decomposition.

The DMD is then applied to the same 3D dataset to extract dynamically meaningful modes. DMD approximates the eigenvalues and eigenvectors of a linear operator A that best advances the system in time such that $X' = AX$, X and X' being the data matrix and its time-advanced counterpart. The DMD spectrum, which maps each mode's temporal frequency and growth/decay rate, indicates the flow's temporal coherence and stability characteristics.

3 RESULTS AND DISCUSSION

The convergence analysis of POD for the 2D variant of the cavity flow demonstrates that the dominant energetic structures are accurately captured with fewer than 600 snapshots. The cumulative energy captured by the leading

¹ Communicating Author: Satya Prakash, satya.ada@gov.in

modes reaches a plateau beyond this limit, indicating statistical convergence. This confirms that the low-dimensional subspace spanned by the first few POD modes effectively represents the principal dynamics of the flow, making the decomposition suitable for reduced-order modelling and further DMD analysis.



Fig. 2: Pressure POD mode convergence: snapshot counts being (a) 1000, (b) 2000, (c) 4000, (d) 8000.

3.1 DMD OF BASELINE AND PASSIVELY CONTROLLED CAVITY

The DMD complex eigenvalue plot for the baseline cavity presents eigenvalues near the unit circle, indicating modes of neutral stability. These modes correspond to Rossiter frequencies also seen in the PSD and SPL plots (not shown). The DMD amplitude spectrum shows pronounced peaks at those frequencies, with mode shapes depicting large-scale shear-layer vortices extending along the span and into the cavity interior (not shown). The baseline flow is thus dominated by coherent, feedback-sustained Rossiter modes: shear-layer perturbations amplify downstream, impinge on the aft wall, create acoustic waves that travel upstream, and continuously reinforce the oscillation cycle.

When a cylindrical spoiler is introduced at the leading edge, significant modifications to the flow dynamics are observed. The DMD spectrum for the controlled cavity shows the disappearance of distinct Rossiter peaks and the emergence of broader, lower-energy spectral content. The spatial modes (not shown) become less organized and display reduced spanwise uniformity, indicative of weakened coherence across the cavity width.

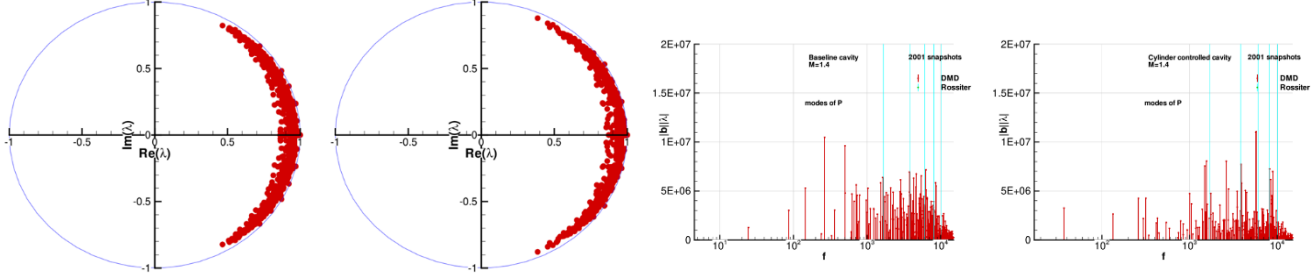


Fig 2: DMD spectrum (a) baseline, (b) controlled case (c) mode amplitudes – baseline, (d) controlled cavity

4 SUMMARY

The combined POD-DMD analysis provides valuable insight into the underlying dynamics and control of supersonic cavity flows. In the baseline 3D cavity, DMD identifies coherent Rossiter modes with strong spanwise organization and discrete spectral peaks. Introduction of a cylindrical spoiler effectively disrupts that coherence, suppresses dominant modes, and redistributes energy into broadband fluctuations, thereby breaking the feedback resonance. These findings support the hypothesis that the effectiveness of passive control in supersonic cavities stems from breaking modal coherence, rather than merely damping individual modes.

5 REFERENCES

- [1] Rossiter, J. E., Wind-tunnel experiments on the flow over rectangular cavities at subsonic and transonic speeds, Aeronautical Research Council Reports and Memoranda 3438, 1964.
- [2] Rowley, C. W. and Williams, D. R, On self-sustained oscillations in two-dimensional compressible flow over rectangular cavities, Journal of Fluid Mechanics, vol. 453, pp. 315-346, 2002.
- [3] Heller, H. H. and Bliss, D. B., Flow-induced pressure oscillations in cavities, vol. 8, no. 2, pp. 240-253, 1968.
- [4] Barkooz, G., Holmes, P., and Lumley, J.L., The proper orthogonal decomposition in the analysis of turbulent flows, Annual Review of Fluid Mechanics, vol. 25, pp. 539-575, 1993.
- [5] Lawson, S.J., Barakos, G.N., and Simson, A., Understanding cavity flows using proper orthogonal decomposition and signal processing, Int. Journal of Aeroacoustics, vol. 9, no. 3, pp. 291-322, 2010.
- [6] Schmid, P. J., Dynamic mode decomposition of numerical and experimental data. J. Fluid Mech., vol. 656, pp. 5-28, 2010.
- [7] Tu, J.H., Rowley, C.W., Luchtenburg, D.M., Brunton, S.L., and Kutz, J.N., On dynamic mode decomposition: Theory and Applications, J. Comput. Dynamics., vol. 1, no. 2, pp. 391–421, 2014.
- [8] Satya Prakash, Avijit Chatterjee, and Aniruddha Sinha, DMD-Aided Assessment of Control of the Aeroacoustic Environment in a Generic Weapon Bay Cavity, 30th AIAA/CEAS Aeroacoustics Conference, Rome, Italy, June 4-7, 2024.

On the evolution of Lamb vector in pulsating transonic jet flows

Subhro Halder¹, Debayan Das², Ribhu Pal³, Satvik Jaiswal⁴, and Arnab Roy^{5*}

^{1,2,3,4,5}Department of Aerospace Engineering, IIT Kharagpur, Kharagpur, India

*Communicating Author: Arnab Roy, arnab@aero.iitkgp.ac.in

1. Introduction

Impinging jet studies have played a significant role in exploring its various engineering applications, such as rocket propulsion, turbine blade cooling, and short takeoff and vertical landing (STOVL) systems. Several studies have extensively investigated different aspects of the complex flow phenomena involved, including tonal noise production and its dependence on jet temperature, standoff distance, and initial jet velocity. The aeroacoustic feedback loop mechanism was first examined by Powell [1], while Henderson and Powell [2] later also investigated the influence of shock waves on this feedback loop. Other studies have discussed coherent structures and the effects of impingement distance, as well as the occurrence of helical and axisymmetric instability modes [3]. Our primary research objective in this study is to analyze the role of the Lamb vector transport equation in the coupling between the velocity and vorticity fields for an axisymmetric pulsing jet, where the base Mach number at the jet inlet is $\overline{Ma} = 0.72$, and the Reynolds number, based on the jet diameter and base velocity, is $Re = \frac{\overline{UD}}{\nu} \approx 7.77 \times 10^4$, with $D = 0.005$ m. Lamb vector analysis is significant from multiple perspectives: from a kinematic perspective, Lamb vector closely resembles Coriolis acceleration, which plays a role in the jet spreading; divergence of Lamb vector denotes the balance between energy contained in the fluid strain head, and in fluid rotational head; while fluctuations in Lamb vector appears as a source term in the Acoustic Perturbation Equation which provides insights into far-field noise characteristics of the jet.

2. Numerical setup

In the present study, numerical simulations of transonic axisymmetric pulse jet impinging on a flat plate, have been carried out by solving the unsteady compressible Navier–Stokes equations using the *rhoCentralFoam* solver in the OpenFOAM platform. No turbulence model has been implemented to model the Reynolds stresses. The governing equations have been solved on a structured non-uniform quadrilateral mesh with clustering of cells near the solid wall as depicted in Figure 1.

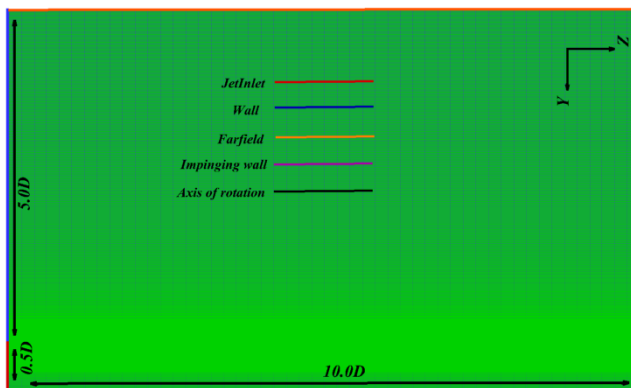


Figure 1: The axisymmetric rectangular computational domain for the present study. The jet inlet is in the form of an orifice on the left wall, with $p = 101325\text{Pa}$, $T = 300\text{K}$, and $\mathbf{u} = [0, 0, 250 + 150 \sin(8000\pi t)]$. The sinusoidal perturbation component is responsible for the pulsation of the jet. At the far-field, outflow boundary conditions: $\frac{\partial(p,T,u)}{\partial n} = 0$ has been prescribed. The jet impinges on a rigid, isothermal wall with boundary conditions as: $\frac{\partial p}{\partial n} = 0$, $T = 300\text{K}$, and $\mathbf{u} = [0, 0, 0]$.

3. Results

Lamb vector appears in the convective part of the Navier-Stokes equation and which acts as analogous to Coriolis force due to self-induced vorticity field. In order to derive greater insights about the spreading of the jet and energy cascade mechanism due to coupling between velocity and vorticity field, in the present study, we

study the effect of various terms of the Lamb vector $\mathbf{L} = \boldsymbol{\omega} \times \mathbf{u}$ transport equation to investigate the sources of Lamb vector production, redistribution, and dissipation in the flow field. The transport equation is as follows:

$$\frac{D\mathbf{L}}{Dt} = \underbrace{(\boldsymbol{\omega} \cdot \nabla) \mathbf{u} \times \mathbf{u}}_{\text{A}} - \underbrace{[\boldsymbol{\omega} (\nabla \cdot \mathbf{u})] \times \mathbf{u}}_{\text{B}} + \underbrace{\left(\frac{1}{\rho^2} \nabla \rho \times \nabla p \right) \times \mathbf{u}}_{\text{C}} + \underbrace{\boldsymbol{\omega} \times \left(-\frac{1}{\rho} \nabla p \right)}_{\text{D}} + \underbrace{\left[\nabla \times \left(\frac{1}{\rho} \nabla \cdot \boldsymbol{\tau} \right) \right] \times \mathbf{u}}_{\text{E}} + \boldsymbol{\omega} \times \left(\frac{1}{\rho} \nabla \cdot \boldsymbol{\tau} \right)$$
(1)

where term A represents the the vortex-stretching/tilting through velocity field. The term B represents the contribution of compressibility effects and term C represents the coupling between the baroclinic torque and velocity field. The effect of the C term becomes significant near shock waves in the flow field. The term D corresponds to the interaction between the vorticity field and the pressure gradient. In our case, terms B and D contribute significantly to the coupling of the velocity and vorticity field. The term E is coming from the viscous related terms from both momentum transport and vorticity transport equation. The variations for cases B, C, and D are shown in Figure 2.

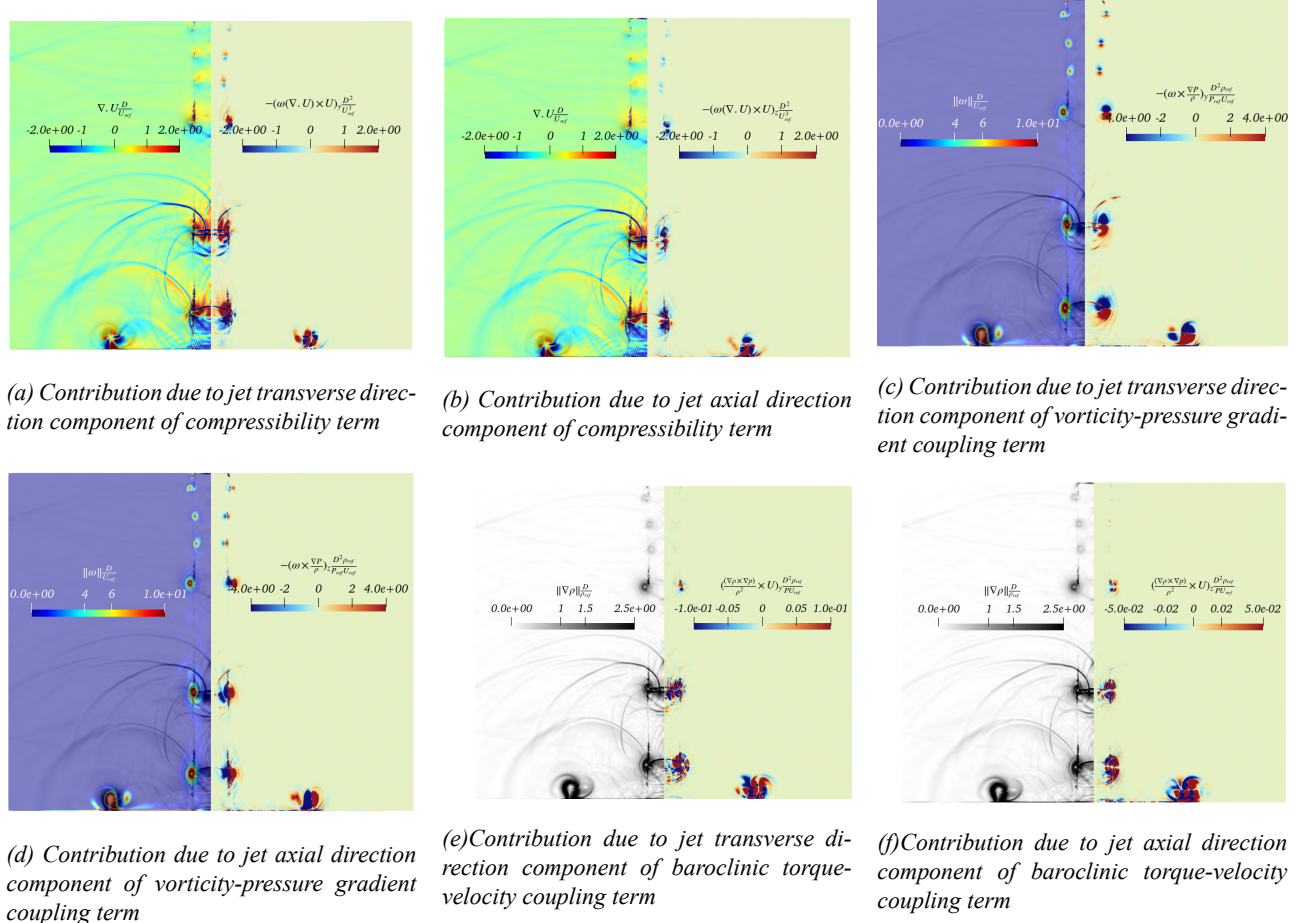


Figure 2: Contribution of various term during the jet impinging

References

1. Powell, A., "On Edge Tones and Associated Phenomena," Acta Acustica United with Acustica, Vol. 3, No. 4, 1953, pp. 233–243.
2. Henderson, B., and Powell, A., "Experiments Concerning Tones Produced by an Axisymmetric Choked Jet Impinging on Flat Plates," Journal of Sound and Vibration, Vol. 168, No. 2, 1993, pp. 307–326.
3. Henderson, B., Bridges, J., and Wernet, M., "An Experimental Study of the Oscillatory Flow Structure of Tone-Producing Supersonic Impinging Jets," Journal of Fluid Mechanics, Vol. 542, Nov. 2005, pp. 115–137.

Parameter Estimation of BLDC Motor Using Nonlinear Least Square Method

Rajib Mandi,^{a*} N. K. Peyada,^b

^a Research Scholar, Department of Aerospace Engineering, Indian Institute of Technology Kharagpur, Kharagpur, India

^bAssociate Professor, Department of Aerospace Engineering, Indian Institute of Technology Kharagpur, Kharagpur, India

1. INTRODUCTION AND OBJECTIVE

Recent advancement in aviation systems is paving the way for deployment of power optimized aircraft (POA) via Fly-by-Wire (FBW) and Powered-by-Wire technologies. The goal is to replace existing actuators that are powered by the central hydraulic system with intelligent electro-mechanical (EMA) and electro-hydraulic (EHA) actuators [1]. The EMA uses mechanical gearing and ball screws to amplify the motor torque and provide linear actuation. This Approach may make it difficult to meet the safety requirement of a primary flight control surface with multiple actuators to ensure continued operation in the event of a unit failure. When an EMA fails due to mechanical gearing, the result can be jammed actuator, which may also prevent the backup units from operating [2]. The EHA is a local, electrically powered hydraulic actuation system that performs similar functions to a hydraulic system. When multiple EHA actuators are used in parallel on a flight control surface, a simple hydraulic bypass valve can be used to accommodate the failure of one unit. This allows the failed unit's hydraulic ram to move freely while the flight control surface moves under the control of the remaining healthy units [2]. A fundamental element that drives the EHA/EMA actuator is the DC motor. Nowadays. DC motors are being replaced by BLDC motors [2]. Due to their unique design and absence of a commutator, high-speed brushless direct current (BLDC) motors have the advantages of high mechanical reliability, high power density and efficiency, greater longevity, and compact construction [3]. As a result, in space, where the operational environment is unique and harsh, are ideal for these motors. Besides the aerospace, BLDC motors are used in automotive, pumping, and many others industries. Though the BLDC motors are gaining interest in industrial and commercial applications, the future of the BLDC motors faces indispensable concerns and open research challenges.

In its use, of course, this BLDC motor requires control so that it can be used according to its function. In this research paper unknown parameters of the BLDC motor are estimated using nonlinear least square method.

2. METHOD OF ANALYSIS

The BLDC motor is constructed with a permanent magnet rotor and three-phase star or delta connected stator, and a drive unit. Therefore, in the BLDC motor, three phase currents, angular speed, and angular position are output of the system and three phase voltages are input to the system, i.e., BLDC motor is a MIMO system. But, the nonlinear least square method is developed for SISO system[4]. Therefore, to estimate the parameters of the BLDC motor using nonlinear least square method, firstly the equations of the BLDC motors are discretized using Euler's discretization method. By discretizing BLDC motor's equation, three equations for three phase currents, one for angular speed, and one for angular position are derived. From the three phase current equations, unknown parameter resistance (R), inductance (L), and back-EMF constant (Ke) are estimated and from the equation for angular speed unknown parameter moment of inertia (J) is estimated. In this parameter estimation method, Gauss-Newton (GN) and Levenberg-Marquardt (LM) optimization method is used.

* Communicating Author: Rajib Mandi
Email id: rajibaero.4@gmail.com/rajibmandi@iitkgp.ac.in
Address: Aerospace Engineering Department,
Indian Institute of Technology Kharagpur, West Bengal 721302, India
Contact No: 8145320747

3. RESULTS

The initial values of the parameters are chosen as $R = 1.4$, $L = 6.15 \times 10^{-3}$, $Ke = 0.105$, and $J = 7.1 \times 10^{-3}$ for both the optimization method. The parameters, resistance converges to 1.4711, inductance converges to 6.1500002×10^{-3} , back-EMF constant converges to 0.1074, and moment of inertia converges to 0.0083. The changes from initial value to converged value in case of inductance are very less compared to other parameters. The converged value of the parameter inductance is rounded off to four decimal places as 0.0062. The estimated parameters are listed in Table 1 and are compared with the true value of the parameters.

Table 1: Estimated Parameters

| Parameter | True Value | GN Method | Absolute % of error in GN Method | LM Method | Absolute % of error in LM Method |
|-----------------------|-------------------------|-----------|----------------------------------|-----------|----------------------------------|
| $R (\Omega)$ | 1.5 | 1.4711 | 1.9277 | 1.4711 | 1.9277 |
| $L (H)$ | 6.1×10^{-3} | 0.0062 | 0.8197 | 0.0062 | 0.8197 |
| $Ke (V/(rad.s^{-1}))$ | 0.1074 | 0.1078 | 0.3536 | 0.1078 | 0.3537 |
| $J (kgm^2)$ | 8.2614×10^{-3} | 0.0083 | 0.4619 | 0.0083 | 0.4619 |

4. CONCLUSIONS

The parameters estimated are very close to its true value. Only the resistance has around 2% error, and the other parameters has less than 1% error. The GN method and LM method are in very good agreement in terms of estimating parameters of BLDC motors. These two estimation methods are very sensitive to the initial value of the parameters. A little change of initial value will change the value of parameters drastically and it will diverge.

REFERENCES

- [1]. Vladimir Hubik, Martin Sveda, and Vladislav Singule. On the development of bldc motor control run-up algorithms for aerospace application. In 2008 13th international power electronics and motion control conference, pages 1620–1624. IEEE, 2008.
- [2]. Xiaoyan Huang, Keith Bradley, Andrew Goodman, Chris Gerada, Pat Wheeler, Jon Clare, and Chris Whitley. Fault-tolerant brushless dc motor drive for electro hydrostatic actuation system in aerospace application. In Conference record of the 2006 IEEE industry applications conference forty-first IAS annual meeting, volume 1, pages 473–480. IEEE, 2006.
- [3]. Jian Feng, Kun Liu, and Qing Wang. Scheme based on buck-converter with three-phase hbridge combinations for high-speed bldc motors in aerospace applications. IET Electric Power Applications, 12(3):405–414, 2018.
- [4]. Karel J Keesman and Karel J Keesman. System identification: an introduction, volume 2. Springer, 2011.

Parametric study of friction characteristics of IRS rail steel using ball-on-disk experiments

Shreedhar Sahoo^a, D S Kushan^b, Mayank Kumar^b and Vikranth Racherla^c

^aResearch Scholar, Department of Mechanical Engineering, Indian Institute of Technology Kharagpur, Kharagpur, India

^bProject Officer, Centre for Railway Research, Indian Institute of Technology Kharagpur, Kharagpur, India

^cProfessor, Department of Mechanical Engineering, Indian Institute of Technology Kharagpur, Kharagpur, India

1. INTRODUCTION AND OBJECTIVE

Railway track materials endure complex tribological stresses under varying operational conditions. IRS-grade rail steels, widely used in Indian Railways, require robust evaluation to ensure long-term performance and safety. Among laboratory-scale methods, the ball-on-disk test offers a controlled simulation of contact wear, enabling parametric insights into surface degradation.

Previous studies have explored wear behavior of rail and stainless steel materials under varied tribological conditions. Ball-on-disk tests have demonstrated sensitivity to load and sliding speed, with increased values leading to elevated wear rates and COF under dry conditions [1]. The use of tungsten carbide balls has been validated as a reliable proxy for rail-wheel contact, especially when isolating disk wear [2]. Additionally, asymmetric wear patterns and repeatable tribometer setups have been reported under spin creepage and varied lubrication states [3]. These findings underscore the relevance of controlled lab-scale tribometry in predicting field performance and motivate the current study's focus on IRS-grade rail steel.

This study presents a full factorial investigation of IRS rail steel using a tungsten carbide (WC) ball-on-disk tribometer. The parameters varied include normal load (40–60 N) and surface roughness obtained through different grit polishing. Tungsten carbide was selected as the counterface to minimize ball wear and isolate the disk's tribological response.

Wear track widths were measured across all runs, and surface morphology was analyzed using SEM. Elemental changes were studied via EDS, comparing track vs base under coarse finish (220#) and assessing load effects under fine finish (1000#). The objective is to quantify the influence of load and surface finish on wear behavior, and to identify dominant wear mechanisms relevant to rail applications.

2. METHODS OF ANALYSIS

A full factorial matrix was constructed with two independent variables, namely, normal load (40 N, 50 N, 60 N) and surface roughness by polishing to 220# and 1000# grit, while maintaining a constant sliding speed of 52.36 mm/s.

1. Ball-on-disk wear tests were conducted using a tungsten carbide (WC) ball to minimize counterface wear and isolate the disk material response.
2. Post-test wear tracks were examined using a contact profilometer to measure track width, area of depression, and maximum depth, which serves as a proxy for wear across all runs.
3. Scanning Electron Microscopy (SEM) was employed to identify dominant wear mechanisms such as abrasion, adhesion, and delamination on selected tracks.
4. Energy Dispersive Spectroscopy (EDS) was performed to compare elemental composition between worn tracks and unworn base material:
 - Under 220# finish, track vs base comparison was conducted.
 - Under 1000# finish, EDS was used to study the effect of varying load.

3. RESULTS

a. WEAR TEST:

- For higher roughness disk, with increasing load, the steady state coefficient of friction rises; Whereas for higher finish disk, with increasing load, the steady state coefficient of friction reduces. At 60N load, the steady state coefficient of friction is around 0.2. For higher finish disk, the initial coefficient of friction is higher than the rough disk.
- For rough disk, the initial coefficient of friction increases with load, but the delay in the drop reduces. Thus, at 60N, the drop is quickly achieved than at 40N.

b. CONTACT PROFILOMETRY:

- Rougher surfaces (220#) consistently showed wider tracks across all loads, supporting multi-asperity contact behavior.
- For both samples, increasing load generally led to deeper and wider tracks, though Sample 1000# showed an unexpected reduction in depth at 60N, possibly due to peak interference.

c. WEAR MECHANISM:

- Delamination is visible for all samples, with few traces of abrasive wear on some samples.

d. ELEMENTAL ANALYSIS:

- The delaminated tribo-oxide layer reveals the beneath ferrous surface evident through the EDS mapping, with less percent ball material also found in the tribo-oxide layer on track.

4. CONCLUSIONS

The following can be concluded based on the above experiments:

- Surface finish and load significantly influence frictional behavior, with smoother discs showing reduced steady-state friction at higher loads.
- Contact profilometry confirms wider wear tracks for rougher surfaces, indicating multi-asperity contact and distributed deformation.
- Delamination is the dominant wear mechanism across samples, with minor abrasive features observed selectively.
- Elemental analysis reveals tribo-oxide formation and partial ball material transfer, exposing the underlying ferrous substrate.

REFERENCES

- [1] D. V. Lindberg and H. K. H. Lee, “Optimization under constraints by applying an asymmetric entropy measure,” *J. Comput. Graph. Statist.*, vol. 24, no. 2, pp. 379–393, Jun. 2015, doi: 10.1080/10618600.2014.901225.
- [2] A. Ay and A. Çelik, “Investigation of friction and wear behavior of Turkish rail steels using ball-on-disk tests,” *Wear*, vol. 330–331, pp. 507–517, 2015, doi: 10.1016/j.wear.2015.01.058.
- [3] J. Xia, J. S. S. Lee, and R. Lewis, “A novel twin-disc method for investigating spin creepage in rail-wheel contact,” *Tribol. Int.*, vol. 113, pp. 1–10, 2017, doi: 10.1016/j.triboint.2017.03.007.

Prediction of Store Trajectory Using Domain-Decomposed Reduced-Order Modelling

Navdeep Pandey^{*1}, Jaysinh Jagdishchandra Patel^{†2}, and Aniruddha Sinha^{‡1}

¹Dept. of Aerospace Engineering, Indian Institute of Technology Bombay, Mumbai 400076, INDIA

²Defence Research and Development Laboratory, Hyderabad 500058, INDIA

I. Introduction

A meticulous analysis is crucial to certify the safe-separation flight envelope of aircraft store (missile, payload etc.) duo, whenever an existing one undergoes any design modification or a new one is inducted. The trajectory followed by the store after its release from the aircraft is computed to predict the safe flight envelope of aircraft. There are mainly three conventional approaches to predict the store trajectory: flight testing, wind tunnel experiment, and computational fluid dynamics (CFD) investigation. All of these pose some constraints related to safety, time consumption, and economic viability. In the present work, we perform a store trajectory estimation based on empirical reduced-order modelling (ROM) integrated with domain-decomposition that we proposed recently [1, 2]. It is an efficient, albeit approximate, alternative to the steady RANS-based approach. The proposed ROM uses proper orthogonal decomposition (POD) to identify the underlying reduced-order topology of the flow which necessitates that all the empirical flow data supplied are for the same geometry (and mesh). the position of the store changes continuously throughout its trajectory. Consequently, the usual POD-ROM approach for single-body aerodynamics cannot be employed for the full-flow domain here. Considering this limitation, our proposed approach decomposes the full-domain into multiple subdomains such that POD-ROM can be employed for the maximal portion of the flow domain, and the remaining subdomain that involves changing geometry/mesh is solved using the full-order model (FOM). The overall approach is termed domain-decomposed ROM (DDROM). Our previous work [1–3] demonstrated the feasibility of the approach. Here, we extend the work for predicting the full trajectory of the store on more complicated and realistic three-dimensional problem.

II. Theory and approach

A. POD & Reduced-order model

Let us denote the flow vector field by $\mathbf{q}(\mathbf{x}; \boldsymbol{\mu})$, where $\mathbf{x} := (x, y)$ is the 2D Cartesian coordinate and $\boldsymbol{\mu}$ is the parameter vector. In POD, we assume that the flow vector field can be approximated as $\mathbf{q}(\mathbf{x}; \boldsymbol{\mu}) \approx \bar{\mathbf{q}}(\mathbf{x}) + \sum_{n=1}^{N_p} \eta^n(\boldsymbol{\mu}) \tilde{\mathbf{q}}^n(\mathbf{x})$. where, $\bar{\mathbf{q}}(\mathbf{x})$ is the mean flow vector field and the remaining ‘fluctuations’ are approximated as linear combinations of spatial basis functions $\{\tilde{\mathbf{q}}^n(\mathbf{x})\}_{n=1}^{N_p}$ called POD modes, weighted by POD coefficients $\{\eta^n(\boldsymbol{\mu})\}_{n=1}^{N_p}$ whose determination follows the established ‘snapshot’ POD approach [4–6].

The ROM predicts the flow field for a new parameter vector $\boldsymbol{\mu}_0$ by invoking the governing equations. This is a more robust and accurate approach than the more straightforward interpolation in the parameter space. The POD-based ROM technique employed here was originally developed for steady single-body aerodynamics [7–11]. The particular details relevant to this work can be found in Ref. [6].

B. Domain decomposition

As discussed in section I, we can not implement POD-ROM for the full domain due to the continuous change in the geometry (mesh). To avoid this problem, We adopt the domain decomposition strategy to deploy a POD-based reduced-order model (ROM) to solve the flow problem over the largest possible portion of the flow domain i.e., *Aircraftbox*, Ω_A and *Capsule*, Ω_C , along with a full-order model (FOM) solution restricted to the remaining small subdomain i.e., *Dropbox*, Ω_D [1, 2, 12].

The capsule and aircraftbox are subdomains where the geometry (and even the mesh) can remain same across all possible configurations of the store. Thus, we will pursue POD-based ROM in these two subdomains. On the other hand, the dropbox is the only subdomain whose geometry (and hence the mesh) must change across various possible positions of the store. Hence, POD-ROM is inapplicable here, and we have to revert to FOM calculations instead. A more detailed discussion will be included in final paper.

III. Results

A. Geometry and mesh

The geometries of the aircraft and the store are borrowed from a standard test case carried out by Heim1991. All geometry parameters, including those of the pylon, can be found in Heim1991.

^{*}Graduate student

[†]Scientist E

[‡]Associate Professor; Corresponding author: as@aero.iitb.ac.in

The mesh is generated using the commercial software Pointwise (v18.2). The total cell count of the grid is 3.54 million. To achieve the y^+ constraint of unity at any wall for the $k - \omega$ (SST) turbulence model, prism layers have been generated on the store with the first cell layer height of 1 micron, and stretching factor of 1.2.

B. Performance of DDROM

In this preliminary work, we present the verification of the DDROM technique to predict force and moment coeffs. on the store for a new parameter set. Performance is evaluated in the sets of parameters of the ‘test’ and the results are presented in table 1. All coefficients are multiplied by 100 to obtain numbers that are easier to present in the table. The ‘truth’ values of the coefficients come from a FOM trajectory calculation for the test case. The absolute errors of the DDROM predictions are not insignificant as a fraction of the corresponding truth values; indeed, there is 180% relative error in roll moment prediction for the case of $M = 0.6$ and $\alpha = 7.5^\circ$. However, this is somewhat misleading as the truth value of the same happens to be very close to zero. A more representative metric is the maximum absolute error as a percentage of the range of the respective coefficient observed in the learning database, as presented in the final row. Even in this perspective, the DDROM performance may only be deemed as adequate, but it leaves much ground for improvement. The final paper will include the full trajectory results using DDROM approach corresponding to the test cases.

Table 1 Performance of DDROM in terms of absolute prediction error of force and moment coefficients at the initial points of the 4 test trajectories. The last row gives the maximum error encountered in tests as a percentage of the respective truth ranges.

| M | α [deg] | Quantity | C_x | C_y | C_z | $C_{m,x}$ | $C_{m,y}$ | $C_{m,z}$ |
|---|----------------|----------|-------|-------|-------|-----------|-----------|-----------|
| 0.6 | 2.5 | Error | 1.02 | 1.92 | 0.36 | 0.05 | 9.23 | 2.43 |
| 0.6 | 7.5 | Error | 0.56 | 3.84 | 4.78 | 0.18 | 0.24 | 1.89 |
| 0.7 | 2.5 | Error | 1.59 | 4.97 | 0.79 | 0.38 | 1.57 | 0.49 |
| 0.7 | 7.5 | Error | 2.34 | 5.88 | 0.30 | 0.08 | 7.71 | 2.20 |
| Max error as % of range of truth values | | | 7.66 | 6.89 | 7.28 | 35.23 | 9.03 | 6.50 |

IV. Conclusions

We extend our previous work on efficient albeit approximate computation of store-separation trajectories from aircraft. The adopted strategy has at heart an empirical reduced-order model (ROM) based on proper orthogonal decomposition (POD) that is applied to the majority of the flow domain. To overcome the issue of the changing grid and geometry inherent in the store-separation problem, a domain decomposition strategy has been adopted wherein the remainder of the domain is solved with the full-order model, and the subdomains’ solutions are iteratively matched at the interfaces. Encouraging preliminary results are presented in table 1 but approach needs to be improved substantially for predicting full trajectory. We foresee that these will be overcome in final paper, thus delivering a viable efficient alternative to CFD-intensive store separation trajectory calculation.

References

- [1] Sinha, A., and Garg, S., “Reduced-order modeling of steady aerodynamics for 2D store separation analysis,” *2018 Applied Aerodynamics Conference, Paper 3168*, 2018. <https://doi.org/10.2514/6.2018-3168>.
- [2] Pandey, N., Tembhare, R., Singh, N., and Sinha, A., “Domain-Decomposed Reduced-Order Modelling of Steady Aerodynamics for 2D Store Separation Analysis,” *AIAA Scitech Forum, Paper 1004*, 2023. <https://doi.org/10.2514/6.2023-1004>.
- [3] Pandey, N., Patel, J. J., and Sinha, A., *Store Trajectory Prediction Using Domain-Decomposed Reduced-Order Modelling*, ????. <https://doi.org/10.2514/6.2024-4444>, URL <https://arc.aiaa.org/doi/abs/10.2514/6.2024-4444>.
- [4] Sirovich, L., “Turbulence and the dynamics of coherent structures. I - Coherent structures. II - Symmetries and transformations. III - Dynamics and scaling,” *Quarterly of Applied Mathematics*, Vol. 45, 1987.
- [5] Holmes, P., Lumley, J. L., Berkooz, G., and Rowley, C. W., *Turbulence, coherent structures, dynamical systems and symmetry*, Cambridge University Press, 2012. <https://doi.org/10.1017/cbo9780511919701>.
- [6] Sinha, A., Kumar, R., and Umakant, J., “Reduced-order model for efficient generation of a subsonic missile’s aerodynamic database,” *The Aeronautical Journal*, Vol. 126, 2022, pp. 1546–1567. <https://doi.org/10.1017/aer.2022.4>.
- [7] LeGresley, P. A., and Alonso, J. J., “Investigation of non-linear projection for pod based reduced order models for aerodynamics,” *39th Aerospace Sciences Meeting, Paper 926*, 2001. <https://doi.org/10.2514/6.2001-926>.
- [8] Alonso, D., Vega, J. M., and Velazquez, A., “Reduced-order model for viscous aerodynamic flow past an airfoil,” *AIAA Journal*, Vol. 48, No. 9, 2010, pp. 1946–1958. <https://doi.org/10.2514/1.j050153>.

Predictive Multiphysics Simulation of Fluid–Structure Interaction in Deformable Microchannels for Biomedical Applications

Satyabrata Podder¹ (satyabrata.podder.ece@gmail.com); Tapan Sarkar¹ (tapansarkar.met@gmail.com); Amit Dhar¹ (mtdhar96@gmail.com); Animesh Das¹ (animeshdas990@gmail.com); Shantanu Dutta^{2*} (shantanudut@gmail.com)

¹Elitte College of Engineering, affiliated to Maulana Abul Kalam Azad University of Technology (MAKAUT), India

²Sanaka Educational Trust's Group of Institutions, affiliated to Maulana Abul Kalam Azad University of Technology (MAKAUT) Malandighi Durgapur-713212, India *Corresponding author

Abstract: Deformable microchannels are pivotal in biomedical microfluidic devices, enabling dynamic control of biofluid transport in lab-on-a-chip and organ-on-chip platforms. This study presents a two-dimensional multiphysics simulation of fluid–structure interaction (FSI) in a soft polymer microchannel using COMSOL Multiphysics. The incompressible Navier–Stokes equations for Newtonian biofluid are coupled with linear elasticity for PDMS walls via the Arbitrary Lagrangian–Eulerian (ALE) method. We investigate flow-induced wall deformation under inlet pressures from 500 Pa to 2000 Pa, quantifying effects on flow rate, dimensionless compliance number (Ca), and transient wall dynamics. Results show that wall compliance nonlinearly enhances flow rate by up to 8 %, with a critical $Ca \approx 0.05$ marking the onset of strong coupling. Time-dependent analysis reveals damped oscillations in wall displacement, whose decay rate depends on solid damping. These findings provide quantitative design guidelines for optimizing deformable microchannels in biomedical applications.

Keywords: Microfluidics; fluid–structure interaction ;COMSOL Multiphysics ;deformable microchannels; compliance number

1. INTRODUCTION & OBJECTIVE

Deformable microchannels fabricated from soft polymers such as PDMS critically influence microscale biofluid transport by coupling viscous flow with wall elasticity; numerical studies have demonstrated that this fluid–structure interaction alters hydraulic resistance, modifies velocity and shear distributions, and can produce measurable flow enhancement in compliant regimes [1]. These devices form the technical foundation for many biomedical lab-on-a-chip and organ-on-chip platforms, and design guidelines linking material stiffness, geometry, and operating pressures are summarized in comprehensive texts on microfluidic devices for biomedical applications [2].

2. METHODS OF ANALYSIS

The model is a two-dimensional slice through a deformable microchannel with total outer width 300 μm and height 150 μm . Its adopted from Fig1. The fluid domain is the central cut out of height 30 μm , whose side transitions are defined by two semicircular arcs of radius 15 μm . Top and bottom PDMS walls each have a uniform thickness of 60 μm . A straight channel length of 5 mm is extruded in the flow (x) direction to capture fully developed conditions.

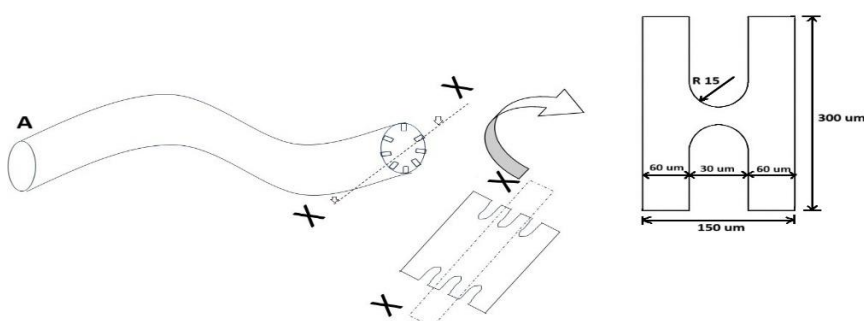


Figure 1. Tubular & X-X Cross-sectional geometry of the deformable microchannel used in simulations[1].

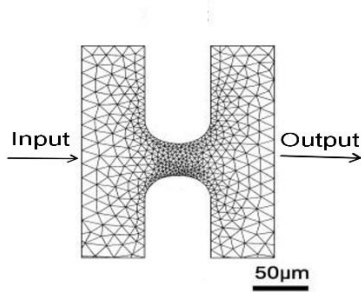


Figure 2. A fully unstructured triangular mesh is used, with element size refined to $0.5 \mu\text{m}$ at the fluid–solid interfaces and along the semicircular arc with inlet and outlet

The incompressible Navier–Stokes equations govern fluid flow (density $\rho = 1000 \text{ kg/m}^3$, viscosity $\mu = 1 \times 10^{-3} \text{ Pa}\cdot\text{s}$). Solid mechanics in PDMS walls (Young’s modulus has an $E = 1.8 \text{ MPa}$, Poisson’s ratio $\nu = 0.49$) and follows linear elasticity. Fluid–structure coupling employs the Arbitrary Lagrangian–Eulerian (ALE) formulation to map mesh deformation in response to wall displacement. The Inlet prescribed pressure gradient varied from 500 Pa to 2000 Pa. The Outlet is set to zero gauge pressure. The walls are no-slip on fluid boundaries; fixed constraint on outer PDMS exterior. Symmetry is enforced at the channel center-plane if modeling half-domain. A fully unstructured triangular mesh is used, with element size refined to $0.5 \mu\text{m}$ at the fluid–solid interfaces and along the semicircular arcs (Fig 2). A mesh-independence study ensures less than 1 % variation (approx) in peak displacement and pressure drop. Ca was used to characterize the relative importance of viscous forcing to solid stiffness as (1)

$$\text{Ca} = \frac{\mu U}{E h} \quad (1)$$

where μ is fluid dynamic viscosity ($\text{Pa}\cdot\text{s}$), U is characteristic fluid velocity ($\text{m}\cdot\text{s}^{-1}$), E is Young’s modulus of the wall material (Pa), and h is a representative wall length scale (m), here taken as the PDMS wall thickness. In this study U was taken as the mean centerline velocity corresponding to the steady pressure-driven flow at each inlet pressure, and $h = 60 \mu\text{m}$. The transition observed near $\text{Ca} \approx 0.05$ therefore corresponds to the onset where viscous forcing produces appreciable elastic deflection under the chosen geometry and material parameters.

3. RESULTS

Under increasing inlet pressure, maximum wall deflection rises non-linearly from $2 \mu\text{m}$ to $12 \mu\text{m}$, altering the cross-sectional area and enhancing flow rate by up to 8 %. Velocity profiles shift from parabolic to flattened shapes as compliance increases. Dimensionless analysis shows that the compliance number ($\text{Ca} = \mu U/E h$) governs the deformation regime, with a transition at $\text{Ca} \approx 0.05$ marking onset of significant coupling. Time-dependent simulations reveal damped oscillations in wall displacement when a pressure step is applied, with decay rates sensitive to the solid damping coefficient. Also by replacing **linear elasticity** with **hyperelastic models** (e.g., Mooney–Rivlin) for PDMS walls we establish large deformations affect flow rate and stress distribution. Under a Mooney–Rivlin hyperelastic model, wall deflection rises from $\sim 2.5 \mu\text{m}$ to $\sim 12 \mu\text{m}$ before plateauing at high inlet pressure.

4. CONCLUSIONS

- The multiphysics model accurately predicts the coupled dynamics of fluid flow and wall deformation in soft microchannels.
- The compliance number (Ca) serves as a key design parameter to tune flow enhancement and structural stability.
- The results provide quantitative guidelines for optimizing wall thickness and material stiffness in responsive microfluidic devices for drug delivery and organ-on-chip applications.

REFERENCES

[1] J. W. Hyun, D. B. Freeman, and M. L. Stone, “Fluid–Structure Interaction in Deformable Microchannels: A Numerical Study,” *Lab Chip*, vol. 11, pp. 1302–1313, 2011. <https://doi.org/10.1039/C0LC00500F>

[2] N.-T. Nguyen and S. T. Wereley, *Microfluidic Devices for Biomedical Applications*, Artech House, Boston, MA, 2006.

Random Eigenvalue Characterization for Free Vibration of Centrifugally Loaded Euler-Bernoulli Beams

Jammu Sarath^a, Ravi Prakash Prajapati^b and Korak Sarkar^c

^aM.Tech., Mechanical Engineering, Indian Institute of Technology Kharagpur, India

^bResearch Scholar, Mechanical Engineering, Indian Institute of Technology Kharagpur, India

^cAssistant Professor, Mechanical Engineering, Indian Institute of Technology Kharagpur, India

1. INTRODUCTION & OBJECTIVE

Numerous engineering materials demonstrate considerable spatial randomness in their mechanical and thermal properties [1]. Here, we specifically study the centrifugally loaded Euler-Bernoulli beams, which are used to model important structures like helicopter blades, propellers, turbines, and wind-turbine blades. The randomness stems from intricate interactions among material composition, microstructure, manufacturing processes, and environmental conditions, leading to statistical fluctuations in the properties of these beams, including their natural frequencies and mode shapes. Estimating statistical properties, including the mean and variance of random eigenvalues, is crucial for real-world applications, especially since these structures are prone to resonant phenomena. Consequently, it is essential to obtain precise analytical expressions for these quantities as functions of the statistical variations in beam properties. In this work, we establish a direct mathematical relationship between flexural stiffness and fundamental natural frequency using an inverse problem approach. The probability density function (PDF) of the flexural stiffness is determined by knowing the PDF of the fundamental frequency. The coefficient of variation (COV) for the stiffness distribution is calculated, which is then used to optimize the centrifugally loaded beam profile for a maximum manufacturing tolerance, that is, we determine the optimal value of the parameters such that the COV of flexural stiffness is maximum when compared to the COV of the fundamental natural frequency.

2. METHODS OF ANALYSIS

A mathematical relationship is established between flexural stiffness $EI(x)$ and the pre-specified fundamental natural frequency ω by assuming a quadratic mass distribution $m(x)$, and an assumed fundamental mode shape $\phi(x)$ which satisfies all four boundary conditions in the governing equations for a rotating Euler-Bernoulli beam.

$$m(x) = a_0 + a_1x + a_2x^2 = a_0(1 + r_1x + r_2x^2) \quad (1)$$

$$EI(x) = 1/10080[28(k(26L^4 + 16L^3x + 6L^2x^2 - 4Lx^3 + x^4) - 2(13L^4 + 26L^3x - 6L^2x^2 - 8Lx^3 + 5x^4)\Omega^2)a_0 + 4(k(142L^5 + 102L^4x + 62L^3x^2 + 22L^2x^3 - 18Lx^4 + 5x^5) - 2(71L^5 + 142L^4x + 3L^3x^2 + 4L^2x^3 - 30Lx^4 + 20x^5)\Omega^2)a_1 + (k(465L^6 + 362L^5x + 259L^4x^2 + 156L^3x^3 + 53L^2x^4 - 50Lx^5 + 15x^6) - 15(31L^6 + 62L^5x + 9L^4x^2 + 12L^3x^3 + L^2x^4 - 10Lx^5 + 7x^6)\Omega^2)a_2] \quad (2)$$

where $k = \omega^2$, a_i -s are mass parameters, Ω is the rotation speed, and L is the length of the beam. Equation (2) can be written as $EI(x) = c(x)k + d(x)$, where $c(x)$ and $d(x)$ are polynomials in x . We consider frequency ω as a random variable denoted by U and flexural stiffness distribution $EI(x)$ as a random field denoted by $V(x)$. Thus, a random field $V(x)$ can be expressed as the function of a random variable $U(x)$, which is $V(x) = c(x)U^2 + d(x)$. Knowing the probability density function (PDF) for the normal distribution of the random variable U , we can formulate the PDF of the $V(x)$. The average coefficient of variation c_T of the random field $V(x)$ for the coefficient of variation $c_V(x)$ over the length of the beam, given by

$$c_T = \frac{\int_0^L c_V(x)dx}{L} \quad (3)$$

3. RESULTS AND/OR HIGHLIGHTS OF IMPORTANT POINTS

The maximum feasible value of the average coefficient of variation is obtained as 0.44231 in Fig. 1(a), corresponding to the design parameter $r_1 = -1.8145$ and $r_2 = 0.8416$. We determine the value of $a_0 = 27.4512$, $a_1 = 49.808$ and $a_2 = 22.363$ assuming a total mass 10 kg. The optimal mass and flexural stiffness distribution on the optimized design parameter value (a_0, a_1, a_2), fundamental natural frequency $\omega = 140$ rad/sec, length $L = 1$ m, and uniform rotation speed $\Omega = 1100$ RPM is given by

$$m(x) = 27.4512 - 49.808x + 22.363x^2 \quad (4)$$

$$EI(x) = 1314.07 - 5368.76x + 5952.29x^2 + 5270.75x^3 - 15523.3x^4 + 10795.2x^5 - 2438.76x^6 \quad (5)$$

Figure 1(b) shows the structurally optimized rotating beam having a rectangular cross-section and a material density $\rho = 7840 \text{ kg/m}^3$ and Young's modulus $E = 2 \times 10^{11} \text{ Pa}$. The coefficient of variation of the structurally optimized beam of the quadratic mass distribution is 44.23%, which shows an improvement of approximately 5% in comparison to a linear mass distribution [1].

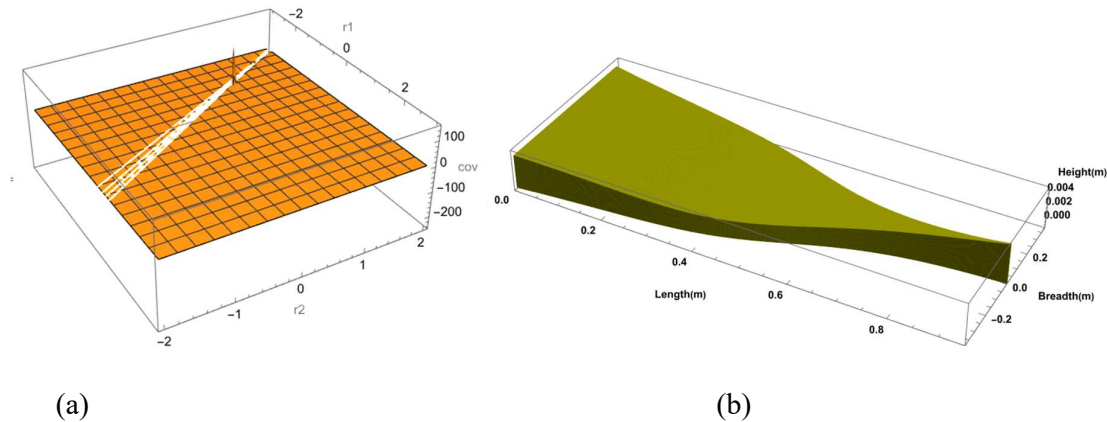


Figure 1: (a) Variation of the average COV of a random field $V(x)$ as a function of $r_1 = \frac{a_1}{a_0}$ and $r_2 = \frac{a_2}{a_0}$, (b) Breadth and height variation of an optimized rotating cantilever beam.

4. CONCLUSIONS

We derive exact analytical expressions for the flexural stiffness distribution $EI(x)$ of cantilever Euler–Bernoulli beams under centrifugal loading with quadratic mass variation, directly linked to a prescribed natural frequency ω . A probabilistic framework establishes closed-form relations between the probability density functions of $EI(x)$ and ω , offering benchmark solutions for validating stochastic simulations. These distributions yield the COV of stiffness, which is optimized to maximize the average COV to mitigate sensitivity to geometric imperfections, which means that even if there is a significant variation in the geometry due to manufacturing defects or operational wear and tear, its effect on the natural frequency will be insignificant.

5. REFERENCES

- [1] K. Sarkar, R. Ganguli, D. Ghosh, and I. Elishakoff, “Random Eigenvalue characterization for free vibration of axially loaded Euler–Bernoulli beams,” *AIAA Journal*, vol. 56, no. 9, pp. 3757–3765, Jun. 2018, doi: 10.2514/1.j056942.

Communicating Author: Ravi Prakash Prajapati, Email ID- ravipp@kgpian.iitkgp.ac.in

RBFN-based reliability analysis of thermally loaded variable fiber spacing composite plates with damage

Prateek Chandrakar^{a*}, Narayan Sharma^b, Dipak Kumar Maiti^a

^aDepartment of Aerospace Engineering, Indian Institute of Technology Kharagpur, Kharagpur, West Bengal

^bAmity Institute of Defence Technology, Amity University, Noida, Uttar Pradesh

1. INTRODUCTION & OBJECTIVE

Laminated composite structures are increasingly used in modern aerospace and mechanical systems owing to their high specific stiffness, strength, and corrosion resistance. In aerospace applications, especially in high-speed flight, the structural skins of aircraft and re-entry vehicles are subjected to intense aerodynamic heating. Such thermal environments can induce material property degradation and generate thermal stresses due to constrained expansions, which may lead to buckling or even catastrophic failure. Hence, analyzing the thermal buckling behavior of composite structures under realistic loading and environmental conditions is of critical importance.

Traditionally, composite laminates have been manufactured with uniformly distributed fibers, referred to as uniformly distributed fiber composites (UDFC). However, recent advances in manufacturing have enabled spatial regulation of fiber distributions within a ply to achieve improved structural performance. Such laminates, termed variable fiber spacing composites (VFSC), offer enhanced control over stiffness, strength, and interlaminar stress profiles. Shiau and Chue [1] demonstrated that VFSC configurations could significantly reduce or even eliminate free-edge interlaminar stresses, while Shiau and Lee [2] extended this concept using higher-order elements with additional degrees of freedom.

Despite these developments, composite structures are inherently prone to manufacturing-induced imperfections and material uncertainties, which can strongly affect their thermal buckling responses. These uncertainties arise from variations in fiber volume fraction, matrix properties, and fabrication-induced defects. Several researchers have addressed this issue: Valliappan et al. [3] developed a finite element model incorporating anisotropic damage for elastic constitutive relationships. The authors' previous works [4,5] also examined stochastic response prediction of advanced composite laminates. Simonetti et al. [6] further analyzed the thermal buckling of functionally graded beam structures under multiple boundary conditions.

While these studies provide valuable insights, the combined effects of thermal loading, damage, and material uncertainty on the reliability of VFSC plates remain relatively unexplored. Furthermore, high-fidelity stochastic analyses such as Monte Carlo simulations (MCS) are computationally demanding, motivating the development of efficient surrogate-based frameworks.

2. METHODS OF ANALYSIS

1. To develop a finite element (FE) formulation based on higher-order shear deformation theory (HSDT) for predicting the critical thermal buckling temperature of composite plates.
2. To study the influence of three non-uniform fiber distribution patterns on thermal buckling behavior under simply supported (SSSS) boundary conditions.
3. To incorporate two damage scenarios (ratio: 3 and 5) at two locations (corner and mid-region) and evaluate their effects on thermal stability.
4. To construct an RBFN-based surrogate model for quantifying the impact of composite property uncertainties on the critical buckling response and assess its accuracy against Monte Carlo MCS.

*Communicating Author: Prateek Chandrakar (pch.prateek@gmail.com)

- To estimate stochastic reliability parameters of VFSC plates under varying levels of uncertainty using the First-order reliability method (FORM) and RBFN model.

3. RESULTS AND HIGHLIGHTS OF IMPORTANT POINTS

The results show that the angle-ply laminates exhibit significantly higher critical buckling temperatures compared to the cross-ply laminates for all fiber distribution cases. The critical temperature decreases progressively from DT1 to DT3, indicating a loss in stiffness with decreasing average fiber density. Even under the least average fiber density case (DT3), the angle-ply configuration maintains almost double the buckling strength of the cross-ply. This demonstrates that fiber orientation and distribution play a crucial role in enhancing thermal buckling resistance of composite laminates.

Table 1: Critical buckling temperature (°C) of VFSC for various conditions

| Lamination sequences | Fiber distribution | Critical buckling temperature |
|----------------------|--------------------|-------------------------------|
| Cross-ply | DT1 | 25.965 |
| | DT2 | 19.115 |
| | DT3 | 15.441 |
| Angle-ply | DT1 | 53.772 |
| | DT2 | 37.730 |
| | DT3 | 29.406 |

4. CONCLUSIONS

The results revealed that the choice of the VFSC distribution function has a pronounced influence on the thermal buckling performance of composite laminates. By selecting suitable lamination sequences and fiber spacing functions, it is possible to enhance the critical buckling temperature and mitigate the detrimental effects of damage.

Among the damage cases considered, damage located at the mid-region of the laminate caused the greatest reduction in the critical buckling temperature for all stacking sequences. The relationship between input uncertainties and output responses was found to be linear, with comparable variability across all configurations. This demonstrates the capability of VFS laminates to maintain reliable buckling strength even in the presence of material randomness.

In terms of reliability, the VFS laminates—particularly those with the angle-ply configuration—exhibited superior resistance to failure. This configuration not only maximized thermal buckling strength but also showed a smaller increase in failure probability when damaged, indicating robust structural performance. Overall, the angle-ply VFS laminate proved to be the most effective configuration, offering high buckling capacity, moderate sensitivity to uncertainty, and an extended structural collapse range.

5. REFERENCES

- [1] L.-C. Shiau and Y.-H. Chue, “Free-edge stress reduction through fiber volume fraction variation,” *Composite Structures*, vol. 19, no. 2, pp. 145–165, 1991.
- [2] L. C. Shiau and G. C. Lee, “Stress concentration around holes in composite laminates with variable fiber spacing.” *Composite structures*, vol. 24, pp. 107–115, 1993.
- [3] S. Valliappan, V. Murti, and Z. Wohua, “Finite element analysis of anisotropic damage mechanics problems,” *Engineering Fracture Mechanics*, vol. 35, no. 6, pp. 1061–1071, 1990.
- [4] P. Chandrakar, N. Sharma, and D. K. Maiti, “Stochastic RBFN-based reliability estimation of variable fiber spacing composite plates under thermal loading,” *International Journal of Advances in Engineering Sciences and Applied Mathematics*, vol. 16, no. 2, pp. 108–116, 2024.
- [5] P. Chandrakar, N. Sharma, and D. K. Maiti, “Buckling variability analysis in damaged composite laminates subjected to thermally varying environment,” *Journal of Thermal Stresses*, pp. 1–23, 2024.
- [6] S. K. Simonetti, G. Turkalj, and D. Lanc, “Thermal buckling analysis of thin-walled closed section FG beam-type structures,” *Thin-Walled Structures*, vol. 181, no. 110075, p. 110075, 2022.

Real-Time Obstacle Avoidance for Waypoint Following of UAVs

Heavenly Dadala^{a*}, Sayantan Pal^b, and Sikha Hota^c

^aUndergraduate Student, Department of Aerospace Engineering, IIT Kharagpur, India

^bResearch Scholar, Department of Aerospace Engineering, IIT Kharagpur, India

^cAssociate Professor, Department of Aerospace Engineering, IIT Kharagpur, India

*Communicating Author: Heavenly dadala, seeyonuraj@kgpian.iitkgp.ac.in

1. INTRODUCTION & OBJECTIVE

Unmanned Aerial Vehicles (UAVs) are widely employed in surveillance [1], inspection, and military missions, where they often must traverse cluttered environments while precisely following a specified trajectory. Existing path-following methods include virtual target point (VTP) techniques, valued for simplicity and efficiency; the L_1 guidance law [2] is especially effective for tracking straight line and circular paths. Recent advances in vector-field guidance [3] inspire the use of geometric ideas in this tangent-based approach to avoid obstacles.

This paper uses a variable L_1 guidance law instead of a constant one to decrease the time of convergence to the desired path and combines both convergence modes into a Real-time Tangent-based algorithm for UAV navigation. Circular convergence begins at an entry point determined via tangents from the UAV's current position, ensuring favorable geometry. The shift from straight to circular paths is handled smoothly by L_1 guidance. Based on the analysis of Park [2], the L_1 guidance law was proved to be asymptotically stable. Obstacles are modeled as circles (any convex polygon can be approximated by its smallest enclosing circle). Results show the UAV successfully tracks waypoints, avoids obstacles, and maintains low computational load while respecting minimum-turn-radius constraints.

2. METHODS OF ANALYSIS

UAV Kinematic Model: The UAV is modeled as a 2-D kinematic system with position $\mathbf{p} = [x, y]^T$ and velocity $\mathbf{v} = [\dot{x}, \dot{y}]^T$. The motion follows

$$\ddot{\mathbf{p}} = \mathbf{v}, \quad \dot{\mathbf{v}} = a_s \hat{\mathbf{n}},$$

where a_s is the commanded lateral acceleration and $\hat{\mathbf{n}} = [-v_y, v_x]/\|\mathbf{v}\|$ is the unit normal to the velocity vector. The L_1 guidance law commands the lateral acceleration as

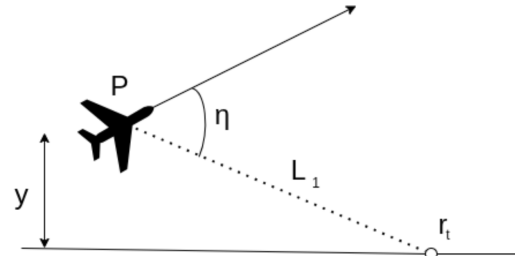
$$a_s = \frac{2v^2}{L_1} \sin(\eta),$$

where $v = \|\mathbf{v}\|$ is airspeed, L_1 is the look-ahead distance, and η is the angle between the velocity and look-ahead vector $\mathbf{L}_1 = \mathbf{r}_t - \mathbf{p}$, with \mathbf{r}_t being the target point on the desired path. The look-ahead distance is linearly varied as

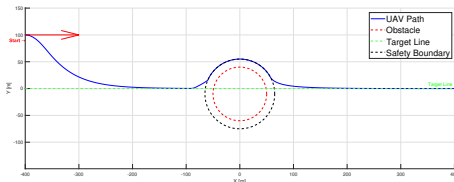
$$L_1 = \max(L_{\min}, L_{\min} + k_L |y|),$$

to ensure smooth convergence, where L_{\min} is the minimum look-ahead which comes from the maximum lateral acceleration constraint $a_s \max$ and k_L is a proportional gain, and y is the cross-track error, that is the normal distance between the UAV and the desired path as illustrated in Figure 1a.

Tangent-Based method: Each obstacle is defined by its center $\mathbf{c} = [c_x, c_y]^T$ and effective radius $R_{\text{eff}} = R + r_{\text{buffer}}$, where R is the obstacle radius and r_{buffer} ensures safe clearance. When a segment between two waypoints is blocked, two tangent points are computed from the UAV position \mathbf{p} to the obstacle and the tangent forming the



(a) Illustration of L_1 guidance law.



(b) Implementation of the Algorithm for one obstacle

Figure 1: (a) shows the L_1 guidance and (b) shows that trajectory of UAV

smaller heading change with the desired path is chosen to calculate the *entry point* into the avoidance mode. We choose that entry point as the next target point of the UAV, which is the starting point of the avoidance mode (tracking the outer boundary circle with the effective radius). An *exit tangent* is selected by choosing the tangent point (on the circle) from the next target point on the path. This ensures smooth switching between path modes while maintaining continuous L_1 control.

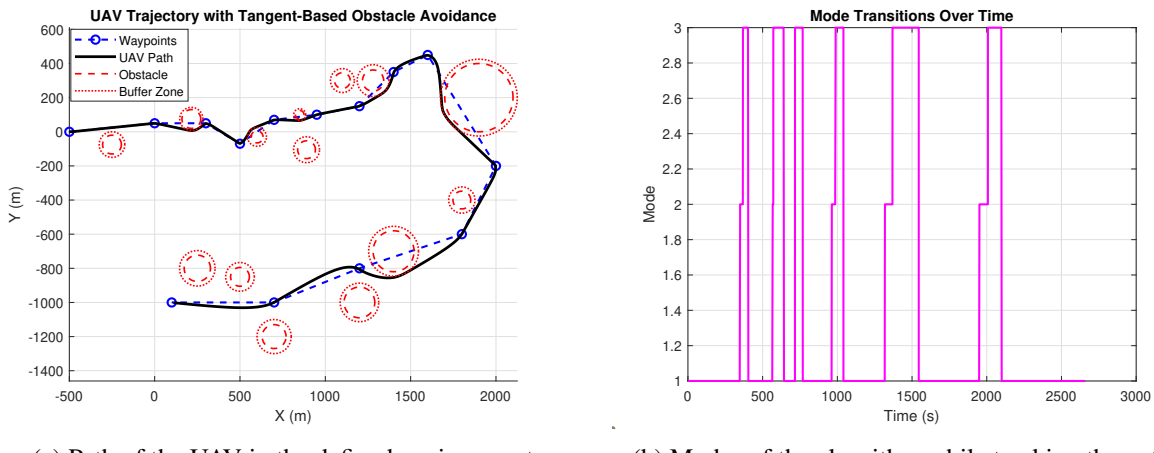
All simulations were performed in MATLAB R2024b using identical nonlinear L_1 guidance dynamics.

3. RESULTS AND/OR HIGHLIGHTS OF IMPORTANT POINTS

UAV Trajectory and Modes of Convergence

Figure 2a shows the UAV trajectory using the proposed tangent-based guidance. The vehicle successfully tracks the predefined waypoints while avoiding all circular obstacles with adequate buffer clearance (waypoints starting from (-500m, 0m) and ending at (100m, -1000m), 15 waypoints with 6 of the obstacles blocking the waypoint segments). Smooth transitions between straight and circular paths are observed, confirming accurate tangent computation and L_1 -based curvature control.

Figure 2b illustrates the corresponding mode transitions over time. The sequence between modes 1 (straight), 2 (circular avoidance), and 3 (post-exit blending) validates correct switching logic. Each obstacle encounter results in a transition to circular mode, followed by recovery to the next straight segment.



(a) Path of the UAV in the defined environment

(b) Modes of the algorithm while tracking the path

4. CONCLUSIONS

This work presented a real-time guidance algorithm for real-time obstacle avoidance using a variable L_1 guidance law. The method enables a UAV to follow a sequence of waypoints while smoothly avoiding circular obstacles by switching between straight line convergence and obstacle-avoiding modes through tangent geometry. Simulation results demonstrated accurate path tracking, stable mode transitions, and safe clearance around obstacles, validating the effectiveness of the proposed approach. The framework maintains low computational cost, curvature limits, and can be extended for three-dimensional environments including wind disturbances in future studies.

REFERENCES

- [1] X. Wang, S. Baldi, X. Feng, C. Wu, H. Xie, and B. De Schutter, “A fixed-wing uav formation algorithm based on vector field guidance,” *IEEE Transactions on Automation Science and Engineering*, vol. 20, no. 1, pp. 179–192, 2022.
- [2] S. Park, J. Deyst, and J. How, “A new nonlinear guidance logic for trajectory tracking,” in *AIAA guidance, navigation, and control conference and exhibit*, 2004, p. 4900.
- [3] S. Pal and S. Hota, “Vector field guidance with curvature constraint for uavs,” in *AIAA SCITECH 2025 Forum*, 2025, p. 0523.

Real-Time Tiny Object Detection and Tracking for High-Altitude UAVs Using Customized YOLO Architectures

V Aditya Shankar^a and Devshree Kumar^b

^aUndergraduate Student, Birla Institute of Technology and Sciences, Hyderabad Campus, Hyderabad, India

^bScientist, Department of Aerospace Engineering, CSIR-National Aerospace Laboratories, Bangalore, India

^bCommunicating Author: Devshree Kumar, devshree.nal@csir.res.in

1. INTRODUCTION & OBJECTIVE

High-altitude UAVs encounter challenges due to tiny object scales (<16x16 pixels), variation in scale, dynamics including spatial and semantic imbalances [2], hinder accuracy of real-time detection and tracking in autonomous flight navigation critical for applications like surveillance and other civilian or security services. Recent advancements in YOLO-based detection [3, 4] and tiny object datasets [1] highlight the need for customized models. The objective of this study is to develop a deep learning pipeline for real-time tiny object detection and tracking at 3–4 km altitudes, integrating customized YOLO variants, active learning with outputs feeding a model predictive control (MPC) framework to enhance UAV navigation under high-altitude constraints, advancing vision based object detection making it more reliable

2. METHODS OF ANALYSIS

The pipeline spans dataset labeling, model preparation, real-time inferencing/tracking. Dataset labeling uses manual annotation (Roboflow) and semi-automated inference with pretrained models, reducing labelling significantly by around 40% (more than 1600 images). Model preparation involves testing YOLO variants (v12, v13) on the AI-TOD-v2 dataset [1], transfer learning, and custom YOLOv12 modifications, including a lightweight multi-scale attention module, better optimiser, learning rate and other hyper parameters including weights, modified loss function with NWD for tiny object robustness. Active learning (uncertainty sampling) selects 30% of samples, complemented by semi-supervised (pseudo-labeling) and supervised methods. NWD(Normalised Wasserian Distance) over IoU(Intersection over Union) and Euclidean distance [1] improve anchor assignment and bounding box based detection for sparse objects. Experiments simulated at 3–4 km altitude executed on Google Colab's T4 GPU. Detection outputs (bounding boxes, class confidence score) inform an MPC controller, optimizing trajectories under constraints like turbulence and noisy data. Initial RL efforts (reward-based decision systems) and better tracking algorithms are in progress

3. RESULTS AND/OR HIGHLIGHTS OF IMPORTANT POINTS

Experiments yield YOLOv12 at 79.4% mAP@0.5, 75.2% MOTA, and 63 FPS, surpassing YOLOv8 (71.2% mAP@0.5) by 8.2%, with training metrics (train_loss: 0.0073, val_loss: 0.00019, best_val_loss: 0.000074 at epoch 27) indicating robust convergence. The custom YOLOv12, with multi-scale attention, achieves superior performance in occlusion scenarios, aligning with SOTA benchmarks [3]. Several experimental outputs validate robustness across noise blur and low illumination, with Figure 1 showing multi-class detection (e.g., vehicles, person,) under augmented variations. The video at [https://youtu.be/aNN0AFcufT0] demonstrates real-time tracking. Optimized model contributes a 9% mAP gain for tiny objects, and preliminary results Figure 2 and 3 promise for extension to a decision-making system. Further discussion of constrained optimization in aerial perception can be found in Tsui et al. [1] and Albalawi [3].



[Figure 1: Multi-class tiny object detection and tracking in simulated high-altitude conditions with bounding boxes and labels.]

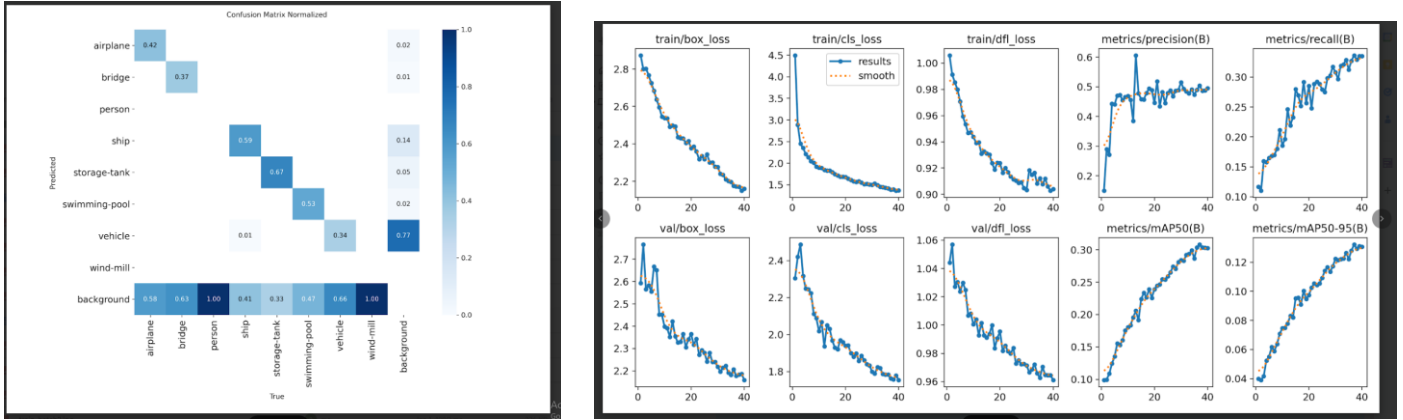


[Figure 2: Class wise Confusion matrix of detections]

[Figure 3:Loss functions and mAP metrics across 40 epochs of trained data]

4. CONCLUSIONS

This pipeline advances high-altitude UAV autonomy through customized YOLOv12 models, active learning, and NWD+RKA, addressing mechanics challenges like turbulence, occlusion, and scale variations. By integrating detection with MPC, it enhances trajectory optimization for autonomous navigation. Future work includes full AI-TOD-v2 integration, reinforcement learning-based decision systems, hybrid detection-tracking frameworks, transformer-based modeling, and edge deployment by October 2025, with applications in UAV surveillance and air traffic management.

5. REFERENCES

- [1] C. Tsui et al., “AI-TOD-v2: A Relabeled Dataset and Benchmark for Tiny Object Detection in Aerial Images,” Available: <https://chasel-tsui.github.io/AI-TOD-v2/>.
- [2] M. El-Taie and A. Y. Kraidi, “Enhancing Information Fusion from UAV-Captured High-Altitude Infrared Imagery through Machine Learning,” Am. Soc. Prof. Growth, 2024.
- [3] N. S. Albalawi, “High-Precision Multi-Class Object Detection Using Fine-Tuned YOLOv11 Architecture: A Case Study on Airborne Vehicles,” Int. J. Adv. Comput. Sci. Appl., vol. 16, no. 1, 2025.
- [4] M. K. A. Maaroof and M. S. Bouhlel, “Real-Time Object Detection Using YOLO-8 Model: A Drone-Based Approach,” J. Object. Wireless Ubiquitous Comput., vol. 1, no. 1, 2025.
- [5] J. Redmon et al., “You Only Look Once: Unified, Real-Time Object Detection,” Proc. CVPR, 2016.
- [6] M. Lei, S. Li, Y. Wu et al., “YOLOv13: Real-Time Object Detection with Hypergraph-Enhanced Adaptive Visual Perception,” arXiv preprint arXiv:2506.17733, 2025.

Reliability analysis of uncertain vibration response in bidirectional sandwich structures using a direct probability integral approach

Narayan Sharma^a, Pawan Kumar^b, Prateek Chandrakar^{c*}, and Dipak Kumar Mait^d

^a Assistant Professor, Amity Institute of Defence Technology, Amity University, Noida, 201303, Uttar Pradesh, India

^b Associate Professor, Department of Mechatronics, Manipal Institute of Technology, Manipal Academy of Higher Education, Manipal, 576104, Karnataka, India

^c Research Scholar, Department of Aerospace Engineering, IIT Kharagpur, Kharagpur, 721302, West Bengal, India

^d Professor, Department of Aerospace Engineering, IIT Kharagpur, Kharagpur, 721302, West Bengal, India

1. INTRODUCTION & OBJECTIVE

Research on uncertainty quantification and propagation in complex structural systems has gained significant attention, particularly in systems where uncertainties have a critical influence on performance and reliability. The source of uncertainty could be the manufacturing defects, environmental conditions, and various other factors, and this randomness could significantly influence the system response. Thus, assessment of such systems under uncertain vibration is essential to avoid premature failure of the structures, or overly conservative designs. Since traditional deterministic based reliability evaluation assumes constant parameters and fails to capture real-world variability, hence, stochastic based reliability computation provides a realistic framework to develop robust and high-performance structures. There are several models available to solve the reliability of composite structures, however, these models fail to provide efficient solutions. Monte Carlo is one of the robust and versatile models to perform reliability analysis, however, the implementation of this model to complex structures is difficult due to high computation cost and time requirement to perform the simulations [1]. To mitigate the issue direct probability integral (DPI) based reliability model is developed to compute reliability parameters at various levels of uncertainty in the systems. DPI complies with the probability conservation principle and offers an efficient framework for solving complex structural dynamic problems with fast convergence and required accuracy [2]. Chen et al. [3] integrates Voronoi model and Generalized F-Discrepancy technique to generate better distributed samples, where each sample points assigned discrete probability value. The developed model was utilized for structural optimization and random vibration analysis and performed well for all the studied cases.

The present work introduces a novel DPI-based reliability model to evaluate the reliability parameters of bi-directional graded sandwich structures. Literature shows that while Monte Carlo simulation (MCS) delivers high accuracy in reliability estimation, its application becomes impractical for complex structures due to the significant computational cost. To address this, the proposed DPI-based model integrates Voronoi space and the Generalized F-Discrepancy (GFD) model, enabling accurate predictions with substantially fewer samples. The proposed meta-model, combined with a higher order layerwise FE model, offers an efficient solution for determining the reliability parameters of complex structural systems

2. METHODS OF ANALYSIS

DPI based reliability model is developed to estimate reliability parameters. For stochastic dynamic analysis, several selective points (x_q) are generated through Voronoi space method and assigned some probabilistic weight to ensure non-overlapping domain. The total probability can be estimated through the following equation:

$$P_q = \int_{V_q} P_x(x_q) dx_q \quad (1)$$

Where $q = 1, 2, 3, \dots, N$ is the selected points, uncertain parameters are $x_q = (x_{1,q}, x_{2,q}, x_{3,q}, \dots, x_{n,q})$, and n representing the number of uncertain parameters. For each representative point the stochastic PDF curve is obtained using equation:

$$\phi_f(f) = \sum_{q=1}^N \frac{1}{\sqrt{2\pi S}} \exp \left\{ \frac{-(f - g(x_q))^2}{2S^2} \right\} \cdot P_q \quad (2)$$

In equation (2), f representing the output vector, $\phi_f(f)$ gives PDF output vector. The input and

output relation can be established using the mapping function $g(x)$. The accuracy of DPI model is predicted depending on the smoothing parameter ($\$$), and the selection of smoothing parameters is taken from refs. [4]. Implementing the GFD based point selection method, the reliability parameter of the stochastic system can be estimated as:

$$R_s = \sum_{q=1}^N H[g(x_q)] \cdot P_q \quad (3)$$

where, $H[g(x_q)] = \begin{cases} 0, & g(x_q) \leq 0 \\ 1, & g(x_q) > 0 \end{cases}$

3. RESULTS AND DISCUSSIONS

To assess accuracy of DPI based reliability model, the PDF curve generated from ~ 1000 samples is compared with the Monte Carlo results obtained from 15,000 samples, as shown in Figure 1. The DPI-based PDF curve exhibits close agreement with the MCS results, and the converged sample size will be adopted for subsequent reliability analyses.

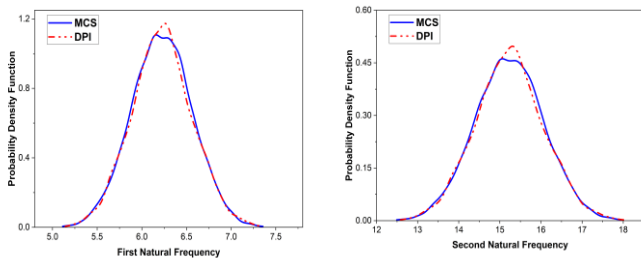


Figure 1: Comparison of PDF curve from the DPI based stochastic model with Monte Carlo results for first and second modes ($\times 10^2$ Hz)

threshold, stochastic analysis highlights the importance of premature failures. It is also observed that increasing randomness does not shift the mean values but rather broadens the distribution, leading to greater output variability.

The present DPI based reliability model evaluates the reliability curves for different levels of randomness in material properties, with violin plots included to capture the detailed scattering pattern of the natural frequencies under varying uncertainty levels. Figure 2 shows that as the randomness increases; the probability of structural failure significantly below the mean response of the structure. While deterministic approaches typically consider the mean value as the failure threshold, stochastic analysis highlights the importance of accounting for variability to prevent premature failures. It is also observed that increasing randomness does not shift the mean values but rather broadens the distribution, leading to greater output variability.

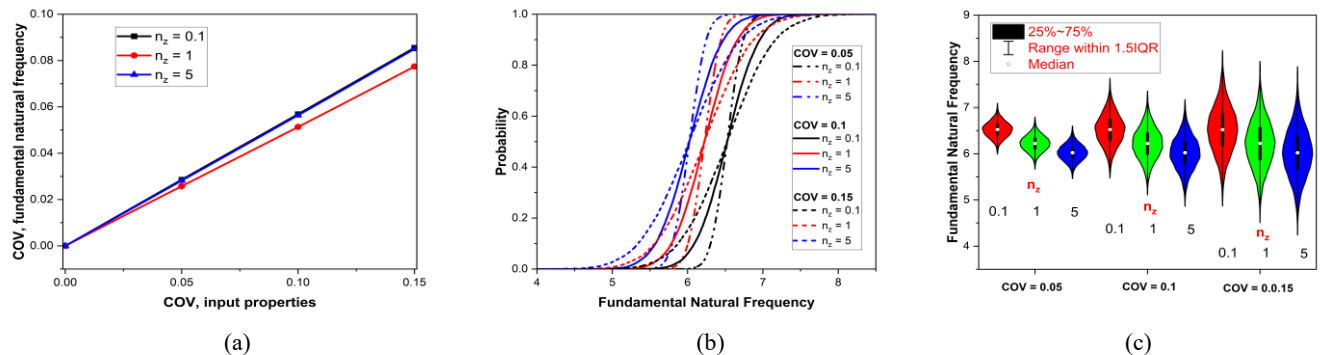


Figure 2: COV plot (a), Reliability plot (b) and Violin plot (c) of the first natural frequency of bi-directional FG sandwich structures for various transverse gradation indices, (a) $n_x = 0$, (b) $n_x = 1$, (c) $n_x = 5$, for degrees of randomness in inputs

REFERENCES

- [1] Oh, D. H., and L. Librescu. "Free vibration and reliability of composite cantilevers featuring uncertain properties." *Reliability Engineering & System Safety* 56, no. 3 (1997): 265-272.
- [2] Chen, Yugeng, Rui Zhong, Qingshan Wang, Liming Chen, and Bin Qin. "Uncertain stochastic vibration characteristic analysis of composite laminated rectangular plate based on improved kriging model." *Composite Structures* 340 (2024): 118180.
- [3] Chen, Guohai, and Dixiong Yang. "Direct probability integral method for stochastic response analysis of static and dynamic structural systems." *Computer Methods in Applied Mechanics and Engineering* 357 (2019): 112612.
- [4] Chen, Guohai, and Dixiong Yang. "A unified analysis framework of static and dynamic structural reliabilities based on direct probability integral method." *Mechanical Systems and Signal Processing* 158 (2021): 107783.

Response Dynamics of Bio-Inspired Morphing Aerofoils

Hibah Saddal^a, Lucky Jayswal^a, Chandan Bose^{a*}

^aAerospace Engineering, School of Metallurgy and Materials, University of Birmingham, United Kingdom

**Email for correspondence: c.bose@bham.ac.uk*

1. INTRODUCTION & OBJECTIVE

Recently, the flexibility of birds' wings has attracted significant research attention as they differ significantly from the rigid wings commonly used in current unmanned aerial vehicles (UAVs) and aircraft design. Unlike conventional rigid wings, birds' wings exhibit a high degree of flexibility, composed of multiple layers of feathers with varying flexibilities, enabling complex shape adaptation during flight. Fluid-structure interaction plays a crucial role in their superior agility and stability under unsteady aerodynamic conditions, such as gusts or turbulent flight. The impressive flight capabilities of birds have motivated the study of bio-inspired morphing wing designs in UAVs, as an alternative to active flow control mechanisms. Studies have demonstrated that flexible wings can outperform rigid ones due to their ability to passively deform in changing conditions, improving manoeuvrability and aerodynamic efficiency [1]. Morphing wings, which allow wings to change shape during flight, are a promising way to mimic the advanced capabilities of birds' wings [2]. This approach has the ability to delay stall and increase lift compared to rigid aerofoils, which suffer from flow separation, limiting performance. However, it is yet to be clearly understood how the flexible morphing wings can mitigate the effects of transient gusts through the passive deformation. Furthermore, the role played by the chordwise variability of the flexibility of bioinspired wing sections in mitigating gust effects has not been studied. To that end, in the present study, we conduct fluid-structure interaction simulations using partitioned strong coupling to investigate the gust response of passively morphing bioinspired wings and compare it with that of a conventional NACA0012 wing section.

2. METHODS OF ANALYSIS

To model the morphing wing sections, we set up the 2D problems illustrated in Figs. 1(a) and 1(b). Three wing sections were considered: a conventional NACA0012 aerofoil and from two bio-inspired wings, a peregrine falcon and a barn owl wing section.

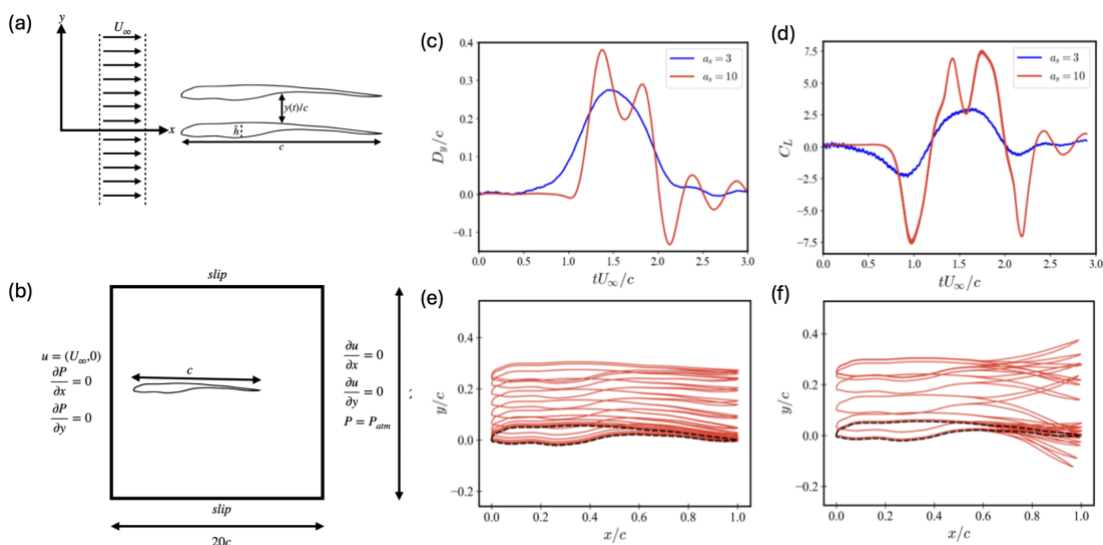


Figure 1: (a) the schematic of the problem set-up, and (b) the computational domain with the dimensions and boundary conditions (not drawn to scale). A comparison of different gust parameters for the falcon wing section for $K_B = 5$ and $\rho^* = 100$: (a) trailing-edge displacement, (b) lift coefficient, and the deflection envelop for (c) $a_s = 3$, and (d) $a_s = 10$.

Gust was mimicked in terms of accelerated plunging motion. Two key non-dimensional parameters are used in this study, the dimensionless bending rigidity (K_B) and the density ratio (ρ^*), defined as follows: $K_B = \frac{EI}{\rho_f U_\infty^2 c^3}$, and $\rho^* = \frac{\rho_s}{\rho_f}$. Here, E is Young's modulus, I is moment of inertia, ρ_s and ρ_f are the solid and fluid densities, respectively. A two-way coupled fluid-structure interaction framework is employed using a partitioned strong coupling strategy. Incompressible fluid flow is governed by the Navier-Stokes equations and solved using the finite volume method-based code - OpenFOAM. Mesh deformation during the wing movement is enabled through a quadratic inverse-distance diffusion-based dynamic meshing technique. The structural part is simulated using the finite element method-based solver CalculiX, governed by the Neo-Hookean constitutive law for hyperelastic materials. The coupling between fluid and structural solvers is facilitated with radial basis function interpolation, ensuring accurate data exchange across the fluid-solid interface. A parallel implicit coupling scheme, accelerated using the Interface Quasi-Newton Inverse Least Squares (IQN-ILS) scheme, ensures convergence.

3. RESULTS

Figure 1 compares D_y/c and C_L for a flexible bio-inspired falcon wing with $K_B = 5$ and $\rho^* = 100$, under two different transition speeds ($a_s = 3$ and $a_s = 10$). Here, the transition speed characterises the translational gust with $a_s = 3$ corresponding to a weaker, more gradual onset, while $a_s = 10$ represents a stronger, more abrupt gust. For $a_s = 3$, the trailing-edge displacement is minimal (see Fig. 1(c)), with the motion mostly following the prescribed translational gust kinematics. In contrast, the $a_s = 10$ case exhibits substantially greater displacement, consistent with the stronger gust input. This difference is also reflected in the lift response in Fig. 1(d), where $a_s = 10$ has the higher peaks and deeper troughs in C_L . The deflection envelopes further emphasise this contrast, with the $a_s = 3$ case showing little deformation (Fig. 1(e)), whereas the $a_s = 10$ gust produces significantly larger structural deformation (Fig. 1(f)). The gradual onset of the accelerated plunge kinematics at $a_s = 3$ leads to a smooth increase in displacement, while the abrupt transition at $a_s = 10$ induces a stronger transient response.

4. CONCLUSIONS

The present study demonstrates that all trailing-edge flexible wing configurations with moderate stiffness outperformed the rigid baseline case. Among the three wing geometries tested, the owl-inspired design achieved the highest lift and vertical displacement, accompanied by the formation of a strong and coherent leading-edge vortex. For the falcon-inspired wing, comparison between two gust intensities showed that the stronger gust produced greater structural deformation and the shedding of more energetic vortices, which significantly influenced the trailing-edge deflection and overall camber adaptation. Future work should extend these two-dimensional simulations to fully three-dimensional cases to more accurately represent realistic flight conditions and incorporate spatially varying flexibility to mimic the natural transition from rigid to compliant regions observed in avian wings.

5. REFERENCES

1. Harvey, C., & Inman, D. J. (2021). Aerodynamic efficiency of gliding birds vs comparable UAVs: a review. *Bioinspiration & Biomimetics*, 16(3), 031001.
2. Boughou, S., Batistić, I., Omar, A., Cardiff, P., Inman, D. J., & Boukharfane, R. (2024). Investigation on aeroelasticity of morphing wing through dynamic response and virtual structural damping. *Physics of Fluids*, 36(9).

Role of Particle Shape in Fabric Evolution during Compressive Creep Failure of Concrete

Subham Mukherjee^{a*}, Kumar Anjneya^a, Arghya Deb^b

^aGraduate Student, Department of Civil Engineering, Indian Institute of Technology, Kharagpur, India

^bProfessor, Department of Civil Engineering, Indian Institute of Technology, Kharagpur, India

1. INTRODUCTION & OBJECTIVE

Concrete creep has long been recognized as an essential phenomenon effecting the serviceability and safety of structures. However, conventional studies of creep are limited to low to medium stress levels ($\leq 0.7f_c$), often neglecting the higher stress regimes when tertiary creep and eventually failure of concrete occur[1]. Moreover, due to computational constraints for long-term analysis, mesoscale analysis of creep in this zone is further challenging. In mesoscale analysis of concrete using the discrete element method (DEM), concrete is modelled as a heterogeneous material. The concept of “fabric” is used to quantify the amount of heterogeneity present within the material[2]. Primarily, fabric is a tensor refers to the spatial arrangement and orientation of constituent particles and cracks. In contrast to macroscopic mechanical properties, fabric provides a mesoscale perspective, capturing how the local interactions between particles evolve under external loading and over time. Particle assembly constituted by round particles tends to exhibit uniform stress transfer and more isotropic arrangements, whereas angular particles induce stress concentrations and more anisotropic contact evolutions[3]. Consequently, the role of particle geometry on fabric evolution is indispensable for elucidating the mesoscale origins of the macroscopic creep phenomenon. In this study, a DEM framework is employed to investigate the evolution of fabric with different stages of creep at stress level $0.8f_c$ and $0.9f_c$. Particular emphasis is placed on the evolution and localization of cracks and the effect of particle morphology at these stress levels. The insights gained aim to advance the understanding of creep mechanisms at high stress limits, while simultaneously boosting the material’s safety and serviceability for complex structures.

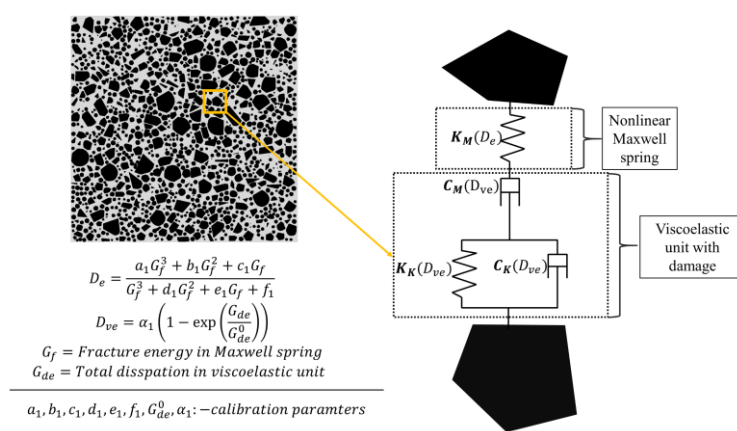


Figure 1. Meso scale constitutive model to simulate nonlinear creep of concrete

2. METHODS OF ANALYSIS

In the DEM analysis of concrete, the constituent particles are explicitly modelled, and the interaction between two particles, which resembles the cement paste, is not modelled separately.

*Communicating Author: Subham Mukherjee(msubham94@gmail.com)

Instead, the interactions are modelled by using spring dashpot system. In this study, nonlinear Burger's model with damage is introduced to represent the aggregate interactions (Figure 1). Generally, in traditional DEM, explicit time integration is used and the stable time increment is extremely small (on the order of 10^{-8}) for irregular particle geometries. The modified adaptive dynamic relaxation algorithm proposed by Mukherjee and Deb[4] is implemented to address this bottleneck.

3. RESULTS

The evolution of the degree of fabric anisotropy(J_2^*), which is determined from the second-order deviatoric tensor computed from the Fabric tensor(\mathcal{N}), is presented in Figure 2. Mathematically, the fabric tensor \mathcal{N}_{ij} is defined as the average of the outer products of the contact normal vectors over all particle contacts. From Figure 2, it is evident that for both the specimens, J_2^* is less at $0.8f_c$, compared to the $0.9f_c$, indicating that the lesser localization of cracks happens at $0.8f_c$.

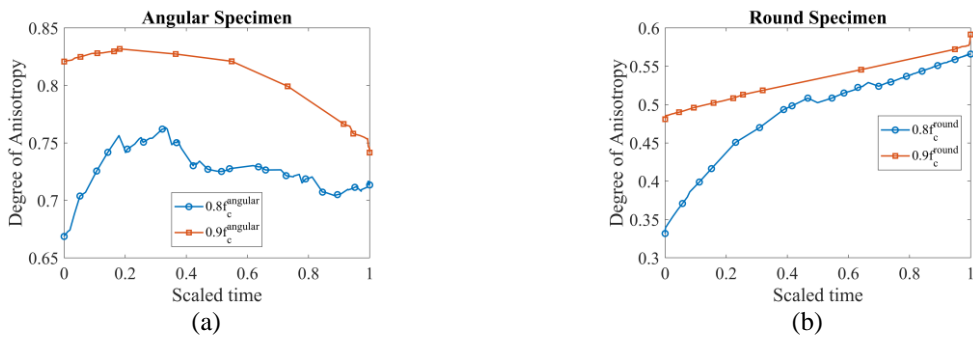


Figure 2. Evolution of the degree of anisotropy for (a) Angular and (b) Round specimens at stress levels of 80% and 90% of their respective ultimate stress levels.

4. CONCLUSIONS

This study highlights that fabric evolution is a primary drivers of creep response and failure at high stress levels, rather than only the damage magnitude. At higher compressive load ($\geq 0.7f_c$), specimens composed of angular particles develop a higher degree of fabric anisotropy, meaning more distributed cracks and lesser localization, which can be attributed to the greater axial failure strain. However, round particle assemblies show a lesser degree of anisotropy, indicating more damage localization, and therefore fail early compared to the angular particle assemblies. The degree of anisotropy emerges as a state variable that tracks the amount of damage and the formation and distribution of cracks within the particle assemblies.

5. REFERENCE

- [1] I. Boumakis, G. Di Luzio, M. Marcon, J. Vorel, and R. Wan-Wendner, "Discrete element framework for modeling tertiary creep of concrete in tension and compression," *Eng. Fract. Mech.*, vol. 200, pp. 263–282, 2018.
- [2] M. Oda, S. Nemat-Nasser, and J. Konishi, "Stress-Induced Anisotropy in Granular Masses," *Soils Found.*, vol. 25, no. 3, pp. 85–97, 1985, doi: https://doi.org/10.3208/sandf1972.25.3_85.
- [3] S. Ghosh and A. Deb, "The role of material fabric in concrete under uniaxial compression," *Int. J. Solids Struct.*, vol. 226–227, p. 111079, 2021, doi: [10.1016/j.ijsolstr.2021.111079](https://doi.org/10.1016/j.ijsolstr.2021.111079).
- [4] S. Mukherjee and A. Deb, "A fast and accurate adaptive dynamic relaxation technique for discrete element analysis of granular media," *Powder Technol.*, vol. 457, p. 120909, 2025, doi: <https://doi.org/10.1016/j.powtec.2025.120909>.

Scaling laws for thrust generated from pitching foils

Mahesh K Sawardekar^a and Ratnesh K Shukla^{b*}

^{a,b} Mechanical Engineering, Indian Institute of Science, Bengaluru, India

1. INTRODUCTION & OBJECTIVE

Miniaturization of propulsion systems results in a reduced lift-to-drag ratio owing to a lower Reynolds number (Re). The conventional fixed-wing thrusters become inefficient, necessitating alternatives such as biomimetic flapping-wing-based thrusters. A pitching foil configuration serves as a canonical model for complex natural swimmers or flyers. In this study, we analyze a NACA0012 foil pitching about its quarter chord length in an incompressible constant velocity inflow. We impose a sinusoidal rotation pitch $\theta = \theta_0 \sin(2\pi ft)$, with a frequency f and a pitch amplitude of $\theta_0 = 5^\circ$. The non-dimensional parameters incorporating the imposed kinematics and the fluid flow are the Strouhal number $St = \frac{fA}{U_\infty}$ and $Re = \frac{U_\infty c}{\nu}$, where the max trailing edge excursion $A = 1.5 \sin(\theta_0)$, U_∞ is the inflow velocity, and ν is the kinematic viscosity of the fluid.

2. METHODS OF ANALYSIS

We consider a flapping foil in an incompressible Newtonian fluid flow, governed by the Navier-Stokes equations, which are solved numerically using the projection method within an adaptive mesh framework. To incorporate a moving rigid body, such as a flapping foil, we employ a sharp interface immersed boundary method with a level set-based interface description. We perform simulations across a vast parametric space, spanning Re from 100 to 10000 and St from 0 to 1 for each Re . We analyze the total mean thrust (\bar{C}_T) and its pressure ($\bar{C}_T^{(P)}$) and viscous components ($\bar{C}_T^{(v)}$), acting on the foil. Furthermore, we compute the surface force distribution over the foil and investigate the scaling laws that the local forces exhibit with respect to Re and St .

3. RESULTS AND/OR HIGHLIGHTS OF IMPORTANT POINTS

The Re and St affect the flow field, resulting in different flow regimes and the forces experienced by the foil. The Fig. 1a depicts the total thrust on the foil for various Re , as a function of St . The foil experiences a net drag over a range of St for a given Re , before transitioning to a thrust-producing state above a Strouhal number corresponding to zero net drag, a state referred to as the self-propelling state.

We investigate the relation between the St and Re at the self-propelling state, which indicates a scaling relation of the form $St \sim Re^{-0.375}$, consistent with the prior studies of Das *et al.* [1]. At the self-propelling state, the foil has zero net thrust, indicating a balance of pressure and viscous components of total thrust. Therefore, we investigate the individual scaling relations of these components with St and Re . The Fig. 1b depicts the variation of the pressure component of thrust with St , that scales as $\bar{C}_T^{(P)} \sim St^2$ while remaining independent of the Re . The viscous component $\bar{C}_T^{(v)}$ however, varies with both Re and St , as the Fig. 1c depicts. Utilizing the viscous drag scaling of $C_D \sim Re^{-0.56}$ [1], inspired by the boundary layer scaling, the data collapses as evident from Fig. 1d. Furthermore, employing the boundary layer thinning hypothesis [2], we get a scaling for viscous drag $\bar{C}_T^{(v)} \sim Re^{-0.56} \sqrt{St}$. Utilizing these scalings and applying a drag thrust balance yields a scaling relation of $St \sim Re^{-0.375}$, which aligns with the numerical data. At the self-propelling state, the flow remains attached over the range of Re considered, and the leading edge vortices emerge at much higher St , ensuring the applicability of the boundary layer thinning hypothesis. We further investigate the mean force distribution over the

*Communicating Author: Ratnesh K Shukla (ratnesh@iisc.ac.in)

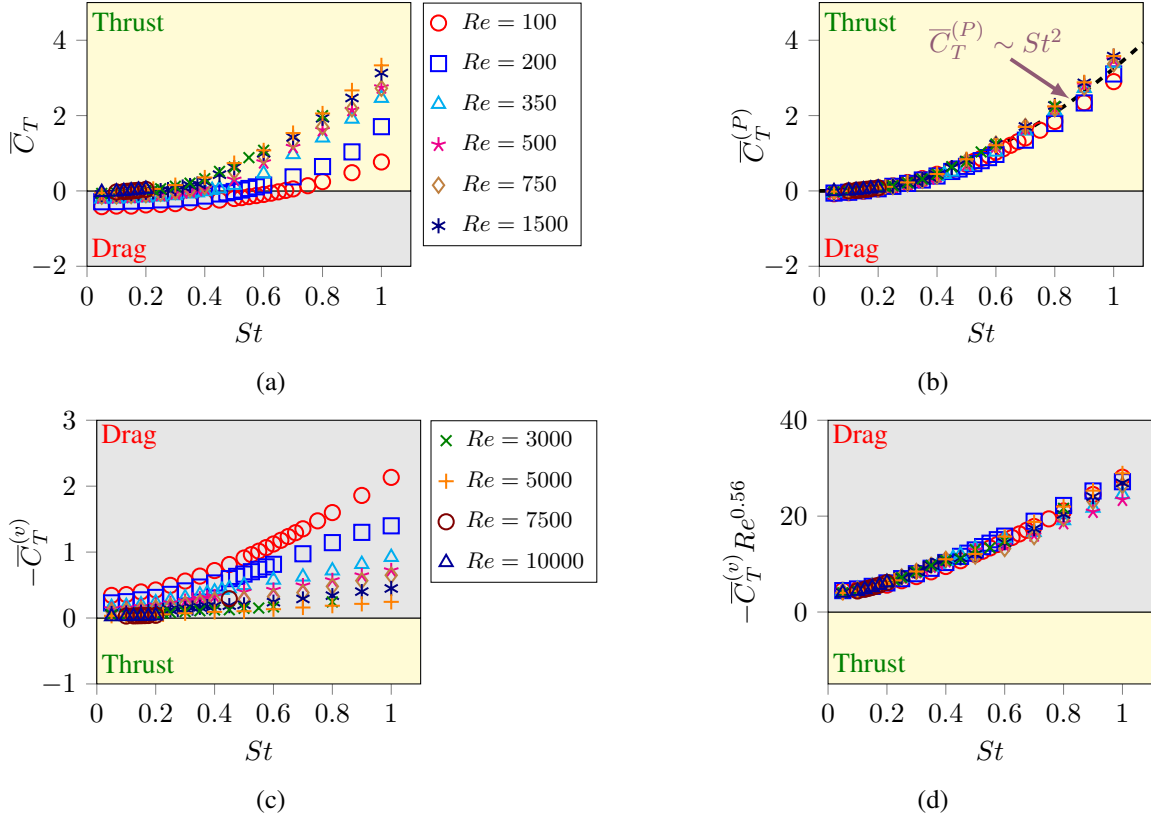


Figure 1: (a) Total mean thrust coefficient \bar{C}_T , (b) the pressure contribution $\bar{C}_T^{(P)}$, (c) The viscous contribution $\bar{C}_T^{(v)}$ and (d) scaled viscous contribution, as a function of St for different Re

foil surface and verify that the local mean forces over the foil surface also follow these scaling relations obtained from the balance of mean pressure thrust and viscous drag.

4. CONCLUSIONS

In the present study, we numerically investigate the flow past a pitching foil over a vast parametric space to identify the scaling laws governing the bio-inspired propulsion. Through the analysis of the mean forces acting on the foil and identifying the self-propelling state, we arrive at a scaling relation, $St \sim Re^{-0.375}$. The pressure component scales as $\bar{C}_T^{(P)} \sim St^2$, whereas the viscous component, applying the boundary layer thinning hypothesis, exhibits a scaling of the form $\bar{C}_T^{(v)} \sim Re^{-0.56}\sqrt{St}$. We derive the St - Re relation through a drag-thrust balance at the self-propelling state, asserting the numerically arrived scaling laws. We further extend our analysis to incorporate the mean local force distributions over the foil surface, which asserts that both pressure thrust and viscous drag adhere to these scaling laws.

5. REFERENCES

- [1] A. Das, R. K. Shukla, and R. N. Govardhan, “Existence of a sharp transition in the peak propulsive efficiency of a low-Re pitching foil,” *Journal of Fluid Mechanics*, vol. 800, pp. 307–326, 8 2016.
- [2] U. Ehrenstein, M. Marquillie, and C. Eloy, “Skin friction on a flapping plate in uniform flow,” *Philosophical Transactions of the Royal Society A: Mathematical, Physical and Engineering Sciences*, vol. 372, no. 2020, 7 2014.

Semi-analytical estimates for three phase elastomeric self-healing composite systems

Jayram Desai ^{a*}, and Vikranth Racherla ^a

^a Department of Mechanical Engineering, Indian Institute of Technology Kharagpur, India

1. INTRODUCTION & OBJECTIVE

Inspired by the self-healing phenomenon in living organisms, extrinsic self-healing polymers carry “healing fluid” in the vascular channels inside the polymeric matrix. In the event of external damage, this fluid is delivered to the damage region for healing and restoring the material integrity [1-3]. To increase the healing efficiency and to attain multiple cut-healing events, researchers had proposed a pressurized delivery of the healing fluid to the damaged region [4,5]. The fluid flow behavior is inherently complex and involves dependency on material properties, channel geometry, and external loads. This fluid flow behavior was studied experimentally where the fluid in the channel was pressurized by suitable external means. In other research, a flow rate-pressure drop relationship was determined for a fluid flow in a channel with soft wall which established that the mechanical compliance of the solid phase governs variations in flow rate and pressure dynamics [6-8].

To address the limitations of extrinsic self-healing polymers based on conventional methods and external pressurization methods, a novel composite system is proposed here. The three phase composite consists of an incompressible elastomer matrix which has channels made of compressible elastomer and the healing fluid. An initial compression is applied on the matrix to pressurize the fluid in the channel. Upon occurrence of a cut, this pressurized fluid is delivered to the damaged region for healing.

2. METHODS OF ANALYSIS

The healing fluid is stored in a circular channel inside an annular cylinder made of the compressible elastomer. The compressible elastomer is placed inside an incompressible elastomeric matrix. An initial compression boundary condition applied on the composite results in stresses within the elastomer phases and causes pressurization of the stored fluid. Once the channel is cut open due to external damage, fluid flows onto the cut face under pressure. The rate of change of strain energy in the elastomer and rate of energy dissipation in the fluid are derived in terms of system parameters like moduli of the elastomer and dynamic viscosity of healing fluid, fluid fraction, channel geometry, and initial loading. The energy release rate in elastomer and the energy dissipation rate in healing fluid are balanced to obtain the fluid flow characteristics in dynamic time marching scheme.

Flow characteristics for healing fluid are estimated using a semi-analytical framework as a function of elastomer, fluid properties, initial elastomer compression, channel geometry, fluid fraction, etc. To validate the results obtained from the proposed framework, numerical simulations are modeled in COMSOL multiphysics software. 2D - axisymmetric models are used to determine the system response from an initial compression and from the relaxation due to the fluid flow after the cut event.

3. RESULTS & HIGHLIGHTS OF IMPORTANT POINTS

The developed semi-analytical method is used to estimate the fluid flow velocity, volume flow rate and the volume of the fluid delivered to the damage region in a specific time after cut. The theoretical results are found to be in agreement with those obtained through numerical simulations performed in COMSOL multiphysics.

*Communicating Author: Jayram Desai, E-mail address: jayramdesai@iitkgp.ac.in

For the elastomer self-healing composite, the proposed three phase architecture provides significant advantages relative to the two phase system comprising healing fluid and compressible elastomer. In a two phase system with the incompressible elastomer, pressurization of the healing fluid in the channel by an initial compression is not feasible. Whereas in the three phase system, the incompressible elastomer transfers all load to the compressible phase which enables the pressurized delivery of fluid. Thus, a small volume fraction of the compressible phase can facilitate the pressurized fluid delivery. Also, for a given amount of an initial compression, the three phase system would result in more pressurization of the fluid and hence more volume of fluid delivery compared to the two phase system. In the other observation, it was found that more volume of healing fluid can be delivered to the damage region if the compressible elastomer has higher elastic moduli.

4. CONCLUSIONS

The present research explores an interesting class of extrinsic type of elastomer self-healing composite comprising three phases which shows promising results in the context of fluid flow behavior required for effective self-healing. While designing such a type of composite, in comparison to 2D or 3D numerical simulations, the developed semi-analytical framework will be computationally effective to decide the system parameters like fluid fraction, geometric properties along with properties of elastomer and healing fluid. Since there are two phases of the elastomer – compressible and incompressible, it would be suitable to tailor the composite architecture to achieve the desired self-healing performance while ensuring that structural capability of the composite is uncompromised.

5. REFERENCES

- [1] J. W. C. Pang and I. P. Bond, "‘Bleeding composites’—damage detection and self-repair using a biomimetic approach," *Compos. Part A: Appl. Sci. Manuf.*, vol. 36, no. 2, pp. 183–188, 2005, doi: 10.1016/j.compositesa.2004.06.016.
- [2] B. J. Blaiszik, S. L. B. Kramer, S. C. Olugebefola, J. S. Moore, N. R. Sottos, and S. R. White, "Self-healing polymers and composites," *Annu. Rev. Mater. Res.*, vol. 40, pp. 179–211, 2010.
- [3] M. D. Hager, P. Greil, C. Leyens, S. van der Zwaag, and U. S. Schubert, "Self-healing materials," *Adv. Mater.*, vol. 22, no. 47, pp. 5424–5430, 2010.
- [4] K. R. Hart, S. M. Lankford, I. A. Freund, J. F. Patrick, B. P. Krull, E. D. Wetzel, N. R. Sottos, and S. R. White, "Repeated healing of delamination damage in vascular composites by pressurized delivery of reactive agents," *Compos. Sci. Technol.*, vol. 151, pp. 1–9, 2017, doi: 10.1016/j.compscitech.2017.07.027.
- [5] A. R. Hamilton, N. R. Sottos, and S. R. White, "Pressurized vascular systems for self-healing materials," *J. R. Soc. Interface*, vol. 9, no. 70, pp. 1020–1028, 2012.
- [6] M. M. Inamdar, X. Wang, and I. C. Christov, "Startup flow in deformable shallow microchannels," *Phys. Rev. Fluids*, vol. 5, no. 6, 064101, 2020.
- [7] Y. Yang, X. Zhu, H. Cui, and Z. Wu, "A fluid-structure interaction model for flow in a soft hydrogel microchannel," *Polymers*, vol. 12, no. 9, 1898, 2020.
- [8] X. Wang and I. C. Christov, "On the flow rate–pressure drop relation for deformable shallow microfluidic channels," *J. Fluid Mech.*, vol. 858, pp. 670–701, 2019, doi: 10.1017/jfm.2018.782.

Shock-Tandem Bubble Interaction: The Effect of Inter-Bubble Gap on the Bubble Flow Dynamics

Nithin Krishnan S^{a*}, Ribhu Pal^a, Arnab Roy^b and Parthasarathi Ghosh^c

^a Research Scholar, Aerospace Engineering Dept., IIT Kharagpur, West Bengal, India

^b Professor and HOD, Aerospace Engineering Dept., IIT Kharagpur, West Bengal, India

^c Professor, Cryogenic Engineering Centre, IIT Kharagpur, West Bengal, India

1. INTRODUCTION & OBJECTIVE

The interaction of a moving normal shock wave with an inhomogeneous medium is a very interesting phenomenon in the field of multiphase compressible flows. The inhomogeneity could be a gas or a liquid bubble immersed in a surrounding medium. Instabilities start developing in the interface along with the strong production of vorticity that grows with the evolution of time. Based on the Atwood number ($A = \frac{\rho_{bubble} - \rho_{air}}{\rho_{bubble} + \rho_{air}}$), two configurations with different flow parameters arise. The main objective of the current numerical study is to analyse the flow morphologies of shock-tandem bubble interaction for a lighter bubble-air and heavier bubble-air combinations for different horizontal separation distances H , $1.25H$ and $1.5H$ ($H=55\text{mm}$) along the shock propagation axis between the trailing edge of the first bubble and the leading edge of the second bubble.

2. METHODS OF ANALYSIS

The two-dimensional numerical study is performed by solving the two-phase compressible unsteady Euler equations. The ECOGEN CFD solver developed by Schmidmayer et al. [1] is used to carry out the study, which solves the partial differential equations (PDEs) by the finite volume discretization technique to treat the spatial derivatives and the diffused interface method to capture the interface between the two media. The software utilizes the MUSCL approach for space and time discretisation, the THINC (Tangent of Hyperbola for INterface Capturing) method as the interface capturing method. The computational domain as seen in fig. 1 consists of a normal shock wave moving with an incident Mach number of 1.22 which interacts with two bubbles surrounded by ambient air. Two gases are considered as the bubble material – helium (lighter) and R22 (denser). Each set of simulations for the tandem bubble employs identical bubbles at separation distances of H , $1.25H$ and $1.5H$, respectively.

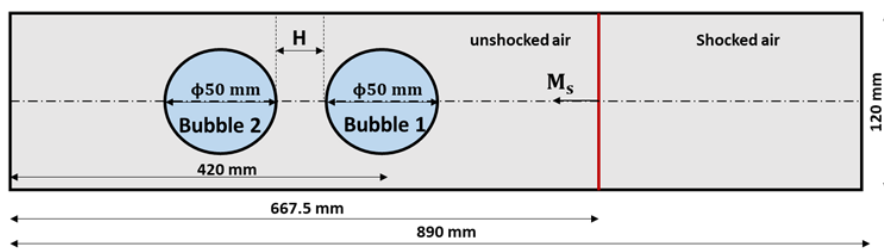


Fig 1: Computational domain in mm (Source: Quirk and Karni [2]).

3. RESULTS

The longitudinal deformation of the bubble can be expressed as $L(t) = x_{max}(t) - x_{min}(t)$. Similarly, the vertical deformation as $H(t) = y_{max}(t) - y_{min}(t)$. Till the modified shock interacts with the second bubble, the deformation is identical for the first bubble in the tandem bubble cases to that in the corresponding single phase case for both gases. As the modified shock impinges on the second bubble, clear divergence in deformation can be observed. The tandem bubble, as it gets deformed due to the impact of the shock, it alters the flow field in the downstream of the first bubble, generating additional vortical structures and shear layers, enhancing the axial stretching of the first bubble. Hence, the longitudinal deformation for the tandem case will grow faster than the single bubble case. These can also be visually observed from the gradient of mixture density contours at different time instants for lighter bubble case fig. 2. (a,b,c and d) and heavier bubble case fig. 3 (a,b,c and d).

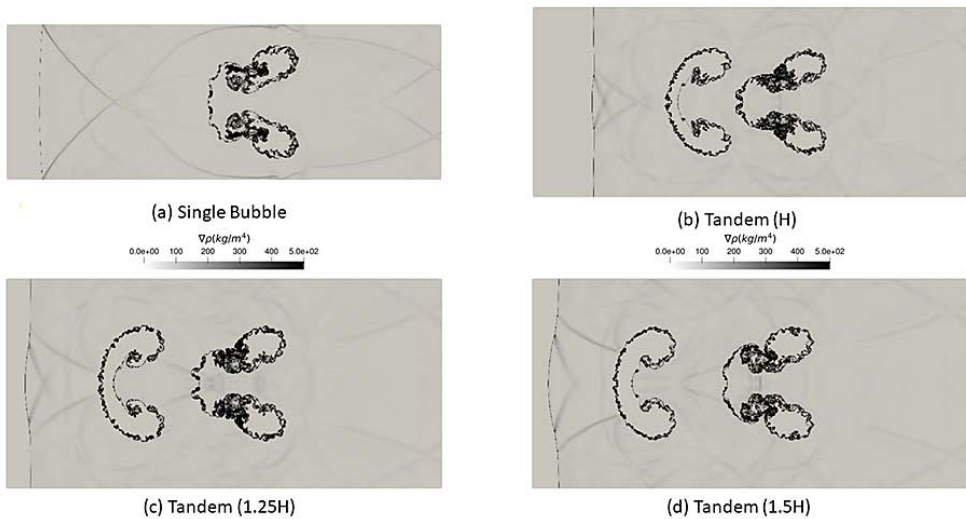


Fig 2: Numerical Schlieren contours at 960 μ s for four configurations (lighter helium bubble).

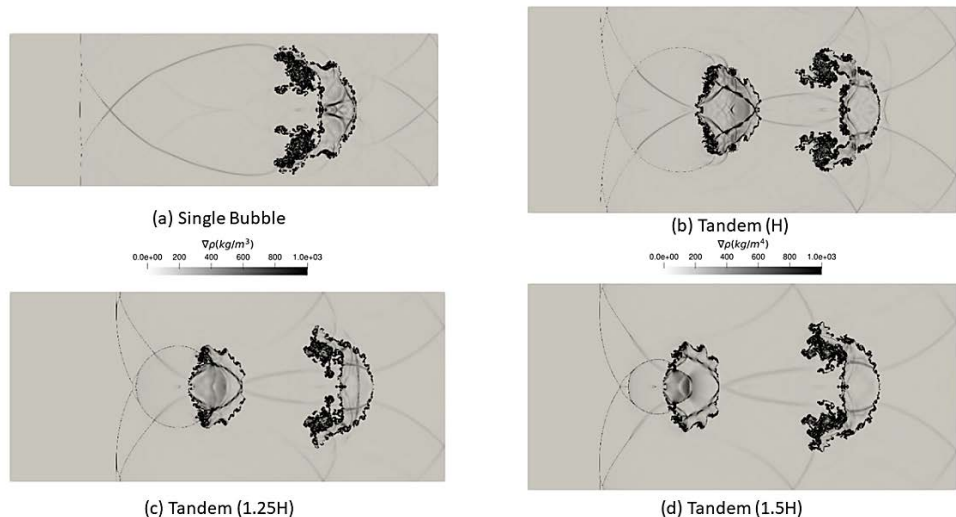


Fig 3: Numerical Schlieren contours at 960 μ s for four configurations (heavier R22 bubble).

4. CONCLUSIONS

At closer bubble separation distance, there is strong interaction between the bubbles through the vortical structures leading to greater deformation. At larger bubble separation distance, the transmitted shock has more time to reorient back before reaching the second bubble. This may result in a stronger impact on the second bubble. Thus, the Atwood number plays a significant role in driving the flow evolution and interface development (Singh et al. [3]) and the different flow properties will have distinguishing effect on vorticity production and bubble deformation.

5. REFERENCES

- [1] James J Quirk and Smadar Karni, “On the dynamics of a shock–bubble interaction, Journal of Fluid Mechanics,” *Journal of Fluid Mechanics.*, vol. 318, pp. 129–163, 1996, doi: 10.1017/S0022112096007069.
- [2] Kevin Schmidmayer, Fabien Petitpas, Sébastien Le Martelot, and Eric Daniel, “ECOGEN: An open source tool for multiphase, compressible, multiphysics flows,” *Computer Physics Communications.*, vol. 251, pp. 107093, 2020, doi: 10.1016/j.cpc.2019.03.011.
- [3] Satyvir Singh, Ahmed Hussein Msmali, Mohammad Tamsir, Abdullah Ali H. Ahmadini, “Mechanisms of coupling-induced instabilities in shock-accelerated tandem light square bubbles,” *Physics of Fluids.*, vol. 37, no. 8, pp. 082101-1-082101-28, 2025, doi: 10.1063/5.0278548.

Simulation of Voltage Generation in Thermophotovoltaic (TPV) Cells Using FE Analysis

Samanth Martis^a and Krishnendu Haldar^{b,*}

^a BTech Student, Department of Aerospace Engineering, Indian Institute of Technology Bombay, Mumbai, India

^b Associate Professor, Department of Aerospace Engineering, Indian Institute of Technology Bombay, Mumbai, India

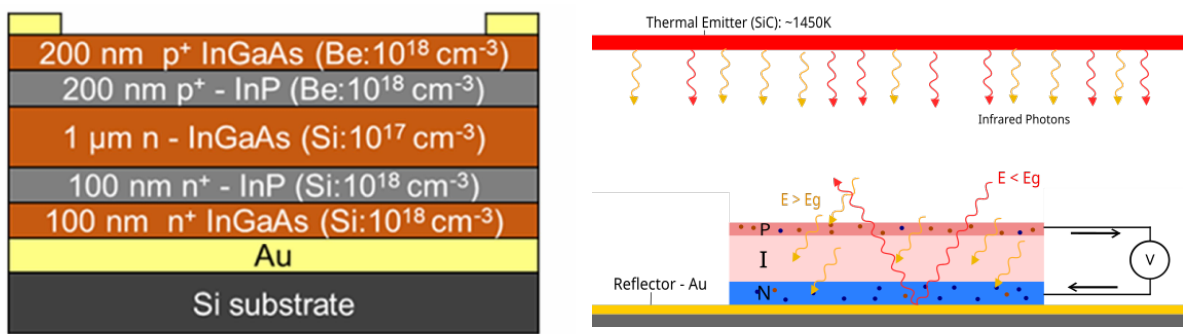
1. INTRODUCTION & OBJECTIVE

Thermophotovoltaic (TPV) cells hold significant potential for efficient heat-to-electricity conversion. Similar to solar cells, they operate by converting photons into electrical energy. The key difference lies in their spectral response: TPV cells are optimised to operate in the infrared, making them well-suited for recovering waste heat and enabling higher overall system efficiency. This also makes them highly fuel-agnostic, as they can be driven by heat sources such as fossil fuels, nuclear, concentrated solar, etc.

A major efficiency gain can be achieved by incorporating a back surface reflector (BSR), which reflects out-of-band (OOB) photons back to the emitter, allowing the unused energy to be recycled.

Modelling such cell architectures accurately is an important step towards prototyping and refining the technology. This work aims to contribute to that process by performing finite element simulations of various TPV designs, beginning with a thin-film cell with an Au back surface reflector.

2. MATHEMATICAL FORMULATION



(a) Conventional thin-film TPV cell with Au reflector

(b) Operation of TPV with OOB photon reflection.

Figure 1: Schematics of TPV composition and functioning

The 3D TPV unit cell is reduced to a 2D rectangular domain under the assumption that out-of-plane effects are negligible due to the cell depth. The emitter's far-field effect is modelled using a rectangular waveguide port boundary condition in combination with a scattering boundary condition to allow scattered rays to pass through without further reflection. The lateral walls of the domain are set to periodic boundaries to capture cell patterns. The Si substrate is modelled with an impedance boundary.

The electromagnetic field equations (a) are then solved in this domain with the boundary conditions using frequency-domain analysis to obtain the steady-state electric field distribution.

$$\nabla \times \nabla \times \mathbf{E} - k_0^2 \epsilon_r(\omega, T) \mathbf{E} = 0 \quad (a)$$

Here, ω is the angular frequency of the electric field \mathbf{E} , $k_0 = \omega/c$ is the free-space wavenumber, and ϵ_r is the material's relative permittivity. From the electric field distribution, the absorbed power and

corresponding carrier generation can be calculated:

$$P_{abs}(\mathbf{x}, \omega, T) = \frac{1}{2} \omega \epsilon_0 \epsilon''(\omega, T) |\mathbf{E}(\mathbf{x}, \omega)|^2, \quad G(\mathbf{x}, \omega, T) = \frac{P_{abs}(\mathbf{x}, \omega, T)}{\hbar \omega}$$

The stationary generation rate $G(x, \omega)$ can then be used to solve for the carrier concentrations via the charge continuity and drift-diffusion equations with the Ohmic contacts approximation. Power output can be determined by applying voltage boundary conditions and solving for the current densities.

3. RESULTS

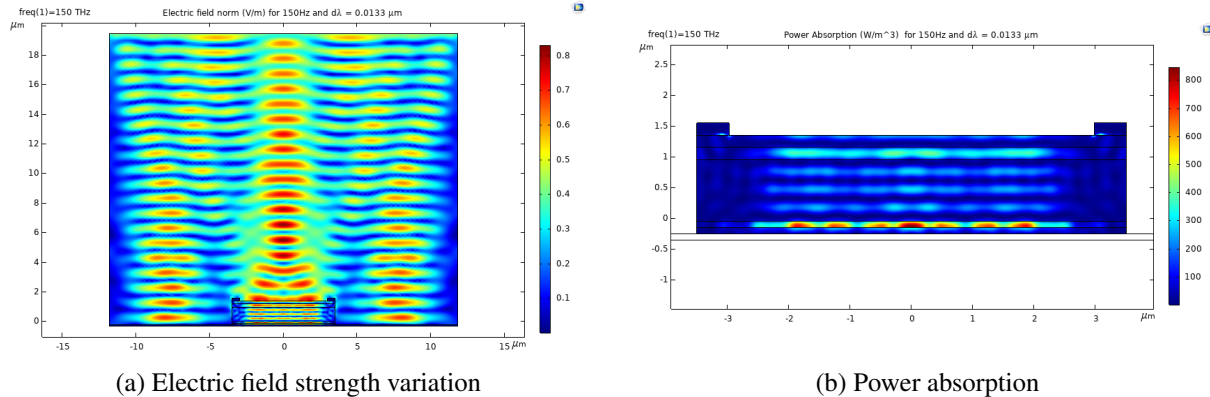


Figure 2: Resultant \mathbf{E} distribution and TPV cell power absorption for 150 THz and $\Delta\lambda = 13.3$ nm

We simulate a conventional thin-film TPV cell with a gold BSR as described by Fan *et al.* [1]. The simulation was carried out in COMSOL with a chosen frequency of 150 THz, corresponding approximately to the peak emission frequency of a blackbody at 1450 K, and with a port input power of 6.8 nW. The resultant field norm and attenuation are shown in Figure 2.

4. CONCLUSIONS

This work presents a finite element simulation of a thin-film thermophotovoltaic (TPV) cell with a back surface reflector (BSR). The 3D geometry was reduced to a 2D formulation, and the EM field distribution was obtained under realistic material conditions. Continuing the work, we aim to model more complex geometries such as air bridges and solve for the current densities.

REFERENCES

- [1] D. Fan, T. Burger, S. McSherry, B. Lee, A. Lenert, and S. R. Forrest, “Near-perfect photon utilisation in an air-bridge thermophotovoltaic cell,” *Nature*, vol. 586, no. 7828, pp. 237–241, 2020.
- [2] B. Roy-Layinde, J. Lim, C. Arneson, S. R. Forrest, and A. Lenert, “High-efficiency air-bridge thermophotovoltaic cells,” *Joule*, vol. 8, no. 7, pp. 2135–2145, 2024.
- [3] A. LaPotin, K. L. Schulte, M. A. Steiner, K. Buznitsky, C. C. Kelsall, D. J. Friedman, E. J. Tervo, R. M. France, M. R. Young, A. Rohskopf, *et al.*, “Thermophotovoltaic efficiency of 40%,” *Nature*, vol. 604, no. 7905, pp. 287–291, 2022.
- [4] M. M. A. Gamel, H. J. Lee, W. E. S. W. A. Rashid, P. J. Ker, L. K. Yau, M. A. Hannan, and M. Z. Jamaludin, “A review on thermophotovoltaic cells and their applications in energy conversion: issues and recommendations,” *Materials*, vol. 14, no. 17, p. 4944, 2021.
- [5] J. Lim, B. Roy-Layinde, B. Liu, A. Lenert, and S. R. Forrest, “Enhanced photon utilisation in single-cavity-mode air-bridge thermophotovoltaic cells,” *ACS Energy Letters*, vol. 8, no. 7, pp. 2935–2939, 2023.

* Corresponding Author: Krishnendu Haldar, krishnendu@aero.iitb.ac.in

Some Acoustic Measurements on a Thrust-Vectoring Biconical Jet

SaiPhaneendra Karuchola^{a,*}, Deeksha Yadav^b, Revathy R K^a, Arun Kumar Perumal^a and Ashoke De^a

^aDepartment of Aerospace Engineering, IIT Kanpur, India

^bDepartment of Aerospace Engineering and Applied Mechanics, IIEST Shibpur, India

1. Introduction

Supersonic jets radiate turbulent mixing noise and, under off-design expansion, broadband shock-associated noise as large-scale turbulence interacts with quasi-periodic shock cells [1]. Injecting a secondary stream is a practical active control that changes the flow structure, acoustic radiation, and thrust vectoring without moving parts [2].

This study examines a biconical nozzle designed for $M_j = 1.85$ with asymmetric secondary air injection fixed at $x_i/D_e = -0.6$. We report overall sound pressure level (OASPL) for an *overexpanded* condition ($P_e/P_a = 0.88$) and quantify how injection alters directivity. The injector follows established design principles for fluidic manipulation of supersonic jets [3]. Our goal is a concise mapping of OASPL trends and key sensitivities relevant to flow-control implementation.

2. Experimental Facility and Instrumentation

Experimental investigations were carried out in the Jet Acoustics & Flow Control Laboratory at IIT Kanpur. Dry, filtered air supplied an open-jet rig with the settling-chamber total pressure P_{0j} regulated precisely. The test article is a biconical convergent-divergent nozzle designed for a fully expanded $M_j = 1.85$ with $D_{th} = 14$ mm, $D_e = 17.12$ mm, and divergent length 35.73 mm. Secondary air is injected asymmetrically at $x_i/D_e = -0.6$ within the divergent section (design per [2]). Acoustic measurements were made in a $4 \times 4 \times 2.3$ m anechoic room using five 1/4-inch free-field microphones (PCB 378C01, $S \approx 2.0 \text{ mV Pa}^{-1}$) arranged on a circular arc of radius $R/D_e = 68$ (Fig. 1a). Signals were acquired with an NI-9232 at $f_s = 80$ kHz for $T = 5$ s; a 500 Hz low-cut was applied before computing OASPL.

The polar angle is denoted by ϕ (measured from the jet axis) and the azimuthal angle by θ (in the transverse plane), as illustrated in Fig. 1b. Data were taken for $\phi = 20^\circ:5^\circ:115^\circ$ at $\theta \in \{0^\circ, 90^\circ, 180^\circ\}$, and results reported here correspond to an *overexpanded* operating condition.

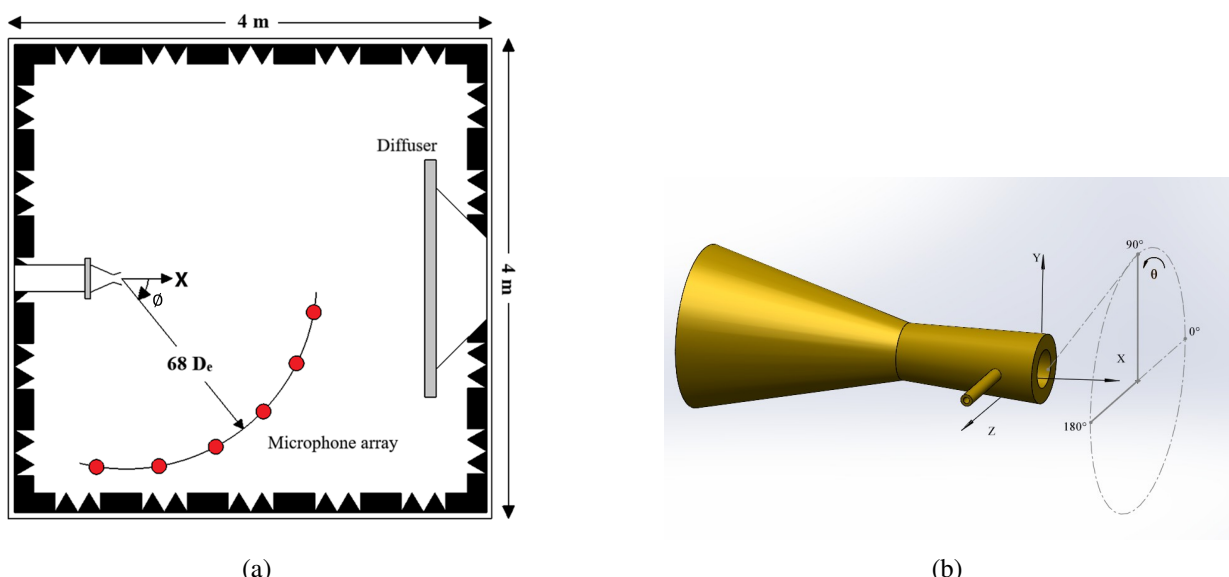


Figure 1: (a) Schematic of the anechoic chamber, indicating microphone positions on a circular arc at a radial distance of $68 D_e$. (b) Convention for the *azimuthal* angle θ , showing $\theta = 0^\circ, 90^\circ$, and 180° .

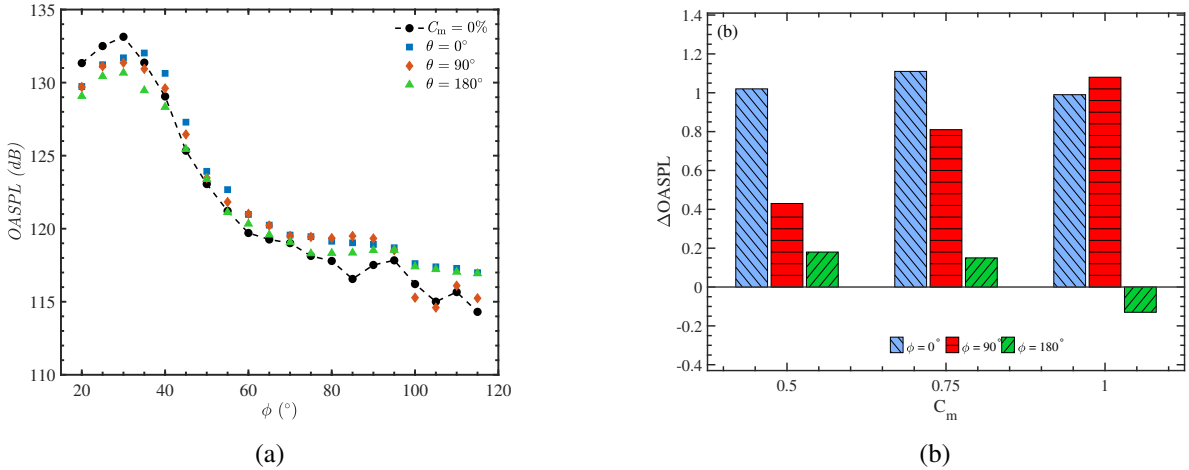


Figure 2: (a) Dependence of OASPL on θ for the natural and manipulated jet at $P_e/P_a = 0.88$ and various azimuthal angles (ϕ) for $C_m = 0.5\%$. The deflection angle δ at $C_m = 0.5\%$ is 1.43° . (b) Difference in overall sound pressure level (ΔOASPL) as a function of C_m for azimuthal angles $\phi = 0^\circ$, 90° , & 180° .

3. Results and Discussions

Figure 2(a) shows OASPL directivity at $P_e/P_a = 0.88$ for $C_m = 0.5$ and $x_i/D_e = -0.6$ across azimuthal angles $\theta \in \{0^\circ, 90^\circ, 180^\circ\}$. At shallow polar angles ($\phi = 20^\circ$ to 50°), the highest radiation occurs near $\phi = 20^\circ$ to 35° at ≈ 129 – 132 dB. The $\theta = 90^\circ$ case is ~ 0.6 – 1.2 dB above the baseline, while $\theta = 180^\circ$ is typically ~ 0.5 – 1.0 dB lower, with $\theta = 0^\circ$ in between. A rapid decline of about 10–12 dB sets in beyond $\phi \approx 45^\circ$ to 60° (Fig. 2(a)).

At the sideline ($\phi = 75^\circ$ to 95°), levels plateau near 118–120 dB; $\theta = 90^\circ$ remains the loudest by ≈ 0.5 – 1.0 dB, $\theta = 0^\circ$ is within ≈ 0.3 – 0.8 dB of the baseline, and $\theta = 180^\circ$ is at or up to ~ 0.5 dB below the baseline (Fig. 2(a)). Upstream ($\phi = 95^\circ$ to 115°), OASPL reduces further to ≈ 115 – 116 dB and the separation among θ narrows to $\lesssim 1$ dB, with the ordering $\theta = 90^\circ \gtrsim \theta = 0^\circ \gtrsim \theta = 180^\circ$ (Fig. 2(a)).

4. Conclusions

Asymmetric secondary injection at $x_i/D_e = -0.6$ reshapes radiation from the Mach 1.85 biconical nozzle at NPR = 5.5. For $C_m = 0.5$, OASPL peaks at $\phi = 20^\circ$ – 35° (129–132 dB), then drops by ~ 10 – 12 dB by $\phi \approx 60^\circ$ (Fig. 2(a)). At the sideline ($\phi = 75^\circ$ – 95°) it plateaus at 118–120 dB; $\theta = 90^\circ$ is highest by ~ 0.5 – 1.0 dB and $\theta = 180^\circ$ is at slightly below baseline. Upstream ($\phi = 95^\circ$ – 115°) it settles at 115–116 dB with < 1 dB spread.

ΔOASPL versus C_m (Fig. 2(b)) increases in the symmetry/cross planes: $\theta = 0^\circ$ gives +1.0, +1.1, +1.0 dB at $C_m = 0.5, 0.75, 1.0$; $\theta = 90^\circ$ gives +0.43, +0.81, +1.07 dB; whereas the injection plane remains small or slightly negative ($\theta = 180^\circ$: +0.18, +0.15, -0.15 dB). Overall, injection redistributes acoustic energy, penalizing $\theta = 0^\circ$ and 90° most, and leaving $\theta = 180^\circ$ unchanged or modestly quieter.

References

- [1] C. K. W. Tam, “Supersonic Jet Noise,” *Annual Review of Fluid Mechanics*, 27 (1995), 17–43.
- [2] B. Henderson, “Fifty Years of Fluidic Injection for Jet Noise Reduction,” *International Journal of Aeroacoustics*, 9(1&2) (2010), 91–122.
- [3] A. K. Perumal and E. Rathakrishnan, “Design of Fluidic Injector for Supersonic Jet Manipulation,” *AIAA Journal*, (2022), 1–10.

* Communicating Author: SaiPhaneendra K (saidp21@iitk.ac.in).

Stability characteristics of ORV at Transonic and Supersonic Mach number

Nalin Singh Sirohi*, M Jathaveda*, Dileep K N†, and G Vidya‡

* Fluid Mechanics and Thermal Analysis Division, ADSG, AERO, VSSC, ISRO, Trivandrum – 695022, India

†Head, Fluid Mechanics and Thermal Analysis Division, ADSG, AERO, VSSC, ISRO, Trivandrum – 695022, India

‡Group Director, ADSG, AERO, VSSC, ISRO, Trivandrum – 695022, India

1. INTRODUCTION & OBJECTIVES

Aerodynamic characterization of Orbital re-entry vehicle is a challenging task as it undergoes various Mach regimes i.e. hypersonic, supersonic, transonic, and subsonic from re-entry to landing phase. Each Mach regime is governed by different flow physics. Subsonic and supersonic aerodynamics characteristic studies of ORV for longitudinal plane and zero slip angle were carried out earlier and presented[1,2]. In this paper, numerical studies have been carried out for wind tunnel scale model in transonic and supersonic Mach number 0.95, 1.1 and 1.6, for various angle of attack and side slip angle using commercial CFD code *Ansys Fluent* with undeflected control surface. Results are compared with experimental data [3]. Flow features like stagnation C_p , flow interaction between wing and vertical tail are captured.

2. METHODS OF ANALYSIS

Steady state CFD simulations have been carried out in wind tunnel scale and wind tunnel conditions at $M = 0.95, 1.1, 1.6$ and angle of attack (α) range from 0° to 10° and for side slip angle $\beta = 0$ and 5° . The sign convention for angle of attack and sideslip is depicted in Figure 1.

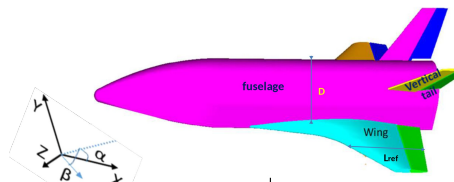


Figure 1: Study configuration and sign convention

Computational domain and boundary conditions considered for simulation shown in Figure 2. Unstructured grid with 32.07 million cell count is made using *Ansys mesh*. Inflation layers are used to capture the boundary layer on the wall. SST k- ω model is used for turbulence modeling. Force coefficients are monitored for solution convergence.

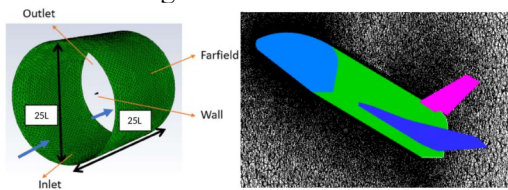


Figure 2: Computational domain, boundary condition, view of symmetry plane grid along with body

3. RESULTS AND DISCUSSION

Results are presented here for Mach 0.95, 1.1 and 1.6 for side slip angle 5° and angle of attack range from $0-10^\circ$. Mach and C_p palette at various planes are presented here to show the flow features.

Mach palette in horizontal plane is shown in Figure 3 for Mach 1.6 for $\alpha = 5^\circ$ and $\beta = 5^\circ$, which shows flow asymmetry due to side slip angle. Flow features like stagnation point at nose cap, flow

expansion in fuselage straight body (FSB) and base region are clearly visible. Symmetry plane C_p is shown in Figure 3. Maximum C_p is observed in nose cap region due to shock formation and low C_p in base region due to suction effect.

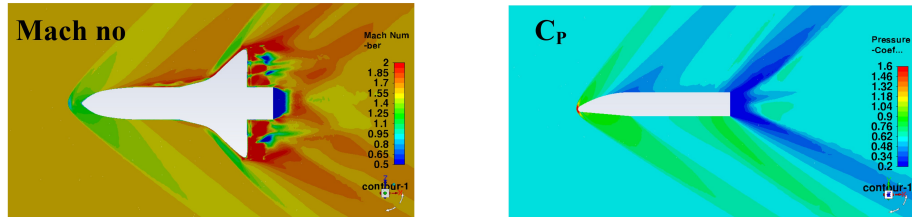


Figure 3: Mach contour in horizontal plane and C_p contour in vertical symmetry plane for M 1.6 at typical α and $\delta\alpha=5^\circ$

Figure 4 shows the good match between CFD and experimental results in transonic and supersonic regime for stability coefficients. Negative slope of CPM shows the longitudinal stability, however it reduces with angle of attack. Negative rolling moment indicates lateral stability for both transonic and supersonic flow. Vehicle becomes directionally unstable for supersonic as sign change from negative to positive for Yawing moment coefficient from transonic to supersonic regime.

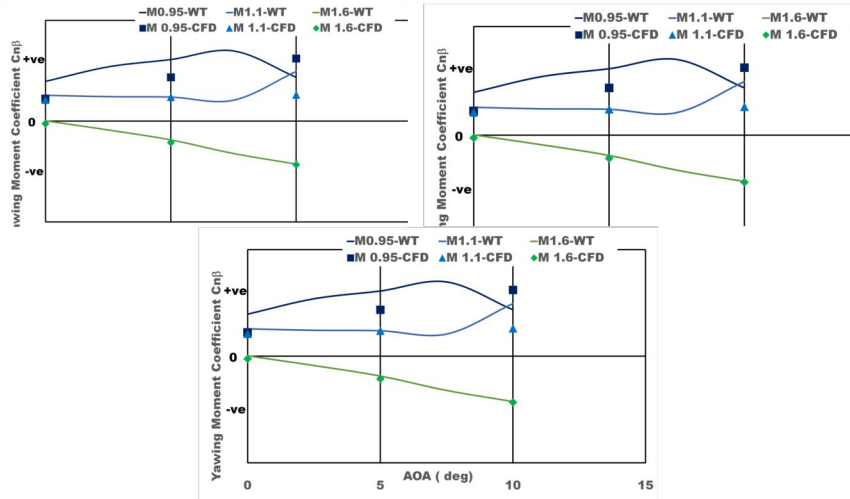


Figure 4 : Comparison of stability coefficients with experimental data

4. CONCLUSIONS

Stability characteristics of orbital reentry vehicle has been studied for transonic and supersonic Mach number using CFD simulations in *Ansys Fluent* for selected angle of attack range and side slip angle. CFD results have been compared with experimental results and good match is observed. ORV is directionally unstable for supersonic flow. Detailed results will be presented in full paper.

REFERENCES

1. M Jathaveda, Kunal Garg, G Vidya, M M Patil and V Ashok, "Subsonic aerodynamics of a winged reusable launch vehicle", NCAE 2022, IIT Kanpur branch
2. M Jathaveda, Kunal Garg, G Vidya, M M Patil and V Ashok, "Flow features and aerodynamic characteristics of RLV-TD at supersonic Mach number", Proceedings of the 1st International Conference in Fluid Thermal and Energy Systems, June 9-11, 2022, NIT Calicut, Kerala, India
3. G Vidya, et al, Aerodynamic Design, "Characterisation and Flight performance of RLV-TD", Current Science, Vol.114, No. 1, 10 January 2018, pp 48-63.

Strength and Environmental Durability of Epoxy/Graphene Oxide Composites: An AI-Driven Framework for UAV Applications

S. Maharana^a, S.K. Maharana^b and R. Vijayakumar^c, Anand M Raikar^d

^a*Dept of Mech. Engg., Odisha University of Tech. and Research, Bhubaneswar, Odisha, India*

^b*Dept. of Aerospace Engg., Faculty of Engineering and Technology, Ramaiah University of Applied Sciences, Bangalore, Karnataka, India*

^c*Dept. of Aeronautical Engg., MVJ College of Engineering, Bangalore, Karnataka, India*

^d*Dept. of Aerospace Engineering, Ramaiah Institute of Technology, Bengaluru, Karnataka, India*

1. INTRODUCTION

Unmanned Aerial Vehicles (UAVs) are increasingly used for defense, surveillance, disaster management, and commercial applications [1]. Their performance critically depends on the structural integrity and durability of lightweight composite materials. Epoxy/Graphene Oxide (E/GO) composites are promising due to their high strength-to-weight ratio and tunable mechanical properties [2]. However, existing research largely emphasizes static mechanical performance, with limited attention to long-term environmental durability under UV, moisture, and thermal cycling. Given the operational variability of UAV environments, it is essential to assess both the strength and durability of such composites.

Recent advances in Artificial Intelligence (AI), particularly Neural Networks, provide a powerful framework for predictive modeling of composite behavior under multi-factorial loading and environmental conditions [3]. The integration of accelerated aging data with AI-based predictive frameworks can reveal hidden degradation trends and enable data-driven design of composites with improved environmental resilience [4].

2. OBJECTIVE

The study aims to develop a strength assessment and environmental durability prediction framework for E/GO composites used in UAV structures. Specifically, it intends to:

1. Evaluate the static and dynamic strength of E/GO composites.
2. Investigate the effects of accelerated aging conditions (UV, humidity, thermal cycling) on mechanical properties.
3. Extend AI-based prediction models to incorporate environmental durability parameters for long-term performance assessment.

3. METHODOLOGY

The research involves a hybrid experimental–computational approach:

- **Material Preparation & Testing:** Epoxy/Graphene Oxide composites are fabricated and tested for tensile, flexural, and impact properties following ASTM standards.
- **Accelerated Aging:** Samples are subjected to accelerated aging protocol (e.g., ASTM) to simulate UV exposure, moisture ingress, and thermal cycles.
- **Data Acquisition:** Retention of strength properties is measured over aging intervals.

- **AI-Extended Framework:** A Neural Network model is trained with experimental data, with input features including GO concentration, environmental exposure parameters (time, humidity, temperature), and mechanical loading conditions. The model is designed to predict degradation trends and residual strength under coupled aging effects.

4. HIGHLIGHTS OF IMPORTANT POINTS

Preliminary results show that incorporation of GO enhances the initial tensile and flexural strength compared to neat epoxy [1]. Aging experiments reveal a progressive decline in mechanical properties, with moisture absorption and UV degradation as dominant factors [2]. The Neural Network model successfully captures nonlinear degradation trends, demonstrating predictive accuracy within $\pm 5\%$ of experimental results. The AI-extended framework highlights the feasibility of long-term durability prediction, which traditional empirical methods cannot efficiently address.

5. CONCLUSIONS

This study provides a dual contribution: (i) establishing the superior strength potential of E/GO composites for UAV applications, and (ii) introducing an AI-extended environmental durability framework that enables predictive modeling of composite performance under aging effects. The approach not only advances the reliability of UAV structures but also opens new directions for AI-driven material design and lifecycle assessment in aerospace engineering.

6. REFERENCES

- [1] S. I. Abdullah and M. N. M. Ansari, “Mechanical properties of graphene oxide (GO)/epoxy composites,” *HBRC Journal*, vol. 11, no. 2, pp. 151–156, 2015.
- [2] J. L. Thomason and L. Yang, “Temperature dependence of the interfacial shear strength in glass-fibre epoxy composites,” *Composites Science and Technology*, vol. 96, pp. 7–12, 2014.
- [3] B. Rasuo, A. Grbovic, and D. Petrasinovic, “Investigation of fatigue life of 2024-T3 aluminum spar using extended finite element method,” *SAE International Journal of Aerospace*, vol. 6, no. 2, pp. 408–416, 2013.
- [4] M. Z. Rong, M. Q. Zhang, and W. H. Ruan, “Surface modification of nanoscale fillers for improving properties of polymer nanocomposites: A review,” *Applied Surface Science*, vol. 255, no. 5, pp. 3422–3431, 2008.

Communicating Author: First Author, email id: santha_ruby@yahoo.com

Study of Lamb Wave Propagation for Sandwich Plates of Fiber-Reinforced Functionally Graded Transverse Isotropic Material with an adhesive modelled as linear elastic material with voids using Frobenious Method

Rokkam Saketh[a] and Tatipaka Ananda[b].

[a].Btech-3rd year , Mechanical Engineering, Indian Institute of Technology Bhubaneshwar, Jatni, Khordha, India.

[b].Btech-3rd year , Mechanical Engineering , Indian Institute of Technology Bhubaneshwar, Jatni, Khordha, India.

1. INTRODUCTION & OBJECTIVE

Essentially, the present study is an extension of two different scientific studies that appeared earlier. Over time, we observe that adhesive-bonded composite structures often develop voids within adhesive regions. While a limited presence of voids may enhance desirable structural responses of a material, such as mechanical strength, excessive void formation can significantly degrade the mechanical integrity and performance of a composite structural element. Previous studies by Vasudeva and Govinda Rao [1,2] have explored the influence of distributed voids on Lamb wave propagation in symmetric sandwich plates, where both facings are made from the same type of fibre-reinforced elastic material. In the present study, we extend their investigation by examining the dispersion characteristics of Lamb waves in sandwich plates whose facings are functionally graded along their thickness. We retain the mathematical model of the adhesive as a linear elastic material with voids, as applied in [1].

This work is also concerned with a study carried out by our seniors Ujjwal Shende and Madapati Nikhil [3], who presented their work at the 64th CONGRESS OF ISTAM conference held at IIT Bhuvaneswar. In [3], they studied surface wave-like modes in Lamb wave propagation for plates of fibre-reinforced functionally graded material using the Frobenius method. We consider Lamb wave propagation in sandwich plates whose facings are a functionally graded transverse isotropic material and the adhesive is a linear elastic material with voids. Material moduli govern the mechanical behaviour of any structure, and the characteristics of Lamb wave propagation can be known by tracing dispersion curves of the propagating waves. A method devised by Srikanth and Gopinathan [4] is made use of to obtain features of Lamb wave propagation in the above sandwich plate, which is obtained through the dispersion of the waves. The material of the facings has five elastic constants, which are assumed to be varying along the thickness of the facings. Finding a numerical approximation to a root of the dispersion equation of Lamb wave propagation in the chosen plate medium [3] is not only desirable but also essential to bring out the structural health of the plate medium. The root-finding algorithm devised by Srikanth and S. Gopinathan [4] is utilised here for the determination of a root of the secular equation [3] for low-frequency Rayleigh waves.

2. METHODS OF ANALYSIS

For all numerical computation We employed MATHEMATICA.

3. RESULTS AND/OR HIGHLIGHTS OF IMPORTANT POINTS

Our main objective is to reproduce the results of Vasudeva and Govinda Rao [1] using the functionally graded facing equations described by Ujjwal Shende and Nikhil [3], and obtain the dispersion relations to our current problem. Although we cannot present the dispersion curves at this time due to ongoing semester commitments, we are on track to complete this work and present our findings at the conference.

4. CONCLUSION

We are trying to reproduce the results of Vasudeva and Govinda Rao [1] using the functionally graded facing equations described by Ujjwal Shende and Nikhil [3] and obtain the dispersion relations to our current problem. The motivation to take up this task was the extensive study of functionally graded plates in recent years, and our hope is that our present work might open doors for new applications which would cause a positive impact on various fields.

5. REFERENCES

- [1] R. Y. Vasudeva and P. Govinda Rao," Influence of Voids in Interface Zones on Lamb-Mode Spectra in Fiber-Reinforced Composite Laminates," *Journal of Applied Physics* **71**, 612, 1992.
- [2] R. Y. Vasudeva and P. Govinda Rao, "Influence of voids in interface zones on Lamb wave propagation in composite plates ",*J. Acoust. Soc. Am.* 89, 516–522 (1991).
- [3] Ujjwal shinde and madapati Nikhil "An analysis of Surface Wave like Modes in Lamb Wave Propagation for Plates of Fiber-Reinforced Functionally Graded Material using Frobenious Method".
- [4] Ganti Srikanth and Gopinathan Sudheer "A note on the solutions of cubic equations of state in low temperature region" *Journal of Molecular Liquids* Volume 315, 1 October 2020, 113808
- [5] X. Wu, On zeros of polynomial and vector solutions of associated polynomial system from Vieta theorem, *Appl. Numer. Math.* 44 (2003) 415–423, [https://doi.org/10.1016/S0168-9274\(02\)00145-9](https://doi.org/10.1016/S0168-9274(02)00145-9).

Tailoring Flow-Induced Vibrations of Flexible Plates via Perforation

Shubham Giri, V. Kartik, Amit Agrawal, Rajneesh Bhardwaj

Department of Mechanical Engineering, Indian Institute of Technology Bombay, Mumbai 400076, India

*Corresponding author (email: rajneesh.bhardwaj@iitb.ac.in)

1 INTRODUCTION & OBJECTIVE

Flow-induced vibration (FIV) of flexible plates has a wide range of practical applications, including flag flapping [1], plant biomechanics [2], paper flutter [3], and energy harvesting [4]. Bio-inspired porous structures, such as dandelion filaments [5] and bird wings [6], demonstrate the aerodynamic advantages of porosity in natural systems. Further, engineering studies have illustrated that perforation can effectively modulate flow behavior [7] and influence flow-induced reconfiguration [8].

Motivated by these insights, the present study investigates the effect of perforation on the FIV of a cantilevered flexible plate mounted behind a cylinder in axial parallel flow. In particular, we vary the plate porosity by changing the hole diameter, number, and arrangement, and analyze its dynamic response.

2 METHODS OF ANALYSIS

FIV of perforated plates is investigated experimentally in a low-speed wind tunnel as shown in Fig. 1(a). The test section of the wind tunnel (Sunshine Measurements Pvt. Ltd., India) has dimensions of $1.2 \times 0.5 \times 0.5 \text{ m}^3$, with a turbulence intensity below 2% and a blockage ratio lesser than 10%. The plates are attached to the lee side of an upstream cylinder of diameter $D = 26.7 \text{ mm}$, positioned at the center of the test section. The plates are fabricated from a plastic sheet of thickness 0.2 mm, with density $\rho_s = 1210 \text{ kg/m}^3$ and Young's modulus $E = 1.105 \text{ GPa}$. Two plate lengths, $L = 5D$ and $L = 7D$, are considered with extra 20 mm length kept inside the cylinder, while the span is fixed at $W = 5D$. The porosity ($\beta = \frac{A_p}{A_T}$), defined as the ratio of perforated area (A_p) to the solid-plate area without perforation (A_T), is varied in the range $0 \leq \beta \leq 0.2$. Multiple perforated plates are tested to characterize the oscillation dynamics. Figure 1(b1–b4) shows four perforated plates with a regular 16-hole arrangement, where the porosity (β) varies from 0 to 0.1. Wind velocity is measured using an electronic manometer (Sunshine Measurements Pvt. Ltd., India; EM 0901), and plate displacement at the probe point (center of the plate) is measured using a laser displacement sensor (Micro-Epsilon Inc., Germany; ILD1220-500, range: 500 mm).

3 RESULTS AND DISCUSSION

Figure 1(c) and (d) show the root-mean-square (RMS) displacement ($\bar{\xi}_{p, exp}$) and dominant frequency ($f_{p, exp}$) response with varying wind velocity (U) for four perforated plate with $\beta = [0, 0.1]$. $\bar{\xi}_{p, exp}$ decreases with increasing β in the high amplitude oscillation regime (lock-in), while the dominant frequency ($f_{p, exp}$) of plate flapping remains nearly constant in the lock-in regime for a given plate dimension. This trend is consistent across both regular and irregular hole arrangements distributed over the plate surface. Uncertainty from repeated measurements is higher in the pre-critical regime (small oscillations) and negligible in the lock-in regime, as shown by the error bars in Fig. 1(c,d). Further, the experimental uncertainties may arise from geometry measurement, velocity estimation, calibration errors, and material nonuniformity.

For the same porosity and different hole arrangements, the $\bar{\xi}_{p, exp}$ and $f_{p, exp}$ response of the $L = 5D$ plate remain almost identical, whereas the $L = 7D$ plate exhibits greater variation in $\bar{\xi}_{p, exp}$. Furthermore, the critical velocity for the onset of high-amplitude limit-cycle oscillations is found to vary with porosity. An optimum porosity ($\beta = 0.05$) is identified at which the plate achieves high-amplitude oscillations at relatively low flow velocity. Flow visualization shows that flow passing through the perforations reduces the pressure difference across the plate, thereby decreasing $\bar{\xi}_{p, exp}$ with increasing β .

4 CONCLUSIONS

We experimentally investigate the flow-induced vibration (FIV) of a perforated plate, mounted in the standard flag orientation behind a cylinder and subjected to uniform axial flow. The porosity and wind velocity are varied in the ranges 0–0.2 and 2–15 m/s, respectively. The initial measurements reveal that both

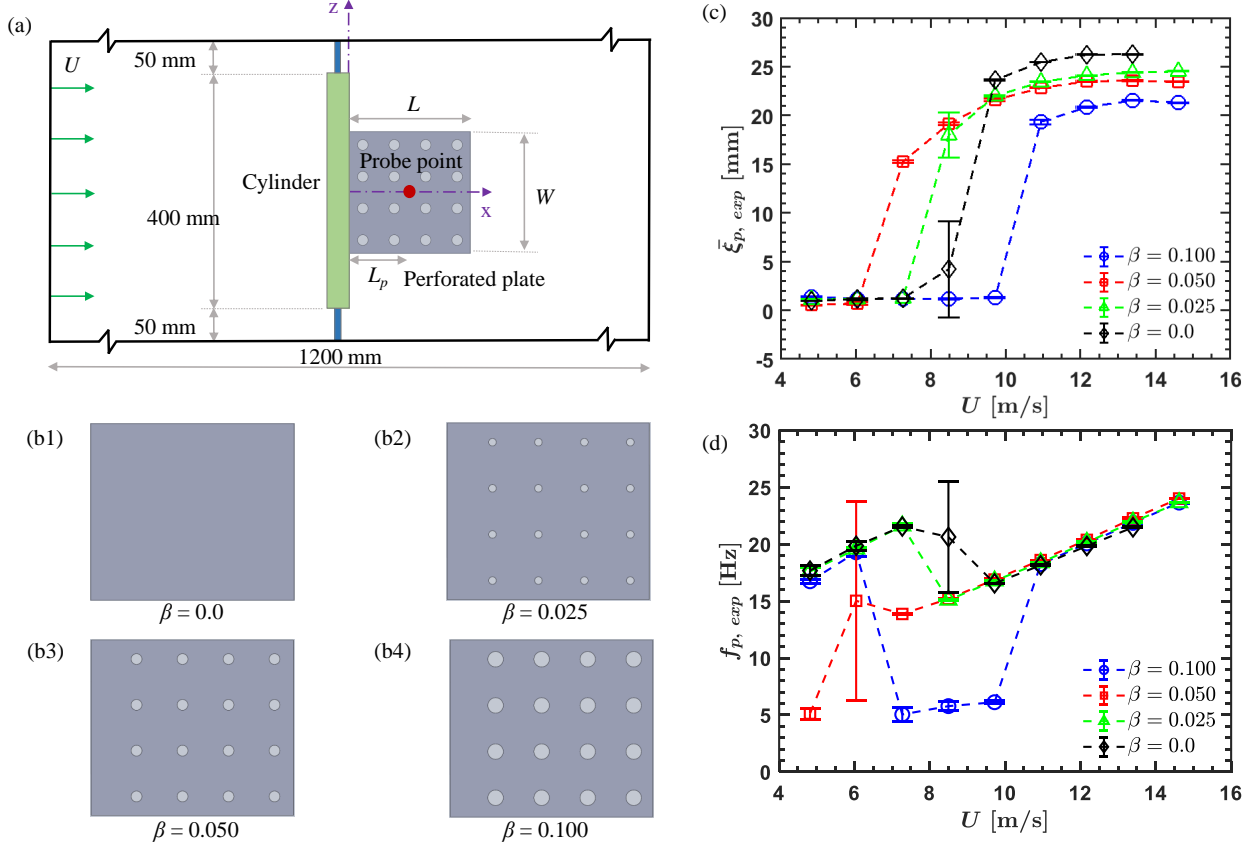


Figure 1: (a) Experimental setup in the wind tunnel test section. (b1–b2) Photographs of the four perforated plates. (c) RMS displacement ($\bar{\xi}_{p, \text{exp}}$) and (d) frequency response ($f_{p, \text{exp}}$) as functions of flow velocity (U).

the plate dynamics and the critical velocity for flapping are strongly influenced by porosity. These findings indicate that the FIV of a cantilever flexible plate can be tuned through perforation, either enhanced (the lock-in onset velocity reduces by up to 25% for $\beta = 0.05$ relative to $\beta = 0$) or suppressed (the maximum $\bar{\xi}_{p, \text{exp}}$ decreases by about 18% for $\beta = 0.1$ relative to $\beta = 0$), depending on the application. A detailed study of the structural and flow dynamics of perforated plates is a promising direction for future work.

References

- [1] Y. Yu *et al.*, “A review on fluid-induced flag vibrations,” *Appl. Mech. Rev.*, vol. 71, no. 1, 2019.
- [2] M. J. Shelley *et al.*, “Flapping and bending bodies interacting with fluid flows,” *Annu. Rev. Fluid Mech.*, vol. 43, no. 1, pp. 449–465, 2011.
- [3] Y. Watanabe *et al.*, “An experimental study of paper flutter,” *J. Fluids Struct.*, vol. 16, no. 4, pp. 529–542, 2002.
- [4] S. Giri *et al.*, “Energy harvesting using piezoelectric sheet fixed on a flexible plate attached to a cylinder in free stream flow,” *Phys. Fluids*, vol. 37, no. 2, 2025.
- [5] C. Cummins *et al.*, “A separated vortex ring underlies the flight of the dandelion,” *Nature*, vol. 562, no. 7727, pp. 414–418, 2018.
- [6] Y. L. Lin *et al.*, “Fluid–structure interactions of bristled wings: the trade-off between weight and drag,” *J. R. Soc. Interface*, vol. 20, no. 206, p. 20230266, 2023.
- [7] M. M. Cicolin *et al.*, “Vortex shedding behind porous flat plates normal to the flow,” *J. Fluid Mech.*, vol. 985, p. A40, 2024.
- [8] M. Pezzulla *et al.*, “Deformation of porous flexible strip in low and moderate reynolds number flows,” *Phys. Rev. Fluids*, vol. 5, no. 8, p. 084103, 2020.

Temperature-Driven Deformation Mechanisms in CNT- and Graphene-Reinforced Al_{0.3}CoCrFeNi High-Entropy Alloys: A Molecular Dynamics Approach

Subrata Barman^a, Sudip Dey^b

^aResearch Scholar, National Institute of Technology Silchar, India

^bAssociate Professor, National Institute of Technology Silchar, India

1. Introduction and Objective

High-entropy alloys (HEAs) are a new class of metallic materials containing multiple principal elements in near-equiatomic ratios, leading to exceptional strength, hardness, and thermal stability [1]. Among them, AlCoCrFeNi alloys exhibit remarkable tunability of microstructure and mechanical properties, with Al_{0.3}CoCrFeNi being widely studied for its stable FCC structure and superior toughness [2]. Beyond compositional optimization, reinforcing HEAs with nanomaterials has emerged as an effective strategy to enhance mechanical performance. Carbon-based nanostructures, such as carbon nanotubes (CNTs) and graphene (Gr), possess extraordinary stiffness and strength, enabling efficient stress transfer and grain refinement in HEA composites [4]. Experimental studies have demonstrated that CNT addition enhances yield strength, hardness, and wear resistance in HEAs through interfacial load transfer and carbide formation. Similarly, graphene reinforcement improves hardness, tribological behavior, and corrosion resistance, driven by dislocation pinning and interfacial strengthening. However, while these studies confirm significant improvements, the atomistic mechanisms governing the mechanical behavior—especially the temperature-dependent effects of different carbon nanostructures—remain inadequately understood. Molecular dynamics (MD) simulations provide atomistic insights into deformation and failure mechanisms [4]. Previous works revealed that reinforcement geometry, interface bonding, and temperature collectively govern load transfer and plasticity in nanocomposites [5]. Yet, a systematic comparison between CNT- and graphene-reinforced HEAs under varying temperature conditions is still lacking. This study employs MD simulations to investigate the tensile behavior of Al_{0.3}CoCrFeNi HEAs reinforced with CNT and Gr of equivalent surface areas at temperatures ranging from 100–900 K. The objectives are to: (i) compare their temperature-dependent stress-strain responses; (ii) quantify variations in yield and ultimate strengths; and (iii) elucidate atomistic mechanisms such as stress distribution, dislocation evolution, and interfacial deformation. The results (Figure X) show that CNT-reinforced HEAs exhibit higher strength and thermal stability than Gr-reinforced systems, attributed to enhanced interfacial confinement and efficient load transfer.

2. Methodology

Molecular dynamics (MD) simulations were performed using the LAMMPS package to investigate the tensile behavior of Al_{0.3}CoCrFeNi high-entropy alloys (HEAs) reinforced with carbon nanotubes (CNTs) and graphene (Gr) of equivalent surface areas. The HEA matrix was modeled with a near-equiatomic atomic distribution and equilibrated using the embedded atom method (EAM) potential, while carbon–metal interactions were described using a Lennard–Jones (LJ) potential. The composite models were first energy-minimized and equilibrated under the NPT ensemble at temperatures ranging from 100 K to 900 K for 200 ps. Uniaxial tensile loading was applied along the z-direction under the NVT ensemble at a constant strain rate of 10⁸ s⁻¹. Periodic boundary conditions were applied in all directions. The virial stress–strain response, atomic configurations, and von Mises stress distributions were analyzed to elucidate deformation mechanisms, interfacial load transfer, and failure characteristics associated with CNT and graphene reinforcement geometries.

3. Results

The results clearly demonstrate the influence of temperature on the mechanical behavior of HEA–CNT and HEA–Gr composites. Both systems exhibit a progressive decrease in yield strength and ultimate tensile strength with increasing temperature, indicating thermal softening of the HEA matrix and weakening of interfacial bonding between the reinforcement and the alloy. At lower temperatures (100 K and 300 K), the composites show higher strength and pronounced strain hardening due to restricted atomic mobility and efficient load transfer across the interface. In contrast, at elevated temperatures (600 K and 900 K), reduced interfacial adhesion and enhanced atomic diffusion lead to lower peak stresses and smoother deformation profiles. Overall, CNT-reinforced HEA exhibits higher strength and superior thermal stability compared to its graphene-reinforced counterpart, owing to the enhanced load-bearing capacity and stronger interfacial confinement offered by the tubular CNT structure.

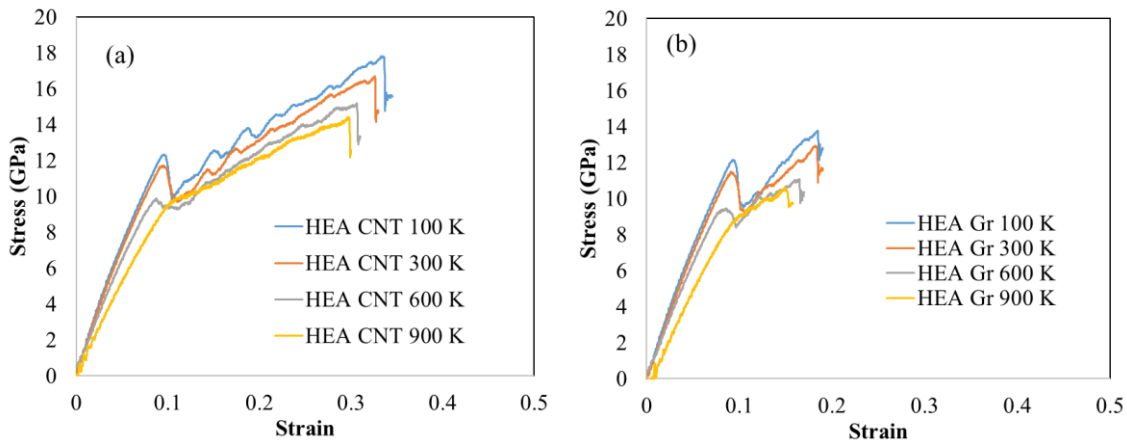


Figure 1. Tensile stress–strain response of HEA nanocomposites reinforced with equivalent surface areas of (a) carbon nanotubes (CNTs) and (b) graphene (Gr) at different temperatures.

4. Conclusion

Molecular dynamics simulations revealed that both CNT- and graphene-reinforced Al_{0.3}CoCrFeNi HEAs exhibit temperature-dependent tensile behavior, with strength decreasing as temperature increases. CNT-reinforced composites consistently demonstrated higher yield and ultimate strengths than their graphene counterparts due to superior interfacial confinement and efficient load transfer arising from their tubular geometry. In contrast, graphene interfaces showed greater thermal sensitivity, leading to earlier softening. Overall, CNT reinforcement offers enhanced mechanical stability, making it more suitable for high-temperature structural applications of HEA-based nanocomposites.

References

- Yeh, J. W. et al. Nanostructured high-entropy alloys with multiple principal elements: Novel alloy design concepts and outcomes. *Adv. Eng. Mater.* **6**(5), 299–303 (2004).
- Feng, R. et al. Design of lightweight high-entropy alloys. *Entropy* **18**(9), 333 (2016).
- Tang, Z. et al. Aluminum alloying effects on lattice types, microstructures, and mechanical behaviour of high-entropy alloys systems. *JOM* **65**, 1848–1858.
- Rafiee, R. & Mahdavi, M. Molecular dynamics simulation of defected carbon nanotubes. *Proc. Inst. Mech. Eng. Part L J. Mater. Des. Appl.* **230**(2), 654–662 (2016).
- Barman, S., Gupta, K. K. & Dey, S. Enhancing mechanical performance of Al_{0.3}CoCrFeNi HEA films through graphene coating: Insights from nanoindentation and dislocation mechanism analysis. *Model. Simul. Mater. Sci. Eng.* **32**(3), 035012 (2024).

The assessment to study the free vibration of edge cracked bi-directional SFGM plate with modified inverse hyperbolic shear deformation theory (m-IHHSDT).

Rahul Sudam Kamble^a, Achchhe Lal^b, Bhrigu Nath Singh^c

^a Research Scholar, Department of Mechanical Engineering, SVNIT, Surat, India

^b Associate Professor, Department of Mechanical Engineering, SVNIT, Surat, India

^c Professor (HAG) on lien, Department of Aerospace Engineering, IIT Kharagpur, Kharagpur, India

ABSTRACT

Nowadays, the sectors like defence, construction, and nuclear energy are growing rapidly. In the applications of such fields the crack failure is needed to be avoided. The bidirectional variation of properties is chosen to compare similar studies with available literature with unidirectional approach. Hence, this work has addressed the free vibration behaviour of porous bi-directional sigmoid functionally graded (SFGM) edge cracked plate by newly modified inverse hyperbolic higher order shear deformation theory (m-IHHSDT). The gradation or variation of effective material properties is assumed in x and z directions with the sigmoid law. Parametric analysis is employed to study the effect of volume fraction exponent, type of porosity, crack length, crack angle, and boundary conditions (BCs) on natural frequencies of bi-directional functionally graded material. The value of porosity coefficient influences the natural frequency considerably. The natural frequency is strongly influenced by the volume fraction exponent (n) and boundary conditions also. This work will help to design bidirectional functionally graded structures for the applications of combustion chambers, I.C. engine components, nuclear reactors, etc.

Keywords: Edge crack, Square plate, Free vibration, Bi-directional porous SFGM, IHHSDT.

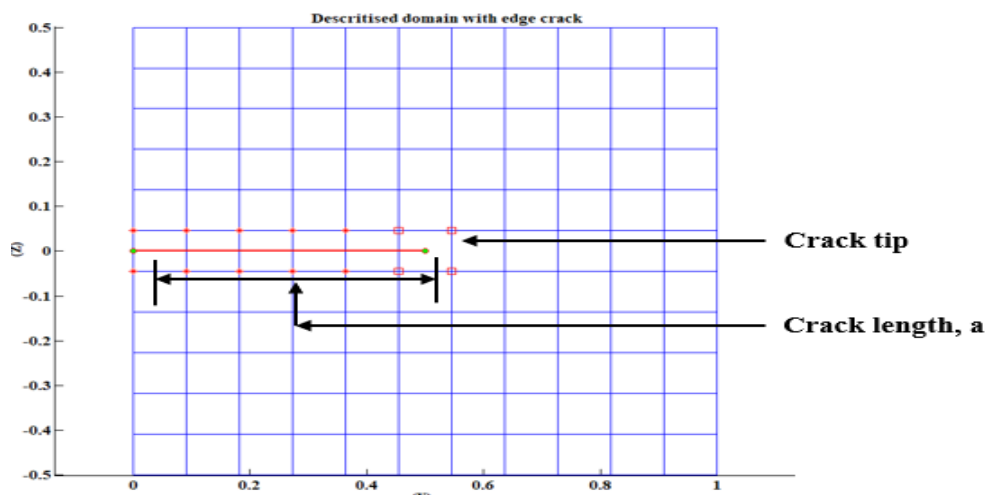


Figure 1. The edge crack propagation of bidirectional SFGM in free vibration.

Figure 1. Shows the square edge cracked FGM plate having length (l), and breadth (b), with gradation index in thickness direction (n_z), and longitudinal direction (n_x) are taken into consideration. X and Z are considered as cartesian coordinates respectively. The variation of material properties of bidirectional SFGM (Ramteke & Panda, 2021) with uniform porosity distribution can be expressed as:

$$E(Z, X) = E_m + 0.5 * (E_c - E_m) \left(\frac{2Z}{h} + 1 \right)^{n_z} \left(\frac{X}{a} \right)^{n_x} - 0.5 * V_e * (E_c + E_m)$$

for $-\frac{h}{2} \leq Z \leq 0$ and $-\frac{a}{2} \leq X \leq 0$ (1)

$$E(Z, X) = E_m + (E_c - E_m) \left\{ 1 - 0.5 \left(1 - \frac{2Z}{h} \right)^{n_z} \left(\frac{X}{a} \right)^{n_x} \right\} - 0.5 * V_e * (E_c + E_m)$$

$$for 0 \leq Z \leq \frac{h}{2} \text{ and } 0 \leq Z \leq \frac{a}{2} \quad (2)$$

The modified m-IHHSDT can be written as,

$$f(Z) = Z \tan^{-1} h \left(\tanh \left(2\pi \left(\frac{PZ}{h} \right)^2 \right) \right) - \left(\frac{3P\pi Z}{2} \right) \quad (3)$$

Where, Ve = porosity fraction, Em and Ec are modulus of elasticities of aluminium and alumina respectively.

Validation and parametric study:

Table 1. Effect of thickness ratio on the vibration responses (nondimensional) of bidirectional SFGM porous square plate. ($a/h = 10$, SSSS, $\bar{\omega} = \omega \left(\frac{b^2}{h} \right) \sqrt{\frac{\rho_c}{E_c}}$)

| Power law index, (n) | | Porosity distribution (Ve) | | | | Ref. |
|----------------------|-------------|----------------------------|--------|--------|--------|-------------------------|
| | | Even | | Uneven | | |
| $n_z = 0$ | $n_x = 0$ | 0.1 | 0.2 | 0.1 | 0.2 | (Ramteke & Panda, 2021) |
| | $n_x = 0.5$ | 4.2426 | 4.1683 | 4.3394 | 4.3818 | |
| | $n_x = 1$ | 3.9285 | 3.7979 | 4.0545 | 4.0834 | |
| | $n_z = 0.5$ | 4.5393 | 4.4787 | 4.6216 | 4.6635 | |
| | $n_x = 0.5$ | 4.0862 | 3.9541 | 4.2063 | 4.2323 | |
| | $n_x = 1$ | 3.8103 | 3.6263 | 3.9565 | 3.9713 | |
| $n_z = 0$ | $n_x = 0$ | 5.7488 | 5.8219 | 5.7672 | 5.8534 | Present study |
| | $n_x = 0.5$ | 5.2499 | 5.4649 | 5.2194 | 5.3472 | |
| | $n_x = 1$ | 1.1221 | 2.6048 | 2.0647 | 1.4880 | |
| | $n_z = 0.5$ | 4.6206 | 4.5663 | 4.7057 | 4.7526 | |
| | $n_x = 0.5$ | 4.3871 | 4.4249 | 4.4503 | 4.5090 | |
| | $n_x = 1$ | 2.8836 | 1.8309 | 3.2716 | 3.0998 | |

In Table 1. The effects of type of porosity and varying power indices on NDF's can be observed. The results obtained in this work by using modified version of IHHSDT (Kumar et al., 2019) are matching with the (Ramteke & Panda, 2021). Hence, it is concluded that the developed code can be employed to study the free vibration behavior of bidirectional SFGM square plate with edge crack.

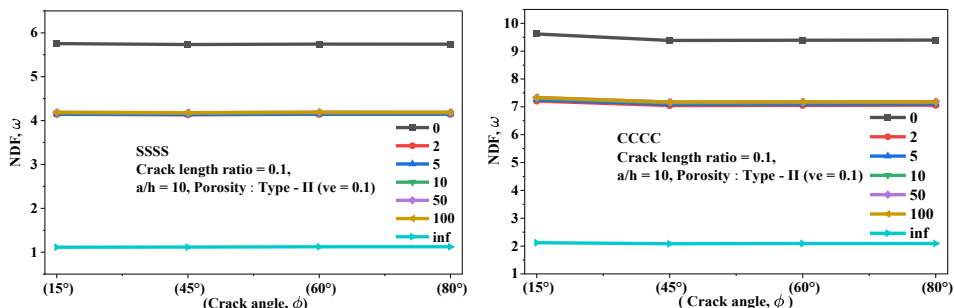


Figure 2. The effect of crack angle on nondimensional frequency of bidirectional SFGM

References:

- Kumar, R., Lal, A., Singh, B. N., & Singh, J. (2019). Meshfree approach on buckling and free vibration analysis of porous FGM plate with proposed IHHSDT resting on the foundation. *Curved and Layered Structures*, 6(1), 192–211. <https://doi.org/10.1515/cls-2019-0017>
- Ramteke, P. M., & Panda, S. K. (2021). Free Vibrational Behaviour of Multi-Directional Porous Functionally Graded Structures. *Arabian Journal for Science and Engineering*, 46(8), 7741–7756. <https://doi.org/10.1007/s13369-021-05461-6>

Thermo-elastic vibration characteristics of graphene-reinforced composite stiffened spherical panels

Pabitra Maji^{a,b*}, Poonam Kumari^b and Bhrgu Nath Singh^{a,c}

Aerospace Engineering, Rajiv Gandhi National Aviation University (RGNAU), India.

^b Department of Mechanical Engineering, Indian Institute of Technology Guwahati, India.

^c Aerospace Engineering, IIT Kharagpur-721302, India.

1. INTRODUCTION:

An innovative sort of composite material known as graphene-reinforced composites is utilized to enhance the strength of multilayer structures. Graphene is a lightweight structure composed of two dimensions of carbon. Its mechanical, electrical, and thermal properties are all excellent. It is possible to improve composites' thermal, mechanical, and electrical qualities by adding a small amount of graphene. It is well recognized that graphene and carbon nanotubes (CNTs) are the two primary nanoscale materials used to strengthen composites. Not only does graphene have more surface area than carbon nanotubes (CNTs), but it also interacts better with polymer matrix (PMMA). Also, compared to CNTs, graphene can be made efficiently and cheaply. Extra beams or sections that are attached to the panels on one side or both sides are known as stiffeners. Their purpose is to help the structure stronger. In addition, when comparing panels of the same weight, stiffened panels can support a more significant load. The doubly curved stiffened spherical shell can be used in various structural engineering applications.

2. THEORETICAL FORMULATIONS:

2.1 SPHERICAL SHELL ELEMENTS FORMULATION:

A graphene-reinforced composite stiffened spherical shell panel with the principal radius of curvature along X and Y directions, R_x and R_y , respectively, are illustrated in Figure 1. Shell dimensions are $a=b=h$ with a uniform thickness and a radius of curvature $R_x=R_y=R$. The geometry of the stiffened shells is modelled based on the first-order shear deformation theory (FSDT).

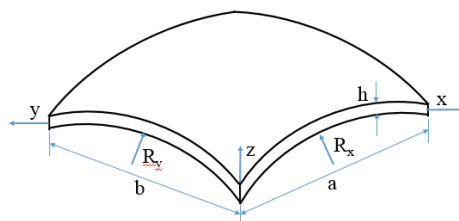


Figure 1: The shape of the stiffened graphene-reinforced composite (GRC) spherical shells.

$$u(x, y, z) = u^0(x, y) + z\theta_x(x, y) \quad (1)$$

$$v(x, y, z) = v^0(x, y) + z\theta_y(x, y) \quad (2)$$

$$w(x, y, z) = w^0(x, y) \quad (3)$$

where the transverse displacement of the mid-plane of the GRC panels is represented by the in-plane displacements u^o , v^o , and w^o respectively. The values of θ_x and θ_y represent the rotation of the X and Y axes, respectively.

2.2 STIFFENERS FORMULATIONS:

In the process of modelling the stiffener, three nodded curved isoparametric beam elements are utilized. These elements have four degrees of freedom, which include two translations and two rotations. For the purpose of the stiffener, a rectangular section composed of graphene-reinforced composite materials with a constant width (b_t) and depth (d_t) is being evaluated.

2.3 THE MATERIAL PROPERTY OF STIFFENED SPHERICAL SHELLS:

Four different types of grades are taken into consideration, and these grades are dispersed throughout the thickness of the stiffened spherical shell panels.

3. RESULTS AND DISCUSSIONS:

The finite element code is being developed to offer numerical results with the aim of analysing the free vibration characteristic of graphene-reinforced stiffening composite (GRC) plates. It is clear that the current results closely align with those of Shen et al. [1] and Kiani [2] are shown in Table 1. The validations listed above have shown that the current formulation is accurate and correct.

Table 1: Assessment of first three frequency of various graded patterns GRC square plates with $b/h = 10$.

| Temp | Source | Ω_1 | Ω_2 | Ω_3 |
|------|-----------------|------------|------------|------------|
| 300K | Shen et al. [1] | 29.5212 | 65.7134 | 65.8394 |
| | Kiani [2] | 30.0881 | 68.2699 | 68.3945 |
| | Present | 30.0917 | 68.3233 | 68.4472 |

4. CONCLUSIONS:

The finite element analysis (FEM) is used to look at the free vibration behaviour of GRC stiffened spherical panels based on the first-order shear deformation theory. A three-nodded beam element is taken into consideration for modeling the stiffeners. In this study, four different types of grades are taken into consideration, and these grades are dispersed throughout the thickness of the stiffened spherical shell panels. Various parametric studies and convergence studies are performed to check the correctness and precision of the current formulation.

5. REFERENCES

- [1] C.T. Sun, J.K. Chen, "On the Impact of Initially Stressed Composite Laminates". *J Compos Mater* Vol. 19, No. 6, pp. 490-504. Nov 1985. <https://doi.org/10.1177/002199838501900601>.
- [2] Y. Kiani, "Isogeometric large amplitude free vibration of graphene reinforced laminated plates in thermal environment using NURBS formulation". *Comput Methods Appl Mech*, Vol. 332, pp 86–101, Apr 2018. <https://doi.org/10.1016/j.cma.2017.12.015>.

*Corresponding Author: Dr. Pabitra Maji, Email: pabitrajumech2@gmail.com.

Thermo-Mechanical Analysis of thermally Autofrettaged Functionally Graded Disk

Mohit Rajput^{a*}, S.M Kamal^b, R. U. Patil^a

^a*Department of Mechanical Engineering, Indian Institute of Technology Jammu, India*

^b*Department of Mechanical Engineering, Tezpur University, Tezpur, Assam, India*

*2020rme2068@iitjammu.ac.in

smkmech@tezu.ac.in

roshan.patil@iitjammu.ac.in

Introduction and objective

Functionally graded (FG) materials [1] are gaining widespread application in industries requiring superior thermal and mechanical properties, such as high-pressure bearing components, pressure vessels, and pipelines transporting high-pressure fluids. These materials are crucial in preventing structural failure caused by extreme internal pressure or thermal gradients. However, the homogeneous cylinder or disk used in building aerospace, automobile or many other engineering structures are subjected to high tensile stresses in service. In traditional thick-walled metallic cylinders or disks, this issue is commonly addressed through a prestressing method known as autofrettage [2]. This technique, widely used for over a century, enhances the strength and durability of high-pressure components, ranging from large cannon to small fuel injection systems. The autofrettage process generates the compressive residual stresses near the cylinder or disk inner surface, which significantly improves its load-bearing capacity. The complete details of autofrettage process, including traditional autofrettage methods such as hydraulic, swage, and explosive autofrettage as well as recent advancements including thermal and rotational autofrettage are given in references [2,3]. A recent approach known as thermal autofrettage was introduced by Kamal and Dixit [4]. This method used a thermal gradient across the disk wall thickness to generate the plastic deformation at its interior wall. After achieving the desired plastic deformation, gradual cooling to room temperature which resulting the residual compressive stresses, enhancing the pressure capacity of the disk.

The increasing preference for FG materials over homogeneous materials in aerospace, nuclear, and pressure vessel industries has led to a growing interest in studying their mechanical behavior. Analytical solutions for FG cylinders under internal pressure and temperature gradients using yield criterion of Tresca with an elastic perfectly plastic model, were obtained by Parvizi et al. [5]. Alikarni and Parvizi [6] extend the same work using combined pressure and thermal loading and validated the theoretical results with finite element results using Abaqus software. Rodriguez Castro et al. [7] investigated the mechanical and microstructure behaviour of FG Al/SiC composite material. Belhaou et al. [8] introduced a model to analyse residual stress formation in autofrettaged FG cylinders under internal pressure. The method used a power-law distribution for material properties and accounted for strain hardening as well as the Bauschinger effect during unloading. A mathematical model for thermal autofrettage in thick-walled functionally graded cylinders was recently developed by Rajput et al. [9].

Based on the existing literatures, no prior investigations have examined the residual stress in FG disk. These advanced composite materials possess continuous gradation of material properties in the radial direction. During thermal loading, FG thick-walled hollow disk is presumed to exhibits elastic-perfectly plastic behavior under the assumption of plane stress. The formulation for thermo-elastic plastic stresses of the FG disk is derived by a plastically deforming temperature difference and considering the yield criterion of von Mises. The advantageous effect of thermal autofrettage to induce the compressive residual stresses after unloading to enhance the disk pressure carrying capacity is examined. The mathematical formulation of the thermal stresses in an FG disk made of aluminium (Al) and silicon carbide (SiC) undergoing thermal autofrettage is carried out. The analysis shows that thermal autofrettage can generate substantial compressive residual stresses, approximately 99 % of the yield strength, at the disk inner radius, which increases its pressure capacity during service. In the current study, the allowable internal pressure for an FG disk with a thickness ratio of 3 may increase up to approximately 30.68%.

Results and Discussion

The material properties of FG disk are considered from references [5],[7]. In the present case, considering the Al A359 aluminum alloy matrix reinforced with 20 % and 30% SiC volume fraction at the inner and outer surface respectively. The material properties are varied along the radial direction based on power law. The temperature of the FG disk at the inner surface is 25°C. For achieving autofrettage in the FG disk, a thermal gradient of 418°C is considered. The analytical solution of elastic-plastic stresses using yield criterion of von Mises under thermal loading is given in Fig 1(a). It is analyzed that the hoop stress exhibits a considerably higher magnitude compared to the radial stress. While the radial stress remains tensile throughout the wall thickness, the hoop stress transitions from tensile to compressive toward the outer radius.

Residual stress refers to the internal stress that remain in a material after a thermal gradient is removed as revealed in Fig 1(b). The formation of compressive residual stresses around the disk inner wall which marks the FG disk as being thermally autofrettaged. It is analyzed that a significant amount of residual hoop stress at the disk inner radius is induced, which is of the order of -309.3 MPa. The radial stress shows a consistent compressive trend.

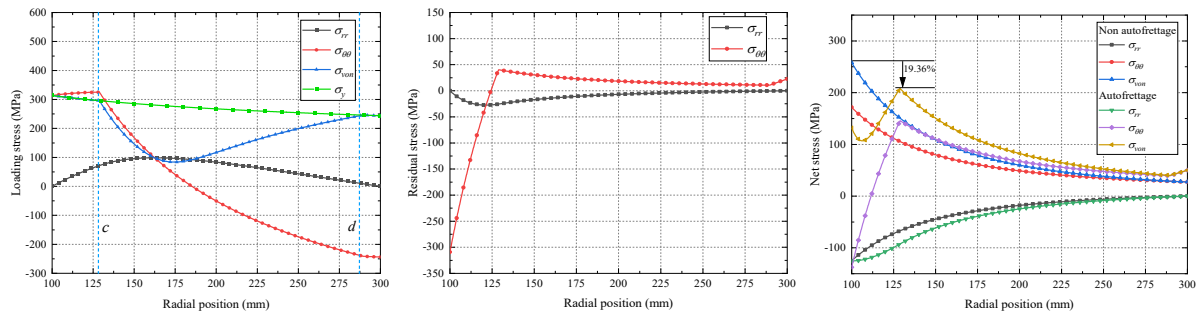


Fig 1: Distribution of (a) loading stress due to the thermal gradient of 418 °C, (b) residual stresses of FG disk after unloading (c) net stress during service under the internal pressure of 125 MPa

After the introduction of thermally induced residual stresses, the pressure resistance of the FG disk is examined by applying an internal pressure of 125 MPa, as depicted in Fig. 1(c). The outcomes indicate that the maximum equivalent von Mises stress in the thermally autofrettaged disk decreases by about 19.36% compared to the non-autofrettage disk. Consequently, the autofrettaged disk is capable of sustaining an high internal pressure of 151.48 MPa before yielding, whereas the autofrettaged disk can withstand only up to 101.47 MPa. Hence, thermal autofrettage yields an improvement of approximately 30.68% in the maximum pressure capacity of the functionally graded disk.

References

- [1] J. N. Reddy and C. D. Chin, "Thermomechanical analysis of functionally graded cylinders and plates," *J. Therm. Stress.*, vol. 21, no. 6, pp. 593–626, 1998.
- [2] R. Shufen and U. S. Dixit, "A Review of Theoretical and Experimental Research on Various Autofrettage Processes," *J. Press. Vessel Technol. Trans. ASME*, vol. 140, no. 5, pp. 1–15, 2018.
- [3] U. S. Dixit, S. M. Kamal, and R. Shufen, "Autofrettage Processes: technology and modelling," CRC Press, 2019.
- [4] S.M. Kamal , U.S.Dixit. "Feasibility study of thermal autofrettage process," *Top Mining, Metall Mater Eng* 2015; 81–107. Springer, New Delhi
- [5] A. Parvizi, R. Naghdabadi, and J. Arghavani, "Analysis of Al A359/SiCp functionally graded cylinder subjected to internal pressure and temperature gradient with elastic-plastic deformation," *J. Therm. Stress.*, vol. 34, no. 10, pp. 1054–1070, 2011.
- [6] S. Alikarami and A. Parvizi, "Elasto-plastic analysis and finite element simulation of thick-walled functionally graded cylinder subjected to combined pressure and thermal loading," *Sci. Eng. Compos. Mater.*, vol. 24, no. 4, pp. 609–620, 2017.
- [7] R. Rodríguez-Castro, R. C. Wetherhold, and M. H. Kelestemur, "Microstructure and mechanical behavior of functionally graded Al A359/SiCp composite," *Mater. Sci. Eng. A*, vol. 323, no. 1–2, pp. 445–456, 2002.
- [8] M. Belhaou, N. E. Laghzale, and A. H. Bouzid, "Residual stresses in autofrettaged functionally graded pressurized thick cylinders," *Int. J. Press. Vessel. Pip.*, vol. 208, pp. 105143, 2024.
- [9] M. Rajput, S. M. Kamal, R. U. Patil, and S. Deka, "Analysis of thermal autofrettage for functionally graded thick-walled cylinders," *Int. J. Press. Vessel. Pip.*, vol. 216, pp. 105505, 2025.

Thrust Vectoring of an Actively Controlled Supersonic Jet

Mayank Kumar, SaiPhaneendra Karuchola ^{*}, Arun Kumar Perumal, Ashoke De
Indian Institute of Technology Kanpur, Kanpur–208016, India.

1 Introduction

Thrust vectoring enables rockets and space vehicles to steer their exhaust without mechanical gimbals by deflecting the primary jet. This study explores fluidic thrust vectoring (FTV) of a supersonic jet as a practical alternative to passive or mechanical methods, preserving a fixed nozzle geometry and associated structural simplicity.

Building on the extensive experimental investigation of jet deflection angle (δ°) in a Mach 1.85 jet by Yadav *et al.* [1], we examine the influence of fluidic parameters—the injector-to-main mass flow ratio C_m , injector axial location x_s/L_d , diameter ratio (d/D_e), and expansion ratio P_e/P_a —across multiple design Mach numbers ($M_d = 1.35, 1.50, 1.85$). The objective is to document the effect of P_e/P_a and C_m on δ° for all three nozzles and relate the observed trends to the underlying shock/jet structure.

2 Experimental Facility and Instrumentation

Experiments were conducted in the Jet-Acoustics and Flow-Control Laboratory at IIT Kanpur (same facility as [1]). Three axisymmetric CD nozzles with semi-divergence angle 2.5° and throat diameter $D_{th} = 14$ mm were designed for $M_d = \{1.35, 1.50, 1.85\}$. Exit diameters were 15.19 mm, 17.12 mm, and 17.12 mm (Area-Mach relation), yielding calibrated nozzle pressure ratios $NPR_d = \{2.96, 3.67, 6.20\}$. Figure 1a shows the nozzle schematic.

Following [1], the secondary fluidic injection was implemented via a single injector of $d/D_{th} = 0.087$ located at $x_s/L_d = -0.3$ (negative denotes upstream of the exit). The injector mass flow rate \dot{m}_i was measured using an Alicat MCR-2000 SLPM controller; the primary mass flow was obtained via a choked-flow estimate. Pressures within the jet were recorded using a 16-channel PSI-9116 transducer (range 0–2.1 MPa). The deflection angle δ° was determined from a Pitot rake placed downstream of the nozzle exit as in [1, 2]. The rake position y_{peak}^* relative to the nozzle centerline (non-dimensionalized by D_e) yields

$$\delta^\circ = \tan^{-1} \left(\frac{y_{peak}^*}{x_{rake}^*} \right), \quad (1)$$

where x_{rake}^* is the streamwise non-dimensional location.

3 Results and Discussions

Figure 1b presents the variation of δ° with C_m at $P_e/P_a = 1$ and $x_s/L_d = -0.3$ for $M_d = \{1.35, 1.50, 1.85\}$. A strong dependence on C_m is observed: for same C_m , $M_d = 1.35$ nozzle exhibits the largest deflection (e.g. $\delta^\circ \approx 5.94^\circ$ at $C_m = 1.75\%$), consistent with its lower design NPR_d . Increasing M_d tends to reduce δ° , indicating reduced sensitivity to vectoring at higher design expansion.

Time-averaged Schlieren images in Fig. 2 compare natural jets (a–c) and manipulated jets (d–f) for $(C_m, x_s/L_d) = (0.75\%, -0.3)$ at $P_e/P_a = 1$. The natural jets show the canonical shock-cell structure, while the manipulated jets display an induced shock that turns the primary flow away from the centerline, in line with the mechanism summarized in [1, 2]. The qualitative shift of the jet core and the induced shock angle highlighted in panel (e) are consistent with the increasing δ° trends in Fig. 1b.

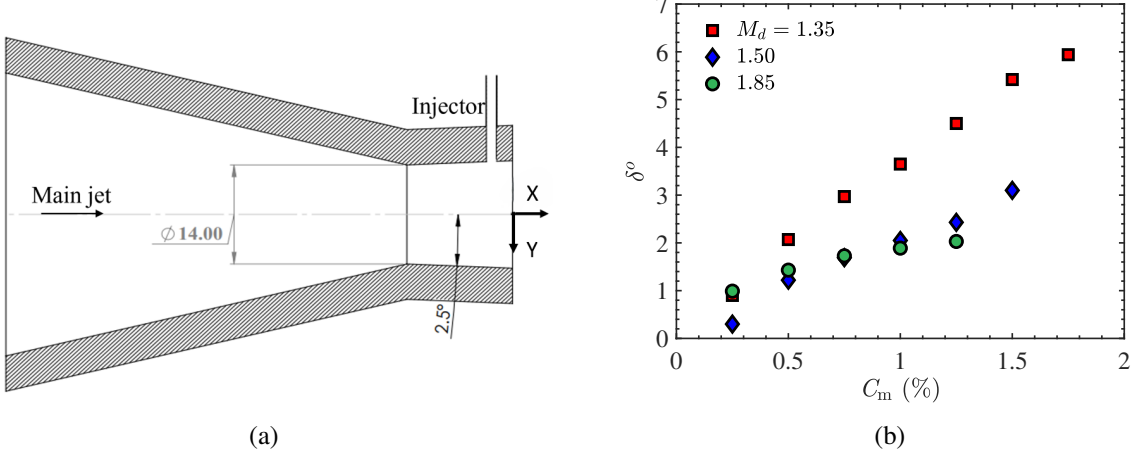


Figure 1: (a) Schematic of the nozzle and (b) Variation of δ° with C_m for all three nozzles at $P_e/P_a = 1.0$, and $x_s/L_d = -0.3$.

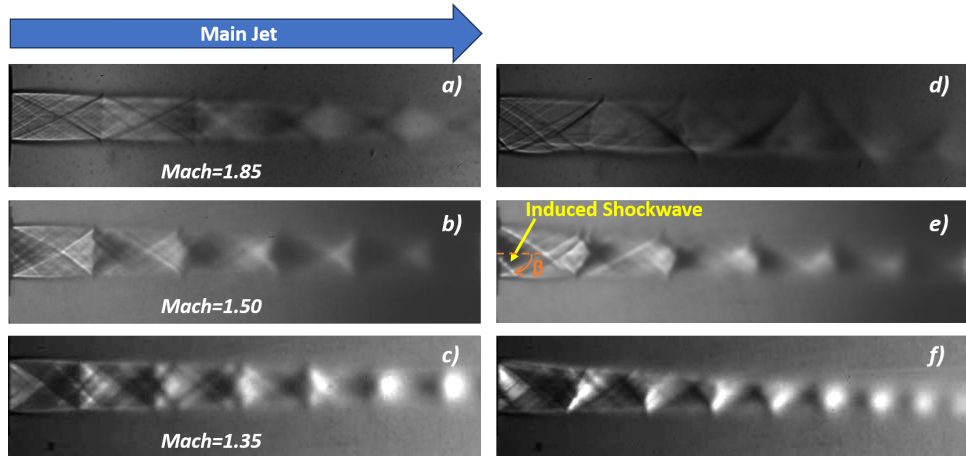


Figure 2: Time-averaged Schlieren images of (a - c) natural jet and (d - f) manipulated jets for $C_m = 0.75\%$, $x_s/L_d = -0.3$ at $P_e/P_a = 1.0$.

4 Conclusions

Fluidic thrust vectoring of supersonic jets is strongly governed by C_m and by the nozzle design Mach number. For a fixed P_e/P_a and injector location, lower M_d produces larger δ° , whereas higher M_d reduces sensitivity to vectoring. Schlieren imaging confirms the presence of an induced shock that steers the jet away from the centerline, providing a physical basis for the measured deflection. Detailed parametric results for $P_e/P_a < 1$ (overexpanded) and $P_e/P_a > 1$ (underexpanded) will be presented in the full paper.

References

- [1] A. Yadav, R. Vignesh, and A. K. Perumal, “Parametric Study on the Thrust Vectoring of a Supersonic Jet Manipulated by Fluidic Injection,” in *AIAA Aviation 2023 Forum*, p. 4084, 2023.
- [2] A. K. Perumal, “Performance Analysis of Fluidic Injector for Supersonic Jet Manipulation,” *AIAA Journal*, vol. 61, pp. 5658–5668, 2023.

* Communicating Author: SaiPhaneendra K (saidp21@iitk.ac.in).

Transonic flutter prediction of delta wings using coupled CSD-CFD approach

Arun Kumar A^a, Amit K Onkar^{a1}, Rahul B Choudhary^a, Arun K^a, Raja S^a

^a Structural Technological Division, CSIR-National Aerospace Laboratories, Bangalore 560017, India

1. INTRODUCTION & OBJECTIVE

Aeroelastic flutter is a critical phenomenon in aircraft design, and its accurate prediction is essential for certification. While established techniques exist for flutter clearance in subsonic and supersonic regimes, their applicability to transonic flows is limited due to simplified assumptions in flow-field modelling. The transonic regime, characterized by shock waves and complex boundary layer interactions, demands more advanced computational approaches. Computational Fluid Dynamics (CFD), coupled with Computational Structural Dynamics (CSD), has emerged as a viable solution for transonic flutter prediction, capable of capturing key aerodynamic phenomena. The objective of the present work is to employ a Fluid-Structure Interaction (FSI) approach based on coupled CFD-CSD approach to study the transonic flutter characteristics of delta wing and clipped delta wing models [1].

2. METHODS OF ANALYSIS

The FSI approach adopted here is based on a staggered or explicit coupling approach where both CFD solver (CFD++) and CSD solver (CSM++) interact sequentially in time. For flutter prediction, CFD solves the unsteady form of the RANS equations in a coupled manner with the turbulence modelled using the 2-equation SST model. For the finite element analysis, CSD solves the structural dynamic equations in modal coordinates and time integration is carried out using the Newmark/HHT time integration algorithm. The morphing of the CFD grid in FSI problems is modelled using a radial basis interpolation function.

3. NUMERICAL RESULTS

Figure 1(a) shows the geometric details of the clipped delta wing. The model has a 72° sweep with aspect ratio of 0.54. The wing cross-section is made of a 3.0-percent-thick modified biconvex airfoil. The leading edge and trailing edge of the model are rounded as indicated in figure providing smooth aerodynamic contour resulting in modified biconvex airfoil section.

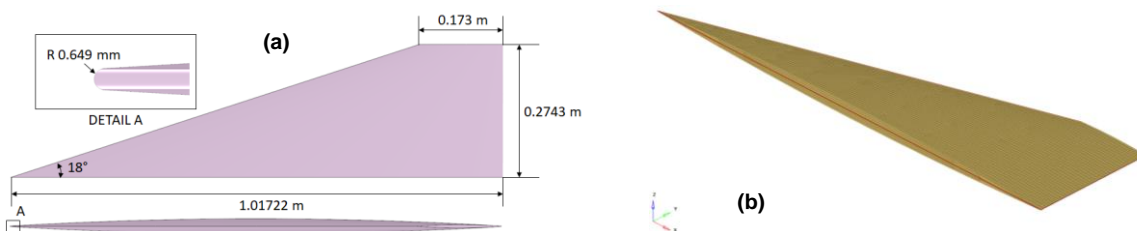


Figure 1: Geometry of clipped delta wing, and its finite element model

The finite element model of the clipped delta wing is shown in Fig. 1(b). It consists of 61594 nodes and 275128 solid elements. The model is constructed using two different materials [1]: 0.051 inch thick aluminium alloy plate (2024 T3) at the middle covered by balsa wood. The aluminium plate is rounded along its edges and the balsa wood is faired into these rounded edges to provide a smooth aerodynamic contour. The total weight of the model is 1.04 kg. Free vibration analysis is then carried out and the obtained natural frequencies are compared with the experimental data [1] (indicated in bracket) as follows: Mode 1: 22.1 Hz (20.8 Hz), Mode 2: 46.548 Hz (45.2 Hz), Mode 3: 79.134 Hz (84.4 Hz), and

¹ Communicating Author: Amit K Onkar and aeroamit@nal.res.in.

Mode 4: 106.287 Hz (104 Hz). All the modal frequencies match well with experiment with a maximum difference of ~6% observed for Mode1, and Mode3.

The CFD domain considered is shown in Fig. 2(a) where hemispherical far-field is chosen with a radius of 50 m. The total cell count is 3845247 with 1st cell height of 1.2e-5 m and maximum skewness angle of 84.2°. The boundary conditions applied in CFD analysis are also indicated in the figure.

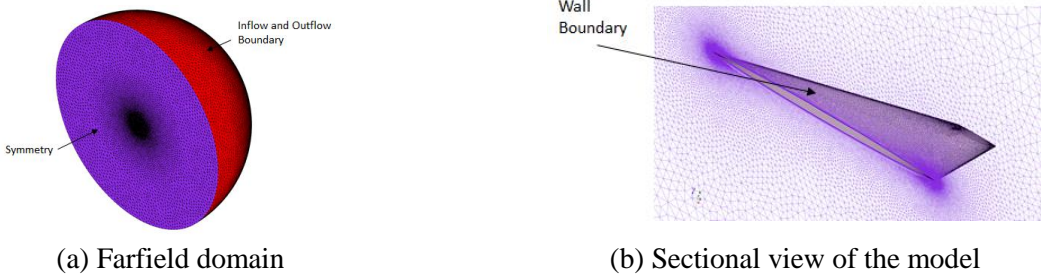


Figure 2: CFD model of clipped delta wing

For flutter analysis at a given Mach number and mass ratio, steady flow solution at zero angle of attack is used as an initial condition for FSI simulation. Here, the structure is excited with a step input of infinitesimal pressure for a duration of 3 timesteps. Then, the excitation is removed and the system is allowed to respond to the surrounding flow field. The unsteady RANS equations are solved using CFD solver and the structural dynamics in modal coordinates using CSD solver, with five modes retained. A time step of 2.5e-4 s, 10 inner CFD iterations, and a CFL of 50 are employed. Simulations are run for 0.5s, monitoring wing-tip displacements at various velocity indices (VI). The flutter index (FI) is identified at velocity where oscillations reach a small constant amplitude. Figure 3(a) shows the time histories of wing tip displacements for various VI at $M=0.9$. Figure 3(b) shows the comparison of flutter index and flutter frequency between the present computation and experiment [1] at various Mach numbers. The present results show a good agreement with the experimental data. It is also observed that the simulated flutter index and frequency are slightly over-predicted for all Mach numbers considered.

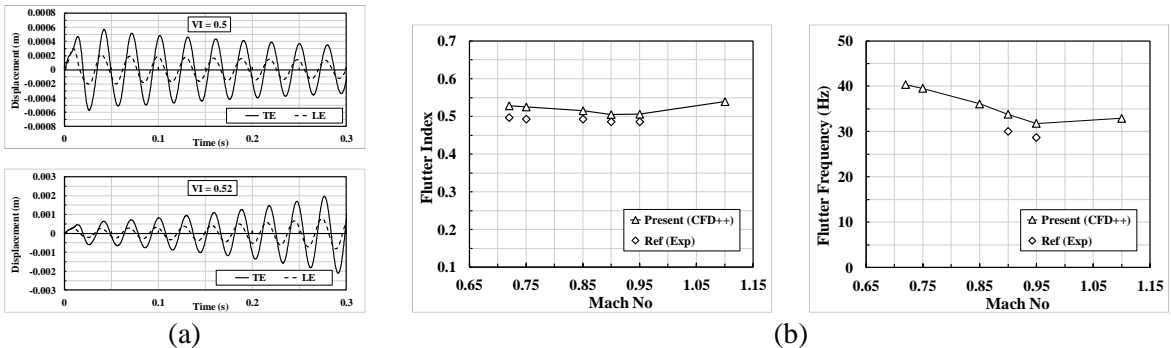


Figure 3: (a) Time history of wing tip displacements at $M = 0.9$ and (b) Comparison of flutter index and flutter frequency of clipped delta wing

4. CONCLUSIONS

In this study, a FSI framework based on coupled CSD - CFD is employed to predict the transonic flutter boundary of a clipped delta wing. The applicability of the present approach is investigated by comparing the present results with the available WT data. The present results show a good agreement with the experimental data with small discrepancy potentially arise from the structural model.

5. REFERENCES

- [1] R. V Doggett Jr, D. L. Soistmann, C. V Spain, E. C. Parker, and W. A. Silva, "Experimental transonic flutter characteristics of two 72 deg-sweep delta-wing models," NASA TM 101659, 1989.

Validating Combined Vector Field Approach With Full Quadrotor Dynamics

Sikha Hota^a and Dheeraj^{b*}

^aProfessor, Department of Aerospace Engineering, Indian Institute of Technology Kharagpur, India

^bStudent, Department of Aerospace Engineering, Indian Institute of Technology Kharagpur, India

*Communicating Author: Dheeraj (prajapatidheeraj25042004@gmail.com)

1. INTRODUCTION & OBJECTIVE

Autonomous unmanned aerial vehicles (UAVs) are increasingly employed in surveillance, reconnaissance, and environmental monitoring missions that demand precise path following under uncertain and dynamic conditions. The Combined Vector Field (CVF) approach proposed by Liang and Jia (2016) [1] provides a generalised mathematical framework for guiding UAVs along arbitrary twice-differentiable curves in both 2D and 3D spaces, using the Helmholtz decomposition of conservative and solenoidal vector fields to ensure convergence and smooth tangential motion. However, the validations have been limited to simplified kinematic models. This study aims to bridge the gap by integrating the CVF guidance law with the complete quadrotor dynamics model and robust control strategy. The quadrotor dynamics and Sliding Mode Control (SMC) law are developed following the methodology of Herrera et al. (2015) [2], enabling accurate attitude and position tracking under external disturbances. The primary objective of this work is to validate, through numerical simulation, the feasibility and effectiveness of the Combined Vector Field Approach when applied to a realistic quadrotor system, assessing its path-following accuracy, convergence, and robustness.

2. METHODS OF ANALYSIS

The simulation framework developed in this study integrates the Combined Vector Field (CVF) based guidance algorithm proposed in [1] with a complete quadrotor dynamic model and Sliding Mode Control (SMC) structure described in [2].

The Combined Vector Field method generates continuous reference velocity directions for arbitrary twice-differentiable paths defined implicitly as $f(x, y) = 0$ for 2D paths, or $f(x, y, z) = 0$ and $g(x, y, z) = 0$ for 3D paths. The conservative and solenoidal vector fields are computed and combined as described in [1], given by

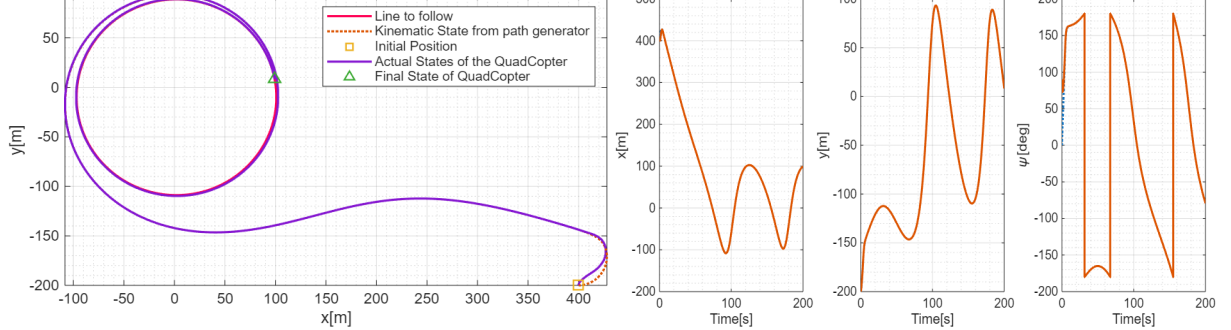
$$\mathbf{v}_d = -V_g \tanh(\kappa r) \mathbf{v}_c + s V_g \operatorname{sech}(\kappa r) \mathbf{v}_s \quad (1)$$

where, V_g is ground speed, \mathbf{v}_c and \mathbf{v}_s are normalized conservative and solenoidal vector fields, r is the indirect measure of the distance from the desired curve defined by $f = 0$ and/or $g = 0$ ($r = f$ or $r = \sqrt{f^2 + g^2}$), $s (= \pm 1)$ determines the direction of the solenoidal vector field (clockwise or anticlockwise). And κ is the tunable parameter that adjusts the rate of convergence. This formulation ensures a smooth, continuous, and feasible guidance vector field that guarantees asymptotic convergence to the desired path while maintaining tangential motion along it.

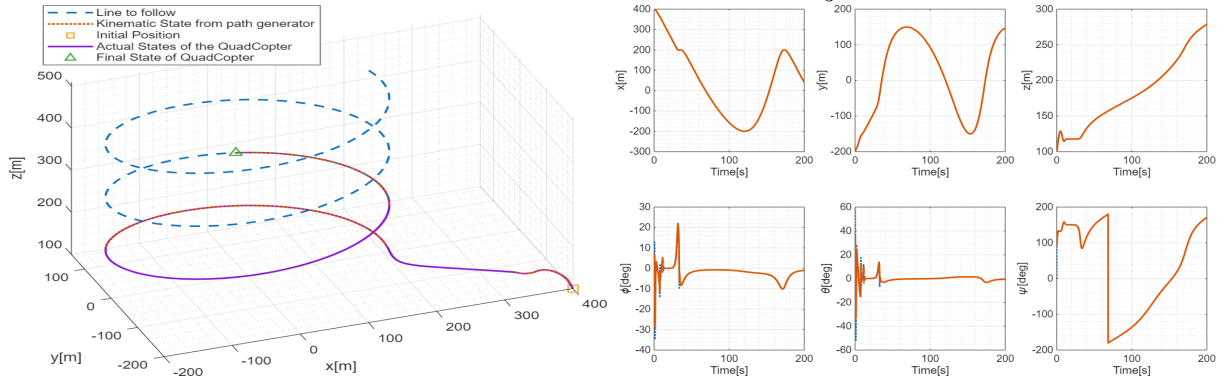
A proportional derivative (PD) saturated controller, incorporating limits on maximum course and climb rates, is employed to align the vehicle's orientation with the CVF-generated reference directions. The resulting kinematic variables are then used as desired inputs for the quadrotor simulation developed following [2], where the Sliding Mode Controller provides robustness against disturbances and model uncertainties.

3. RESULTS

3.1 Simulating for the 2D circular curve given by $f(x, y) = (x - 2)^2 + (y + 10)^2 - 9775$, with parameters as initial position $[400, -200]m$, initial course angle $\frac{\pi}{2} rad$, constant air speed, $v_a = 10m/s$, wind speed $w = [3, 4]m/s$, $s = +1$, vector field convergence parameter, $\kappa = 5$ and maximum course rate is $0.5rad/s$.



3.2 Simulating for the 3D inclined star curve given by, $f(x, y, z) = x - 200 \cos\left(\frac{z}{20}\right)$ and $g(x, y, z) = y - 150 \sin\left(\frac{z}{20}\right)$, with all other same parameters specified for the 2D case, with additional/updated parameters such as initial position $[-400, -200, 100]m$, initial climb angle $\frac{\pi}{4} rad$, maximum climb rate, $0.3rad/s$, maximum allowable roll and pitch angle for the quadrotor, $\frac{\pi}{3}$.



4. CONCLUSIONS

The numerical simulations demonstrate that the Combined Vector Field (CVF) guidance law, when integrated with Sliding Mode Control (SMC) and full quadrotor dynamics, achieves accurate path following for both 2D circular curves and 3D helical curves in a reasonable time. Although, as mentioned in [1], the main limitation of this approach is that the UAV might diverge or take too much time if the residual values of the intersecting function surfaces ($f(x, y, z)$ and $g(x, y, z)$) are not same order of magnitude; also, different curves require different convergence gain κ (as seen in the above figures). The future work can be extended to have fixed-time convergence to the specified curve and can also be used to guide the UAV swarm.

REFERENCES

- [1] Y. Liang and Y. Jia, “Combined vector field approach for 2d and 3d arbitrary twice differentiable curved path following with constrained uavs,” *Journal of Intelligent & Robotic Systems*, vol. 83, no. 1-4, pp. 133–160, 2016.
- [2] M. Herrera, W. O. Chamorro, A. P. Gómez, and O. Camacho, “Sliding mode control: An approach to control a quadrotor,” in *2015 IEEE Andean Country Congress (ANDESCON)*, 2015.

Venting analysis of a Typical Launch Vehicle Inter Stage Structure near to strapon nose cone

Darshit Gajera^a and Sanjoy Kumar Saha^{b*}

^aScientist/Engineer - SD, Vikram Sarabhai Space Centre, ISRO, India

^bDivision Head, ACD/AERO, Vikram Sarabhai Space Centre, ISRO, India

*Communicating Author: Sanjoy Kumar Saha, Email: sanjoy_kumar@vssc.gov.in.

1. INTRODUCTION

During the ascent of a typical launch vehicle through the atmosphere, ambient pressure decreases with altitude. Hence differential pressure (ΔP^1) builds up across the close structures of the launch vehicle, necessitating the implementation of intentional venting schemes to maintain ΔP within its structural design limits. To achieve this, generally vent valves or ports are strategically installed on the wall of the structures by comprehensive venting analysis (Detailed design of the vent system can be found from monograph published by NASA (Reference [1])).

For the India's most powerful rocket, Inter Tank Structure (ITSc) between Liquid Oxygen (LOX) and Liquid Hydrogen (LH₂) tanks near to the strapons of the vehicle has been modified and is made closed, isolated structure (Figure 1). Hence, the design of the venting system of the isolated ITSc compartment is of paramount importance for the structural integrity of the launch vehicle during its ascent phase.

A comprehensive venting study was conducted to determine the optimal vent port location on ITSc structure, with a focus on assessing the impact of vent port placement on the venting efficiency of the ITSc isolated compartment. Based on preliminary analysis, two potential locations for venting were identified on the ITSc structure. The first vent scheme involved implementing three vents on the cutout (CO) panels (CO1, CO2, and CO3) located on the cylindrical region of the ITSc (Figure 2). Each cutout was equipped with 12 vent ports of 40mm diameter. The number of vent ports was finalized based on experience gained from previous launch vehicle flights. An alternative vent implementation was also investigated, which involved relocating the vent scheme from the cutout panels to the aft-end side closure plates/panels, as depicted in Figure 1. While this approach resolved the issue of water logging inside the ITSc, it posed significant challenges due to the need for drilling holes on the hardware, which would be difficult to correct without replacing the entire ITSc structure.

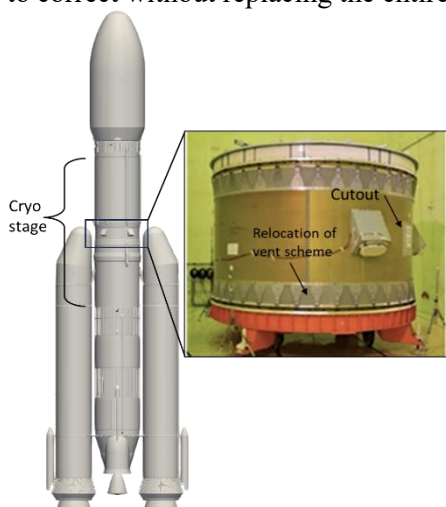


Figure 1: Closed Inter Tank Structure of ITSc

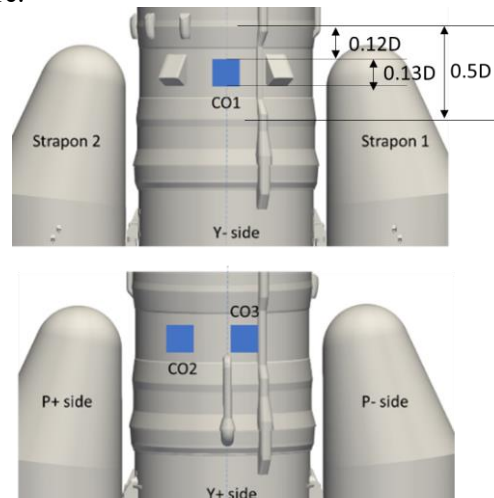


Figure 2: Location of the cutouts on ITSc

The Fortran code developed in-house is used for the venting analysis of ITSc compartment. This is a code being successfully used vent analysis of the launch vehicle compartments [2]. The code uses expression of isentropic mass flow rate across the vent ports which are obtained from the conservation

¹ Differential pressure ΔP is defined as $P_C - P_\infty = C_{PL} * q_\infty - (P_L - P_C)$, where C_{PL} , P_C , P_∞ and P_L stands for the local C_P , compartment, freestream, and local pressure respectively, q_∞ is freestream dynamic pressure

equations for energy and mass flow rate for inviscid flow. The viscous and external freestream effects are accounted using coefficient of discharge (C_d) values obtained from in-house wind tunnel experiments in the code [3].

2. RESULTS

The venting behaviour of the ITSc compartment was investigated when vent ports are located on cutouts as well as on aft-end closure panels. The result, presented in Figure 3, demonstrate the upper bound (UB), nominal, and lower bound (LB) venting profiles for ITSc estimated using CFD simulations at 4° angle of attack. The UB/LB venting profiles were generated using upper bound/lower bound trajectory details and respective dispersions in C_p and C_d coefficients. Notably, the UB venting profile produces the highest positive differential pressure for ITSc, while the LB venting profile yields lower and slightly negative differential venting pressure values, particularly at subsonic Mach numbers. These profiles govern the structural design of the ITSc. From the Figure 3, it can be noticed that differential pressure (ΔP) of ITSc is higher (by 5%) for the vent scheme implemented on cutouts. This is due to relatively higher C_p on all the cutout port locations due to presence of strapons. Higher C_p leads to lower mass flow rate through the ports. For the case of venting on closure panel, vent ports on leeward side have much lower (yet positive) C_p at almost all studied Mach numbers and hence more mass flow rate outside of the compartment is observed. The other main difference is observed in the case of lower bound case, where aft-end closure panel vent scheme has realized more -ve differential pressure.

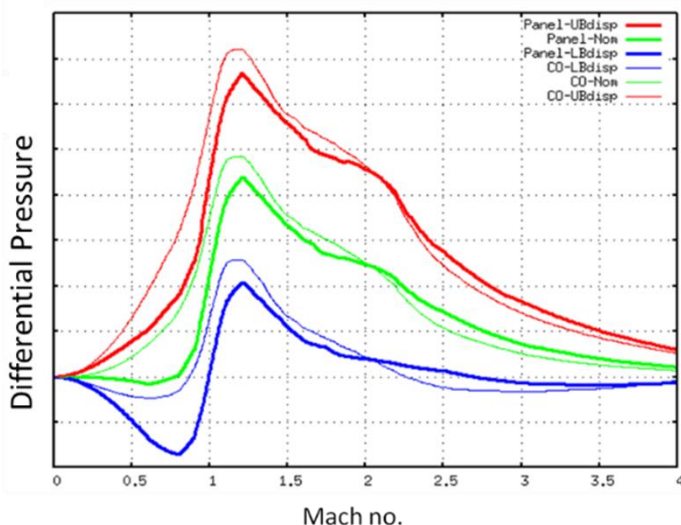


Figure 3: Comparison of ITSc cutout (CO) venting and closure panel venting performances

3. CONCLUSIONS

The venting behaviour of the ITSc compartment of the upper stage of the launch vehicle was investigated using in-house developed software, with a focus on the implementation of vent ports/valves to ensure a safe and efficient venting system for the closed structure. Based on several studies, two vent schemes have been finalised. These two vent scheme configurations are venting through cutouts and venting at aft-end closure panels, with varying vent areas. It was found that venting at the aft-end closure panel is relatively more efficient compared to venting through cutouts. Although both schemes were well within the structural design limits of the ITSc.

4. REFERENCES

- [1] Tech report, November 1970, "NASA Space vehicle Design criteria (Structures) Compartment venting", NASA SP-6060.
- [2] Proceedings, November 08-09, 2013, Dehradun, India," Venting system design and analysis for a typical launch vehicle compartment", National Convention of Aerospace Engineers (27th NCAE)
- [3] Proceedings, August 23-24, 2013, Thiruvananthapuram, "Experimental determination of Discharge Coefficient (C_d) of vent port", National conference on wind tunnel testing (NCWT-03)

Vibration-Based Energy Harvesting Using Mass-in-Mass Metamaterial with Piezoelectric Coupling

Subrata Barman^{1*}, P. Pandey², H. Haddad Khodaparast², T. Mukhopadhyay³, H. Madinei², M. I. Friswell², S. Dey¹

Department of Mechanical Engineering, National Institute of Technology Silchar, India

¹ Department of Mechanical Engineering, Swansea University, United Kingdom

² Department of Aeronautics and Astronautics, University of Southampton, United Kingdom

1. Introduction

Vibration-based energy harvesters (VEHs) have emerged as a promising technology to convert ambient mechanical vibrations into usable electrical energy for low-power applications such as wireless sensor networks (WSNs) and microelectromechanical systems (MEMS) [1]. Among the different VEH mechanisms—electromagnetic, electrostatic, and piezoelectric—piezoelectric energy harvesters (PEHs) are particularly attractive due to their high-power density, compactness, and ease of integration [2]. They exploit the direct piezoelectric effect, where strain-induced deformation generates electrical charge across the material. The integration of metamaterial concepts into PEHs has opened avenues for improved vibration absorption and broadband energy conversion [3]. Specifically, mass-in-mass metamaterial configurations, consisting of vertical beams with tip masses interconnected through springs, can induce local resonances and effectively capture vibrational energy across multiple frequencies [4]. By attaching piezoelectric (PZT) patches at the beam roots, the induced strain energy from these local resonances can be converted into electrical energy. This study investigates the dynamic behavior and energy harvesting potential of such a metamaterial-based PEH system. The objective is to develop and validate a numerical and experimental model that captures the coupled electromechanical response of the multi-degree-of-freedom (MDOF) mass-in-mass metamaterial system. The focus lies on evaluating the voltage and power outputs under different resistive loads, identifying optimal parameters, and assessing the feasibility of the design for structural vibration energy harvesting applications.

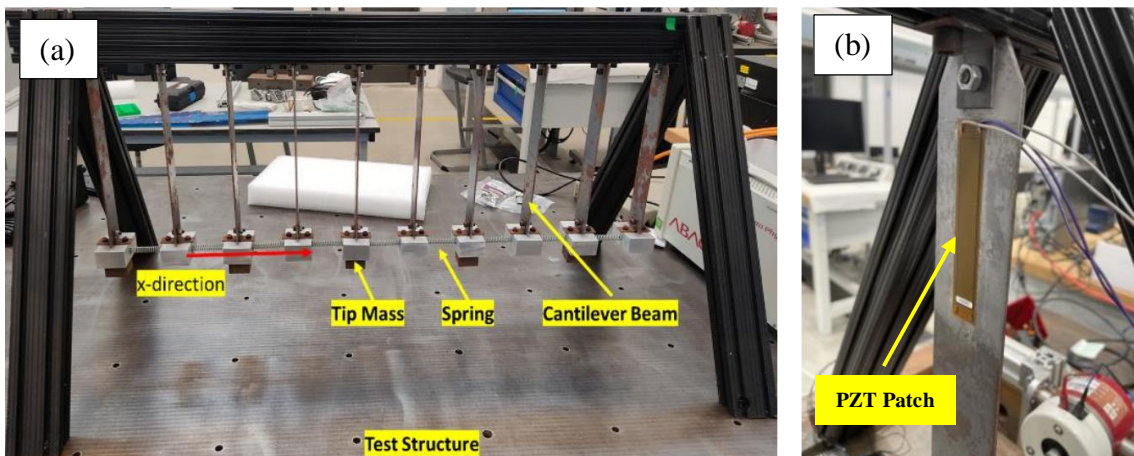


Fig 1. (a) Mass-in-mass metamaterial arrangement, (b) PZT patch adheded to the beam root

2. Methodology

The metamaterial-inspired energy harvester consists of multiple vertical beams with alternating tip masses coupled through linear springs, forming a mass-in-mass chain structure as presented in Fig. 1. Each beam acts as a cantilever, with PZT patches bonded near its root to harvest strain-induced energy. The governing dynamics of the system are derived using Newton's second law and Euler–Bernoulli beam theory, leading to the coupled electromechanical equations of motion. For the i^{th} beam-mass subsystem, the mechanical and electrical coupling is described as:

- Communicating Author: Subrata Barman, subrata21_rs@mech.nits.ac.in

$$m_i \ddot{x}_i - c_i \dot{x}_{(i-1)} + (c_{i-1} + c_i) \dot{x}_i - c_{i+1} \dot{x}_{i+1} - k_i x_{i-1} + (k_{i-1} + k_i + k_{eq_i}) x_i - k_{i+1} x_{i+1} - \theta_i v_i = 0 \quad (1)$$

$$C_p \dot{V}_i + \frac{1}{R_{L_i}} V_i + \frac{\theta_i}{C_{p_i}} \dot{x}_i = 0 \quad (2)$$

where m_i , c_i and k_i denote mass, damping, and stiffness, respectively; θ_i is the electromechanical coupling coefficient; v_i is voltage; and R_L is the load resistance [5]. The system is expressed in state-space form and solved using MATLAB's Runge–Kutta (ODE45) algorithm. Frequency response functions (FRFs) are computed and experimentally validated using a shaker-based test setup with accelerometers and data acquisition modules.

3. Results and discussion

The experimental and numerical analyses reveal good agreement in identifying natural frequencies and mode shapes of the metamaterial PEH system. The first mode, which corresponds to the primary beam with attached PZT patches, exhibits dominant energy conversion characteristics. The model demonstrates very close prediction of the resonance behavior, with the first natural frequency occurring near 8.7 Hz experimentally and 10.7 Hz numerically. The power output is strongly dependent on the load resistance, reaching an optimal value of approximately 60.36 μW at 140 $\text{k}\Omega$, while an experimental output of 8.56 μW is recorded at 10 $\text{k}\Omega$. The frequency response indicates multiple resonance peaks corresponding to higher modes, confirming broadband harvesting potential inherent to the mass-in-mass metamaterial configuration. Results confirm that the resonance condition significantly enhances voltage generation, validating the role of dynamic coupling between masses and local resonators in amplifying strain energy at the PZT interfaces. The model thus serves as a reliable predictive tool for design optimization, enabling future exploration of system miniaturization and multi-mode energy capture.

4. Conclusion

A vibration-based metamaterial energy harvester comprising vertical beams, tip masses, and PZT patches has been successfully modeled and experimentally validated. The structure demonstrates strong electromechanical coupling and effective energy conversion at resonance, achieving up to 60 μW output. The mass-in-mass configuration provides broadband response potential, making it suitable for low-frequency ambient vibration environments. Future work will focus on optimizing stiffness and mass distribution, incorporating multiple PZT layers, and miniaturizing the system for aerospace and structural health monitoring applications.

References

1. Iqbal, M., Nauman, M.M., Khan, F.U., Abas, P.E., Cheok, Q., Iqbal, A. and Aissa, B., 2021. Vibration-based piezoelectric, electromagnetic, and hybrid energy harvesters for microsystems applications: a contributed review. *International journal of energy research*, 45(1), pp.65-102.
2. Wang, G., Song, R., Luo, L., Yu, P., Yang, X. and Zhang, L., 2024. Multi-piezoelectric energy harvesters array based on wind-induced vibration: Design, simulation, and experimental evaluation. *Energy*, 300, p.131509.
3. Fayyaz, Bashmal, S., Nazir, A., Khan, S. and Alofi, A., 2025. Damping optimization and energy absorption of mechanical metamaterials for enhanced vibration control applications: a critical review. *Polymers*, 17(2), p.237.
4. Chaurha, A., Malaji, P.V. and Mukhopadhyay, T., 2022. Dual functionality of vibration attenuation and energy harvesting: effect of gradation on non-linear multi-resonator metastructures. *The European Physical Journal Special Topics*, 231(8), pp.1403-1413.
5. P Pandey, S Barman, H Haddad Khodaparast, T Mukhopadhyay, H Madinei, S Dey, H Madinei & MI Friswell, Optimizing Mass in Mass Metamaterials for Enhanced Energy Harvesting: via Analytical and Machine Learning Approach. *International Conference on Noise and Vibration Engineering, ISMA2024*, 9-11 September 2024, Leuven, Belgium, 2279-2293.

- Communicating Author: Subrata Barman, subrata21_rs@mech.nits.ac.in

Wake Modifications arising from a Bio-inspired Flexible Filament placed on NACA0012 Airfoil

Thangavel Sudeep^a and Sachin Yashavant Shinde^{b*}

^a M. Tech. Student; ^b Associate Professor

^{a,b} Department of Mechanical Engineering, Indian Institute of Technology Kanpur, Kanpur, U.P., 208016, India

1. INTRODUCTION & OBJECTIVE

Flow separation and vortex shedding behind lifting surfaces are key contributors to unsteady aerodynamic forces and form drag. Controlling these wake structures is crucial for improving aerodynamic efficiency, especially in low-to-moderate Reynolds number flows where separation occurs readily at higher angles of attack (α). In nature, several bird species manipulate or exploit vortical structures to minimize energy expenditure during locomotion. For instance, flexible surface features such as the covert feathers of birds adaptively deform to suppress large-scale vortex formation and stabilize flow separation regions (e.g., Gong et al. [1]). Motivated by such bio-inspired flow–structure interactions, we investigate the use of a thin, flexible filament attached to the suction surface of a symmetric airfoil as a passive flow-control element. In the case of a symmetric airfoil at higher angles of attack (usually, $\alpha > 15^\circ$), the flow separation from the suction surface produces a strong leading-edge vortex (LEV), which rolls up and sustains a periodic Bénard–von Kármán (BvK) vortex street in the wake. The presence of the filament, however, introduces a small but significant obstruction to the backflow that is responsible for the LEV formation. This interference limits the growth of the LEV and thus, its shedding. From an aerodynamic standpoint, weakening of the vortex street corresponds to a reduction in the wake momentum deficit, implying a drag-reduction effect (Zarketa-Astigarraga et al. [2]). Such trends have been numerically demonstrated by Agriss et al. [3] for the NACA0012 airfoil equipped with small separation-control devices, where modification of the shear layer roll-up has been shown to improve the lift-to-drag ratio. The objective of the present study is therefore to experimentally demonstrate this wake-modification phenomenon using flow visualizations in a quasi-two-dimensional soap-film tunnel and to provide physical insight into the fluid–structure interaction between a separated shear layer and a compliant filament, which can be thought of as a biomimetic analogue of a covert wing.

2. METHODS OF ANALYSIS

The experimental setup consists of a gravity-driven inclined soap film tunnel developed in-house. The flow is generated by directing a soap solution through a nozzle onto two closely spaced nylon wires. When stretched, these wires form the desired soap film. The flow rate of the soap solution is regulated using a rotameter. To investigate the effect of a covert feather in a two-dimensional environment, we use a symmetric NACA0012 airfoil with a flexible filament attached at a specific location on its suction surface (we call it as ‘airfoil model’). Once a stable and uniform soap film is formed, the airfoil model mounted on a plane platform is pierced into the film. The flow field is visualized from the top using a Sony DSLR camera operating at 1000 frames per second. Illumination is provided by a 55W SOX lamp, positioned such that the monochromatic light is reflected off a planar white board before striking the soap film. Two sets of experiments were conducted under identical flow conditions. In the first case, the flow is visualized for a bare airfoil (i.e., without attaching any flexible filament). In the second case, a spandex 70D flexible filament, half a chord in length, is attached to the airfoil suction side at the mid-chord location.

3. RESULTS AND/OR HIGHLIGHTS OF IMPORTANT POINTS

The qualitative comparison of the flow visualizations revealed a noticeable alteration in the wake structure when the flexible filament is attached to the suction side of the airfoil surface. Figure 1 clearly shows the differences in the wake produced by attaching a flexible filament to the airfoil when it is kept at a 15° angle of attack. Without the filament attached, as expected, the wake behind the airfoil exhibited the distinct Bénard–von Kármán vortex street, characterized by the generation of counter-rotating vortex pairs and their periodic shedding (see Fig. 1(a)). Upon attaching the flexible filament, a clear reduction in the intensity and coherence of the wake vortices is observed, as shown in Fig. 1(b). The flexible filament, initially aligned along the airfoil surface, lifts up to a certain angle upon introduction into the flow, and then remains there with a slight fluttering motion about the new mean position it assumes.

The other major effects introduced by attaching the flexible filament include a reduction in the strength and size of the shed vortices, more diffused vortex cores, a slight increase in intervortex spacing, a delay in the roll-up of the shear layers in the near-wake, and a reduction in wake width (by ~20%), thus indicating a weakening of the wake structure and a lower shedding frequency. This wake modification can be attributed to the filament's passive interaction with the separated shear layer. The filament obstructs the reverse flow on the suction surface, thereby hindering the formation and growth of the LEV, and breaks it into small vortices. The resulting attenuation of the LEV circulation limits the downstream roll-up of vortices, producing a less energetic wake. Although the present study is primarily qualitative, using Particle Image Velocimetry (PIV), a quantitative flow characterization of the velocity deficit, circulation, and wake width is planned. Such analysis will help correlate the observed reduction in vortex strength with an effective drag reduction estimate and an improvement in the lift-to-drag ratio.

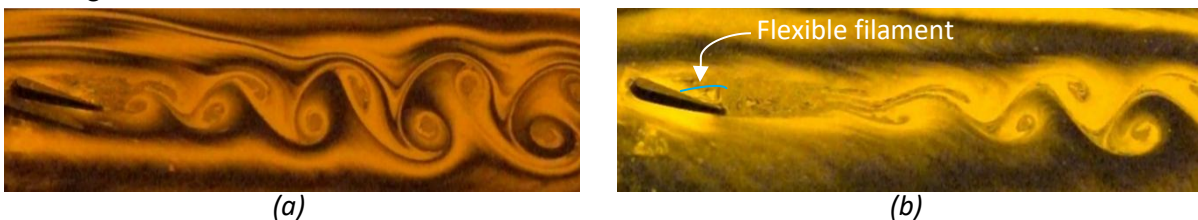


Fig. 1. Wake flow visualization for NACA0012 airfoil at $\alpha = 15^\circ$ in the soap-film tunnel: (a) without any filament; (b) with flexible spandex filament attached on the suction surface. The filament's presence visibly weakens the Bénard–von Kármán vortex street and reduces overall wake intensity.

In a recent study, Verma *et al.* [4] showed that a passive bionic flap stabilized flow separation and improved post-stall performance; similarly, the flexible spandex filament here acts as a compliant obstruction that limits vortex growth while adapting to local flow fluctuations.

4. CONCLUSIONS

This experimental investigation using a quasi-2D soap film flow demonstrates that attaching a thin, flexible filament to the suction surface of a NACA0012 airfoil passively modifies the wake dynamics. The filament's interaction with the separated shear layer suppresses leading-edge vortex formation and weakens the downstream Bénard–von Kármán vortex street. As a result, the wake becomes less coherent and energetic, implying a reduction in unsteady pressure forces and, hence, in pressure drag. Overall, the filament-induced modulation of the wake illustrates the broader principle of passive flow control, where small surface-mounted features (e.g., vortex generators) manipulate vorticity distribution to delay or weaken separation. The observed passive modulation of wake structure by a compliant filament suggests potential applications in the design of biomimetic airfoils and micro aerial vehicles (MAVs), where flexible surface features inspired by covert feathers could offer self-adaptive flow control. Future biomimetic designs could therefore integrate flexible appendages to achieve enhanced aerodynamic stability, as seen in Airbus's *AlbatrossONE* concept by Wilson *et al.* [5], where semi-aeroelastic hinged wingtips passively alleviate wing loads experienced due to gusts.

5. REFERENCES

- [1] Z. Gong, W. Liu, L. Zhang, and T. He, "Defining aerodynamic modes of large-scale birds' covert feathers," *Appl. Phys. Lett.*, vol. 127, no. 12, pp. 123 – 130, Sep. 2025, doi: 10.1063/5.0293353.
- [2] A. Zarketa-Astigarraga, A. Martin-Mayor, M. Martinez-Agirre, M. Peñalba-Retes, Assessing the statistical validity of momentum-deficit-based C_D measurements in turbulent configurations, *Measurement*, vol. 181, Aug. 2021, doi: 10.1016/j.measurement.2021.109592.
- [3] A. Agriss, M. Agouzoul, and A. Ettaouil, "Drag Reduction of a NACA Aerodynamic Airfoil: A numerical study," *J. Fluid Flow, Heat and Mass Transfer (JFFHMT)*, vol. 10, pp. 97 – 105, Oct. 2023, doi: 10.11159/jffhmt.2023.013.
- [4] A. Verma, V. Kulkarni, and S. Shinde, "Experimental investigations of self-adjusting bionic flaps on low-aspect-ratio wings," *J. Appl. Fluid Mech.*, vol. 18, no. 4, pp. 992 – 1006, Feb. 2025, doi: 10.47176/jafm.18.4.2922.
- [5] T. Wilson, J. Kirk, J. Hobday, A. Castrichini, "Small-scale flying demonstration of semi-aeroelastic hinged wing tips". *Proceedings of the International Forum on Aeroelasticity and Structural Dynamics (IFASD)*, pp. 1-19, Jun. 2019

* Communicating Author: Sachin Yashavant Shinde, email: sachin@iitk.ac.in

Wave Propagation Mechanisms for Enhanced Jet Impulse in Squid-Inspired Flexible Nozzles

Paras Singh^{a,b}, Daehyun Choi^b, Halley Wallace^b, Gourav Samal^b, Saad Bhamla^b, Chandan Bose^{a*}

^aAerospace Engineering, School of Metallurgy and Materials, University of Birmingham, United Kingdom

^bGeorgia Institution of Technology, Atlanta, Georgia, United States

*Email for correspondence: c.bose@bham.ac.uk

1. INTRODUCTION & OBJECTIVE

Cephalopods, such as squids and jellyfish, achieve high propulsive efficiency through pulsed jets expelled from their flexible, deformable funnels. The wave propagation along the flexible funnel influences the strength and convection speed of the jet vortex rings and the associated jet impulse. Pulsed jets, produced by the ejection of a finite volume of fluid with high momentum into a surrounding medium, are fundamental to propulsion and fluid transport in both natural and engineered systems. The pulsatile flows ejected from nozzles are dominated by the formation and evolution of vortex rings, which provide thrust through the combined effects of fluid momentum and pressure impulse at the nozzle or body exit [1]. The efficiency of such pulsed-jet propulsion has been linked to the ability of the compliant structure to interact dynamically with the surrounding fluid, a feature common in biological systems where flexibility and resonant deformation augment vortex formation and energy recovery [2]. In rigid nozzles, the generated impulse composed of jet momentum and nozzle exit pressure contribution (which can vary with jet vortex dynamics depends on the jet generator (e.g. piston and impeller) and the nozzle geometry. However, in flexible nozzle, the fluid–structure interaction with the jet significantly affect the generated impulse as well as the efficiency. Inspired by this biological mechanism, we design passive flexible nozzles for underwater propulsion and analyse their propulsive performance.

2. METHODS OF ANALYSIS

We use three-dimensional strongly coupled partitioned fluid-structure interaction simulations based on the Arbitrary Lagrangian-Eulerian framework. We investigate how nozzle flexibility and shape influence impulse generation, as well as nonlinear deformations governed by wave propagation and vortex ring formation. To optimize performance, we parameterize nozzle geometries using spline curves defined by control points and apply a multi-fidelity Bayesian optimization (BO) with spline control points and wall thickness as design variables. For the multi-fidelity BO, we do an initial design space exploration using our simulation framework and evaluate optimal solutions for subsequent nozzle generations using experimental load cell measurements.

3. RESULTS

Figure 1 illustrates the influence of nozzle flexibility on the deformation dynamics and the resulting jet flow characteristics. Panel (a) shows the instantaneous deformation of the nozzle and the associated flow structures identified by the iso-surface of the Q-criterion, coloured by the normalized streamwise velocity. Compared to the rigid nozzle ($Eh = \infty$), the flexible nozzle ($Eh = 75 \text{ N m}^{-1}$) exhibits significant shape deformation during the ejection phase, leading to enhanced jet acceleration near the exit; where E is the Young's modulus and h is the thickness of the nozzle. Panel (b) depicts the evolution of the near-field vorticity and velocity vectors for varying flexibilities. Increasing flexibility promotes stronger and more coherent vortex ring formation, accompanied by asymmetric roll-up and higher entrainment of the surrounding fluid. The temporal evolution of the primary vortex circulation, shown in panel (c), reveals a monotonic increase in circulation strength with increasing flexibility, indicating more efficient momentum transfer and thrust generation. Correspondingly, panel (d) shows that the axial displacement of the primary vortex core increases more rapidly for softer nozzles, suggesting that

structural compliance enhances vortex convection and jet impulse. Overall, these results demonstrate that nozzle flexibility can be strategically exploited to augment vortex strength and propulsion efficiency in bio-inspired jet systems.

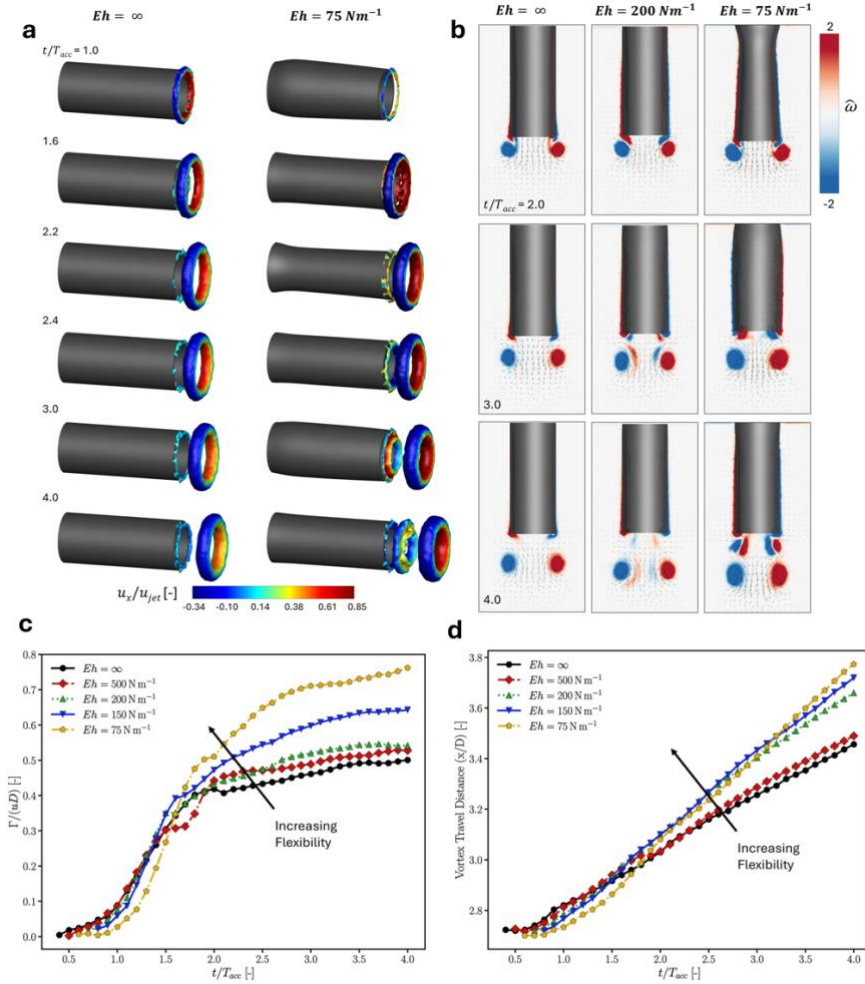


Figure 1 (a) Snapshots of 3D nozzle deformation and iso-surface of Q criteria = 200 for rigid and flexible nozzle ($Eh = 75 \text{ N/m}$) coloured by the normalized x-component of jet velocity. (b) Evolution of jet flow (vorticity and velocity vectors) for different nozzle flexibilities. (c) Temporal evolution of primary vortex circulation for different flexibilities. (d) Temporal evolution of primary vortex core displacement along nozzle axis for different flexibilities.

4. CONCLUSIONS

The resulting optimized nozzle exhibits enhanced impulse performance compared to both a baseline flexible cylindrical nozzle and rigid counterparts. We observe that the optimised jet impulse is strongly correlated with the tuned wave propagation speed through the nozzle. Interestingly, the optimised geometry also mirrors key morphological features observed in natural cephalopod funnels.

5. REFERENCES

1. Krueger, P. S., & Gharib, M. (2003). The significance of vortex ring formation to the impulse and thrust of a starting jet. *Physics of fluids*, 15(5), 1271-1281.
2. Dabiri, J. O. (2009). Optimal vortex formation as a unifying principle in biological propulsion. *Annual Review of Fluid Mechanics*, 41(1), 17-33.

Wind-Aware Dubins-Inspired L₁ Guidance for Faster Convergence with Bounded Continuous Curvature and Sliding Mode Tracking for UAVs

Pradyumn Mahajan^a, Sayantan Pal^b and Sikha Hota^{c*}

^aUndergraduate Student, Department of Aerospace Engineering, Indian Institute of Technology Kharagpur, India

^bResearch Scholar, Department of Aerospace Engineering, Indian Institute of Technology Kharagpur, India

^cAssociate Professor, Department of Aerospace Engineering, Indian Institute of Technology Kharagpur, India

1. INTRODUCTION & OBJECTIVE

Unmanned Aerial Vehicles (UAVs) are often required to operate autonomously in many applications, making path planning and control systems essential parts of the autonomous UAV system. These generated trajectories need to be not only time-efficient but also dynamically feasible and robust to disturbances such as wind, while respecting the physical capabilities of the vehicle. Dubins paths [1] provide the time-optimal solution to path following, subject to the minimum turn radius of the UAV in the absence of wind, but these paths are only C¹-continuous. L₁ guidance [2], on the other hand, provides a C²-continuous path for path following, but takes a long time to converge to the desired path.

This work proposes a novel Dubins-inspired modified L₁ guidance law that first follows the Dubins straight-line segment before converging to the main path using a wind-aware kinematic formulation [3]. The method retains the C²-continuity of L₁ guidance, respects the minimum turn radius of the UAV, and significantly reduces convergence time, bringing performance closer to the minimum-time solution. To validate dynamic feasibility, the generated trajectories are tracked using a Sliding Mode Controller (SMC) [4] on a 6-DOF quadrotor model.

2. METHODS OF ANALYSIS

The L₁ guidance law is a Virtual Target Point (VTP) based approach in which a lateral acceleration command is generated to guide the vehicle along circular arcs towards the desired path by following a VTP at a constant look-ahead distance L₁. In the proposed approach, the VTP is first moved along the straight-line segment of the Dubins path, which is the time-optimal path in the absence of wind, before transitioning to the desired path. The look-ahead distance L₁ is chosen to respect the minimum turning radius of the UAV. Since L₁ guidance inherently produces C²-continuous trajectories, the resulting path remains smooth, while also significantly reducing the convergence time, bringing it closer to the minimum time solution. Wind disturbances are explicitly incorporated into the UAV kinematic model by using the ground speed and course angle formulation. The generated trajectories are then supplied as reference inputs to a 6-DOF quadrotor model, where they are successfully tracked using a Sliding Mode Controller (SMC) to demonstrate the dynamic feasibility of the wind-aware guidance law.

3. RESULTS

The proposed guidance and control framework was tested for following straight-line and loiter paths by a quadrotor in altitude-hold mode. Figures 1(a) and 1(b) show the generated paths using the modified L₁ guidance logic, guided by the Dubins straight segment, along with the corresponding SMC-tracked paths with a quadrotor under different constant wind conditions. The results demonstrate that the

*Communicating Author: Sikha Hota (email: sikhahota@aero.iitkgp.ac.in)

proposed guidance law achieves significantly faster convergence as compared to the traditional L_1 guidance, while maintaining its C^2 -continuity and bounded curvature. This improvement arises from initially following the Dubins straight-line segment before transitioning to the main path, thereby avoiding the large detour taken by L_1 . The generated trajectories are robustly tracked by a 6-DOF quadrotor model using SMC, validating their dynamic feasibility. Further results, including comparison with standard L_1 guidance, curvature plots, cross-track error plots, and the evolution of course and heading angles, will be presented in the full paper.

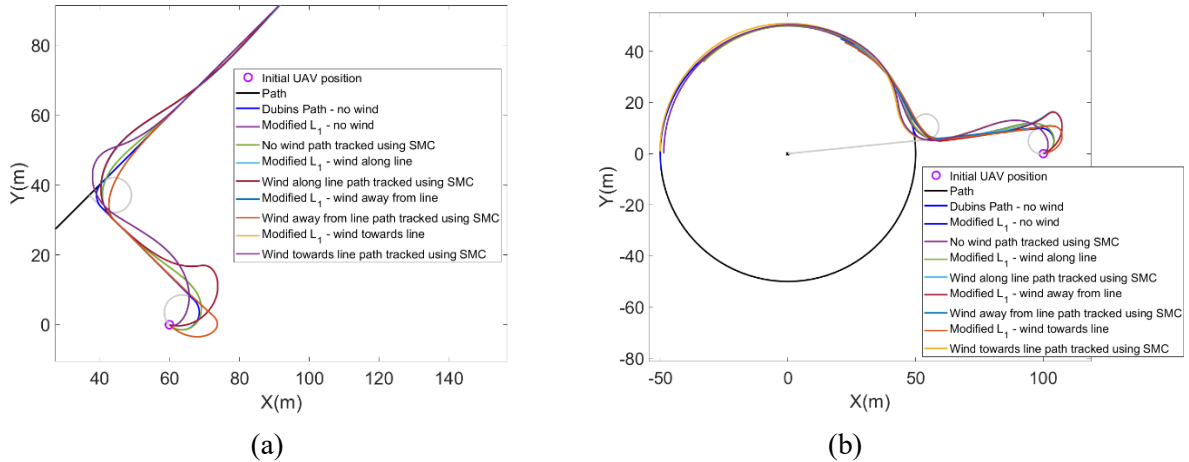


Fig 1: (a) Straight-line and (b) loiter path following with Modified L_1 Guidance under different wind conditions

4. CONCLUSIONS

This work presented a novel Dubins-inspired modified L_1 guidance law for UAV path following in the presence of wind. This approach retained the C^2 -continuous nature of the traditional L_1 guidance logic, respects the UAV's minimum turning radius, and achieves significantly faster convergence in comparison to L_1 guidance by first applying L_1 to follow the Dubins straight-line segment, defined without wind, before transitioning to the main path. The guidance law was made robust to wind disturbances by explicitly modelling the UAV kinematics using the course angle and ground speed formulation, which directly incorporates wind effects into the guidance law. These generated wind-aware trajectories were then finally tracked by a 6-DOF quadrotor model using a Sliding Mode Controller (SMC), hence validating the dynamic feasibility of the trajectories.

5. REFERENCES

- [1] L. E. Dubins, "On curves of minimal length with a constraint on average curvature, and with prescribed initial and terminal positions and tangents," Amer. J. Math., vol. 79, no. 3, pp. 497–516, 1957.
- [2] S. Park, J. Deyst, and J. How, "A new nonlinear guidance logic for trajectory tracking," in AIAA Guidance, Navigation, and Control Conference and Exhibit, 2004, p. 4900.
- [3] Y. Liang and Y. Jia, "Combined vector field approach for 2D and 3D arbitrary twice differentiable curved path following with constrained UAVs," J. Intell. Robot. Syst., vol. 83, no. 1, pp. 133–160, 2016.
- [4] M. Herrera, W. Chamorro, A. P. Gómez et al., "Sliding mode control: An approach to control a quadrotor," in 2015 Asia-Pacific Conference on Computer Aided System Engineering (APCASE), Quito, Ecuador: IEEE, 2015, pp. 314–319, doi: 10.1109/APCASE.2015.62.

*Communicating Author: Sikha Hota (email: sikhahota@aero.iitkgp.ac.in)

Simulation-Based Performance Analysis of Fiber-Reinforced Particle Polymer Composites Using R–Abaqus Multiscale Framework

Ajoy Kumar Bhowmick^{a*}, Salil Halder^b and Nipu Modak^c

^a PhD Scholar, Department of Mechanical Engineering, Jadavpur University, Kolkata, India

^b Professor, Department of Mechanical Engineering, IEST Shibpur, Howrah, India

^c Professor, Department of Mechanical Engineering, Jadavpur University, Kolkata, India

1. INTRODUCTION & OBJECTIVE

Fiber-reinforced particle polymer composites (FRPPCs) provide enhanced stiffness, strength, impact resistance, and cost-to-performance benefits due to hybrid reinforcement mechanisms [1]. However, their mechanical behavior exhibits uncertainties arising from fiber orientation, particle dispersion, and interfacial interactions at multiple scales.

To reduce experimental dependency and ensure reliable structural design, a simulation-driven multiscale modeling approach is essential.

This work introduces a reproducible and statistically validated R–Abaqus computational framework to evaluate the mechanical and thermal performance of FRPPCs. The objective is to integrate deterministic micromechanics, stochastic uncertainty quantification, and finite-element validation to establish a computationally efficient and prediction-reliable methodology for hybrid composite systems.

2. METHODS OF ANALYSIS

A deterministic micromechanics module was developed in R programming, implementing classical homogenization models including Rule of Mixtures, Halpin–Tsai [2], Mori–Tanaka, and Self-Consistent schemes to predict ply-level elastic constants. To account for microstructural variability, a Monte Carlo simulation (10,000 iterations) was performed to quantify the influence of uncertainty in fiber and particle volume fractions on elastic properties [3].

Laminate-level stiffness matrices [A, B, D] were computed using Classical Laminate Theory (CLT), facilitating upscale of micromechanical predictions to structural scale. Automated R–Abaqus parametric coupling enabled finite element (FE) validation with equivalent constitutive inputs. FE simulations were carried out under tensile, flexural, vibrational, and thermal loading to verify predicted structural responses.

The overall multiscale methodology is depicted in Fig. 1, demonstrating the sequential workflow from microscale homogenization to laminate modeling and FE-based multiphysics evaluation.

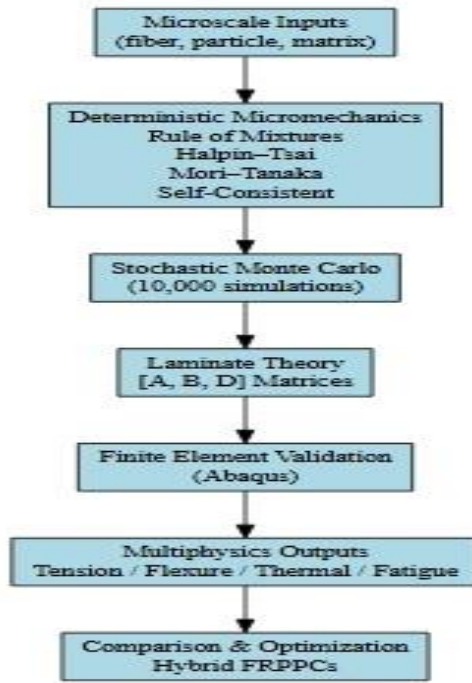


Fig. 1. Representation of the proposed R–Abaqus multiscale modelling framework.

3. RESULTS AND DISCUSSION

Deterministic predictions showed <6% deviation from benchmark literature data, confirming the accuracy of parameter implementation. Monte Carlo analysis revealed coefficients of variation (COV) of 2–5% for stiffness values, consistent with experimentally observed scatter. Laminate stacking reduced variability by ~60%, demonstrating statistical stabilization at structural scale. Abaqus simulations confirmed <6% deviation in elastic and dynamic responses, validating cross-platform fidelity. Hybrid reinforcement showed 11% improvement in shear modulus and 18% reduction in variability compared to pure fiber composites.

4. CONCLUSIONS

A reproducible and statistically valid R–Abaqus multiscale framework was developed for performance evaluation of FRPPCs. The integration of deterministic micromechanics and stochastic uncertainty analysis with FE validation ensures predictive accuracy and confidence. The approach reduces experimental reliance and supports lightweight structural design for aerospace and automotive sectors.

5. REFERENCES

- [1] B. D. Agarwal, L. J. Broutman, and K. Chandrashekara, *Analysis and Performance of Fiber Composites*, 4th ed. Hoboken, NJ, USA: Wiley, 2018.
- [2] J. C. Halpin and J. L. Kardos, “The Halpin–Tsai equations: A review,” *Polymer Engineering & Science*, vol. 16, no. 5, pp. 344–352, 1976, doi: 10.1002/pen.760160512.
- [3] B. Liu, J. Liang, J. Ou, and C. Zhang, “Uncertainty quantification in fiber-reinforced composites using Monte Carlo simulation,” *Composite Structures*, vol. 152, pp. 865–875, 2016, doi: 10.1016/j.compstruct.2016.05.084.

*Communicating Author: First Author, Ajoy Kumar Bhowmick, abhowmick.mech.rs@jadavpur university.in

Index

- A. Abhijith, 141
A.K.L. Srivastava, 31, 32
Aayush Gupta, 67
Abdennour C. Seibi 121
Abdul Sadiq 67
Abhinav Kumar KSN 77
Abhishek Kumar, 46
Abinesh K , 1
Achchhe Lal, 51,101, 102, 201
Adeetya Uppal 36, 71
Aishwarya Kasarla, 127
Ajit Kumar 129, 130
Ajoy Kumar Bhowmick, 223, 224
Akshay Abhyankar, 59
Aman Shukla, 149
Amit Agrawal, 98
Amit Dhar, 165
Amit K Onkar, 115, 209
Amit Sachdeva, 34
Amlan Kumar Bairagi, 105
Anand M Raikar, 109, 193
Animesh Das, 165
Aniruddha Sinha, 91, 155, 156
Ankitha Kamatha, 21
Ankur Nagpal , 34
Ansh Kapoor, 5, 40, 41
Antony J. K. 141, 147
Anubhab Das, 34, 35
Anup Ghosh, 21
Anup Kumar Pathak, 11
Anuttar Jain, 119
Arash Hajisarifi, 131
Arghya Deb, 179
Aritro Ghosha, 91
Arnab Roy, 185
Arun B. S. 147
Arun K, 115, 209
Arun Kumar A, 115, 209
Arun Kumar Perumal 189
Ashik Muhammad, 147
Ashoke De, 189, 207
Aswathy K. S,141
Atharv Mangalkar, 59, 60
Atul Sharma, 98
Avijit Chatterjee, 155, 156
Avinash Kumar Pandey, 15
B. N. Singh, 52, 64, 113, 114
B.Venkat Shivaram Jadav 57, 58
Babasaheb Kisan Varpe 101
Bandaru Bangarraju 87, 88
Bhrigu Nath Singh 201, 203
Bibhas Chand 151
Bibhu Prasad Mahapatra 89
Busi Swathi Priya 93
Chandan Bose 149, 177, 219
Chandra Sekhar Yerramallib 38
D S Kushan 161
Dabeer Anwer Danish 25, 26
Daehyun Choi 219
Danial Arias 121

- Darshit Gajera 213
 Debajyoti Kumar 149
 Debashish Khan 53
 Debayan Das 157
 Deeksha Yadav 189
 Deore N 29
 Devshree Kumar 173
 Dheeraj 211
 Dhruv Bagora 139
 Digpriya 145
 Dileep K N 191
 Dipak Kumar Maiti 67, 73, 169, 175
 G S P J Ronith 135
 G Vidya 34, 43, 57, 192
 Gajavada Sanjeev Kumar 99, 100
 Gianluigi Rozza 131, 132
 Gourav Samal 219
 Gururaj Khurd 103, 104
 H. Haddad Khodaparast 215
 H. Madinei 215
 Halley Wallace 219
 Heavenly Dadal 171
 Hemant V Nair 117
 Hibah Saddal 177
 Iqbal Ahmed 85, 86
 Ishan Phanse 7
 Jagat Rath 129
 Jammu Saratha 167
 Jathaveda.M 57
 Jayant Prakash Varun 99
 Jayram Desai 183
 Jaysinh Jagdishchandra Patel.163
 Jiju R. Justus, 42
 Kabir Bakhshaei 131, 132
 Kevin S. Swamy 13
 Khandare A 29
 Korak Sarkar 167
 Krishnendu Haldar 39, 84, 119, 144,188
 Kumar Anjneya 179
 Kumar N 29
 Kunal Garg 34
 Kushan D S 135
 Lakshita Patil 123
 Lucky Jayswal 177
 M Jathaveda 57, 191, 192
 M Ramji 9, 87, 88
 M S Harihara Sudhan 151
 M. I. Friswell 215
 M. Ramji, 9, 88
 M.N. Saradvani 3
 Machavolu Venkata Sushanth 137
 Mahendra Gattu 27, 28
 Mahesh K Sawardekar 181
 Malaikannan G, 61, 62
 Malapeta Hemasundara Rao, 9, 10
 Manoj Kumar M 141,147
 Manoj T Nair 65
 Manokaran K, 42
 Manoranjan Sinha, 36 133, 153
 Mayank Kumar 135, 161
 Mohamed Aniffa S, 19
 Mohammad A. S. Masoum 121
 Mohammed Rabius Sunny, 23
 Mohit Rajputa 205
 Mutturaj H Medar 115
 N. K. Peyada 159
 N.Chikkanna 109
 N.K. Peyad 17, 159
 Nalin Singh Sirohi 191
 Narayan Sharma 169
 Navdeep Pandey 5, 40, 175
 Nazim Khan ,1

- Nikita Pavle 153
 Nipu Modak 223
 Nithin Krishnan S 185, 186
 Nitin Pal 17
 Nivin Francis 44
 Omkar Bilawar 125
 P. Pandey 215
 Pabitra Majia 203
 Panasa Pranav Kumar 49
 Pankaj Meena 55
 Parag Deshpande 77
 Paras Singh 219
 Pardeep Duneri 139
 Parth Madure 103
 Parthasarathi Ghosh 185
 Patel J, 29, 164
 Patel Namra 129
 Patil A 29, 206
 Pawan Kumar 5, 40, 175
 Pawar Raju Sidhu 51
 Poonam Kumari 203
 Prabhash Kumar Yadav 31, 32
 Prabir Sikdar 151
 Pradeep K Sahoo 3
 Pradeep Moise 145
 Pradyumn Mahajan 221
 Prahlad V Deshpande 139
 Prasant Kumar Swain 5, 6
 Prashanta Kr Mahato 99
 Prasun Jana 89
 Prateek Chandrakar 169, 175, 176
 Praveen Shakya 85, 121
 Pritam Chakraborty 1, 2
 Pritam Mondal 99
 Priyakshi Goswami 69
 Prof. Krishnendu Halder 39, 84, 144, 188
 Prof. Manoranjan Sinha 36, 133, 153
 R. Sharma 55, 56
 R. U. Patil 81, 82, 205, 206
 R. Vijayakumar 193
 Rabius Sunny 23, 85
 Rahul B Choudhary 115, 209
 Rahul Halder 131, 132
 Rahul Kumar Saini 83
 Rahul Ranjan 71
 Rahul Sudam Kamble 51, 201
 Raja S 115, 209
 Rajat Mittal 15
 Rajdip Mukherji, 1
 Rajeev Nayan Gupta 73
 Rajesh Ranjan 145
 Rajib Mandi 159
 Rajneesh Bhardwaj 15, 197
 Rakesh Kumar Sahoo 36, 153
 Rakesh Sahoo 133
 Rakesha Chandra Dash 40, 75, 76
 Ram Kumar Yadav 155
 Ratan Joarder 46
 Ratnesh K Shukla 181
 Ravi Dodamani 77
 Ravi Prakash Prajapati 167, 168
 Revathy R K 189
 Ribhu Pal 185
 Ritesh Srivastava 107
 Rokkam Saketh 195
 S. Dey 215
 S. Maharana 193
 S.K. Maharana 109, 193
 S.M Kamal 205, 206
 Saad Bhamla 219
 Sachin Kumar 121
 Sachin S B 97

- Sachin Yashavant Shinde 217, 218
 Sai Phaneendra Karuchola 190, 207, 208
 Sai Sidhardh 10, 87, 88
 Saikat Ranjan Maity 73
 Salil Haldar 223
 Samanth Martis 187
 Sanjay R. 91
 Sanjay Satish 44, 141, 147
 Sanjoy Kumar Saha 65, 79, 213
 Satheeshkumar S.44
 Satvik Jaiswal 157
 Satya Prakash 155, 156
 Satyabrata Podder 165
 Sayantan Pal7, 49,103, 117, 217, 221
 Shantanu Dutta 165
 Shashank K Shankaregow 73, 74
 Shivaprasad M V 115, 217
 Shivendaraj Godbole 143
 Shreedhar Sahoo 135, 161
 Shrimukhi G Shastry 3
 Shrreya Rajneesh 133, 153
 Shubham Giri 197
 Sibaram Patro 38
 Sikha Hota 7, 8,117, 211, 217, 221, 222
 Smruti Ranjan Sahoo 113
 Somnath Bhowmick 1
 Somnath Ghosh 69, 70
 Somnath Roy 149
 Sonage S 29
 Sreenivasulu Juluri 79
 Subhabrata Koley 111, 112
 Subham Mukherjee 179
 Subhro Halder 157
 Subrata Barman 73, 199, 213, 215, 216
 Sudip Dey 73, 199, 216
 Sukanta Chakraborty 25
 Suman Chakraborty 61
 Sundeep Kumar Epuri 42
 Sunetra Sarkar 19
 Sunil Manohar Dash 151, 152
 Supen Kumar Sah 21
 Suplal Tudu 95
 Suraj J Warang 139
 Surendra Verma 113
 Sushma Santapuri 53
 T. Mukhopadhyay 215
 Tapan Sarkar 165
 Tatipaka Ananda 195
 Thangavel Sudeep 217
 Thivya Ranee 59
 Umakant Meher 121
 V Aditya Shankar 173
 V. Kartik 197
 Vaibhav Joshi 13, 14
 Vanshika Anand 5, 40
 Velmurugan Ramachandran 95
 Vidya G 42, 79
 Vijay Suresh 141,
 Vikranth Racherla 135, 161, 183
 Vinod Kumar Jat 81
 Viswasarathi NM 89
 Vivek Kumar Patel 107
 Yadwinder Singh Joshana 53



IIT Kharagpur PLATINUM JUBILEE

Publishing by:
Vidya Kutir Publications
Registered Office: 137, Asola Village, New Delhi -110074
Phone: 9910321772
Email: vidyakutirpublications@gmail.com